

AD

ARCCB-SP-96032

**PROCEEDINGS OF THE  
EIGHTH U.S. ARMY SYMPOSIUM  
ON GUN DYNAMICS**

**NEWPORT, RHODE ISLAND**

**14-16 MAY 1996**

19970117 199

**G. ALBERT PFLEGL, EDITOR**



**US ARMY ARMAMENT RESEARCH,  
DEVELOPMENT AND ENGINEERING CENTER  
CLOSE COMBAT ARMAMENTS CENTER  
BENÉT LABORATORIES  
WATERVLIET, N.Y. 12189-4050**



**APPROVED FOR PUBLIC RELEASE; DISTRIBUTION UNLIMITED**

#### DISCLAIMER

The findings in this report are not to be construed as an official Department of the Army position unless so designated by other authorized documents.

The use of trade name(s) and/or manufacturer(s) does not constitute an official indorsement or approval.

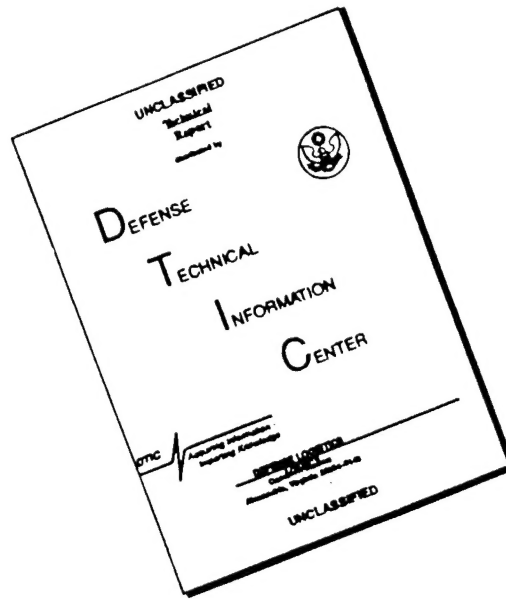
#### DESTRUCTION NOTICE

For classified documents, follow the procedures in DoD 5200.22-M, Industrial Security Manual, Section II-19 or DoD 5200.1-R, Information Security Program Regulation, Chapter IX.

For unclassified, limited documents, destroy by any method that will prevent disclosure of contents or reconstruction of the document.

For unclassified, unlimited documents, destroy when the report is no longer needed. Do not return it to the originator.

# DISCLAIMER NOTICE



THIS DOCUMENT IS BEST QUALITY AVAILABLE. THE COPY FURNISHED TO DTIC CONTAINED A SIGNIFICANT NUMBER OF PAGES WHICH DO NOT REPRODUCE LEGIBLY.

REPORT DOCUMENTATION PAGE			Form Approved OMB No. 0704-0188	
Public reporting burden for this collection of information is estimated to average 1 hour per response, including the time for reviewing instructions, searching existing data sources, gathering and maintaining the data needed, and completing and reviewing the collection of information. Send comments regarding this burden estimate or any other aspect of this collection of information, including suggestions for reducing this burden, to Washington Headquarters Services, Directorate for Information Operations and Reports, 1215 Jefferson Davis Highway, Suite 1204, Arlington, VA 22202-4302, and to the Office of Management and Budget, Paperwork Reduction Project (0704-0188), Washington, DC 20503.				
1. AGENCY USE ONLY (Leave blank)		2. REPORT DATE November 1996		3. REPORT TYPE AND DATES COVERED Final
4. TITLE AND SUBTITLE PROCEEDINGS OF THE EIGHTH U.S. ARMY SYMPOSIUM ON GUN DYNAMICS			5. FUNDING NUMBERS AMCMS No. 6226.24.H191.1	
6. AUTHOR(S) G. Albert Pflegl, Editor				
7. PERFORMING ORGANIZATION NAME(S) AND ADDRESS(ES) U.S. Army ARDEC Benet Laboratories, AMSTA-AR-CCB-O Watervliet, NY 12189-4050			8. PERFORMING ORGANIZATION REPORT NUMBER ARCCB-SP-96032	
9. SPONSORING/MONITORING AGENCY NAME(S) AND ADDRESS(ES) U.S. Army ARDEC Close Combat Armaments Center Picatinny Arsenal, NJ 07806-5000			10. SPONSORING/MONITORING AGENCY REPORT NUMBER	
11. SUPPLEMENTARY NOTES Presented at the Eighth U.S. Army Symposium on Gun Dynamics, Newport, RI, 14-16 May 1996. This symposium was sponsored by the U.S. Army Armament Research, Development, and Engineering Center and the U.S. Army Research Laboratory.				
12a. DISTRIBUTION/AVAILABILITY STATEMENT Approved for public release; distribution unlimited.			12b. DISTRIBUTION CODE	
13. ABSTRACT (Maximum 200 words)  This publication represents a compilation of the technical papers concerning modeling, analyses, design, measurements, and instrumentation of gun dynamics. The authors represent a cross section of the scientific and technical community, including universities, industrial, and government research laboratories.				
14. SUBJECT TERMS Ballistics, Barrel Vibration, Dynamics, Precision, Controls, Target Acquisition, Accuracy, Heating, Erosion			15. NUMBER OF PAGES 494	
			16. PRICE CODE	
17. SECURITY CLASSIFICATION OF REPORT UNCLASSIFIED	18. SECURITY CLASSIFICATION OF THIS PAGE UNCLASSIFIED	19. SECURITY CLASSIFICATION OF ABSTRACT UNCLASSIFIED	20. LIMITATION OF ABSTRACT  UL	

**CONTENTS**

**A CHRONOLOGY OF GUN DYNAMICS SYMPOSIA**

*ii*

**FOREWORD**

*iii*

**ATTENDEES**

*iv*

**ALPHABETICAL INDEX OF AUTHORS**

*ix*

**SESSION 1**

*Gun Accuracy*

1-1

**SESSION II**

*Thermal and Chemical Effects/  
Experimental Methods and Measurements*

6-1

**SESSION III**

*Metrology and Design*

13-1

**SESSION IV**

*Modeling, Simulation, and Finite Element Analysis*

17-1

**SESSION V**

*Kinetics, Vibrations and Wave Motion*

25-1

## **A CHRONOLOGY OF GUN DYNAMICS SYMPOSIA**

### **In-Bore Dynamics Symposium**

Naval Postgraduate School, Monterey, CA, 8-9 July 1976. Thomas N. Tschirn, Chairman.

### **First Conference of the Dynamics of Precision Gun Weapons**

Rock Island, IL, 26-27 January 1977. Proceedings: R-TR-77-008, E.J. Haug, Editor

### **Second U.S. Army Symposium on Gun Dynamics**

The Institute on Man & Science, Rensselaerville, NY, 19-22 September 1978.  
Thomas E. Simkins, General Chairman. Proceedings:ARLCB-SP-78013

### **Third U.S. Army Symposium on Gun Dynamics**

The Institute on Man & Science, Rensselaerville, NY, 11-14 May 1982. Thomas E. Simkins, General Chairman. Proceedings:ARLCB-SP-82005

### **Fourth U.S. Army Symposium on Gun Dynamics**

Riviera Beach, FL, 7-9 May 1985. Thomas E. Simkins, General Chairman.  
Proceedings:ARLCB-SP-85009

### **Fifth U.S. Army Symposium on Gun Dynamics**

The Institute on Man & Science, Rensselaerville, NY, 23-25 September 1987.  
Thomas E. Simkins, General Chairman. Proceedings:ARCCB-SP-87023

### **Sixth U.S. Army Symposium on Gun Dynamics**

Tamiment, PA, 15-17 May 1990. Thomas E. Simkins, General Chairman.  
Proceedings:ARCCB-SP-90015

### **Seventh U.S. Army Symposium on Gun Dynamics**

Newport, RI, 11-13 May 1993. Thomas E. Simkins, General Chairman.  
Proceedings:ARCCB-SP-93034

## FOREWORD

### **-The Eighth Symposium-**

Enclosed herein are the Proceedings of the Eighth U.S. Army Symposium on Gun Dynamics held at Newport, Rhode Island, 14-16 May 1996. These proceedings contain twenty-nine papers presented by authors from the military, academia, and industry. Papers from France, Germany, the U.K., and the U.S. are included. The topics include gun accuracy, projectile motion both inside and outside the barrel, vibrations, heating, bore erosion, testing, instrumentation, modeling & simulation, control theory and applications, and mathematical methods.

Past symposia have been sponsored by a single government laboratory or organization or as a collaborative effort of such units. This symposium was sponsored by Arrow Tech Associates, Inc. of South Burlington, Vermont with joint endorsement by the US Army Armaments Research, Development, and Engineering Center (ARDEC), the US Army Research Laboratory (ARL), and the US Army Research Office (ARO). By agreement the collection, selection, and publishing of the papers has been done by Benet Laboratories, U.S. Army ARDEC, Watervliet, NY.

The symposium announcement and resultant selection of papers reflects a continued effort to broaden the scope of topics yet still retain the connection to gun systems. Thought was given to changing the name to reflect this expansion but recognition has been developed over the twenty years of these meetings so the name 'U.S. Army Symposium on Gun Dynamics' still stands.

I wish to thank everyone who contributed to the success of this eighth symposium, whether by contribution of a paper, chairing a session, or just by attending. Special thanks to Dr. Tom Simkins, who worked so hard to champion these meetings while at Benet Laboratories and who has done so once again. This collection of the presented papers is a statement of the continued interest and effort of these people.

Bert Pflagl, Editor  
Eighth U.S. Army Symposium on Gun Dynamics

## ATTENDEE LIST

Allen, Craig  
OPM-TMAS  
SFAE-ASM-TMA-AS  
Picatinny Arsenal, NJ 07806-5000

Andrade, Charles A.  
Benet Laboratories  
Watervliet Arsenal, B40-2  
Watervliet, NY 12189-4050

Avinoam, Bartal  
Military Attache Office  
Israel Embassy  
Washington, D.C

Bidorini, Philippe  
Etablissement Technique De Bourges  
CE/DEA/ATT  
Carrefour De Zero-Nord  
Route De Guerrey  
Bourges Cedex, France

Bretl, Donald S.  
Federal Cartridge Company  
Ehlen Drive  
Anoka, MN 55303

Bundy, Dr. Mark  
US Army Research Lab  
AMSRL-WT-PB  
Aberdeen Proving Grounds, MD 21005-5066

Burns, Dr. Bruce P.  
US Army Research Laboratory  
AMSRL-WT-PD  
Aberdeen Proving Ground, MD 21005-5066

Burton, Lawrence R.  
US Army Research Laboratory  
AMSRL-WT-PD  
Aberdeen Proving Grounds, MD 21005-5066

Conroy, Paul J.  
US Army Research Lab  
AMSRL-WT-PA  
Aberdeen Proving Grounds, MD 21005-5066

Cording, Charles  
OPM-TMAS  
SFAE-ASM-TMA-AS  
Picatinny Arsenal, NJ 07806-5000

Corsello, John  
OPM-CRUSADER  
SFAE-FAS-CR-A  
Picatinny Arsenal, NJ 07806-5000

Couvin, Bertrand  
Direction Techniques  
13, route de la Miniere  
78022 Versailles Cedex, France

Cruzado, Manuel  
PM-CRUSADER  
Bldg. 3159  
Picatinny Arsenal, NJ 07806-5000

D'Andrea, Dr. Giuliano  
Benet Laboratories  
CCB-T  
Watervliet Arsenal  
Watervliet, NY 12189-4050

Dahdouh, Francois  
ARDEC  
CCAC-B65N  
Picatinny Arsenal, NJ 07806

Dillon, Dr. Robert E.  
Department of Mechanical Engineering  
Rose-Hulman Institute of Technology  
Wabash Ave.  
Terre Haute, Indiana 47803

Dowding, Robert J.  
US Army Research Laboratory  
AMSRL-MA-I  
Aberdeen Proving Ground, MD 21005-5069

Doyle, Paul J.  
US Army Missile Command  
AMSMI-RD-ST  
Redstone Arsenal, AL 35898

Eisler, Elwood  
Benet Laboratories  
AMSTA-AR-CCB-DE, Bldg. 40-2  
Watervliet, NY 12189-4050

Erline, Thomas F.  
US Army Research Lab  
AMSRL-WT-PD  
Aberdeen Proving Grounds, MD 21005-5066

Fischer, Leo  
United Defense, L.P.  
Armament Systems Division  
East River Road  
Minneapolis, MN 55421-1498

Gast, Dr. Ronald  
Benet Laboratories  
AMSTA-AR-CCB-DE  
Watervliet Arsenal  
Watervliet, NY 12189-4050

Groff, John N.  
General Dynamics Land Systems  
Mound Road, Dept., 9663  
Sterling Heights, MI 48310-3200

Groves, Alan  
Defense Research Agency  
Structural Materials Centre  
Fort Halstead  
Sevenoaks, Kent UK TN14 7BP

Grumann, H.  
Fraunhofer-Institut für Kurzeitdynamik  
Ernst-Mach-Institut  
Weil am Rhein  
Germany

Guyott, C.C.H.  
Frazer-Nash Consultancy  
Stonebridge House  
Dorking Business Park  
Dorking, Surrey RH4 1HJ, UK

Hathaway, Alan F.  
Arrow Tech Associates, Inc.  
Suite D-8, Pierson House  
Shelburne Road  
South Burlington, VT 05403

Held, Major Bruce  
Office of Project Manager  
Tank Main Armament Systems  
Picatinny Arsenal, NJ 07806

Kathe, Eric  
Benet Laboratories  
AMSTA-AR-CCB-TC  
Watervliet Arsenal  
Watervliet, NY 12189-4050

Kuhl, Frank P.  
US Army ARDEC  
AMSTA-AR-FSF-R  
Picatinny Arsenal, NJ 07806-5000

Lam, Dr. Vincent C.  
United Defense LP  
Armament Systems Division  
East River Road  
Minneapolis, Minnesota 55421

McMullen P.J.  
Concurrent Technologies  
Scalpe Ave.  
Johnstown, PA 15904

Miller, Craig S.  
Concurrent Technologies  
Scalpe Ave.  
Johnstown, PA 15904

O'Hara, Peter  
Benet Laboratories  
Bldg. 115  
Watervliet Arsenal  
Watervliet, NY 12189-4050

Perry, Joseph  
Israel Military Industries  
Tel Aviv 67070  
Israel

Pflegl, Bert  
Benet Laboratories, Bldg. 115  
Watervliet Arsenal  
Watervliet, NY 12189-4050

Purdy, Dr. David  
CAMSE, SEAS  
RMCS Shrivenham  
Swindon, SN68LA  
England

Rao, Dr. Vittal S.  
Intelligent Systems Center  
University of Missouri-Rolla  
Rolla, Missouri 65401

Ribe, Dr. Floyd S.  
OPM-CRUSADER  
SFAE-FAS-CR-A  
Bldg. 3159  
Picatinny Arsenal, NJ 07806-5000

Rivera, Dr. Mario P.  
Benet Laboratories  
AMSTA-AR-CCB-DE  
Bldg. 40-2  
Watervliet, NY 12189-4050

Scarton, Dr. Henry A.  
Dept. of Mechanical Engineering  
Rensselaer Polytechnic Institute  
JEC4008  
Troy, NY 12180

Schmidt, Edward M.  
US Army Research Laboratory  
AMSRL-WT-P  
Aberdeen Proving Grounds, MD

Seiler, Dr. Friedrich  
Institut Franco-Allemand de Recherches  
de Saint-Louis  
Boite postale 34  
F 68301 Saint Louis Cedex, France

Simkins, Tom  
Lance Ave.  
Troy, NY 12180

Sites, Joseph  
BRTRC, Inc.  
Willow Oaks Corp. Dr.  
Suite 800  
Fairfax, VA 22031

Soifer, Dr. Martin T.  
Lockheed Martin  
Plastics Ave., Room 2168  
Pittsfield, MA 01202

Storey, Steve  
Simatics, Limited  
Main Street  
Little Thetford  
Cambridgeshire  
CB6 3HA, UK

Tzeng, Jerome  
US Army Research Lab  
AMSRL-WT-PD  
Aberdeen Proving Grounds, MD 21005-5066

Vasilakis, Dr. John D.  
Benet Laboratories  
AMSTA-AR-CCB-TC, Building 115  
Watervliet Arsenal  
Watervliet, NY 12189-4050

Warkin, D.  
Fraunhofer-Institut für Kurzeitdynamik  
Ernst-Mach-Institut, Hauptstrasse 18  
Weil am Rhein  
Germany

Whyte, Robert  
Arrow Tech Associates, Inc.  
Shelburne Road  
Suite D-8 Pierson House  
South Burlington, VT 05403

Wilkerson, Dr. Stephen  
US Army Research Lab  
AMRSL-WT-PD  
Aberdeen Proving Grounds, MD 21005-5066

Zimmerman, LTC Eric  
Dept. of Civil and Mechanical Engineering  
Military Academy  
West Point, NY 10996

Zvi, Hadas  
Tank Program Authority  
Ministry of Defense  
Israel

## SESSION I - GUN ACCURACY

Chairman: Dr. Bruce Burns, Chief, Mechanics and Structures Branch,  
US Army Research Laboratory, Aberdeen Proving Ground, MD

THE EFFECTS OF VEHICLE AND BARREL MOTION  
ON THE ACCURACY OF A REPEAT FIRE SMALL CANNON ..... 1-1  
*David N. Bulman*

---

ACCURACY ENHANCEMENT OF THE 120MM XM291 TANK GUN ..... 2-1  
*Dr. Ronald Gast*

---

TECHNIQUES FOR MODELING BULLET EXIT STATE CONDITIONS  
PREDICTED BY TRANSIENT FINITE ELEMENT MODELS ..... 3-1  
*David Hopkins and Stephen Wilkerson*

---

EXPERIMENTAL INVESTIGATION OF THE INFLUENCE OF MUZZLE  
AND PROJECTILE TAIL SYMMETRIES ON THE FLIGHT AND HIT  
PERFORMANCE  
OF SPIN-STABILIZED PROJECTILES ..... 4-1  
*D. Warken*

---

COMPARISON OF COMPUTED AND MEASURED FLIGHT CHARACTERISTICS  
OF FIN STABILIZED PROJECTILES ..... 5-1  
*Dr. Robert E. Dillon*

---

**SESSION II - THERMAL, CHEMICAL AND TEMPERATURE EFFECTS/  
EXPERIMENTAL METHODS AND MEASUREMENTS**

Chairman: Dr. John Vasilakis, Chief, Physical Sciences Branch, Technology Division,  
US Army Benet Laboratories, Watervliet, NY

THERMALLY CONTROLLED BORE STRAIGHTNESS DURING FIRING ..... 6-1  
*Dr. Mark L. Bundy*

---

SURFACE CHEMISTRY EFFECTS ON EROSION IN HIGH PERFORMANCE  
TANK AMMUNITION ..... 7-1  
*Paul J. Conroy, Paul Weinacht and Michael J. Nusca*

---

BORE EROSION AND HEAT TRANSFER MEASUREMENTS IN  
20 AND 60MM CALIBER COMPARED WITH PREDICTION  
OF MODEL CALCULATIONS ..... 8-1  
*F. Seiler, K. Zimmerman, J. Raupp and G. Zettler*

---

COMPARISON OF EXPERIMENTAL AND PREDICTED RESULTS FOR  
THE BARREL HEATING OF AN 81 MM MORTAR SYSTEM ..... 9-1  
*C.C.H. Guyott*

---

COMPARISON OF NUMERICAL PREDICTIONS FOR GUN BARREL  
TEMPERATURES WITH EXPERIMENTAL TEST RESULTS ..... 10-1  
*C.S. Miller and K.C. Bearden*

---

AN ALIGNMENT BLOCK EXPERIMENT FOR THE M256 GUN SYSTEM ..... 11-1  
*Dr. Stephen Wilkerson, David Lyon*

---

TECHNIQUE FOR REDUCTION OF LAUNCH-INDUCED PERTURBATIONS ... 12-1  
*Edward M. Schmidt and William F. Donovan*

---

**SESSION III - METROLOGY and DESIGN**  
Chairman: Mr. Bert Pflegl, Modeling and Simulation Branch,  
US Army Benet Laboratories, Watervliet, NY

DEVELOPMENT OF RF COUPLERS FOR THE INTERIOR BALLISTICS  
MICROWAVE INTERFEROMETRY AND CONSTRUCTION OF A  
MICROWAVE INTERFEROMETER ..... 13-1  
*H. Grumann*

---

FIRST ORDER DYNAMIC TOOLS FOR RAPID ASSESSMENT OF  
SMALL CHANGES TO MAJOR GUN AND PROJECTILE  
DYNAMIC PARAMETERS ..... 14-1  
*Thomas F. Erline and Leo L. Fischer*

---

DESIGN TRADEOFFS FOR A VERY LIGHTWEIGHT 155MM HOWITZER  
FOR THE US ARMY LIGHT FORCES ..... 15-1  
*Lawrence R. Burton, Christopher P.R. Hopple,  
and Robert P. Kaste*

---

DESIGN SOFTWARE AND VERIFICATION STUDIES FOR  
FIBRE COMPOSITE OVERWRAPPED TANK BARREL ..... 16-1  
*A. Groves, A. Howard and M.J. Hinton*

---

## SESSION IV - MODELING, SIMULATION, AND FINITE ELEMENT ANALYSIS

Chairman: Dr. Thomas E. Simkins

---

### THERMO-CHEMICAL EROSION MODELING OF M242 GUN SYSTEMS ..... 17-1

*Samuel Sopok, Bert Pflegl, G. P. O'Hara,  
Stuart Dunn, and Douglas Coats*

---

### ELASTIC-PLASTIC COMPARISON OF THREE THREAD FORMS ..... 18-1

*G. Peter O'Hara*

---

### APPLICATION OF SUB-MODELS TO EXPLORE GEOMETRIC EFFECTS IN MEDIUM CALIBRE GUN BARRELS ..... 19-1

*P.J.McMullen*

---

### MODELLING OF A WEAPON CONTROL SYSTEM FOR A MAIN BATTLE TANK ..... 20-1

*Dr. David J. Purdy*

---

### GLOBAL MODELING FOR A MEDIUM CALIBRE TURRET SYSTEM ..... 21-1

*Sylvain Carlier, Bertrand Couvin and Josette Dias-Alves*

---

### SIMULATION OF PROJECTILE BALLOTING IN HYPERVELOCITY LAUNCHERS ..... 22-1

*Burdett K. Stearns and John R. Burnett*

---

### AIRCRAFT TRAJECTORY PREDICTION USING A RADIUS OF CURVATURE MODEL ..... 23-1

*Luis C. Cattani, Paul J. Eagle, and Frank P. Kuhl*

---

### NEURAL NETWORK BASED SMART STRUCTURAL CONTROL SYSTEMS .... 24-1

*Rajendra Damle and Dr. Vittal S. Rao*

---

## SESSION V - KINETICS, VIBRATIONS AND WAVE MOTION

Chairman: Alan F. Hathaway, Arrow Tech Associates, Inc.,  
South Burlington, VT, USA

GAS DYNAMICS OF BORE EVACUATOR EJECTORS .....	25-1
<i>C.A. Andrade and D.G. Messitt</i>	
<hr/>	
MODAL ANALYSIS OF MORTAR BASE PLATES .....	26-1
<i>Dr. Mario P. Rivera, Elwood Eisler, and Carlos Gutierrez</i>	
<hr/>	
DYNAMIC RESPONSE OF OVERWRAPPED COMPOSITE GUN TUBES SUBJECTED TO A MOVING PRESSURE .....	27-1
<i>Jerome Tzeng, David Hopkins, and Rodney Hubbard</i>	
<hr/>	
DESIGN OF PASSIVE VIBRATION ABSORBER TO REDUCE TERRAIN INDUCED GUN BARREL VIBRATION IN THE FREQUENCY DOMAIN .....	28-1
<i>Eric Kathe</i>	
<hr/>	
BEATING THE CRITICAL VELOCITY PROBLEM .....	29-1
<i>Dr. Thomas E. Simkins</i>	
<hr/>	

## ALPHABETICAL INDEX OF AUTHORS

Andrade, C. ....	25-1	Pflegl, B. ....	17-1
Bearden, K. ....	10-1	Purdy, D. ....	20-1
Bulman, D. ....	1-1	O'Hara, G. ....	17-1, 18-1
Burton, L. ....	15-1	Rao, V. ....	24-1
Bundy, M. ....	6-1	Raupp, J. ....	8-1
Burnett, J. ....	22-1	Rivera, M. ....	26-1
Carlier, S. ....	21-1	Scarton, H. ....	...
Cattani, L. ....	23-1	Schmidt, E. ....	12-1
Coats, D. ....	17-1	Seiler, F. ....	8-1
Conroy, P. ....	7-1	Simkins, T. ....	29-1
Couvin, B. ....	21-1	Sopok, S. ....	17-1
Damle, R. ....	24-1	Stearns, B. ....	22-1
Dias-Alves, J. ....	21-1	Tzeng, J. ....	27-1
Dillon, R. ....	5-1	Warker, D. ....	4-1
Donovan, W. ....	12-1	Weinacht, P. ....	7-1
Dunn, S. ....	17-1	Wilkerson, S. ....	3-1, 11-1
Eagle, P. ....	23-1	Zettler, G. ....	8-1
Eisler, E. ....	26-1	Zimmerman, K. ....	8-1
Erline, T. ....	14-1		
Fischer, L. ....	14-1		
Gast, R. ....	2-1		
Groves, A. ....	16-1		
Grumann, H. ....	13-1		
Gutierrez, C. ....	26-1		
Guyott, C. ....	9-1		
Hinton, M. ....	16-1		
Hopkins, D. ....	3-1, 27-1		
Hopple, C. ....	15-1		
Howard, A. ....	16-1		
Hubbard, R. ....	27-1		
Kaste, R. ....	15-1		
Kathe, E. ....	28-1		
Kuhl, F. ....	23-1		
Liang, P. ....	...		
Lyon, D. ....	11-1		
McMullen, P. ....	19-1		
Messitt, D. ....	25-1		
Miller, C. ....	10-1		
Nusca, G. ....	7-1		

**SESSION I**  
**GUN ACCURACY**

## THE EFFECT OF VEHICLE AND BARREL MOTION ON THE ACCURACY OF A REPEAT FIRE SMALL CANNON

David N Bulman  
Professor of Dynamics  
School of Engineering and Applied Science  
Royal Military College of Science  
Shrivenham,  
Swindon, SN6 8LA.  
UK

### ABSTRACT:

The modelling of barrel and shot motion during firing is now an accepted part of gun design procedure. Most simulations include some form of barrel mounting which range from simple linear spring bearings, to complex flexible cradles which include non-linear sliding bearings and clearance. These models are usually perfectly acceptable with single shot simulations. They will even give useable results with repeat fire cases where the mounting of the 'cradle' is unlikely to move during the firing sequence. However, larger guns are being mounted on lighter vehicles, and also there is an increasing requirement for small cannons with high accuracy during a repeat fire sequence. In these cases it is becoming increasingly evident that the motion of the vehicle is a significant factor in the accuracy of such weapons.

The paper describes the introduction of a vehicle model into an existing gun dynamics simulation package. The full simulation included the flexible barrel, a rigid spinning shot or a flexible non-spinning shot, a flexible cradle with three bearings all with clearance, the elevation mechanism, and a four wheeled vehicle. The suspension, wheels and tyre characteristics were included.

The simulation was able to show how, during a repeat fire case, the motion of the vehicle had a significant effect on the accuracy of the weapon. Certain parameters, particularly the damping characteristics of the system, were shown to be important. It was also demonstrated how a modification to the firing rate could improve the consistency of the system.

### BIOGRAPHY:

David N Bulman is Professor of Dynamics in the School of Engineering and Applied Science at the Royal Military College of Science, UK. He has worked in the field of Gun Dynamics since 1976, and also Vehicle Dynamics since 1973. He has lectured extensively in these subjects, and been involved in large research contracts to produce and validate codes for Gun Dynamics Analysis. He is the principal author of the commercial code SIMBAD, which is in use in over 11 countries throughout the world. He has also produced codes for vehicle ride and motion analysis, including special codes for active suspension systems.

## THE EFFECT OF VEHICLE AND BARREL MOTION ON THE ACCURACY OF A REPEAT FIRE SMALL CANNON

DAVID N BULMAN  
SCHOOL OF ENGINEERING AND APPLIED SCIENCE  
ROYAL MILITARY COLLEGE OF SCIENCE  
SHRIVENHAM, SWINDON, UK. SN6 8LA.

### INTRODUCTION

The modelling of barrel and shot motion during firing is now an accepted part of gun design procedure [1-7]. Analysis has been carried out on guns with bore sizes ranging from 12.5mm to 155mm, and in some cases it is known that the models have been used on a bore size as small as 6mm. Most simulations include some form of barrel mounting which range from simple linear spring bearings, to complex flexible cradles which include non-linear sliding bearings and clearance [8,9,10,11].

These models are usually perfectly acceptable with single shot simulations. They will even give useable results with repeat fire cases where the mounting of the 'cradle' is unlikely to move significantly during the firing sequence. However, larger guns are being mounted on lighter vehicles, and also there is an increasing requirement for small cannons with high accuracy during a repeat fire sequence. In these cases it is becoming evident that the motion of the vehicle is a significant factor in the accuracy of such weapons.

Before the study of gun dynamics, it may have been considered acceptable to investigate the motion of the vehicle in isolation of the barrel flexing or the consequent motion of the shot in bore. In this case, the new angular position of the vehicle at each round would have been used to give an indication of the dispersion of the shots. Visual observation of some of the thinner more flexible barrels shows that this is an unrealistic way to proceed. Any modelling must include not only the motion of the vehicle, but also the complete dynamics of the barrel, its mounting and the shot.

The gun dynamics simulation program SIMBAD allows for sub-models to be built around the main gun dynamics model. It is even possible to use the program to build complete models independent of the gun dynamics simulation, and although this is unlikely, it allows for the testing of any sub-models in isolation. SIMBAD was therefore used to study the firing of a 40mm cannon mounted in a four wheeled vehicle.

The aim of the study was to predict the dispersion of a series shots fired in a burst sequence at different elevations, and determine how much of the dispersion was caused by vehicle motion.

It was also required to determine if the firing rate could be modified to reduce the dispersion. A secondary aim was to use the model to study the effect of ground inputs on barrel motion, so that firing on the move could be simulated. The model was therefore prepared with this aim, but firing on the move is not discussed in this paper.

## THE GUN MODEL

The gun model used standard SIMBAD file input [12]. The barrel was 2.8m. long, with a 40mm bore. It was supported in a flexible cradle at three bearing points. The rear bearing point on the barrel (the point through which the resulting bearing force acts) moved as the gun recoiled. The centre and front bearing points were fixed on the barrel, but moved in the cradle. The front bearing point was well forward along the barrel, 2m from the breech face. There was clearance in each bearing.

The cradle was relatively rigid, but by using the flexible cradle model, it enabled the trunnion and elevation gear forces to be positioned correctly in the vehicle. Also by setting the trunnion as either fixed or free, it made it relatively easy to exclude or include the vehicle model.

The buffer characteristics were simulated using measured data, and entered in a function data file. The recuperator was a large coiled spring, and the spring constant was used directly.

The shot was a rigid spinning shot, although a non-spinning flexible sabot shot was used in later investigations [13,14].

## THE VEHICLE MODEL

The gun was supported on a four wheeled vehicle which was initially modelled in a 2D plane as shown in Figure 1. It represents the vehicle in pitch and bounce. A full 3D model has been produced which also allows for roll, and therefore can simulate the gun firing over the side of the vehicle, but this paper concentrates on the results from the 2D model.

It will be noted that the vehicle is defined by its own set of axes,  $x$  and  $y$ , the origin of which is at the centre of gravity, and rotation is defined by  $\theta$  (the pitch of the vehicle). In this case positive  $x$  is forward from the centre of gravity, positive  $y$  is vertically upwards from the centre of gravity, and positive pitch is such that the front of the vehicle rises relative to the rear. The gun may be in elevation, hence the trunnion and elevation gear forces have been resolved into the  $x$  and  $y$  directions.

The suspension was considered to have linear spring stiffnesses and damping, with separate bump and rebound rates. Suspension travel was assumed to be relatively small so that bump stops were not included. Each wheel was represented as a lumped mass with a linear tyre stiffness. Later simulations did show that suspension movement was very small, and therefore the use of linear parameters was considered valid.

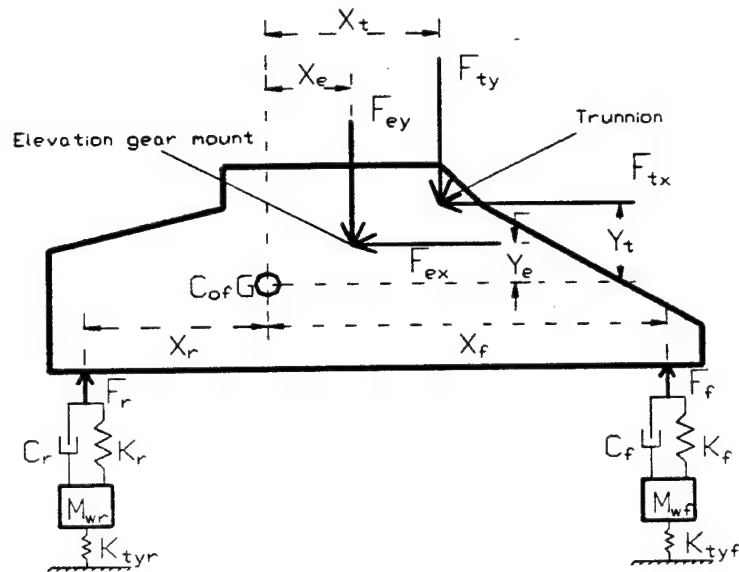


Figure 1. 2D representation of a four wheeled vehicle

We define the physical constants as:

$M_b$	the mass of the body
$I_b$	the moment of inertia of the body about the centre of gravity
$M_{wr}$	the mass of the rear wheel
$M_{wf}$	the mass of the front wheel
$K_r$	the rear suspension stiffness
$K_f$	the front suspension stiffness
$C_r$	the rear damping coefficient (different for bump and rebound)
$C_f$	the front damping coefficient (different for bump and rebound)
$K_{tyr}$	the rear tyre stiffness
$K_{tyf}$	the front tyre stiffness
$X_r$	the x coordinate of the rear wheel (Note, this will be negative)
$X_f$	the x coordinate of the front wheel
$X_t$	the x coordinate of the trunnion
$Y_t$	the y coordinate of the trunnion
$X_e$	the x coordinate of the elevation gear
$Y_e$	the y coordinate of the elevation gear

and the variables as:

$x_b$	the horizontal body displacement at the centre of gravity
$y_b$	the vertical body displacement at the centre of gravity
$\theta$	the angular deflection of the body (pitch)
$y_{wr}$	the rear wheel vertical displacement

$y_{wf}$	the front wheel vertical displacement
$F_{tx}$	the trunnion force in the x direction
$F_{ty}$	the trunnion force in the y direction
$F_{ex}$	the elevation gear force in the x direction
$F_{ey}$	the elevation gear force in the y direction
$F_r$	the spring and damper force from the rear wheel
$F_f$	the spring and damper force from the front wheel
$F_{tyr}$	the rear tyre force
$F_{tyf}$	the front tyre force

Note that it is assumed that the trunnion force and the elevation gear force are defined as positive when acting on the cradle. The reactions on the vehicle are therefore equal and opposite as shown in Figure 1. It is also assumed that rotations are small, and for this case the vehicle does not move in the x direction, hence although included in the calculations for the forces,  $x_b = 0$ .

The notation  $y_b'$  and  $y_b''$  will be used to indicate the first and second differential of  $y_b$  with respect to time, ie the vertical velocity and acceleration of the vehicle body. Similar notation will be used for other variables.

The equations for the body are now given by:

$$M_b \cdot y_b'' = F_r + F_f - F_{ty} - F_{ey} \quad (1)$$

$$I_b \cdot \theta'' = F_r \cdot X_r + F_r \cdot X_f - F_{ty} \cdot X_t + F_{tx} \cdot Y_t - F_{ey} \cdot X_e + F_{ex} \cdot Y_e \quad (2)$$

Note that  $X_r$  will be negative.

The forces are:

$$F_r = (y_{wr} - y_b - \theta \cdot X_r) \cdot K_r + (y_{wr}' - y_b' - \theta' \cdot X_r) \cdot C_r \quad (3)$$

$$F_f = (y_{wf} - y_b - \theta \cdot X_f) \cdot K_f + (y_{wf}' - y_b' - \theta' \cdot X_f) \cdot C_f \quad (4)$$

$$F_{ex} = (x_b - \theta \cdot Y_e - x_{eg}) \cdot K_{eg} \quad (5)$$

$$F_{ey} = (y_b + \theta \cdot X_e - y_{eg}) \cdot K_{eg} \quad (6)$$

$$F_{tx} = (x_b - \theta \cdot Y_t - x_{tru}) \cdot K_{tru} \quad (7)$$

$$F_{ty} = (y_b + \theta \cdot X_t - y_{tru}) \cdot K_{tru} \quad (8)$$

where  $x_{tru}$  is the displacement of the cradle trunnion node in the body x direction.  
 $y_{tru}$  is the displacement of the cradle trunnion node in the body y direction.  
 $x_{eg}$  is the displacement of the cradle elevation gear node in the body x direction.  
 $y_{eg}$  is the displacement of the cradle elevation gear node in the body y direction.  
 $K_{eg}$  is the elevation gear stiffness.  
 $K_{tru}$  is the stiffness of the trunnion relative to the body.

It may be noted that the calculation of  $F_{ex}$  and  $F_{ey}$  will depend on the design of the elevation gear. In the case under consideration, only the vertical force  $F_{ey}$  was used. Also, an elevation

gear stiffness is already defined in the standard routines of SIMBAD. This could not be used because of the internal calculation of the elevation gear force within the program. Therefore the elevation stiffness in the cradle file was set to zero, and another variable was introduced for the elevation gear stiffness as defined above.

The equations for the wheel are:

$$M_f \ddot{y}_{wr} = -F_r + F_{tyr} \quad (9)$$

$$M_f \ddot{y}_{wf} = -F_f + F_{tyf} \quad (10)$$

where:

$$F_{tyr} = -y_{wr} K_{tyr} \quad (11)$$

$$F_{tyf} = -y_{wf} K_{tyf} \quad (12)$$

Equations 1 to 12 can now be used to simulate the motion of the vehicle when the gun is fired.

## THE LINK BETWEEN THE GUN AND VEHICLE MODEL

The link between the gun and the vehicle is through the trunnion and elevation gear mountings as described in equations 5 to 8. The variables  $x_{tru}$ ,  $y_{tru}$ ,  $x_{eg}$ , and  $y_{eg}$  are all variables directly obtained from the standard gun dynamics simulation program. The following FORTRAN code was used to extract these trunnion and elevation gear mounting displacements in the vehicle x and y directions:

```

Trunnion_node_disp_x = Cdisps((Trunnion_node-1)*Flag3d+1)*
&                          COS(ElevationAngle) -
&                          Cdisps((Trunnion_node-1)*Flag3d+2)*
&                          SIN(ElevationAngle)

Trunnion_node_disp_y = Cdisps((Trunnion_node-1)*Flag3d+1)*
&                          SIN(ElevationAngle) +
&                          Cdisps((Trunnion_node-1)*Flag3d+2)*
&                          COS(ElevationAngle)

Elev_gear_node_disp_y = Cdisps((Elev_gear_node-1)*Flag3d+1)*
&                          SIN(ElevationAngle) +
&                          Cdisps((Elev_gear_node-1)*Flag3d+2)*
&                          COS(ElevationAngle)

Elev_gear_node_disp_x = Cdisps((Elev_gear_node-1)*Flag3d+1)*
&                          COS(ElevationAngle) -
&                          Cdisps((Elev_gear_node-1)*Flag3d+2)*
&                          SIN(ElevationAngle)

```

In this case: Trunnion\_node\_disp\_x is the variable  $x_{tru}$   
 Trunnion\_node\_disp\_y is the variable  $y_{tru}$   
 Elev\_gear\_node\_disp\_x is the variable  $x_{eg}$   
 Elev\_gear\_node\_disp\_y is the variable  $y_{eg}$

The ElevationAngle is a new variable giving the elevation angle of the gun. The other variables are standard variables as defined in SIMBAD.

Equations 1, 2, 9 and 10 were solved by using the inbuilt integration routines of the program, and the forces given by equations 3 to 8, plus 11 and 12 were calculated at each time step.

## SIMULATIONS MADE

The purpose of the simulations was to determine the dispersion of a series of shots fired in a burst sequence. It was also required to know the effect that vehicle motion had on dispersion. An initial set of simulations were therefore made without the vehicle motion to establish a set of base results. These simulations were made using bursts of five rounds, with the time between rounds varying from 0.2 to 0.5 seconds.

The vehicle was then included in the simulation and the runs repeated for various elevation angles. This gave a total of 150 shot simulations. These simulations were then repeated for various vehicle suspension parameters, various barrel bearing clearances, and modifications to certain parameters which had initially to be estimated, eg shot band stiffnesses [15].

## RESULTS

The quantity of results produced in this investigation was considerable, and therefore only those of particular significance are shown and discussed in this paper. In particular, the gun configuration with the lowest dispersion, when fired without the vehicle, was used to produce the figures below. This highlights the effect of the vehicle motion on the dispersion of a series of 5 rounds. The results shown are with an elevation angle of 5 degrees.

The vertical jump figures for a burst of five rounds, with and without the vehicle are shown in Table 1. The time between rounds for the simulation without the vehicle is 0.3 seconds, the results with the vehicle are for times of 0.2, 0.3, 0.4 and 0.5 seconds.

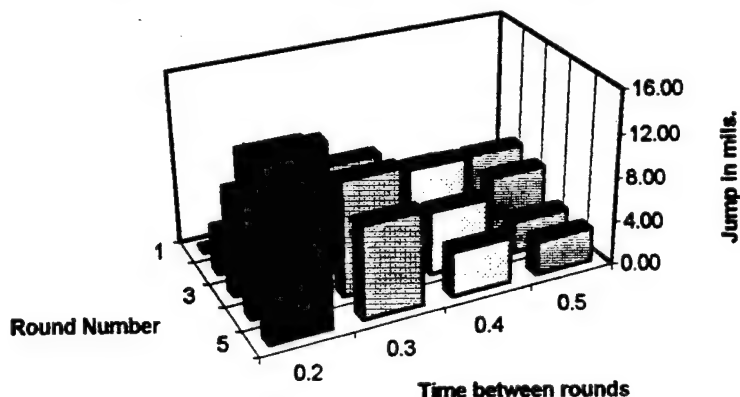
**Table 1. Vertical Shot Jump for various Shot Timings.**

	Time between Rounds	Vertical Jump values in mils.				
		Round1	Round 2	Round 3	Round 4	Round 5
No Vehicle	0.3	-0.071	0.041	-0.002	0.010	-0.001
With Vehicle	0.2	-0.03	3.85	9.28	14.30	16.40
	0.3	-0.03	4.94	9.83	10.40	8.36
	0.4	-0.03	5.81	7.84	5.74	4.08
	0.5	-0.03	5.78	5.34	2.95	3.05

The first point to note is how the inclusion of the vehicle increases dispersion considerably. The jump figures without the vehicle are considered to be small, and dispersion is also small,

the greatest difference between any of the five rounds being just over 0.1mils. When the vehicle is included, the first round still has a relatively small jump figure. In the case of 0.3 second timing, the second round jump has increased to nearly 5mils, and by the third and fourth is around 10mils. At this point the change in jump to the fifth round is reduced.

**Chart 1. Jump Values for Different Timings**



This pattern is different for each of the simulated timings and can clearly be seen in Chart 1. The reason for this change in pattern, with different timings, is because of the way in which each firing point matches a different phase in the pitching of the vehicle.

**Fig 2. Vehicle pitch & muzzle angle.**

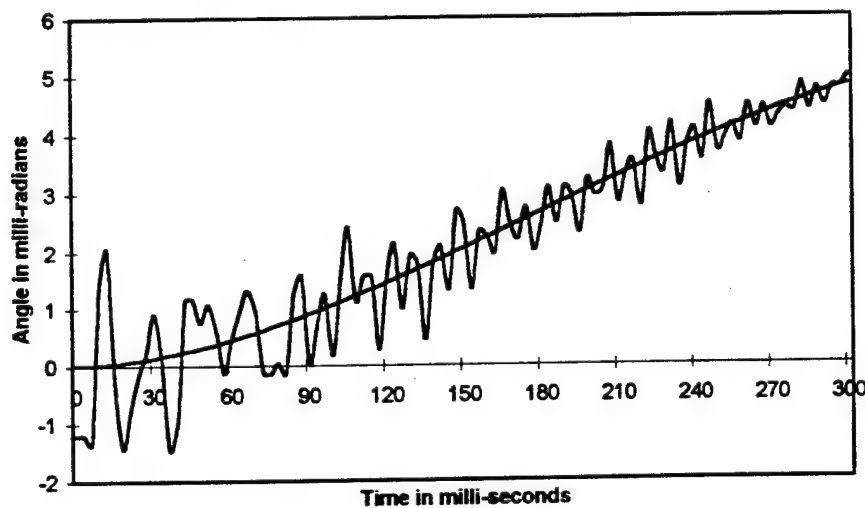
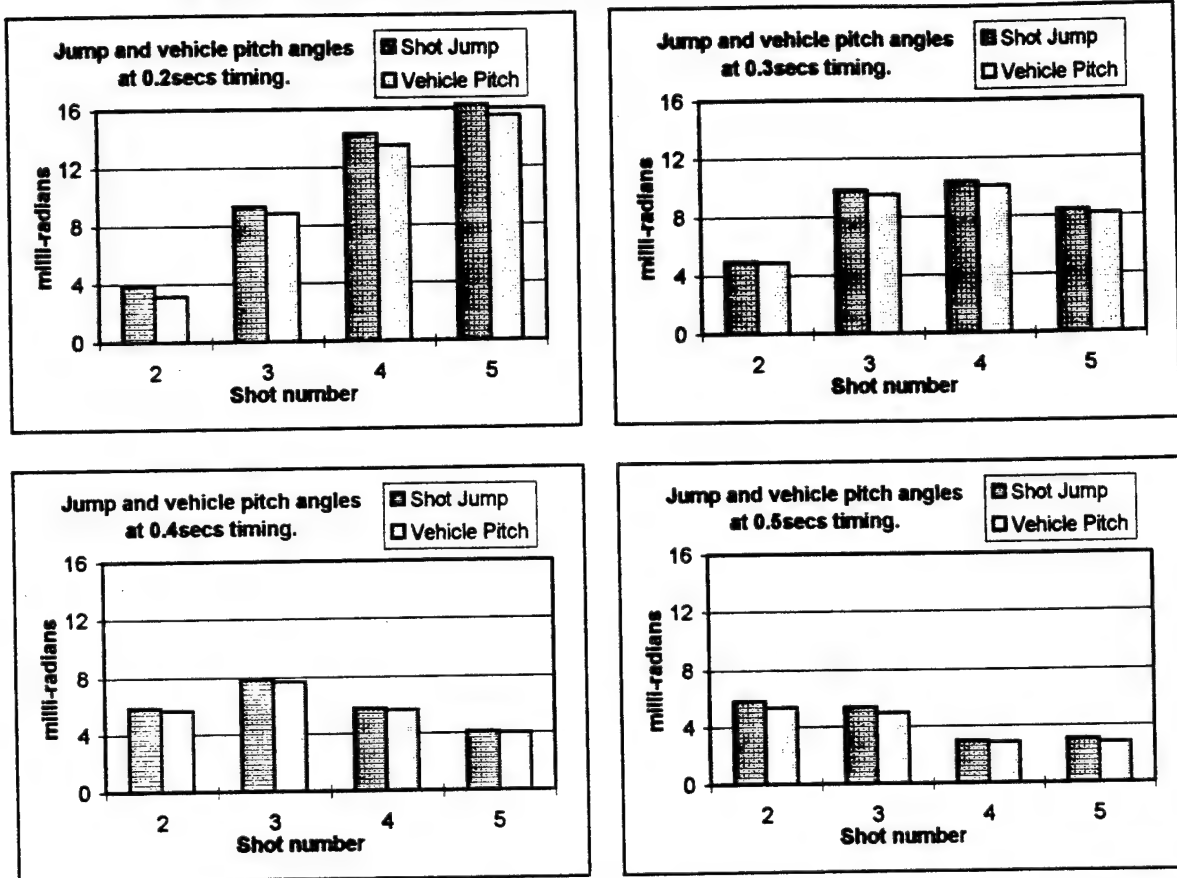


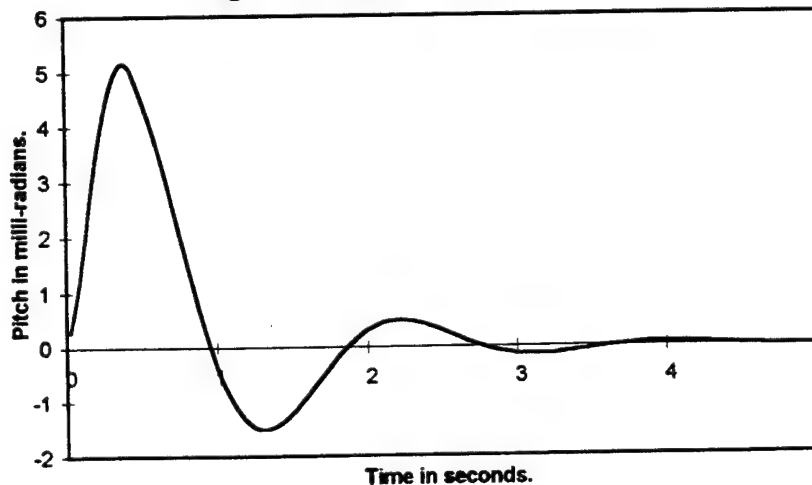
Figure 2 shows a plot of the muzzle angle from a time immediately after round 1 has left the barrel, to a the time when round 2 is about to be fired. Vehicle pitch is also shown on this graph. It is the smooth curve, and it can be seen how the overall muzzle angle is following the vehicle pitch. The barrel has a higher frequency of vibration, and this is seen superimposed upon the overall motion. Muzzle angle continues to follow vehicle pitch, and Chart 2 shows how the jump figures correlate with the vehicle pitch at shot exit.

Chart 2. Correlation between Shot Jump and Vehicle Pitch Angles.



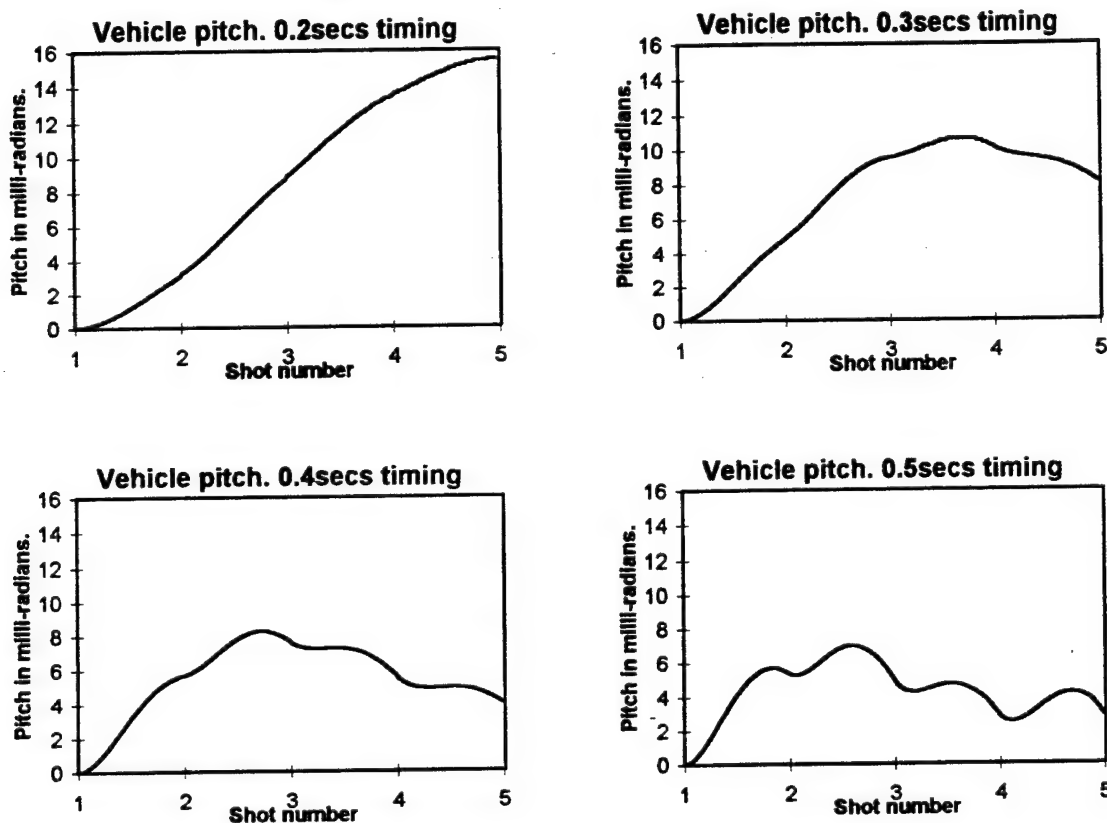
The pitch natural frequency of the vehicle is very low at approximately 0.6Hz. This can be seen in the plot of vehicle pitch for a single shot fired, Figure 3. From this, it might be expected that, if the time between rounds is 0.3 seconds, then when the fourth round was fired, the angle of the gun would be close to the starting angle, and a more cyclic variation of jump would occur than is shown in table 1.

Fig 3. Vehicle pitch after one round.



However, the plots in Figure 4 give an indication of what actually occurs. If the plot showing a timing of 0.3 seconds is examined first it can be seen that the first round starts the vehicle pitching, the second round gives a further impulse to continue pitching, then, just when the pitch starts to reduce, the third round is fired. This causes the pitch to increase still further, but again, just when the pitch starts to reduce, the fourth round is fired. This reduces the rate of decrease in pitch, before the fifth round is fired. It should be realised that if only a single shot had been fired, the pitch would have completed just over half a complete cycle over the same time and the peak value would also have been halved (see Figure 3). It might also be noted that this pitching of the vehicle is very small compared to what would be seen if it was travelling over normal terrain, and visually would hardly be noticed.

Fig 4. Vehicle pitch for various shot timings.



What is highly significant is the change in response of the vehicle with different shot timings. When the time between rounds is 0.2 seconds, the impulses from 5 rounds continue to increase the vehicle pitch, and a progressive increase in shot jump follows (Chart 2). When the time between rounds is 0.5 seconds, the impulses are occurring just after one quarter of a free pitching cycle. This keeps the pitch angle at a lower value overall, and shot jump for rounds 2 to 5 is more consistent.

## FURTHER DISCUSSION

The results above were chosen to show the effect that vehicle motion has upon dispersion of a repeat fire sequence of 5 rounds. The configuration of the gun was chosen to give the minimum dispersion when fired independently of the vehicle. This was with minimum bearing clearances. It may be noted that with maximum bearing clearances, the dispersion without the vehicle was over 1 mil. In this case, when the vehicle was included, the correlation between vehicle pitch and shot jump was not as good as shown in Chart 2. The contribution of the gun dynamics to dispersion could then be as much as 30%, indicating how essential it is to include the full gun dynamic simulation.

Other simulations have shown that when fired without the vehicle, the firing rate also had a large effect on the dispersion. This was particularly noticeable at higher rates of fire, and system damping was significant on the result. This has been shown experimentally, and under certain conditions particular rates of fire with large numbers of rounds gave very high dispersion. This occurred when the rate of fire corresponded with the natural frequencies of the barrel.

A further point is that the vehicle suspension parameters described above were optimised to give good high speed cross country performance. The pitch stiffness was therefore relatively low, with a natural frequency of about 0.6Hz. The level for this type of vehicle would normally be higher, and a simulation in this case showed that a firing interval of between 0.3 and 0.4 seconds gave the optimum value.

A possible method for reducing the effect of vehicle motion on dispersion is to have a lock-out suspension. In this case the vehicle can only move on its tyres. This increases the pitch natural frequency considerably, and further simulations did show that it does improve shot dispersion. The model of the tyres must include damping, usually in the form of relaxation damping.

Another area not discussed in this paper is the mounting position of the gun in the vehicle, the position of the trunnion on the cradle, and the elevation gear stiffness. Some simulations have been made which have shown that by careful choice of these parameters, it is possible to counteract some of the vehicle pitch motion with an equal and opposite motion of the gun about the trunnions. This was achieved by moving the trunnion above the barrel centre-line. The recoil forces then caused a downward pitching motion of the barrel about the trunnions.

## CONCLUSIONS

The work has shown that vehicle motion can have a considerable influence on shot dispersion of a repeat fire cannon. Firing rate is significant, and can be used to optimise the dispersion. This further depends upon the vehicle pitch natural frequency.

Other work has shown that careful selection of mounting parameters can help minimise the effect of vehicle pitch on the gun response. In particular, the positions of the trunnions on the vehicle and on the cradle relative to the barrel centre-line, are significant.

## REFERENCES

1. D. N. Bulman. Simulation of Gun Dynamics to Improve Accuracy and Consistency. 15th International Symposium on Ballistics, Jerusalem, Israel. 21 - 24 May, 1995
2. T. F. Erline, M. D. Kregel. Modelling Gun Dynamics with Dominant Loads. 5th. US Army Symposium on Gun Dynamics, Rensselaerville, NY. 23-25 September 1987.
3. M. T. Soifer, R. S. Becker. DYNACODE-G/P and its Application to the 120mm Tank Gun. 5th. US Army Symposium on Gun Dynamics, Rensselaerville, NY. 23-25 September 1987.
4. D. N. Bulman. A comparison of theoretical jump for rifled and non rifled barrels. 5th US Army Symposium on Gun Dynamics, Rensselaerville NY, 23-25 Sept 87.
5. S. E. Powell, P. G. H. Penny. The Theoretical Modelling of the Dynamics of Initially Non-straight Barrels using Finite Difference Techniques. 6th. US Army Symposium on Gun Dynamics, Rensselaerville, NY. 23-25 September 1987.
6. D. A. Hopkins. Modelling Gun Dynamics with Three-Dimensional Beam Elements. 6th US Symposium on Gun Dynamics, Tamiment, Pennsylvania, 14-17 May 1990.
7. D. A. Rabern, K. A. Bannister. Finite Elements Models to Predict the Structural Response of 120mm Sabot/Rods During Launch. 6th. US Army Symposium on Gun Dynamics, Tamiment, Pennsylvania, 15-17 May 1990.
8. D. N. Bulman. Theoretical and Experimental Observations on the Effect of Bearing Spacing, Pressure Time Curve, Bearing and Barrel Damping on Barrel Motion. Gun Dynamics Workshop, KTA6, RARDE, UK, 24-26 September 1984.
9. D. N. Bulman. The Effect of Bearing Clearance and Barrel Expansion on Barrel Response. 4th US Army Gun Dynamics Symposium, Florida, 7-9 May 1985.
10. D. N. Bulman, S. E. Powell. The Theoretical Modelling of the Effect of Cradle Flexibility on Gun Barrel Response during the Firing Phase. 11th International Symposium on Ballistics, Brussels, 9-11 May 1989.
11. D. N. Bulman, J. B. Hoyle. A Comparison of Theoretical and Experimental Results with Regard to the Effects of Gun Cradle Design on Barrel and Shot Motion. 6th US Symposium on Gun Dynamics, Tamiment, Pennsylvania, 14-17 May 1990.
12. SIMBAD User Manual (November 1995), Danby Engineering Ltd, High Gill House, Richmond, DL11 6NE, England, UK. Tel: +44 (0) 1748 886345.
13. D. N. Bulman. The In-bore Bending Dynamics of Long Rod Projectiles. 13th International Symposium on Ballistics, Stockholm, 1-3 June 1992.
14. D. N. Bulman, J. B. Hoyle. An experimental Validation of the SIMBAD Gun Dynamics simulation Package for Flexible Saboted Long Rod Projectiles. 7th US Symposium on Gun Dynamics, Newport, Rhode Island, 11-13 May 1993.
15. E. M. Patton. Projectile Foundation Moment Generation. 4th US Army Gun Dynamics Symposium, Florida, 7-9 May 1985.

**TITLE:** Accuracy Enhancement of the 120-mm XM291 Gun  
Ronald G. Gast, Michael Soja, Mary Soja,  
Donald Trudeau, Michael Gully, John Keating, Barbara Cunningham  
Benet Laboratories, Close Combat Armaments Center, Armament  
Research Development Engineering Center  
Watervliet Arsenal, Watervliet New York, 12189-4050

## **ABSTRACT**

The 120-mm XM291 tank gun was conceived in the mid-1980s. It contained all of the 'lightweight' features of developmental tank armament of the period, namely; long slender tube, boxlike mount structure, and an external recoil system. When fired from a fixed mount, its performance in terms of accuracy was as good as or better than contemporary fielded guns, however, when installed in the vehicle and fired on the move, it suffered high levels of vertical dispersion.

To determine the root cause of these elevated dispersion levels, a firing test was conducted using three versions of the gun. The design differences were the overall length of the gun tube, namely; standard length tube XM291 version (long tube), M256 length tube (short tube), and one between these two lengths (medium tube). All three were subjected to vehicle-mounted mobility firing at the Aberdeen Test Center (ATC). The test consisted of firing at targets while traveling at 10, 15, and 20 miles per hour (mph). The figure of merit is the target impact dispersion (TID) for each tube at each speed. The lower the value of the TID, the tighter the shot pattern. Testing indicated TID levels for the standard XM291 tube that were much greater than those of the short tube, as well as the current tank cannon which is the M256.

This report details Benet Laboratories effort to confront and resolve this accuracy problem within the constraints of the design, the most compelling of which is that the tube had to remain at its present length of 265 inches.

## **BIOGRAPHY:**

**PRESENT ASSIGNMENT:** Mechanical Engineer, Infantry & Special Projects Branch,  
Development Engineering Division, Benet Laboratories (1994 to present)

**PAST EXPERIENCE:** Mechanical Engineer, Tank Turret Branch (1971-1993) and Infantry  
Weapons Section, Development Engineering Division, Benet Laboratories (1968-1971)

**DEGREES HELD:** B.S.M.E. (1968), M.S.M.E. (1978) Ph.D. (1988) all at Rensselaer  
Polytechnic Institute.

Accuracy Enhancement of the 120-mm XM291 Gun  
Ronald G. Gast, Michael Soja, Mary Soja,  
Donald Trudeau, Michael Gully, John Keating, Barbara Cunningham  
Benet Laboratories, Close Combat Armaments Center, Armament  
Research Development Engineering Center  
Watervliet Arsenal, Watervliet New York, 12189-4050

## BACKGROUND

The 120-mm XM291 tank gun was conceived in the mid-1980s to replace the current M256 gun. It contains all of the 'lightweight' features applied to development tank armament of this period, namely; long slender tube, boxlike mount structure, and external recoil system. With respect to the current fielded tank gun (M256), the length of the XM291 is about five feet longer with thinner cross-sectional areas. For testing purposes, three versions of the XM291 cannon were built and tested, namely; standard length tube (long tube), M256 length tube (short tube), and one between these two lengths (medium tube).

All three were subjected to vehicle-mounted firing tests at Aberdeen Test Center (ATC) between December 1993 and April 1994. The tests consisted of firing at targets while traveling at various speeds. An indication of a dispersion problem was uncovered upon analysis of the firing data for the subject weapon. The figure of merit is the target impact dispersion (TID) for each tube at each speed. The short tube responded quite favorably, whereas the standard (long) tube had dispersion levels which were unacceptable as well as being greater than those of the short tube. The medium length tube fell between the two.

Additionally, in June 1994 at the request of Benet Labs, ATC conducted a vehicle mobility non-firing test, which consisted of traversing the vehicle over known terrain (i.e., 'bump' course) at various speeds with the stabilization system engaged and continuous monitoring of the muzzle reference system (CMRS) data. The results of these tests are summarized in Figure 1. The data points consist of root mean square (RMS) muzzle slope data calculated at specific time slices over the course of a test run. Two plots are shown in each graph, namely: the results for the long tube (closed boxes) and the short tube (open boxes). The top graph shows these results for a vehicle speed of 10 mph, whereas the remaining two are for 15 and 20 mph, respectively.

As indicated in the figure, the muzzle is much more active for the long tube than for the short tube. At 10 mph, the slope value for the short tube is about half that of the long tube for most of the test run. At 20 mph the results for the short tube are less than half those of the long tube, while at 30 mph the short tube shows less activity early in the run but approaches the long tube at the end of the test run. These results seem to indicate that it is more difficult for the stabilization system to control the standard length XM291 gun. Due to range and penetration requirements, the long tube is needed; however, from an accuracy standpoint the increased muzzle activity may mitigate target defeat. In summary, for the system to function as required, the XM291 cannon must be modified to reduce the tube's flexural motion.

This report details Benet Laboratories effort to confront and resolve the accuracy problem within the constraints imposed upon the solution. The most significant constraint is that the tube's length of 265 inches must be retained due to target defeat requirements.

### 120mm XM291 VIBRATION STUDY

COMPARISON of TEST DATA from JUNE 1994  
VEHICLE STABILITY TEST at APG  
CMRS MUZZLE SLOPE (RMS-VALUES) vs TIME

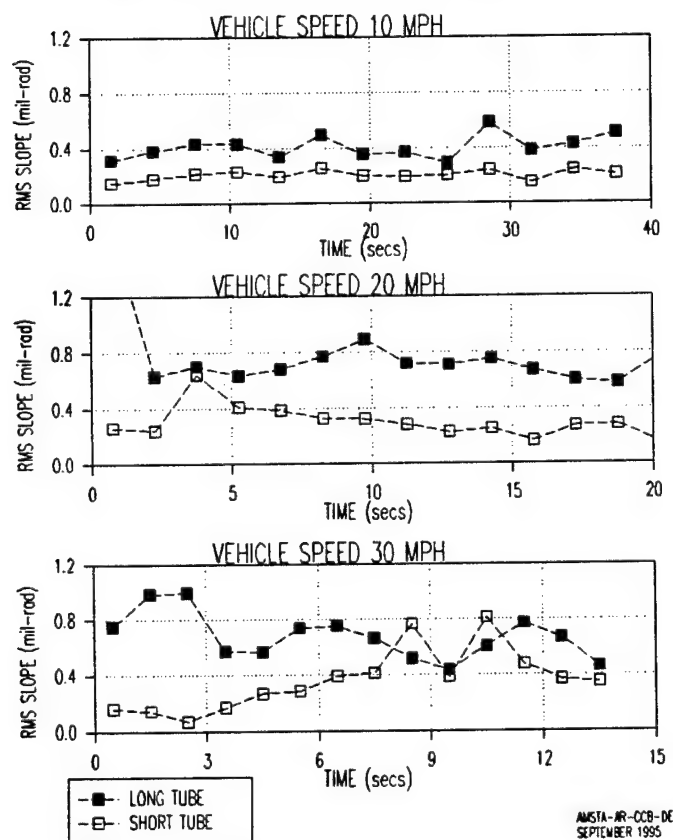


Figure 1. Muzzle Slope Test Data (RMS Values) vs Tube Length

## SOLUTION RATIONALE

The basic problem lies in the increased flexibility of the prototype XM291 cannon over the current production M256 cannon. The M256 is much stiffer due to its shorter length and greater wall ratio. In order for the XM291 system to be a viable replacement, system modifications that decrease cannon flexibility are needed. This may be accomplished through:

- Increasing wall ratio
- Decreasing tube length
- Decreasing the 'cantilevered' length of the tube

To minimize the manufacture and test of prototype candidates, an analytical method of rating the benefit of a potential modification will be conducted prior to a design decision. Benet's gun vibration model called the Uniform Segments Method (USM), which has been in use since the mid-1980s to rate tube dynamics for various ballistic and design contributions, is the analytical tool of choice [1]. It has the capability of 'driving' the gun system with ground-induced support motions (much like those that produced the muzzle slope results in the previous section). It would seem appropriate to claim that the relative 'quietness' of competing prototype systems, which are subjected to a series of analytical simulations, will respond similarly during field use. Basically, the response to actual field-generated signals will be proportional to the response of signals produced by simulations.

### Proposed System Modifications to Reduce Flexibility

Various methods were discussed in regard to reducing system flexibility. Preliminary calculations indicated that increasing the tube's wall ratio near the front support would have a negligible effect on kinematics at the muzzle. In fact, unless a Mann barrel (i.e., tube with large wall ratio used for ballistic evaluation) were used, any reasonable increase in tube stiffness through increasing wall thickness would have very little effect. Since decreasing tube length (a very effective way of decreasing flexibility) was not viable, the only alternative was to increase the length of the support structure, thus decreasing the overhanging portion of the tube. Preliminary analytical evaluations using the USM driven by single-frequency support displacements indicated a decrease in muzzle activity as support length increases. In general, the greater the length, the better the response. Unfortunately, increasing support length also increases weight and exacerbates an already muzzle heavy gun. Discretion had to be incorporated into length selection.

To accommodate the increased support length, the existing cradle structure had to be redesigned. An extension weighing 415 pounds and measuring approximately 22 inches was welded onto the existing cradle. This extension moved the center of gravity of

**XM291 CANNON EXTENDED SUPPORT MODIFICATION**

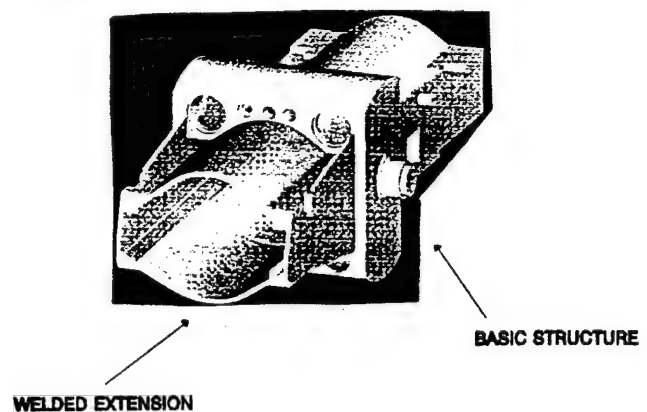


**Figure 2. Modified Cradle / Extended Support**

Figure 2. The extension located at the forward end was welded to an existing cradle.

The USM was used to rate the vibration attenuation provided by this modification. Two simulation tests were conducted on the standard and modified mount configurations. The first was a frequency response test using single-frequency transverse displacement signals at the support locations. The response for the short tube was included in these runs. The second test utilized mount acceleration data (vertical and pitch) from a vehicle mobility test collected by ATC in June 1994.

Figure 3 shows results of the first set of simulations. Frequency is depicted along the

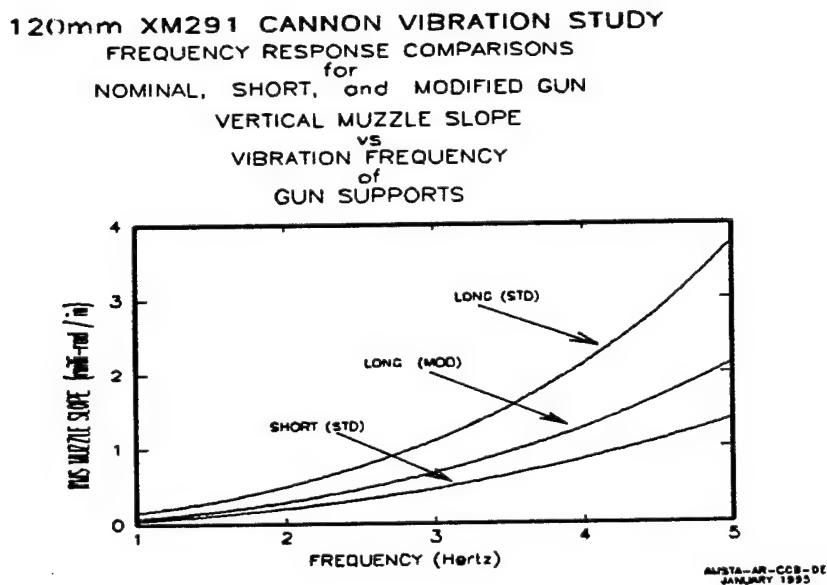


Figure 3. Predicted Muzzle Slope vs Tube Length

horizontal axis and RMS muzzle slope along the vertical axis. The input signals applied at each support are single-frequency sinusoidal displacements of 1-inch amplitude. As indicated, the short tube response is the 'quietest' of the three. Its RMS slope response monotonically increases to a maximum value of 1.40 mrad at a frequency of 5 Hertz (Hz). The other two show similar trends with much greater amplitude. For the gun employing the modified support, the slope response at 5 Hz is slightly above 2.0 mrad. For the standard support, the response of the gun at this frequency is about 3.75 mrad. The decrease in muzzle slope for the standard length gun employing a modified support is roughly 35 percent overall. This test indicates that the extended length support should favorably mitigate excessive muzzle motions when firing on the move.

Figure 4 shows results of the second set of simulations. Three graphs are depicted in this

figure. The upper graph is for a vehicle speed of 10 mph. The middle graph is for 20 mph, and the lower is for 30 mph. The horizontal scale is time in seconds, whereas the vertical scale is RMS muzzle slope in milliradians. The data points on each graph are the RMS slope values calculated for a finite time slice commensurate with the vehicle speed. For example, at a vehicle speed of 10 mph, the data in the graph correspond to the average RMS slope value for a 3-second slice through the transient data. (If the entire transient signal were shown, a comparison of results would be virtually impossible.)

Since muzzle slope values for the extended support design are less than those for the standard length support nearly 100 percent of the time, the gun employing the extended length support indicated improvement. The percentage of the benefit varied with time for a given simulation as well as for different speeds. At 10 mph the slope reductions realized by using the extended support were not as great as those for a vehicle speed of 30 mph. However, this test indicates much improvement for the extended support mount as well as for the single-frequency simulation tests. The results are more applicable to actual conditions in the field since they were developed using field measured data. In the sections to follow, the results of a laboratory test and USM simulations similar to the ones reported here will be addressed for the gun employing the extended support.

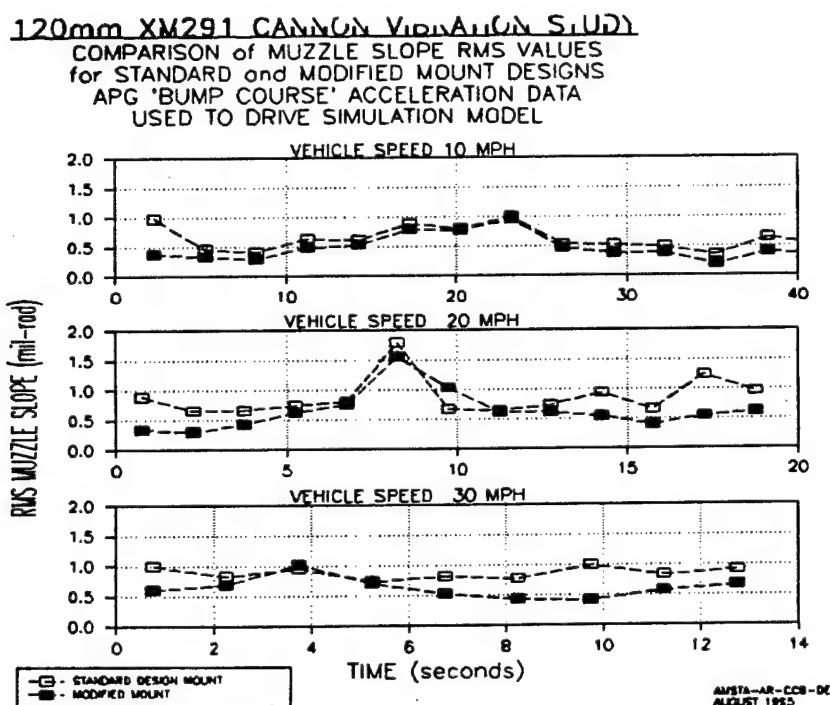


Figure 4. Predicted Slope Response in Field

## CONDUCTION OF CONTROLLED VIBRATION TEST

In order to assess the characteristics of the design modifications, a two-pronged method was utilized. Both an in-house dynamics vibration test and additional simulations would be conducted. Hopefully correlation between the two would exist and the muzzle motions would be reduced, as indicated in the preliminary analysis.

### Test Setup and Procedure

A schematic of the test setup is shown in Figure 5. Vertical accelerations were measured on the gun mount and tube as shown. The test consisted of sending programmed displacement signals to the simulator and recording accelerations. The two accelerometers on the mount provided information as to the displacement of the base, whereas the tube-mounted accelerometers measured accelerations near the muzzle. Various single and multi-frequency sinusoidal displacement signals were sent to the simulator via a computer linkup. Equation (1) shows the makeup of the signals and Table 2 shows the parameters.

## XM291 CANNON VIBRATION STUDY: TEST SETUP EXTENDED SUPPORT GUN

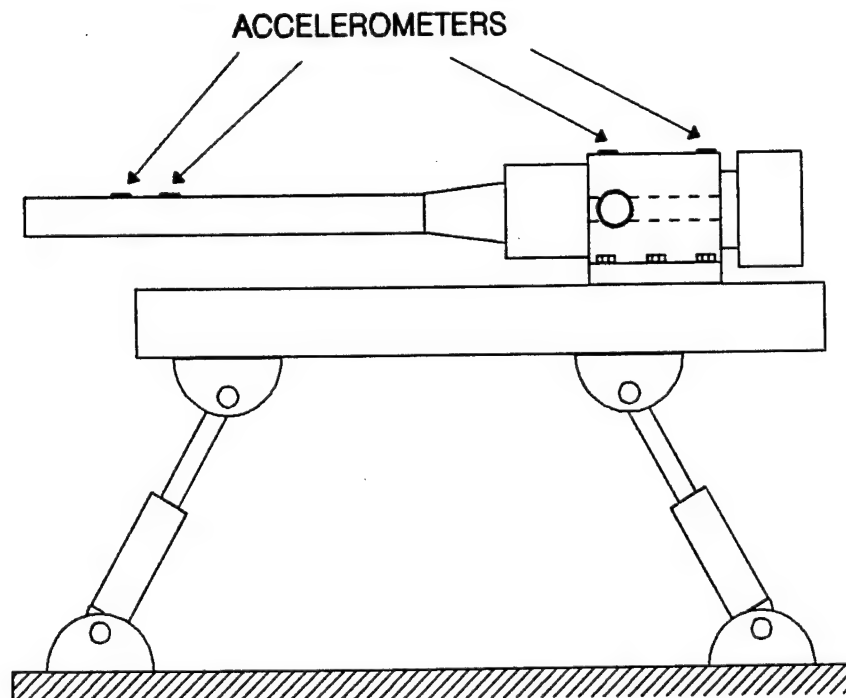


Figure 5. Schematic of Test Setup for Extended Support Gun

$$D(t) = A_i \sum_{i=0}^{I=5} \sin(2\pi f_i t) \quad (1)$$

$D(t)$ : displacement signal sent to machine in inches  
 $A_i$ : amplitude of the  $i_{th}$  sinusoid in inches  
 $f_i$ : frequency of the  $i_{th}$  sinusoid in Hz  
 $t$ : time in seconds

The first five signals are single-frequency sinusoids from 2 through 6 Hz at an amplitude of 0.75 inch. Signals 6 through 11 are of multi-frequency content at various amplitudes comparable to those found in typical acceleration data from ATC vehicle tests conducted on the XM291 system in 1994.

**Table 1. Characteristics of Test Signals** (NOTE: 2 runs for each input signal)

S - #	A	$a_1$	$f_1$	$a_2$	$f_2$	$a_3$	$f_3$	$a_4$	$f_4$	$a_5$	$f_5$
1	0.75	1.0	2	-	-	-	-	-	-	-	-
2	0.75	1.0	3	-	-	-	-	-	-	-	-
3	0.75	1.0	4	-	-	-	-	-	-	-	-
4	0.75	1.0	5	-	-	-	-	-	-	-	-
5	0.75	1.0	6	-	-	-	-	-	-	-	-
6	0.75	0.50	2	0.35	4	0.20	5	0.20	6	-	-
7	0.75	0.50	1	0.40	3	0.35	5	0.35	7	-	-
8	0.25	1.0	0.75	1.50	1.50	1.50	2	1.0	4	-	-
9	0.25	1.0	1.25	1.0	1.75	1.0	2.25	1.0	3	1.0	4
10	0.25	1.0	1.25	1.0	1.50	1.0	1.75	1.0	3	1.0	4
11	0.25	1.0	0.50	1.0	0.85	1.0	1.25	1.0	2.5	1.0	3.75

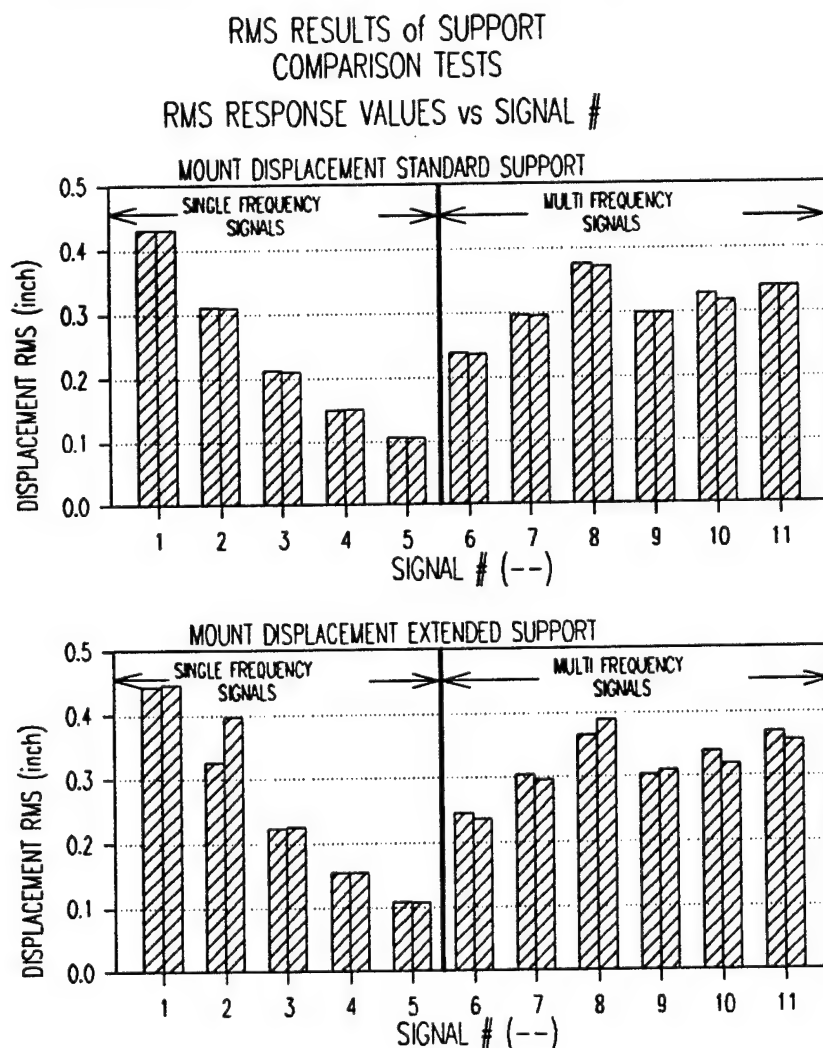
Test data were captured by a Nicolet digital oscilloscope and transferred to 5.25-inch data disks for processing by VuePoint™. Each test run contained four sets of data, namely; the four accelerometer signals all recorded in volts. A zero input range was captured at the beginning and end of each test signal. This was for the purpose of determining the zero level for all signals and the indication of any acceleration 'drift' at the completion of a test run. Data processing included the following:

- Scaling each signal to appropriate engineering units
- Shifting, filtering, and twice integrating the acceleration data to produce displacements

Data Reduction and RMS Ratings

The plethora of data generated during this test required a succinct method of presentation for a valid comparison of the benefits of the extended support gun. Since all of the input signals are periodic, the entire content of the both input and response may be characterized by its RMS value.

Figure 6 plots the mount displacement RMS values against signal number. As noted, signals 1 through 5 are single-frequency signals from 2 to 6 Hz, and signals 6 through 11 are multi-frequency signals. Two data points are shown for each signal. With one exception (signal 2 extended support), repeatability for a given signal and test gun is very good. In addition, when comparing support types, the mount displacement RMS response is about the same for a given signal. The primary characteristic of these responses is the diminished amplitude as frequency increases as shown for signals 1 through 5. Recalling, the amplitude for each single-frequency signal fed by the signal-generating computer was the same. However, as frequency increased, the

120 mm XM291 CANNON VIBRATION STUDY

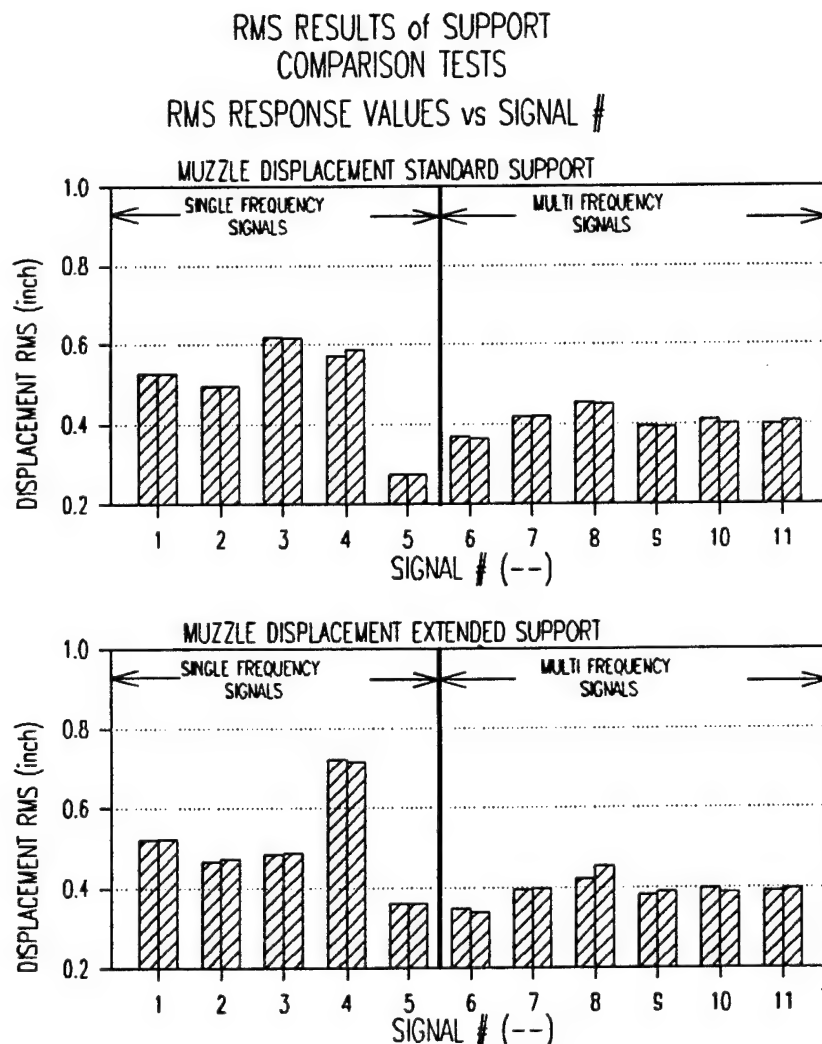
AMSTA-AR-CCB-DE  
NOVEMBER 1995

Figure 6. Mount Displacement RMS Values for Standard and Modified Gun

simulator could not respond due to servo-valve saturation. For multi-frequency signals, amplitude responses were more consistent. The variation ranged from a low of 0.25 inch to a high of 0.40 inch.

Figure 7 plots the muzzle displacement RMS values against signal number. Consistency between responses for a given signal type and support condition again prevails. For the single-frequency signals, the response between support type differs substantially. For the standard support, a rather benign peak of 0.62 inch occurs for signal 3 (4 Hz), whereas a sharp peak of 0.72 inch occurs for signal 4 (5 Hz) for the extended support case. The extended support responses are lower than those for the standard support for signals 1 through 3, however, the reverse is true for signals 5 and 6. For the remaining 6 signals, the responses for the extended support are slightly less than those for the standard support.

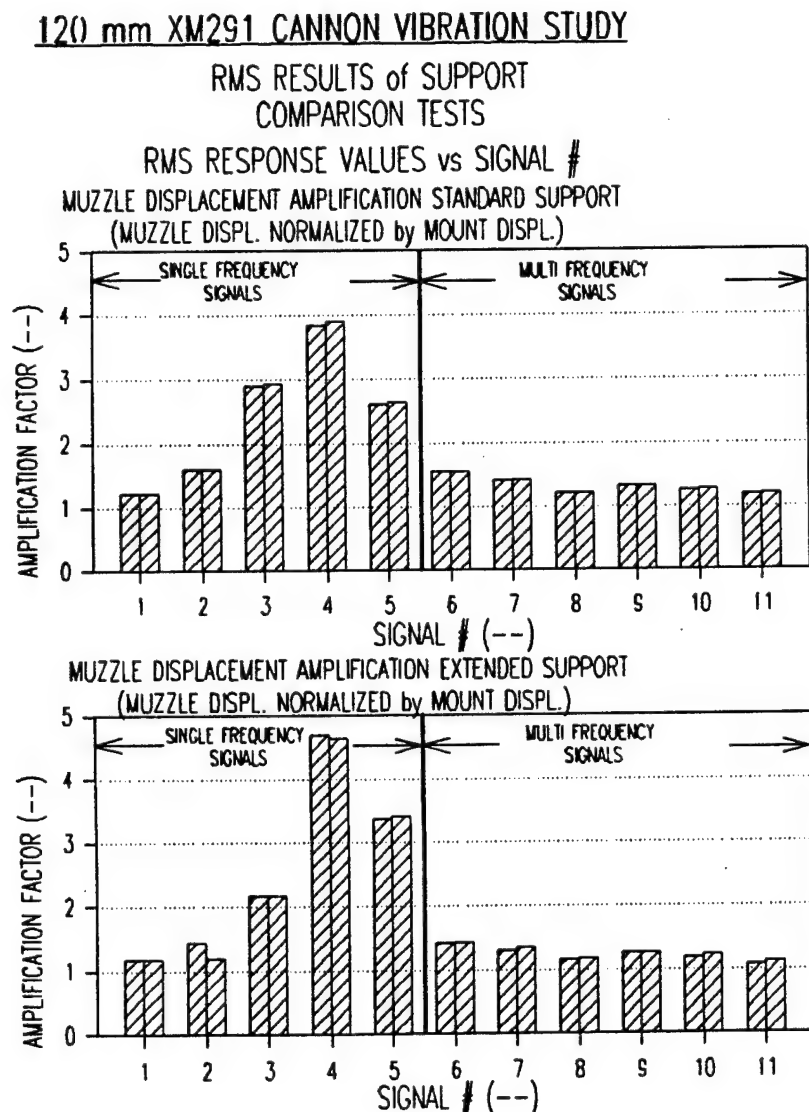
### 120 mm XM291 CANNON VIBRATION STUDY



AMSTA-AR-CCB-DE  
NOVEMBER 1995

Figure 7. Muzzle Displacement RMS Values for Standard and Modified Gun

The true benefit of the extended support is graphically portrayed in Figure 8 in which the muzzle displacement amplification factor is plotted against signal number. The amplification factor is the ratio of the RMS muzzle displacement values to the mount displacement values for a given test run. This type of representation of the displacement data indicates the true frequency response of the system (signals 1 through 5) and the response to generic ground-induced motions (signals 6 through 11). For the frequency response portion, the peaks for each system are very well defined. For the standard support, signal 4 (5 Hz) produced the greatest amplification of just under 4, while for the extended support at this frequency the amplitude was about 4.6. For signals 1 through 3, the extended support system shows less amplification, whereas for 5 and 6 amplification is greater. This indicates that for the extended support, a positive shift of the



AMSTA-AR-CCB-DE  
NOVEMBER 1995

**Figure 8. Muzzle Displacement Amplification for Standard and Modified Gun**

fundamental harmonic frequency occurs. This is a favorable condition, since it renders the system less responsive to the low frequency motions present in ground-induced vibration. Further exemplification of this is shown for the multi-frequency signals. In all cases the extended support gun indicates a 5 to 10 percent reduction in the motion at the muzzle.

The best comparison is shown in Figure 9. This figure plots the percent reduction in muzzle displacement for the extended support gun against frequency on the upper graph, and against signal number on the lower graph. For the single-frequency response, reduction increases from 5 percent at 2 Hz to 27 percent at 4 Hz, then abruptly decreases to -20 percent at 5 Hz and -30 percent at 6 Hz. This distribution indicates a 1.5 Hz positive shift in the fundamental harmonic for the extended support system. Although a greater shift would have been more favorable, the result is as expected since the overhang of the cannon has been decreased by only 10 percent. For the multi-frequency cases, the reduction is positive for all 6 signals and ranges from 4.5 to 8.5 percent.

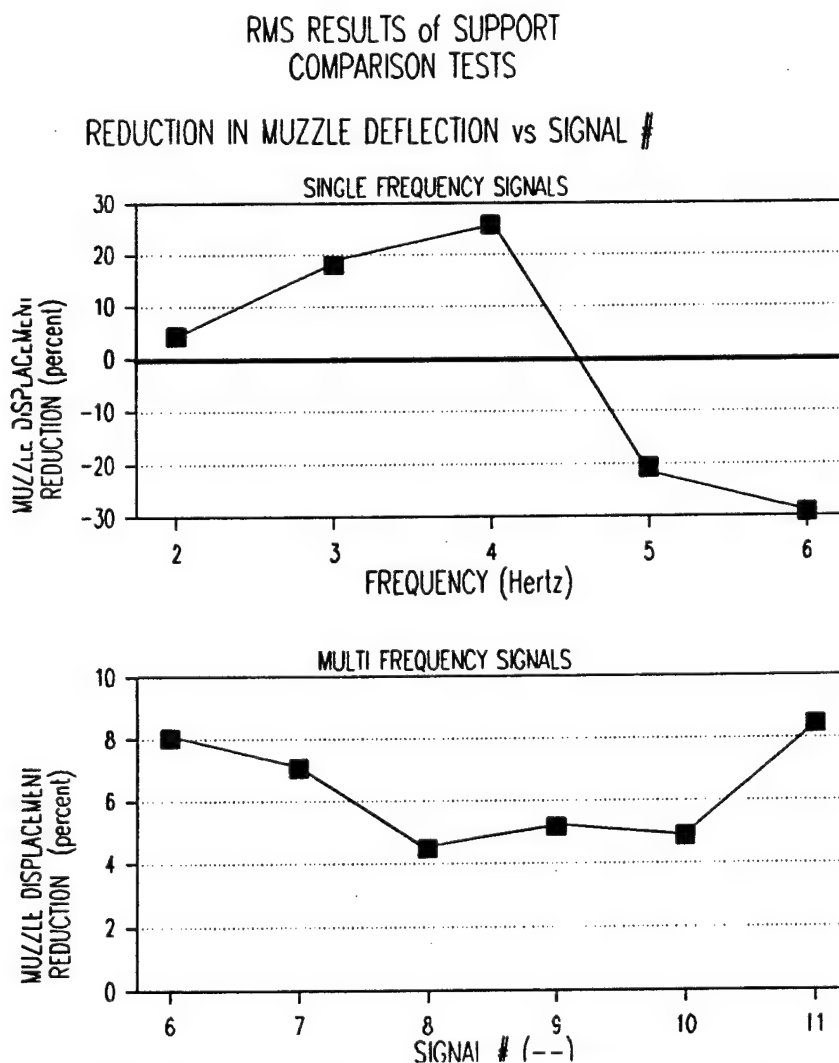


Figure 9. Percentage Reduction in Muzzle Motion for Modified Gun

In the following section, the results of a dynamic analysis of the test will be compared with the data. Both RMS ratings and actual transient results will be presented and discussed.

## DYNAMIC ANALYSIS OF RESULTS USING USM

To solidify the model's validity, test results at the muzzle end were compared to their USM prediction using the mount data as the driving load. In this verification exercise, the dynamics models of both cannons were subjected to the same mount displacement and pitch distributions that were measured during the test. In each case the models were subjected to several seconds of the driving loads, and the muzzle displacement results were retained and analyzed in a manner similar to the test data.

### Comparison of RMS Ratings for Test and Model

In a manner similar to comparing the test data's reproducibility, similar graphs have been constructed to compare test data and modeling results. These RMS comparisons are found in Figures 10 and 11.

Figure 10 illustrates the mount displacement comparisons. The left bar represents the RMS value of the test data for run 'a' of the signal number. The right bar represents the model's average response of the displacements for the two support points on the gun tube. As shown, the correlation between test and model is quite good. This is expected since the 'ground' support in the model (cradle) is very stiff and coupled quite rigidly to the gun tube at these locations. The gun and mount move nearly as a unit.

Figure 11 illustrates similar comparisons for the average muzzle displacement. The left bar represents data and the right bar represents the model's response. The correlation between test and model is good, however, not as good as that for the mount locations. The largest discrepancies occur for the extended support and the multi frequency signals. The model under-predicts the test result by about 5 percent. For the standard support cases, the correlation is much better. For single-frequency signals, the results are within 2 percent of the model and for multi-frequency signals, the correlation is even better. The discrepancy issue will be addressed in the following portion of this section when the transient results are presented and discussed.

# 120 mm XM291 CANNON VIBRATION STUDY

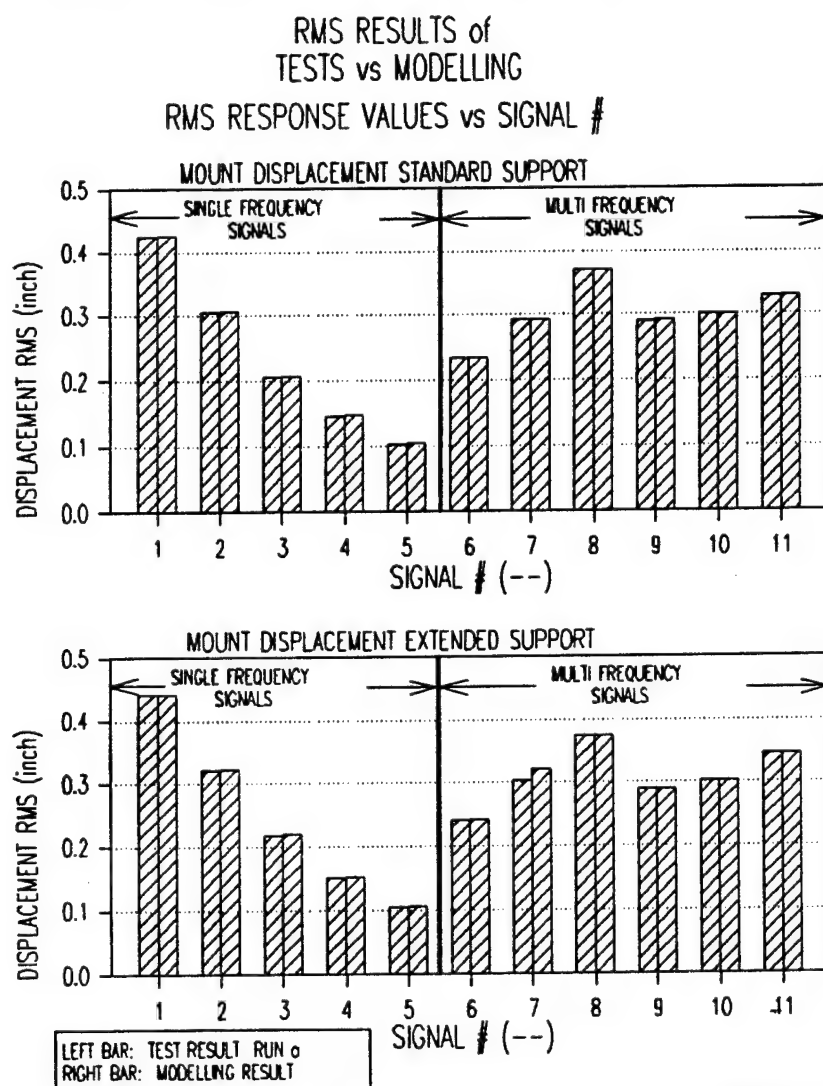
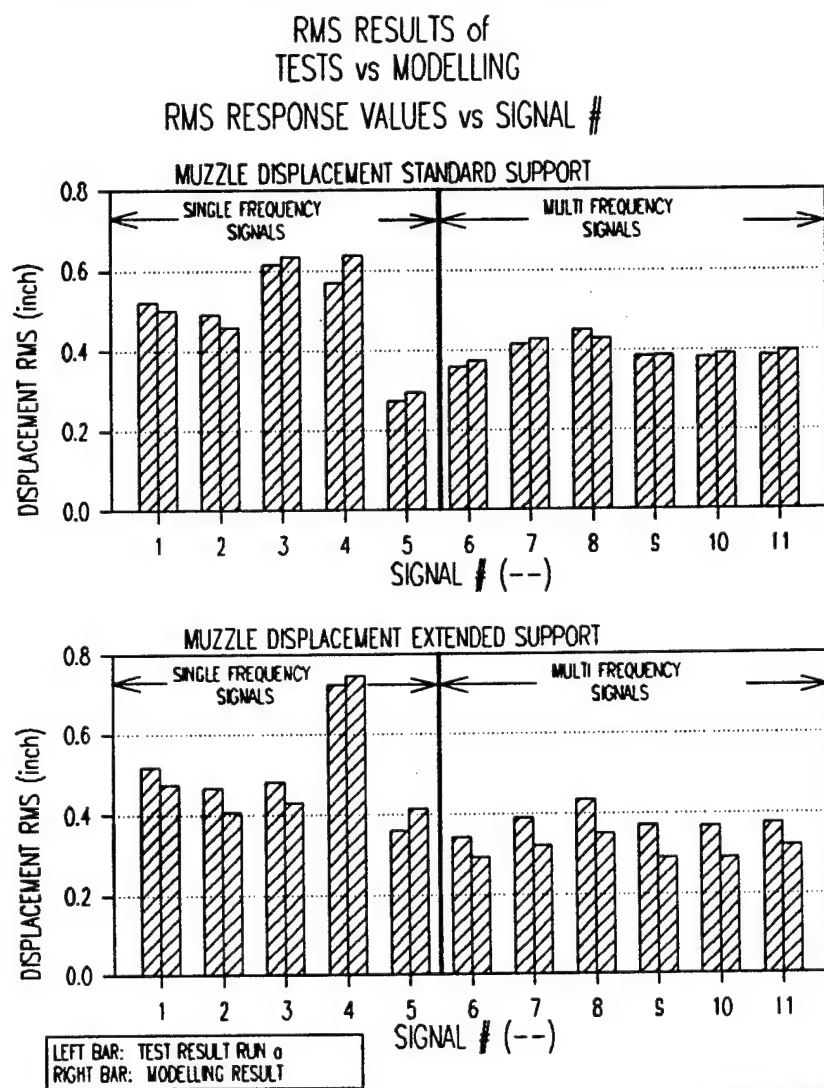


Figure 10. Mount Displacement RMS Values; Comparison of Test and Model

120 mm XM291 CANNON VIBRATION STUDY**Figure 11. Muzzle Displacement RMS Values; Comparison of Test and Model**Comparison of Transient Results for Test and Model

To better illustrate the reliability of the simulations, transient results from the test and model will now be compared. Only a few of these results will be presented since they are polarized into only two groups, namely; those that reproduced the test results quite well and those that did not. Fortunately, the latter group is sparsely populated. The greatest discrepancies occurred for the simulation of the modified gun driven by signals 2a, 3a, and 7a. The transient comparisons are illustrated in Figures 12, 13, and 14, respectively.

Figures 12 and 13 show the data and modeling results for signals 2a and 3a employing the modified mount. Although the amplitudes are quite comparable, the signals seem to be offset in time with signal 3a seemingly 180° out-of-phase. The problem may lie in the selection of startup time for the test results. Although all signals used the same criterion for indication of startup,

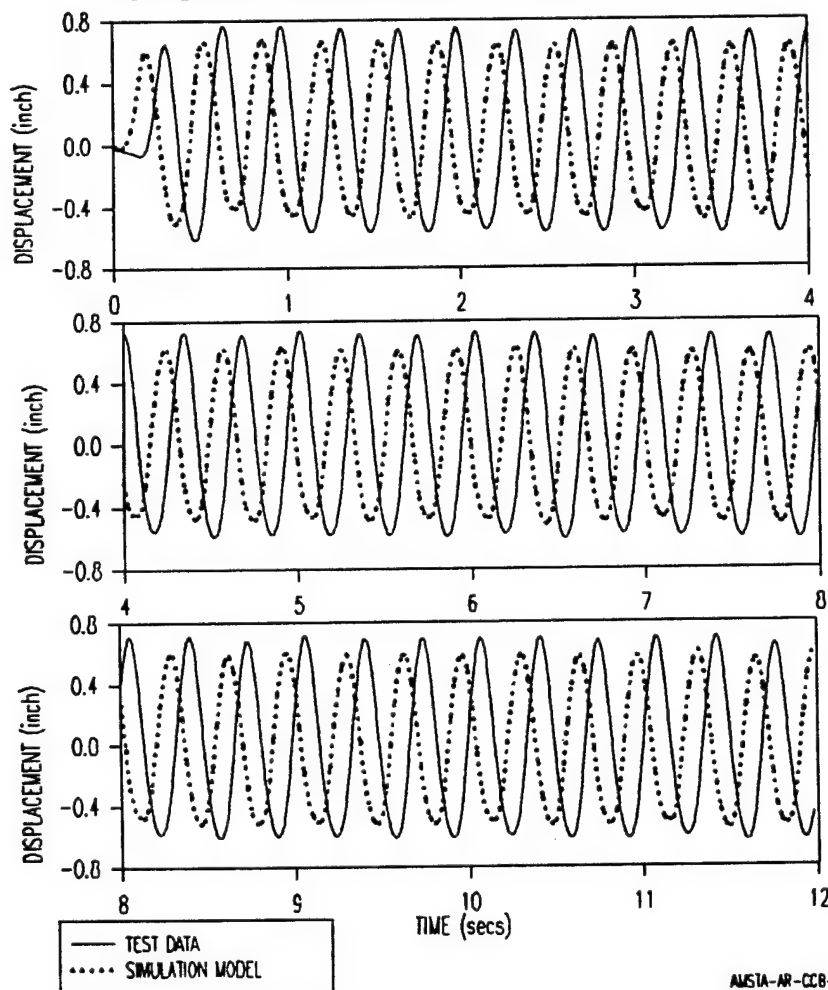
these two may contain some anomalies that cause the shift indication. The situation for signal 7a is much different. Figure 14 shows the data and results for signal 7a. The problem here is purely an amplitude shift for the model. The startup portion of the simulation highly under-predicts the displacement indicated in the test. The situation corrects itself for the second period of application (1 to 2 seconds), however, the discrepancy returns for the next few periods. In the steady-state condition (time greater than 3 seconds), the only points of correlation occur for the low amplitude portions near the end of each period. The discrepancies may be a result of the data processing of the test results. Recalling, each signal was subjected to a low-pass rejection filter to attenuate the accelerometer drift. Although not evident in the displacement data, the shift could be in the mount data that are used in the modeling exercise. In future exercises of this nature, additional care will be used in the processing of these data. In retrospect, the results mentioned above are the only ones containing discrepancies with the test data.

Figures 15, 16, and 17 show the transient results for the test and simulation for the standard support system driven by signals 2a, 3a, and 7a, respectively. These are the standard support counterpart runs for the above cases. By comparison these results show excellent correlation to the test data. Only signal 7a shows slight deviations near the high frequency low-amplitude peaks (e.g., just prior to 1 second). For further information, all of the transient results are available with this author.

In the next section, the USM model will be used to predict muzzle slope responses for both gun types using mount acceleration data collected by ATC during actual 'bump' course testing. This type of comparison will truly indicate the quantitative benefits of the extended support gun.

### 120mm XM291 VIBRATION STUDY

COMPARISON of TEST DATA to DYNAMIC SIMULATION  
for MODIFIED MOUNT DESIGN: TEST RUN #2a  
DISPLACEMENT 13" from MUZZLE vs TIME



AMSTA-AR-CCB-DE  
JANUARY 1996

Figure 12. Comparison of Test and Simulation; Signal #2a Modified Gun

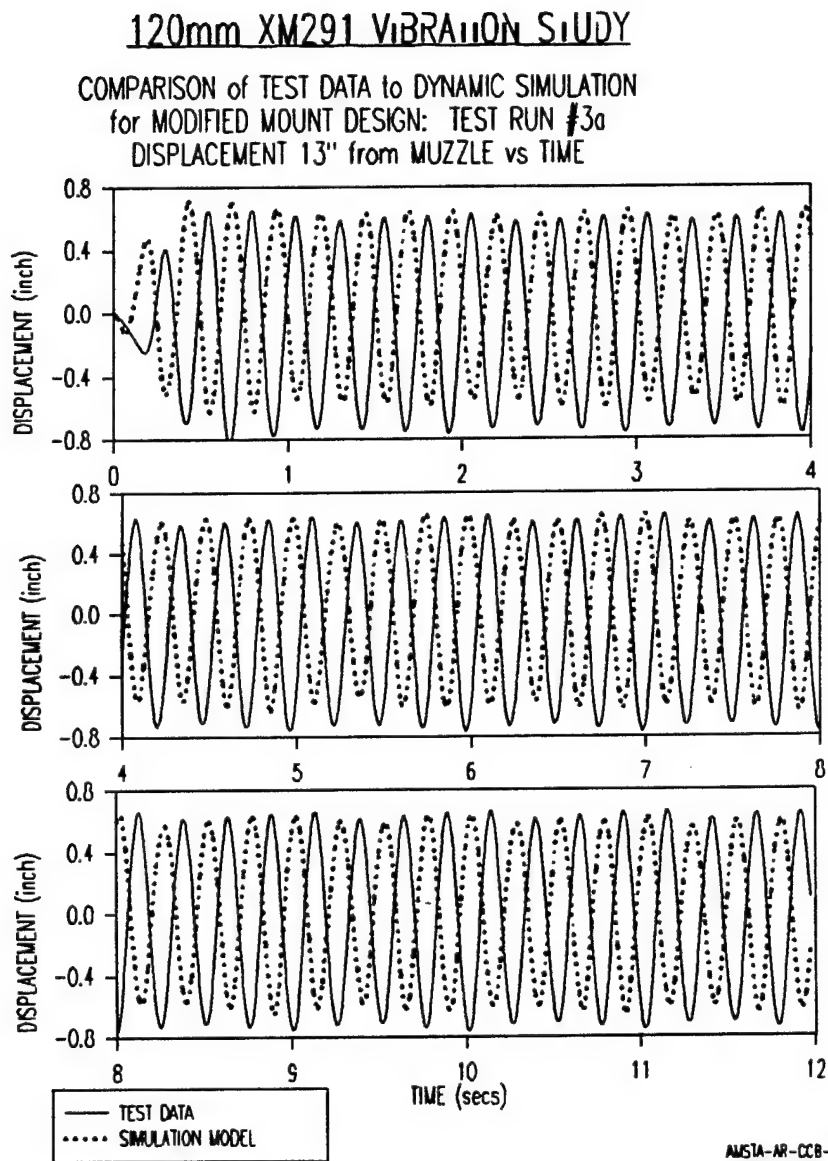
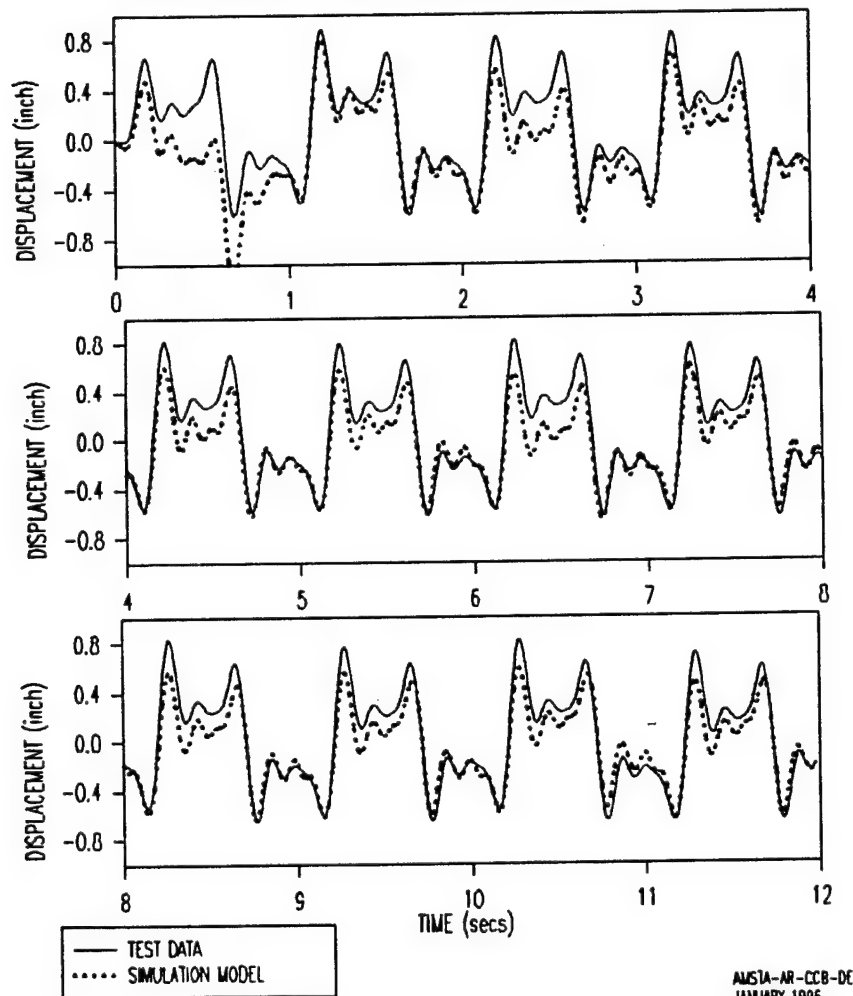


Figure 13. Comparison of Test and Simulation; Signal #3a Modified Gun

### 120mm XM291 VIBRATION STUDY

COMPARISON of TEST DATA to DYNAMIC SIMULATION  
for MODIFIED MOUNT DESIGN: TEST RUN #7a  
DISPLACEMENT 13" from MUZZLE vs TIME



AMSTA-AR-CCB-DE  
JANUARY 1996

Figure 14. Comparison of Test and Simulation; Signal #7a Modified Gun

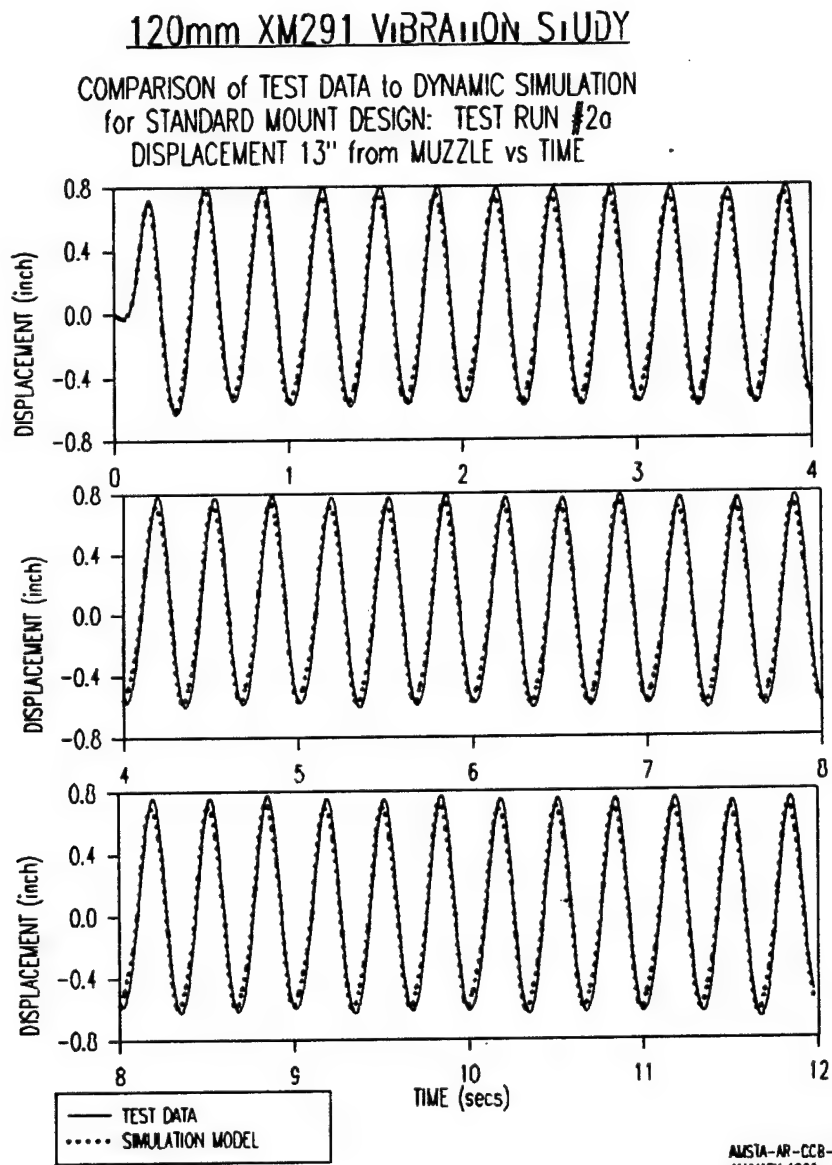
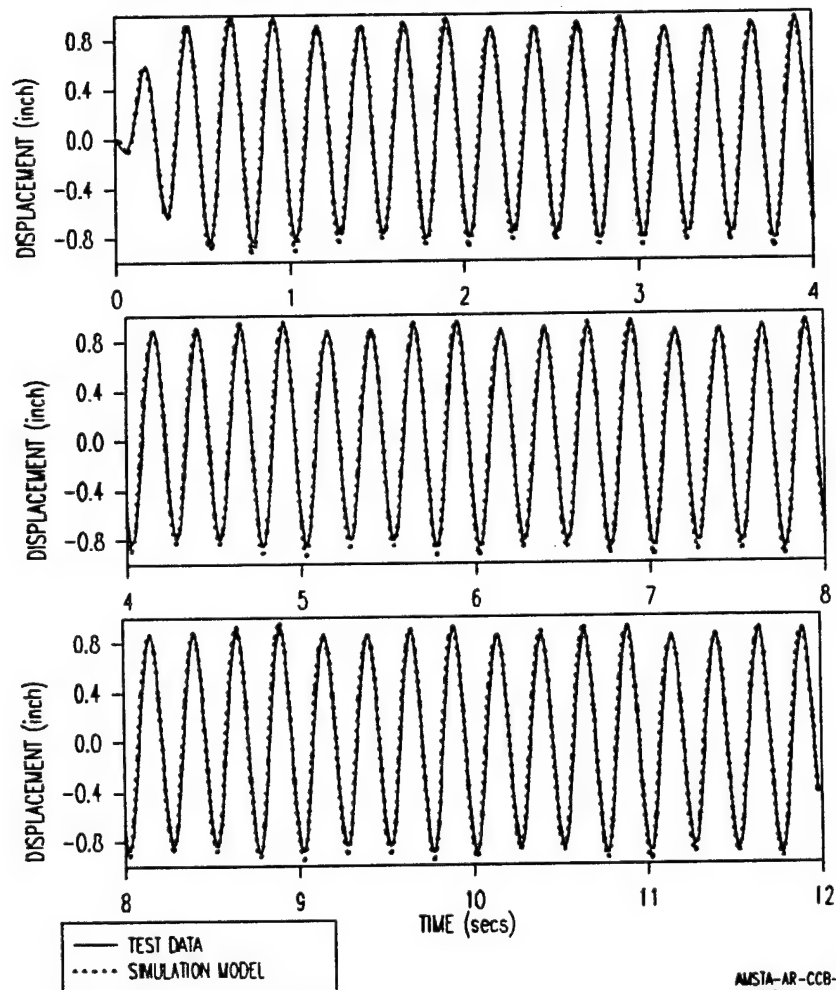


Figure 15. Comparison of Test and Simulation; Signal #2a Standard Gun

### 120mm XM291 VIBRATION STUDY

COMPARISON of TEST DATA to DYNAMIC SIMULATION  
for STANDARD MOUNT DESIGN: TEST RUN #3a  
DISPLACEMENT 13" from MUZZLE vs TIME



AMSTA-AR-CCB-DE  
JANUARY 1996

Figure 16. Comparison of Test and Simulation; Signal #3a Standard Gun

### 120mm XM291 VIBRATION STUDY

COMPARISON of TEST DATA to DYNAMIC SIMULATION  
for STANDARD MOUNT DESIGN: TEST RUN #7a  
DISPLACEMENT 13" from MUZZLE vs TIME

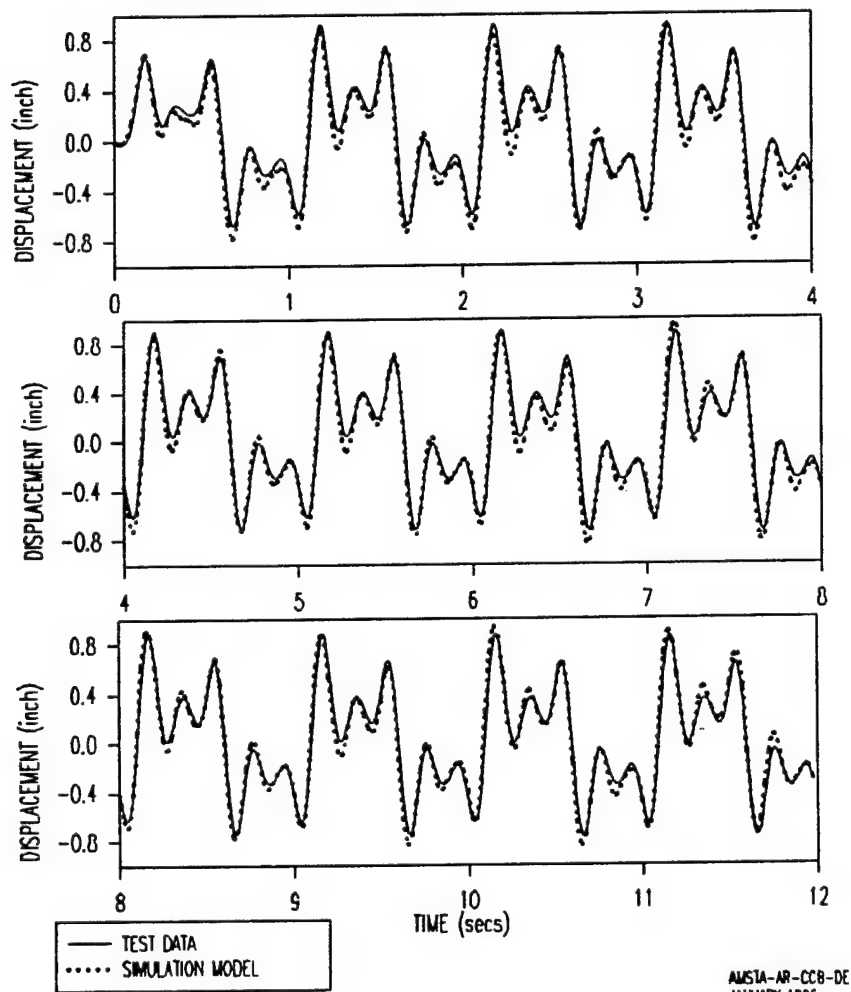


Figure 17. Comparison of Test and Simulation; Signal #7a Standard Gun

## PREDICTED RESPONSE FOR FIELD INDUCED SIGNALS

In order to fully appreciate the worth of the extended support modification for the XM291 gun, a comparison of modeling results driven by field-generated signals for the standard and extended support gun mount will be discussed. The signals driving the model are those that were measured by ATC during the June 1994 test of the subject weapon. Restating a portion of the text from the Background section:

"...at the request of Benet Labs, ATC conducted a vehicle mobility non-firing test, which consisted of traversing the vehicle over known terrain (i.e., 'bump' course) at various speeds with the stabilization system engaged and continuous monitoring of the muzzle reference system (CMRS) data."

Part of the collected data from this test is the mount transverse and rotational accelerations. These data have been filtered to exclude low frequency drift of the accelerometer signals. The displacement signals, which are derived by twice integrating the accelerations, are used to drive the gun mount, whereas the calculated MRS signals are reported and compared for both mount types.

The results of this exercise are reported in Figures 18, 19, and 20. Each figure represents three instances of a different vehicle speed over the 'bump' course. Each of the three graphs per figure contains the results for one run at the given speed. Each gun type (i.e., standard or extended support) was driven by the same acceleration data for a given instance. The graphs show the transient RMS muzzle slope values calculated over fixed increments of time. The closed symbols represent the response for the standard support system and the open symbols represent the response for the extended support system.

Figure 18 shows the results for a vehicle speed of 10 mph. For run #1 the overall level of RMS slope is fairly quiescent at about 0.60 mrad. A mild peak for both support types is shown at 18 seconds. This is the only instance where the response for the extended support gun performs poorer than its standard support counterpart. Between 20 and 30 seconds, the extended support system shows a 25percent benefit. Overall the average reduction in RMS muzzle slope is roughly 10 percent. For runs #2 and #3, the distributions over time are highly transient with high levels of response at the beginning and varying levels for the rest of the run. For run #2 the standard support response is much more variable than that of the extended support system. As was the case for run #1, the extended support system shows a lower level of response for all but one point in the run. The overall benefit is about 10 percent. For run #3 both systems track along the same trajectory, however, the extended support shows lower levels of response in nearly all instances. In all, the benefit at 10 mph is about 10 percent.

Figure 19 shows the results for a vehicle speed of 20 mph. For run #1 the level of RMS slope varies considerably with time. At the beginning of the run, RMS values for both systems are on the order of 2.25 mrad. Five seconds later this value drops to 0.50 mrad and then increases back up to 1.75 mrad. The benefit of the extended support system is not as well defined at this speed as it was for 10 mph, however, it still shows a slightly lower response level (especially between 5 and 10 seconds) than the standard support system. For run #2 the distribution is quite different in that it begins at about 1.0 mrad for 7 seconds then peaks rather quickly at 11 seconds and decays back to 1.0 mrad for the remainder of the run. Both support types track nearly the

same, however, the response of the extended support configuration is less than that for the standard support in nearly all instances. For run #3 the distribution is not as variable as for run #2. It is rather flat at the beginning and end of the run with a mild peak for the extended support system at 9 seconds. So far this is the only instance where the two systems did not closely track one another. The response comparison looks like two waves that are completely out-of-phase. Where the standard support system shows a local maximum, the extended support system shows a local minimum and vice versa. Overall this response shows very little benefit for use of the extended support system. The reason may be in the nature of the driving load used for this case. Further study of the content of this load is required. With the exception of run #3, the benefit for use of the extended support at 20 mph is about 7 percent.

Figure 20 shows the results for a vehicle speed of 30 mph. For run #1 the level of RMS slope varies from a value of about 1.25 mrad at the beginning of the run then levels off to a value of about 0.75 mrad for the remainder of the run. In all instances except one, the extended support system's response is lower than its standard support counterpart. Except for the initial part of the run, which shows a reduction of 33 percent, the average reduction is about 5 percent for the rest of the run. The same level of benefit is shown for the remaining two runs, however, the distributions over time are considerably different than those for run #1. For run #2 the extended support system is less sensitive to the signal, as indicated by its flatter response near the middle of the run. For run #3 a lower level of response is shown from the middle to the end of the run. The peaks near the midpoint are nearly the same. Overall benefit for use of the extended support system is about 10 percent.

In general, it appears that the extended support system will respond more favorably in terms of lessening the muzzle's slope response for field-generated motions. The level of benefit is between 7 and 10 percent, depending upon the magnitude and frequency of the input signal. In addition, at a speed of 20 mph the system appears (i.e., muzzle slope) to be quite sensitive in that for all runs at this speed the response signals were different and transient in nature.

# 120mm XM291 VIBRATION STUDY

ANALYTICAL COMPARISON  
of STANDARD to EXTENDED SUPPORT MOUNT  
DRIVEN by FIELD GENERATED ACCELERATIONS

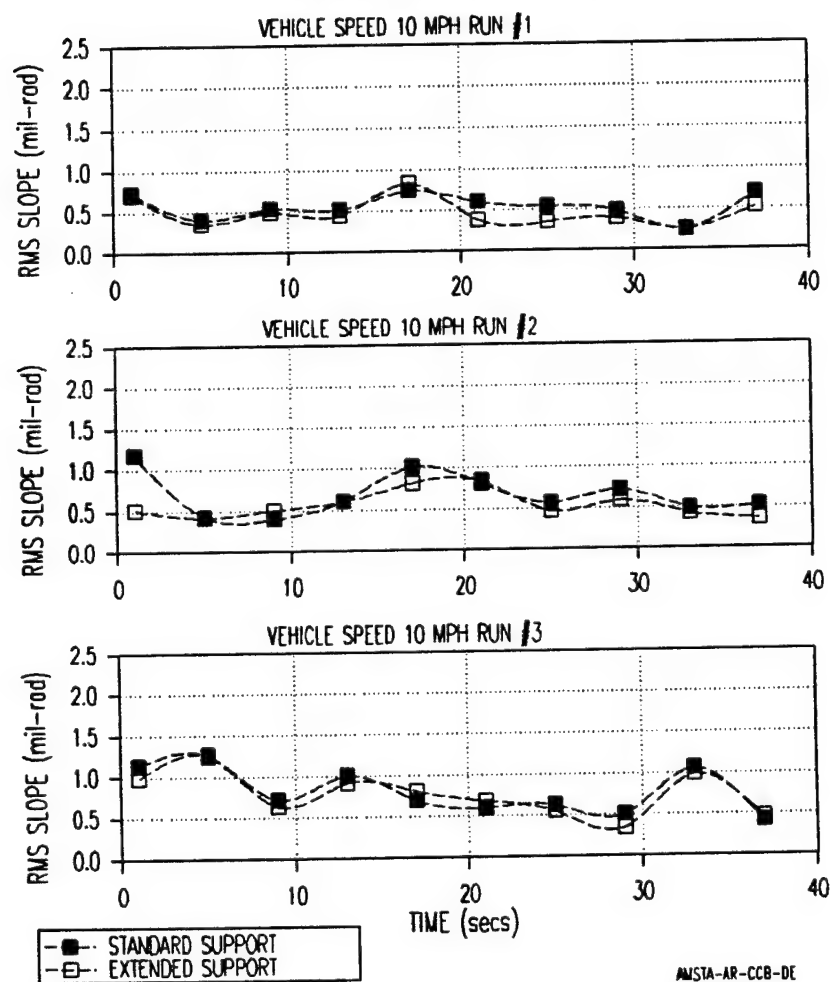


Figure 18. Comparison of RMS Muzzle Slope Values at Vehicle Speed of 10 MPH

# 120mm XM291 VIBRATION STUDY

ANALYTICAL COMPARISON  
of STANDARD to EXTENDED SUPPORT MOUNT  
DRIVEN by FIELD GENERATED ACCELERATIONS

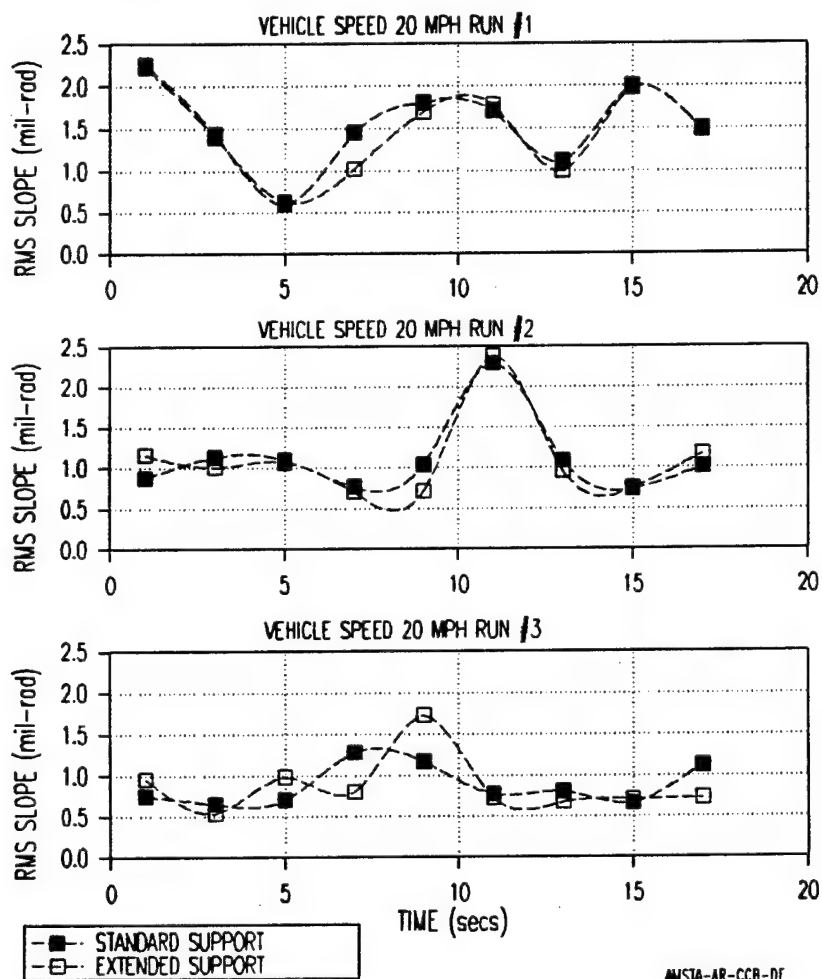


Figure 19. Comparison of RMS Muzzle Slope Values at Vehicle Speed of 20 MPH

# 120mm XM291 VIBRATION STUDY

ANALYTICAL COMPARISON  
of STANDARD to EXTENDED SUPPORT MOUNT  
DRIVEN by FIELD GENERATED ACCELERATIONS

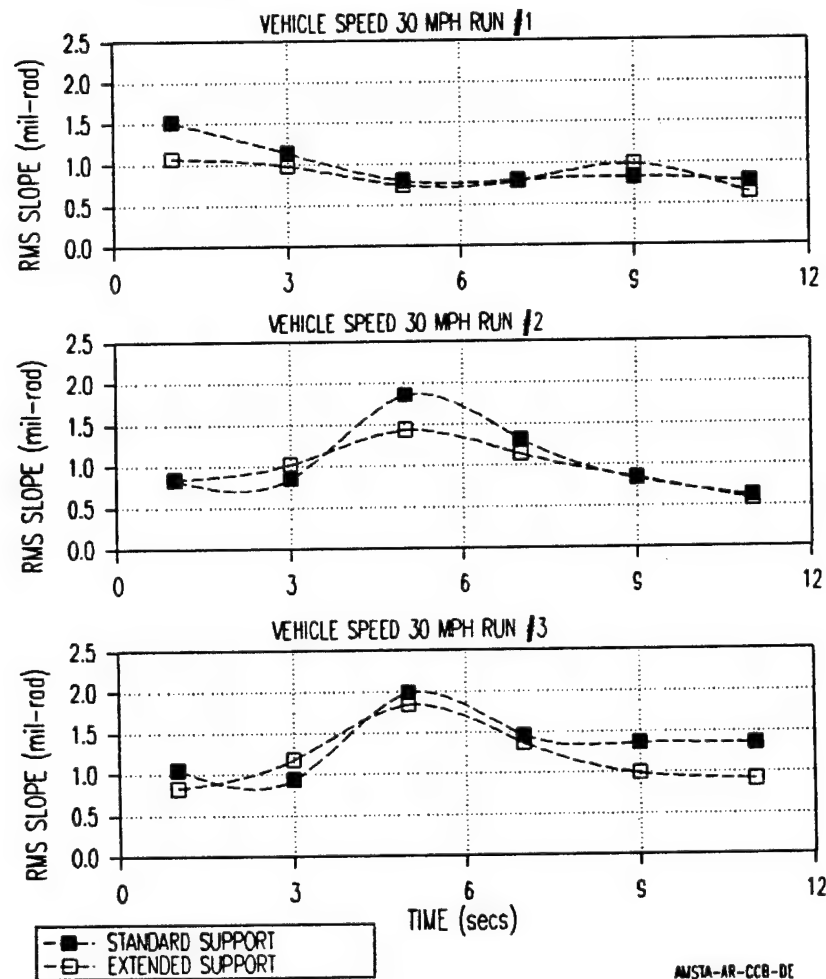


Figure 20. Comparison of RMS Muzzle Slope Values at Vehicle Speed of 30 MPH

## CONCLUSIONS

This redesign program was conducted to increase the accuracy of the 120-mm XM291 tank cannon. In tank-mounted 'on-the-move' firing tests, the vertical dispersion of shot groups was excessive, thus compromising the accuracy features of the weapon. It was decided that the problem was due to the increased flexibility of the gun tube with respect to the current M256 cannon. This report details Benet's efforts at solving the classical engineering problem of shifting the fundamental harmonic frequency of a flexible beamlike structure, thus increasing the stiffness and low frequency rejection of ground-induced motion. Due to constraints imposed upon the solution, the most effective method of decreasing the tube length was not an option.

In attacking the problem, a hybrid approach was used. First, a dynamic computer model of the structure was built and excited by simulated single and multiple-frequency ground motions. These motions are similar in content to those that drive the actual structure. Second, the structure was exercised on a dynamic simulator (i.e., shake table) using the same drive signals as those in the virtual simulation. The responses were compared and appropriate adjustments to the model were made. For this exercise the model reproduced the data quite well and no adjustment was needed. With a validated model in hand, many redesign options may be applied to the model and rated by the virtual simulation. Due to the reduced number of redesign options, only a few were tried. The first was to increase the cross-sectional area of the tube near the breech end. Using reasonable judgment regarding maximum dimensions, this option was not very fruitful. The next method was to lengthen the mounted portion of the cannon such that the overhang is shortened without decreasing the length of the tube. This method showed some improvement when simulated and was pursued as the only viable option.

The mount was lengthened by approximately 2 feet, which shifted the fundamental harmonic frequency approximately +1.5 Hz. Although marginal, it decreased the muzzle motions by 8 to 10 percent across the board for all signals tested and simulated. The dynamic response would have diminished more if the mount length were increased, however, the gross weight and imbalance of the system would have become too great.

In retrospect, if a complete model of the system (i.e., gun and tank) were built and tested by computer simulation early in the system design phase, problems such as this would have been discovered early. The redesign space would have been much greater, thus a truly optimum result could have been found. This is the way things should be done in the future.

## REFERENCES

1. Gast, R.G., "Modal Analysis of the Dynamic Flexure in Tank Weapons by the Uniform Segments Method," PhD Thesis, Rensselaer Polytechnic Institute, Troy, NY, April 1988.
2. Gast, R.G., "120-mm XM291 Vibration Study: Calibration of the Link Six Degree of Freedom Simulator," In-House Report, Benet Laboratories, Watervliet, NY, August 1995.

**WILKERSON, HOPKINS, AND HELD**

**TITLE:** Techniques for Modeling Bullet Exit State Conditions Predicted by Transient Finite Element Models

Steve Wilkerson,\* Dave Hopkins, and Bruce Held

U.S. Army Research Laboratory

ATTN: AMSRL-WT-PD

Aberdeen Proving Ground, MD 21005-5066

**ABSTRACT:**

To understand the accuracy of tank cannons, an analytical and numerical effort has been made to uncouple and quantify the influences from the bullet and gun design. A number of issues are addressed using state-of-the-art finite element techniques. In this paper, the effects of gun tube shape and projectile geometry on projectile exit state conditions are examined using these techniques.

Recently, a live fire test was conducted, which compared long and short 120-mm tank ammunition. Examination of the limited data indicated a potential correlation between ammunition type and gun tube centerline profile. Two gun tubes were chosen for comparison. The two gun tubes selected were based on the very large differences in vertical mean jump between the two tubes. Centerline profiles, obtained at the Watervliet Arsenal, of the two gun tubes were incorporated into the existing finite element models of the M256 system. Additionally, finite element models of the short and long bullets were constructed. The projectile models were then computationally "fired" through the gun models to predict the net effect of the tube shape on the bullet's exit state velocities and rotational rates. This paper presents those results and also compares dynamic response between the longer, more flexible bullet and the short and stiff kinetic energy bullet. Finally, an overview of the techniques used to estimate the bullet's exit state condition is reviewed.

**BIOGRAPHY:** Dr. Wilkerson has been employed by the U.S. Army Research Laboratory since 1989, working in the Mechanics and Structures Branch, Propulsion and Flight Division, Weapons Technology Directorate.

**PRESENT ASSIGNMENT:** Investigate the influences of gun and bullet dynamics on gun accuracy.

**PAST EXPERIENCE:** He has worked in the field of gun accuracy for the past 7 1/2 years, primarily in the study of numerical techniques to simulate gun and projectile interactions.

**DEGREES HELD:** B.S. Mechanical Engineering, Johns Hopkins University, Baltimore, MD, 1982; M.S. Civil Engineering, George Washington University, Washington, D.C., 1985; Ph.D. Mechanical Engineering, Johns Hopkins University, Baltimore, MD, 1990.

WILKERSON, HOPKINS, AND HELD

TECHNIQUES FOR MODELING BULLET EXIT STATE CONDITIONS  
PREDICTED BY TRANSIENT FINITE ELEMENT MODELS

Steve Wilkerson,\* Dave Hopkins, and Bruce Held  
U.S. Army Research Laboratory  
ATTN: AMSRL-WT-PD  
Aberdeen Proving Ground, MD 21005-5066

OVERVIEW

The numerical modeling is based on transient finite element methods. Using the manufacturing drawings and some simplifying geometric assumptions, the gun tubes and projectile geometries are discretized into a collection of eight noded brick elements through the use of the pre- and post-processing routine Patran [1,2]. These brick elements, along with appropriate loading histories and boundary conditions, are converted by the Patran translator for use with the DYNA3D finite element program [3]. DYNA3D analysis is accomplished with a solver employing a force balance approach (i.e.,  $F = ma$ ). The DYNA3D solver produces results which are further analyzed using Taurus, Masseuse, and the Patran program. Taurus is a package that was developed to work in conjunction with DYNA3D. It is a general-purpose program that graphically displays stress and strain conditions in the structure. Patran is also used in a similar manner and is often preferred over Taurus for its superior graphic capabilities. Masseuse was developed [4] for extracting specific data relevant to the launch dynamics of kinetic energy (KE) bullets (e.g., exit state conditions) and is used here for that purpose. In general, all three programs are used extensively for the extraction of data obtained from the finite element analysis.

The gun system model is composed of four subcomponents: the gun tube, the breech block, the recoil system, and the support mechanisms. The gun tube is approximately 208.7 inches long with a 4.72-diameter bore (120 mm). The thickness of the gun tube wall varies along its length. At the rear end of the cannon is a chamber area approximately 6.22 inches in diameter. As the propellant burns, the resulting high-temperature, high-pressure gas accelerates the projectile down the tube. These attributes are included in the model by coupling an interior ballistics code calculation\* with the DYNA3D solver.† The breech consists of two primary components, the breech housing and the breech block, which slide over the chamber opening to seal off the propellant gases. Both components are approximated by a single block with equivalent mass properties and geometry. The actual breech is connected to the gun tube by a series of opposing threads and a locking bolt; though, after the first millisecond of propellant burning, the internal pressure is sufficient to fasten these parts together in a nearly rigid condition. As a result, the breech/gun tube interface can be adequately represented in the model by rigidly fastening the breech to the gun tube. The tube is then overwrapped by the piston, adapter bearing, and king and thrust nut assembly. These parts constitute the recoiling components of the gun system. All of these interconnecting parts are modeled as a single unit for the DYNA3D simulation and are fastened rigidly to the tube at the

---

\* The interior ballistics code IBHVG2 [5] was originally used for the three-dimensional calculations. However, other codes, such as XNOVAKTC [6] and Nova [7], are also employed by interior ballisticians.

† Several different methodologies have been developed, first by Hopkins [8] and then by Hopkins and Wilkerson [9], to simulate the pressure front in the gun barrel.

locations that approximate the bearing surfaces in the actual system. A cradle interfaces with the piston using sliding interfaces. Gaps between the cradle and piston are modeled to simulate the actual dimensional tolerances. These gaps were found to be important in simulating specific attributes of the recoil cycle and are now included in all gun models of the M256 gun system [10]. A mantlet overwraps the cradle and connects the M256 cannon to the tank at the trunnions. The trunnions allow the whole system to rotate only in the vertical plane. This rotation is resisted by the elevation mechanism, which is simulated with a single spring whose constant was determined in static load tests [11]. The recoil spring, located between the piston and cradle, is simulated by 24 smaller springs, spaced at 15° increments. The constant for these springs was approximated as a linear combination of the actual spring's preload and its spring constant. The resulting approximation was shown to be accurate in capturing the recoil motion of the gun for the first 1.5 inches of recoil distance, which is roughly the distance the gun recoils while the projectile is in-bore [12]. Figure 1 shows the complete system with each component labeled.

Two KE projectiles were modeled, a short and a long kinetic energy bullet. The short bullet is a KE training round, and the long bullet is a tactical KE round. They are similar rounds in that each is composed of two primary components, a lightweight, three-piece sabot and a long rod penetrator. There are significant differences between the two rounds, however. The short bullet is a training round and has a much lower length-over-diameter (L/D) ratio than the long bullet. Additionally, the short round uses a hard steel rod with a steel windscreen and a conical stabilizer, while the longer bullet has a high-strength, depleted uranium (DU) rod, an aluminum windscreen, and aluminum tail fins. The shorter sabot is made of a high-strength aluminum, while the longer sabot is constructed of a graphite composite material. Finally, the short round has a rubber obturator, while the longer round's obturator is nylon.

Despite the differences, the similarities between the rounds allow them to be modeled in a similar manner. In each case the sabots are modeled by three independent petals, each with a 120° span. Actual sabot petals interface with the penetrator through a series of opposing grooves or threads. This interface is approximated by smearing the penetrator and sabot threads into an equivalent mass and modulus representation of the region. This approximation is necessary due to the number of threads the model would require to match the detail of the actual bullet.\* As a result, the stresses in the region of the threads are understood to be inaccurate. The approximation is felt to be adequate however, since the pressure on the rear ramp of the projectile clamps the rod and sabot rigidly together after 1 ms of pressure buildup. The sabot petals have sliding interfaces between one another. There are also sliding interfaces between the gun tube and the sabot in the bulkhead and front scoop regions. The sabot models also include the obturator on the rear bulkhead surface, and a sliding interface is used between it and the gun tube wall. The interfaces between sabot petals include gaps roughly equivalent to those that exist in the actual rounds at room temperature. A not-to-scale shaded image of the finite element model is given in Figures 2 and 3 of the short and long bullets, respectively.

---

\* In other words, the discretization required to model the grooves would increase the number of elements in the model, slowing the analysis time and increasing the initial stages of setting up the problem significantly. It is believed that this additional work would not benefit the model sufficiently to justify the costs.

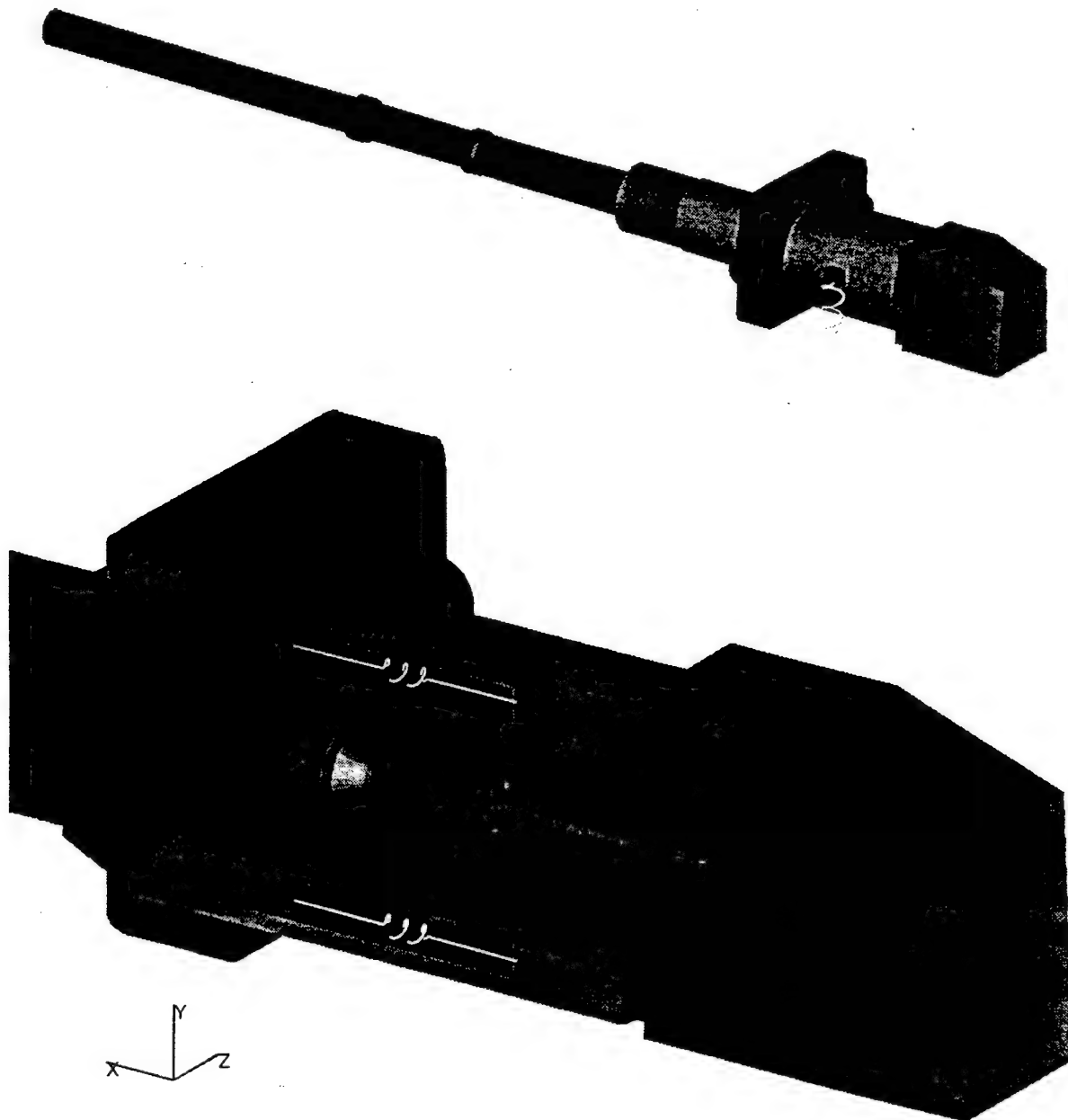


Figure 1. Finite element model of the M256 gun system.

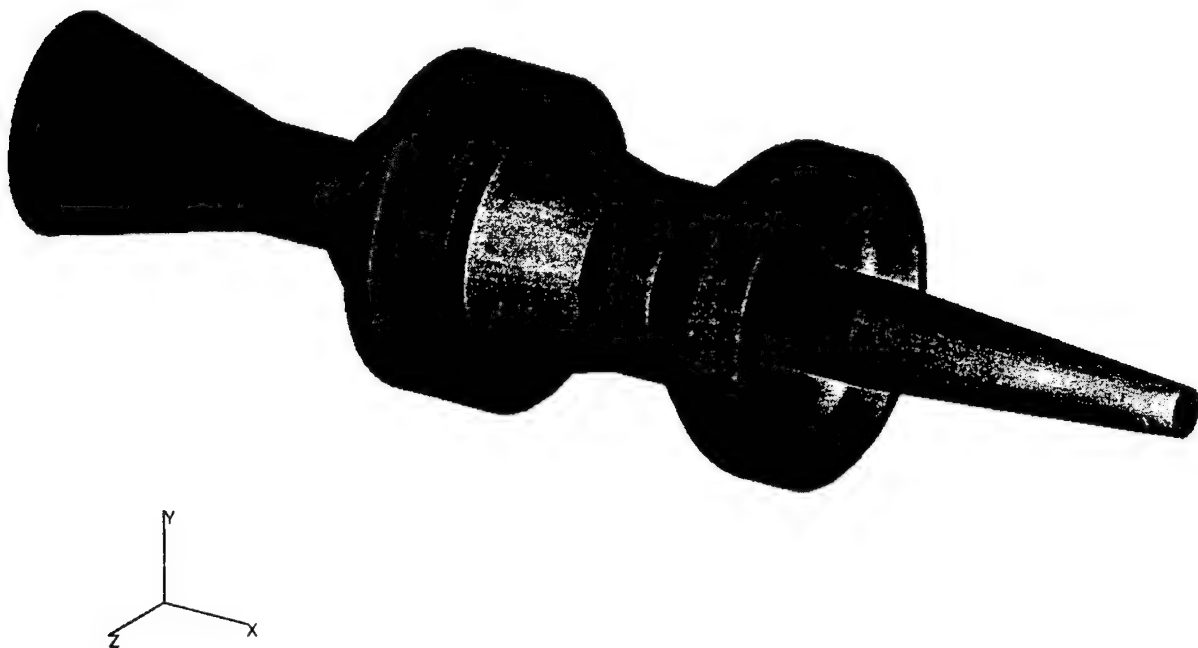


Figure 2. Finite element model of the short bullet.

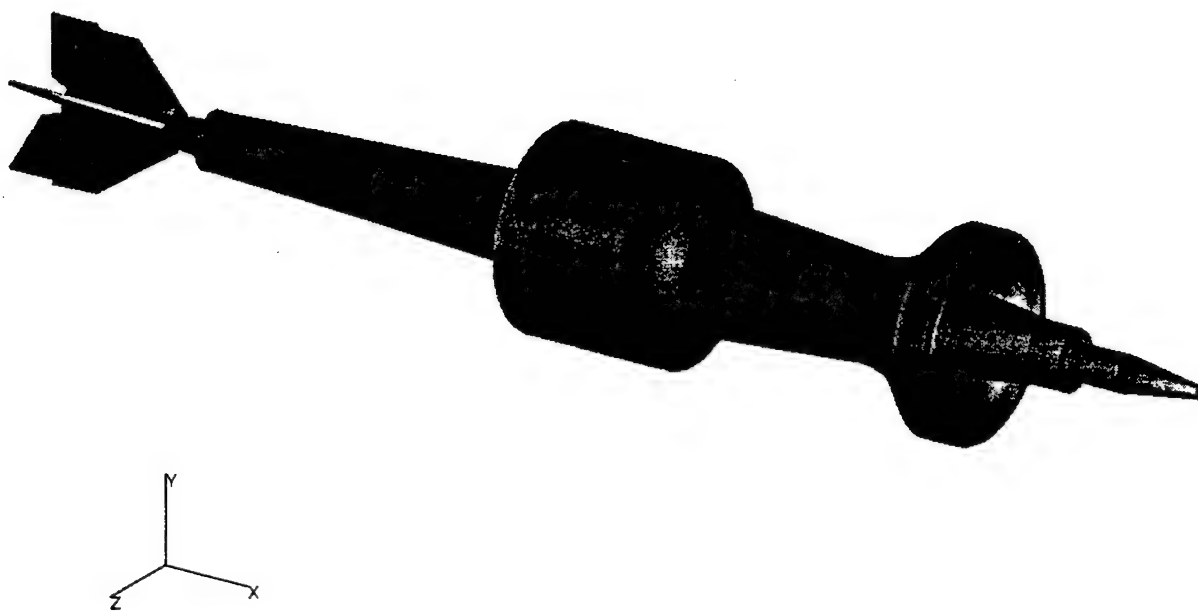


Figure 3. Finite element model of the long bullet.

## RESULTS

During the fall of 1994, a large firing test was conducted at Aberdeen Proving Ground. During this test, both long and short ammunition were fired. A total of 12 gun tubes were used during this test. Out of this sample, two gun tubes (serial numbers 5064 and 4087) were selected for numerical simulations on the basis of how they shot the long and short ammunition: tube 4087 tended to shoot short and long ammunition much lower on the target than average, while 5064 tended to shoot much higher. The centerline profiles of the two gun tubes were obtained from the Watervliet Arsenal Quality Assurance Division, which records the final profile at the end of the manufacturing process [13]. It is important to note that the centerline profiles for both gun tubes fell within the acceptable tolerances. These profiles were incorporated into the DYNA3D gun dynamics simulation so that the influence of centerline profile could be examined for a simulated firing. It is important to note that the results of the simulation are considered to be accurate in terms of predicting trends, but are probably not reliable in terms of absolutes. Therefore, the modeling was ideal for this application.

Gun tube 5064 and 4087 centerline profiles are summarized in Figures 4 and 5. The Watervliet Arsenal centerline data (both horizontal and vertical) includes two sets of measurements. In one, the gun tube is oriented as it will be mounted in the tank. In the other, the gun tube is rotated 180° and remeasured.\* The two measurements provide all the information necessary to determine the tube's shape independent of gravity droop and approximation of the shape of the tube in the tank. Use of both sets of measurements also allows an estimation of the measurement error. As can be seen in the figures, the tubes mirror one another in the vertical planes.

Table 1 summarizes the exit state conditions obtained from the simulations for the two different projectile types in the two different gun tubes. Column one in Table 1 gives the results for the short round's exit state condition just as it exits the muzzle of gun tube 4087. The vertical velocity is calculated by summing the vertical momentum of each element and dividing the total by the total mass. The horizontal velocity is obtained in the same manner. Pitch and yaw rates are found by summing the moment of momentum about the center of gravity of the projectile in the vertical and horizontal planes, respectively. The short round firing simulations from gun tube 5064 are summarized in column 2. As can be seen, the two different tube shapes have a considerable effect on the vertical and horizontal velocities of the bullet at shot exit. However, they do not change the rotational rates significantly. Columns 3 and 4 provide similar summaries for the longer, more flexible round. For the longer, more flexible projectile, the difference in tube shape seems to have a much greater effect on the rotational rates. The large differences in the long round's rotational rates between the gun tubes helps explain the large difference that was observed in the mean point of impact for the longer ammunition when fired from the two gun tubes.

---

\* The first measurement is done with supports at 405 and 1,853 mm from the breech end of the gun tube with the site of the gun at dead-top-center. When the tube is rotated 180°, the actual vertical profile is rotated with it. However, the gravity droop remains unchanged so long as the supports remain the same. Hence, based on these two measurements, the true profile resulting from the manufacturing process and the gravity droop can be determined using the linear relationship obtained during the measurement process. The error associated with the measurement is approximately 15% on the average. For further details, see Wilkerson [14].

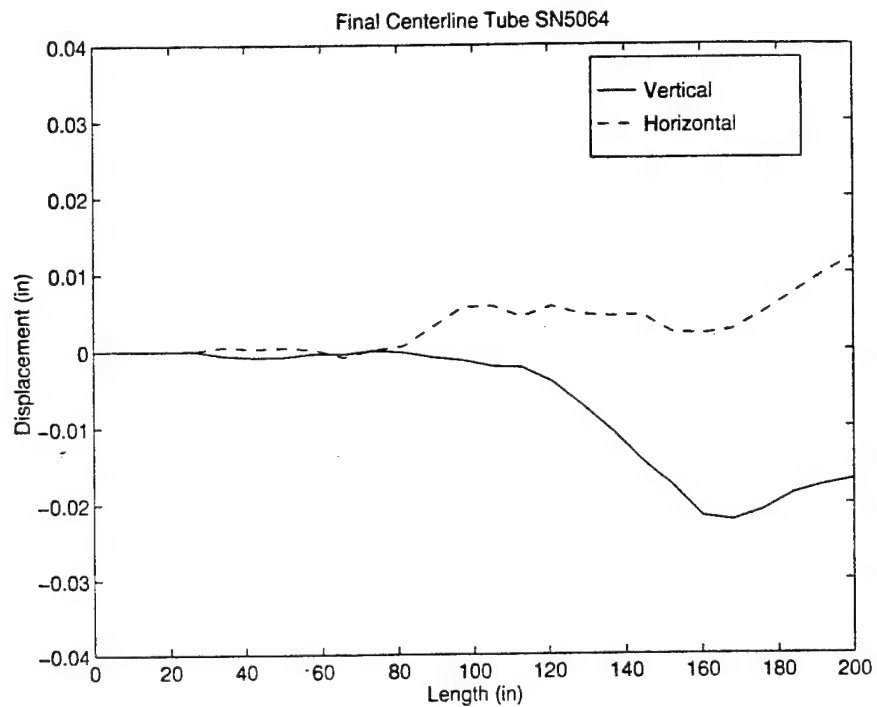


Figure 4. Vertical (solid) and horizontal (dashed) centerline profiles of tube 5064.

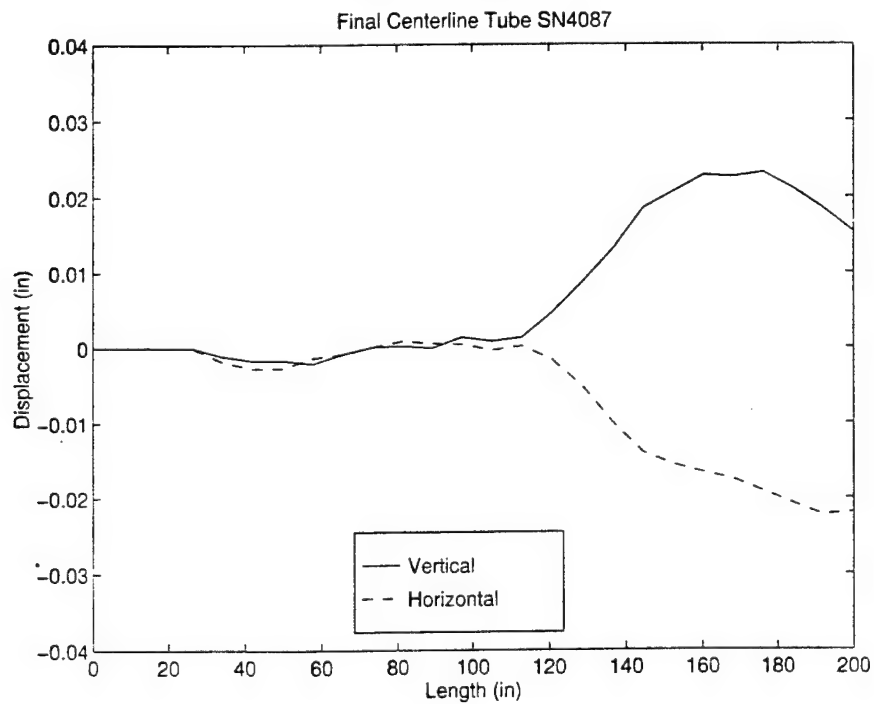


Figure 5. Vertical (solid) and horizontal (dashed) centerline profiles of tube 4087.

Table 1. Short vs. Long Ammunition Comparison

Two Tubes (No. 4087 and No. 5064)

	Short Round G/T 4087	Short Round G/T 5064	Long Round G/T 4087	Long Round G/T 5064
Vertical Velocity	-128.5	15.8	-46.21	0.558
Horizontal Velocity	59.1	87.7	22.76	45.2
Pitch Rate	6.2	6.15	-1.5	-3.13
Yaw Rate	-5.97	-5.08	-4.26	2.1

Another observation that can be made from the simulation is that a correlation between the projectile's vertical and horizontal velocities and the gun tube shape may exist. At shot exit, the projectile horizontal and vertical velocity vectors, for both projectile types, is less positive from tube 4087, than it is from tube 5064.

## CONCLUSION

The long and short 120-mm tank ammunition was fired from several gun tubes, and differences were seen in the mean point of impact between the various gun tubes. The magnitude of the difference was greater for the longer round than for the shorter one. An attempt was made to simulate the firing of the two ammunition types from two different gun tubes. The goal of this simulation was to extract the exit state conditions of the projectiles as they exited the gun tubes. These conditions were then used to explore possible reasons for the gun tube and ammunition differences noted during the firing test. The gun tubes chosen had vertical profiles which were mirror images of one another and also exhibited very large differences in their mean points of impact. When the simulations were run using the DYNA3D finite element code, trends which could help explain the firing test results were seen. Linear velocity states were consistent across a gun tube and, most importantly, change in tube shape seemed to affect the longer bullet more than the shorter one in terms of pitch and yaw rate.

## REFERENCES

1. PDA Engineering. "PATRAN Plus Users Manual Release 2.4." Patran Division, Costa Mesa, CA, 1987a.
2. PDA Engineering. "PAT/DYNA Interface Guide." Patran Division, Costa Mesa, CA, 1987b.
3. Hallquist, J., and R. Whirley. "DYNA3D Users Manual (Non-Linear Dynamics Analysis of Structures in Three-Dimensions)." UCID-19592, rev 5, Lawrence Livermore National Laboratory, Livermore, CA, May 1989.

WILKERSON, HOPKINS, AND HELD

4. Hopkins, D. Private communication, U.S. Army Research Laboratory, Aberdeen Proving Ground, MD, 1993.
5. Anderson, R., and K. Fickie. "IBHVG2 - A Users Guide." BRL-TR-2829, U.S. Army Ballistic Research Laboratory, Aberdeen Proving Ground, MD, July 1984.
6. Gough, P. "The Nova Code - A User's Manual." Indian Head Contract Report IHCR 80-8 Naval Ordnance Station, Indian Head, MD, 1980.
7. Gough, P. "The XNOVAKTC Code." BRL Contract Report BRL-CR-627, U.S. Army Ballistic Research Laboratory, Aberdeen Proving Ground, MD, 1990.
8. Hopkins, D. A. "Predicting Dynamic Strain Amplification by Coupling a Finite Element Structural Analysis Code With a Gun Interior Ballistics Code." BRL-TR-3269, U.S. Army Ballistic Research Laboratory, Aberdeen Proving Ground, MD, July 1990.
9. Hopkins and Wilkerson. "Modeling of Gun Systems Including Pressurization Effects," poster paper, 14th International Symposium Ballistics, Quebec, Canada, September 1993.
10. Wilkerson, S., and D. Hopkins. "Analysis of a Balanced Breech System for the M1A1 Main Gun System Using Finite Element Techniques." ARL-TR-608, U.S. Army Research Laboratory, Aberdeen Proving Ground, MD, November 1994.
11. Wilkerson, S., V. Fulton, and J. Thiravong. "M256 Static Load Test." ARL-TR-182, U.S. Army Research Laboratory, Aberdeen Proving Ground, MD, August 1992.
12. Wilkerson, S. Unpublished ANSYS Analysis of M256 System. U.S. Army Research Laboratory, Aberdeen Proving Ground, MD, unpublished 1992.
13. Howd, C. "In Process Straightness Measurement of Gun Tubes." WVA-QA-9101, Watervliet Arsenal, Watervliet, NY, August 1991.
14. Wilkerson, S. "A Consistent Method for Determining Gun Tube Straightness on the M256 120-mm Gun." International Symposium on Gun Dynamics, Newport, RI, April 1993.

Warken

**TITLE:** Experimental Investigation of the Influence of Muzzle and Projectile Tail Asymmetries on the Flight and Hit Performance of Spin-Stabilized Projectiles

**Dieter Warken**

Fraunhofer-Institut für Kurzzeitdynamik, Ernst-Mach-Institut

Hauptstrasse 18, D - 79576 Weil am Rhein, Germany

**ABSTRACT:**

The ambitious requirements for a high first round hit probability of guns have been more and more extended by the additional demand for a defined dispersion. Today these stringent requirements are typical for the development of modern gun systems. Asymmetric muzzle and projectile tail geometries are two of several reasons for a non-optimum flight and hit performance of spin-stabilized projectiles. To investigate these effects a 7.62 mm rifled test fixture was used to fire NATO standard ammunition. For the experiments described, the normally small muzzle and projectile asymmetries were enlarged in a well defined way in order to exceed other minor effects. Inclinations of 0° (normal shape), 5°, 10° and 15° were machined at the projectile base and at the muzzle. At muzzle exit time the asymmetries were oriented into different directions. Under these conditions firings were performed separately for muzzle and projectile asymmetries. In addition, also the influence of the combination of both was investigated. The deviation measured for the "worst" combination was more than 3 mrad. For all firings the hit point could be related to the orientation and the amount of the asymmetries.

**BIOGRAPHY:**

Study of physics at the University of Saarbrücken, Germany  
Since 1974 scientist at the Ernst-Mach-Institut, Weil am Rhein

**PRESENT ASSIGNMENT:**

Head of High Velocity Ballistics Group

**PAST EXPERIENCE:**

Transitional, exterior and interior ballistics

**DEGREES HELD:**

Diplom-Physiker (MA)

**Experimental Investigation of the Influence of Muzzle and Projectile Tail Asymmetries  
on the Flight and Hit Performance of Spin-Stabilized Projectiles**

Dieter Warken

Fraunhofer-Institut für Kurzzeiddynamik, Ernst-Mach-Institut  
Hauptstrasse 18, D - 79576 Weil am Rhein, Germany

## INTRODUCTION

The ambitious requirements for a high first round hit probability of guns have been more and more extended by the additional demand for a defined dispersion. Today, these stringent requirements are typical for the development of modern gun systems. If these demands are not achieved this could lead to a rejection of the whole gun system. Therefore, it is necessary for the designer of new weapon systems to know the effects which influence the hit accuracy. Asymmetric muzzle and projectile tail geometries are two of several reasons for a non-optimum flight and hit performance of spin-stabilized projectiles.

Separation of a projectile from its launcher involves not only the termination of mechanical support but also a release of the gas seal which retains the propellant gases [1,2]. Since the initial flow velocities in this field are significantly higher than the projectile launch velocity, the projectile is rapidly engulfed in the muzzle gas flow (Figure 1). The typical blunt body shock standing at the stern of the projectile clearly illustrates that the projectile is being subject to intense gasdynamic loadings. Asymmetric projectile and/or muzzle geometries can cause an amplification of the effects of these loadings experienced by the projectile in passing through the flow which directly and indirectly influences its resultant trajectory. Therefore, it is of interest to examine the nature and the consequences of these loadings.

For the experiments described below, the normally small muzzle and projectile asymmetries were enlarged (cf. Figure 2). The inclination as well as the orientation of the asymmetries were changed for the different firings. Under these conditions tests were performed separately for muzzle and projectile asymmetries. In addition, also the influence of the combination of both cases was investigated. The hit and flight performance was recorded by means of the free flight range equipment.

The flight and hit performance of the projectiles is widely established during the transitional ballistic phase (muzzle exit until muzzle blast leaving). A direct influence on the projectile trajectory is given, for example, by the asymmetric pressure distribution within the muzzle blast. In

addition, the undisturbed flight path is changed indirectly by the stimulation of the angular motion of the projectiles ("aerodynamic jump"). The static and dynamic unbalance of the projectiles, a consequence of the inclined tail geometry (Fig. 3), is an example of a mixture of both direct (static unbalance) and indirect (dynamic unbalance) influence on the hit performance.

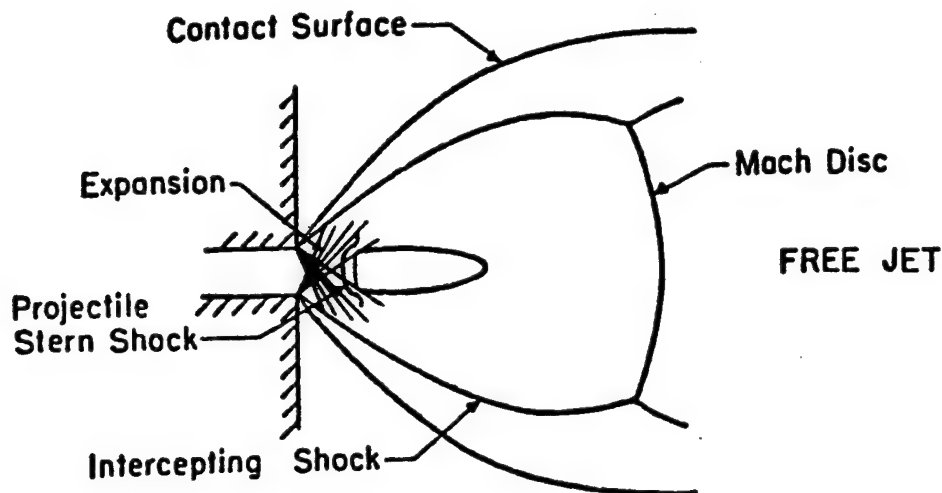


Figure 1 Steady flow model (taken from [1]); propellant gas shock structure

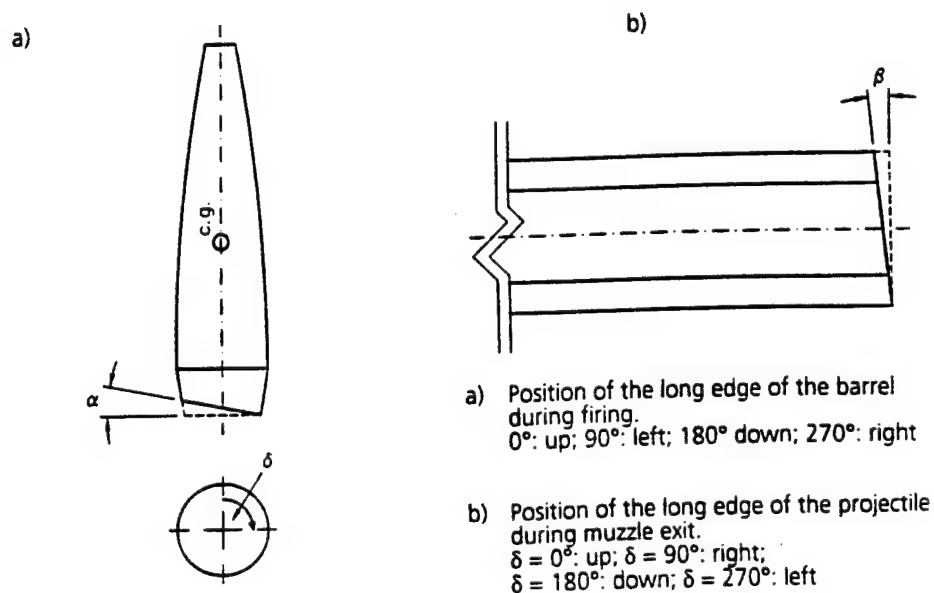


Figure 2 Positions of the long edges of muzzle and projectile during firing

Preceding test firings proved that mutual mechanical gun projectile interactions did not significantly influence the flight and hit performance of the projectiles. The initial velocities were measured to range from 810 m/s to 825 m/s.

For the experiments described the normally small muzzle and projectile asymmetries were enlarged in a well defined way in order to exceed other minor effects (cf. Figure 2). Inclinations of  $0^\circ$  (normal shape),  $5^\circ$ ,  $10^\circ$  and  $15^\circ$  were machined at the projectile base and at the muzzle. At muzzle exit time the asymmetries were oriented into different directions ( $0^\circ$ : up;  $90^\circ$ : right;  $180^\circ$ : down;  $270^\circ$ : left). The projectile fired in these tests is from a 7.62 mm NATO standard ammunition. Physical and aerodynamic properties of such a bullet are summarized below [5]:

$L = 28.9 \text{ mm}$	$I_2 = 56 \text{ g mm}^2$	$C_{M8} = 1.8$
$D = 7.62 \text{ mm}$	$I_t = 445 \text{ g mm}^2$	$s_g = 2.2$
$m_p = 9.45 \text{ g}$	$C_{D0} = 0.3$	$s = 10.7 \text{ mm}$
$v_0 = 820 \text{ m/s}$	$C_{L5} = 2.3$	rifling = 40 cal/rev.

The data of the machined projectiles are presented in Figure 3.

Tests were conducted in the EMI aeroballistic range [3] using the instrumentation shown in Figure 4. Data are taken from ten range stations and an impact card downrange. Each range station takes a set of orthogonal direct spark shadowgraphs of the projectiles and records the time of spark breakdown. Thus, a set of stations may be used to measure projectile position, orientation and direction of motion as a function of time.

The actual aeroballistic testing was conducted in two phases. Phase I only recorded the amount and the orientation of the deviation as a function of the projectile or the muzzle asymmetry. Some shots were fired additionally to demonstrate the combined influence of both. For these tests we only had to evaluate the projectile position in the plane of the impact card downrange related to the aiming point of the gun system.

In phase II we tried to find out the physical reasons for the deviations measured. Therefore, we had to evaluate the free flight data recorded using the free flight range. In normal use, the measured yawing motion of a spin-stabilized projectile is fit by a least squares analysis to the equation of the damped epicycle and used to evaluate aerodynamic coefficients. For the present test data, only the yawing motion of the projectile in the immediate vicinity of the muzzle is of interest. Thus, a simplified data reduction was performed. In particular, the yawing velocity at the muzzle was computed. Comparisons of these data for the various muzzle configurations indicate the effect of gasdynamic loadings due to the presence of asymmetries. In addition, projectile impacts into the yaw card downrange indicate the effect of these muzzle loadings on the mean projectile trajectory.

a)

$\alpha$ [°]	$m_p$ [g]	$\epsilon$ [ $\mu\text{m}$ ]	$\phi$ [mrad]	$s$ [mm]
5	9.35	17	0.6	10.8
10	9.25	27	1.5	11.1
15	9.12	40	2.4	11.5

b)

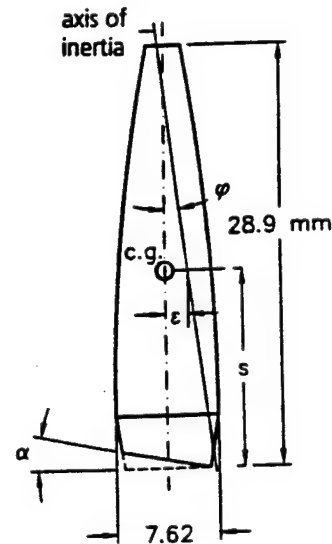


Figure 3 Change of the static ( $\epsilon$ ) and the dynamic ( $\phi$ ) unbalance by varying the inclination  
 a) Projectile data as a function of  $\alpha$ ; b) Schematic drawing of the projectile

## DESCRIPTION OF THE FACILITY

The free flight tests were conducted in the 100 m aeroballistic range of the Ernst-Mach-Institut (EMI) (Figure 4). It is part of the research facilities of the EMI Propulsion Division. This facility is an indoor range used to examine the exterior ballistics performance of various free flight configurations in a caliber range between 5 mm and 40 mm and in a velocity range from 300 m/s up to 3000 m/s [3,4]. It contains a gun room including blast chamber, a control room and the instrumented range. Presently up to 20 direct photo stations are available which can be shifted in the flight direction and replaced or completed by yaw cards, if necessary. Every station yields a set of orthogonal shadowgraphs. Infrared light sensors detect the passage of the projectile separately at all photographic stations and trigger the spark sources. Since the film is illuminated directly, high quality photographs are obtained (Figure 5). The nominal operating conditions of the range are 20 degrees Celsius and standard atmospheric pressure.

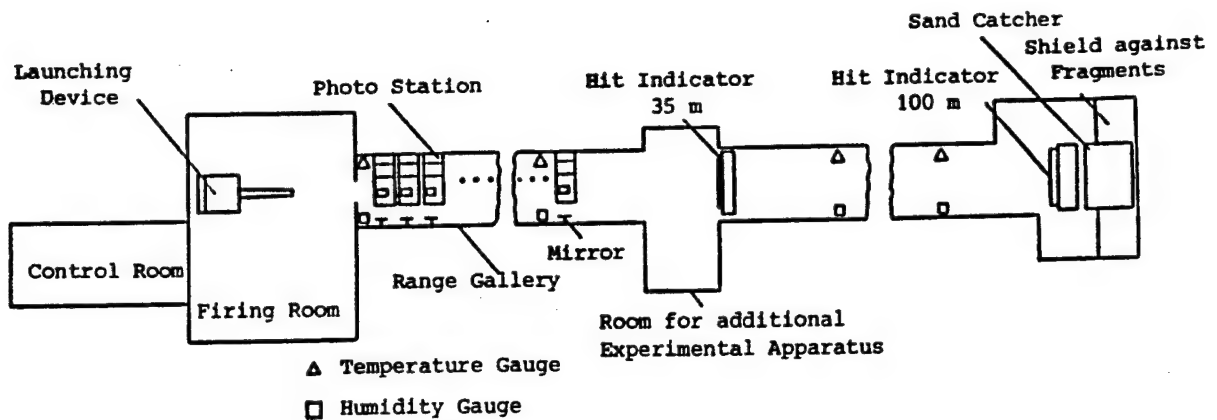


Figure 4 The 100 m free flight aeroballistics range of the Ernst-Mach-Institut

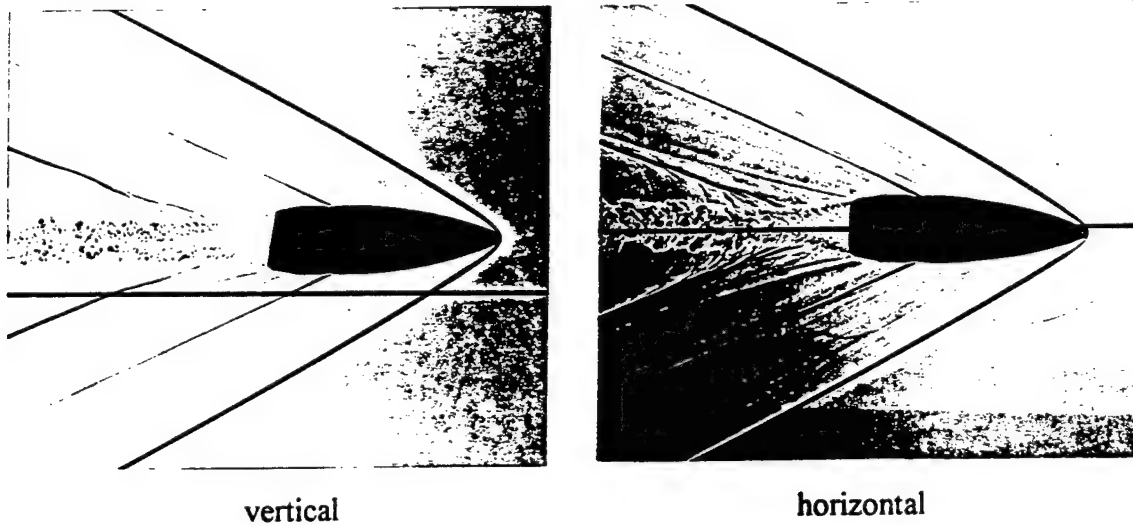


Figure 5 Set of orthogonal direct photographs taken in the free flight range ( $v_0 = 815 \text{ m/s}$ ; 7.62 NATO standard ammunition; machined projectile,  $\alpha = 10^\circ$ )

## EXPERIMENTAL TEST CONDITIONS AND EVALUATION

Since it was planned to carry out fundamental tests to demonstrate the effects mentioned above, a small caliber equipment could be employed in order to save costs. Therefore, a 7.62 rifled test fixture was used to fire NATO standard ammunition.

## EXPERIMENTAL RESULTS AND DISCUSSION

Data are presented in the range coordinate system looking from the breech of the gun downrange. The yaw is also represented in the  $\delta$ - $\psi$ -plane.

In phase I of the investigation we only were interested in the projectile downrange impacts as a function of the muzzle and projectile tail asymmetries. For different muzzle asymmetries ( $\beta = 5^\circ; 10^\circ; 15^\circ$  - Fig. 2) Figure 6 indicates the deviations measured at a distance of 100 m for different orientations of the muzzle inclination ( $0^\circ; 90^\circ; 180^\circ; 270^\circ$  - Fig. 2). The deviations of the averaged impact data from three shots were directed right to the plane of inclination.

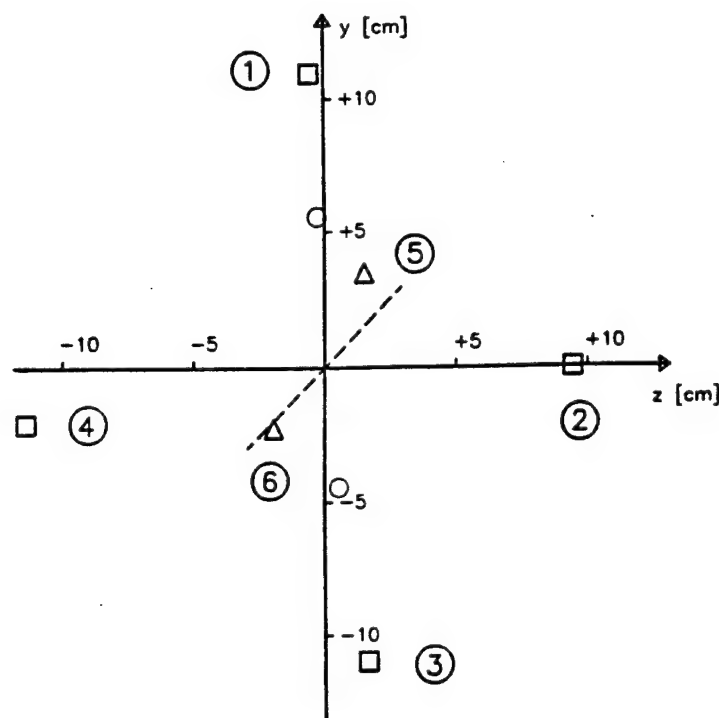


Figure 6 Yaw card impacts (averaged impact data from three shots) 100 m from the muzzle. Standard ammunition without asymmetry. Variation of muzzle inclination and orientation of muzzle inclination.  $\Delta$ :  $\beta = 5^\circ$ ;  $O$ :  $\beta = 10^\circ$ ;  $\square$ :  $\beta = 15^\circ$   
Orientation of muzzle inclination (Fig. 2):  
1:  $180^\circ$ ; 2:  $270^\circ$ ; 3:  $0^\circ$ ; 4:  $90^\circ$ ; 5:  $225^\circ$ ; 6:  $45^\circ$

For the next series of firings within phase I we only changed the projectile tail asymmetry ( $\alpha = 5^\circ; 10^\circ; 15^\circ$  - Fig. 2) and the orientation of this asymmetry at muzzle exit ( $0^\circ; 90^\circ; 180^\circ; 270^\circ$  - Fig. 2). The averaged impact values are given in Figure 7. Again, the amount of the deviations did grow with the angle of the inclination, but the direction of the deviation was no longer directed

right to the projectile tail inclination. There was an additional clockwise angular rotation which nearly was equal for all impact values. This will be discussed together with the results obtained in phase II.

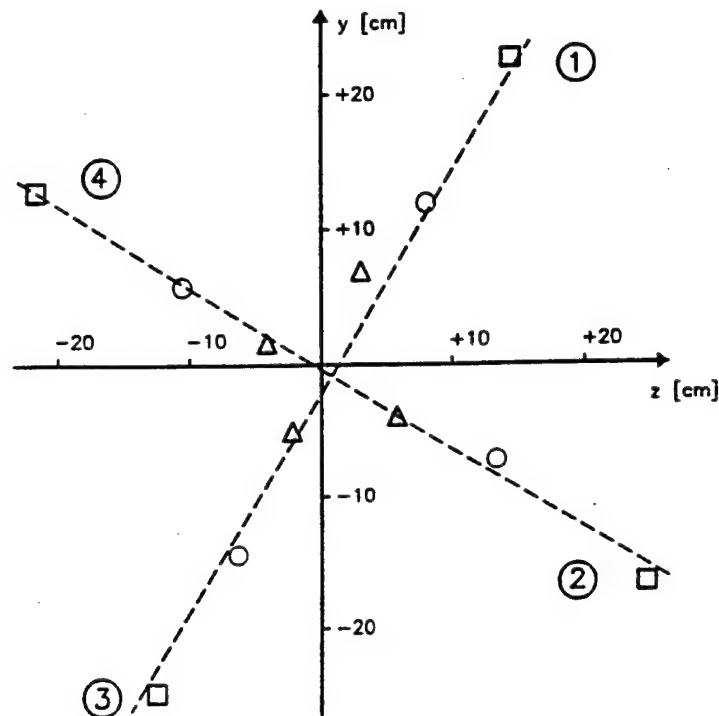


Figure 7 Yaw card impacts (averaged impact data from three shots) 100 m from the muzzle. Muzzle without asymmetry. Variation of projectile tail inclination and orientation of the inclination at muzzle exit.  $\Delta$ :  $\alpha = 5^\circ$ ;  $O$ :  $\alpha = 10^\circ$ ;  $\square$ :  $\alpha = 15^\circ$   
Orientation of muzzle inclination (Fig. 2): 1:  $0^\circ$ ; 2:  $90^\circ$ ; 3:  $180^\circ$ ; 4:  $270^\circ$

For eight additional single shots we combined muzzle and projectile asymmetries. These firings demonstrated that the amount  $|a|$  as well as the orientation  $\gamma$  of the impact data reported above nearly add independently. Figure 8 shows the result of four of these single firings.

Evaluating the phase II firings we tried to get information about the physical reasons for the deviations measured in phase I. Assuming that for our test conditions mechanical as well as direct gasdynamic loadings do not affect significantly the projectile motion it seemed to be reasonable that the deviations caused by the aerodynamic jump [6] and the static unbalance [7] could explain the hit and flight performance of the projectiles.

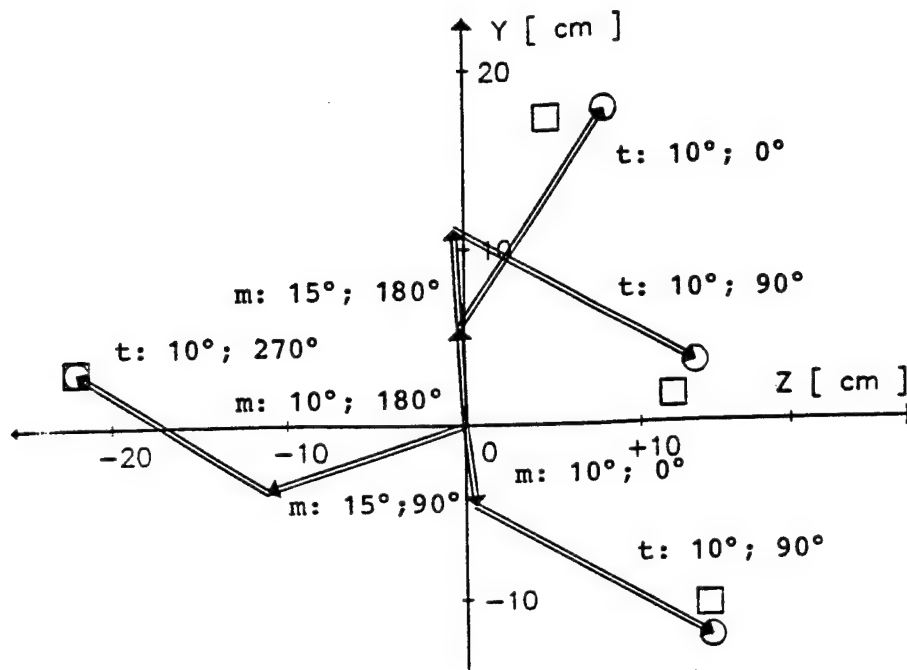


Figure 8 Comparison of single shot impacts  $\square$  (muzzle (m) and tail (t) asymmetries) with the vectorial addition of the data recorded separately for muzzle and projectile tail asymmetries (see also Figures 6 and 7)

Employing the free flight range photo stations we recorded in seven single shots the down-range yawing motion of the projectiles and determined the angular velocity at the muzzle by extrapolation. Using equation (1)

$$I_A = - \frac{I_t}{m_P D \cdot v} \cdot \frac{C_{L_\alpha}}{C_{M_\alpha}} \cdot \dot{\delta}_0 \quad (1)$$

we could calculate the aerodynamic jump deflection caused by the angular motion of the projectile in the free flight phase [6]. Equation (2) gives the relation between the static unbalance of the machined projectiles ( $\epsilon$ ) (see also Figure 3) and the deviation [7].

$$\delta^*_{stat} = \frac{\omega_0 \cdot \epsilon}{v_0} \quad (2)$$

This part of the total deflection is responsible for the clockwise impact rotation shown in Figure 7. The consequence of the dynamic unbalance ( $\varphi$ ) concerning the projectile impact is given in formula (3) [7].

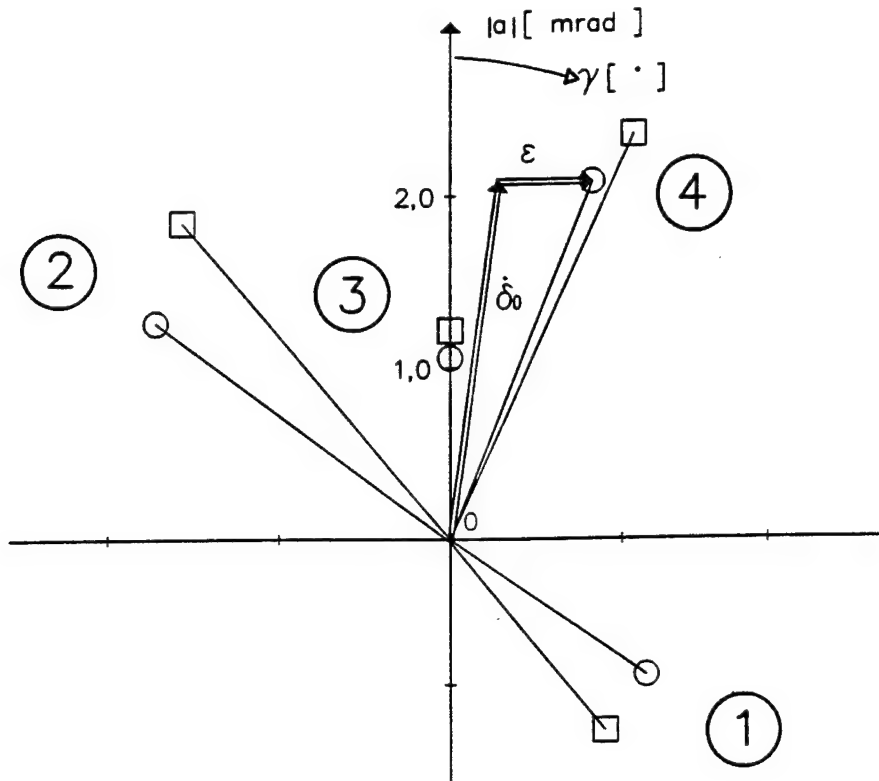
$$\delta_{\text{stat}}^* = -\frac{C_{L\delta}}{C_{M\delta}} \frac{I_t}{m_P D v_0} \dot{\delta}_0 + i \frac{C_{L\delta}}{C_{M\delta}} \cdot \frac{I_a \omega_0}{m_P D v_0} \delta_0 \quad (3)$$

For a new barrel the initial angle of attack  $\delta_0$  within the barrel is assumed to be zero. Therefore, the second term of equation (3) can be neglected. Since the dynamic unbalance part of the total deviation is already included in the evaluated free flight data we can confine to the aerodynamic jump and the static unbalance as explanation of the projectile deviation.

Figure 9 shows for four shots a comparison between the experimental impact data and the computed ( $I_A + \delta_{\text{stat}}^*$ ) values. For shot number 4 ( $\alpha = 10^\circ$ , orientation  $0^\circ$ ;  $\beta = 10^\circ$ , orientation  $180^\circ$ ) the aerodynamic jump part ( $\dot{\delta}_0$ ) and the static unbalance part ( $\epsilon$ ) are specified. In this case the values of  $\epsilon$  and  $\dot{\delta}_0$  are  $27 \mu\text{m}$  and  $218 \text{ rad/s}$ . For the other six shots the data are given in Table 1. The agreement between the calculated the measured impact data is good.

Table 1. Comparison of computed and experimental hit points for seven single shots (computation includes aerodynamic jump and static unbalance effects).  
See also Figure 9

Shot No.		a  [mrad] exp.	a  [mrad] theory	$\gamma$ [°] exp.	$\gamma$ [°] theory
1	$\alpha = 10^\circ; 90^\circ$ $\beta = 0^\circ$	1.41	1.40	141	124
2	$\alpha = 15^\circ; 270^\circ$ $\beta = 0^\circ$	2.39	2.11	321	306
3	$\alpha = 0^\circ$ $\beta = 10^\circ; 180^\circ$	1.19	1.04	0	0
	$\alpha = 0^\circ$ $\beta = 15^\circ; 180^\circ$	2.37	1.88	0	0
4	$\alpha = 10^\circ; 0^\circ$ $\beta = 10^\circ; 180^\circ$	2.54	2.35	24	20
	$\alpha = 10^\circ; 180^\circ$ $\beta = 15^\circ; 180^\circ$	1.76	1.34	317	309
	$\alpha = 10^\circ; 90^\circ$ $\beta = 15^\circ; 180^\circ$	1.48	1.54	39	44



- Experiment  
 ○ Computation: - aerodynamic jump,  $\dot{\delta}_0$   
                   - static unbalance,  $\epsilon$

- |   |   |
|---|---|
| ① $\alpha = 10^\circ, 90^\circ$<br>$\beta = 0^\circ$  | ② $\alpha = 15^\circ, 270^\circ$<br>$\beta = 0^\circ$           |
| ③ $\alpha = 0^\circ$<br>$\beta = 10^\circ, 180^\circ$ | ④ $\alpha = 10^\circ, 0^\circ$<br>$\beta = 10^\circ, 180^\circ$ |

Figure 9 Comparison of computed and experimental impact data of four different shots

## CONCLUSION

An experimental program was designed which permits variations in projectile trajectory due to muzzle and/or projectile asymmetries. Neglecting other minor effects aerodynamic jump and static unbalance deflections could explain the projectile impact data concerning the amount and the orientation of the deflections. The resulting comparison of experimental and computed data provides insight into the gasdynamic effects which influence the projectile motion in presence of muzzle and/or projectile tail asymmetries.

## LIST OF SYMBOLS

$ a $	Deviation
$b$	Outer barrel diameter at the muzzle
$C_{D0}$	Drag coefficient at zero angle of attack
$C_{L\delta}$	Lift force coefficients
$C_{M\delta}$	Static moment coefficient
$D$	Caliber
$I_A$	Aerodynamic jump
$I_x$	Axial moment of inertia
$I_t$	Transverse moment of inertia
$L$	Projectile length
$M$	Mach number
$m_p$	Projectile mass
$s$	Center of gravity distance to the projectile stern
$s_g$	Gyroscopic stability factor
$v_0$	Muzzle velocity
$x, y, z$	Coordinates
$\alpha$	Angle of projectile tail inclination
$\beta$	Angle of muzzle inclination
$\gamma$	Orientation of the deviation
$\delta$	Angle of attack
$\dot{\delta}_0$	Angular velocity at muzzle exit
$\delta^*_{stat}$	Deviation caused by a static unbalance
$\epsilon$	Eccentricity - static unbalance
$\varphi$	Axis of inertia orientation
$\omega_0$	Spin rate at the muzzle
$\psi$	Angle of precession

## ACKNOWLEDGEMENT

The author gratefully acknowledges the assistance of Mr. H. Hänßler (EMI) who prepared the tests and installed the measuring technique. Together with Mr. E. Prange he also carried out the experiments thoroughly. I also thank Mrs. E. Messner for preparing the manuscript.

## LITERATURE

- [1] E. M. Schmidt  
The Effect of Muzzle Jet Asymmetry on Projectile Motion  
AIAA Mechanics and Control of Flight Conference, Anaheim, CA, USA, August 1974

## Warken

- [2] E. M. Schmidt, D. D. Shear  
The Flow Field About the Muzzle of an M-16 Rifle  
U. S. Army Ballistic Research Laboratory, APG, MD, BRL Report 1692, January 1974
- [3] D. Warken, H. Hänßler  
Die 100-m-Freifluganlage des Ernst-Mach-Instituts  
Fraunhofer-Institut für Kurzzzeitdynamik, Ernst-Mach-Institut, Weil am Rhein, EMI-Bericht 7/82, 1983
- [4] D. Warken  
Beschußversuche mit Modellprojektilen im Kaliber 40 mm,  $L/D = 30$ ,  $v_0 = 2500$  m/s  
Fraunhofer-Institut für Kurzzzeitdynamik, Ernst-Mach-Institut, Weil am Rhein, EMI-Bericht E 14/95, 1995
- [5] W. F. Braun  
Aerodynamic Data for Small Arms Projectiles  
U. S. Army Ballistic Research Laboratory, APG, MD, BRL Report 1630, January 1973
- [6] C. H. Murphy  
Free Flight Motion of Symmetric Missiles  
U. S. Army Ballistic Research Laboratory, APG, MD, BRL Report 1216, July 1963
- [7] D. Warken  
Einfluß der Unwucht drallstabilisierter Geschosse auf die Trefferlage  
Fraunhofer-Institut für Kurzzzeitdynamik, Ernst-Mach-Institut, Weil am Rhein, EMI-Bericht 6/81, 1981

DILLON

**TITLE: Comparison of Computed and Measured Flight Characteristics of Fin Stabilized Projectiles**

Robert E. Dillon, Jr., Associate Professor  
Department of Mechanical Engineering  
Rose-Hulman Institute of Technology  
Terre Haute, Indiana

**ABSTRACT:**

A six degree of freedom exterior ballistic code (BANG) was used to model the flight dynamics of 120mm fin stabilized hypervelocity projectiles. The code was used to predict the flight characteristics and impact of the 120mm M866 projectile. These predictions were then compared with corresponding data from actual firing tests. For the impact prediction study, the initial conditions at the muzzle were determined from the gun dynamics code, LITTLE RASCAL. No sabot discard contribution to projectile jump was studied in this work. The current study found the projectile aerodynamic coefficients were very sensitive to predicting the flight characteristics of the projectile, especially in the vicinity of the muzzle. BANG was able to predict the flight of the projectile with good results and predict the impact of the M866 projectile to within 0.52 and 0.4 milliradians of actual impact measurements for tubes 85 and 104, respectively.

**BIOGRAPHY:**

**PRESENT ASSIGNMENT:** Associate Professor of Mechanical Engineering

**PAST EXPERIENCE:** Armor Officer 21 years, world-wide experiences; R&D Coordinator, Benet Weapons Laboratory; Associate Professor, US Military Academy.

**DEGREES HELD:** BS, US Military Academy, West Point, NY, 1975; M. Eng. (Aero), Rensselaer Polytechnic Institute, Troy, NY, 1981; Ph.D., (Aero), Rensselaer Polytechnic Institute, Troy, NY, 1983.

## Comparison of Computed and Measured Flight Characteristics of Fin Stabilized Projectiles

R. E. Dillon, Jr.

Rose-Hulman Institute of Technology  
Terre Haute, Indiana 47803-3999Abstract

A six degree of freedom exterior ballistic code (BANG) was used to model the flight dynamics of 120mm fin stabilized hypervelocity projectiles. The code was used to predict the flight characteristics and impact of the 120mm M866 projectile. These predictions were then compared with corresponding data from actual firing tests. For the impact prediction study, the initial conditions at the muzzle were determined from the gun dynamics code, LITTLE RASCAL. No sabot discard contribution to projectile jump was studied in this work. The current study found the projectile aerodynamic coefficients were very sensitive to predicting the flight characteristics of the projectile, especially in the vicinity of the muzzle. BANG was able to predict the flight of the projectile with good results and predict the impact of the M866 projectile to within 0.52 and 0.4 milliradians of actual impact measurements for tubes 85 and 104, respectively.

Introduction

The need for greater accuracy in tank main guns has dictated greater emphasis be placed on, among other things, the flight dynamics of fin stabilized projectiles. These hypervelocity projectiles, fired out of conventional cannons, follow a ballistic trajectory that is strongly influenced by the conditions at the muzzle at the start of flight. Currently there are large efforts to quantify the influence of each parameter on the overall accuracy of a particular gun/ammunition combination. This present work presents an alternative method to the existing exterior ballistic repertoire to study the dynamic behavior of hypervelocity projectiles.

The goal of this present study is to predict the strike of a hypervelocity discarding sabot projectile on target. In order to do this, all sources of error associated with the launch and flight of the projectile must be accounted for. Much study has been done in the past to determine the sources of error and the importance of each (references 1-8). The importance

of understanding the sources of error is critical when one attempts to hit a target at ranges of 3000 meters. The launch process consists of a sequence of coupled mechanical and gasdynamic interactions leading up to free flight of the projectile. The different codes used to describe each process were first coupled by reference 15.

The projectile in this present study is a rigid metal rod with fins. It is held in the gun bore by three sabot petals which are discarded after the projectile clears the muzzle. Since the gun tube is not straight due to manufacturing tolerances, the gun and projectile experience large lateral forces as the projectile is accelerated down this bent tube. These lateral forces cause the muzzle of the gun to move from its initial position by the time the projectile reaches the muzzle. At the muzzle, the gun is pointing away from the initial aim point, it is moving with some velocity in the vertical and horizontal planes, and the projectile has some initial yaw and yaw rate. The sabot petals, once clear of the muzzle experience some elastic decompression due to the large spring factors they possess being released from the compressing force of the gun tube. Depending on the design of the projectile, the sabot will have three or four petals. Ideally these will all clear the muzzle, rotate away from the subprojectile, pick up large aerodynamic drag due to their large angles of attack and fall away from the subprojectile in a symmetrical manner.

Since the gun tube is not straight and consequently the projectile has initial yaw angles and velocities as well as the sabot petals having an asymmetrical discard pattern, the ideal launch of the projectile is rarely, if ever, seen. The asymmetric discard of the sabot petals places large asymmetric forces on the subprojectile which further adds to the difficulty of predicting impact.

The inbore dynamics have been estimated with LITTLE RASCAL, ref. 10 and SHOGUN, refs. 11 and 12. The muzzle blast loading has been calculated analytically, ref. 13, and the Sabot discard has been calculated, ref. 14. The existing works in the literature have calculated the trajectory analytically ref. 15. This present work uses the gun

dynamics code, LITTLE RASCAL, ref. 10, to calculate the muzzle conditions of the projectile and these conditions are then used in the exterior ballistic code, BANG, ref. 9, to calculate the trajectory from the muzzle to the target. These calculated results are compared with the experimental results of two gun tubes reported in reference 15.

### Theoretical Development

A body-fixed reference frame was chosen for this study since the dynamic behavior of the vehicle is the main object of study. Since body axes have played an important role in flight dynamics, the traditional notation associated with them is used here, ref. 16-18. The equations of motion for a rigid body in free flight are developed using a body-fixed coordinate system, figure 1. The origin of the body axes is the vehicle center of mass, C. The angular velocity of the body relative to an inertial frame is  $\omega$  ( $p, q, r$ ) and the components of the velocity,  $V$  are ( $u, v, w$ ).

The earth is treated as flat and non-rotating in this study since the time of flight for these vehicles is on the order of 1 second. Thus, the earth's surface can be considered an inertial reference frame. In order to describe the orientation of the body-fixed coordinate system relative to an earth bound observer, we must define three angles,  $\psi, \theta, \phi$  which are the consecutive rotations about the axes,  $z, y, x$ . These are the Euler angles.

In order to properly account for the yaw of the projectile with respect to the relative wind, two aerodynamic angles must be defined. The *angle of attack*,  $\alpha$ , is the angle between the vehicle and the relative wind. The *angle of inclination*,  $\beta$ , is the inclination of the plane containing the relative wind vector. Now the equations of motion can be developed using this coordinate system.

### Equations of Motion in Body Axes

The aerodynamic force in body axes is denoted as  $[X, Y, Z]$ . The scalar equations can then be written as

$$\begin{aligned} X - mg \sin \theta &= m[u' + qw - rv] \\ Y + mg \cos \theta \sin \phi &= m[v' + ru - pw] \\ Z + mg \cos \theta \cos \phi &= m[w' + pv - qu] \end{aligned} \quad (1)$$

The projectiles being considered here are essentially bodies of revolution (with the exception of the fins of course) so the simplest form of the moment equations is

$$\begin{aligned} L &= I_x p' \\ M &= Iq' - (I - I_x)rp \\ N &= Ir' - (I_x - I)pq \end{aligned} \quad (2)$$

The Euler angular rates then become

$$\begin{aligned} \phi' &= p + q \sin \phi \tan \theta + r \cos \phi \tan \theta \\ \theta' &= q \cos \phi - r \sin \phi \\ \psi' &= q \sin \phi \sec \theta + r \cos \phi \sec \theta \end{aligned} \quad (3)$$

The position of the vehicle relative to the earth can now be given by

$$\begin{aligned} x'_E &= u \cos \theta \cos \psi + v(\sin \phi \sin \theta \cos \psi - \cos \phi \sin \psi) \\ &\quad + w(\cos \phi \sin \theta \cos \psi + \sin \phi \sin \psi) \\ y'_E &= u \cos \theta \sin \psi + v(\sin \phi \sin \theta \sin \psi + \cos \phi \cos \psi) \\ &\quad + w(\cos \phi \sin \theta \sin \psi - \sin \phi \cos \psi) \\ z'_E &= +u \sin \theta - v \sin \phi \cos \theta - w \cos \phi \cos \theta \end{aligned} \quad (4)$$

The aerodynamic forces used in equation 1 are given by

$$\begin{aligned} X &= -\frac{\rho V_\infty^2 A}{2} [C_x + C_{x2} \alpha^2] \\ Y &= -\frac{\rho V_\infty^2 A}{2} C_{na} \frac{v}{V_\infty} \\ Z &= -\frac{\rho V_\infty^2 A}{2} C_{na} \frac{w}{V_\infty} \end{aligned} \quad (5)$$

The moments used in equation 2 are given by

$$\begin{aligned}
 L &= \frac{\rho V_\infty^2 AD}{2} \left[ C_{l_{dd}} + \frac{pD}{2V_\infty} C_{lp} \right] \\
 M &= \frac{\rho V_\infty^2 AD}{2} \left[ C_{ma} \frac{w}{V_\infty} + \frac{qD}{2V_\infty} C_{mq} \right] \\
 N &= \frac{\rho V_\infty^2 AD}{2} \left[ -C_{ma} \frac{v}{V_\infty} + \frac{rD}{2V_\infty} C_{mq} \right]
 \end{aligned} \quad (6)$$

The aerodynamic coefficients were obtained from ref. 19 and vary with Mach number and angle of attack. For this present work the coefficients used are the axial force coefficients,  $C_x$  and  $C_{x2}$ ; the normal force coefficient,  $C_{na}$ ; the spin producing coefficient,  $C_{l_{dd}}$ ; the spin damping coefficient,  $C_{lp}$ ; the yaw moment coefficient,  $C_{ma}$ ; and the yaw damping coefficient,  $C_{mq}$ .

The magnitude of the relative wind velocity in the body reference frame is

$$V_\infty = \sqrt{u^2 + v^2 + w^2} \quad (7)$$

The angle of attack,  $\alpha$ , and the angle of inclination,  $\beta$ , are given by

$$\begin{aligned}
 \alpha &= \arctan\left(\frac{\sqrt{w^2 + v^2}}{u}\right) \\
 \beta &= \arcsin\left(\frac{w}{V_\infty}\right)
 \end{aligned} \quad (8)$$

With these equations, the motion of the vehicle in flight can be modeled.

### Numerical Results

#### Comparison Between Experiment and Predictions

##### Flight Characteristics

The first objective of this present study was to compare the predicted flight characteristics of the projectile to those obtained from firing tests. To this end Dr. Plostins, ref. 20, provided valuable data from the firing test of the projectile modeled in this present study. The initial conditions for BANG were

set to the initial conditions observed in the firing tests and the results compared. Table 1 shows the initial projectile conditions for the flight characteristics comparison. The projectile in the firing tests was observed to have a much higher frequency of oscillation in both yaw and pitch. Subsequent examination of the aerodynamic coefficients obtained from the firing tests could have accounted for the observed differences. BANG was then used with the initial conditions of the firing test as well as the experimentally observed values for the aerodynamic coefficients. The results are seen in figures 2a-c. In figure 2a the total angle of attack is seen as a function of the downrange distance. The results agree fairly well with the projectile showing a slightly higher pitch rate than that predicted by the code. Figure 2b shows the Euler pitch angle vs. downrange distance. The greatest discrepancy is seen here. Again the magnitude of the pitch angle is predicted fairly well but the pitch rate is under predicted. Figure 2c shows the Euler yaw angle which is good agreement with the data of reference 20. For longer range flights, the calculations were extended to a target 985 meters downrange. The motion of the projectile calculated by BANG is shown in figures 3 and 4. Figure 3 shows the three Euler angular rates, while figure 4 shows the angle of attack along with the Euler pitch and yaw angles. The initially high displacements and rates characteristic of launch are seen along with their subsequent aerodynamic damping. With these results a prediction of the impact by two gun using the predicted values of the muzzle conditions will be attempted.

##### Impact Prediction

LITTLE RASCAL was set up for the 120mm, M256 system firing the M866 projectile through tubes 85 and 104. Earlier works have demonstrated the validity of LITTLE RASCAL in predicting gun tube motion, ref. 15. Table 2 shows the launch properties predicted by LITTLE RASCAL.

The center of impact of all the rounds fired from tubes 85 and 104 are presented in Table 3 along with the predictions of LITTLE RASCAL and BANG.

Figure 5 presents these results graphically which shows the predictions close to the center of impact locations. For tube 85 the predictions were within 0.52 milliradians of the center of impact. This is seen as good agreement since the dispersion of this type of ammunition is accepted as about 0.3 milliradians. For tube 104 the results were slightly

better and were much better than the analytical predictions of ref. 10. The predictions for tube 104 were within 0.4 milliradians of the center of impact measurement.

A detailed closure diagram representative of this round is shown in figure 6. The largest single source of error is the muzzle pointing angle with the projectile yaw angles, and projectile yaw rates causing lesser effects. The work of reference 15 showed that for the projectile types and velocities here the effect of muzzle blast on accuracy is negligible.

#### Summary and Conclusions

A method for predicting the strike of fin stabilized discarding sabot ammunition is presented along with a comparison between predicted and measured flight characteristics and the strike of a

120mm fin stabilized discarding sabot projectile. The aerodynamic coefficients were found to strongly influence any efforts at predicting the flight performance of these projectiles. The LITTLE RASCAL/BANG combination predicted the strike of the M866 projectile with good results.

A better estimate of the impact point could be made by incorporating the sabot discard in BANG. This would allow the sabot discard aerodynamics to be directly coupled to the six degree of freedom exterior ballistic code, presumably yielding more accurate results.

The LITTLE RASCAL/BANG code combination shows a very good ability to treat the different gun tubes used in this study. Further use with different tubes would strengthen this assertion. Finally, it appears feasible and very attractive to use the approach presented here to create a virtual zero for every tank in the inventory.

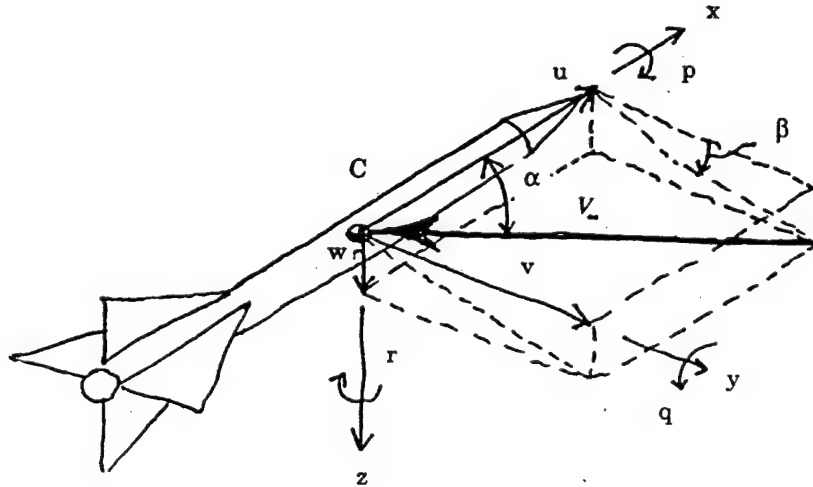


Figure 1. Body Axis Coordinate System used in BANG.

Table 1. Initial Conditions from Firing Test

	Azimuth	Elevation
Projectile Yaw Angle (milliradians)	5.74	8.26
Projectile Yaw Rate (rad/s)	8.62	1.65

Table 2. LITTLE RASCAL Predicted Launch Properties

Muzzle Pointing Angle (milliradians)	Azimuth	Elevation
Tube 85	-0.289	0.752
Tube 104	-0.104	0.643
Projectile Yaw Angle (milliradians)		
Tube 85	-1.08	0.641
Tube 104	-0.264	1.07
Projectile Angular Rate (rad/s)		
Tube 85	-0.504	0.843
Tube 104	0.149	-0.331

Table 3. Comparison of Predicted and Measured Impacts

	RASCAL BANG		Center of Impact	
	Azimuth	Elevation	Azimuth	Elevation
Tube 85	-1.05	0.66	-1.42	0.30
Tube 104	-0.29	1.17	-0.66	1.32

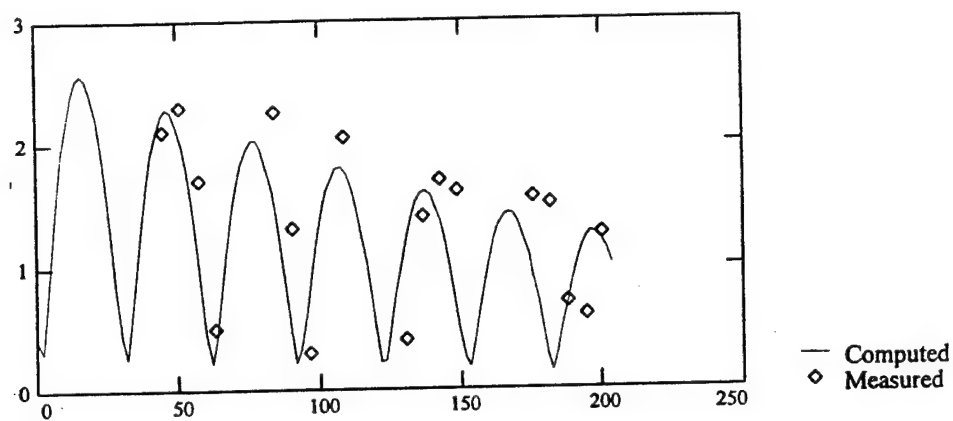


Figure 2a.  $\alpha(\text{deg})$  versus  $x(\text{m})$ .

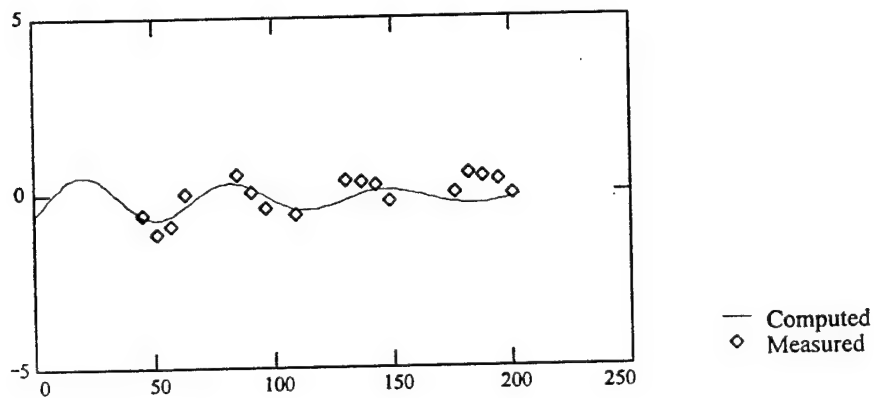


Figure 2b.  $\theta(\text{deg})$  versus  $x(\text{m})$ .

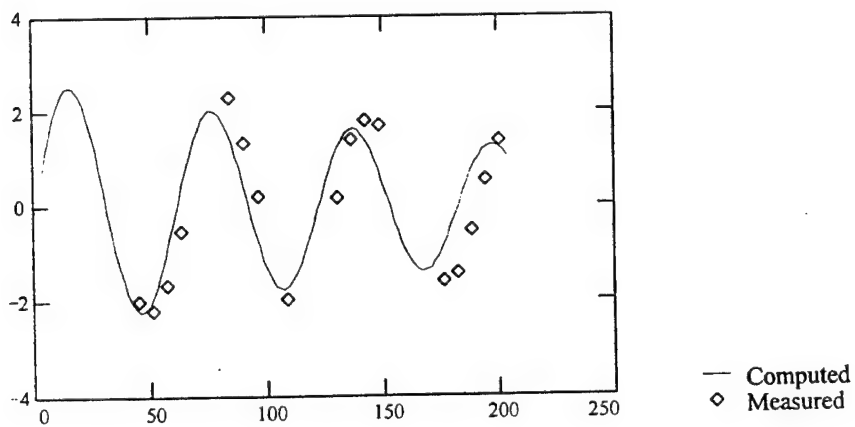


Figure 2c.  $\psi(\text{deg})$  versus  $x(\text{m})$ .

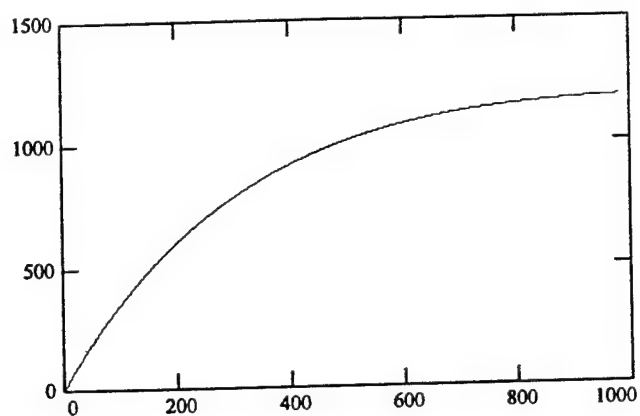


Figure 3a.  $p$ (rad/s) versus  $x$ (m).

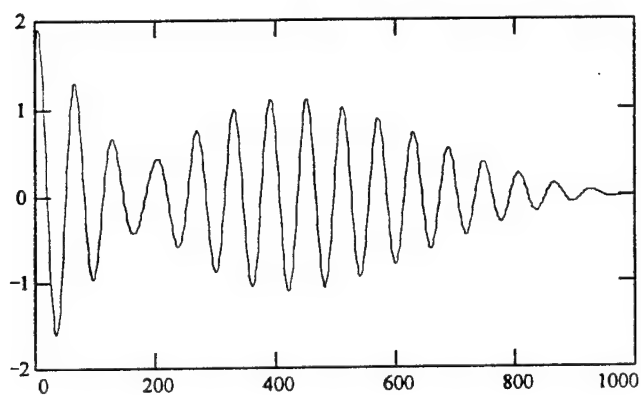


Figure 3b.  $q$ (rad/s) versus  $x$ (m).

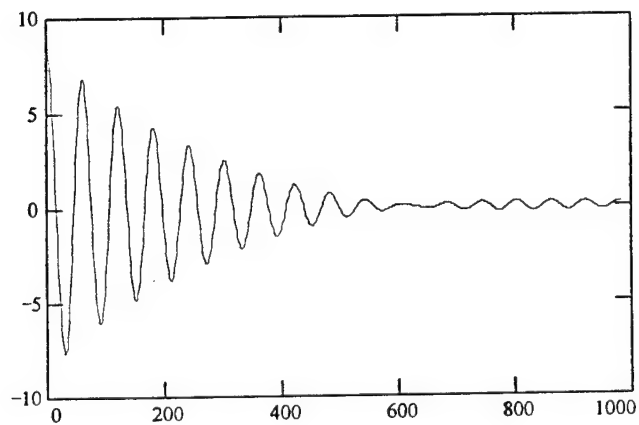


Figure 3c.  $r$ (rad/s) versus  $x$ (m).

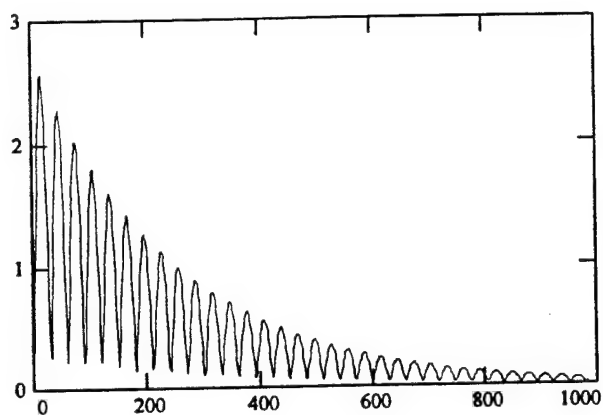


Figure 4a.  $\alpha(\text{deg})$  versus  $x(\text{m})$ .

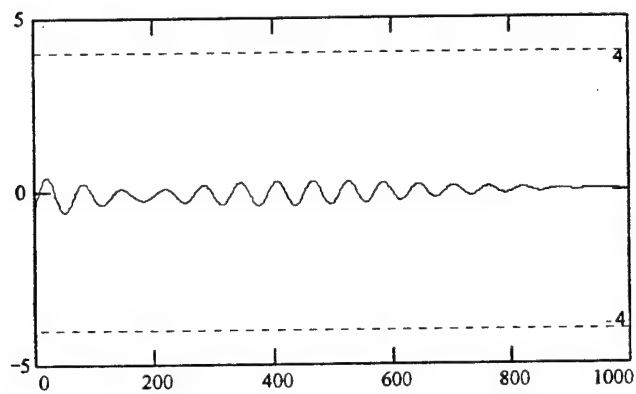


Figure 4b.  $\theta(\text{deg})$  versus  $x(\text{m})$ .

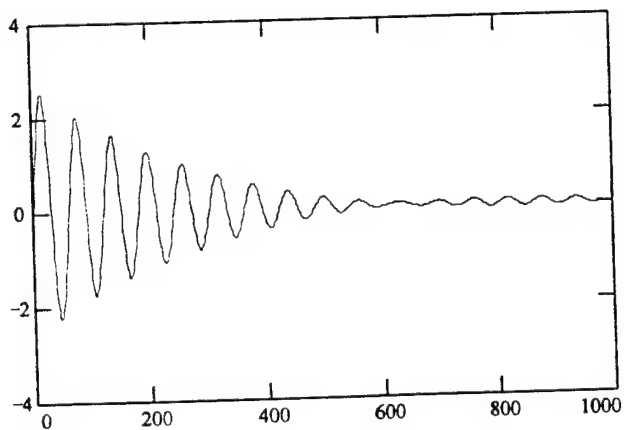


Figure 4c.  $\psi(\text{deg})$  versus  $x(\text{m})$ .

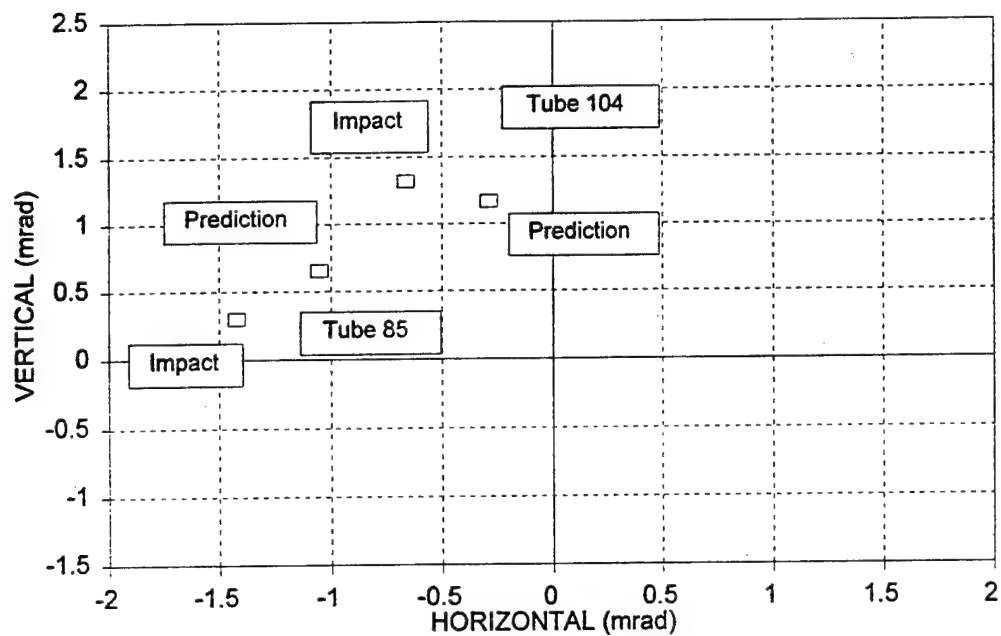


Figure 5. Comparison of measured and predicted impacts.

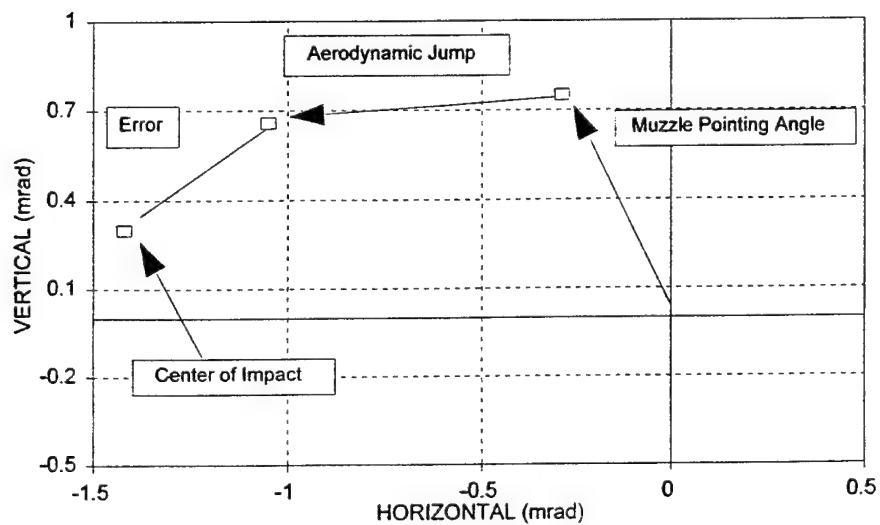


Figure 6. Error closure diagram, Tube 85.

## References

1. Gay, H. P., and Elder, A. S., "The Lateral Motion of a Tank Gun and Its Effect on the Accuracy of Fire," US Army Ballistic Research Lab., BRL Rept. 1070, Aberdeen Proving Ground, MD, March, 1959.
2. Murphy, C. H., "Free Flight Motion of Symmetric Missiles," U.S. Army Ballistic Research Lab., BRL Rept. 1216, Aberdeen Proving Ground, MD, July 1963.
3. Lieske, R. F., and McCoy, R. L., "Equations of Motion of a Rigid Projectile," U.S. Army Ballistic Research Lab., BRL Rept. 1244, Aberdeen, MD, March 1964.
4. Lieske, R. F., and Reiter, M. L., "Equations of Motion for a Modified Point Mass Trajectory," U.S. Army Ballistic Research Lab., BRL Rept. 1314, Aberdeen Proving Ground, MD, March, 1966.
5. Schmidt, E. M., "Disturbance to the Launch of Fin Stabilized Projectiles," Journal of Spacecraft and Rockets, Vol. 19, No. 1, Jan-Feb, 1982, 30.
6. Plostins, P., Celmins, I., and Bornstein, J., "The Effect of Sabot Front Borerider Stiffness on the Launch Dynamics of Fin-Stabilized Kinetic Energy Ammunition," AIAA Paper presented at the 28th Aerospace Sciences Meeting, Reno, NV, Jan. 8-11, 1990.
7. Bornstein, J., Celmins, I., Plostins, P., and Schmidt, E., "Launch Dynamics of Fin-Stabilized Projectiles," Journal of Spacecraft and Rockets, Vol. 29, No. 2, March-April, 1992, 166-172.
8. Plostins, P., Bornstein, J., and Celmins, I., "The Effect of Sabot Wheelbase and Position on the Launch Dynamics of Fin-Stabilized Kinetic Energy Ammunition," AIAA Paper 92-0648 presented at the 30th Aerospace Sciences Meeting and Exhibit, Reno, NV, Jan 6-9, 1992.
9. Dillon, R. E., "Flight Dynamics of Fin Stabilized Projectiles," AIAA Paper 96-0458 presented at the 34th Aerospace sciences Meeting, Jan 15-18, 1996, Reno, NV.
10. Erline, T. F., "Flexible Projectile Modeling Using the LITTLE RASCAL Gun Dynamics Program," 6th U. S. Army Symposium on Gun Dynamics, Tamiment, PA, 14-17 May 1990.
11. Hopkins, D., "Modeling Gun Dynamics with Three-Dimensional Beam Elements," 6th U. S. Army Symposium on Gun Dynamics, Tamiment, PA, 14-17 May 1990.
12. Soifer, M., and Becker, R., "Dynacode-G/P and its Application to the 120mm Tank Gun," 5th U.S. Army Symposium on Gun Dynamics, Rensselaerville, NY, 23-25 September, 1987.
13. Schmidt, E., and Fansler, K., "Trajectory Perturbations of Fin-Stabilized Projectiles due to Muzzle Blast," Journal of Spacecraft and Rockets, Vol. 14, No. 6, June 1977, 339-344.
14. Siegelman, D., Wang, J., and Crimi, P., "Computation of Sabot Discard," CR-00450, Ballistic Research Lab., Aberdeen Proving Ground, MD, February, 1983.
15. Lyon, D. H., Savick, D. S., and Schmidt, E. M., "Comparison of Computed and Measured Jump of 120mm Cannon", AIAA Paper 91-2898-CP.
16. Etkin, Bernard, *Dynamics of Atmospheric Flight*, New York: John Wiley & Sons, Inc. 1972, pp 109-10.
17. Costello, M., Private communication, West Point, New York, 1994.
18. Dillon, R. E., "120mm Projectile Response to Launch Conditions," AIAA Paper 95-3430 presented at the Atmospheric Flight Mechanics Conference, Aug 5-8, 1995, Baltimore, MD.
19. Plostins, P., Private Communication, West Point, New York, 1995.
20. Plostins, P., Private Communication, Aberdeen, MD, 1996.

**SESSION II**

**THERMAL AND CHEMICAL EFFECTS/  
EXPERIMENTAL METHODS AND MEASUREMENTS**

BUNDY

**TITLE:** Thermally Controlled Bore Straightness During Firing  
Dr. Mark L. Bundy  
U.S. Army Research Laboratory  
Attn: AMSRL-WT-PB  
Aberdeen Proving Ground, MD 21005-5066

**ABSTRACT:**

It is possible that a given lot of ammunition fired at the same aim point by two different tanks will produce center-of-shot impacts (COIs) that differ in magnitude by several times the lot's dispersion. It is difficult to discern what fraction of this variation is due to barrel differences alone, since changing tubes alters both the mounting conditions and the occasion.

A means has been devised to "change tubes" without altering the mount, or the occasion, by merely changing the shape of a given tube within the same mount. This is accomplished by localized control of the barrel's axial thermal expansion, implemented through a series of temperature-controlled heating pads adhered to the outer barrel wall. Using this technique, it was found that a simple, yet very common, bow-shaped curvature to the right vs. left, for example, produced a significant shift in the COI, the magnitude of which was on the order of the ammunition dispersion. In particular, inducing a right bow moved the muzzle to the left and the shot impacts to the right. Conversely, forming a left bow moved the muzzle to the right and the shot impacts to the left.

**BIOGRAPHY:** Dr. Bundy has been employed by the Army Research Laboratory since 1981, working in the Aerodynamics Branch of the Propulsion and Flight Division, Weapons Technology Directorate.

**PRESENT ASSIGNMENT:** Investigate the influence of gun dynamics on the fall of shot.

**PAST EXPERIENCE:** He has worked in the field of gun accuracy for the past ten years, primarily in the abatement of gun barrel heating and cooling asymmetries.

**DEGREES HELD:** B.A. Math & Physics, Augsburg College, Mpls., MN, 1968; M.S. Physics, Drake Univ., Des Moines, IA, 1975; Ph.D. Physics, Univ. of Maine, Orono, ME, 1980.

## THERMALLY CONTROLLED BORE STRAIGHTNESS DURING FIRING

Mark L. Bundy  
U.S. Army Research Laboratory  
Aberdeen Proving Ground, MD. 21005-5066

### INTRODUCTION

The difference between the gravity-, wind-, and drag-corrected aim point and where a projectile actually hits the target is referred to as projectile jump. Projectile jump varies from round to round, but in general, roughly two-thirds of the rounds will hit the target within one standard deviation of the center of shot impacts (COI), for a given lot of ammunition.

However, the COI will vary from tube to tube, mount to mount, and occasion to occasion. In a test with early production tubes (Walbert and Petty [1]), the COIs from six different tank-tube combinations were found to vary by 3 mils (roughly 3 m at 1,000 m) in azimuth and elevation. It is likely that production tubes today would show a smaller variation, maybe half (Webb [2]); nonetheless, a large source of error.

It is difficult to discern what fraction of this variation is due to barrel differences alone, since changing the tubes alters both the mounting conditions and the occasion. The novelty of the test described here is that the centerline is changed without remounting the barrel; thus, there is no doubt that the alteration in the bore profile is the sole source of the COI change.

### CONTROLLING THE CENTERLINE

A series of heating pads was adhered to the outer wall of an M256 barrel (serial number 2971), as illustrated in Figure 1. In the center of each pad was a small hole that accommodated the placement of a thermocouple used to measure the barrel temperature. The temperature of the barrel under each pad could be stabilized by automatic, or manual, control of the heating pad's on-off switch. The heating pads were used to create cross barrel temperature differences (CBTDs) that in turn produced uneven axial thermal expansion, thus changing the bore centerline.

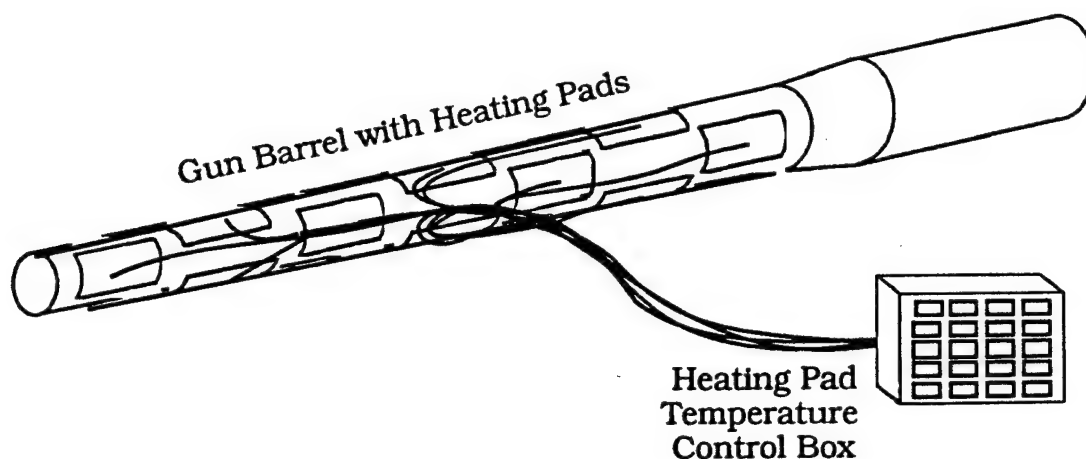


Figure 1. Illustration of temperature-controlled M256 gun barrel.

Since heating the barrel creates a turbulent bore atmosphere, it is not possible to directly measure the CBTD-induced change in bore centerline using conventional, optically based, bore straightness equipment. Instead, a thermal distortion model (Bundy [3]) was used to predict the bore centerline change based on the measured CBTDs. The model was validated by making extensive comparisons between predicted and externally measured shape changes. One such validation test is shown in Figure 2. In general, the predicted vs. measured thermal bend differed by less than 0.2 mm in displacement, and less than 0.1 mil in angular change of the muzzle.

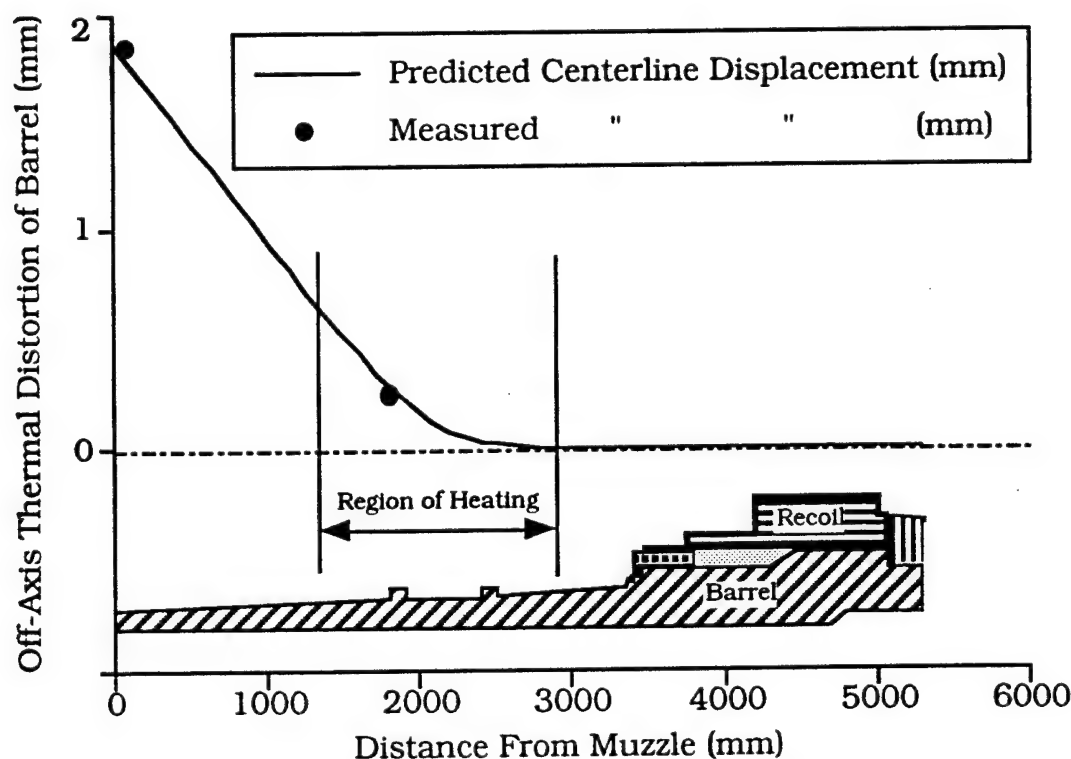


Figure 2. Change in bore straightness due to one-sided pad heating.

This being the first firing test of a thermally controlled barrel, the investigation was limited to the horizontal plane only, where fewer factors influence gun dynamics. That is, in the vertical plane the unidirectional effects of gravity on the barrel and projectile add complexity to the analysis of gun dynamics. Furthermore, it is well known (e.g., Erline and Kregel [4]) that the effects of the breech center-of-gravity offset will overshadow the effects of centerline curvature on vertical plane gun dynamics.

To further simplify the experiment, only a simple bow shape, or half-sine wave curvature, to the left and right, and a near-straight centerline were chosen for analysis. It should be noted, however, that some (Schmidt, et al. [5]) think barrels with multiple changes in curvature produce greater jump than simple bow-shaped barrels.

The magnitude of the bow shape was varied twice in each direction to give a total of five trial cases, which are distinguished as bow left, bow right, large bow left, large bow right, and near straight in the horizontal centerline plots of Figure 3. Bear in mind, these centerline plots are not based on actual measurements; rather, they are based on theoretical predictions, as previously mentioned.

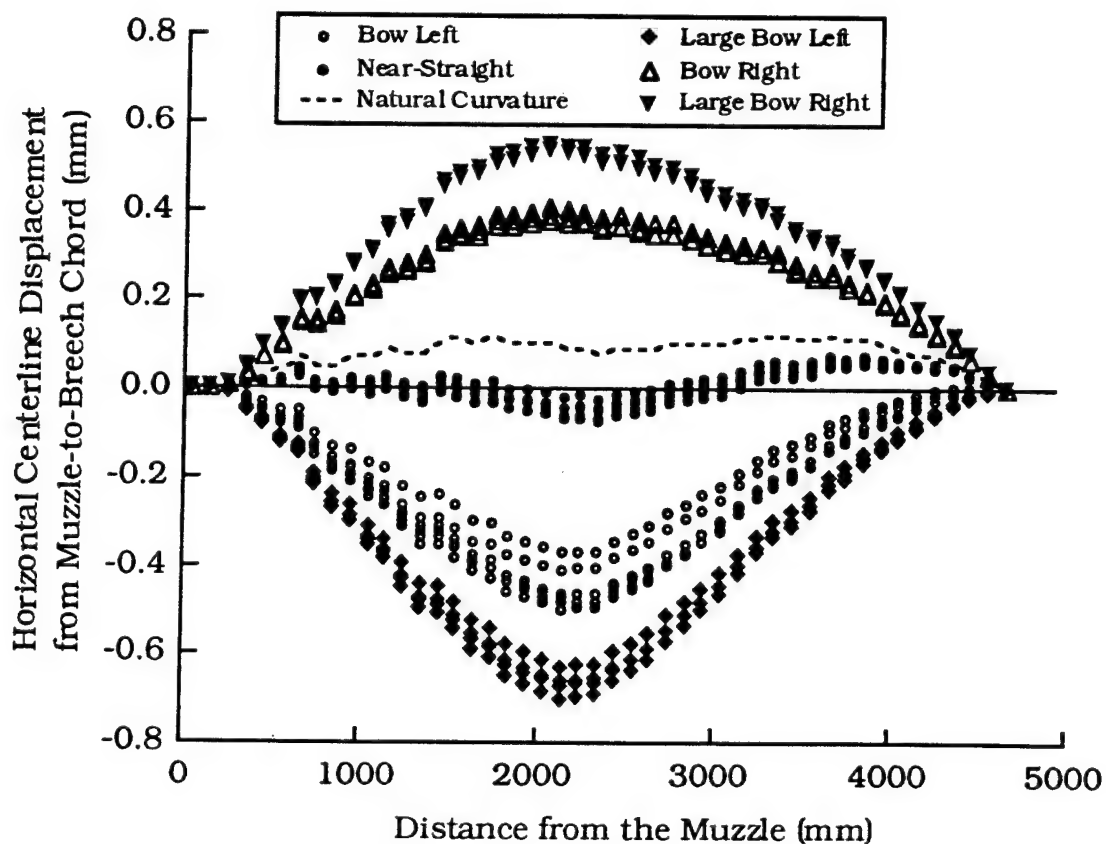


Figure 3. Manufactured and heating-pad-induced horizontal centerline curvatures prior to firing M256 ser. no. 2971.

How do the trial cases of Figure 3 relate to the general population of tube centerlines? In the dispersion study of Wilkerson [6], 20 M256 tubes were examined. Of these 20, 15 (75%) had a simple bow shape in either the horizontal or vertical plane, or both. Ten of the 20 barrels (50%) had bow shapes that were equal to or smaller in magnitude than the bow left and bow right curvatures in Figure 3. Five of the 20 (25%) had bows that were as large as the bow left/right curvatures, but smaller than the large bow left/right curvatures.

There are several centerline plots drawn in Figure 3 for each of the five general curvature cases. For example, there are five distinctly different plots for the bow left case. Each plot represents the centerline profile when a round was fired. The small variation in plots for the same case attests to the fact that it was not possible to maintain exact control over the CBTDs, which affect thermal bend. In actuality, there were six rounds fired for the bow left case, with two plots overlaying each other. However, regardless of the number of plots distinguished, there were at least four rounds fired for each general curvature case.

The ambient temperature during the 5-day testing period never exceeded 20° C. The barrel temperature would, of course, rise above ambient after firing. To maintain a consistent set of starting conditions for each firing, all heating pads were set to maintain a minimum barrel temperature of 25° C. A large-volume air pump was used to blow ambient air through the barrel from the breech to the muzzle after each round; this expedited the return of the barrel to the 25° C minimum starting condition. Once the starting condition was reached, the blower was removed and manual control of specific heating pads was used to raise the barrel temperature above the 25° C minimum, in accordance with the temperature distribution required to create a given centerline profile. For example, the bow-left profile was created by raising three consecutive heating pads on the gunner's left of the barrel to 31° C, 39° C, and 31° C, as indicated in the schematic of Figure 4, while all other heating pads maintained the 25° C minimum barrel temperature. Actually, Figure 4 plots the right minus left CBTDs, rather than the absolute temperatures, since it is temperature difference that determines thermal bend.

## MEASURING THE COI

In total, 29 rounds of same-lot M865 target practice, cone-stabilized, discarding-sabot, training (TPCSDS-T) ammunition, were used in this test. To reduce the dependence of occasion-to-occasion differences on the results, the firings were sequenced so that a round was fired with the centerline bowed to the left; then a near-straight centerline was fired; and then a round was fired with the centerline bowed to the right. This left-straight-right pattern was repeated, with, on average, a round being fired every 30–60 min. (Although the centerline could be changed in 5–10 min, a period of 20–30 min was required to bring the barrel back down to the 25° C starting condition, using the forced air blower.) Six test rounds were fired per day.

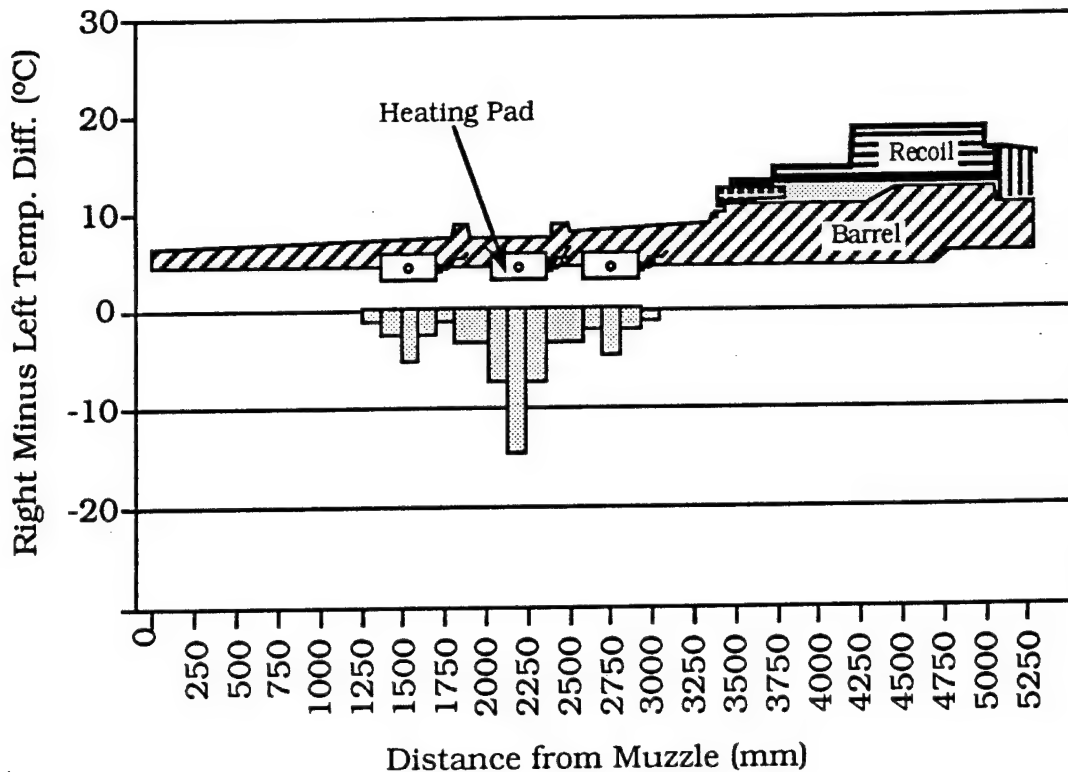


Figure 4. CBTD profile needed to induce bow-left configuration of Figure 3.

A spotter round was fired at the beginning of each day to "set" the gun, which directionally predisposes clearances and tolerances in the gun-mount system. These biases are, for the most part, maintained during the course of subsequent firings, but can "relax" if the period between rounds is excessive (24 hours for example). To gauge the relative motion of the mount, a 20-power telescope (a so-called Wye scope) was placed in a special cradle rigidly attached to the outside wall of the recoil cylinder. The Wye scope was used to read a grid board located 103 m downrange. The accuracy of this reading was considered to be 0.01 mils. Figure 5 shows, as implicated previously, that the largest change in breech angle occurs after the spotter rounds. Thereafter, the mount remained fairly stable. This mount, located at the Army Research Laboratory's (ARL's) Transonic Range, held tube 2971 in an M1A1 recoil that was attached to an Aberdeen Proving Ground (APG) "yoke" through an APG "adapter" plate. The APG yoke was affixed to the recoil system (equilibrator, trunions, and pedestal) of an 8-in M110 howitzer. However, the recoil system was not vehicle mounted; rather, it was rigidly bolted to a concrete ground slab.

The pointing angle of the muzzle end of the gun could be changed by altering the breech angle, or it could be changed by thermal distortion of the barrel between the breech and the muzzle. The muzzle angle was measured using a so-called APG muzzle scope. The reading accuracy of the APG scope is considered to be 0.05–0.10 mil.

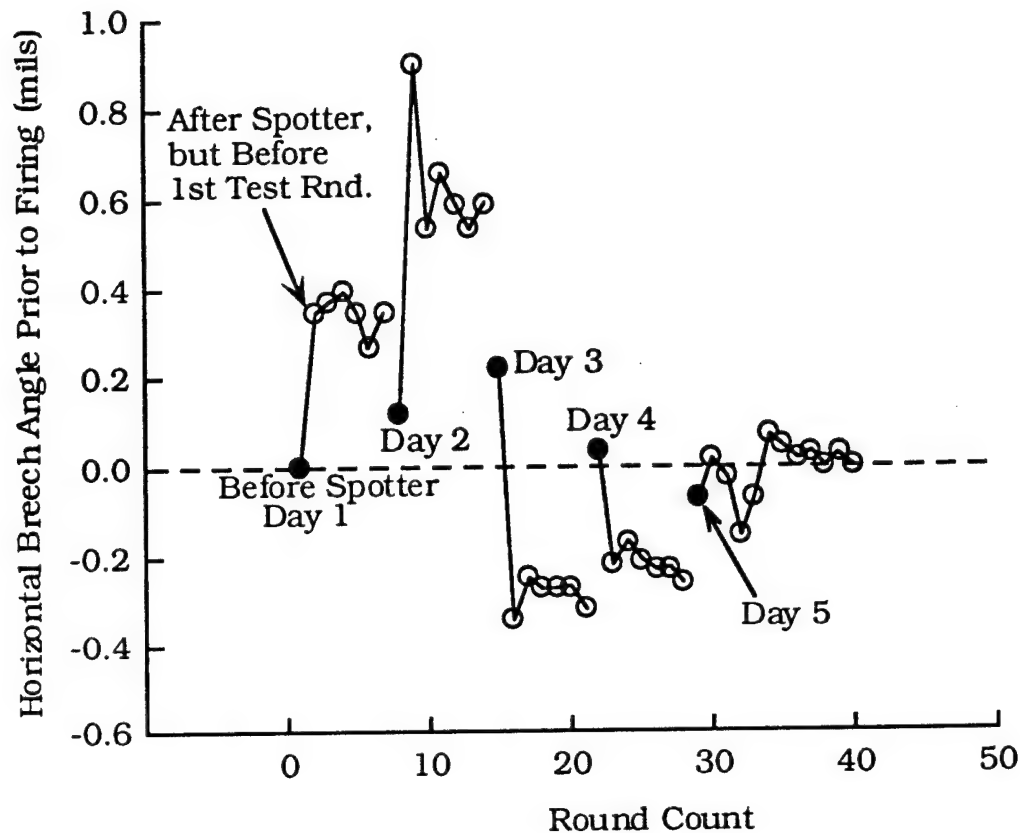


Figure 5. Change in horizontal breech pointing angle during 5-day firing period.

In addition to the baseline breech scope measurement, a baseline muzzle scope reading was taken before each day's firings. In fact, prior to taking these baseline measurements, the azimuth and elevation of the gun mount was adjusted so that the collimated APG scope was pointing at a painted cross on a downrange target cloth. As discussed, however, firing the pretest spotter round would normally move the mount so that the pointing angle of the muzzle after the spotter round, and before the first test round, was not usually directed exactly at the target cross. Rather than move the mount again to align the muzzle angle with the cross, and risk having to fire another spotter round to ensure the mount was once again set in place, the post-spotter-round readings of the breech and muzzle scopes were taken as the pretest-round pointing angles.

After firing each round, the target impact location was marked, and later measured relative to the initial (prespotter) aim point. The horizontal distance from the initial aim point, divided by the distance to the target (953 m), was used to convert the shot impact location into an angular deviation (in mils) off the original "line of fire." Having determined the prefiring muzzle pointing angle and the shot impact angle for each test round, the two angles were differenced

to establish the horizontal jump angle for each round. Finally, the mean horizontal jump angle was computed and defined to be the COI for the group of rounds associated with each specific barrel curvature.

### COMPARISON OF THE COIs WITH CENTERLINE CURVATURES

The first comparison is between the COIs and centerline curvatures of the bow-left, bow-right, and near-straight configurations. An illustration of the results is displayed in Figure 6. For the bow-left case, the horizontal COI falls 0.30 mil to the left of the muzzle pointing angle. Whereas, for the bow-right case, the horizontal COI falls only 0.02 mil to the left of the aim point. For the near-straight barrel, the COI lies in the middle of the bow-left and right result, viz., 0.14 mils to the left of the aim point. It can be seen from the illustration that, relative to the near-straight case, inducing a left bow will move the muzzle to the right and the shot impacts to the left. Conversely, forming a right bow will move the muzzle to the left and the shot impacts to the right.

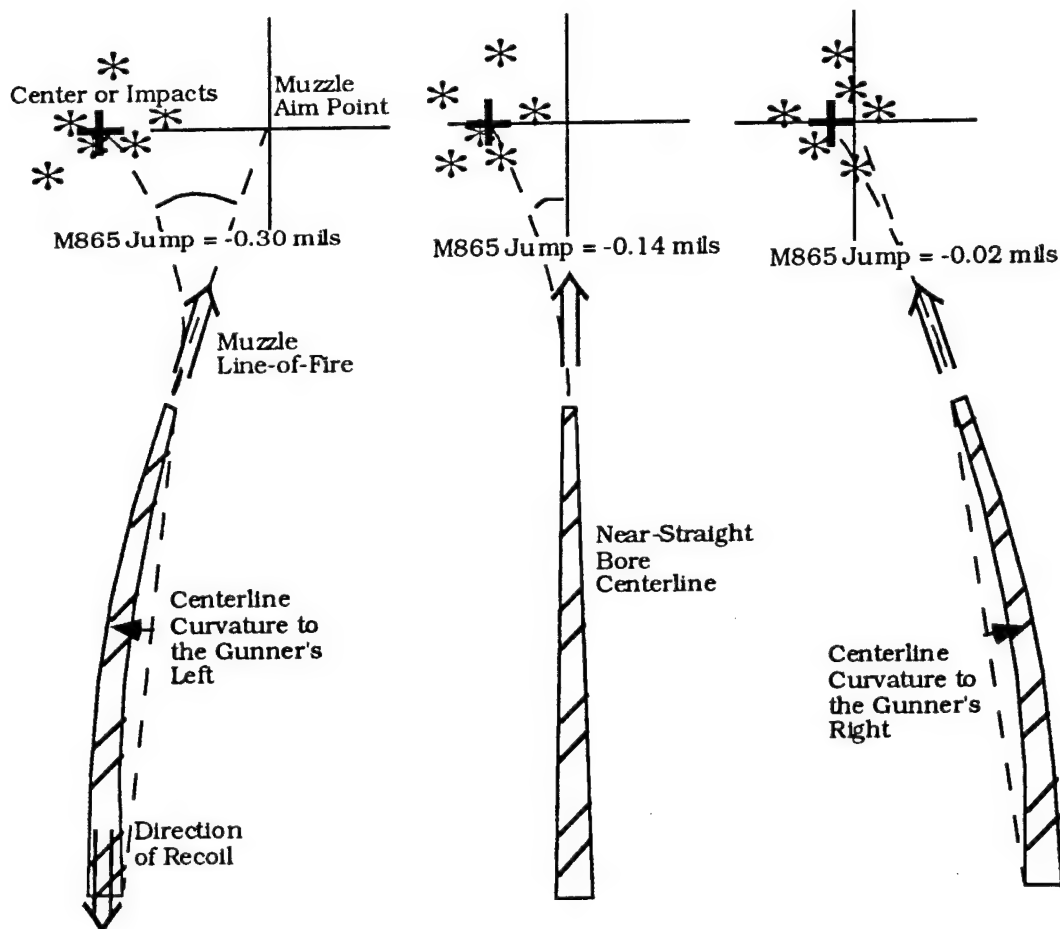


Figure 6. Illustration of M865 COI vs. centerline curvature (in the horizontal plane) for three of five bent barrel cases.

When the barrel is distorted into the large bow-left configuration, the COI lies, surprisingly, at virtually the same location as the smaller bow-left firings—in this case, 0.29 mil to the left of the aim point, Figure 7. Similarly, the COI for the large bow-right firings lies at the same location as the smaller bow-right firings, viz., 0.02 mil to the left of the aim point. The results for all five firing configurations are summarized in Table 1. It should be noted that on day 1 only four of six test rounds were considered "good" data rounds, with no entrees (Table 1) for the bow-right configuration. The exclusion of the bow-right trials was based on the fact that the CBTD patterns for these two rounds were not deemed sufficiently close to the bow right configuration. Such a problem did not occur again during the course of firing because control of the CBTDs was changed from automatic to manual after the first day. This provided better control over the repeatability of centerline curvatures for all configurations.

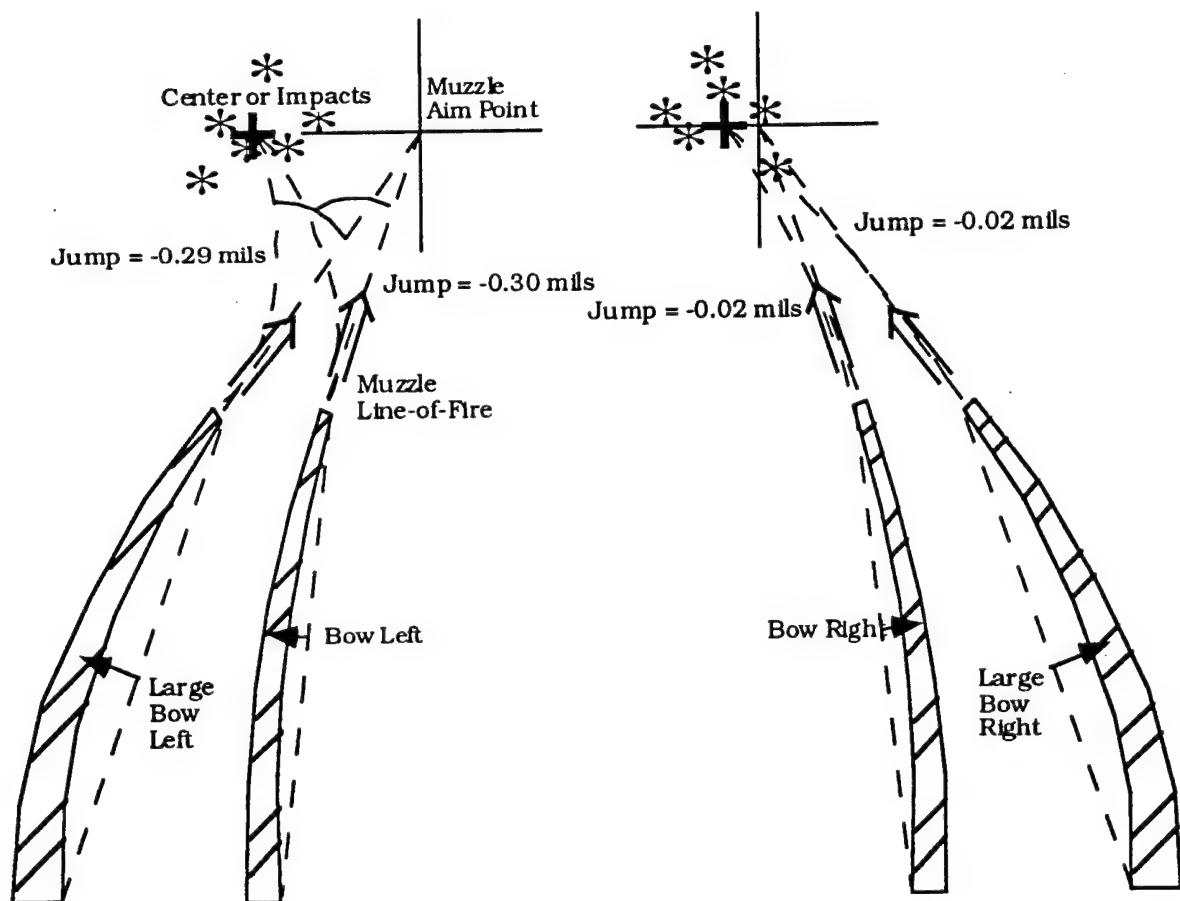


Figure 7. 865 COI vs. centerline for larger vs. smaller barrel bends.

## BUNDY

Table 1. Horizontal jump values for five barrel curvatures

	M865 IMPACT ANGLE MINUS MUZZLE ANGLE (mils)				
	Large Bow Left	Bow Left	Near Straight	Bow Right	Large Bow Right
Day 1		-0.285	-0.308		
		-0.347	-0.204		
Day 2		-0.164	-0.297	-0.049	
		-0.534	-0.067	-0.366	
Day 3		-0.177	-0.115	+0.180	
		-0.270	+0.130	+0.156	
Day 4	-0.345				+0.258
	-0.258				-0.141
	-0.366				+0.179
Day 5	-0.093				-0.136
	-0.262				-0.236
	-0.422				
Avg. Jump	-0.291	-0.296	-0.143	-0.020	-0.015
Std. Dev.	0.116	0.135	0.165	0.252	0.219

The observation that a centerline bowed to the left or right (with muzzle angle moved right or left, respectively) shoots rounds to the left or right, respectively, relative to a straighter centerline, has occurred before. In 1987, for example, during testing of the Gloster Saro thermal shroud on the M256 cannon (Bundy [7]), uneven cooling (due to a design failure in the shroud) caused the barrel to undergo a thermal bend to the gunner's left (bow left). As this occurred, the fall of shot also moved to the gunner's left. The correlation coefficient ( $r$ -value) between the bow-left thermal bend and the shift left in jump was highly significant,  $|r| = 0.76$ . A similar result occurred in a more recent test, with a 25-mm chain gun (Garner et al. [8]); it was found that thermal distortion induced by uneven firing heat input caused the barrel to bow to the right and the shot impacts to move to the right.

## CONCLUSIONS

Controlled changes of the bore centerline with heating pads provide a means to isolate the effects of tube-to-tube variation on the fall of shot, without entailing a mount or an occasion change. Five simple, nevertheless common, centerline profiles were examined. The shape changes were all made in the horizontal plane to avoid the complexities introduced by gravity and the large vertical center-of-gravity offset of the breech.

It was found that same-lot M865 rounds fired through a nearly straight tube were grouped about a COI that was on the gunner's left of the prefiring muzzle aim point (-0.14 mil). When the bore centerline had a bow to the left,

the COI was to the left of the near-straight case (-0.30 mil from the aim point), and when it was bowed to the right the COI was to the right of the near straight case (-0.02 mil from the aim point). However, a change in magnitude of the left and right bows did not change the COI. Overall, the average COI for all five cases was about -0.15 mil.

If we assume the M1A1 fleet has roughly the same number of right-bowed barrels as left, then we might expect the fleet COI for M865s would be close to our "five-barrel" average. However, this is not the case, the fleet COI is considered to be +0.15 mils, which is the same magnitude but opposite direction from our result. This difference begs the question of whether the mount used in our test biased the COIs to the left? In the test of Walbert and Petty [1], it was found that COIs for the same tube mounted in different tanks varied by as much as 0.8 mil. Since the difference between our same-mount, five-tube COI and the fleet COI is only 0.3 mil, it seems plausible that the bias to the left could be mount related.

Regardless of what bias the mount may impart, the change in COIs observed between the bow-left and bow-right centerlines were on the same order of magnitude as the ammunition dispersion. This demonstrates that tube-to-tube variability, even for simple shapes, can be a significant contributor to tank-to-tank variation in shot impacts.

#### REFERENCES

1. Walbert, J. N., and D. W. Petty. "Assessment of Firing of the M1E1 with an Indexed Gun Tube." BRL-MR-3458, U.S. Ballistic Research Laboratory, Aberdeen Proving Ground, MD, August 1985. (AD C037676L)
2. Webb, D. W. Private communications concerning tank-to-tank variation in shot impacts. U.S. Army Research Laboratory, Aberdeen Proving Ground, MD, April 1996.
3. Bundy, M. L. "Gun Barrel Cooling and Thermal Droop Modeling." ARL-TR-189, U.S. Army Research Laboratory, Aberdeen Proving Ground, MD, August 1993.
4. Erline, T. F., and M. D. Kregel. "Modeling Gun Dynamics with Dominant Loads." BRL-MR-3683, U.S. Ballistic Research Laboratory, Aberdeen Proving Ground, MD, July 1988.
5. Schmidt, E. M., J. A. Bornstein, P. Plostins, B. Haug, and T. L. Brosseau. "Jump from M1A1 Tank." BRL-TR-3144, U.S. Ballistic Research Laboratory, Aberdeen Proving Ground, MD, September 1990.
6. Wilkerson, S. "Possible Effects of Gun Tube Straightness on Dispersion." ARL-TR-767, U.S. Army Research Laboratory, Aberdeen Proving Ground, MD, June 1995.

BUNDY

7. Bundy, M. L. "Performance Analysis of a Blanket Type Thermal Shroud for 120 mm Tank Cannon." BRL-MR-3611, U.S. Army Ballistic Research Laboratory, Aberdeen Proving Ground, MD, June 1987. (AD-C041556)
8. Garner, J. M., M. L. Bundy, D. W. Webb, and B. J. Patton. "Variation in Muzzle Pointing Angle and Shot Impact of M2452 Chain Gun." ARL-TR-785, U.S. Army Research Laboratory, Aberdeen Proving Ground, MD, July 1995.

**TITLE: Surface Chemistry Effects on High Performance Tank Ammunition**

P. J. Conroy\*, P. Weinacht, and M. J. Nusca

U. S. Army Research Laboratory, Aberdeen Proving Ground, MD, 21005-5066, USA

**ABSTRACT:**

A theoretical model that addresses thermochemical erosion in gun tubes is presented. The model incorporates two interior ballistics codes, XKTC, IBHVG2, and the thermochemical code BLAKE, to provide the necessary state variables and bulk species concentrations of the core flow as input. This erosion model utilizes a Crank-Nickolson integration scheme, with dynamic gridding capability to account for material ablation, as well as the addition of energy sources and heat transfer augmentation due to surface deviations. A mass transport scheme, utilizing the Lennard Jones 6-12 diffusion model, enables individual species to be transported to the surface from the core flow. Also fully coupled is a separate thermochemical routine which incorporates the NASA Lewis database. The code is written modularly, enabling the inclusion and modification of existing sub-modules. Erosion results comparing a fielded kinetic energy tank round and a candidate next-generation tank round are presented. The thermochemical effects at the surface are also shown and discussed.

**BIOGRAPHY:**

Paul J. Conroy

**PRESENT ASSIGNMENT:** Mechanical Engineer, U.S. Army Research Laboratory, Aberdeen Proving Ground, MD, 1989-Present

**PAST EXPERIENCE:**

Cryogenics at Fermi National Accelerator Laboratory, Batavia, IL.  
Graduate Student at The Pennsylvania State University under  
Professor Kenneth K. Kuo.

**DEGREES HELD:**

B.A. Physics, Millersville State University  
B.S. Mechanical Engineering, The Pennsylvania State University  
M.S. Mechanical Engineering, The Pennsylvania State University

## **Surface Chemistry Effects on High Performance Tank Ammunition**

P. J. Conroy\*, P. Weinacht, and M. J. Nusca  
U. S. Army Research Laboratory  
Aberdeen Proving Ground, MD 21005-5066, USA

### **Introduction**

Gun tubes are typically either erosion or fatigue limited in the number of rounds that can be effectively and safely fired from them. Direct fire weapons are typically erosion-life limited due to the high performance requirements placed upon them. Current ammunition for the M256 tank gun is being designed to maximize the kinetic energy of the projectile at launch. Performance requirements have reintroduced gun bore erosion as a significant design issue because erosion will limit the number of rounds that can be effectively and safely fired over the life of the gun tube. Previous "solutions" had not identified the fundamental cause of the erosion, and some discrepancies between the flame temperature correlations [1,2,3] and the erosivity were never resolved. Attempts to model erosion using first principles have been and are currently being made [4,5,6], although it is believed that significant additional work is still required.

A complete description of the erosion process would include a variety of mechanisms produced by thermal, chemical, and mechanical effects. Generally, thermal erosion is driven by high convective heating produced by the propellant gases that heat the in-bore surface of the gun tube and cause it to melt. Chemical erosion is caused by surface chemical reactions produced by the interaction of the gun tube gases with the inbore surface of the tube. These reactions may erode the inbore surface directly through pyrolysis or produce additional heat to augment the convective heating thus inducing melting. The thermal and chemical erosion mechanisms are common and generally interrelated, while erosion due to mechanical effects is more isolated and somewhat independent. In this current work we have focused on the coupled thermal and chemical erosion mechanisms, while not excluding the possible addition of the mechanical contribution in the future.

### **Model Description**

The model description consists of three fully coupled portions consisting of thermal ablation and heat transfer/conduction, mass transport, and the imbedded thermochemistry, as well as the intercoupling of these portions.

Following a modular engineering approach resulted in the integration of some of the Army Research Laboratories (ARL) well developed tools as well as the development of new modules to

supply additional physics, namely: an interior ballistics code to provide the necessary state variables and gas velocities XKTC [7], and a chemical equilibrium code BLAKE [8] coupled to an interior ballistic code, IBHVG2 [9], thus creating the IBBLAKE [10] code which provides temporal specie concentrations, as well as the gun tube heat transfer-conduction code XBR-2D [11, 12,13].

The current modeling effort considers a melt-wipe model similar to that proposed by Caveny [14], with the addition of surface chemistry. Conceptually, as shown in Figure 1, the surface heats from convection until the chemical activation energy is overcome; at this point a surface reaction occurs, releasing additional energy into the system, and producing various products. The reaction products can either remain, as some solids, or be removed from the area as liquids or gasses, thus resulting in pyrolysis or ablation. As the surface regresses, the solids are refreshed accordingly. The following assumptions have been made in the model:

- (a) 1-D heat conduction
- (b) No subsurface diffusion/ reaction,
- (c) All surface liquids are removed,
- (d) All surface gas products are removed,
- (e) There is no feedback to the interior ballistics,
- (f) Chemical energy released is treated as a source term,
- (g) Species are frozen from core flow to wall.

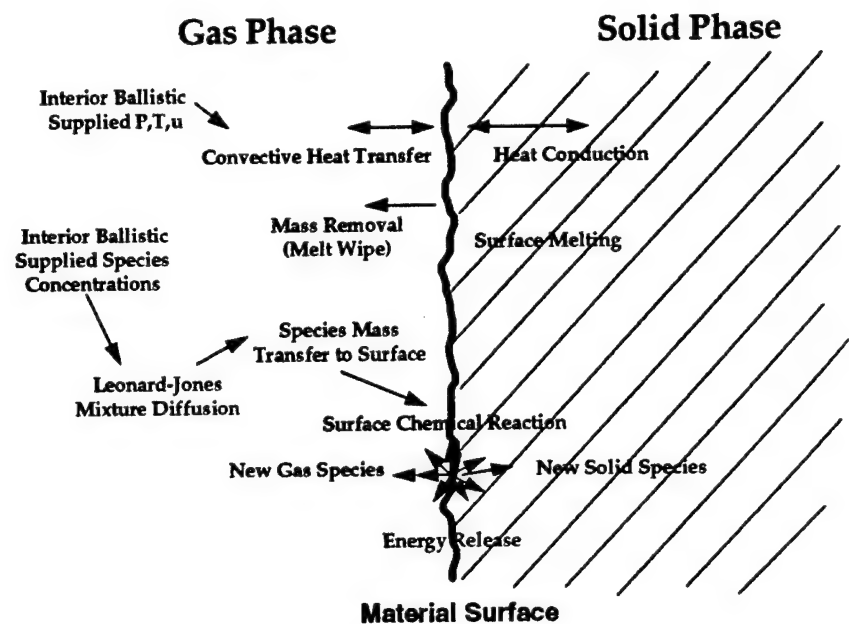


Figure 1 Conceptual erosion model.

### Ablation-Conduction Model and Computational Approach

The in-depth temperature response of the unablated (solid) material is modeled using the one-dimensional heat conduction equation shown below.

$$\rho C_p \frac{\partial T}{\partial t} = \frac{1}{r^\beta} \frac{\partial}{\partial r} \left( r^\beta k \frac{\partial T}{\partial r} \right)$$

By setting  $\beta=0$  or  $\beta=1$ , the planar or axisymmetric form of the governing equation can be obtained. In this form of the equation the relevant material properties, density,  $\rho$ , specific heat,  $C_p$ , and conductivity,  $k$ , the conductivity, may vary (but remain continuous). The feature of variable conductivity was not utilized in the results presented here.

At the internal surface of the gun tube, two separate boundary conditions were applied depending on whether the melting of the surface material was occurring. When the surface material was below the melt temperature, a convective heat transfer boundary condition was applied.

$$h(T_{\infty} - T_{wall}) = -k \frac{\partial T}{\partial r}$$

Using the state variables and gas velocity from the XKTC [7] code, the convective heat transfer coefficient,  $h$ , is determined using the correlation of Stratford and Beavers [15]. Once the surface of the gun tube reaches the melt temperature, melting of the surface material is assumed to occur. When fully molten (complete change of phase from solid to liquid), the liquid metal is immediately removed or ablated by the shearing action of the gun gases. Because surface material is being removed during the ablation process, the surface location (or the regression rate) becomes an additional variable. During the ablation process two boundary conditions are applied as shown below.

$$T_{wall} = T_{melt}$$
$$\rho L \frac{\partial s}{\partial t} = h(T_{\infty} - T_{wall}) = -k \frac{\partial T}{\partial r}$$

The first equality of the second boundary condition simply states that the temperature at the interface while the phase change is occurring is equal to the melt temperature. The melt temperature is assumed to be a known material property. The second equality of the boundary condition is obtained from an energy balance at the melt surface. In addition to the heat transfer due to conduction and convection, the additional energy required due to the change of phase from solid to liquid (latent heat of melting,  $L$ ) is also included. This boundary condition allows the regression rate of the solid material to be computed, given that the latent heat of melting,  $L$ , is a known material property.

To provide closure for the in-depth temperature response of the gun tube, a convective boundary condition is applied to the outer surface of the gun tube.

$$h_{amb}(T_{outer-wall} - T_{\infty-amb}) = -k \frac{\partial T}{\partial r}$$

However, because the erosion process occurs during the first several milliseconds of the firing process, the heat can only penetrate a fraction of the distance from the inner surface of the gun tube to the outer surface of the gun tube. In this case, it may not be necessary to model the radial temperature response of the entire gun tube. By locating the outer edge of the computational domain so that the temperature response is unchanged during the heating process, a smaller computational domain may be analyzed. In this case, one of two boundary conditions may be applied-- a constant temperature boundary condition or an adiabatic wall boundary condition.

The appropriate depth of the computational domain can be estimated using a depth of penetration analysis [16,17]. The depth of penetration,  $\delta$ , gives the approximate distance that the heat would penetrate in a given time  $t$  and is a function of the thermal diffusivity of the material,  $\alpha$ .

$$\delta = \sqrt{12 \alpha t}$$

Using a factor of safety of two or three will place the outer boundary of the computational domain far enough from the bore surface of the gun tube so that the temperature at the outer boundary remains unaffected by the heating of the gun tube during firing. This analysis enables either single firing erosion prediction or rapid, continuous fire capability depending upon the computation approach chosen and the imposed outer boundary condition.

The governing equations and boundary conditions are solved using a Crank-Nicolson finite-difference technique. Prior to the onset of melting, the governing equations and boundary conditions are linear and solutions are obtained in a direct (non-iterative) fashion. During the melting process, the equations become non-linear since the dimensions of the computational domain are coupled with the regression rate. An iterative approach is utilized during melting to appropriately address the non-linearity.

Because the boundary of the computational domain moves during the erosion event, a transformed version of the governing equation is employed. This allows the equations to be solved in a fixed computational space even though the physical boundary is moving. A generalized transformation between the computational coordinate,  $\xi$ , and the physical coordinate,  $r$ , is utilized. The transformed equations are shown below.

$$\rho C_p \left( \frac{\partial T}{\partial t} + \xi_r \frac{\partial T}{\partial \xi} \right) = \frac{1}{r} \xi_r \frac{\partial}{\partial \xi} \left( r k \xi_r \frac{\partial T}{\partial \xi} \right)$$
$$\xi_r = \frac{-r_t}{r_\xi} \equiv \frac{\frac{\partial r}{\partial t}}{\frac{\partial r}{\partial \xi}}$$
$$\xi_r = \frac{1}{r_\xi} \equiv \frac{1}{\frac{\partial r}{\partial \xi}}$$

In this form, the non-linear nature of the governing equation produced by the moving boundary is evident because the metric terms,  $\xi_r$  and  $r_\xi$ , are not constant and are dependent on the erosion rate when the grid is moving.

#### Validation of Ablation-Conduction Model:

Over the past several decades, numerous studies examining the phase change process have been made. Results from two of these studies have been used to validate the currently developed numerical method. Landau [18] has made one-dimensional time-dependent numerical predictions of a melting solid using a technique similar to that utilized here. Landau considered the case of a semi-infinite solid subject to a constant heat flux. Goodman [19] considered similar problems using a heat-balance integral approach which utilizes an assumed form of the temperature profile to analytically determine the heat conduction and ablation process. While exact solutions are not typically obtained, the results are reasonably accurate and are of a simple form. One of the cases addressed by Goodman was the melting of a semi-infinite solid under constant heat flux. In both cases, an ablative boundary condition was utilized; that is, the liquid phase was immediately removed following melting.

The problem of the heating on a semi-infinite solid subject to constant heat flux was addressed using the current numerical method. The solid initially had a uniform temperature distribution of  $T_o$  and a specified melt temperature,  $T_{melt}$ . The results are scaled by the time to melt,  $t_{melt}$ , which is a function of applied heat flux. Figure 2 shows the in-depth temperature profile at several increments in time during the melting process. The results were obtained using material properties corresponding to gun steel. In addition to the numerical results, the analytical results obtained using the heat-balance integral approach of Goodman are also shown at the onset of melting and during steady-state melting. The numerical solution and the analytical results are in excellent agreement at the onset of melting. (Though not shown, both results are also in excellent agreement with the exact analytical solution.) As the melting progresses, the temperature gradient at the heated interface is reduced due to the additional energy required to melt the solid (latent heat of melting). After approximately eight times the time required to reach the melt temperature, the numerical results show that temperature profile has nearly reached the steady-state temperature profile. The differences between the analytical and numerical steady-state temperature profile are less than 2% of the difference between the melt temperature and the initial temperature. Exact agreement between the two results is not expected because the assumed form of the temperature profile in the heat-balance integral approach is not an exact solution.

A comparison of the predicted ablation rate obtained using the current technique with the results of Landau is shown in Figure 3. The current results are in excellent agreement with the results of Landau for three different sets of material properties including properties close

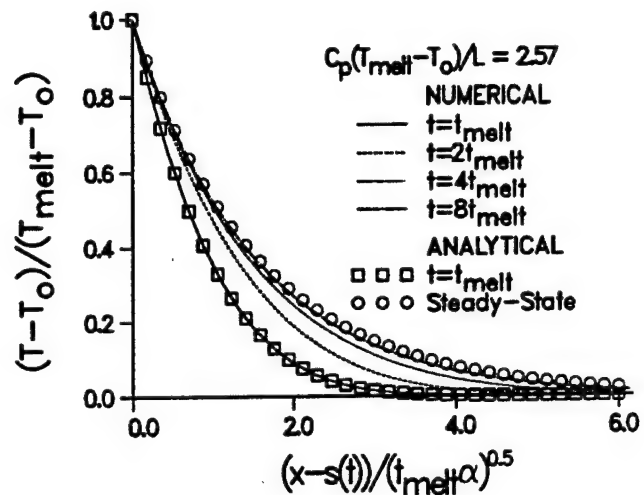


Figure 2 In-depth temperature profile during ablation process for a semi-infinite slab subject to constant heat flux.

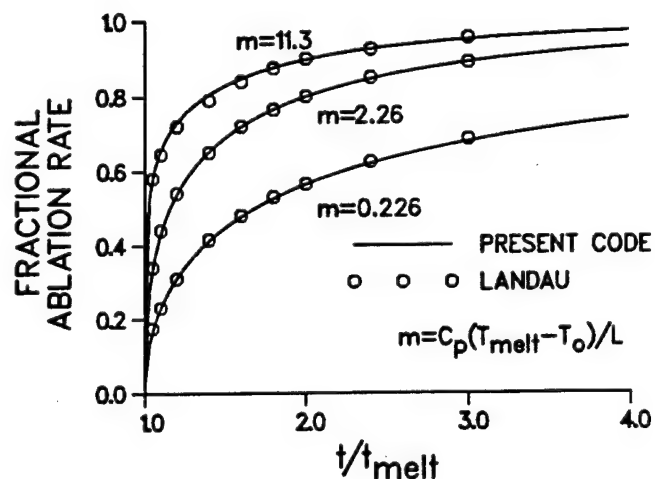


Figure 3 Fractional ablation rate versus time for a semi-infinite slab subject to constant heat flux.

to gun steel. (Differences between the results of Landau and the current result may be more related problems in extracting the data from the original published graphs of Landau than to numerical accuracy.) The steady-state ablation rate for the current result is also in good agreement with the exact analytical results presented by Landau.

### Multi-component Diffusion and Mass Transport Scheme

In order to derive the mass transport coefficient for a specific specie from the Sherwood number  $h_m L/D_{AB}$ , the diffusion coefficient must be determined. A reasonable representation of binary diffusion is provided by the following relationship

$$D_{12} = \frac{0.0026280 \sqrt{T^3(M_1 + M_2)/2M_1M_2}}{P \sigma_{12}^2 \Omega_{12}^{(1,1)*}(T_{12}^*)}$$

Where  $M_1$ ,  $M_2$  are the molecular weights of the species,  $T$  is the temperature, and  $P$  is the pressure. The simplest model to apply to the problem, given the criteria, is the Lennard Jones 6-12 model [20]. The potential function governing the Lennard Jones model is presented as

$$\Psi(r) = 4\epsilon \left[ \left( \frac{\sigma}{r} \right)^{12} - \left( \frac{\sigma}{r} \right)^6 \right],$$

where  $\epsilon$  is the depth of the potential well and  $\sigma$  is the collision diameter for low energy collision. The integral quantities  $\Omega_{12}^*$  are obtained through table interpolation. Both the  $\epsilon$ 's and  $\sigma$ 's are tabulated for various species. The following combinatory analysis is needed in order to correctly apply these tabulated single species values

$$\epsilon_{12} = \sqrt{\epsilon_1 \epsilon_2}, \quad \sigma_{12} = \frac{(\sigma_1 + \sigma_2)}{2}$$

The non-dimensional temperature  $T_{12}^*$  is used as a tabulation parameter for the Lennard-Jones  $\Omega$  integrals

$$T_{12}^* = \frac{Tk}{\epsilon_{12}}$$

The binary diffusion provides the basis for the multi-component diffusion coefficient. Each binary diffusion possibility is used and weighted versus all other possibilities in the following mixture coefficient combinatory function [21].

$$D_{im} = \frac{1 - X_i}{\sum_{j \neq i} \frac{X_j}{D_{ij}}}$$

This function enables the calculation of the diffusion coefficient for a particular specie into a mixture of many species. Equilibrium calculations for all service propellants were performed and all principle products species  $\sigma$ 's and  $k/\epsilon$ 's along with the  $\Omega(T^*)$  were placed into data statements in the diffusion routine. Thus, tracking of an individual species contribution to the erosion process is possible.

Mass transport to the surface is provided through a species concentration potential and a mass transport coefficient  $h_m$  derived from Sherwood number correlations for two ranges of Schmidt numbers,  $Sc = \mu/\rho D_{AB}$ , as shown

$$Mass_i = \iint h_m (\phi_{i\infty} - \phi_{iwall}) dA dt .$$

The gaseous species are assumed to not penetrate the surface at this time. However, the diffusion module is general enough to readily incorporate this possibility in the future.

Mass transport for a transient boundary layer development as shown in Figure 4 has been derived [22] and will be presented here. Considering a periodic transitional sublayer model enables infrequent penetration to the surface by eddies, as well as predictions of transfer rates over the entire range of Schmidt numbers. The thin laminar wall-layer beneath the boundary layer is periodically

replenished, however at a much slower rate than the bulk wall region. The importance of the thin wall-layer determines the treatment of the model. At moderate Schmidt numbers ( $10 < Sc < 1000$ ) the thickness of the boundary layer is much greater than the thickness of the viscous sublayer. This enables the accumulation in the wall-layer to be neglected. Ruckenstein [23] assumed the following linear pressure gradient model to govern the mass transport to the surface through the thin wall-layer

$$\psi = \frac{k}{\delta_1} (P_0 - P_1) ,$$

where  $k$  is the conductivity and  $\delta_1$  is the thickness of the thin wall layer. Utilizing the momentum integral method the following Sherwood number has been derived

$$Sh = \frac{0.0097 Re^{\frac{9}{10}} Sc^{\frac{1}{2}} \left( 1.10 + 0.44 Sc^{-\frac{1}{3}} - 0.70 Sc^{-\frac{1}{6}} \right)}{1 + 0.064 Sc^{\frac{1}{2}} \left( 1.10 + 0.44 Sc^{-\frac{1}{3}} - 0.70 Sc^{-\frac{1}{6}} \right)}$$

For higher Schmidt numbers ( $Sc > 1000$ ) the thickness of the boundary layer becomes of the order of magnitude of the thin wall-layer. The mass transport for this range is governed by the penetration of eddies into the boundary layer, in this case the wall-layer. This description, assuming characteristic distances between eddie disruptions is larger in the wall-layer than it is in the boundary layer and Blasius' expression for the friction factor, leads to the following Sherwood number

$$Sh = 0.0102 Re^{\frac{9}{10}} Sc^{\frac{1}{3}} .$$

These expressions for the Sherwood number have been compared [22] with much experimental data and agree very well within the Schmidt number regions specified.

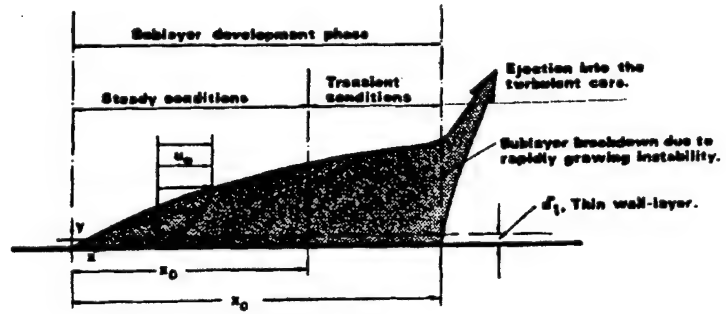


Figure 4 Idealized boundary layer development [22].

## Equilibrium Kinetics:

Equilibrium chemical processes are considered to dominate whenever the characteristic time for a fluid element to traverse the flow field of interest is much longer than the characteristic time for chemical reactions to approach equilibrium. As the pressure and temperature increases the molecular collision frequency and energy per collision increases which leads to smaller characteristic chemical times, and chemical processes approach equilibrium.

Chemical equilibrium is usually described by either of two equivalent formulations; equilibrium constants or minimization of free energy. Several disadvantages of the equilibrium constant method have been noted [24] and most researchers prefer the free-energy minimization formulation. The condition for equilibrium may be stated in terms of any of several thermodynamic functions such as the minimization of the Gibbs free energy or Helmholtz free energy or the maximization of entropy. For a mixture of  $N$  species (e.g. atoms or molecules) with the number of moles of species are denoted  $n_i$ , the Gibbs energy per mole of mixture is given in terms of the Gibbs free energy of the individual species,  $g_i$ , the internal energy,  $e$ , the temperature,  $T$ , the entropy,  $s$ , the pressure,  $p$ , and the specific volume,  $V$ .

$$G = \sum_{i=1}^N n_i g_i = e - Ts + pV$$

The equilibrium method employed in the present study is based on the fact that at equilibrium the total Gibbs energy of the system attains a minimum value. The total Gibbs energy of a single-phase system is given by

$$(G_{total})_{e,V} = G(n_1, n_2, n_3, \dots, n_N)$$

The problem is to find the set of  $n_i$ 's which minimizes  $G_{total}$  for a specified energy and specific volume ( $e, V$ ), subject to the constraints of material balances. The standard solution to this type of problem is based on the method of Lagrange's undetermined multipliers. First we must recognize that the total number of atoms of each element in the system is constant. Denoting a particular atomic species with subscript  $k$ , then  $A_k$  is the total number of atomic masses of the  $k$ -th element in the system, as determined by the initial constitution of the system. Denoting the number of atoms of the  $k$ -th element present in each molecule of chemical species  $i$  by  $a_{ik}$ , then the material balance on each element  $k$  may be written ( $M$  is the number of elements),

$$\sum_{i=1}^N \lambda_k (\sum_{i=1}^N n_i a_{ik} - A_k) = 0 \quad (k=1, 2, \dots, M) \quad [1]$$

introducing Lagrange multipliers,  $\lambda_k$ , for each element. Then a new function,  $F$ , is formed by addition of the last equation to  $G_{total}$ . The function  $F$  is identical to  $G_{total}$  since the summation term is zero. However,  $\partial F / \partial n_i$  and  $\partial G_{total} / \partial n_i$  are different since  $F$  incorporates the constraints of the material balances. The minimum of both  $F$  and  $G_{total}$  occurs when these partial derivatives are zero.

$$F = G_{total} + \sum_{k=1}^M \lambda_k (\sum_{i=1}^N n_i a_{ik} - A_k)$$

$$\left( \frac{\partial F}{\partial n_i} \right)_{e,V,n_j} = \left( \frac{\partial G_{total}}{\partial n_i} \right)_{e,V,n_j} + \sum_{k=1}^M \lambda_k a_{ik} = 0 \quad (\text{for } F_{min})$$

This equation can be rewritten using the definition of chemical potential  $\alpha_i$ , for species  $i$ .

$$\delta_i = \left( \frac{\partial G_{total}}{\partial n_i} \right)_{e,v,n_j} = G_i^\circ + R_u T \ln(\alpha_i),$$

$$\delta_i + \sum_{k=1}^M \lambda_k a_{ik} = 0 \quad (i=1,2,\dots,N) \quad [2]$$

The standard Gibbs-energy change of formation for species  $i$  is denoted  $G_i^\circ$  which is equal to zero for elements in their standard states. The activity for species  $i$  in solution is given by  $\alpha_i$  defined in terms of the equilibrium constant  $K$  as,

$$K = \prod_i \alpha_i^{v_i},$$

where the activities of the components are raised to the corresponding stoichiometric coefficients. For an ideal gas mixture ( $X_i \phi = 1$ ),

$$\alpha_i = f_i = X_i \phi_i p = p,$$

where  $f_i$  is the fugacity and  $X_i$  is the mole fraction for the  $i$ -th species. For liquids and solid phases

$$\ln(\alpha) = 1 - 1/p,$$

which is approximately zero for large pressure, therefore  $\delta_i = G^\circ$ .

There are  $N$  equilibrium equations (Eq. 2), one for each species, and there are  $M$  material-balance equations (Eq. 1), one for each element, a total of  $N+M$  equations. The unknowns in these equations are the  $n_i$ 's, of which there are  $N$ , and the  $\lambda_k$ 's, of which there are  $M$ , a total of  $N+M$ . Thus, the number of equations is sufficient for the determination of all unknowns.

### Surface Erosion Results:

Due to current development programs the first application of the model has been directed toward direct-fire systems. The model is used to compare the relative erosion performance in the M256 cannon firing the M829A1 KE projectile and an advanced KE projectile concept. Both of these rounds are built from similar propellants, although the flame temperature of the M829A1 propellant is lower than that of the advanced concept. The thermal performance of the M829A1 KE round has been investigated previously [25] with excellent agreement between the model and existing experimental data, as was the case with numerous previous applications [12,13].

The U.S. Army Research Laboratory erosion code calculations require a core flow thermochemical output from IBBLAKE, and an XKTC output file including the spatially varying gas pressure, temperature, and velocity [26]. For both calculations the barrel was assumed not to have a chrome layer. Once degraded, the chrome's effectiveness is small [27]. It will be seen that this assumption possibly has some validity for the advanced KE round, while for the less viscorative M829A1 round this assumption appears to be somewhat excessive.

Results of the calculations are shown in Figures 5-10. Figures 5 and 6 show surface temperatures of both the M829A1 and the advanced round at three representative axial locations, 640-mm, 1050-mm, and 1350-mm from the Rear Face of the Tube (RFT). The 640-mm location is

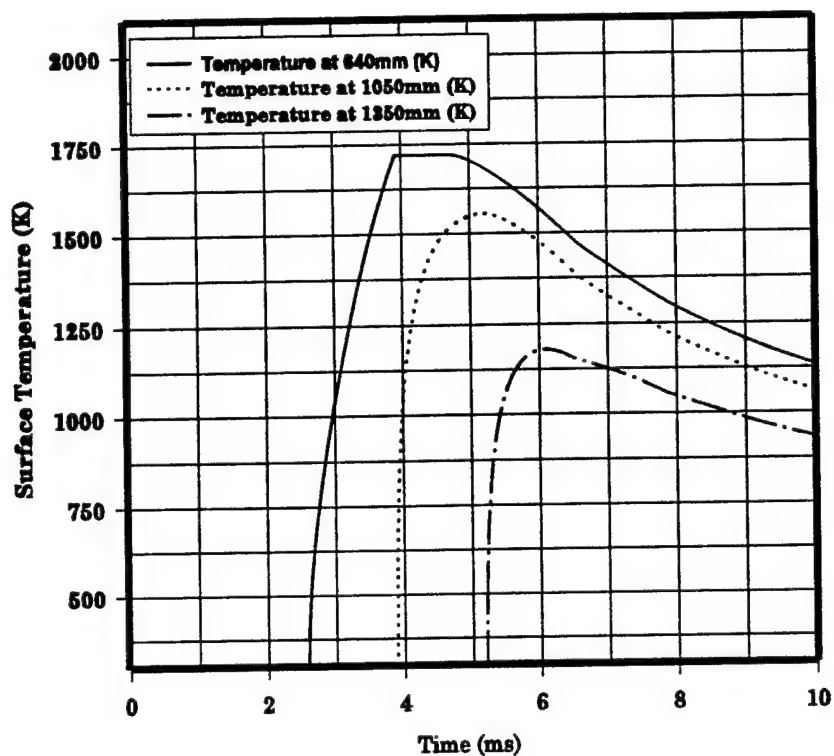


Figure 5 Surface temperatures for the M829A1 KE round in a non-chromed M256 cannon.

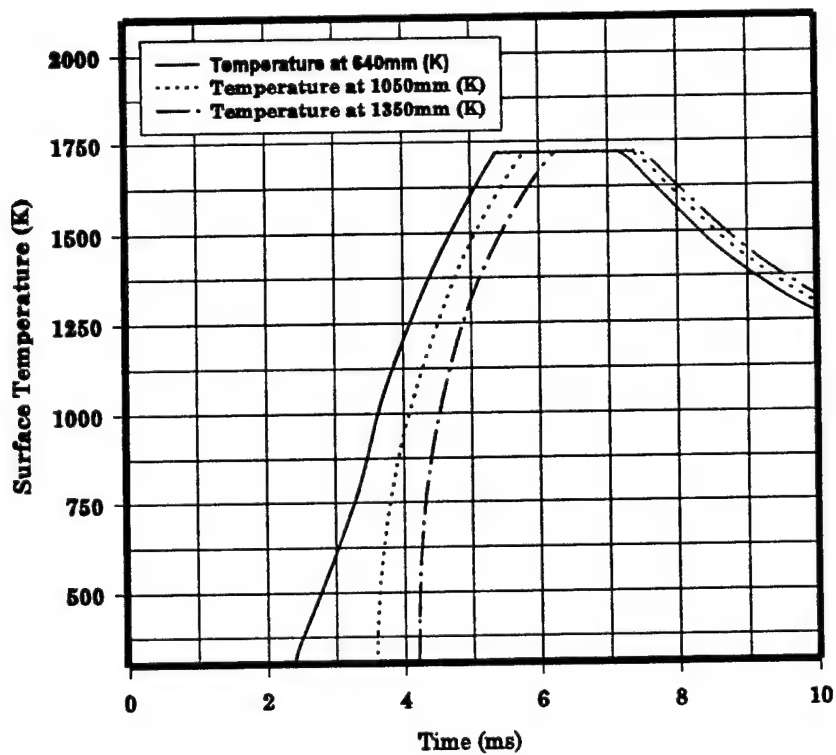


Figure 6 Surface temperatures for an advanced KE round in a non-chromed M256 cannon.

near the forcing cone region. One can see from Figure 5 that the surface just barely reaches the specified melt temperature at the 640-mm axial location, while at the more distant locations down bore the surface does not reach the melt temperature. Experimentally, bore enlargement is noted at this location as well [27]. Looking at Figure 6, what is first noticed is that the melting in this case is much more severe and for a much longer duration at all three axial locations presented (and in between as well). Also noted is that the peak temperature for this round is reached somewhat later and longer in duration than that of the M829A1. This is due to the different propellant grain geometry, which was designed to create just such an effect in the pressure profile, in order to optimize the ballistic performance with the given constraints.

Figures 7 and 8 show the resultant surface heat fluxes due to convection and thermochemical reactions. Notice that in both cases, the level of thermochemical energy imparted to the surface is on the order of 1% of the total energy. This is intuitively correct because convective heat transfer calculations gave very good agreement with experimental data [25]. The M829A1 flux rises and decays much more rapidly than that of the advanced round, again due to the charge design. The advanced round shows a spike at the peak of the flux that is believed to be caused by the "slivering" (the point at which the grain burns through its web) of the grain.

Erosion rates are shown in Figure 9 for both rounds. The erosion rate for the M829A1 is almost an order of magnitude smaller than that of the advanced round. Even though the surface temperature is constant during melting, the erosion rate follows the heat flux contour, including the spike at the peak heating rate. The erosion rate decreases for the advanced round as the axial location increases from the RFT.

Figure 10 reveals the amount of material removed for both rounds. The M829A1 erodes much less at the forcing cone region than the advanced round. The predicted erosion rate is about 16% below the experimental data (average of 39 rounds) for the advanced round and a bit high for the average M829A1 round. For abnormal erosion, the M829A1 calculation was within the data range. The use of constant physical properties in the calculations probably accounted for some of this discrepancy. It is also possible that for the M829A1 rounds, that more chrome existed at the surface, thus preventing much erosion.

### **Surface Chemistry Results:**

Table 1 is representative of the chemistry occurring at the surface at an axial location during one time step. Both the input and output from the thermochemical calculation are presented. A total of 34 species were considered for both the M829A1 and advanced KE penetrator, although many of these were not utilized. A user may choose any material for the surface or any additional gas products from the propellant combustion. For these calculations  $O_2$ ,  $CO_2$ ,  $H_2$ ,  $CO$ ,  $H_2O$ ,  $N_2$ ,  $SO_2$ , and  $NO$  represented about 98% of the combustion products. The surface was considered to be steel consisting of Fe(A),  $Cr_2O_3$ , Ni(B), and C(GR). The following species were included in all of the thermochemical calculations, however they converged to a value within an internally specified tolerance on the mass fraction for zero: Ni, NiO,  $NO_2$ , HNO, HCO RAD, CRO,  $CRO_2$ , SO, COS,  $S_2$ , FEO(S), FEO(L), FE, FEO,  $FEO_2H_2$ , FE(L),  $FE_3O_4(S)$ , OH, OH+, and S.

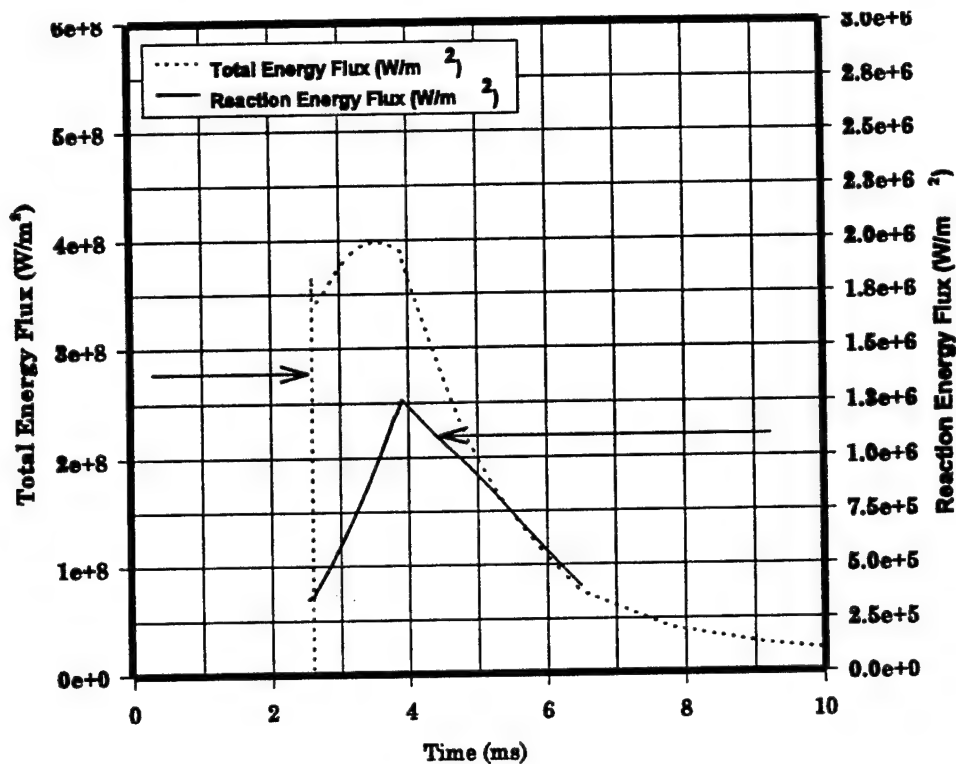


Figure 7 Energy flux distribution at 0.64 m from RFT for an M829A1 KE round in a non-chromed M256 cannon.

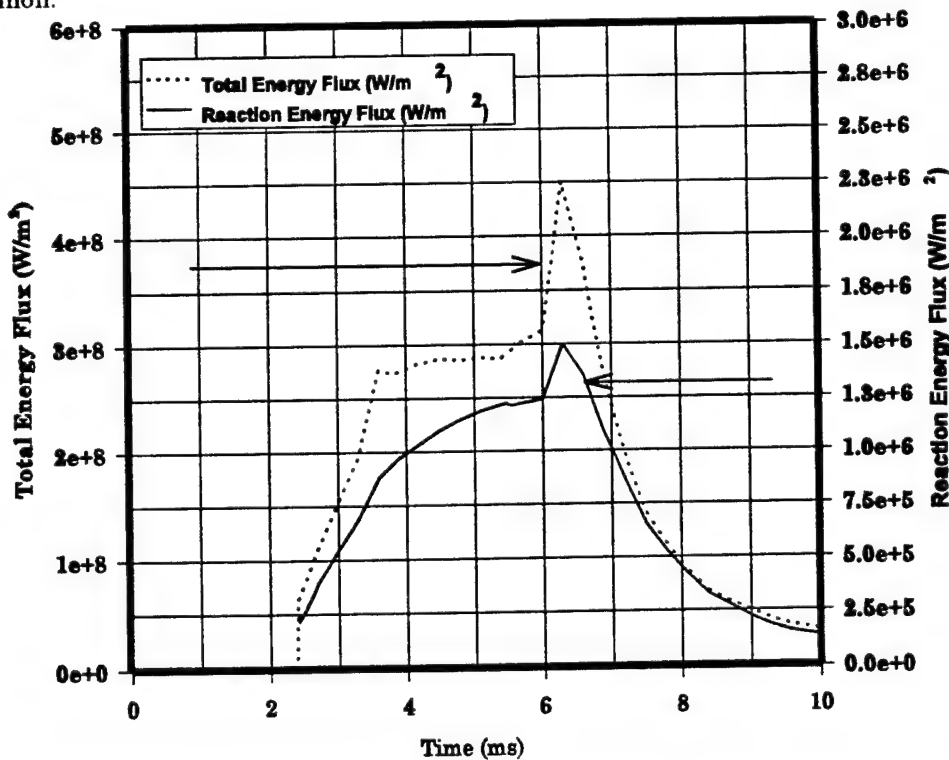


Figure 8 Energy flux distribution at 0.64 m from RFT for an advanced KE round in a non-chromed M256 cannon.

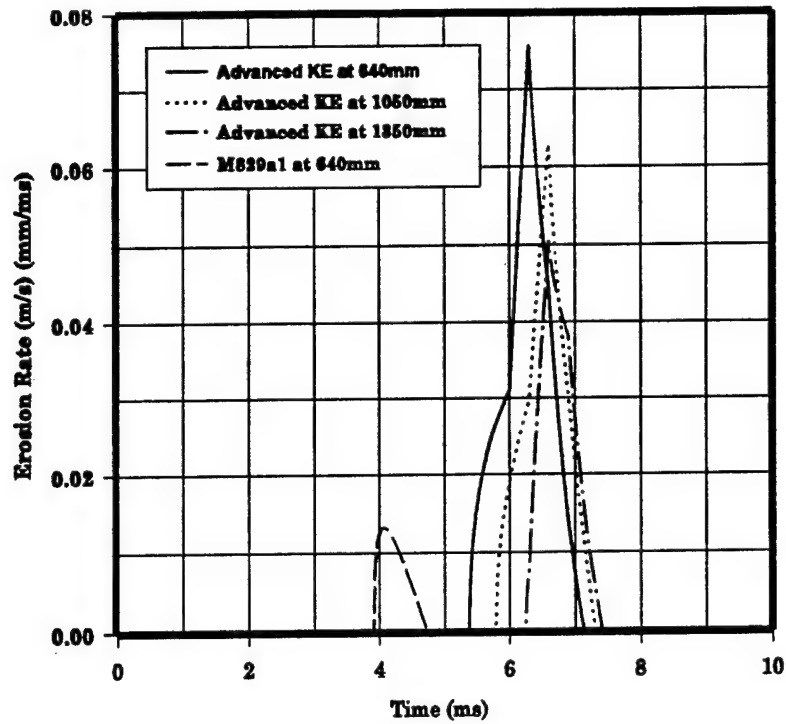


Figure 9 Erosion rates for an advanced KE penetrator at three axial locations and the erosion rate for an M829A1 KE penetrator at one axial location.

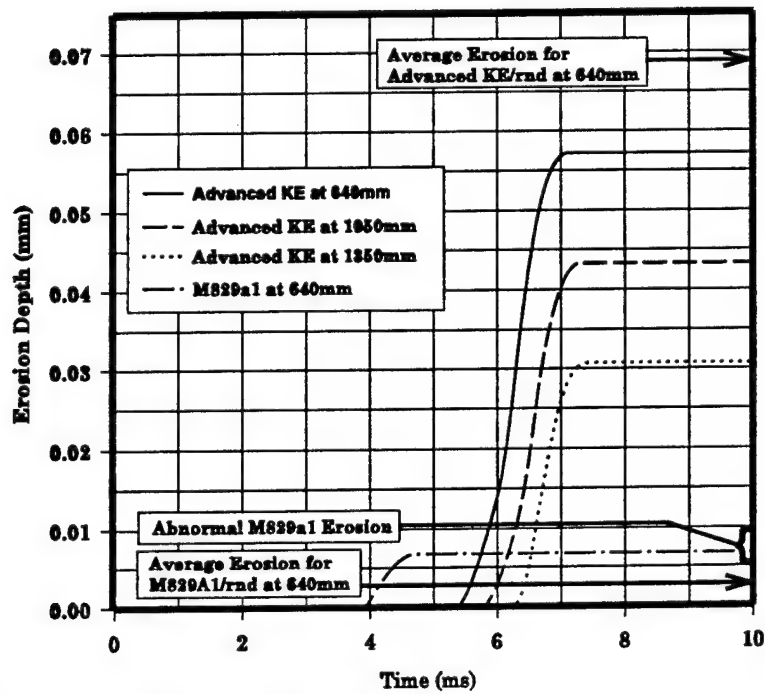


Figure 10 Erosion depths for an advanced KE penetrator at three locations and the erosion depth for an M829A1 KE penetrator at one axial location. Also presented is averaged experimental erosion depths for both penetrators.

The behavioral results from both rounds were basically the same because of the similar propellant formulation. Principally what occurs is that  $\text{CO}_2$  is not the preferred specie at the wall state. This releases the carbon and oxygen from the existing  $\text{CO}_2$ . The molecular oxygen reacts with the molecular hydrogen to make water, while the carbon forms graphite. The added  $\text{FE(A)}$  goes through the phase transition to  $\text{FE(C)}$  and the additional  $\text{NI(B)}$  melts. Please note that during this time step at this location the surface is melting and the surface is being replenished with fresh "steel". The  $\text{CR}_2\text{O}_3$  in the steel acts inertly as does the  $\text{N}_2$  from the gas. One interesting point is that the graphite formed may create a physical property modification if it dissolves or diffuses into the surface of the steel.

TIME (MS) = 5.349E-03		ENERGY RELEASED (J/KG) = 12218.7			
		UNREACTED SPECIES AT THE SURFACE		REACTION PRODUCTS AT THE SURFACE	
	SPECIES	MASS(KG)	FRACTION	MASS(KG)	FRACTION
1	H2	0.4553E-06	0.1147E-01	0.8000E-20	0.2016E-15
2	O2	0.9061E-13	0.2283E-08	0.1270E-18	0.3200E-14
3	CO	0.7709E-05	0.1943E+00	0.9855E-05	0.2483E+00
4	CO2	0.6656E-05	0.1677E+00	0.1747E-18	0.4401E-14
5	H2O	0.3950E-05	0.9953E-01	0.8019E-05	0.2021E+00
6	SO2	0.0000E+00	0.0000E+00	0.2542E-18	0.6406E-14
7	N2	0.1073E-05	0.2704E-01	0.1073E-05	0.2704E-01
8	NO	0.2222E-11	0.5599E-07	0.1191E-18	0.3001E-14
9	C(GR)	0.8020E-07	0.2021E-02	0.9766E-06	0.2461E-01
10	FE(A)	0.1759E-07	0.4432E-03	0.2216E-18	0.5585E-14
11	NI(B)	0.3299E-09	0.8313E-05	0.2330E-18	0.5870E-14
12	CR2O3(S)	0.1634E-06	0.4117E-02	0.1634E-06	0.4117E-02
13	FE(C)	0.1958E-04	0.4934E+00	0.1960E-04	0.4939E+00
14	NI(L)	0.0000E+00	0.0000E+00	0.3299E-09	0.8313E-05
		TOTAL MASS (KG) 0.3969E-04		TOTAL MASS (KG) 0.3969E-04	
		BEFORE SUM OF MASS FRACTIONS = 0.1000E+01		AFTER SUM OF MASS FRACTIONS = 0.1000E+01	

Table 1 Representative chemical reactants and products during melting of the surface.

## **Discussion:**

A numerical method for estimating the erosion which occurs within gun tubes due to high convective and chemically reactive in-bore heating has been developed. The method has been successfully applied to estimate the erosion which may occur during the firing of M829A1 and advanced kinetic energy projectiles fired from a non-chromed M256 cannon. While chrome is present the surface does not reach a high enough temperature to enable the surface to melt. If the surface is gun steel, i.e. the chrome has chipped off, then the predicted levels of erosion are roughly in agreement with experimental observations at the forcing cone. The prediction for the M829A1 is probably high due to the absence of chrome, while the computed values for the advanced KE round were a bit low, possibly reinforcing the assumption that the chrome was overwhelmed. With the addition of currently excluded physics, the predictions should improve.

The current model provides the us with the ability to predict the effects of modifications to the propelling charge, and chemical propulsion technique i.e. liquid or solid propellants. It is evident that small chemical formulation changes greatly alter the erosion behavior [28]. Tracking these chemical modifications and their impact on the erosion behavior is now possible. This tool may be especially useful in estimating the erosive behavior before the development of new charges. It is intended to be used as a platform to build upon to include the mechanical portion of the erosion and to investigate other physics of interest such as the effect of wear reducing additives and surface treatments. Potentially, newer and more direct mitigation techniques may be identified once the causality of a specific erosion problem is determined. Also, this model has been written to incorporate boundary conditions from future interior ballistic codes such as NGEN [29]. NGEN will be fully turbulent, enabling the turbulent reacting boundary layer to be computed. This coupling will strengthen the mass and heat transfer physics and enable more confidence in the solutions.

## **Bibliography:**

1. Proceedings of the Interservice Technical Meeting on: Gun Tube Erosion and Control, Watervliet Arsenal, Watervliet, NY, 25-26 February 1970.
2. Proceedings of the Tri-Service Gun Tube Wear and Erosion Symposium, ARDEC, Dover, NJ, 29-31 March 1977.
3. Lawton, Brian, "Thermal and Chemical Effects on Gun Barrel Wear," Proceedings of the 8<sup>th</sup> International Symposium on Ballistics, Orlando, FL 23-25 October 1984.
4. Evans, Michael R., "User's Manual for Transient Boundary Layer Integral Matrix Procedure TBLIMP," Aerotherm UM-74-55, Prepared for NOSIH, October 1974.
5. Dunn, Stuart, et. al., "Unified Computer Model for Predicting Thermochemical Erosion in Gun Barrels," AIAA 95-2440, July 1995.
6. Conroy, P.J., Weinacht, P., Nusca, M.J., "U. S. Army Research Laboratory Tube Erosion Code (ATEC)," Proceedings of the 32<sup>nd</sup> JANNAF Combustion Subcommittee Meeting, October 1995.
7. Gough, Paul S., "The XNOVAKTC Code," BRL-CR-627, U. S. Army Ballistic Research Laboratory, Aberdeen Proving Ground, MD, February 1990.

8. Freedman, Eli, "BLAKE - A Thermodynamic Code Based on Tiger: Users' Guide and Manual," ARBRL-TR-02411, U.S. Army Ballistic Research Laboratory, APG, MD 21005, July 1982.
9. Anderson, Ronald D., Fickie, Kirt D., "IBHVG2- A Users Guide," BRL-TR-2829, U.S. Army Ballistic Research Laboratory, Aberdeen Proving Ground, MD 21005, July 1987.
10. Janke, P.J., et al., "Electrothermo-Chemical Propellant Extensions to the IBHVG2 Interior Ballistics Simulation: Model Development and Validation," Proceedings of the 31st JANNAF Combustion Meeting, October 1994.
11. Crickenberger, Andrew B., Talley, Robert L., Talley, James Q., "Modifications to the XBR-2D Heat Conduction Code," ARL-CR-126, U. S. ARL, APG, MD, April 1994.
12. Conroy, Paul J., "Gun Tube Heating," BRL-TR-3300, U. S. Army Ballistic Research Laboratory, Aberdeen Proving Ground, MD, December 1991.
13. Keller, George E., Conroy, Paul J., Coffee, Terence P., and Barns, J., "Chamber Heating of the AFAS Gun," ARL-TR-799, U. S. Army Research Laboratory, APG, MD, July 1995.
14. Caveny, Leonard, H., "Steel Erosion Produced by Double Base, Triple Base, and RDX Composite Propellants of Various Flame Temperatures," ARLCD-CR-80016, U.S. Army Armament Research and Development Command, October, 1980.
15. Stratford, B.S., and Beavers, G.S., "The Calculation of the Compressible Turbulent Boundary Layer in Arbitrary Pressure Gradient - A Correlation of Certain Previous Methods," Aeronautical Research Council R&M, No. 3207, 1961.
16. Kakac, S., Yener, Y., Heat Conduction, 2nd Edition, NY, Hemisphere Publishing Co., 1985.
17. Özisik, M. N., Heat Conduction, John Wiley and Sons, Inc., New York, 1980.
18. Landau, H.G., "Heating Conduction in a Melting Solid," Quarterly of Applied Mathematics, vol. 8, 1950, pp. 81-94.
19. Goodman, T.R., "The Heat-Balance Integral and Its Application to Problems Involving a Change of Phase," Transactions of the ASME, vol. 80, 1958, pp. 335-342.
20. Hirschfelder, Curtis Bird, Molecular Theory of Gases and Liquids, John Wiley and Sons Inc., New York, NY, March 1964.
21. Anderson, J.D., Hypersonic + High Temperature Gas Dynamics, McGraw Hill, NY, 1989.
22. Gutfinger, Chaim, Topics in Transport Phenomena, John Wiley and Sons, NY 1975.
23. Ruckenstein, E., "Some Remarks on Renewal Models," Chem Eng Sci, Vol 18, pp.223, 1963.
24. Gordon, S., and McBride, B.J., "Computer Program for Calculation of Complex Chemical Equilibrium Compositions, Rocket Performance, Incident and Reflected Shocks, and Chapman-Jouget Detonations," NASA SP-273, 1971.
25. Conroy, P.J., et al., "Simulated and Experimental In-Wall Temperatures for 120-mm Ammunition," ARL-TR-770, ARL, APG, MD, June 1995.
26. Mr. Andrew Brant of the ARL was instrumental in providing the necessary XKTC, BLAKE, and IBHVG2 databases for the conceptual advanced KE round, March 1996.
27. Bundy, M.L., Gerber, N. and Bradley, J.W., "Evaluating Potential Bore Melting From Firing M829A1 Ammunition," US Army Research Laboratory Technical Report, Aberdeen Proving Ground, MD, ARL-MR-107, October 1993.
28. Downs, David S., et. Al., "Prediction of Wear Characteristics of Artillery Propelling Charges," ARDEC-TR-80016, Large Caliber Weapon Systems Lab, Dover, NJ, March 1981. AD-E400572
29. Nusca, Michael J., "Investigation of Solid Propellant Gun Systems Using the Next-Generation Interior Ballistics Code," Proceedings of the 31<sup>st</sup> JANNAF Combustion Meeting, CPIA Publication no. 620, Vol 1, pp. 279-292, October 1994.

# **BORE EROSION AND HEAT TRANSFER MEASUREMENTS IN 20 AND 60-MM-CALIBER COMPARED WITH PREDICTIONS OF MODEL CALCULATIONS**

**Dr.-Ing. F. Seiler\*, Dipl. Phys. K. Zimmermann, J. Raupp, G. Zettler**

**German-French Research Institute of Saint-Louis (ISL)  
5 rue du Général Cassagnou, 68301 Saint-Louis, France**

## **ABSTRACT**

In the present study, the action of the hot and compressed propellant gas flow inside the barrel of a powder gun on heat transfer and barrel erosion has been investigated (1) theoretically using the boundary layer & ablation model BABEL and (2) experimentally measuring bore temperature and bore surface erosion in ISL's 20-mm- and 60-mm-caliber erosion-guns. For theoretical description, an in-bore boundary layer model was developed using some basic assumptions for the interior gun tube flow. Prandtl's boundary layer equations were used to solve the unsteady, compressible and turbulent boundary layer development at discrete projectile locations. Melting erosion at the inner surface is taken into account in this interior ballistics heat transfer model. This allows the prediction of tube erosion where melting processes at the bore surface are dominant.

The results describing the development of the compressible, turbulent boundary layer at the inner tube wall are compared with heat transfer measurements performed in ISL's 20-mm- and 60-mm-test-gun by use of thermocouples. Erosion measurements are carried out by erosion surface sensors made of barrel steel in 20-mm-caliber and in 60-mm-caliber by measuring directly the diameter increase inside the bore. It can be found that the agreement between the analytical solutions for gun tube heating & ablation with the experimental results of gun-tube firing is quite good, though there are sometimes some differences. To check the model applicability carefully, the calculated results consider the structure of the thermocouples consisting of a thin layer of nickel on a steel sensor tip. For particular reasons the surface of gun tubes is coated, e.g., by chromium. A new idea is to use two thin coating layers, i.e., chromium on copper on gun steel. How the inner tube temperature is affected by this measure will be discussed.

## **1. INTRODUCTION**

In conventional gun tube flows generally the Reynolds number is so high that viscosity and heat conduction are important factors only in the boundary layer at the inner tube wall. Across this wall layer the velocity increases from zero to free stream velocity, and the gas temperature

changes from the temperature at the inner tube surface to the higher gas temperature inside the core flow of the propellant gas. For the theoretical description of the formation of the turbulent boundary layer, usually the conservation equations for mass, momentum and energy are used. The turbulence of the flow is taken into account with a turbulence model, e.g., the k-e model. It is difficult, however, to find an analytical solution for the complex system of equations needed. Thus, the calculation of the complete set of differential equations must be performed with numerical methods, e.g., [1-3].

Compared with these efforts an analytical solution has the advantage to show fastly the influence of important input parameters, although perhaps the solution is due to some simplifications not as exact as with solving the full set of equations. Therefore an analytical solution resulting from Prandtl's boundary layer equations has been developed for predicting the formation of turbulent in-bore boundary layer.

## **2. ANALYTICAL BOUNDARY LAYER MODEL FOR GUN TUBE HEATING**

### **Existing calculation schemes**

If only the boundary layer formation is taken into account, then simplified conservation equations [4] can be applied. Such calculations have been carried out by MAY and Heinz [5] for the case of a compressible and laminar tube boundary layer. The calculations of ADAMS and KRIER [6] involve the unsteady, compressible and turbulent boundary layer using the boundary layer equations combined with a simple turbulence model. Again, numerical methods are required in order to solve the differential equations in references [5] and [6].

The disadvantage of all these theoretical models is that they are time consuming and require a great amount of computer resources. Therefore, it is desirable to have a simplified analytical solution which can run on a work station or a personal computer for predicting the formation of the boundary layer in gun tube flows, even if it yields only an approximate description of the realistic event.

### **Equations for boundary layer development**

The simplified formation of the boundary layer inside a gun tube is illustrated in the schematic of Fig. 1. In the vicinity of the base of the projectile, an unsteady boundary layer is formed at the wall of the gun barrel, called "projectile boundary layer". It develops instationary downstream as the projectile is accelerated down the tube. In addition, a stationary bore boundary layer originates at the breech: "breech boundary layer". The entire boundary layer formation can be described, if one couples both the projectile and breech related boundary layers at equal boundary layer thicknesses.

The formation of the gun tube boundary layer is treated in two dimensions which is justified in case if the boundary layer thickness is small compared with the bore diameter. The time-dependent and unsteady boundary layer development between breech and projectile will be approximated by taking into account the actual flow pattern upstream of the projectile at

successive time intervals  $\Delta t_0, \Delta t_1, \Delta t_2, \dots, \Delta t_n = t_{n+1} - t_n$ , see Fig. 2. During each of the steps  $\Delta t_0, \Delta t_1, \Delta t_2, \dots, \Delta t_n$  the problem is treated as a stationary one, wherefore the time-dependence can be withdrawn of Prandtl's boundary layer equations used [4]. Then the following equation can be obtained for the wall shear stress  $\tau_w$  [7]:

$$\tau_w = \frac{d}{dx} \int_0^\delta \rho u (u_2 - u) + \frac{du_2}{dx} \int_0^\delta (\rho_2 u_2 - \rho u) dy. \quad (1)$$

The experimentally determined velocity profiles in turbulent boundary layers are given approximately by the power-law equation [4]:

$$\frac{u}{u_2} = \left( \frac{y}{d} \right)^{\frac{1}{n}}, \quad 5 \leq n \leq 10. \quad (2)$$

Introducing equation (2) into (1) for both the breech and the projectile boundary layer two sets of differential equations are obtained which are solved with the following boundary conditions inside the outer core flow:

- (1) the flow velocity increases linearly from breech ( $u = 0$ ) to projectile ( $u = u_p$ ),  
 (2) gas pressure  $p$  and temperature  $T$  are assumed to be constant along the tube axis for a given time interval  $\Delta t_n$ .

These quantities  $u, p, T$  change in time with proceeding projectile displacement  $x_p = x_p(t)$  along the gun barrel:  $p = p(t), T = T(t)$ . The flow velocity  $u(x, t) = u_p x/L$  between breech and projectile is approximated linearly to the calculation results given by KRAUTH [14]. From KRAUTH [14] the gas pressure and gas temperature is nearly independent of the  $x$ -coordinate, except the beginning of the firing cycle, wherefore in our calculations the pressure  $p$  and the temperature  $T$  is set only a function of the running time  $t$ :  $p = p(t), T = T(t)$ . Integration of the two differential equations yields analytical solutions for the boundary layer thickness  $\delta$  and the heat flux  $\dot{q}_g$  from gas into the tube surface [8, 9].

**Solution for the projectile boundary layer heat flux:**

$$\begin{aligned} \dot{q}_g(\bar{x}) = & \left( \frac{n+1}{n+3} \right)^{\frac{2}{n+3}} (B(n) \varphi)^{\frac{n+1}{n+3}} c_p (T_r - T_w) \text{Pr}^{-\frac{2}{3}} \rho_e \\ & \cdot \left( \frac{v_2 \delta^{**}}{L \delta} \right)^{\frac{2}{n+3}} u_e^{\frac{n+1}{n+3}} \left[ -\ln \left( 1 - \frac{\bar{x} \delta^*}{L \delta^{**}} \right) \right]^{\frac{2}{n+3}}. \end{aligned} \quad (3)$$

**Solution for the breech boundary layer heat flux:**

$$\dot{q}_g(x) = \left( \frac{n+1}{n+3} \right)^{\frac{2}{n+3}} (B(n)\varphi)^{\frac{n+1}{n+3}} c_p (T_r - T_w) Pr^{-\frac{2}{3}} \rho_e \cdot \left( \frac{\delta^{**}}{\delta} \right)^{\frac{2}{n+3}} \left( u_e \frac{x}{L} \right)^{\frac{n+1}{n+3}} \left( \frac{v_e}{x} \right)^{\frac{2}{n+3}} \quad (4)$$

**3. WALL TEMPERATURE CALCULATION**

The variations of the calculated heat flux along the breech's x-coordinate in equation (4), resp. along the projectile's  $\bar{x}$ -coordinate in equation (3), are very small. Therefore, the heat flux  $\dot{q}_w(x)$ , resp.  $\dot{q}_w(\bar{x})$ , into the tube is approximately one-dimensional in depth (y) and the one-dimensional heat-conduction equation was applied. By integration with the boundary conditions given in [9], one obtains the following solution for the temperature change  $\Delta T_w$  into the tube wall as a function of the heat flux  $\dot{q}_w(x)$ , resp.  $\dot{q}_w(\bar{x})$ , at the surface (y = 0), [10]:

$$\Delta T_w(x, y, t) = \frac{1}{\sqrt{\pi \rho_w c_w \lambda_w}} \int_0^t \frac{\dot{q}_w(x, \tau)}{\sqrt{t-\tau}} \exp\left(\frac{\rho_w c_w y^2}{4 \lambda_w (t-\tau)}\right) d\tau \quad (5a)$$

Introducing the heat flux  $\dot{q}_w(x, y=0, t=t_1, \dots, t_n)$  of equations (3), or (4) in equation (5a) by assuming that the heat flux at the surface at y = 0 is equal on both the gas side and the wall side, with  $\dot{q}_g(x, t) = \dot{q}_w(x, y=0, t)$ , the temperature distribution  $T_w(x, y, t)$  inside the gun barrel can be calculated. The procedure described is carried out for each time interval  $\Delta t_0, \Delta t_1, \Delta t_2, \dots, \Delta t_n$  at all  $x < x_p$  for getting the temperature distribution  $T_w(x, y, t)$  inside the gun tube with projectile displacement in time. Fig. 3 presents schematically the  $\dot{q}_w(x)$ -variation with ongoing time t, with  $\dot{q}_w(x) = \text{constant}$  during each time-step  $\Delta t_n$ . The total bore temperature increase of  $\Delta T_{w, \text{total}}$  is for a certain time-step given as follows:

$$\begin{aligned} t=t_1: \dot{q}_{w,1} &= \dot{q}_{w,1} \\ t=t_2: \dot{q}_{w,2} &= \dot{q}_{w,1} + (\dot{q}_{w,2} - \dot{q}_{w,1}) \\ t=t_3: \dot{q}_{w,3} &= \dot{q}_{w,1} + (\dot{q}_{w,2} - \dot{q}_{w,1}) + (\dot{q}_{w,3} - \dot{q}_{w,2}) \\ &\vdots \\ t=t_n: \dot{q}_{w,n} &= \dot{q}_{w,1} + (\dot{q}_{w,2} - \dot{q}_{w,1}) + (\dot{q}_{w,3} - \dot{q}_{w,2}) + \dots + (\dot{q}_{w,n} - \dot{q}_{w,n-1}) \\ &\downarrow \quad \downarrow \quad \downarrow \quad \downarrow \quad \downarrow \\ \Delta T_{w, \text{total}} &= \Delta T_{w,1} + \Delta T_{w,2} + \Delta T_{w,3} + \dots + \Delta T_{w,n} \end{aligned}$$

$$\Rightarrow \Delta T_{w, \text{total}} = \sum_{k=1}^n \Delta T_{w, k} \quad (5b)$$

The temperature increase for each  $\Delta T_{w, k}$  is calculated with equation (5a) and will be a function of both the heat flux  $\dot{q}_w$  and the depth ( $y$ ).

#### 4. ANALYTICAL ABLATION MODEL

##### Assumptions

It is assumed that ablation occurs only by melting erosion with no evaporation. Melting erosion often takes place when hot gas flows with a high stagnation temperature are in contact with colder walls. This process is extensively treated by many authors, see ADAMS [15]. In the paper of SEILER [16] an analytical ablation model for calculating melting processes on the sharp-nose cone of a ram-projectile is described. This model was used and transformed to predict surface melting in gun barrels. It is assumed that the tube geometry remains approximately unchanged by heating and ablation, i.e., ablation is small. Therefore, the boundary layer formation is considered to be uninfluenced. Due to strong shear stresses it is supposed that the molten material is wiped away from the bore surface immediately as it is produced by heat input in the case that the wall temperature exceeds the melting temperature. That means that no liquid layer develops on the solid surface. Heat addition from melt to gas flow is not considered.

##### Ablation equations

Heating and melting ablation are decoupled during time interval  $\Delta t_n$  at each point  $x$  along the gun tube barrel. Supposing that for  $t < t_n$  the wall temperature  $T_{w, n-1}(x, y, t < t_n) < T_{\text{melt}}$  and for  $t = t_n$  the wall temperature  $T_{w, n}(x, y, t)$  exceeds first time the melting temperature  $T_{\text{melt}}$  by the heat input into the wall  $\dot{q}_{w, n}(x, t) = \dot{q}_g$ , see Fig. 4. Now melting occurs in the layer  $\Delta y_1$  at time interval  $\Delta t_n = t_{n+1} - t_n$  and the melting heat  $h_{\text{melt}}$  of the wall material has to be taken into account. The total heat flux input  $\dot{q}_{w, n}$  must be divided into one part  $\dot{q}_{c, n}(x, t)$  for heat conduction and one part for heat of melting:

$$\dot{q}_{w, n}(x) \Delta t_n = \dot{q}_{c, n}(x) \Delta t_n + \rho h_{\text{melt}} \Delta y_j, \quad j = 1, \dots, m. \quad (6)$$

For obtaining the molten layer  $\Delta y_j (j = 1, \dots, m)$  along the time steps  $n$ , equation (6) can be solved with equations (5) and the additional assumption

$$T_{w, \text{total}, n}(x, y = y_{n+1}) = T_{\text{melt}}. \quad (7)$$

At the end of time interval  $\Delta t_n$  the molten layer  $\Delta y_j$  is wiped away by the shearing forces exerted by the strong wall shear stress  $\tau_w$ . The described processes of melting and shearing are continued during the whole ram acceleration cycle, as:

$$\begin{aligned}
 t < t_n: T_{w,n-1} &< T_m \\
 t = t_n: T_{w,n} &> T_m \xrightarrow{\Delta y_1 = y_{n+1} - y_n} T_{w,n+1} = T_m, \\
 t > t_n: T_{w,n+1} &> T_m \xrightarrow{\Delta y_2 = y_{n+2} - y_{n+1}} T_{w,n+2} = T_m, \\
 & \\
 T_{w,n+m} &> T_m \xrightarrow{\Delta y_m = y_{n+m} - y_{n+m-1}} T_{w,n+m} = T_m.
 \end{aligned} \tag{8}$$

Then, the total erosion  $e$  at position  $x$  is:  $e(x) = \sum_{j=1}^m \Delta y_j(x), j=1, \dots, m.$  (9)

## 5. 20-MM-CALIBER GUN BARREL SET-UP AND INSTRUMENTATION

### The 20-mm-test-gun

For bore temperature determination single-shot experiments have been performed in a test-gun device of 20-mm-caliber. The gun setup consists mainly of the combustion chamber, the gun tube and a cylinder inset, see Fig. 5a. This removable cylinder tube is equipped with bore holes in two measuring cross-sections (A) and (B) which can be instrumented for temperature gauging with thermocouples, pressure gauges and steel erosion sensors for measuring ablation at the sensor surface, see Fig. 5b. The steel used for the sensors of Fig. 6 is the same used for the gun: 35 NCD 16. Typical features of the test-gun device [11] are: The barrel is not rifled. The projectile is starting from the forcing cone. The propellant is loaded into the combustion chamber inside of a bag and the charge is fired via an electrical igniter.

### Temperature measurements

For bore temperature gauging Ni-steel thermocouples have been developed as given in Figure 7. They consist of a steel housing and a centered nickel wire with a non-conductive layer for electric insulation. At the front side of the thermocouple a galvanic nickel layer (thickness 10 up to 100  $\mu\text{m}$ ) was coated. Therefore, the tube temperature is measured in depth at the nickel/steel contact layer and not at the inner bore surface.

## 6. COMPARISON OF HEATING MODEL/20-MM-GUN

### Input parameters

The propellant considered for gun firing is the double-base propellant GB-Pa 125 with an adiabatic flame temperature of 3750 K. A 58 g charge is always used. All computations take

account of the geometry and the interior ballistics of the 20-mm-test device. The analytical solution from code BABEL is based on gas pressure, gas temperature and flow velocity as they are computed as boundary conditions by the numerical method of Heiser et al. [12]. The Prandtl number 0.81 and the exponent  $n = 7$  in equation (2) are used. The thermophysical properties as they are introduced in the solution of the heat conduction equation (5a) for 35 NCD 16 gun steel are as follows: density  $\rho = 7828 \text{ kg/m}^3$ , specific heat  $c = 460 \text{ Ws/kg K}$  and heat conduction  $\lambda = 36 \text{ W/m K}$ . For nickel the values used for  $\rho$ ,  $c$  and  $\lambda$  are: density  $\rho = 8900 \text{ kg/m}^3$ , specific heat  $c = 440 \text{ Ws/kg K}$  and heat conduction  $\lambda = 60 \text{ W/m K}$ . Chromium: density  $\rho = 6900 \text{ kg/m}^3$ , specific heat  $c = 455 \text{ Ws/kg K}$  and heat conduction  $\lambda = 69 \text{ W/m K}$ .

All the following data are taken at the first measuring station (A) down the tube which is 33 mm off the initial starting position of the projectile's base.

#### Tube made of steel

In the following some results calculated with equations (5a,b) applied successively along the time-step procedure are presented and compared with experimental results. Fig. 8 shows the calculated temperature distribution in the inner wall surface in depth of  $y = 0$  (upper curve)/10/ 30/ 50 and 100  $\mu\text{m}$  (lower curve) as they are chosen for the experiment assuming gun barrel 35 NCD 16 steel for the whole wall.

#### Steel tube with nickel layer

The thermocouples used have a nickel layer on the side exposed to the gas flow. To compare more realistically theory and experiment, the nickel layer has to be taken into account in the calculation scheme. A second heat conduction equation has to be solved for the nickel layer on steel [7]. Therefore, two solutions are present. One for the temperature distribution inside the nickel layer, designed with the index (s):

$$\Delta T_w(y \leq d, t) = \frac{1}{\sqrt{\pi \rho_s c_s \lambda_s}} \left\{ \int_0^t \frac{\dot{q}_w(0, \tau)}{\sqrt{t-\tau}} \exp\left(-\frac{\rho_s c_s y^2}{4 \lambda_s (t-\tau)}\right) d\tau + \sum_{n=1}^{\infty} \sigma^n \int_0^t \frac{\dot{q}_w(0, \tau)}{\sqrt{t-\tau}} \right. \\ \left. \cdot \left[ \exp\left(-\frac{\rho_s c_s (2nd+y)^2}{4 \lambda_s (t-\tau)}\right) + \exp\left(-\frac{\rho_s c_s (2nd-y)^2}{4 \lambda_s (t-\tau)}\right) \right] d\tau \right\} \quad (10)$$

$$\sigma = \frac{\sqrt{\frac{\rho_s c_s \lambda_s}{(\rho c \lambda)_{\text{steel}}} - 1}}{\sqrt{\frac{\rho_s c_s \lambda_s}{(\rho c \lambda)_{\text{steel}}} + 1}}$$

and one for the temperature distribution inside the steel tube.

There is no big difference between the results in Fig. 8 (steel tube) and in Fig. 9 (0/10/30/50/100  $\mu\text{m}$  nickel layer on steel), which show the bore temperature variation in depth of  $y = 0/10/30/50/100 \mu\text{m}$ . This comparison means that the nickel/steel thermocouples can be used successfully for temperature gauging in steel tubes. The deviations between both cases, Figs. 8 and 9, are of the order of the measuring error of about 10%.

The experimental results are given in Fig. 10 for the depth of 10/30/50 and 100  $\mu\text{m}$ . The calculation for, e.g., the depth of 10  $\mu\text{m}$  gives about 200 K higher maximal wall temperatures than the experiment compared with the corresponding calculated curves in Figs. 8 and 9. The reason for the deviation can be probably found in the assumption of the theoretical model and/or in the boundary conditions for gas pressure and gas temperature used from numerical calculations [12] which are done for the 20-mm-gun firings under these conditions. In depth the deviation between theory and experiment becomes smaller.

### Steel tube with chromium coating

It is preferred to extend the life-time of barrels with chromium coatings at the inner surface. The upper curve of Fig. 11 shows the surface temperature at  $y = 0$  for the steel tube, the lower one that for a chromium tube. In between there are the curves for chromium coated tubes with 100/200/300  $\mu\text{m}$  coatings. Chromium coating reduces the tube surface temperature. With a chromium layer of already 200  $\mu\text{m}$  a maximum surface temperature reduction can be obtained. An important result is, that in chromium coated steel tubes the temperature under the chromium layer is consequently exerted to smaller temperatures than at the surface of a tube without chromium.

### Ablation

The melting erosion on steel can be calculated with the procedure of equation (9). For the fired gun cycle with the 58 g GB-Pa 125 powder charge, at measuring station (A) 33 mm downstream of the projectile's base at time  $t = 0$ , the surface erosion is estimated with equation (9) to  $e = 1 \mu\text{m}$  per shot. In Fig. 12 the behavior of melting erosion is clearly seen. Erosion becomes dominant only for a short time period at the beginning of the gun firing. Then melting stops and the ablation remains unchanged. Experimental data are available from so-called "Knoop indentations" pressed into erosion sensors, see Fig. 13. In measuring there length before and after firing the loss in depth can be determined [13] to more than 1.25  $\mu\text{m}$  per firing. Though the ablation model is very simple, the calculated and measured erosion rate is of the same order. This comparison shows that, as assumed for the ablation calculation, here mainly melting processes are responsible for tube wear which is some orders higher than without surface melting processes.

## 7. 60-MM-CALIBER EROSION GUN

The 60-mm-caliber erosion gun (Fig. 14) is specially designed for testing inner coatings in steel barrels. The gun barrel begins with a tube segment of 170 mm length which is used for the erosion measurements. This cylindrical inset, see Fig. 15, can be removed for erosion

investigations. This removable segment is equipped with bore holes for temperature and pressure gauging. Erosion data are gathered by determining the increase of the inner bore diameter. As for the 20-mm-gun the bore temperature is measured with the thermocouples shown in Fig. 7.

Pressure and temperature distributions are shown in Fig. 16: pressure P1 at measuring station M1 (combustion chamber), P2 and barrel temperature T2 at station M2. M2 is placed in the middle of the 170 mm long cylindrical erosion inset. The gun powder used is 1.2 kg GB-Tu 125 and the projectile mass is typically 1.5 kg with a nylon driving band. Gun firings have been done with (1) steel erosion tubes (35 NCD 16), (2) erosion tubes coated with 150  $\mu\text{m}$  chromium on steel and (3) coated with 50  $\mu\text{m}$  chromium on a copper layer on steel. Metallographic investigations in the tube inset layers have been carried out but the results are not included in this paper.

The travel of the projectile inside the barrel was calculated taking into account the pressure forces acting at the base of the projectile. The result is given in Fig. 17 with the velocity distribution fitted to the experimentally determined muzzle velocity. The gas pressure and temperature variations in time at the projectile's base along its travel is drawn in Fig. 18. These data are determined for shot no. 20 and are used as input parameters for the boundary layer & ablation BABEL-calculations.

## 8. COMPARISON OF HEATING & ABLATION MODEL/60-MM-GUN

### Input for BABEL-Code

The same input parameters are used as previous discussed for the 20-mm-gun calculations, concerning the thermophysical properties density, specific heat and heat conduction for the gun barrel steel as well as for nickel and chromium. Additionally, the data for copper are enclosed: density  $\rho = 8342 \text{ kg/m}^3$ , specific heat  $c = 476 \text{ Ws/kg K}$  and heat conduction  $\lambda = 359 \text{ W/m K}$ . Reinforced copper is used to make it more resistant against mechanical forces exerted by the projectile and the gas pressure.

### Steel tube with nickel layer/thermocouple

A comparison between temperature measuring results gathered with the thermocouple sensors and BABEL-calculations are compared in Fig. 19 for shot no. 20. The calculations are done for a hypothetical gun tube with a 10  $\mu\text{m}$  nickel layer on gun steel to model the thermocouple design with 10  $\mu\text{m}$  nickel on steel housing. The calculated profile begins as steep as the experimental one. Also the maximum temperature is in good agreement.

### Steel tube

The bore temperature distributions calculated with BABEL for predicting the nickel/steel thermocouple measuring results in depth of 10  $\mu\text{m}$  show, compared with that in steel (Fig. 20: 10  $\mu\text{m}$  depth), a deviation which is smaller than the already mentioned measuring error of 10%.

Therefore the thermocouples could practically be used without temperature transformation to determine the temperature in barrels of steel guns, in case the thermocouple housing is of the same steel type as used for the barrel.

### **Ablation**

Using the procedure of equation (9), the total melting erosion  $e$  was estimated at two positions: 6 cm and 9 cm upstream of measuring station M2. It can be seen that the calculated melting erosion increases towards the erosion tube inlet (upstream) and decreases downstream. The calculated melting ablation is in good agreement within the limits given from the experiment on the one hand at the inlet to the erosion tube (30  $\mu\text{m}$  per shot) and on the other hand at the outlet (10  $\mu\text{m}$  per shot). This result supports the model assumptions of steel melting followed by wiping and shows the good applicability of model BABEL to describe interior gun tube heating and ablation.

### **Steel tube with chromium coating**

A chromium coating reduces the surface bore temperature compared with the case of an uncoated steel tube, see Fig. 22 for 150  $\mu\text{m}$  chromium layer on steel tube. Fig. 23 shows that in depth of 150  $\mu\text{m}$  (contact layer chromium/steel) the bore temperature is slightly higher in a chromium/steel tube compared with the simple steel case. An important result is the fact that with chromium coating the steel barrel is protected against the high maximum temperatures of about  $T = 1800\text{ K}$  seen in Fig. 22. The 150  $\mu\text{m}$  chromium layer decreases the maximum steel temperature by about  $\Delta T \approx 800\text{ K}$  to about  $T = 1000\text{ K}$ .

It is also important to optimize the chromium layer thickness for protecting optimally the steel barrel against too high temperatures. Therefore BABEL-calculations have been done with 50/150/250  $\mu\text{m}$  thick chromium layers on steel barrels. The results are depicted in Figs. 24 and 25. At the inner surface a chromium layer thickness of 50  $\mu\text{m}$  can be tolerated. More than 150  $\mu\text{m}$  is not necessary, see Fig. 24. In order to reduce the temperature of the steel tube, e.g., below  $T = 800\text{ K}$  a chromium layer of minimum more than 150  $\mu\text{m}$  is desirable. A good compromise between a thin chromium layer and a low steel temperature seems to be a coating thickness of 200  $\mu\text{m}$ .

### **Steel tube with chromium coating on a copper layer**

To reduce the bore temperature drastically, a good heat conducting coating material should be used. Calculations with reinforced copper show that the bore temperature can be dropped strongly. Newest calculations with a 50  $\mu\text{m}$  chromium layer to protect the copper layer underline this effect. The surface temperature at the chromium layer is quite high (Figs. 26 and 27), but in depth the steel tube temperature remains nearly unchanged. Future efforts will be to optimize the chromium and copper layer thicknesses or to exchange one or both materials.

## 9. CONCLUDING REMARKS

Temperature informations on gun tube heating are very important in erosion research. Therefore, in the present study the boundary layer formation has been investigated theoretically and experimentally. For theoretical description an analytical approximation beginning with Prandtl's boundary layer equations has been used. The calculation results yield informations on parameters such as boundary layer thickness and heat flux into the tube wall. Surface erosion by melting processes was considered with an ablation model. The results describing the development of the compressible, turbulent boundary layer and the heat transfer at the inner tube wall are used to find an analytical solution of the heat conduction equation for calculating the bore temperature at the inner surface and in depth.

These results are compared with bore temperature measurements in the ISL 20-mm and 60-mm-caliber test-guns using special ISL nickel/steel thermocouples. These thermocouple measurements, carried out in depths up to 100  $\mu\text{m}$  are used to show the good applicability of the interior ballistics boundary layer model at realistic interior flow conditions. In firing, e.g., in the 20-mm-caliber-gun the "hot" GB-Pa 125 propellant, surface melting occurs in the order of more than 1  $\mu\text{m}$  per shot. The erosion rate predicted by the given boundary layer model for gun tubes, BABEL, is of the same range. The 60-mm-gun erosion rates have been gathered from the bore diameter directly. Comparable results are given from the ablation model taking into account melting processes at the steel bore surface.

In summary, it is found that the agreement between the analytical solutions for gun tube heating and melting erosion with the experimental results of gun-tube firing is quite good. The model input parameters are: the pressure distribution at the projectile base and its velocity travel along the gun barrel up to the muzzle. Then, with a CPU-time of some seconds on a IBM 3090 or a PC the computer code calculates the whole heat transfer history using a time-step-procedure along the projectile's in-bore flight. In this theoretical model the experimental firing cycle data mentioned are directly used for the theoretical calculation of tube temperature and melting erosion along the path of the projectile inside of a powder gun. For a full theoretical description it is possible to use a characteristics model, e.g., [14] to provide from theoretical point of view the input parameters mentioned above.

## REFERENCES

1. SCHMITT, J.A., MANN T.L., Calculation of Compressible Flow in the Lagrange Gun by the Interior Ballistics Algorithm ALPHA, Proc. DEA-G 1060, Eglin AFB, USA, 1980
2. HENSEL, D., HEISER, R., Stand der Arbeiten in der Entwicklung des zweidimensionalen Modells AMI für die Innenballistik, ISL-report CO 211/82, 1982
3. HEISER, R., Viscous Modeling of the Interior Ballistic Cycle, Fraunhofer-Institut für Kurzzeitdynamik, Ernst-Mach-Institut, Weil am Rhein, EMI Report 10/91, 1991
4. SCHLICHTING, H., Boundary-Layer Theory, McGraw-Hill, New- York, 1960
5. MAY, H., HEINZ, C., Arbeiten zur Berechnung der laminaren kompressiblen Grenzschicht in einem Rohr, 5. Symposium über innenballistische Leistungssteigerung von Rohrwaffen, BICT, Swisttal-Heimerzheim, Germany (1979)

6. ADAMS, J., KRIER, H., Unsteady Internal Boundary Layer Analysis Applied to Gun Barrel Wall Heat Transfer, *Int. J. Heat Mass Transfer*, Vol. 24, No. 12, 1981
7. OERTEL, H., Stoßrohre, Springer Verlag, Wien-New York, 1966
8. HEISER, R., SEILER, F., ZIMMERMANN, K., Experimental and Theoretical Investigation of Heat Transfer in a Gun Barrel, 13th International Symposium on Ballistics, Stockholm, Sweden, June 1992
9. HEISER, R., SEILER, F., ZIMMERMANN, K., Computational Methods and Measurements of Heat Transfer to the Barrel of a Hot Gas Accelerator Under High Pressure, 6th International Conference on Computational Methods and Experimental Measurements, Siena, Italy, May 1993
10. OERTEL, H., Messungen im Hyperschallstoßrohr, p. 759-848 in "Kurzzeitphysik", Springer Verlag, Wien-New York, 1967
11. ZIMMERMANN, K., et al. Influence of normal and LOVA propellant charges on 20-mm-gun-tube erosion, *Proc. of the 12th International Symposium on Ballistics*, San Antonio, Tx., USA, 1990
12. HEISER, R., SEILER, F., ZIMMERMANN, K., Computational Methods and Measurements of Heat Transfer to Gun Barrels with and without Coatings, 14th International Symposium on Ballistics, Quebec, Canada, September 1993
13. SEILER, F., ZIMMERMANN, K., Methods for Gun Tube Erosion Testing and their Application in a 20-mm-Erosion-Gun, 13th International Symposium on Ballistics, Stockholm, Sweden, June 1992
14. KRAUTH, G., Nichtstationäre Rohrströmung mit Verbrennung, ISL-report R 118/83, 1983
15. ADAMS, Mac C., Recent Advances in Ablation, *ARS Journal*, 1959
16. SEILER, F., Heating and ablation of a sharp-nosed body flying at hypersonic velocity through a tube filled with highly compressed gas mixture, *IUTAM Symp. on Aerothermochemistry and Associated Hypersonic Flows*, Marseille, 1992
17. SEILER, F., Boundary layer model for calculating the heat transfer into a ram projectile fired in a ram accelerator, *Second International Workshop on Ram Accelerator, RAMAC II*, University of Washington, Seattle, USA, 1985

### Acknowledgement

The authors thank very much Dr. R. Heiser from the Ernst-Mach-Institut (EMI) in D-79576 Weil am Rhein, Germany, for the help to draw some of the diagrams presented. These have been plotted for a joint international publication

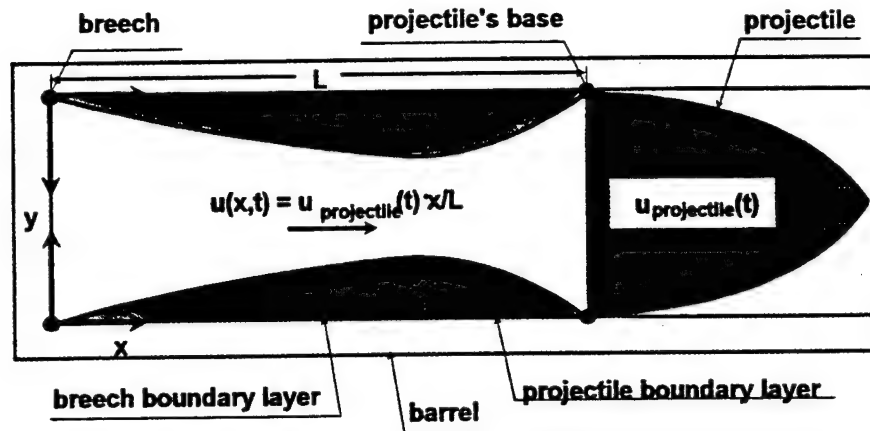


Figure 1. Schematic of boundary layer formation

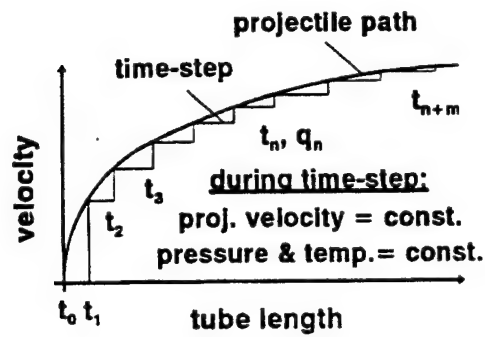


Fig. 2. Time-step approximation

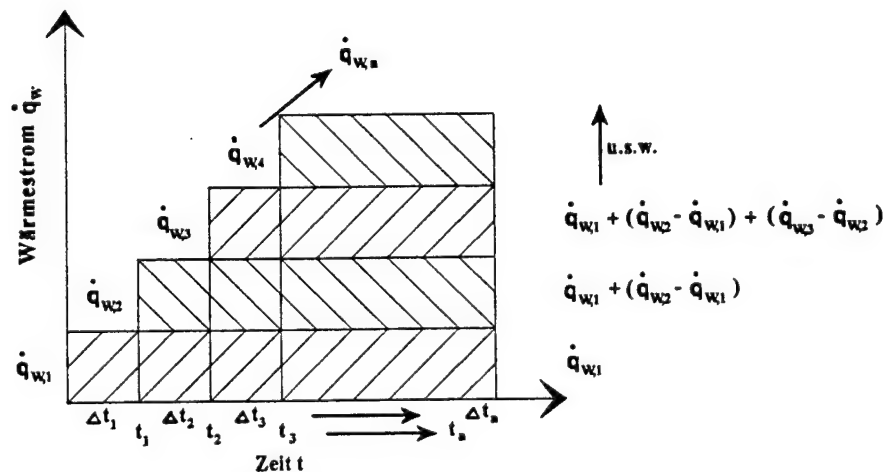


Fig. 3. Bore temperature calculation procedure

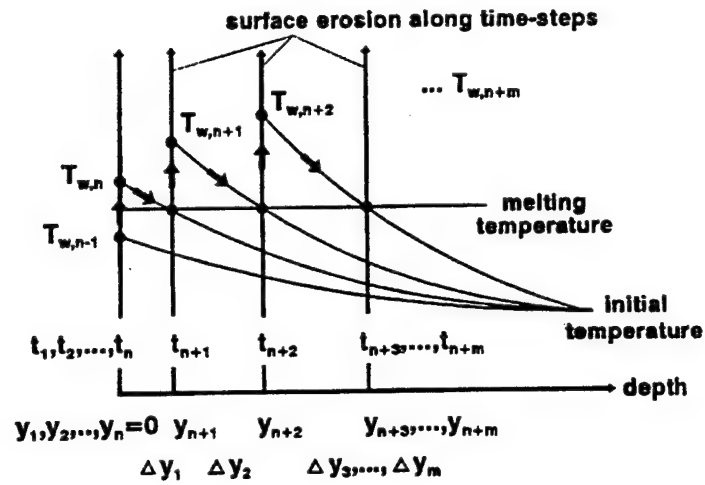


Fig. 4. Temperature  $T_{w,1} \dots T_{w,n+m}$  and ablation  $\Delta y_1 \dots \Delta y_m$  along time-step-procedure

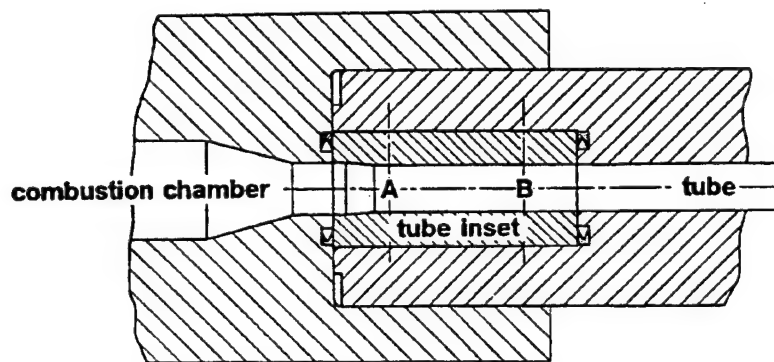


Fig. 5a. Gun tube set-up of 20-mm-caliber device

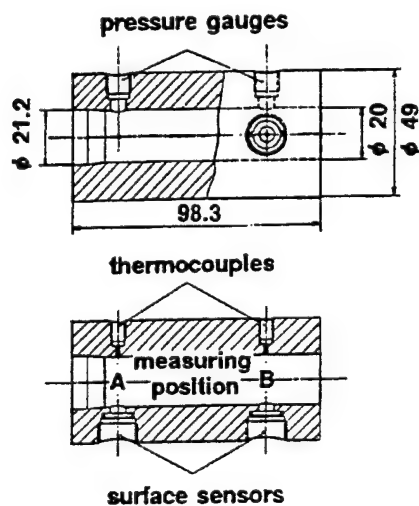


Fig. 5b. Circular erosion tube inset

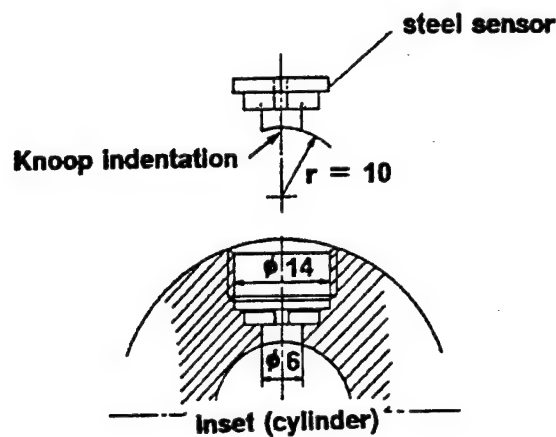


Fig. 6. Surface erosion sensors

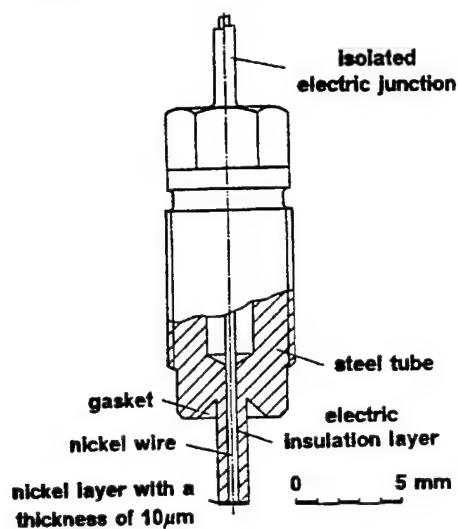


Fig. 7. Thermocouple

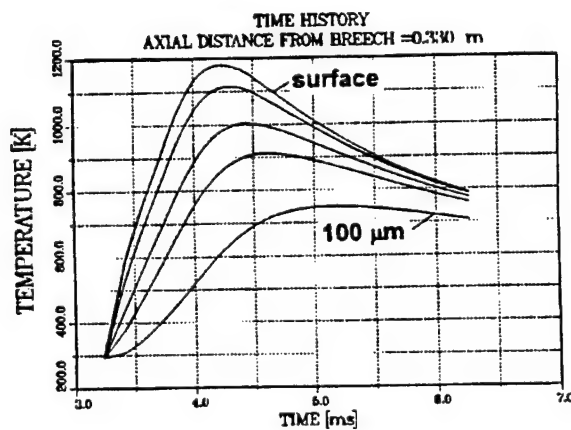


Fig. 8 Calculated bore temperature for steel tube in depth of 0/10/30/50/100  $\mu\text{m}$

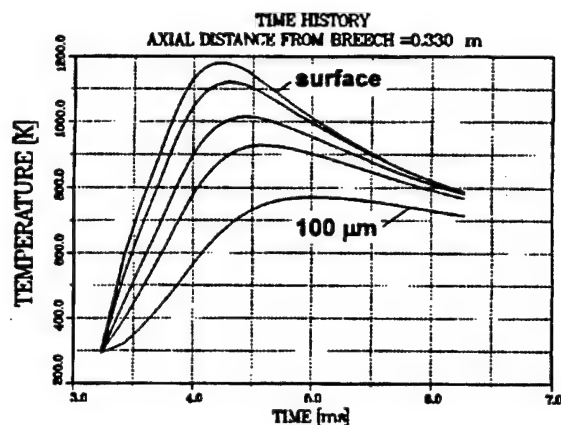


Fig. 9 Calculated bore temperature for a nickel coated steel tube: depth of 0/10/30/50/100 μm

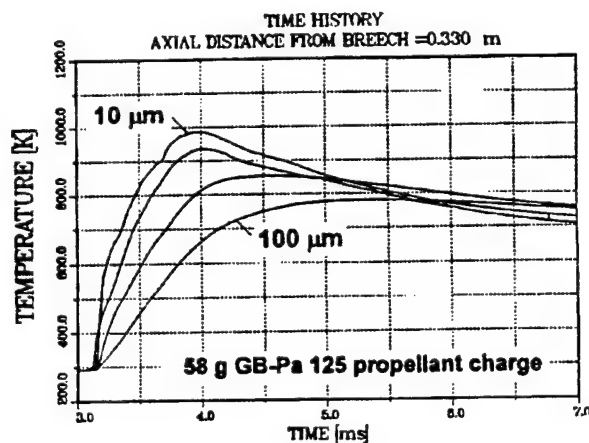


Fig. 10. Measured wall temperature in depth of  $y = 10/30/50/100 \mu\text{m}$

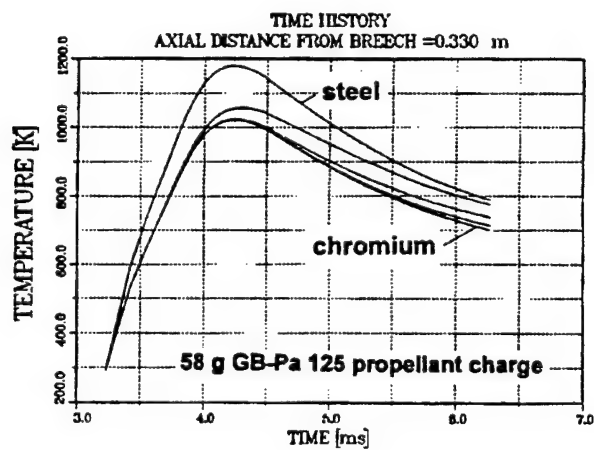


Fig. 11. Surface temperature for steel, 100/200/300 μm chromium coatings, pure chromium

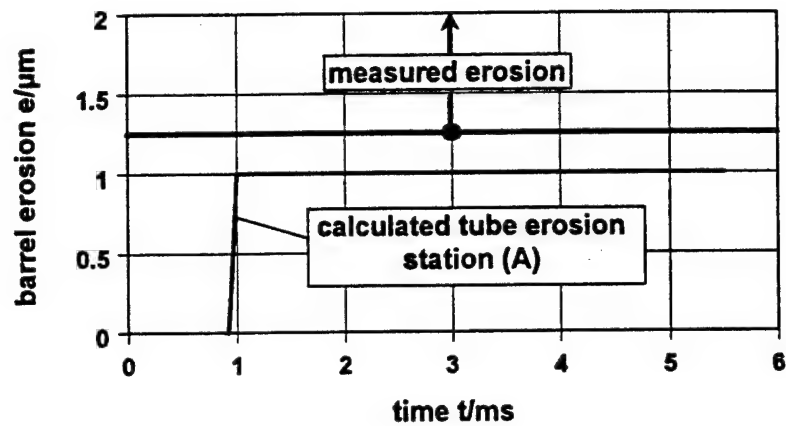
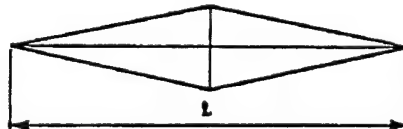
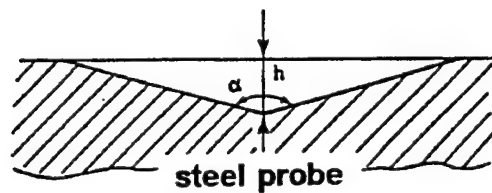


Fig. 12. Calculated and measured 20-mm-gun erosion



$$\alpha = 172^{\circ}30' \pm 5'$$

$$h = \frac{l}{2} \cot \frac{\alpha}{2} \approx \frac{l}{30.5}$$

measured quantity: length  $l$   
 calculated quantity: depth  $h$   
 before shooting: initial depth  $h_1$   
 after shooting: reduced depth  $h_2$

$$\text{erosion: } E = h_1 - h_2$$

Fig. 13. Knoop indentations

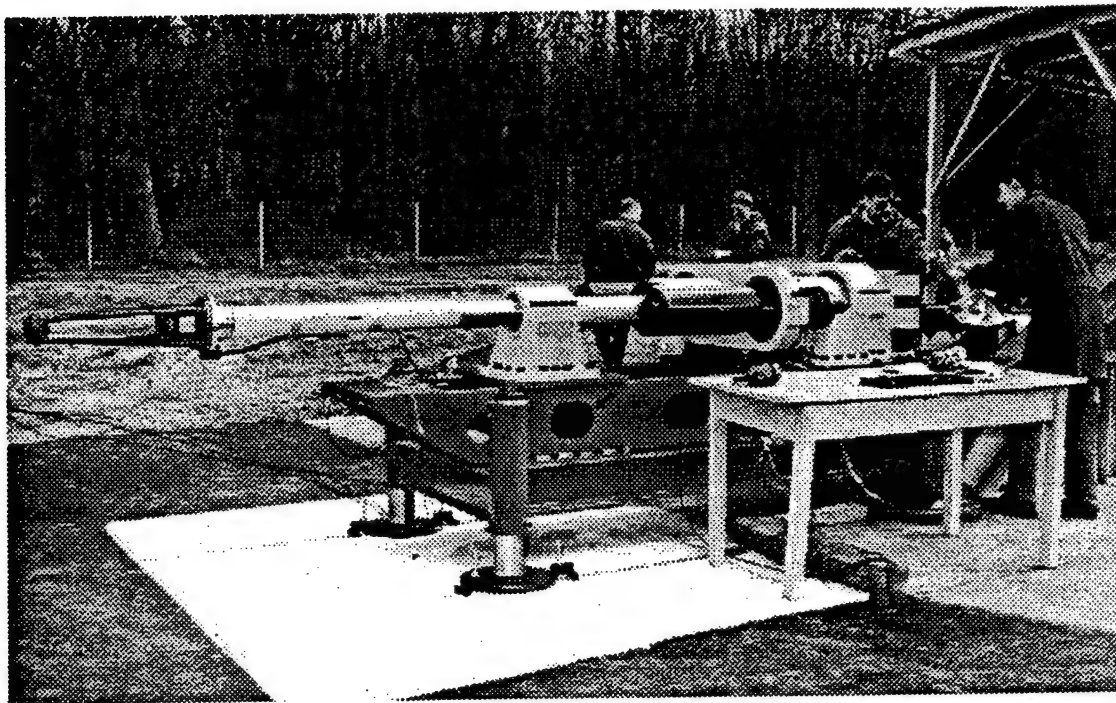


Fig. 14. Photography of 60-mm-caliber erosion gun

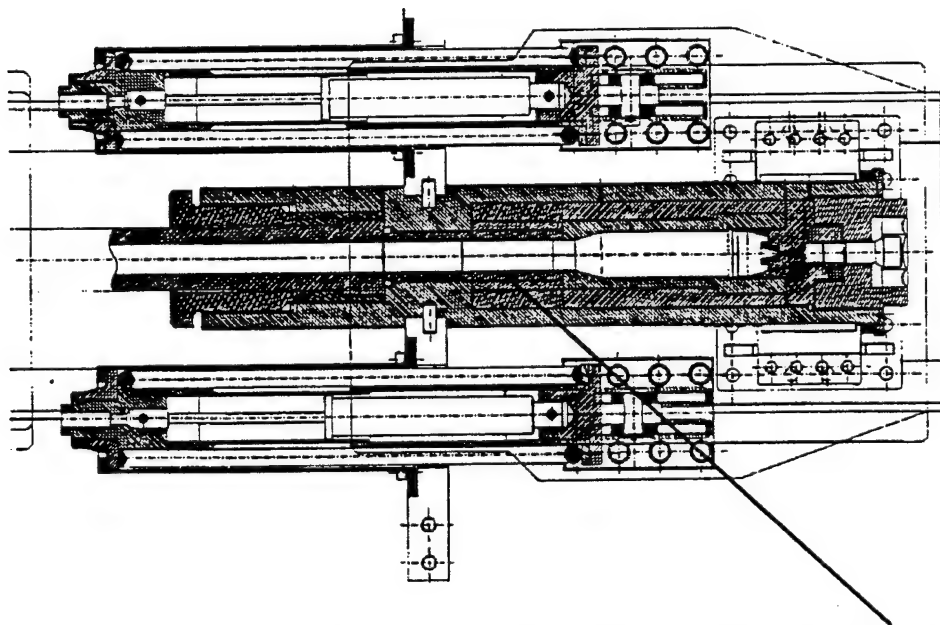


Fig. 15. Schematic set-up of 60-mm-gun with built in erosion tube (cylinder inset)

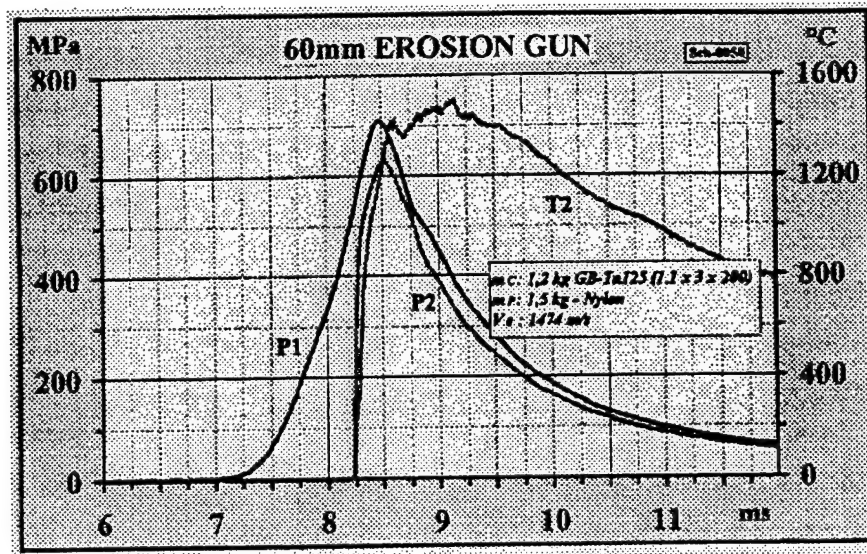


Fig. 16. Pressure and temperature distributions at measuring stations M1 and M2

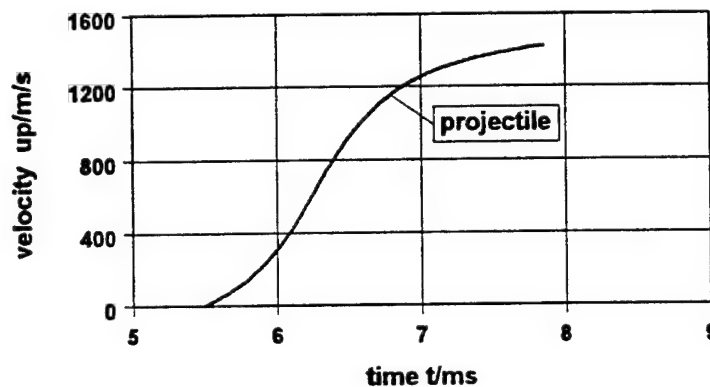


Fig. 17 Calculated projectile velocity

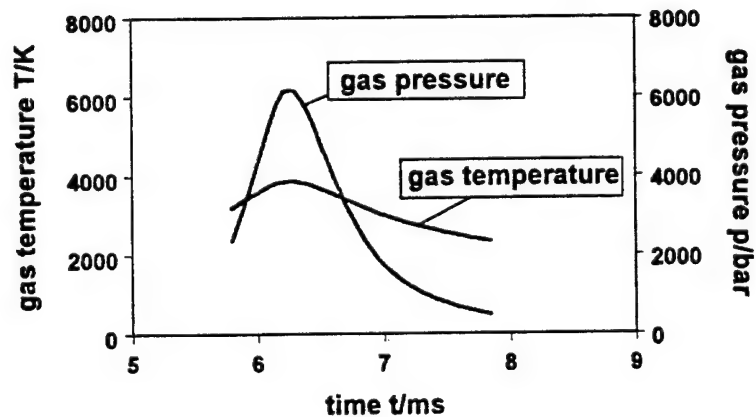


Fig. 18. Gas pressure and gas temperature at projectile base

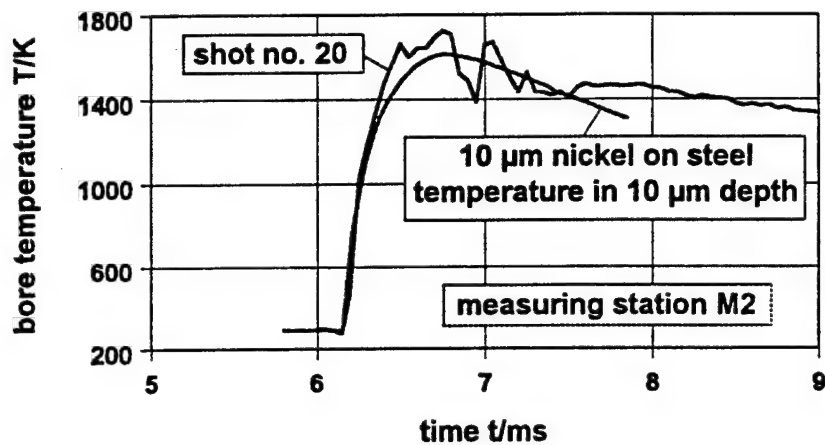


Fig. 19. Measured and calculated bore temperature in depth of 10 µm

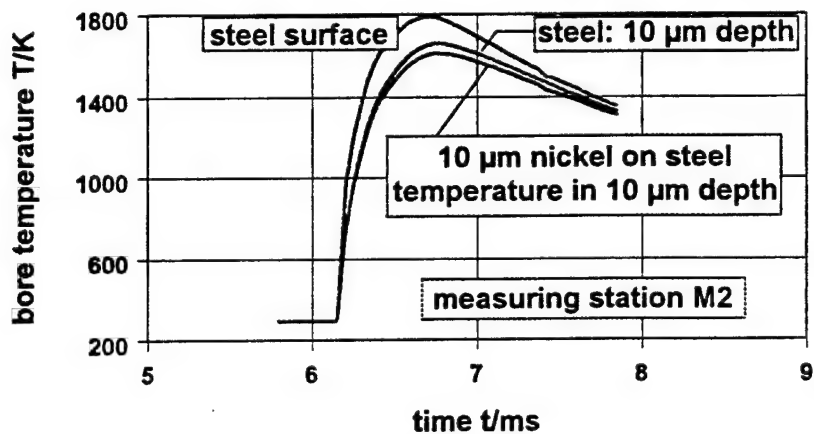


Fig. 20. Bore temperature for steel tubes and tubes coated with 10 µm nickel

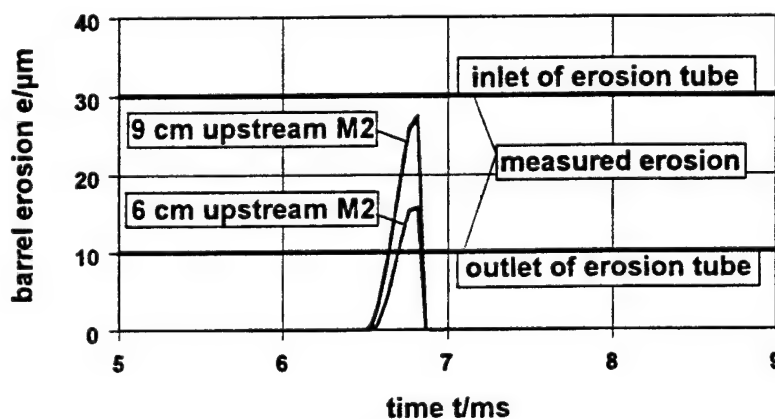


Fig. 21. Experimental and calculated bore melting erosion

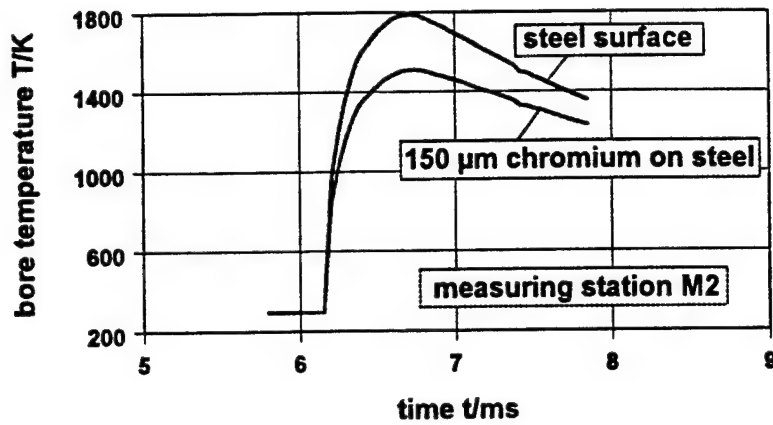


Fig. 22. Bore surface temperature for steel tubes and tubes coated with 150 µm chromium

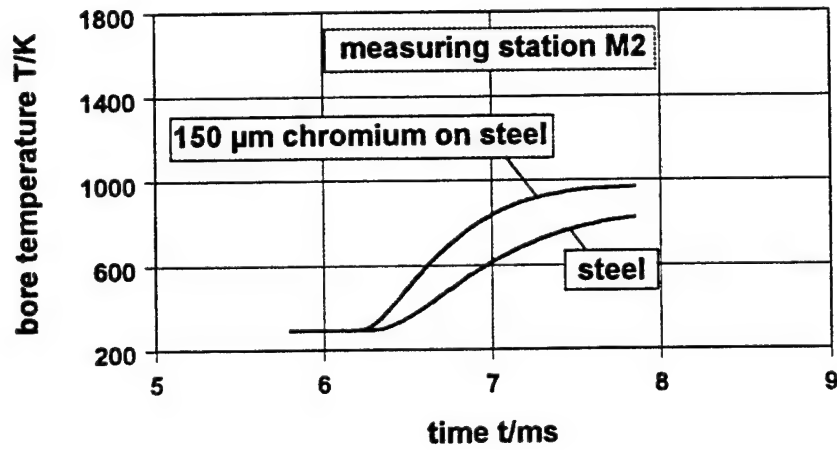


Fig. 23. Bore temperature in depth of 150 µm for steel, steel coated with 150 µm chromium

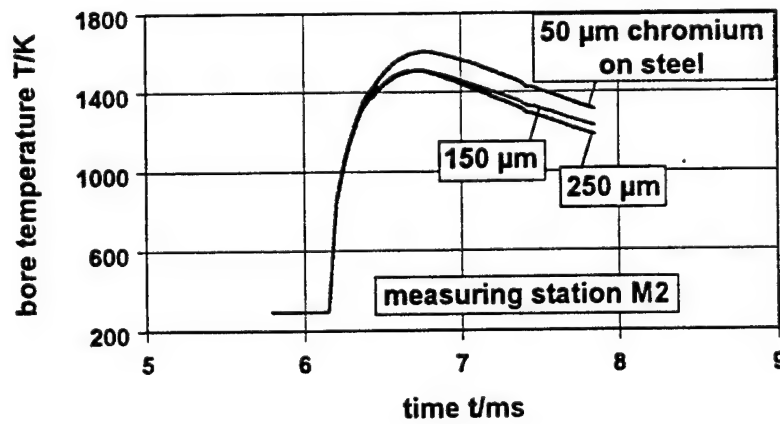


Fig. 24. Bore surface temperature for steel tubes coated with 50/150/250 µm chromium

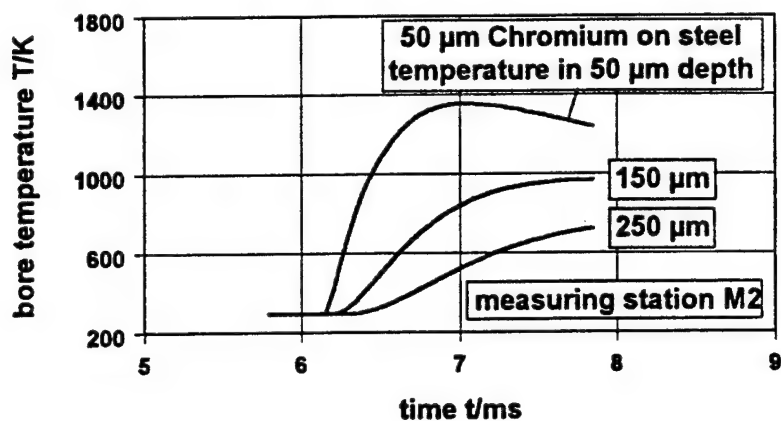


Fig. 25. Temperature distribution at the contact surface in depth between chromium and steel

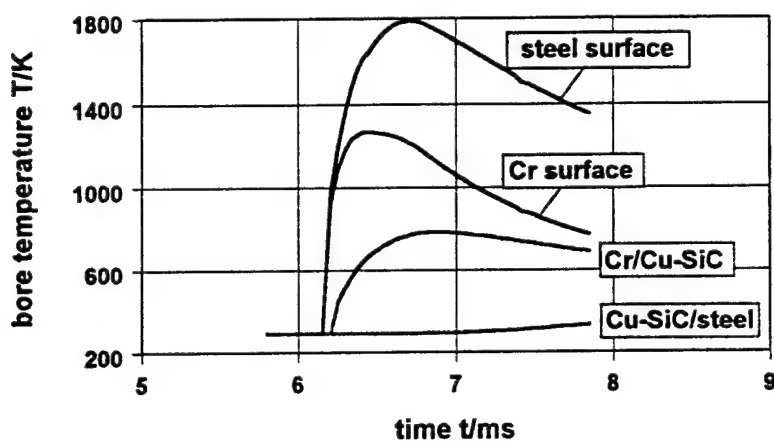


Fig. 26. Temperature distr. at (1) surface, (2) contact surface Cr/Cu and (3) Cu/steel

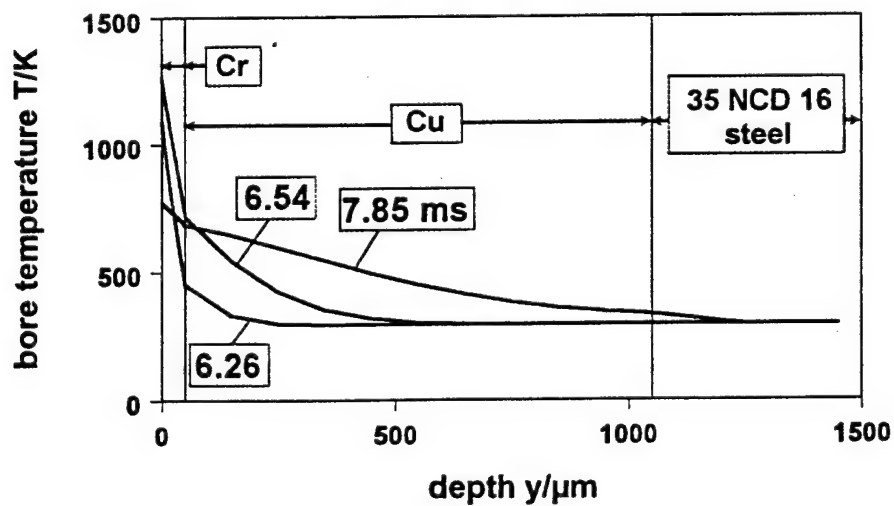


Fig. 27. Temperature distr. in depth at measuring station M2 for Cr/Cu layers on steel

**TITLE: COMPARISON OF EXPERIMENTAL AND PREDICTED RESULTS  
FOR THE BARREL HEATING OF A 81mm MORTAR SYSTEM**

C C H Guyott, BSc(Eng) PhD ACGI DIC

Frazer-Nash Consultancy Limited, Stonebridge House  
Dorking Business Park, Dorking, Surrey RH4 1HJ, UK  
Tel: +44 1306 885050 Fax: +44 1306 886464

**ABSTRACT:**

This paper presents a detailed comparison between experimentally measured barrel temperatures and those predicted using the FNGUN gun design software for an 81 mm mortar system. In particular, it has been shown that simulations can be used to obtain accurate data which can be used to support the design process both rapidly and for a wide range of different firing conditions.

The extensive experimental trials recorded the increase in barrel temperature resulting from the sequential firing of a large number charges followed by the subsequent cooling of the barrel back to ambient temperature. Results were recorded for different charge configurations and different rates of fire. By positioning thermocouples along the length of the barrel it was possible to measure both temporal and axial variation in temperature of the barrel.

Prior to simulating the barrel heating, FNGUN was used to predict the internal ballistic performance of the mortar including the spatial and temporal variation of propellant gas temperature within the barrel. The predicted results for muzzle velocity and peak pressure showed good agreement with the experimental results across the range of charge configurations which were considered e.g. muzzle velocities were predicted within 2-4% of those measured.

Using the propellant gas data as input, the FNGUN Thermal Module was then used to predict the long term heating and cooling of the barrel at a number of positions along the barrel. The simulation of barrel heating was found to be in excellent agreement with the experimental results. For example, after the sequential firing of over 160 rounds FNGUN predicted the maximum barrel temperature to within 2% of that measured. Furthermore the predicted thermal gradient along the barrel showed good agreement with the measured results.

Frazer-Nash Consultancy gratefully acknowledge British Aerospace Defence, Royal Ordnance, Nottingham, UK for permission to use their experimental results for their L16A2 81mm mortar and Mk4 Charge system in this paper.

## **COMPARISON OF EXPERIMENTAL AND PREDICTED RESULTS FOR THE BARREL HEATING OF A 81mm MORTAR SYSTEM**

C C H Guyott

Frazer-Nash Consultancy Limited, Stonebridge House  
Dorking Business Park, Dorking, Surrey RH4 1HJ, UK  
Tel: +44 1306 885050 Fax: +44 1306 886464

### **INTRODUCTION**

Knowledge of the barrel temperature is an important parameter in the design of all types of gun since it plays a role in determining factors such as:

- Permitted Maximum Gun Pressure
- Barrel Fatigue Life
- Barrel Wear or Erosion
- "Cook Off" Delay

In the case of mortars and machine guns the maximum permitted gun pressure is strongly influenced by the temperature profile along the barrel. Since there is often only a small temperature difference between the inner and outer walls of the barrel and the integrity of the gun is usually limited by the hot strength of the barrel steel. This is in contrast to other types of gun where, although the transient bore temperatures may be higher, the barrel walls are often much thicker and there is a significant temperature difference through the wall of the barrel.

While experimental trials provide an important means of determining gun barrel temperatures, they can be expensive to conduct. Consequently, if the gun designer has a reliable means of predicting temperatures from information about the charge and gun barrel trials costs may be substantially reduced, particularly when the effect of different firing patterns needs to be considered.

### **EXPERIMENTAL TRIALS**

One of the main aims of the experimental trials conducted by Royal Ordnance [1] was to determine a definitive temperature profile for the L16A2 mortar barrel under typical operating conditions. This was achieved by firing a series of trials with different charges and at different firing rates.

In order to determine the likely maximum barrel temperatures under hot ambient conditions the trials were carried out using a barrel and rounds which were pre-heated to above ambient temperature i.e. the barrel typically had an initial temperature of 50-45 deg C (120 deg F) whereas the average temperature of the ammunition and charge was 25 deg C (80 deg F). Once firing had commenced, the barrel temperature rapidly increased as would be expected. However, it was not possible to maintain the ambient air temperature in the vicinity of the barrel at its initial value. For example, the air temperature close to the barrel typically decreased from approximately 30 deg C (85 deg F) at the start of the firing to the "global" ambient temperature of approximately 13-15 deg C (60 deg F).

In each trial the temperature of the barrel was recorded at 2 s intervals on its outside surface and at 7 locations along its length, see Figure 1. Two thermocouples were positioned diametrically opposite each other at each location in order to improve the reliability of the results.

In general, firing was continued until the maximum temperature of the barrel reached an equilibrium with the environment i.e. it did not increase further. The exact number of rounds required to reach the equilibrium value depended on the charge type and firing rate. As an example, when Charge 6 was fired at a rate of 12 rounds per minute (r.p.m.) the equilibrium temperature was reached after approximately 160 rounds i.e. 13-14 minutes.

For two of the trials the barrel cooling was also measured for a period of approximately 18 minutes after firing was stopped.

Figure 2 shows a typical set of experimental results from the trials i.e. the recorded temperatures for Charge 6 being fired at a rate of 12 r.p.m. during both the heating and cooling phases. The Figure shows that the maximum temperature is approximately 500 deg C (930 deg F) and that this maximum occurs in a region approximately 300 mm from the breech.

Figures 3 and 4 show the recorded temperatures for Charge 4 being fired at a rate of 12 r.p.m and Charge 6 at 6 r.p.m. during the heating phase only. For these cases, the maximum temperatures decrease to approximately 445 deg C and 370 deg C respectively. The maximum values of temperature occur again in a region approximately 300 mm from the breech.

## INTERNAL BALLISTICS

In order to predict the heating of the barrel it is first necessary to have an accurate knowledge of both the spatial and temporal variation in propellant gas temperature within the gun i.e. it is necessary to carry out an internal ballistics simulation. For the simulations presented here the internal ballistics code FNGUN [2] was used to determine the gas temperatures from details of the propellant type, charge mass, projectile and gun tube layout.

The measured and predicted pressure-time curves for Charge 6 at 21 deg C are shown in Figures 5a and 5b respectively. The two figures show that there is good agreement between the two sets of results. The small "kink" in the pressure time curve corresponds to the reflection of

the shot exit pressure pulse back to the breech and is seen in both traces. The predicted muzzle velocity is within 2% of the measured value. Based on the same propellant information, the predicted muzzle velocity for Charge 4 was found to be within 4% of the measured value.

Figures 6a and 6b show the predicted spatial and temporal variation in gas temperature during the internal ballistic process, each line in Figure 6b represents the predicted gas temperature at 0.1 ms intervals during the internal ballistic process. In particular, Figure 6b shows the high transient gas temperatures which occur close to the point of obturation of the shot and at the breech face where the flow stagnates. In these regions, the gas temperature can be significantly higher than the flame temperature, e.g. circa 3,700 deg C (6,600 deg F) albeit for only a few ms.

## THE SIMULATION OF BARREL HEATING

The FNGUN Thermal Module calculates the barrel temperature by solving the equations for radial and axial conduction through the barrel wall. Forced and, or natural convection is assumed to occur at the outside surface of the barrel, see Figure 7.

The heat input to the barrel is determined from the spatial and temporal variation of propellant gas temperature and is taken directly from the internal ballistics simulation. The heat input to the barrel,  $q$ , is calculated from the following equation within each calculation cell:

$$q = h_w (T - T_w)$$

Where  $T_n$  is the propellant gas temperature within the calculation cell e.g. taken from the data shown in Figure 6,  $T_w$  is the temperature of the barrel wall i.e. taken from the previous time step and  $h_w$  is the heat transfer coefficient at the bore wall. The heat transfer coefficient  $h_w$  is calculated at each time step and at each point along the barrel wall from the local flow using the following dimensionless relationship [2] and [3]:

$$Nu_w = 0.0137 Re_x^{0.864} Pr^{0.333}$$

Where  $Nu$  is the local Nusselt No.,  $Re$  is the local Reynolds No. and  $Pr$  is the local Prandtl No:

$$Nu_x = h_w/k,$$

$$Re_x = \rho C_x x/\mu,$$

$$Pr = C_p \mu/k.$$

Where  $\rho$ ,  $C_p$ ,  $\mu$ , and  $k$  are the gas density, specific heat capacity, dynamic viscosity and conductivity respectively and  $C_x$  is the gas velocity outside the boundary layer.

The FNGUN Thermal Module solves the above equations in two distinct ways which depend on the timescales under consideration. While the shot is still in the barrel and shortly after it has left, i.e. for approximately ten milliseconds in this case, the equations are solved using an explicit time stepping approach where the time step length is typically a fraction of a millisecond and is determined from the rate of heat diffusion. Once the shot has left the barrel, the time up to

the next firing, i.e. typically a period of seconds, is simulated using an implicit solution of the equations. This approach means that overall solution times are kept to a minimum. For example, if an explicit approach is used for whole solution the run times can be extremely long owing to the need for a small time step during the period when the shot is in the barrel [4]. Similarly, the use of an implicit approach can lead to inaccuracies during the very short timescales while the shot is in the barrel.

In practice, the switch over between the two solution techniques is fully automatic. Table 1 gives examples of the run times (based on the use of a 486PC running at 66MHz) for two of the cases presented here.

**Table 1 - Typical Elapsed Run Times for the Simulation of Barrel Heating**

Case	Run Time (mins/secs)
Single Shot Charge 6	45 secs
160 Rounds Charge 6 at 12 r.p.m plus 18 minutes cooling	60 mins

Figure 8 shows an example of the predicted bore temperature at the 7 thermocouple positions for a **single** firing for a total duration of about 20 ms from the time of ignition i.e. including a period of about 14 ms after shot exit. This figure shows that after a single shot the maximum bore temperature is only 200 deg C and that the bore wall cools quite rapidly e.g. it has reduced to 130 deg C in 15 ms. The figure also shows that the maximum temperature occurs close to the point of obturation (Position 2) and that the temperatures nearer the breech (Position 1) and towards the muzzle (Positions 6 and 7) are significantly lower.

## DISCUSSION OF RESULTS

A comparison between the measured and predicted barrel temperature close to the point of shot obturation (Position 2) when firing Charge 6 at 12 r.p.m. is shown in Figure 9. This figure shows that the general form of the simulated temperature rise is in good agreement with the measured results, in particular the maximum temperature following the discharge of approximately 160 rounds is predicted to within 2%.

A similar comparison when firing Charge 6 at the slower rate of 6 r.p.m. is shown in Figure 10. Again it can be seen that the general shape of the heating curve is predicted well and that the maximum temperature agrees within 2%.

Figure 11 gives a comparison between the measured and predicted barrel wall temperatures along the axis of the barrel. This figure shows that, in a similar manner to the predicted results for a single firing (Figure 8), there is a considerable variation in temperature along the barrel with the maximum occurring close to the point of obturation e.g. approximately 300 mm from the breech face.

Close to the breech, the temperature is somewhat lower than the maximum e.g. approximately 300 deg C rather than 500 deg C. As might be expected the temperature is also significantly lower at the muzzle.

The reasons for the variations in temperature along the barrel occur because the temperature of the barrel at any particular point is a function of a number of factors including the following:

- the maximum propellant gas temperature at that point in the barrel
- the time for which that region of the barrel is exposed to the high temperature
- heat transfer at that point which is largely influenced by the local gas velocity

For example, the maximum barrel temperature tends to occur close to the point of obturation because it is exposed to the highest propellant gas temperature anywhere in the barrel and it is subjected to the high temperature for a relatively long period of time (perhaps only 2 ms in absolute terms).

While the region close to the breech is also exposed to high gas temperatures, the local gas velocity and hence heat transfer is lower, therefore the barrel wall temperatures tend to be lower.

Figure 12 shows the predicted variation in pressure as a function of distance along the barrel from the internal ballistic simulation, each line representing the pressure at 0.1 ms intervals during the internal ballistic process. These results can be combined with the corresponding variation in barrel wall temperature (Figure 11) to provide the data necessary to determine the required strength of the barrel.

## CONCLUSIONS

Knowledge of the barrel wall temperature plays an important part in the gun design process since it influences many issues such as gun bore erosion and overall barrel strength, the latter being particularly important in determining the maximum permitted gun pressure in the case of mortars.

While experimental trials will undoubtedly continue to play a major role in the determination of barrel temperatures, the simulation of gun barrel heating can provide a valuable and reliable addition to experimental work. In particular, owing to the expense of trials, it is often only possible to determine barrel temperatures under a relatively limited range of conditions e.g. particular firing patterns and environmental conditions. Consequently, simulation can be

used to supplement trials data by, for example, providing data on the effects of changes to:

- The typical "battle field day" consisting of different rates of fire and pauses between firing.
- The design of the barrel e.g. the extent of the barrel with cooling fins
- The environmental conditions
- The Charge design e.g. using a cooler burning propellant

Furthermore, owing to the speed with which simulations can be carried out, the data from the simulations are available within timescales which can influence the design process in a beneficial manner.

## ACKNOWLEDGEMENT

Frazer-Nash Consultancy gratefully acknowledges British Aerospace Defence, Royal Ordnance, Nottingham, UK for permission to use the results of the experimental trials on their L16A2 81mm mortar and Mk4 Charge system, carried out at Pendine in October 1993, in this paper.

## REFERENCES

1. "81mm Mortar, Barrel Heating Trial Technical Report", Royal Ordnance, Nottingham, UK, Report Ref. No. DD/R/002/94, Jan 1994.
2. "FNGUN Manual v4.4", Frazer-Nash Consultancy, Dorking, UK, Ref FNC/8950R, Oct 94.
3. "Textbook of Ballistics and Gunnery", HMSO, UK, 1984
4. "Modifications to the XBR-2D Heat Conduction Code", Army Research Laboratory Report, Aberdeen, US, Ref ARL-CR-126, April 1994.

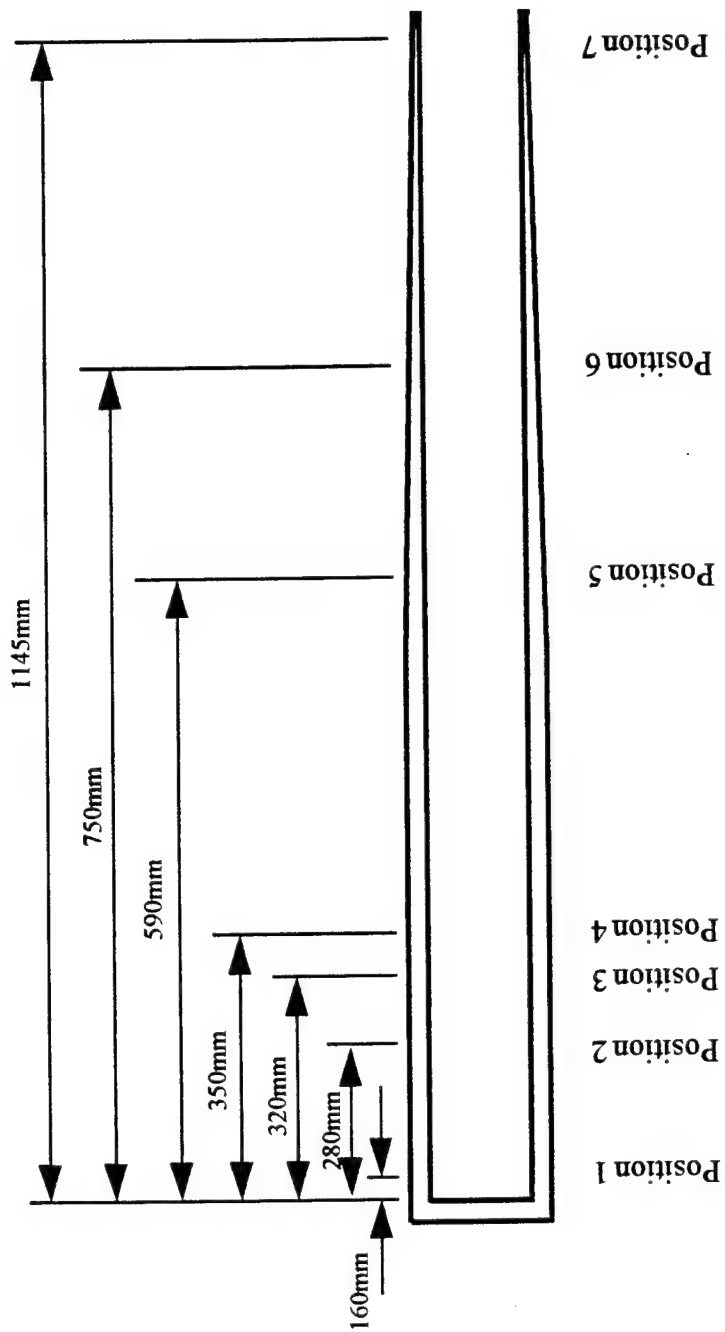


Figure 1 - Schematic View of the L16A2 Barrel Showing Thermocouple Locations

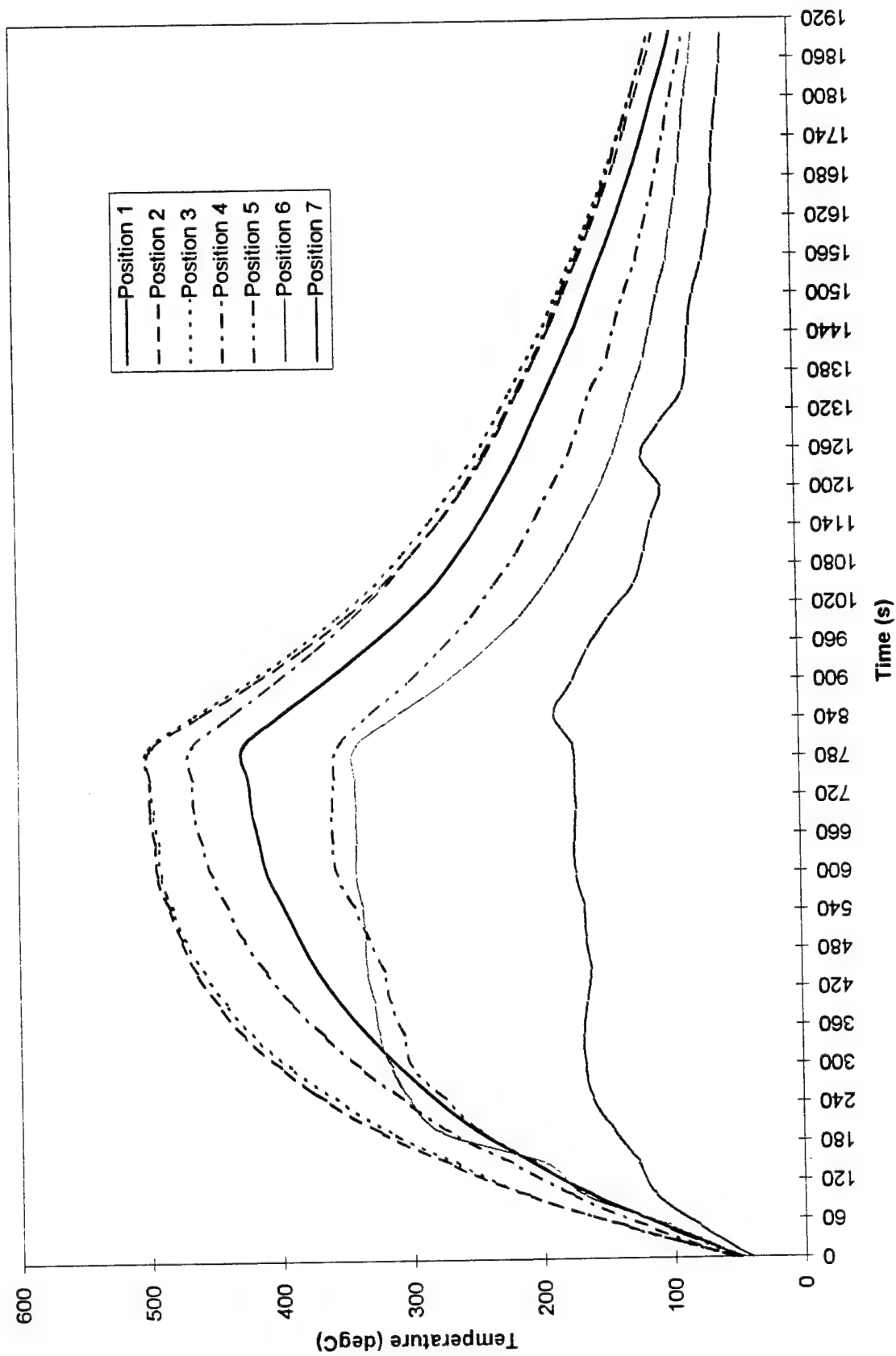


Figure 2 - Experimentally Measured Temperature Rise for the L16A2 Mortar when firing the Mk 4 Charge 6 at 12 rounds per minute

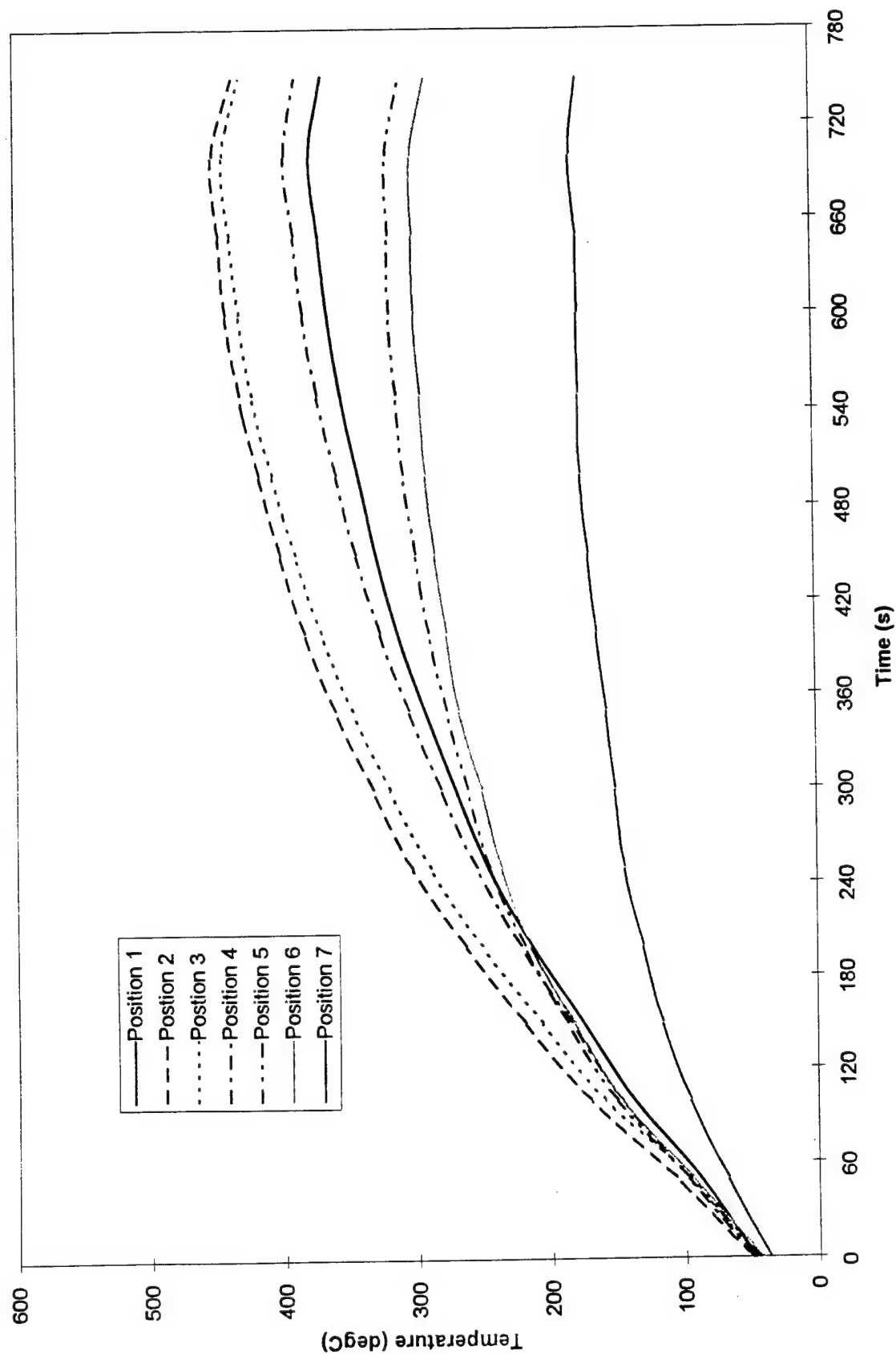


Figure 3 - Experimentally Measured Temperature Rise for the L16A2 Mortar when firing the Mk 4 Charge 4 at 12 rounds per minute

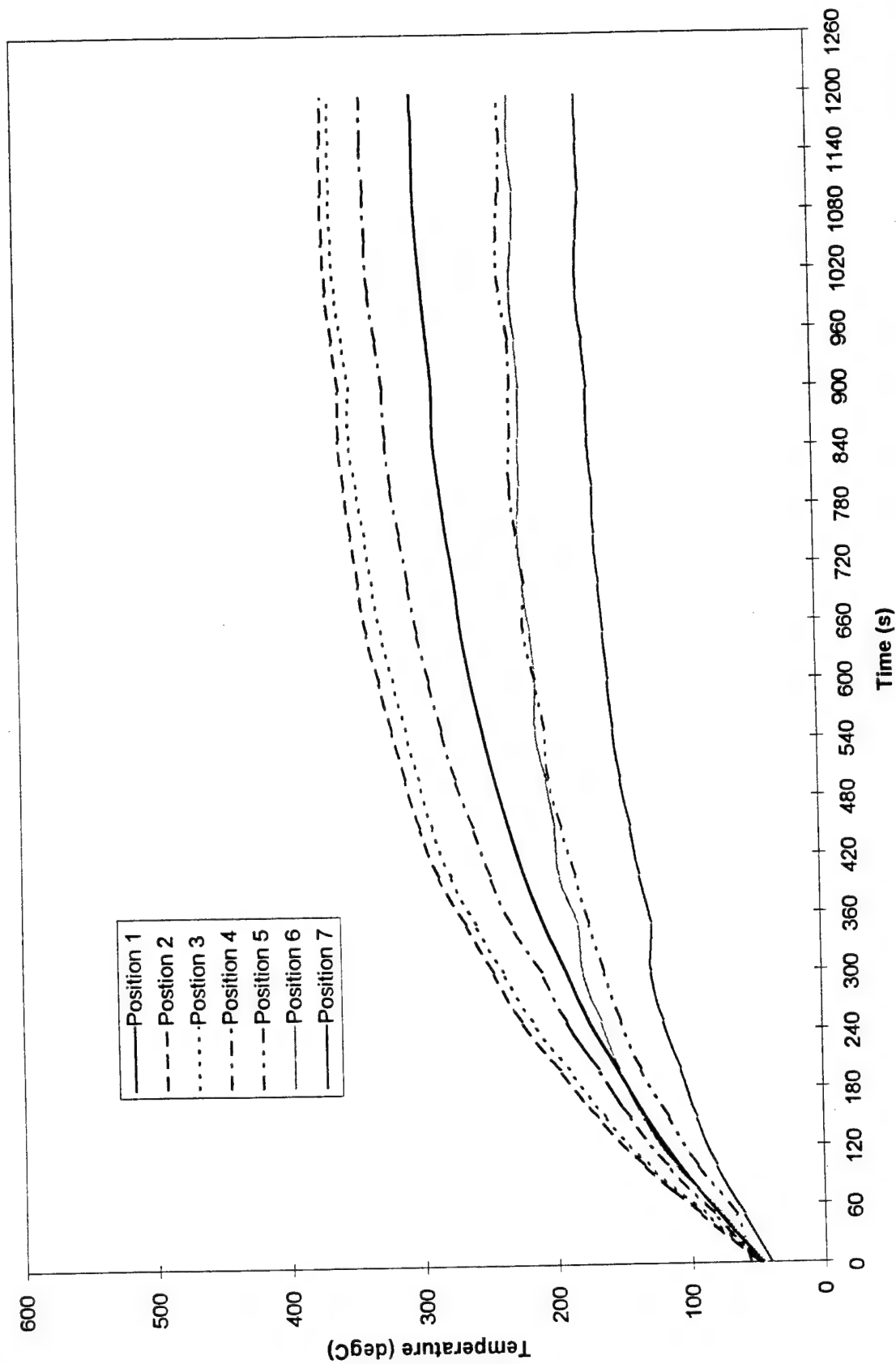


Figure 4 - Experimentally Measured Temperature Rise for the L16A2 Mortar when firing the Mk 6 Charge 6 at 6 rounds per minute

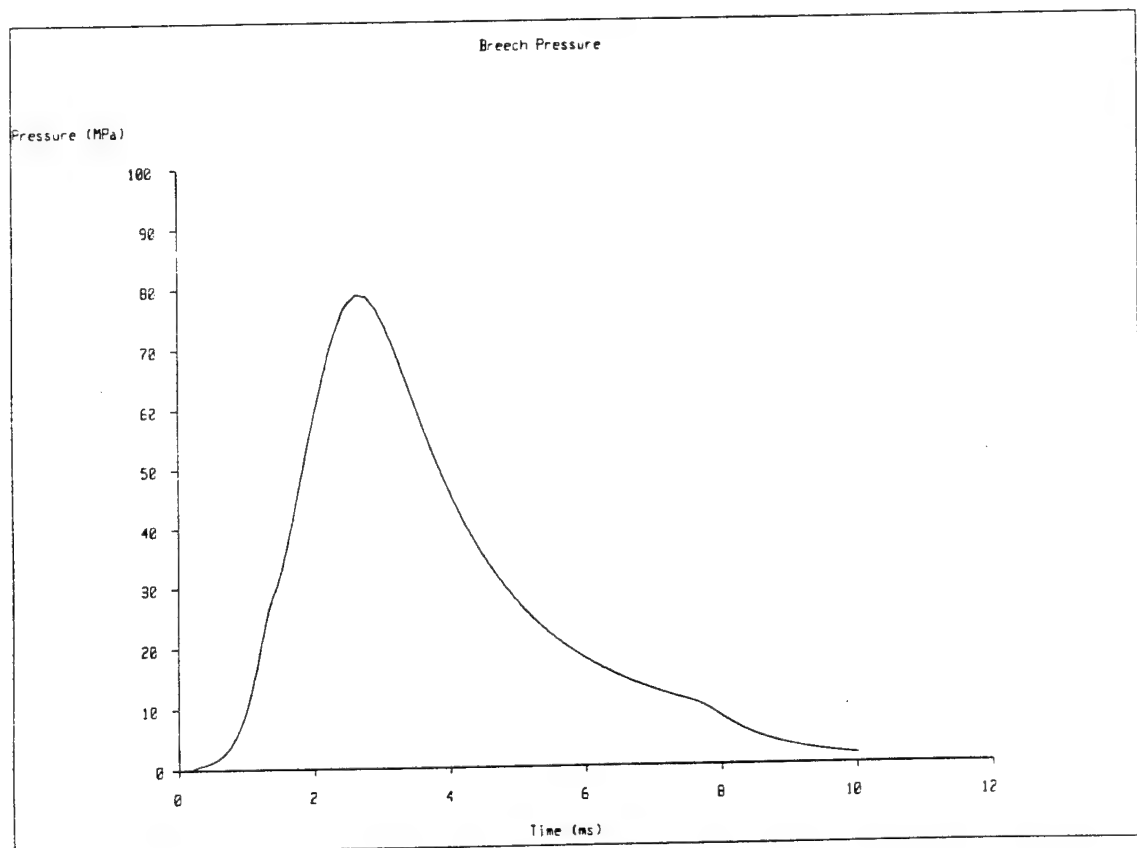
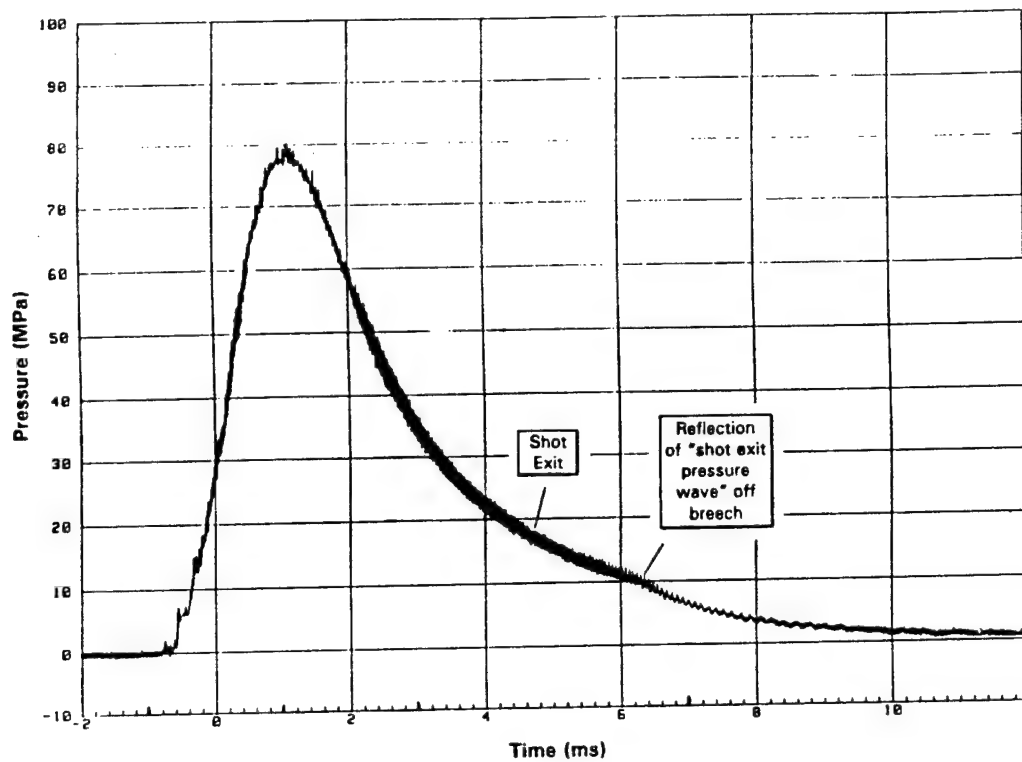


Figure 5 - Pressure-time curve for Charge 6 at 21 deg C (a) Experimental Results (b) Predicted Using FNGUN

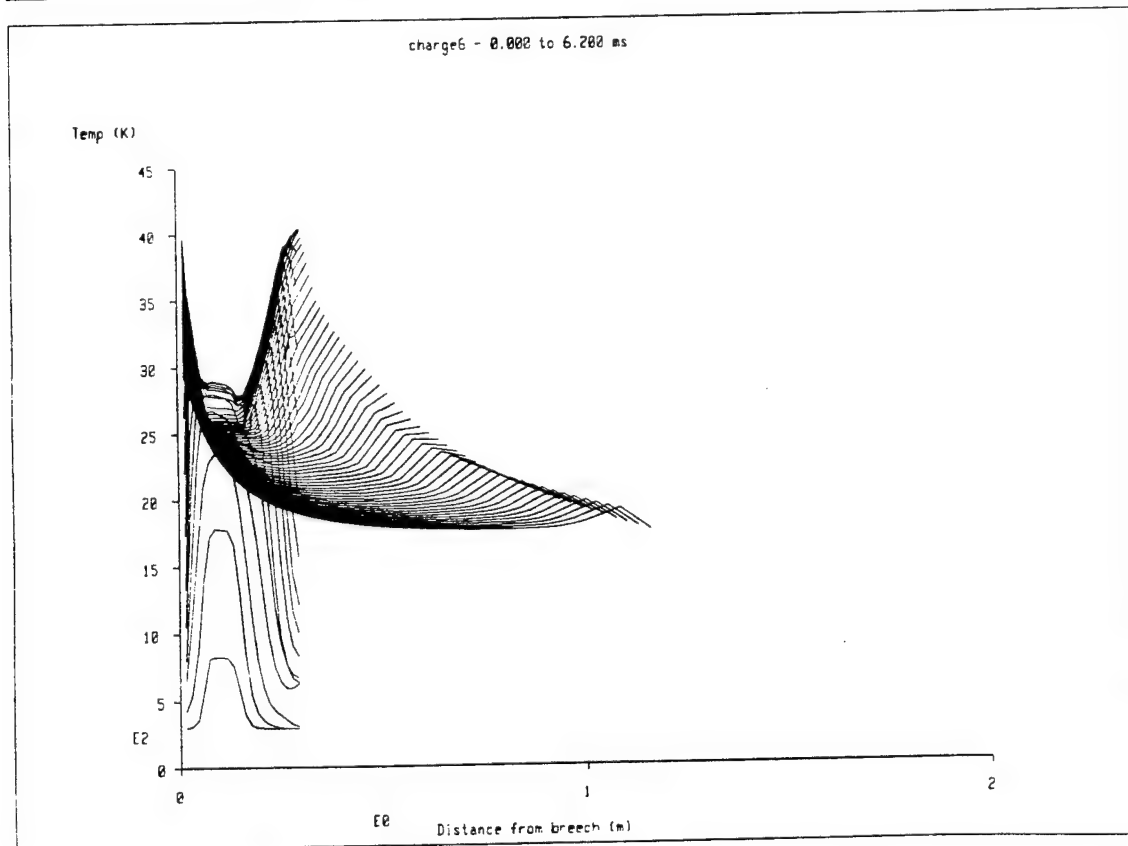
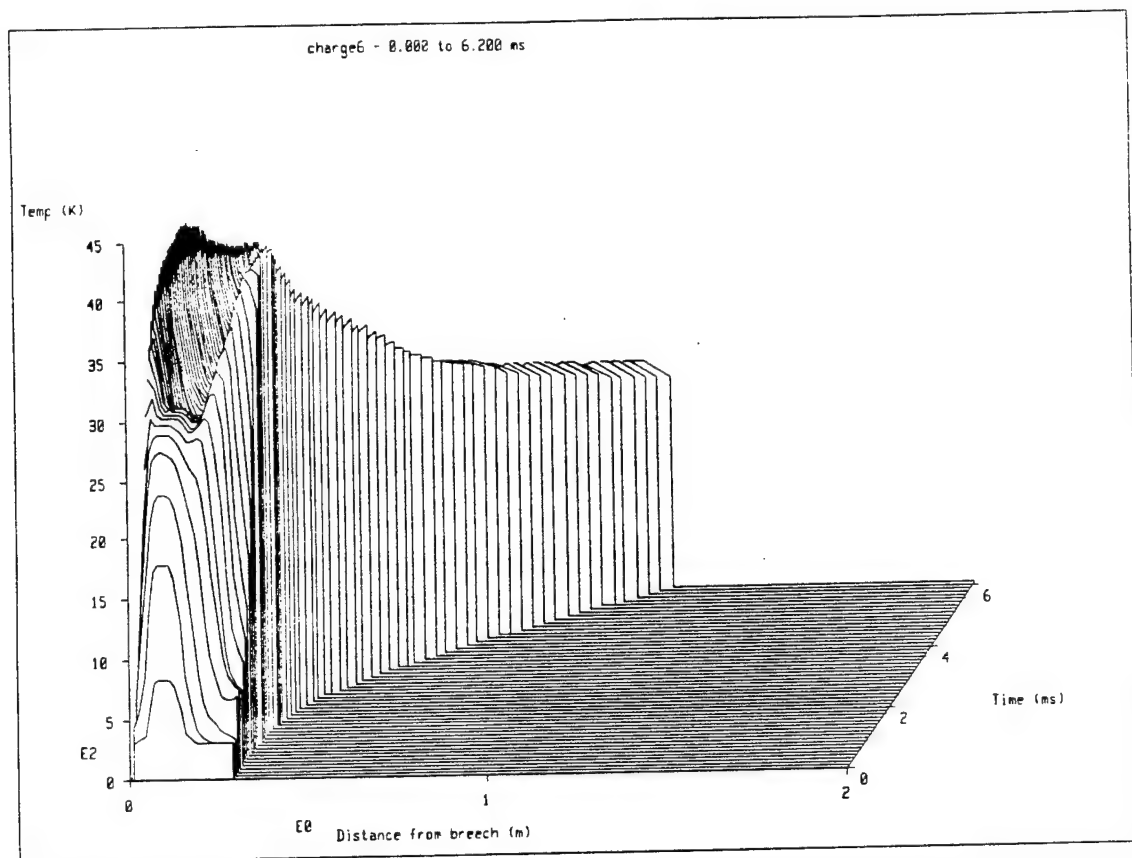


Figure 6 - Predicted Propellant Gas Temperature

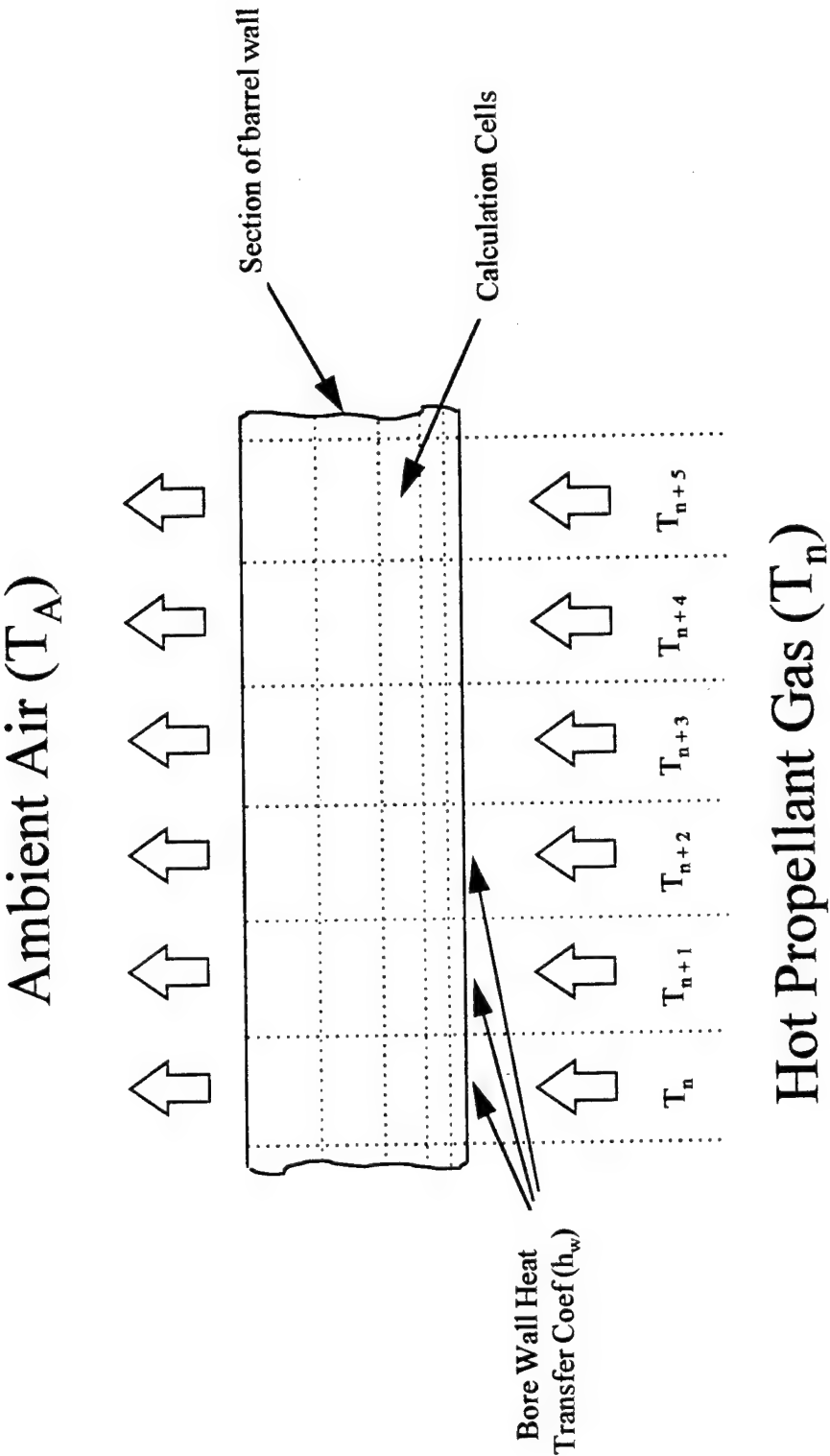


Figure 7 - Schematic Representation of Barrel Heating Problem

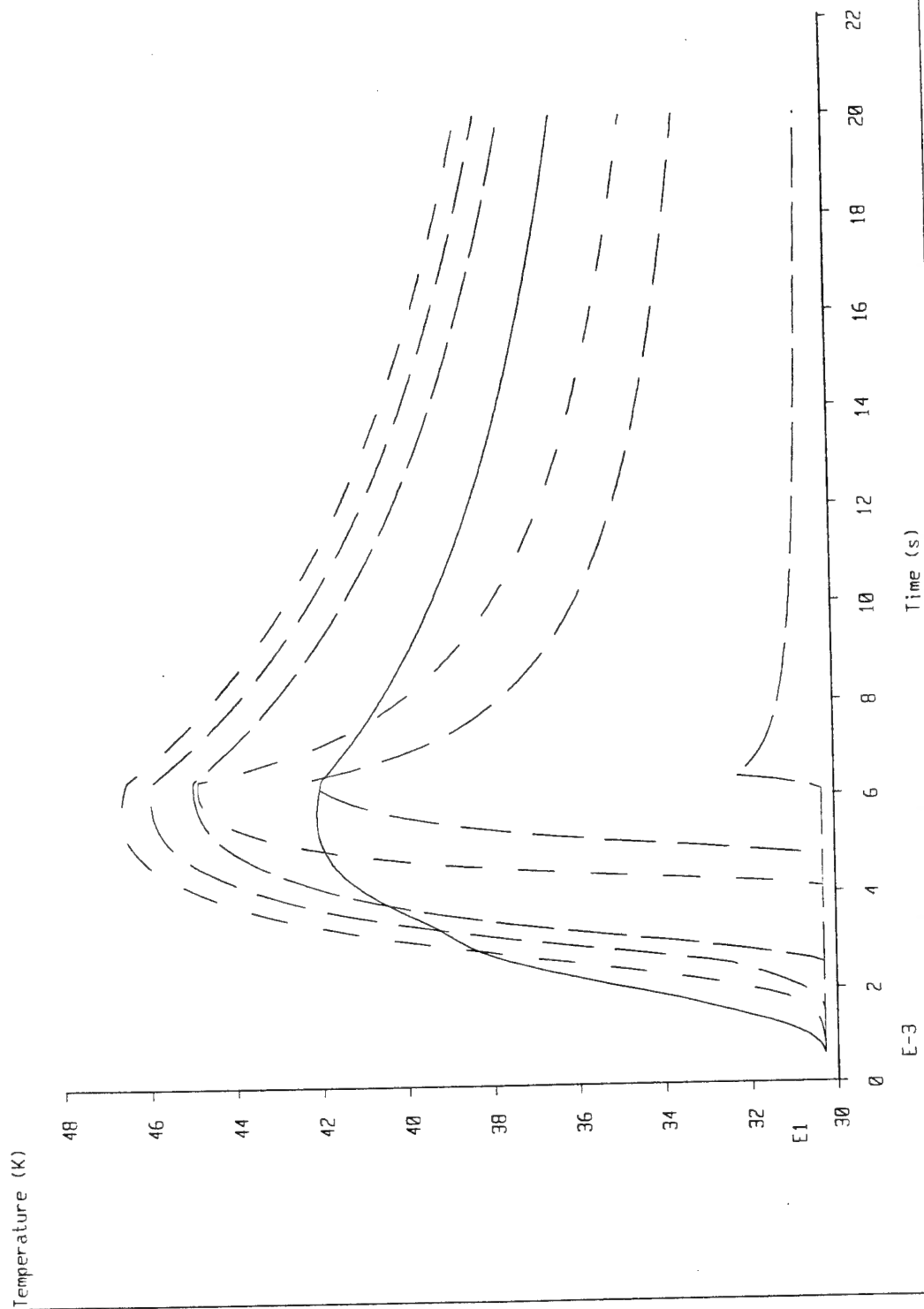


Figure 8 - Predicted Barrel Wall Temperature for a Single Firing of Mk 4 Charge 6

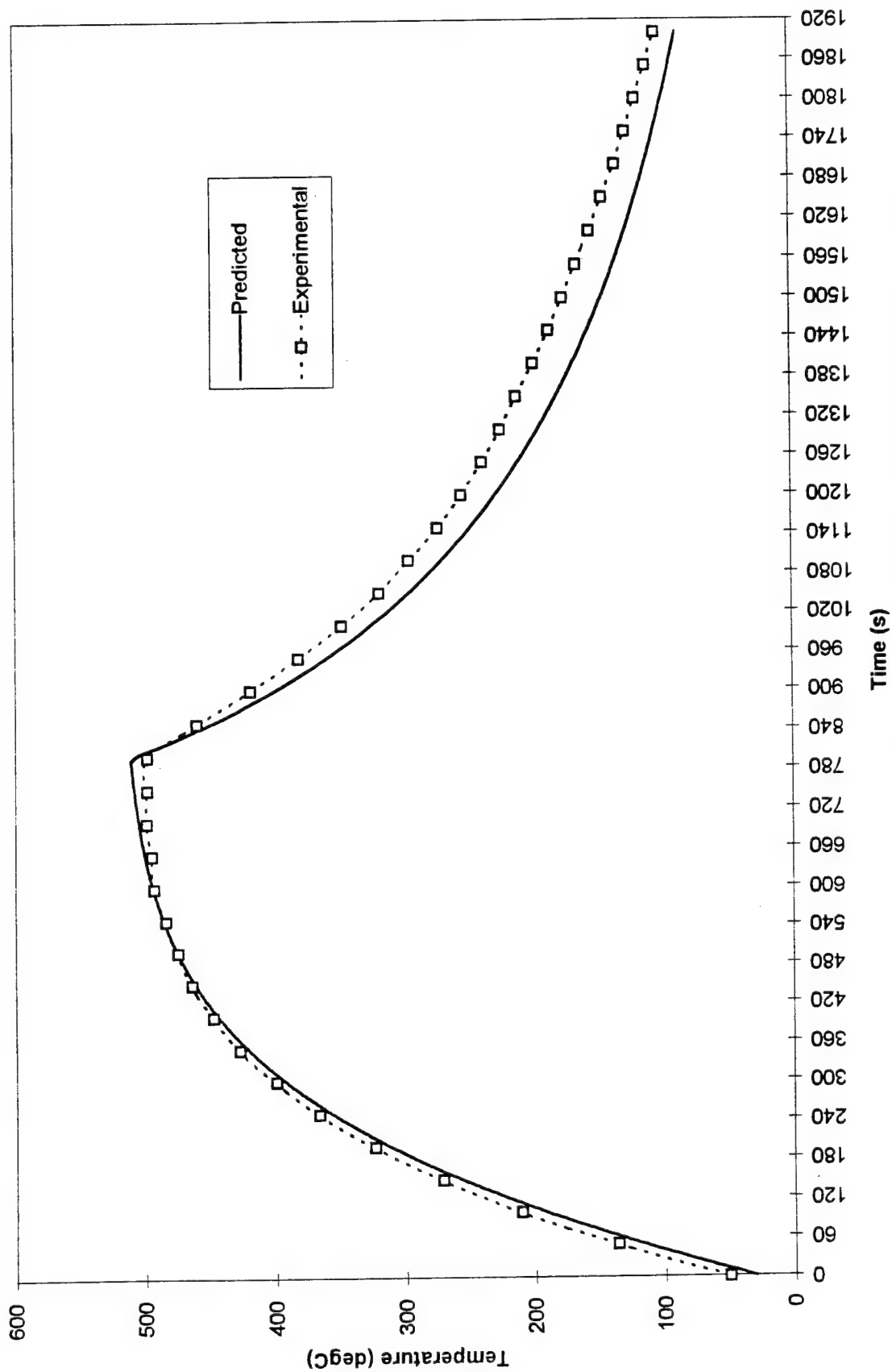


Figure 9 - Comparison of the Measured and Predicted Barrel Wall Temperature at Location 2 when firing the Mk 4 Charge 6 at 12 rounds per minute

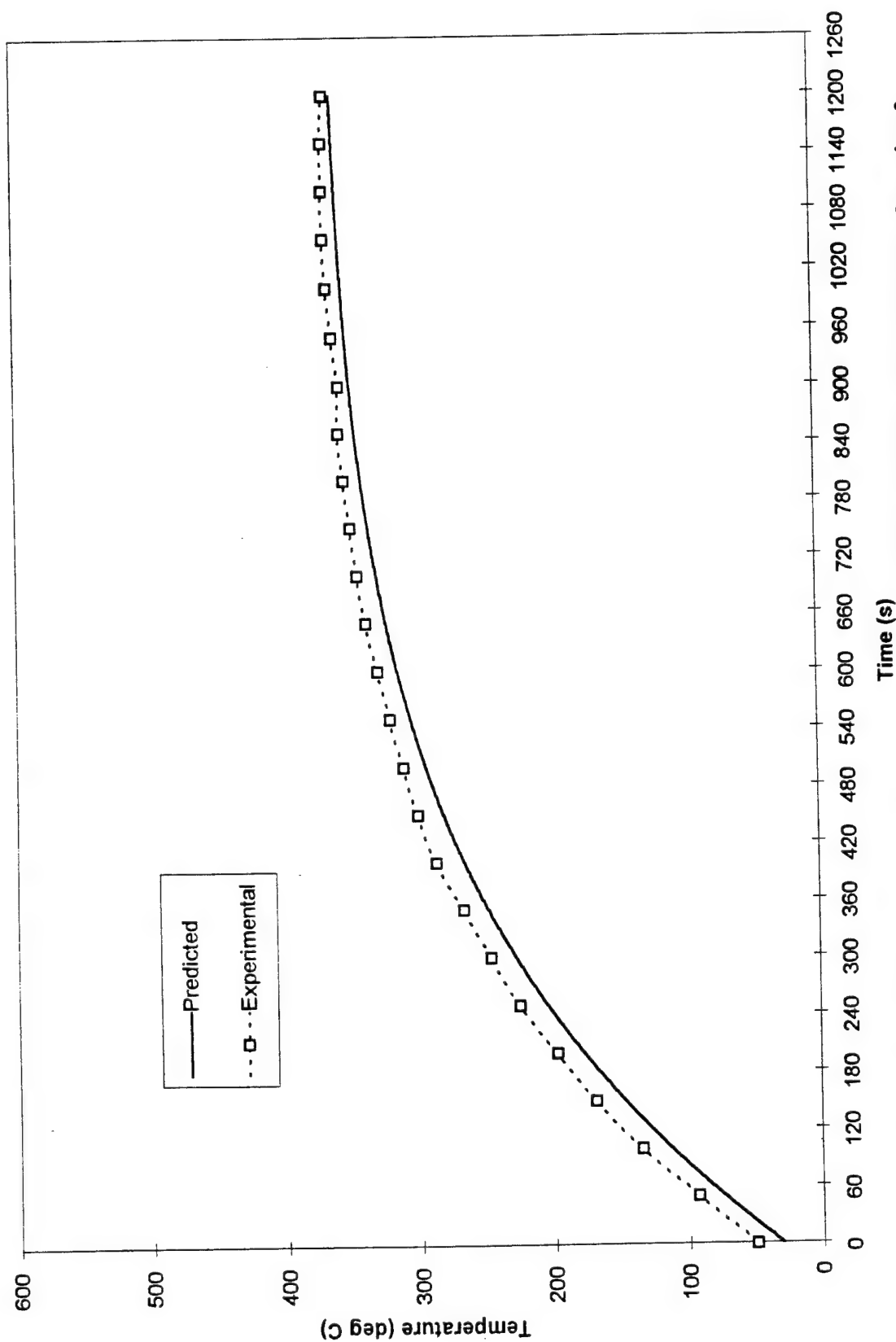


Figure 10 - Comparison of the Measured and Predicted Barrel Wall Temperature at Location 2 when firing the Mk 4 Charge 6 at 6 rounds per minute

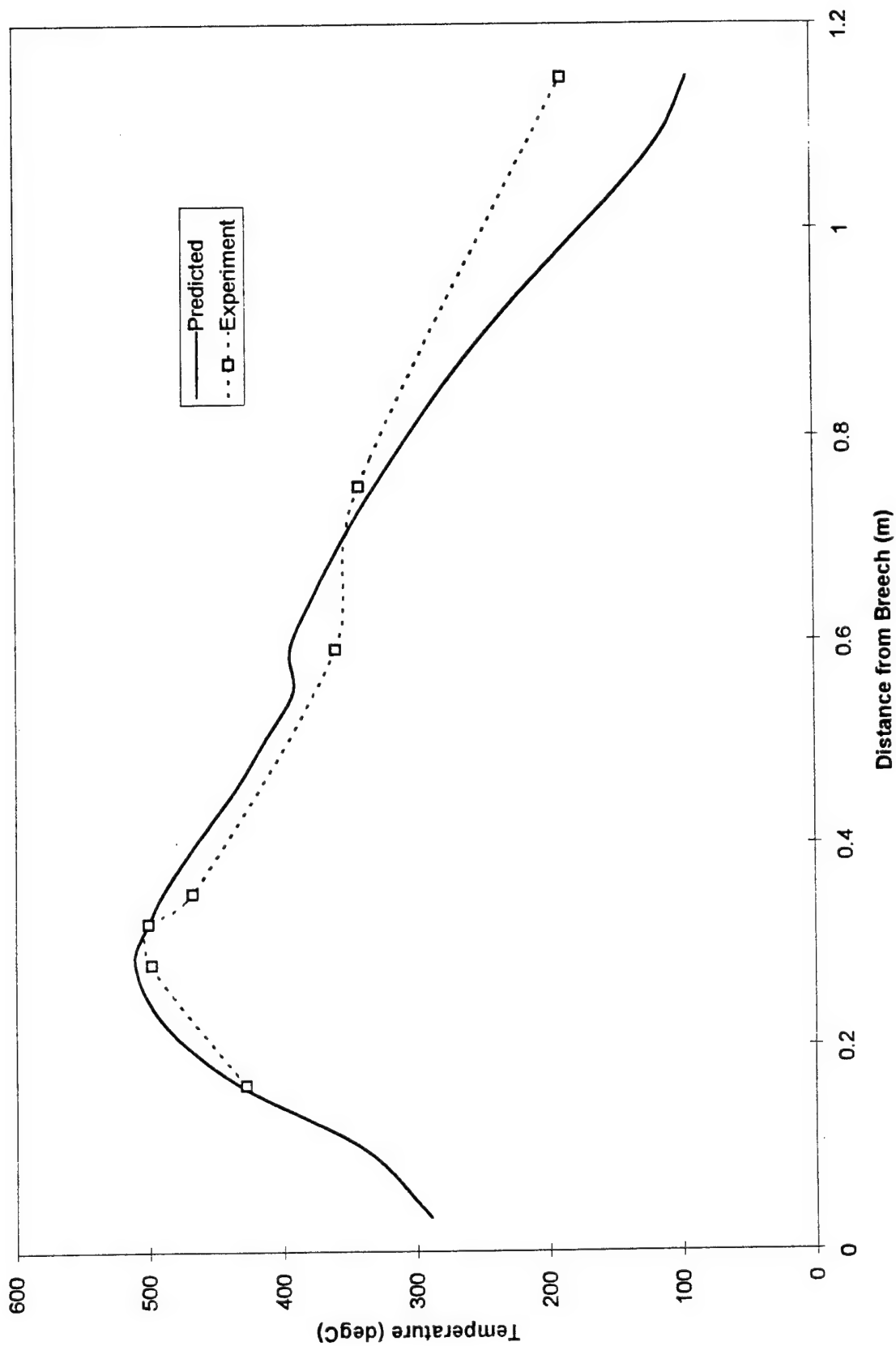
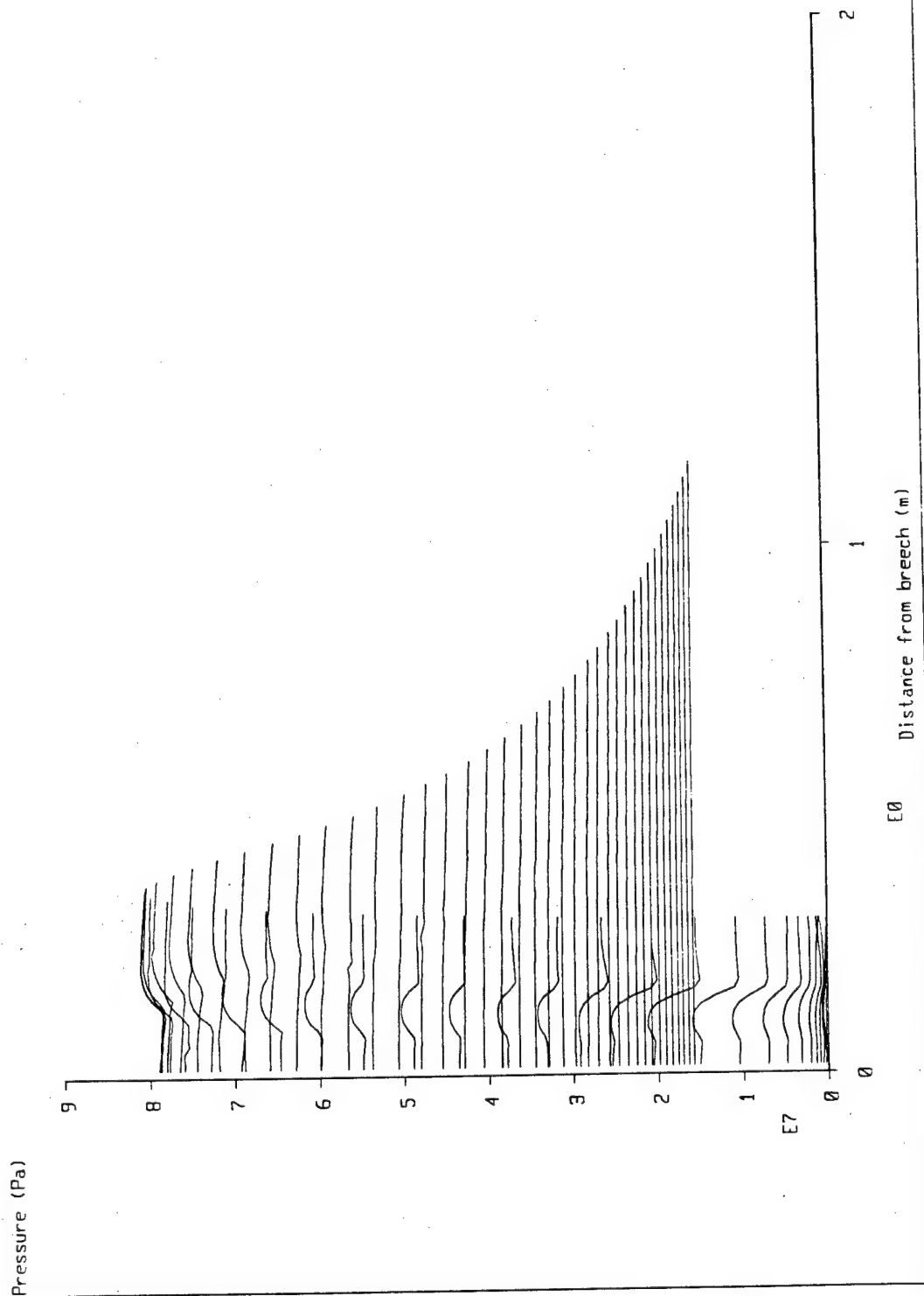


Figure 11 - Comparison of the Measured and Predicted Variation in Temperature along the Axis of the Barrel Wall

charge6 - 0.000 to 6.200 ms

**Figure 12 - Predicted Variation in Pressure along the Axis of the Barrel**

**\*TITLE:** Comparison of Numerical Predictions for Gun Barrel Temperatures with Experimental Test Results

CRAIG S. MILLER\* AND KATHRYN C. BEARDEN  
CONCURRENT TECHNOLOGIES CORPORATION  
1450 SCALP AVENUE  
JOHNSTOWN, PENNSYLVANIA 15904

**\*ABSTRACT**

The firing of a gun is a highly dynamic event that results in rapid temperature excursions in the gun barrel wall, particularly in the bore surface location. In medium caliber weapons using high impetus ammunition, these temperatures can vary by more than 1200C ° within a 0.25 second period. It is critical for the gun barrel designer to have tools that accurately predict the temperature distribution in the barrel to enable the selection of proper gun barrel materials and development of an adequate barrel configuration. Tools such as XKTC, a ballistics code, and FDHEAT, a finite difference heat transfer code have been developed by Benét Laboratories to predict the gun barrel wall temperature distribution. However, continued improvement in these codes and the confidence in applying them to new gun barrel designs and ammunition will depend on verifying their accuracy. A modified medium caliber M242 gun barrel is being designed that will accommodate increased rates of fire with a high impetus ammunition having a flame temperature of 3550K. The barrel uses a partial liner to protect the barrel jacket in the regions of greatest heat input and has an increased mass to provide additional capacity for thermal energy management near the muzzle end.

**\*BIOGRAPHY:** Assistant Staff Mechanical Engineer - Concurrent Technologies Corporation

**\*PRESENT ASSIGNMENT:** Numerical Modeling for the Advanced Gun Barrel Project

**\*DEGREES HELD:** B. S. Mechanical Engineering (1994), West Virginia University

## **Comparison of Numerical Predictions for Gun Barrel Temperatures with Experimental Test Results**

Craig S. Miller and Kathryn C. Bearden  
Concurrent Technologies Corporation  
Johnstown, Pennsylvania, USA 15904

### **ABSTRACT**

The firing of a gun is a highly dynamic event that results in rapid temperature excursions in the gun barrel wall, particularly in the bore surface location. In medium caliber weapons using high impetus ammunition, these temperatures can vary by more than 1200C° within a 0.25 second period. It is critical for the gun barrel designer to have tools that accurately predict the temperature distribution in the barrel to enable the selection of proper gun barrel materials and development of an adequate barrel configuration. Tools such as XKTC, a ballistics code, and FDHEAT, a finite difference heat transfer code, have been developed by Benét Laboratories to predict the gun barrel wall temperature distribution. However, continued improvement in these codes and the confidence in applying them to new gun barrel designs and ammunition will depend on verifying their accuracy. A modified medium caliber M242 gun barrel is being designed that will accommodate increased rates of fire with a high impetus ammunition having a flame temperature of 3550K. The barrel uses a partial liner to protect the barrel jacket in the regions of greatest heat input and has an increased mass to provide additional capacity for thermal energy management near the muzzle end.

### **INTRODUCTION**

To increase their lethality and extend their range, medium caliber gun barrels are required to fire at increasingly higher rates, for longer sustained bursts, with higher impetus ammunition. These high kinetic energy projectiles generate flame temperatures up to 3550K with a corrosive gas that can decrease the useful service life of a barrel manufactured from conventional gun barrel steels to less than 100 rounds. In response to this need, the Advanced Gun Barrel Initiative is being conducted by the National Center for Excellence in Metalworking Technology to improve the performance of a 25mm Bushmaster barrel while minimizing life cycle costs [1]. The ammunition that is being demonstrated is labeled 616W, which is comprised of high impetus propellant from the more familiar M919 round and the standard M791 projectile and plastic obturating band. The use of this ammunition will provide higher lethality and increased stand-off distance for weapon systems such as the McDonnell Douglas M242 chain gun used on the Bradley Fighting Vehicle.

To better accommodate the 616W ammunition, numerical modeling has guided a number of barrel design modifications to the existing M242 barrel [2]. As a baseline,

maximum bore temperature plots were generated using a 150 round burst of high impetus ammunition at 500 shots per minute (SPM) (Figure 1). Temperature dependent material properties were used for the standard gun barrel steel and the chromium bore plating. The gun barrel steel temperature dependent material properties were determined through other NCEMT projects on Atlas of Formability and Thermophysical Properties, which address acquisition of mechanical and physical properties for materials used by the U.S. Navy.

The gun barrel steel melts at approximately 1454°C. The model predicts that this melting temperature is exceeded in the bore for the first 700mm as measured from the breech end. Hence, an advanced material liner is needed to protect the steel in this region as shown in Figure 1. Also shown are predicted curves for the temperature reached on the OD surface of a standard barrel and a modified M242 barrel. For preservation of barrel integrity, a design criterion of 600°C maximum surface temperature is employed. Modeling predicts that this temperature will be exceeded in the muzzle region. The mass of the barrel forward of the barrel support assembly was increased to accommodate the increased heat input from the 616W ammunition and to reduce the average volumetric temperature of the barrel. A constant taper was maintained over the remaining length.

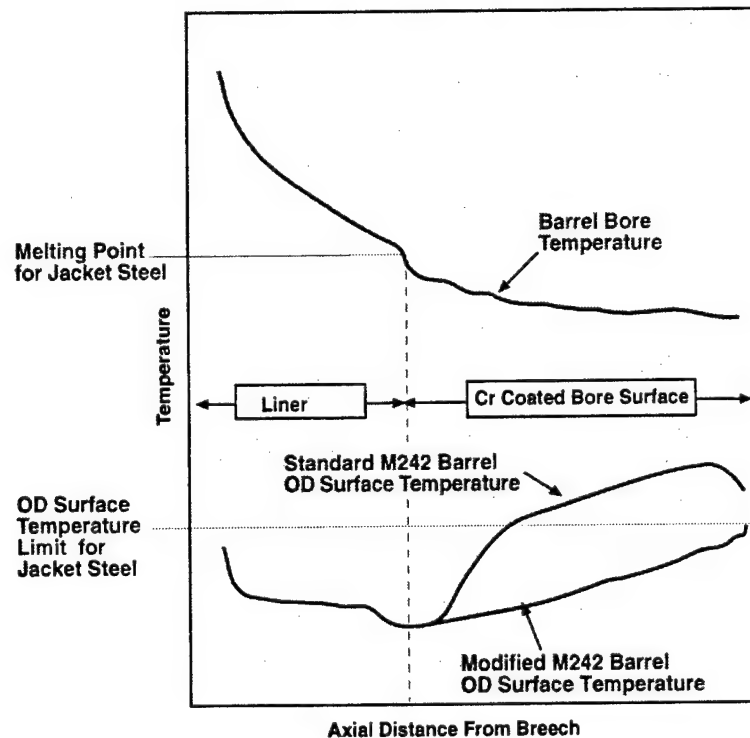


Figure 1: Baseline predictions for M242 modified barrel. Predicted maximum temperature plot after a 150 round burst of high impetus ammunition at 500 SPM

The first barrel produced and tested was an unlined barrel with enough added mass to keep the surface temperature in the muzzle region well under 600°C. This added approximately 10mm of material radially from the standard M242 un-finned barrel design.

This barrel is labeled the M242 Modified Unlined (M242MU) barrel and will provide a baseline for subsequent lined barrel designs. Other barrels to be manufactured under this program include a niobium alloy partially lined barrel with the same muzzle geometry, called the M242ML-F, and a molybdenum alloy partially lined barrel called the M242ML-M. All barrels have gain-twist rifling that initiates after the breech and extends to the muzzle.

The ability of the numerical modeling tools to accurately simulate the temperature distribution in the barrel wall is critical to this barrel design process. A systematic experimental verification program was devised to evaluate the ability of these tools to accurately simulate temperatures in a lined barrel due to firing of high impetus ammunition. The program began with experimental testing of an unlined barrel of modified geometry using conventional M791 ammunition and will progress to firing of lined barrels with high impetus 616W ammunition.

A consistent set of thermocouple locations will be used throughout the test series to facilitate comparison of results. Locations were selected to enable measurement of temperatures near the bore wall, on both sides of the liner and jacket radial interface, and at the axial joint between the liner and jacket. Presently the M242MU barrel has been tested with both M791 and 616W ammunition and these results are presented here. Experimental data from the first series of unlined barrel tests are compared with predictions from the numerical modeling tools. This series of tests will provide the groundwork for future testing of partially lined barrels and further refinement of the modeling tools.

Also, because the barrel experiences large temperature gradients near the bore surface, the thermocouples must be precisely located to enable a valid comparison with model predictions. X-ray tomography has been used to precisely locate the thermocouple position. Furthermore, sub-models have been developed to study the effect that the 1.016mm diameter holes, drilled to accommodate the thermocouples, have on the results.

## APPROACH

### Numerical Modeling

The modeling tools used for this analysis are XKTC [3], a ballistics code, which generates single shot gas temperature, pressure, and film coefficients with respect to time and axial position of the gas column, and FDHEAT [4], a two-dimensional finite difference code that uses the XKTC output and performs the heat transfer analysis for a specific barrel geometry. The temperature time history results from FDHEAT are used to develop a barrel design that will successfully manage the heat output from the ammunition. This model based design approach relies heavily on the accuracy of these codes to predict the steep temperature distributions of different barrel geometries and the thermal output of different ammunitions. The following sections describe the experimental verification program that was constructed to give confidence in the numerical analysis.

### Testing Sequence

The first series of firing tests with the modified unlined barrel (Figure 2) used conventional M791 ammunition and then the experimental 616W high impetus round. These tests were used to refine the data acquisition system and develop the instrumentation needed to capture the mechanical and thermal response of the barrel during this highly dynamic event. The methodologies developed will be used as a basis for future lined barrel testing.

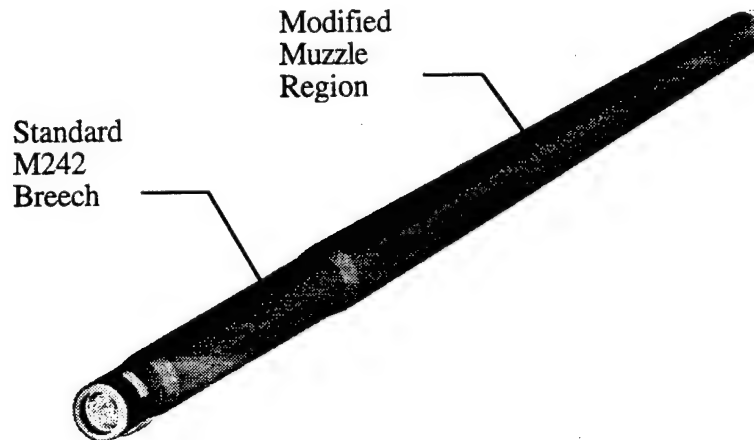


Figure 2: Modified unlined barrel (M242MU) with standard breech geometry for direct insertion into breech assembly, and enhanced muzzle geometry to increase thermal mass

The second barrel scheduled for manufacture and testing uses the same modified barrel geometry but incorporates a 650mm long partial liner in the breech region made of the niobium-base alloy FS-85 (Figure 3). This liner should offer modest thermal protection in the breech region from the high temperature round. Valuable insight will be gained on the design approach taken to accommodate unavoidable mechanical discontinuities introduced with the installation of a partial liner. This test adds some complexity to the data acquisition, but confidence has been gained from the successes in the completed test firings.

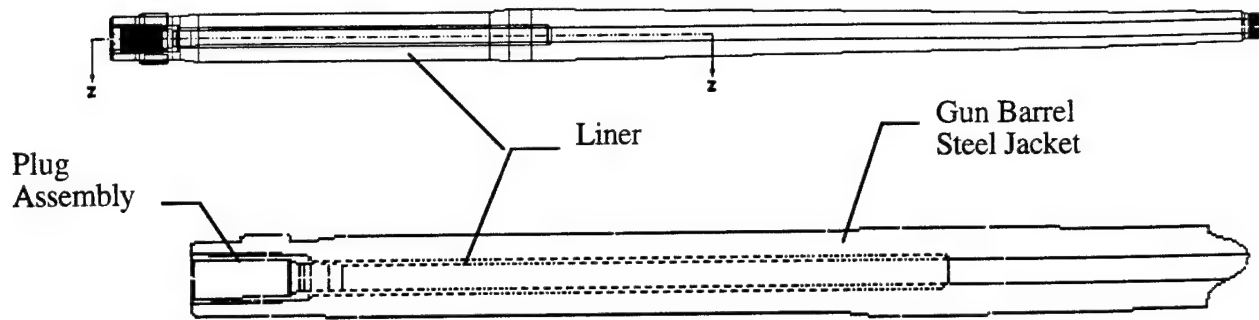


Figure 3: M242ML modified lined barrel. Standard gun barrel steel jacket with FS-85 liner and plug assembly

Experience gained in the second test will then be used for evaluation of a molybdenum alloy liner in a third test barrel and data will be compared to numerical predictions. The molybdenum-based partial liner should yield the greatest thermal and wear protection. This barrel will be designed utilizing the validated models and knowledge gained from the previous tests.

#### Barrel Instrumentation

The barrel was comprehensively instrumented to capture data related to barrel vibration, shock, strain, oscillation, and axial and radial thermal response. Instrumentation included 20 thermocouples, 20 strain gauges, 2 optical sensors, 2 capacitive sensors, and 2 accelerometers [5]. High speed video and state-of-the-art infrared thermal imaging were also used. This study focuses only on the thermal data collected.

#### Axial Thermocouple Locations

In order to provide a direct comparison between lined and unlined tests, a consistent set of thermocouple locations will be maintained. As shown in Figure 4, thermocouples are distributed along the length of the barrel with a concentration around the liner axial joint in order to capture any detrimental thermal effects from this discontinuity. In addition, more thermocouples were placed in the breech end because of the greater bore temperatures in that region. A three-dimensional thermocouple hole profile is displayed in Figure 5.

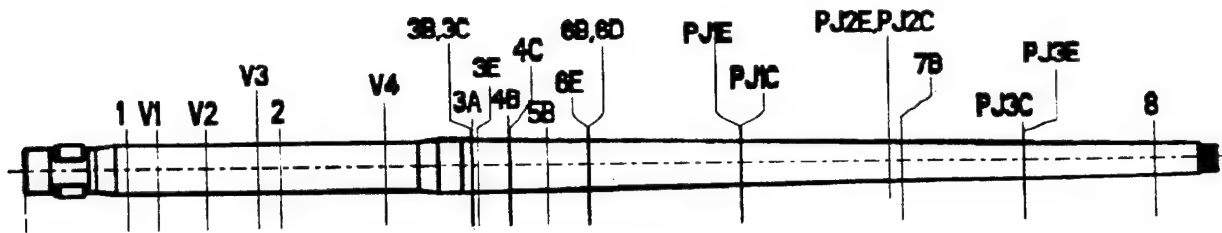


Figure 4: Axial thermocouple locations

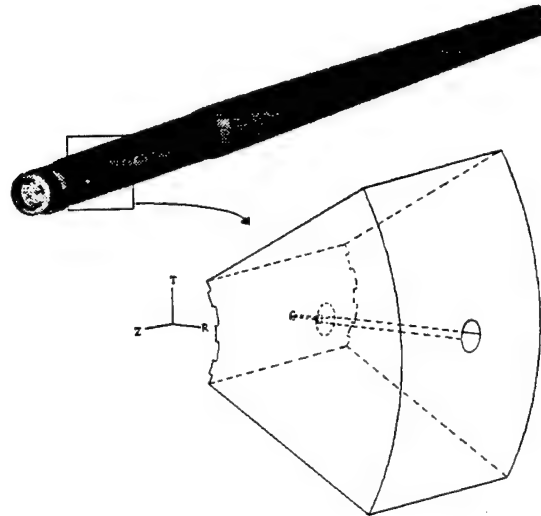


Figure 5: Three dimensional thermocouple hole profile

#### Radial Thermocouple Locations

As many as seven thermocouples at various radial and circumferential locations are placed at any one axial position. To maintain consistent thermocouple locations between the lined and unlined tests, thermocouples were placed in the unlined barrel in the same radial locations as desired for the lined barrels. As displayed in Figure 6, using an alphanumeric code with radial distances as measured from the bore wall: thermocouple A is located 1.27mm from a groove, thermocouple B is located 1.27mm from a land, thermocouple C is located 1.27mm from outer liner surface, thermocouple D is located at the radial liner/jacket interface, and thermocouple E is located on the outer surface of the barrel.

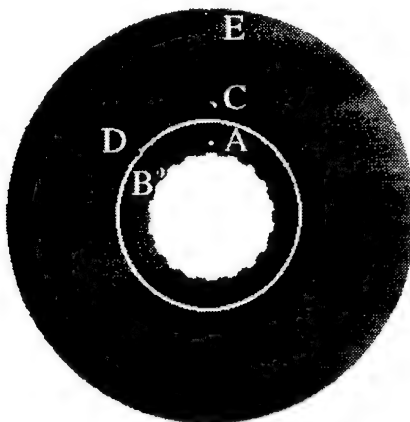


Figure 6: Radial thermocouple locations

Thermocouples A and B were designed to offer a direct comparison between the temperatures in the barrel wall directly over a land and a groove. Thermocouples C and D were designed to capture the thermal effects caused by the insertion of a liner. Surface temperature data provided by thermocouple E will be used to compare with the infrared data collected, and will verify the necessity of the modified barrel geometry.

#### X-ray Tomography

Owing to the large near bore temperature gradient, proper application of the experimental data requires accurate knowledge concerning the location of the thermocouple holes and an understanding of the effect of the holes on the measured temperatures. X-ray Tomography was used to accurately locate the thermocouples, and sub-models were used to study the geometric effect of the holes.

The radial location of the thermocouple relative to the bore was calculated from the depth of the drilled hole. This assumes that the bore and outer machined surface are in perfect concentric alignment. Furthermore, hole locations were placed over lands or grooves by locating the orthogonal surface position using ultrasonic inspection. Even with these precise placement methods, no compensation can be made for any "drift" experienced by the drill bit. Tomography creates a cross-sectional image by allowing X-rays to pass through the barrel and into a receiver. Image dimensions are calculated from their width, height, and pixel size. Eight axial positions were studied with one to three thermocouple holes at each location. Figure 7 shows a typical location [6].

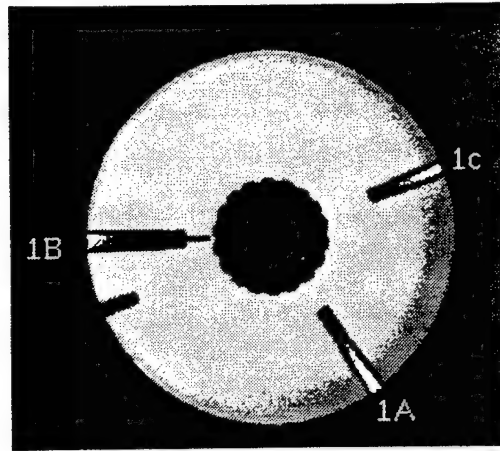


Figure 7: Tomography image at axial location number 1

The critical measurement for analysis is the distance from the bore surface (land or groove) to the bottom of the thermocouple hole. An error of one millimeter in this value could create as much as a  $150^{\circ}\text{C}$  temperature difference. The tomograms revealed major discrepancies in a few locations and the appropriate compensations were made to enable comparison with the predicted results. For example, thermocouple 1A was specified to be 1.27mm from a groove. The tomography image revealed that the hole was drilled to about 2.03mm from a land. The tomograms also show a consistent misalignment of the holes relative to the centerline of the bore. This was probably caused by a slight bias in the machining setup.

The thermocouple locations studied with the tomography images suggest that the techniques used to drill the holes do not yield desired accuracy. Although, the tomography was useful for determining gross misalignment, its accuracy in locating precise hole depths was inadequate. The resolution for this analysis was 0.191mm/pixel; therefore, only major discrepancies were measured.

#### Sub-Modeling

To further understand what additional refinements can be made to the model, sub-modeling investigations are being performed by studying the thermal effects of geometric discontinuities. These include: the effects of the land and groove, the varying chrome thickness, and the actual thermocouple hole void [7]. The exact degree of model adjustment has not been finalized, but valuable insight has been gained as to the magnitude of error introduced by these discontinuities.

## RESULTS

The data from the completed M242MU testing includes a 75 round burst of M791 ammunition at a nominal 200 SPM (test 1), and a 50 round burst of the 616W "hot round" ammunition, also at a nominal 200 SPM (test 2).

Test 1

Figure 8 displays a comparison of the model data with data collected for test 1 at thermocouple 1A. The planned location for this thermocouple was 174mm axially from the breech end and 1.27mm radially from a rifling groove. The thick line is comprised of the actual thermocouple data, which ends abruptly after shot 71 because of a data acquisition problem. Some scatter can be seen in the experimental data. The thin line represents the model predictions.

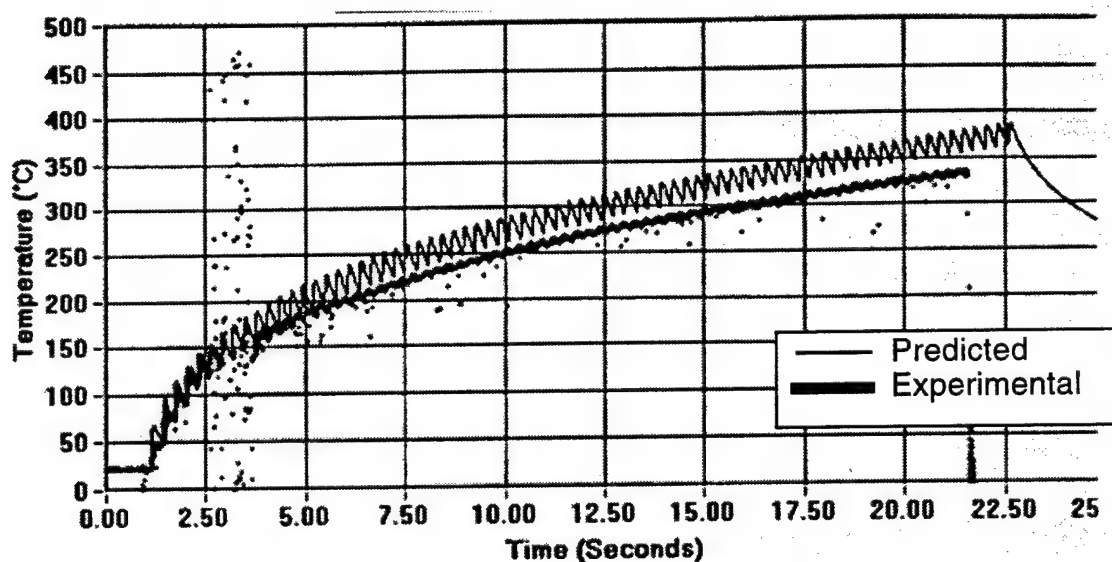


Figure 8: Predicted versus experimental temperature profiles for thermocouple 1A after 75 shots of M791

The tomography study showed that thermocouple 1A was actually at a depth of 2.032mm. Predicted data from this location, displayed in Figure 9, matches very well with the experimental data. This illustrates the importance of accurately knowing the thermocouple location.

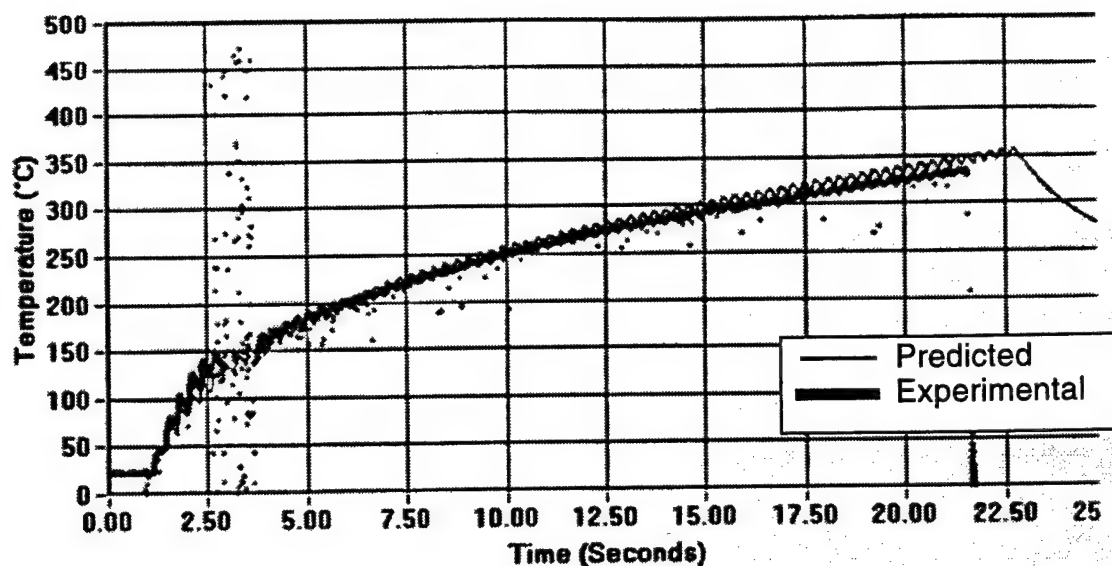


Figure 9: Modified predicted versus experimental temperature profiles for thermocouple 1A after 75 shots of M791

Data from thermocouples 2A and 2B were also collected during test 1. Figures 10 and 11 show a comparison between a thermocouple located within 1.27mm of a groove (2A) and 1.27mm of a land (2B). The data compare fairly well with the numerical predictions. Based on the sub-modeling [7], the experimental data from an A and a B thermocouple located at the same axial position were expected to be different; however, not enough test data were collected to support this conclusion.

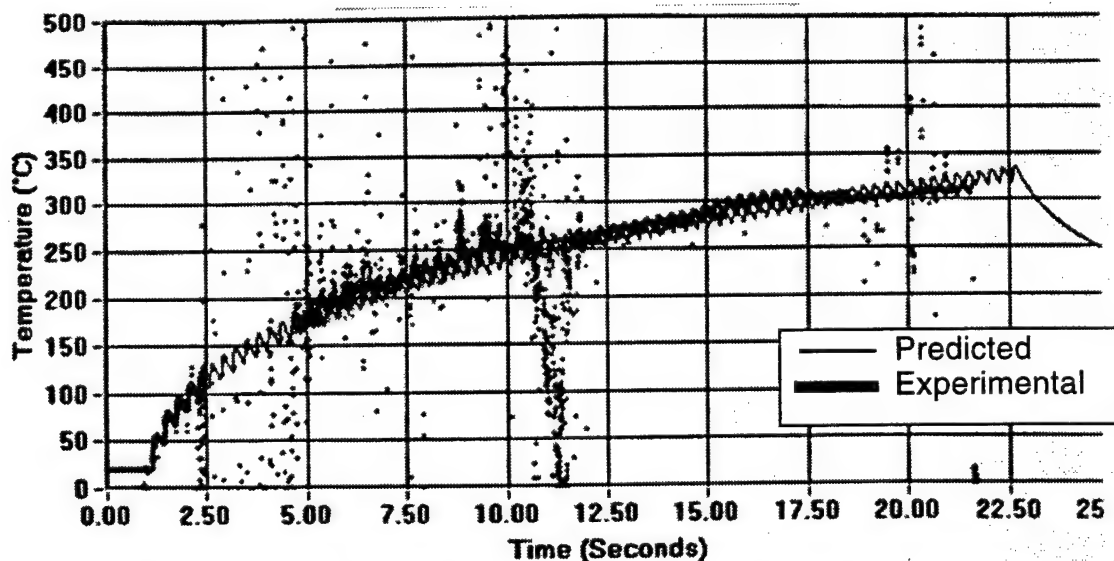


Figure 10: Predicted versus experimental temperature profiles for thermocouple 2A after 75 shots of M791

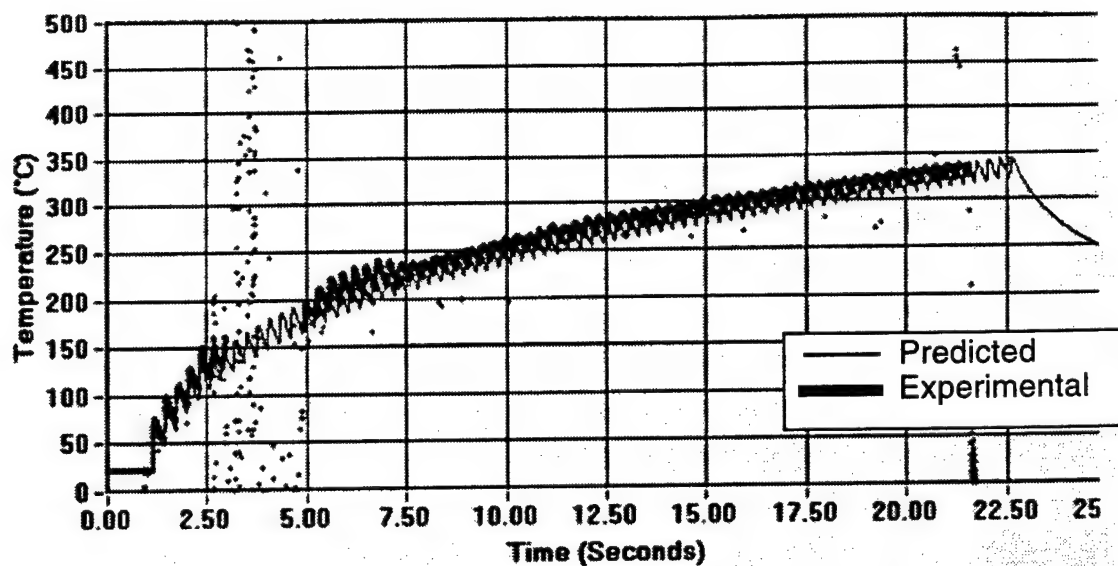


Figure 11: Predicted versus experimental temperature profiles for thermocouple 2B after 75 shots of M791

Figure 12 shows the temperature difference between shot 70 experimental peak and predicted peak for all near bore thermocouples (A and B) along the length of the barrel. The groove thermocouples are represented by diamonds and the land thermocouples are represented by squares. The numerical FDHEAT model is unable to handle land and groove geometry and assumes a smooth bore, therefore, the prediction curve for an A and B thermocouple would be the same unless the tomography showed a misalignment. Again, there are some land and groove differences indicated by the results, but more data are needed before any definitive conclusions can be drawn.

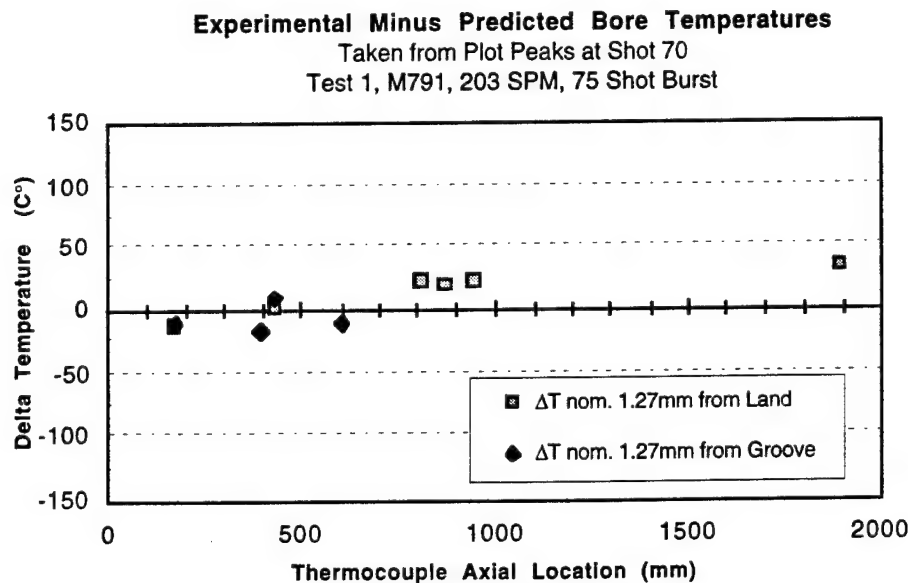


Figure 12: Temperature difference between near bore predicted and experimental data: comparison for test 1

In general, the results indicate that the model predictions in the breech area are fairly close to the experimental results. However, there is a trend towards increasing underprediction towards the muzzle end.

Test 2, 50 shots of 616W, did not provide close correlation between predicted and experimental results. The model consistently under-predicts the actual measured temperatures and no land versus groove conclusions can be drawn. The slope of the curves are also noticeably different. The results from thermocouple 1A are shown in Figure 13. Comparing Figure 13 to Figure 9 shows the significant increase in heat input resulting from the "hot round" ammunition.

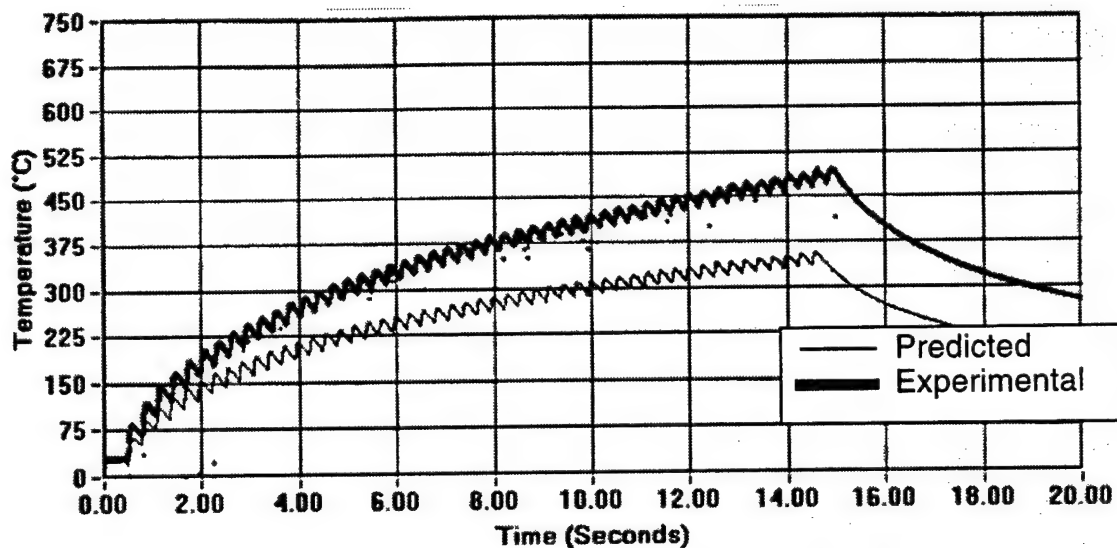


Figure 13: Predicted versus experimental temperature profile for thermocouple 1A after 50 shots of 616W

Another direct comparison between the M791 and 616W ammunition is given by Figures 14 and 15. Thermocouple 6B is located axially 947mm from the breech and 1.27mm radially from the bore. The model under-predicts in both cases, but the error is more severe in test 2. The increased thermal input from the 616W is also as significant at this mid-barrel location as it was for the breech location displayed in Figures 13 and 9. The thermocouple reads a temperature that is almost 100C° higher than the M791 after 50 shots of 616W as compared to the M791.

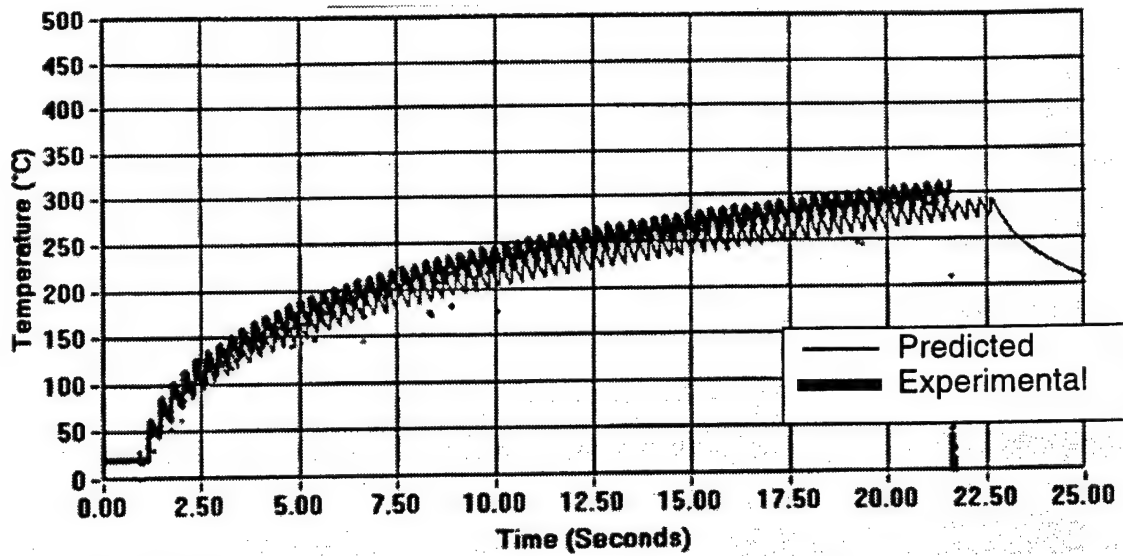


Figure 14: Predicted versus experimental temperature profile for thermocouple 6B after 75 shots of M791

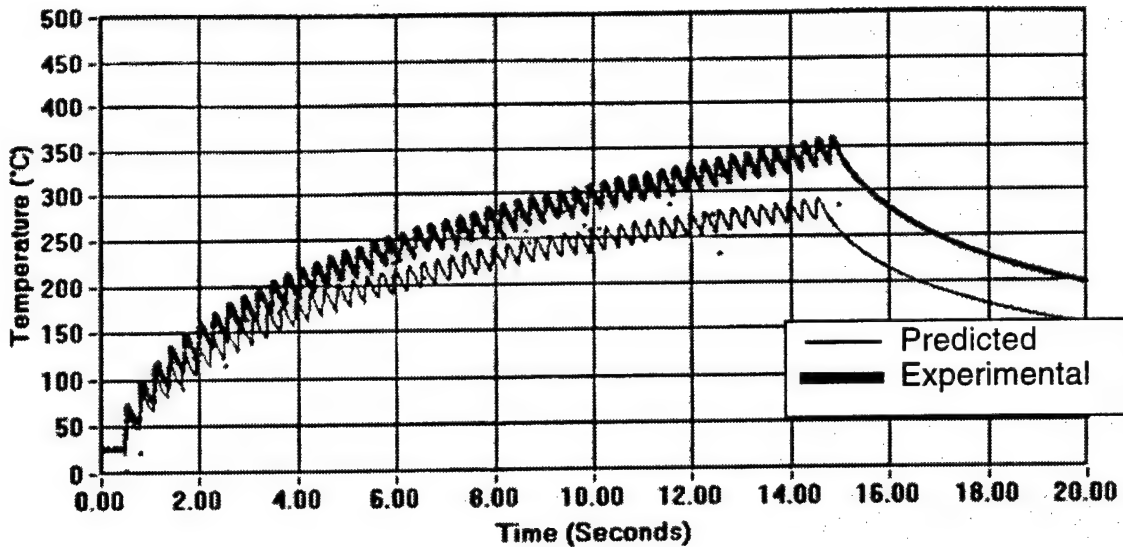


Figure 15: Predicted versus experimental temperature profile for thermocouple 6B after 50 shots of 616W

Figure 16 shows the difference between the experimental peak and predicted peak of near bore thermocouples at shot 50. Comparing this plot to Figure 12 for results with M791 ammunition shows the significant increase in deviations from model predictions shown by experimental data obtained with 616W ammunition.

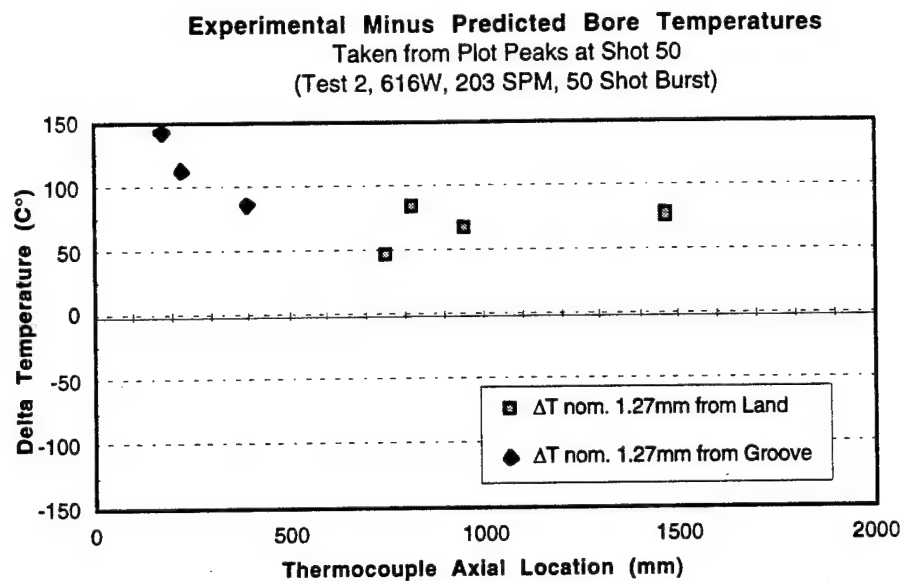


Figure 16: Temperature difference between near bore predicted and experimental data: comparison for test 2

## CONCLUSIONS

Two numerical codes are used to predict gun barrel response during firing. The data from the M791 tests compare fairly well with the predictions, and this provides good verification for both codes. However, this was not the case with the 616W hot ammunition tests. In this case the codes under-predicted the barrel temperatures by a significant amount. This mismatch could be attributed to the inability of one or both codes to handle the hot ammunition. In the case of XKTC, the code may not accurately predict the gas temperature or film coefficients. In the case of FDHEAT, the built-in time steps associated with the heat transfer calculation may not be fine enough to handle the rapid temperature excursions associated with the hot ammunition. In either case, additional study is required to reach a firm conclusion concerning the use of the codes with high impetus ammunition.

The next phase of work will compare the numerical results to experimental results for partially lined barrels. The implementation of a partial liner will compound the modeling challenges, but the groundwork set from the present evaluation will enhance the numerical modeling capabilities. To provide more accurate predictions from the model, this experimental data will be used to determine correction factors for the high impetus ballistics input data. Using the experimentally corrected model will allow extrapolation for designing barrels that can withstand high impetus propellant at high firing rates for an acceptable life. The project calls for bursts of 150 rounds at 500 SPM.

The completed tests have produced excellent data from which much can be learned. After the series of lined barrel tests, a clearer picture of the predictive capabilities of these codes and their proper application as a design tool will be achieved.

## ACKNOWLEDGMENTS

The authors wish to acknowledge Mr. George Pflagl and Mr. Mark Witherell of Benét Laboratories for modeling assistance and Mr. Mike Aesoph for providing the experimental data and data reduction methods.

## REFERENCES

- [1] C. Bagnall, J. R. Cook, K. C. Bearden and J. B. Boley, "Advanced Gun Barrel Technology Initiative Project Plan Revision," National Center for Excellence in Metalworking Technology, TR No. 95-068D, Concurrent Technologies Corporation, Johnstown, PA, 15904, (1995)
- [2] K. C. Bearden, "Analytical Methods Used to Predict M242 Bushmaster Gun Barrel Temperature Profiles," National Center for Excellence in Metalworking Technology, TR No. 00495, Concurrent Technologies Corporation, Johnstown, PA, 15904, (1995)
- [3] P. Gough, "XKTC Interior Ballistics Code," Benét Laboratories, Watervliet, NY, 12189
- [4] M. D. Witherell, "FDHEATCTC1.0 Benét Heat Transfer Code," Benét Laboratories, Watervliet, NY, 12189
- [5] J. R. Cook, M. D. Aesoph, R. Czarnek and B. K. Ott, "Instrumentation and Testing of a Modified M242 Bushmaster Barrel," National Center for Excellence in Metalworking Technology, Concurrent Technologies Corporation, Johnstown, PA, 15904, (1996)
- [6] E. L. Strickland III, "Report on Radiographic and Tomographic Observations of 25mm Gun Barrel," Scientific Measurement Systems, Austin, TX, 78758, (1996)
- [7] P. J. McMullen, "Application of Sub-models to Explore Geometric Effects in Medium Caliber Gun Barrels," National Center for Excellence in Metalworking Technology, Concurrent Technologies Corporation, Johnstown, PA, 15904, (1996)

**TITLE:** The Influence of a Balanced Breech and Modified Alignment Blocks on the Gun Dynamics of the M256 Cannon System  
Steve Wilkerson\* and Dave Lyon  
U.S. Army Research Laboratory  
**ATTN:** AMSRL-WT-PD  
Aberdeen Proving Ground, MD 21005-5066  
Larry Rusch and Bill Simard  
Benet Laboratories  
Watervliet, NY 12189-4050

**ABSTRACT:**

When a modern, high-pressure tank cannon is fired, a complex series of chemical, mechanical, and gas dynamic interactions occur. As a result of these coupled events, a projectile is launched toward the intended target with a high initial velocity. The intricate dynamic interactions that transpire between the recoiling gun system and projectile are not yet fully understood. However, it is known that these interactions are fundamental in controlling the projectile point of impact. It is also known that one of the major contributors to projectile accuracy and dispersion is the dynamics of the gun/projectile system during the firing cycle. As the bullet negotiates the gun tube, which is not perfectly straight, huge forces can be generated and transmitted between the two components. Motions occur as a result of these forces, driven by the gas pressure developed by the burning of gun propellant. Due to clearances in the recoiling parts of the gun coupled with an unbalanced breech, the gun movement is known to vary from shot to shot and occasion to occasion, thereby leading to perturbations in the projectile launch conditions. These disturbances can then induce deviations in the flight path, resulting in a loss of accuracy and an increase in dispersion.

In an attempt to improve the overall performance of the M256 gun system, the Benet Weapons Laboratory redesigned several of the key recoil components along with a method to balance the gun breech. The intent of the modified recoil parts was to constrain the breech motion in the vertical plane, while the bullet was in-bore. Since the breech motion couples directly into the dynamic shape of the gun tube, it was postulated that a reduction in the magnitude of the breech motion would also decrease the dynamic tube shape, thereby providing a straighter, lower disturbance tube for the projectile to negotiate.

A series of preliminary experiments were conducted from an M256 mounted in a hardstand. These experiments had two purposes: (1) to ensure the structural integrity of the modified hardware and (2) to examine how the system was being affected by the addition of these devices. What was observed during these tests was that a substantial reduction in the vertical breech movement could be obtained only when the modifications were adjusted correctly. This result was somewhat unexpected, as it was discovered that a minor adjustment in the alignment blocks could produce a significant impact on the breech motion. This paper will discuss what was learned and what future work remains to understand and utilize the benefits of the modifications in order to minimize the influence of gun dynamics on the M256 gun system.

WILKERSON, LYON, RUSCH, AND SIMARD

**BIOGRAPHY:** Dr. Wilkerson has been employed by the U.S. Army Research Laboratory since 1989, working in the Mechanics and Structures Branch, Propulsion and Flight Division, Weapons Technology Directorate.

**PRESENT ASSIGNMENT:** Investigate the influences of gun and bullet dynamics on gun accuracy.

**PAST EXPERIENCE:** He has worked in the field of gun accuracy for the past 7 1/2 years, primarily in the study of numerical techniques to simulate gun and projectile interactions.

**DEGREES HELD:** B.S. Mechanical Engineering, Johns Hopkins University, Baltimore, MD, 1982, M.S. Civil Engineering, George Washington University, Washington, D.C., 1985; Ph.D. Mechanical Engineering, Johns Hopkins University, Baltimore, MD, 1990.

WILKERSON, LYON, RUSCH, AND SIMARD

THE INFLUENCE OF A BALANCED BREECH AND MODIFIED ALIGNMENT  
BLOCKS ON THE GUN DYNAMICS OF THE M256 CANNON SYSTEM

Steve Wilkerson,\* Dave Lyon, Larry Rusch, and Bill Simard  
U.S. Army Research Laboratory  
ATTN: AMSRL-WT-PD  
Aberdeen Proving Ground, MD 21005-5066

OVERVIEW

The current M256 system has an asymmetrical breechblock causing the center of gravity of the recoiling mass to be different from the centerline of the gun tube. Upon firing, the pressure from the burning propellant, on the breech face, results in an offset between the center of gravity and the center of pressure. Consequently, the force couple imparts motion into the system. It was thought that by balancing the breech this source of motion could be eliminated, thereby reducing the gross movement of the gun tube in the vertical plane. In order to confirm this premise, the U.S. Army Research Laboratory (ARL) conducted a series of experiments in which the breechblock of the M256 tank cannon system was balanced relative to the bore centerline [1]. The goal of these experiments was to greatly reduce breech and tube motion in the vertical plane. What actually occurred was unexpected. Normally, when the gun is fired, the breechblock begins to fall as the gun recoils. Therefore, it was expected that the elimination of the powder pressure couple would result in the breech recoiling with minimal motion in either plane. However, with the breechblock balanced, the breech dropped for approximately the first 3 ms, then rose for the following 3 ms. This was unexpected based not only upon an intuitive sense, but also the fact that the gun dynamics codes, which were employed to simulate the balancing experiment, failed to predict this movement.

Following the firing tests, a series of finite element simulations were made, using the DYNA3D program, in hopes of understanding what might have caused this unexpected movement in the system [2]. These calculations also indicated that the balanced system would be an improvement (i.e., all but eliminate breech vertical motion during recoil). However, the first set of calculations assumed that there were no clearances between the recoiling parts. These assumptions, judged to be valid at the time, were made to simplify the modeling process and reduce the computational burden. Nevertheless, a more detailed examination of the gun/recoil components was conducted and clearance measurements were obtained from numerous gun systems at various stages during their life cycle. When representative clearances were added to the DYNA3D model, the results changed significantly. By orienting the clearances between specific parts, as they would be dictated by gravity, the model was able to predict the unexpected behavior of the balanced system [3]. An interesting note is that in the process of working this problem, a possible improvement to the system was also realized.

Exercising the model with various amounts of clearance revealed that the dynamic response was indeed linked to these clearances. It became apparent that a method to constrict the motion of the recoiling parts would prove beneficial. Of course, adjusting the clearances in the model is trivial compared to designing a hardware modification that would achieve the same effect. To design such a system, ARL teamed with Benet Weapons Laboratories, an organization that possesses expertise in gun and recoil design. Benet then modified the existing breech and recoil mechanism to help guide the breech

during its first 1.5 in of recoil, in an attempt to mimic the case where no clearances existed. Furthermore, a robust design for the breech balancing weights was conceived. The original ARL design resulted in minor cracks, which were initiated from additional holes on the breechblock where the weights were attached. The photographs in Figure 1 show the original, as well as the improved, breech alignment blocks. Figure 2 depicts the balancing weights for the breechblock. This design eliminates the need to drill into the current breechblock, it simply uses existing holes. The second design feature is intended to constrain the breech movement in the vertical plane during the first 1.5-in recoil. In effect, this was simply an extension of the existing alignment block and recoil bracket, which are located below the right and left sides of the breech. An important feature of this design is its simplicity and relative low cost. It is believed that different levels of improvement may be possible using these devices alone or in combination with one another. For example, it may be possible to use the wedges alone to achieve a certain portion of the overall improvement to the system and vice versa.

## EXPERIMENTAL FIRINGS

The experimental firing portion of this project took place at the ARL Transonic Range Facility from an M256 tube SN6823, with breech SN29, mounted in a concentric recoil SN1230468. This gun system was then attached to a nonrecoiling artillery sleigh. The hardstand setup allowed easy access to the recoil system, for adjustment and measurement purposes. Experimental instrumentation included two rings of four each proximity probes, shown in Figure 3, which were located 13.6 and 19.6 in behind the muzzle, respectively. These noncontact devices provide voltage-vs.-time data that can then be manipulated to extract the gun tube motion and muzzle pointing angle while the projectile is in-bore. This technique for obtaining gun dynamics is detailed in Bornstein et al. [4]. Two additional proximity probes were located on the gunner quadrant seats of the breech and one on the right cradle tab, shown in Figure 4. These devices were situated to observe motion in the vertical plane only, whereas the muzzle probes encircled the tube, providing data in both horizontal and vertical planes. A cloth target was then erected 953 m downrange to record target impacts.

After installation of all modified hardware, a single DM-13 APFSDS-T was fired to validate the structural integrity of the system and to identify any difficulties that might occur during installation in an M1A1 tank. Afterwards the parts were examined for integrity and appeared intact. Following this, four additional DM-13 data rounds were fired with the gun system in various configurations. The first two data rounds were fired with the gun in an unmodified condition. The final two rounds were fired with both the breech weights and modified alignment blocks attached. This would allow a direct comparison between the unmodified system (baseline) and the modified system. Raw data from one of the first two baseline rounds include the breech vertical displacement (Figure 5), the cradle movement (Figure 6), and the muzzle probes oriented in the vertical direction (Figure 7).

## RESULTS

Past gun dynamics testing of the M256 system has revealed that the breech exhibits a consistent behavior in that it always drops while the bullet travels down the gun tube (6 to 9 ms). This occurs regardless of ammunition type, ammunition temperature, or whether the gun is mounted in a hardstand or tank [1]. Figure 5 shows the measured motion from the forward breech gage during the first data round



Figure 1a. Original left side alignment, kick block.

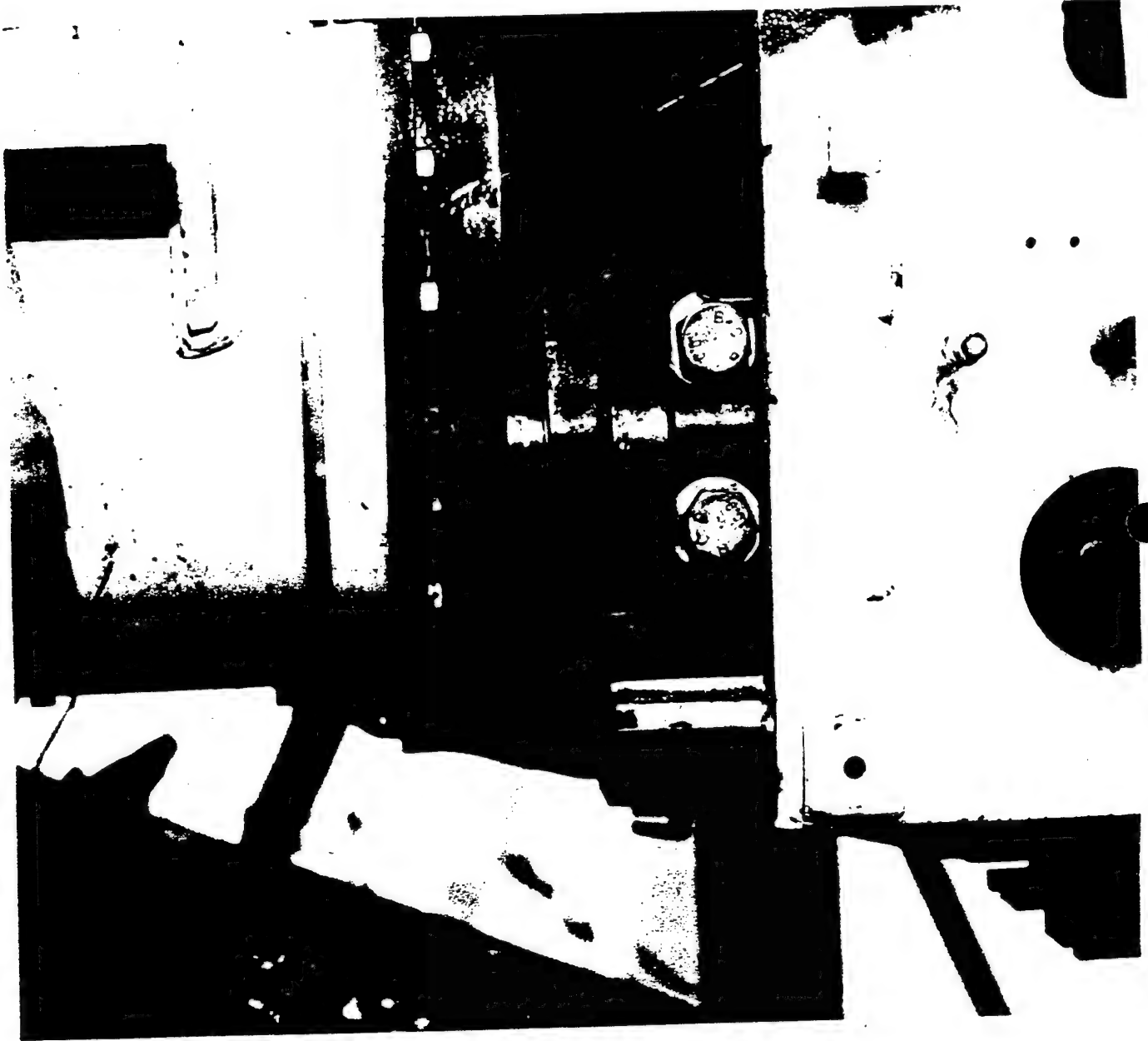


Figure 1b. Modified left side alignment, kick block.



Figure 1c. Right side alignment, kick block.

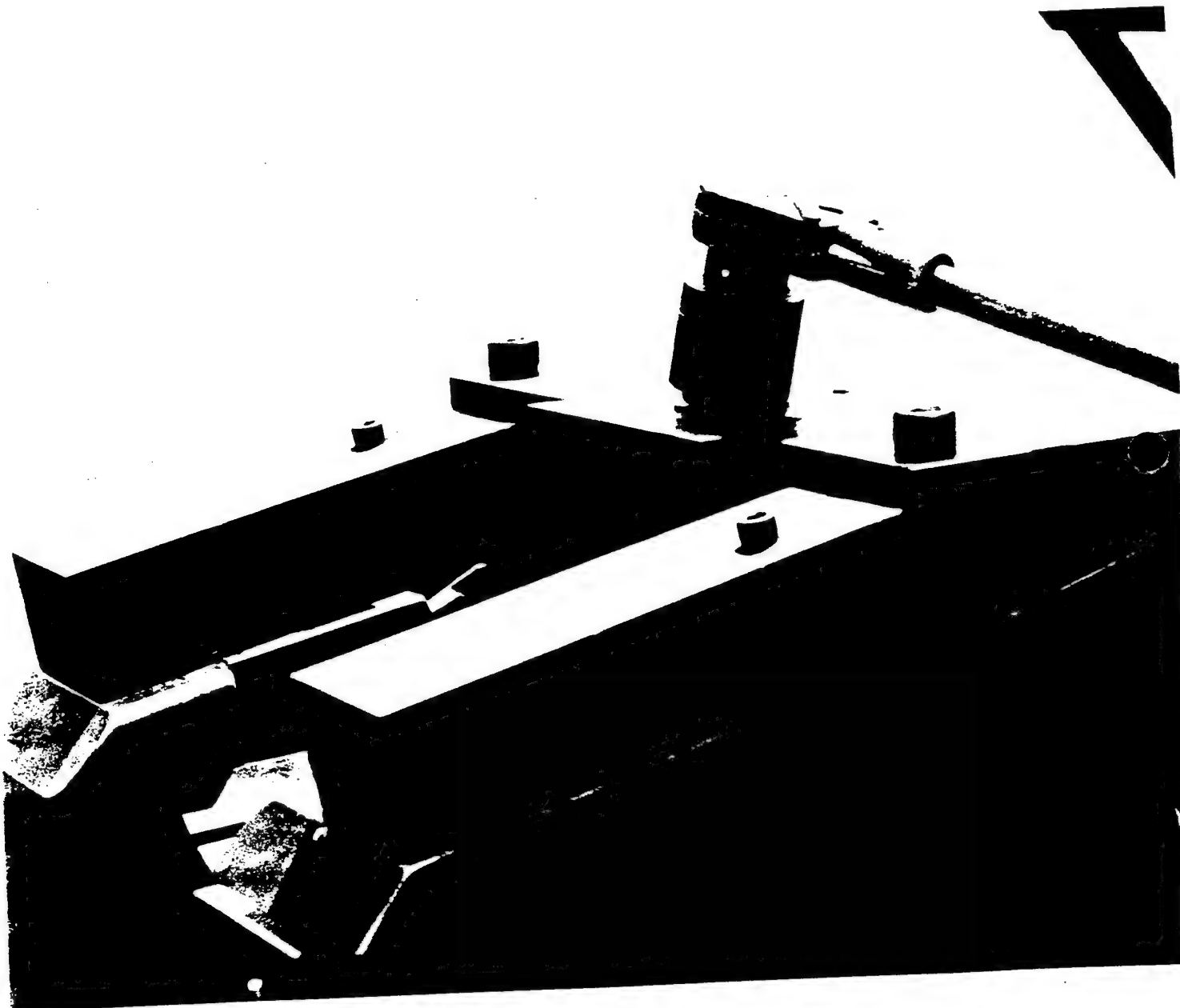


Figure 2. Balancing wedges.

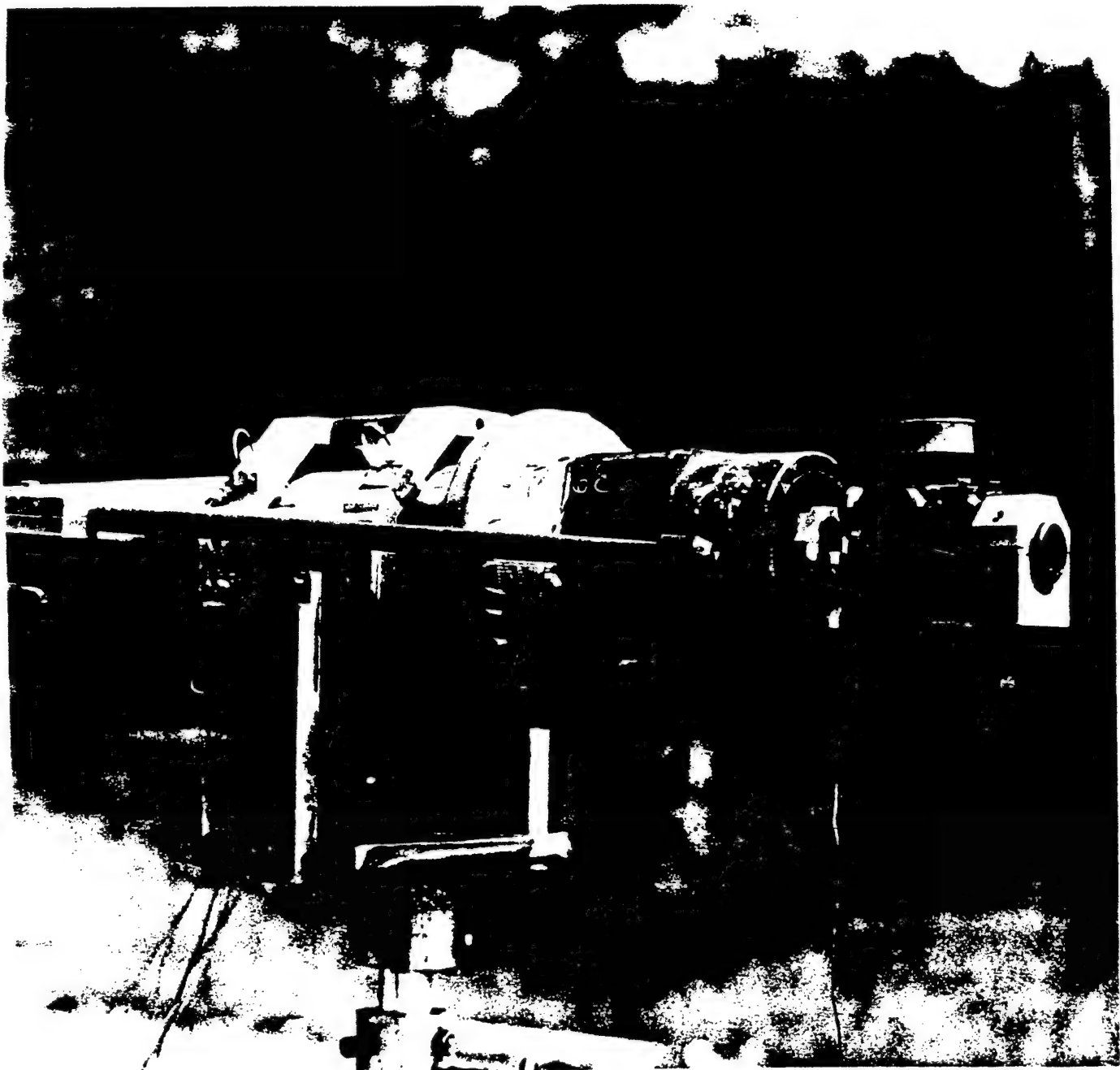


Figure 3. Muzzle gages.

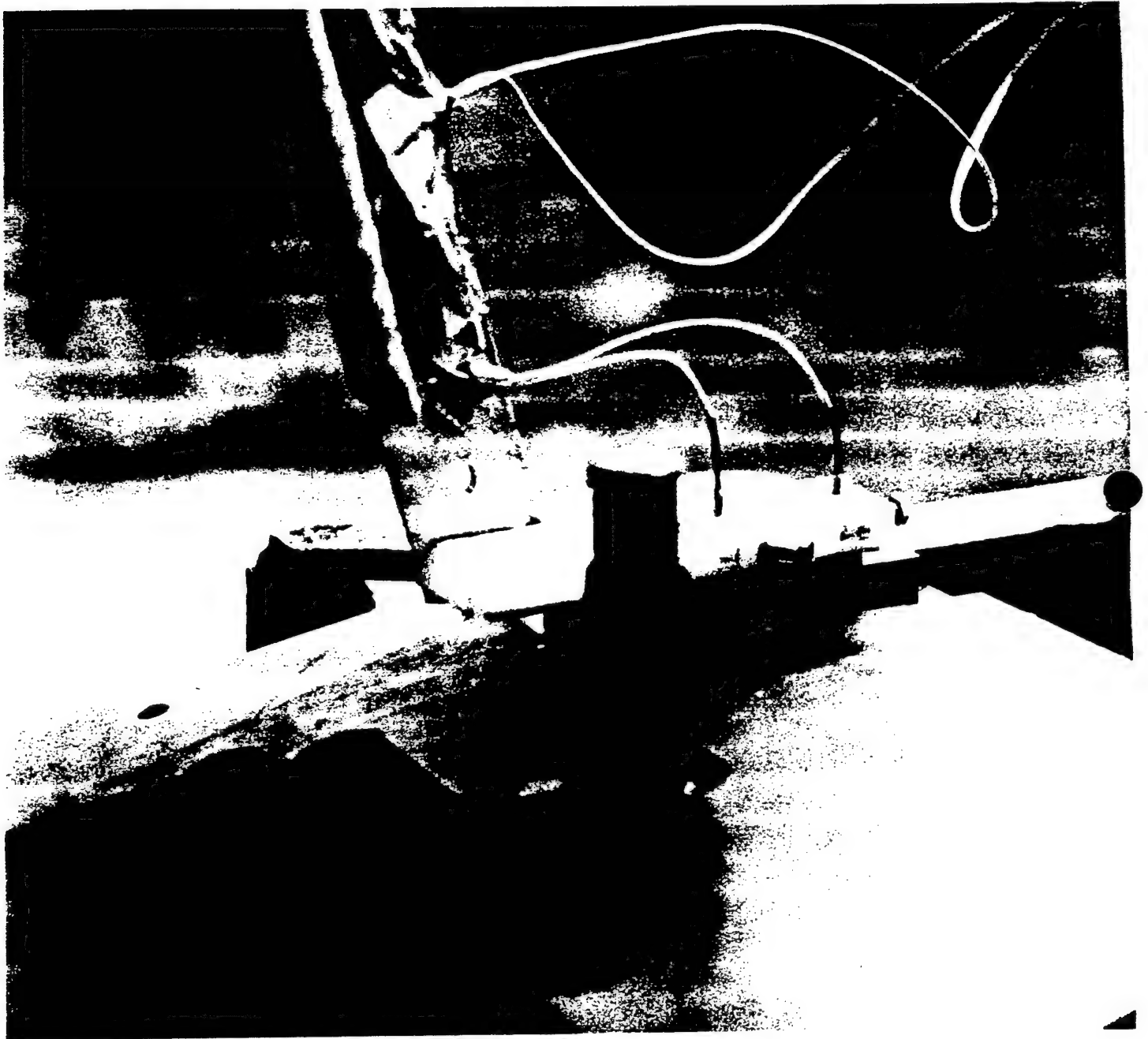


Figure 4a. Breech gages, unmodified system.

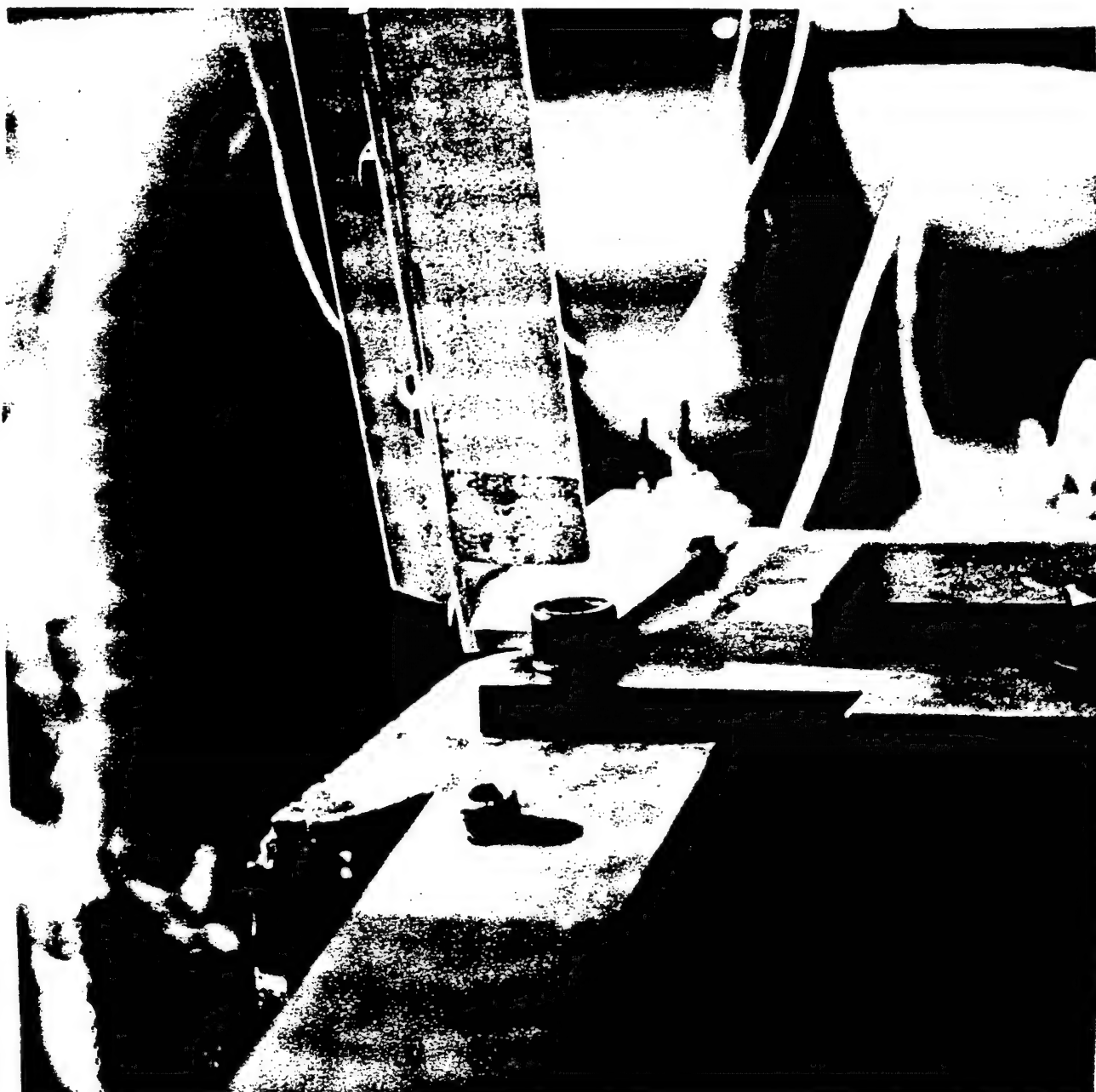


Figure 4b. Breech gages, modified system.



Figure 4c. Cradle gage.

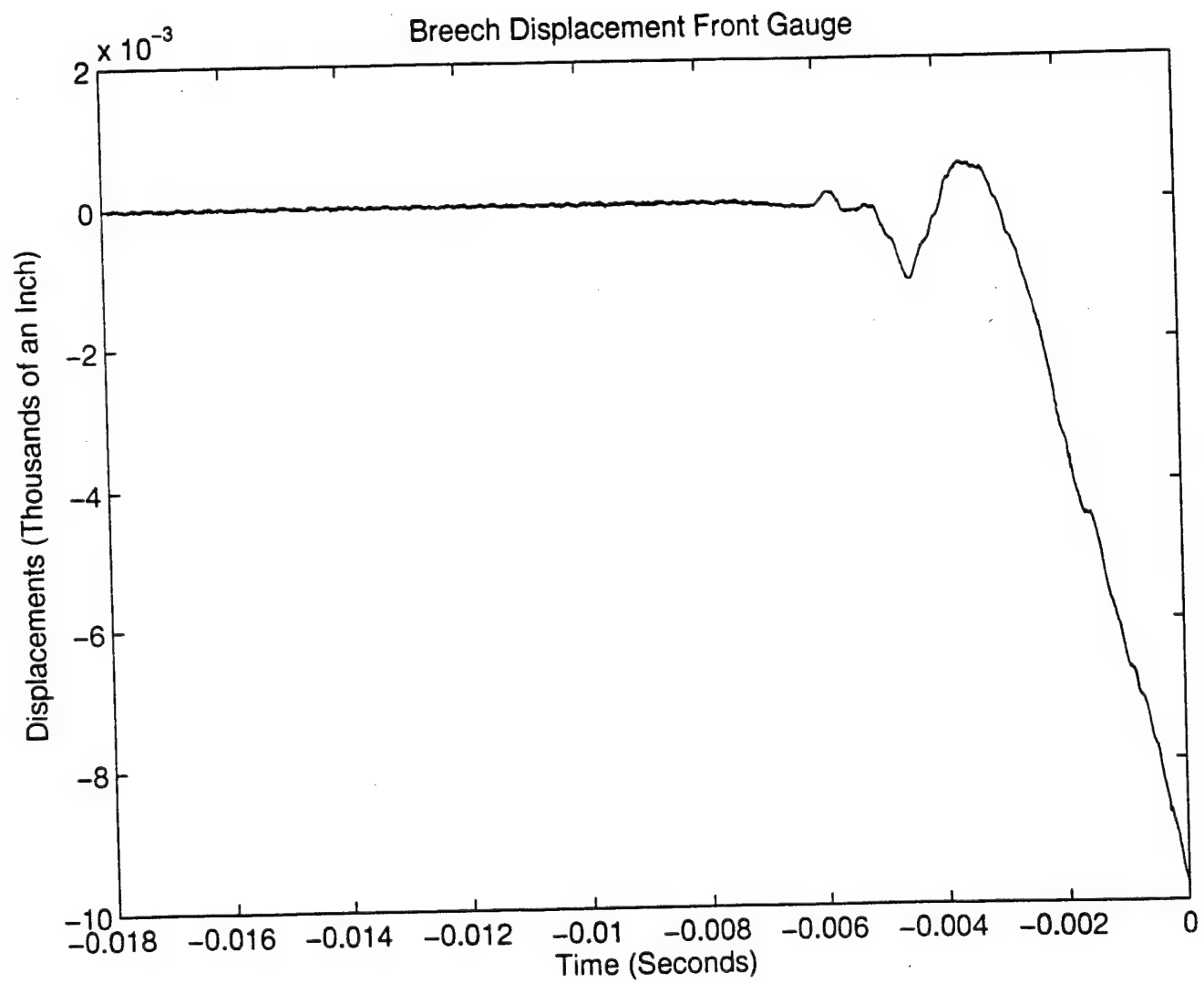


Figure 5. Breech vertical movement (unmodified system).

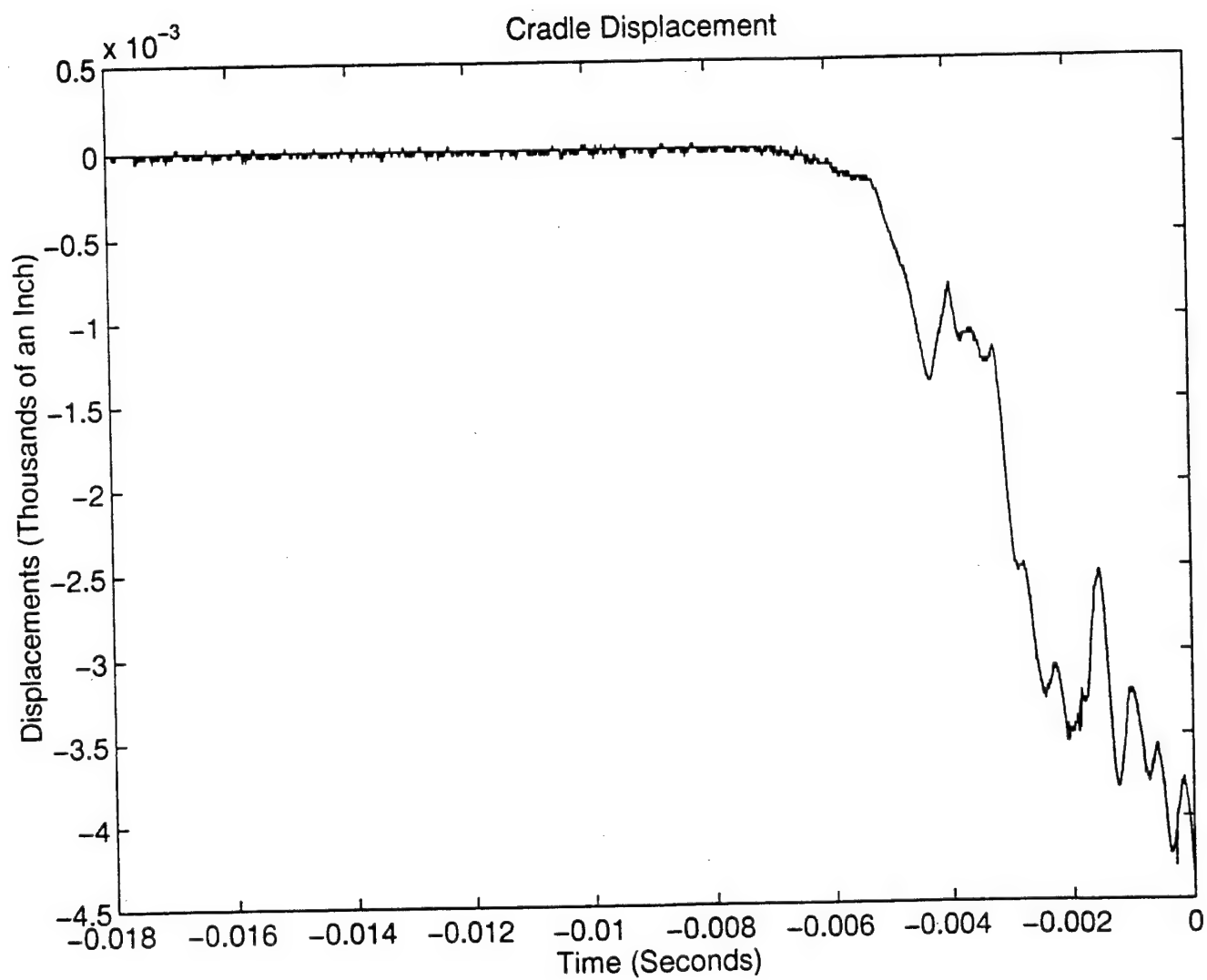


Figure 6. Cradle movement (unmodified system) (first shot).

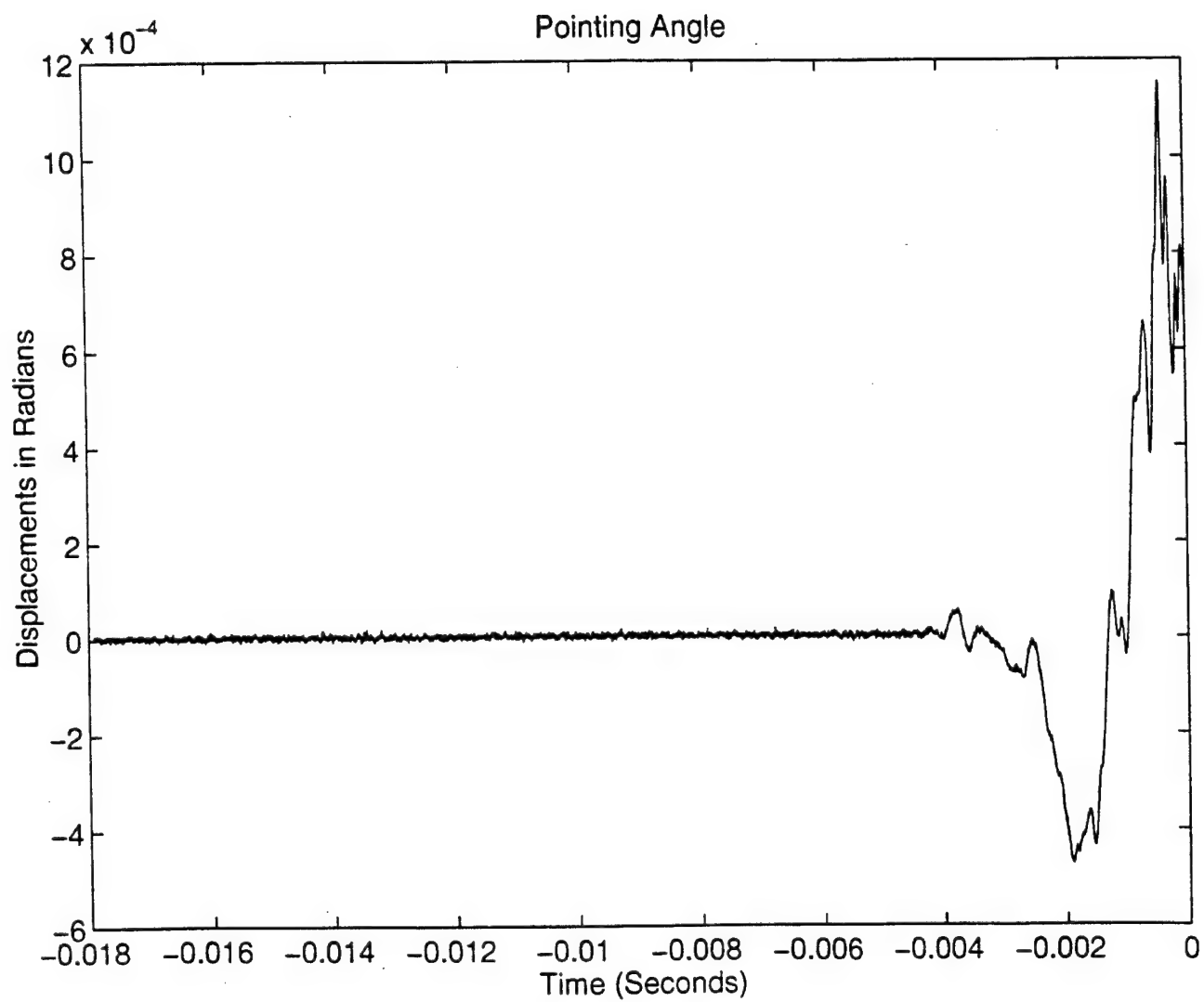


Figure 7. Muzzle displacements.

(no modifications). This plot shows a response very similar to previous test data with the characteristic drop [1]. The rear breech eddy probe also recorded an almost identical motion. Furthermore, when the second baseline data round was fired, the results at both breech gage locations were again identical to Figure 5. Prior to the current testing, it was unknown what vertical motion, if any, the cradle experienced during the in-bore cycle. For this test, an eddy probe was located on a mounting lug of the cradle so that the cradle's movement could be recorded. The displacement-vs.-time plots indicated that during the first shot the cradle dropped, as did the breech, but to a somewhat lesser degree, see Figure 6. However, the second and all subsequent data rounds showed that the cradle dropped initially, then rose later in the in-bore cycle, see Figure 8. Two possible explanations were derived from these observations. The first is that the motion observed at the breech is independent of what occurred at the cradle. The second conclusion was that the motion in the breech could not be explained as a simple rigid body rotation about the trunnions.

The third and fourth data rounds, with breech weights and modified alignment blocks, resulted in significantly different movements of the system. The breech displacement recorded at the forward gage is shown in Figure 9, while the trace from the rear gage is shown in Figure 10. Two aspects of these plots are noteworthy. The first is that the overall movement of the system has been drastically reduced, compared to the baseline; the second is that there appears to be a high-frequency ringing superimposed upon the measurement. Both gages on the breechblock recorded the same motion along with the same ringing phenomenon. It is believed that the high-frequency vibration is a local phenomenon and can be attributed to either the setup of the measurement devices or the breech balancing blocks themselves. Regardless, the modifications appear to have reduced the gross movement of the breechblock in the vertical plane and hence reduce the movement of the gun tube.\* The cradle gage recorded a motion very similar to that observed in the second baseline data round. For the fourth and final data round, a slight modification was made to one alignment block. This consisted of adding a shim (0.002 in thick) to the alignment block on the gunner's left side of the breech, reducing the clearance between the block and the breech. This modification produced breech displacements that were similar to the third round, only of a slightly higher magnitude. The conclusion from these experiments was that the gun/recoil system is sensitive to a subtle adjustment in the alignment blocks.

Another parameter that was measured was the displacement of the muzzle. By recording the displacements at two locations in close proximity, it is possible to estimate the muzzle pointing angle of the gun tube during the in-bore cycle. The muzzle pointing angle, at shot exit, provides a relative measure of the launch disturbance imparted to the projectile. By comparing the pointing angles at shot exit, the dynamic state of the projectile can be deduced, with a reduction in the pointing angle considered favorable. The muzzle pointing angle from the first baseline data round was  $6.4\text{E-}04$  radians, while the second baseline round resulted in  $1.1\text{E-}03$  radians. The sign convention is such that a positive value indicates the muzzle pointing upwards. The third and fourth data rounds, with modifications, yielded  $4.0\text{E-}04$  and  $1.4\text{E-}04$  radians, respectively. It is interesting to note that the fourth data round, with the increased shimming, resulted in a larger breech displacement, but a lower muzzle pointing angle. Comparing the smallest pointing angle (data round four, modified) to the largest pointing angle (data

---

\* For situations involving the dynamics of gun tubes it is believed that lower frequencies are the most detrimental in terms of system accuracy. This belief stems from the fact that lower frequencies tend to produce large amplitude motion and higher frequencies tend to produce small amplitude motion.

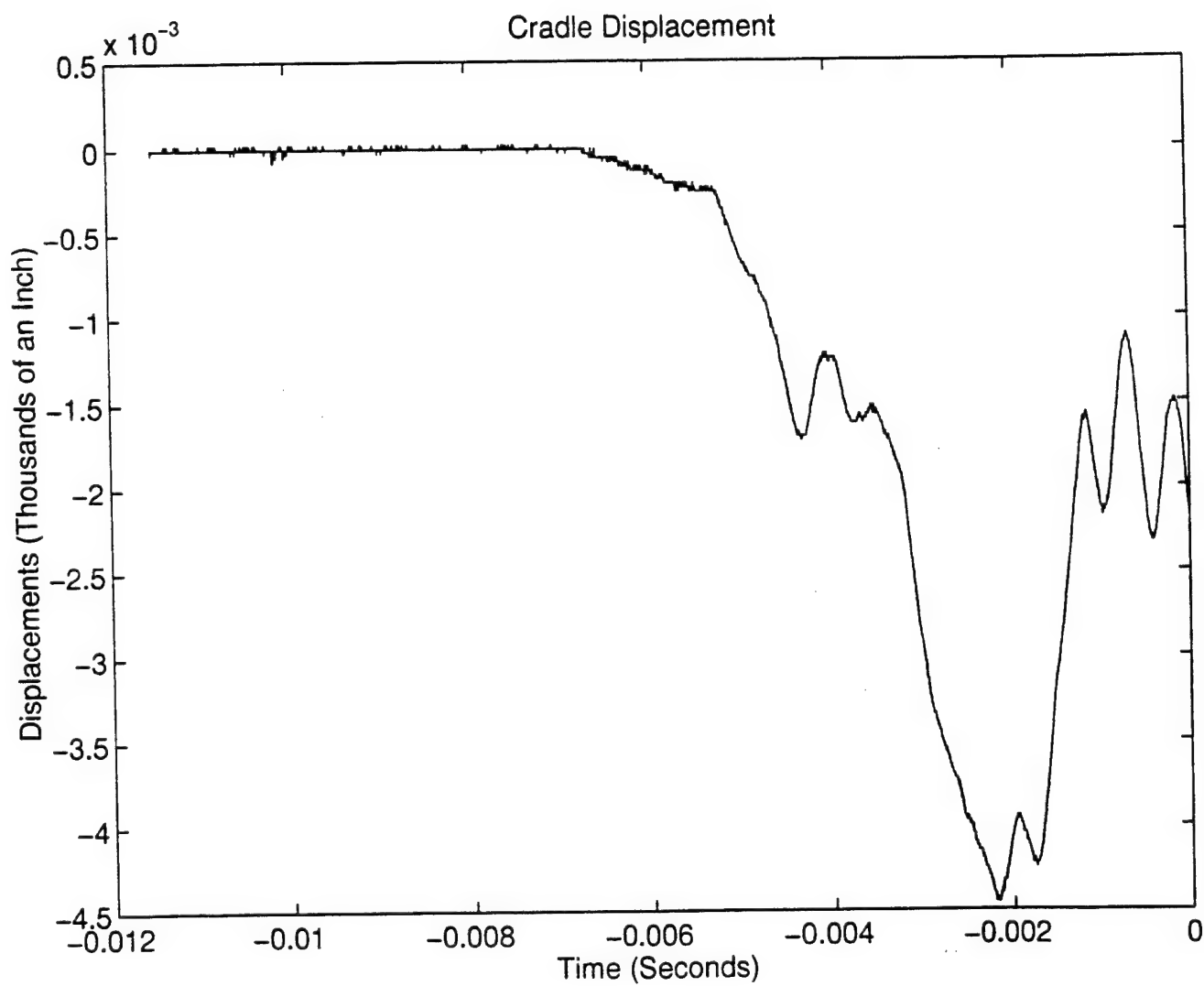


Figure 8. Cradle displacement (unmodified system) (second shot).

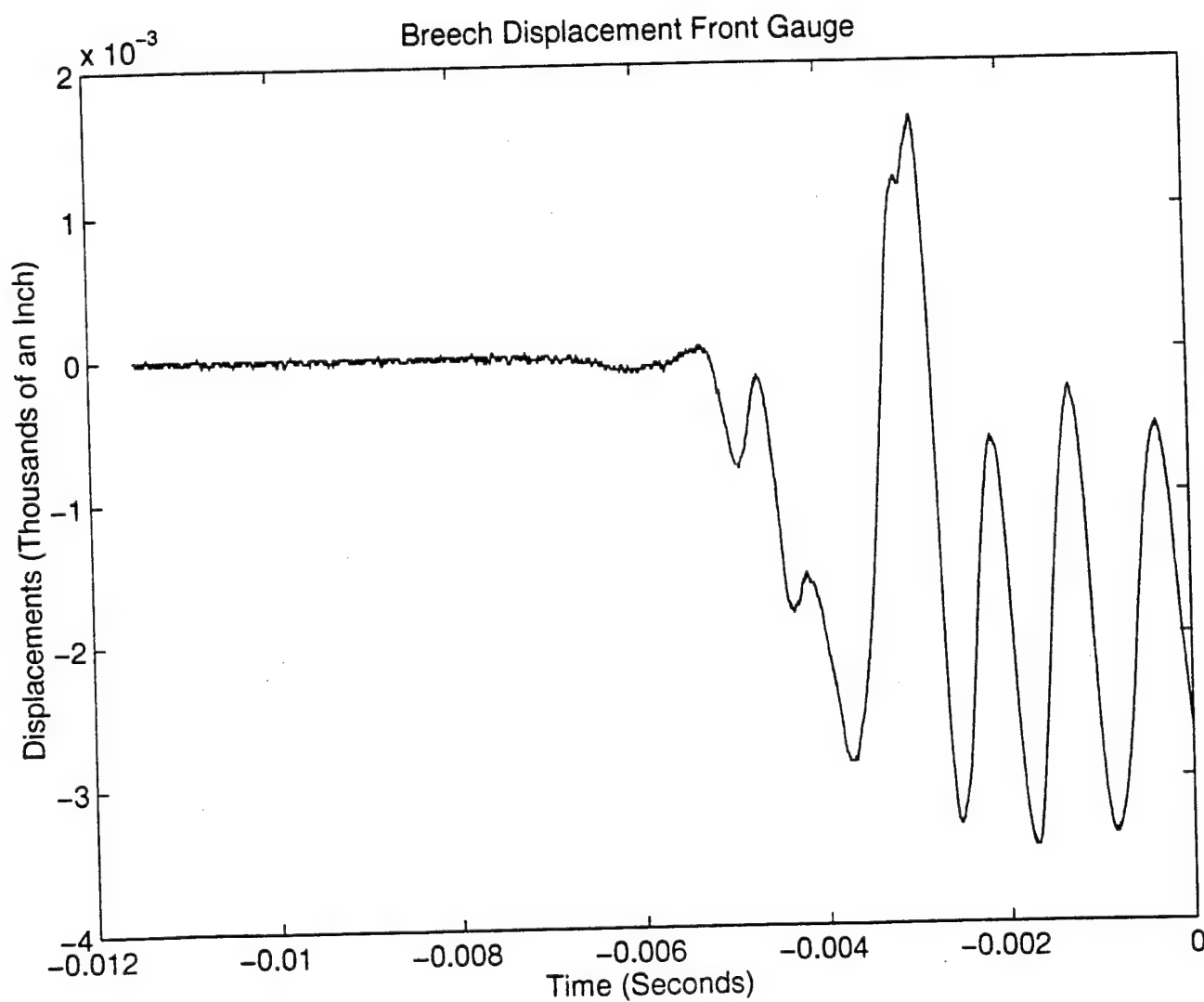


Figure 9. Breech movement (modified system) (first shot).

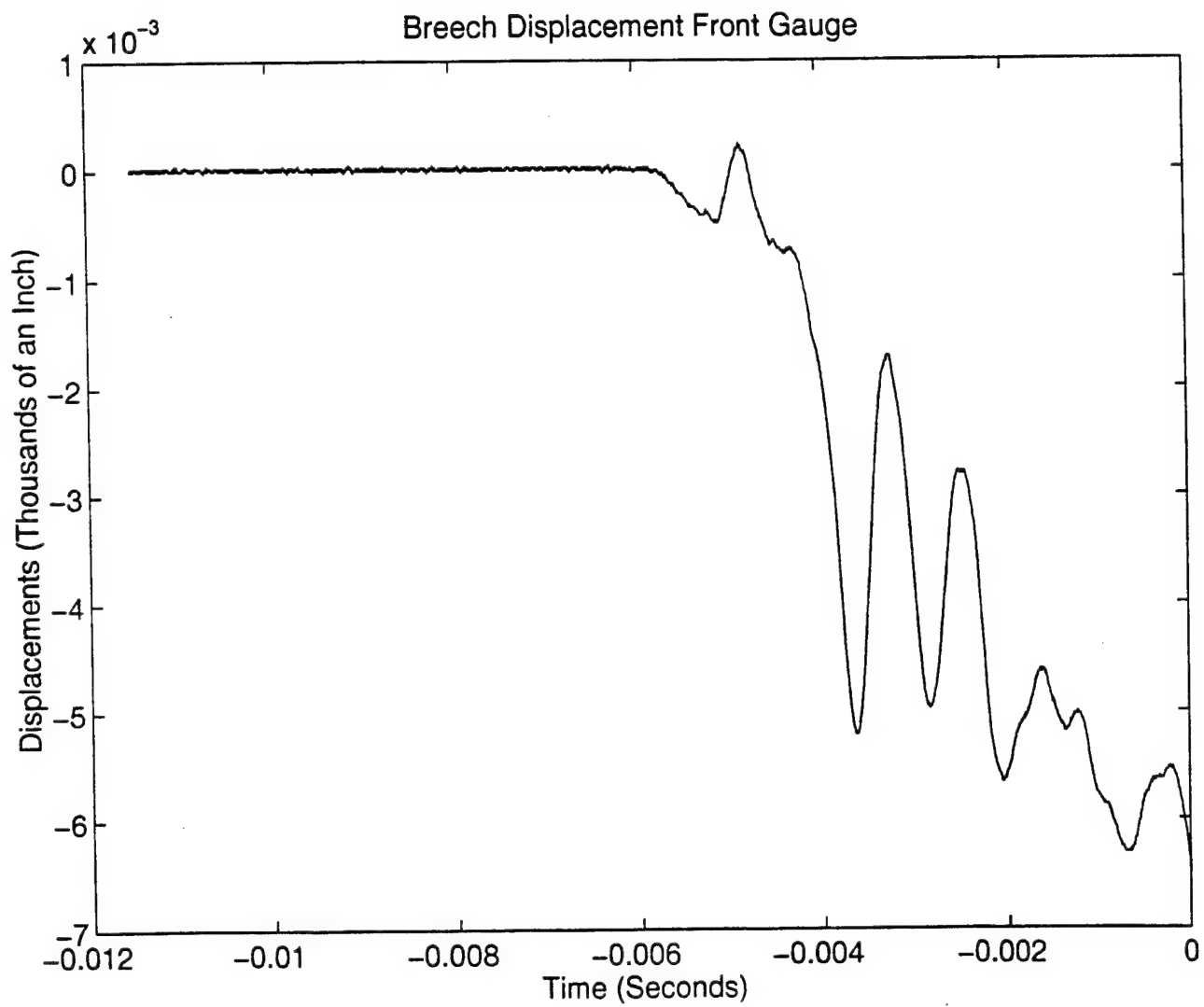


Figure 10. Breech movement (modified system) (second shot +.002 shimming).

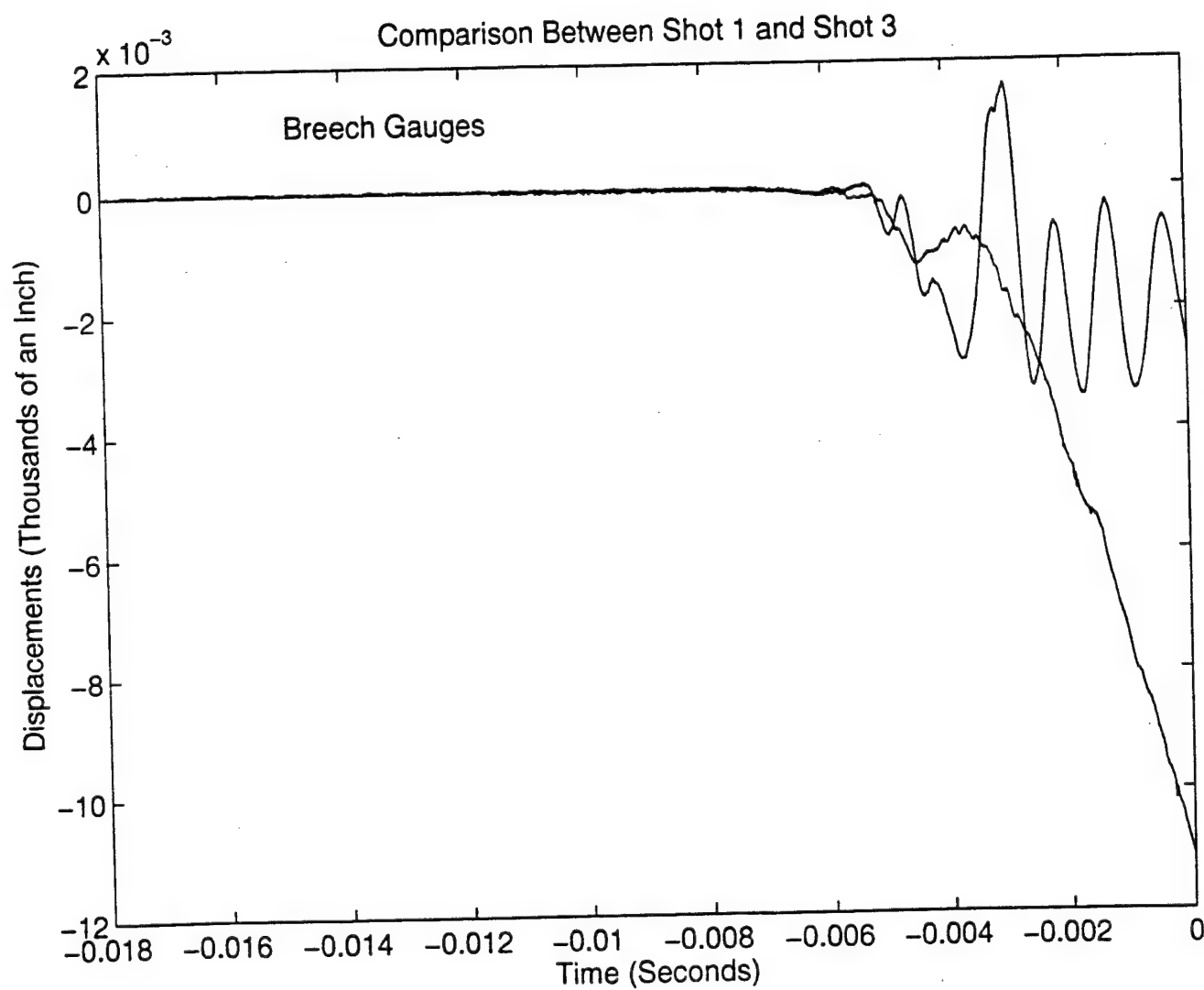


Figure 11. Breech movement, 5 to 1 improvement between modified and unmodified system.

round two, baseline) yields a reduction in the muzzle pointing angle by 87%. Even comparing data round three (modified) to data round one (unmodified) results in a reduction in pointing angle by almost 38%.

## CONCLUSIONS

The most interesting result of these experimental firings can best be summarized in Figure 11. This figure shows a direct comparison of the vertical breech displacement of an M256 gun system for both the baseline case and that of the same gun with a balanced breech and modified alignment blocks. What is apparent is that these alterations drastically reduce the movement of the breechblock while the projectile is in-bore. This is significant because it has been shown that the breech of the baseline system consistently drops in a repeatable manner, regardless of ammunition type [1]. Hence, these adjustments not only modify the dynamic behavior of the M256 breech, but also reduce the magnitude of the motion inherent in the gun tube itself. Furthermore, it was shown that the dynamic motion of the M256 gun system, during the in-bore cycle, can be influenced in a positive manner and that gross gun motion can be reduced through relatively minor alterations. Moreover, these modifications were designed with simplicity in mind, allowing a possible fleet retrofit with minimal expense or complexity.

## REFERENCES

1. Held, B. J., and T. F. Erline. "Dynamics of the Balanced Breech System for the 120-mm Tank Main Gun." BRL-TR-3126, U.S. Army Ballistic Research Laboratory, Aberdeen Proving Ground, MD, January 1991.
2. Wilkerson, S. A. "The Effects of Initial and Gun Mount Conditions on The Accuracy of Kinetic Energy (KE) Projectiles." ARL-TR-895, U.S. Army Research Laboratory, Aberdeen Proving Ground, MD, November 1993.
3. Wilkerson, S. A., and P. A. Hopkins. "Analysis of a Balanced Breech System for the M1A1 Main Gun System Using Finite Element Techniques." ARL-TR-603, U.S. Army Research Laboratory, Aberdeen Proving Ground, MD, November 1994.
4. Bornstein, J., I. Celmins, and P. Plostins. "Launch Dynamics of Fin-Stabilized Projectiles." Proceedings of AIAA Atmospheric Flight Mechanics Conference, Boston, MA, 14-16 August 1989.

# **A TECHNIQUE FOR REDUCTION OF LAUNCH-INDUCED PERTURBATIONS**

Edward M. Schmidt and William F. Donovan  
U.S. Army Research Laboratory  
Aberdeen Proving Ground, MD 21005-5066

## **ABSTRACT:**

A means to improve the stability of fin stabilized projectiles is presented. By allowing the nose of the projectile to move relative to the projectile, it is possible to have it weathervane into the airstream thereby reducing the angle of attack and lift on the nose. This in turn improves the static stability of the round since nose lift results in a positive or destabilizing overturning moment.

## **BIOGRAPHY:**

**PRESENT ASSIGNMENT:** Manager US Army Electric Armament Program

**PAST EXPERIENCE:** Twenty years working in the field of exterior ballistics and tank accuracy at the Ballistic Research Laboratory.

**DEGREES HELD:** BS (64), MS (65), and PhD (69) Polytechnic Institute of Brooklyn

# A TECHNIQUE FOR REDUCTION OF LAUNCH-INDUCED PERTURBATIONS

Edward M. Schmidt and William F. Donovan  
U.S. Army Research Laboratory  
Aberdeen Proving Ground, MD 21005-5066

## INTRODUCTION

Projectile launch always provides a lateral disturbance to the round that results in both linear and angular motion. Within the gun, yaw levels are quite low ( $< 0.1$  deg) but the angular rates can be relatively high ( $> 5$  rad/s). For fin stabilized projectiles, the angular rate can be further enhanced by separation both from the gun and from its sabot. Yaw rates at entry into free flight on the order of 10 rad/s are not uncommon. As the round moves downrange, the yaw cycle is characterized by successive maxima and minima. Eventually, the yaw damps and assumes a low level, circular limit cycle motion. For tank fired kinetic energy projectiles, maximum yaw can be 5 deg near the gun damping to 1.5 deg by 1 km. Unfortunately, yaw in excess of one degree in a high L/D rod degrades penetration due to interference between the penetrator body and the sides of the penetration channel. It is not unusual that a kinetic energy projectile has regions near the weapon where its effectiveness is significantly below specifications. In addition, there is lateral deviation of the shot line, termed aerodynamic jump, associated with yawing motion. If the launch angular rate varies in magnitude and direction, the resulting variation aerodynamic jump will increase round-to-round dispersion (i.e., decrease accuracy).

To reduce the influence of the launch angular disturbance, two approaches are plausible: reducing launch disturbance or increasing stability. Both are reflected in the following expression for first maximum of yaw:

$$\xi_m = \left[ \frac{2I_t}{C_{m_a} \rho V^2 DA} \right]^{1/2} \frac{d\xi_o}{dt}$$

Programs to improve system accuracy generally address the reduction in launch disturbance and through that decrease the initial angular rate. In addition, the aerodynamicist can influence the moment coefficient through a number of factors including nose geometry, fin planform, fin placement, and number of fins; however, traditional design approaches to increase stability will generally increase aerodynamic drag. The present paper describes an alternate approach to dynamically modify the projectile geometry in flight thereby increasing stability without major changes in drag.

## CONCEPT

The moment coefficient is defined by two major sources of lifting force: the projectile nose and the projectile fins. The nose lift is destabilizing while the fins are the major stabilizing surfaces. If the nose lift can be reduced or eliminated, the projectile stability will be increased. One way to reduce nose lift is to make the nose more blunt. This dramatically increases drag. A possible alternative is to gimbal the projectile nose in a fashion that allows it to "weathervane" into the airstream, Fig 1. By placing the center of pressure of the nose aft of the pivot bearing, the aerodynamic moment acts to continually align the nose with the flow velocity vector. Thus, the nose attitude is maintained at zero angle of attack and the nose lift is eliminated.

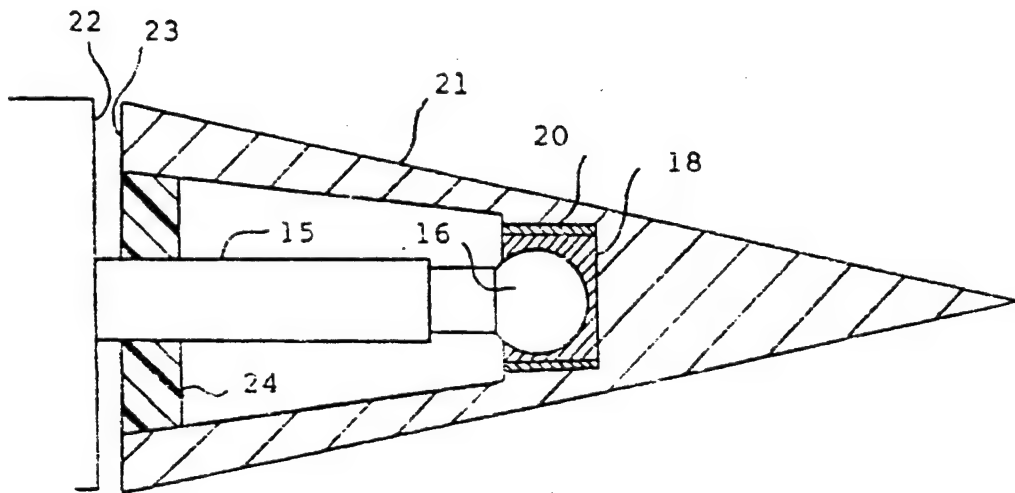


Fig 1. Gimballed Nose

Such configurations have been considered in the past. Dr. Robert Goddard [1] used a gimballed nose connected to a set of actuators as a means of steering a missile. Kranz [2] has a patent which describes a pintal mounted free nose conceptually like that of Fig. 1; however, no analytic or test results are presented. The present concept [3] is somewhat different than that of Kranz in that the nose is gimballed in a fashion that provides positive reinforcement against the longitudinal decompression characteristic of projectile release from guns. It is possible to estimate the effect of perfect weathervaning upon the moment coefficient. In these considerations, a 120mm, DM13 projectile is used as a baseline. The measured moment coefficient has been measured in the ARL Transonic Range and for this simple analysis is assumed to be the sum of two components, nose and tail lift:

$$C_{M_g} = -\Delta_i C_{L_{a_i}} + \Delta_n C_{L_{a_n}} = -16.5$$

according to slender body theory, the nose normal force is

$$C_{N_\alpha} \approx C_{L_\alpha} = 2.0$$

which acts at the center of pressure of the projectile nose a distance of roughly 5.4 calibers (one caliber being the projectile reference diameter of 37.3mm); thus, the moment coefficient with zero nose lift is estimated to be

$$C_{M_\alpha} = -16.5 - \Delta_n C_{L_{\alpha_n}} = -27.4$$

This represents a significant enhancement (66%) of the moment coefficient. Since the first maximum yaw varies inversely with the square root of the moment coefficient it would be expected that for identical launch angular rates, the first maximum yaw with the gimbaled nose would be roughly 25% lower than for the rigid body projectile. There is a tradeoff with this direct decrease in yaw. Yaw damping also depends upon the lift components of the nose and tail and if the nose lift is eliminated, yaw damping is decreased.

The aerodynamic jump is expressed as

$$\Theta = \frac{I_t}{mDV} \frac{C_{L_\alpha}}{C_{M_\alpha}} \frac{d\xi_o}{dt}$$

Using the logic as above, the lift coefficient for the standard DM13 is

$$C_{L_\alpha} = C_{L_{\alpha_t}} + C_{L_{\alpha_n}} = 7.7$$

and for the case of the gimbaled nose

$$C_{L_\alpha} = 7.7 - C_{L_{\alpha_t}} = 5.7$$

The aerodynamic jump varies directly with lift coefficient and inversely with moment coefficient; therefore the gimbaled nose will show a dramatic improvement in jump because both of these coefficients change in a sense that reduces the jump. In fact for equal angular rates, the gimbaled nose should show 55% less aerodynamic jump than the rigid projectile. A series of experiments were performed to explore the ability of actual hardware to reproduce some of these predictions.

## EXPERIMENT

A 120mm, DM13 kinetic energy projectile was modified with a gimballed nose as depicted in Fig. 1. Since the gimbal is supported on a stanchion which will interfere with the free rotation of the cone, the maximum yaw angle of the nose is limited to 10 deg which is less than the maximum yaw expected. Six of these rounds were fired through the ARL Transonic Range. All of the projectiles survived launch with the gimballed noses intact; however, some separation was observed between the base of the cone and the forward shoulder of the projectile. This separation may effect the aerodynamics of the round, particularly the drag. The gimballed nose did function as intended. This is illustrated by the spark shadowgraph in Fig. 2. The projectile body clearly has appreciable yaw while the nose is weathervaned into the flow. The spark shadowgraph was taken just as the round entered the range where the yaw was relatively high. Further downrange, a typical spark station photograph, Fig. 3, shows the nose still intact.

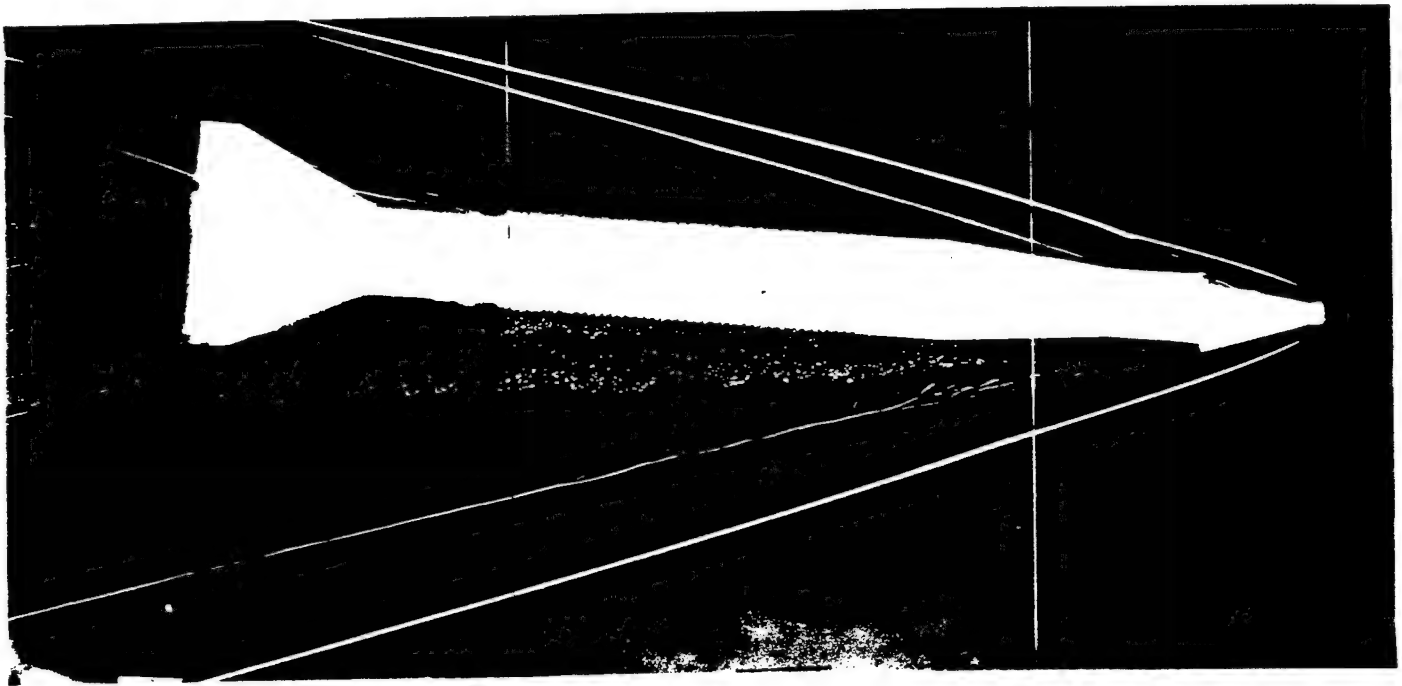


Figure 2. Spark Shadowgraph of Gimbal Nosed Projectile at entry to Transonic Range

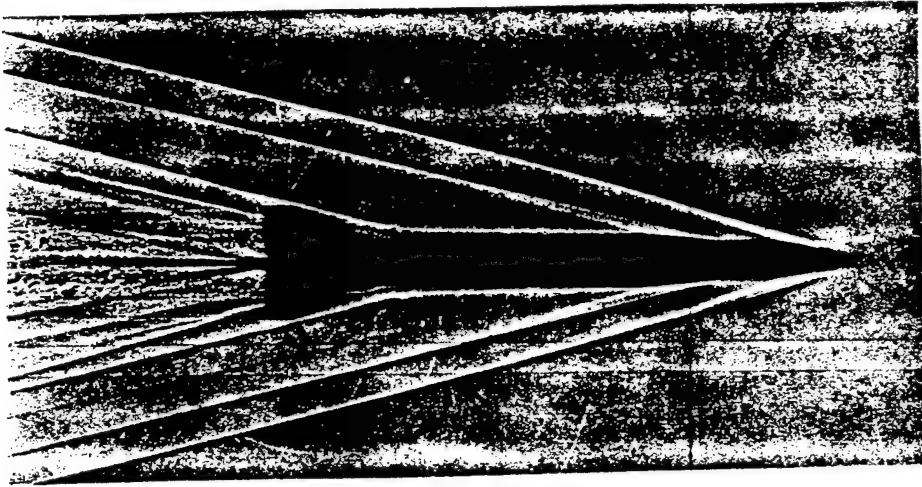


Figure 3. Spark Shadowgraph of Gimballed Nose Projectile at Typical Range Station

A comparison between the measured values of DM13 aerodynamic coefficients with and without the gimballed nose is presented in the table below:

	$C_{D_0}$	$C_{D_\delta^2}$	$C_{L_\alpha}$	$C_{M_\alpha}$
DM13- Standard	0.31	6.30	7.7	-16.5
DM13 - Gimballed	0.35	13.7	6.8	-20.1

The two drag terms represent the zero yaw drag and drag associated with yaw. As can be seen, the zero yaw drag for the two cases is comparable. The gimballed nose projectile has roughly 13% greater drag at zero angle of attack than does the standard DM13. This may reflect the influence of the nose separation following launch. The drag associated with yaw is significantly higher for the gimballed case. This is probably due to the formation of strong shocks off of the projectile shoulder as it is uncovered in the yawed state, Fig 2. As the round moves downrange, the yaw damps and this effect becomes less important. The lift and moment coefficients show the same trend as predicted by the simple estimates in the previous section. The magnitude of the difference between standard and gimballed nose is less than predicted. This may be associated with first, the crudeness of the estimate technique, and second, the effects of nose standoff following launch. Even with these values, it would be expected that for the same launch yaw rate the gimballed nose would show 10% less maximum yaw and 28% less aerodynamic jump than the standard round.

As envisioned by Goddard [1] the gimballed nose could be used in conjunction with a set

of actuators to provide control authority. Another application would employ sensors to measure the angle between the projectile body and the free nose. This could be used as input to a flight control system which could act to counter yaw or to provide for a desired trim angle to the projectile. The latter being essentially to lifting flight needed in range extension techniques.

### **CONCLUSIONS**

A technique is examined to reduce the nose lift on statically stabilized projectiles. It is shown that the possible advantages of the technique in terms of reducing first maximum yaw and aerodynamic jump are substantial. A series of experiments were conducted to demonstrate the concept. The results fell short of simplistic estimates, but did provide worthwhile improvement in flight characteristics. It is necessary to further improve on the initial design to reduce the separation between the nose and the projectile associated with decompression upon release from the gun. The benefit of a fully functional design would then have to be weighed against the addition complexity and cost to the finished projectile.

### **REFERENCES**

1. Goddard, Robert H., "Apparatus for Steering Aircraft," US Patent No. 2,594,766, April 1952.
2. Kranz, Walter, "High Velocity Aerodynamic Body having Telescopic Nose Tip," US Patent No. 4,756,492, July 1988.
3. Schmidt, Edward M and Donovan, William F., "Aerodynamically Compliant Projectile Nose," US Patent No. 4,998,994, April 1991.

**SESSION III**  
**METROLOGY AND DESIGN**

Grumann

**TITLE:** Development of RF Couplers for the Interior Ballistics Interferometry and Construction of a Microwave Interferometer

**Helmut Grumann**

Fraunhofer-Institut für Kurzzeitdynamik, Ernst-Mach-Institut

Hauptstrasse 18, D - 79576 Weil am Rhein, Germany

**ABSTRACT:**

In order to carry out projectile trajectory measurements systematically using interior ballistics microwave interferometry RF couplers for the transfer of RF energy into the barrel were developed which were closely connected to the muzzle. By this means elaborate adjustments of antennas or reflectors are not necessary and measurements also at repeated firings will be possible. The principle and the construction of the RF couplers and the realization of a microwave interferometer operating at 5 GHz will be described.

**BIOGRAPHY:**

Study of electrical engineering at University of Aachen, Germany

**PRESENT ASSIGNMENT:**

Since 1971 scientist at the Ernst-Mach-Institut, Weil am Rhein

**PAST EXPERIENCE:**

Interior ballistics measurements; telemetry; sensor technology

**DEGREES HELD:**

Electromagnetic compatibility of igniters and igniter circuits

Diplom-Ingenieur (MA)

Development of RF Couplers for the Interior Ballistics Interferometry and  
Construction of a Microwave Interferometer

Helmut Grumann

Fraunhofer-Institut für Kurzzeitdynamik, Ernst-Mach-Institut  
Hauptstrasse 18, D - 79576 Weil am Rhein, Germany

## INTRODUCTION

The method mostly used for measuring the projectile movement in a gun tube during firing is the interior ballistics microwave interferometry. The output of the interferometer is a sinusoidal voltage with a frequency that is proportional to the velocity of the projectile. By evaluating this signal the displacement of the projectile as a function of time can be received. From this curve the velocity and the acceleration of the projectile may be deduced by applying the first and the second derivative.

Usually the coupling of the microwave energy into the gun barrel is accomplished by means of simple antennas or passive reflectors, further denoted as RF couplers, which are destroyed when the projectile is fired. The production of the RF couplers as well as their positioning and adjustment is elaborate and expensive. In tests where the flight behavior of the projectile has to be investigated, the interaction with the RF couplers may lead to severe disturbances and consequently to larger deviations from the undisturbed trajectory.

Therefore, it is desirable to have RF couplers which may be reusable for multiple times, which do not disturb the trajectory of the projectile, where elaborate adjustments are not necessary, and which, furthermore, are simply to install and not expensive. The imposed requirements may be fulfilled by RF couplers that are fixed directly to the muzzle of the gun tube.

In [1] a detailed description of such a coupling element can be found for a 105 mm gun tube. An RF coupler which is mounted inside the muzzle break is cited in [2] for the caliber 20 mm. However, there are no details about the construction of this RF coupler.

For the treatment of actual tasks at the Ernst-Mach-Institut (EMI) RF couplers, which are matched to the caliber 40 mm, are necessary. Furthermore, they have to operate with powder guns as well as light gas guns and liquid propellant guns, too. Therefore, in the following the construction of RF couplers which have been developed at EMI for the caliber 40 mm will be described.

Moreover, in a further section the construction of a microwave interferometer as a compact device will be described and examples are given from results which have been achieved with this instrument and the RF couplers constructed at EMI.

## RF COUPLERS

The purpose of RF couplers is to couple the RF energy from the interferometer with high efficiency into the gun barrel and vice versa to return the energy reflected at the projectile into the interferometer. A reflection-free transition between the gun barrel which is regarded as a circular wave guide and the interferometer with its coaxial RF output would be the optimum from the viewpoint of RF engineering. Not regarding the various possibilities for solving this problem, in the following the constructions realized at EMI are described.

As mentioned above, these RF coupling elements are tightly connected to the muzzle of the gun tube.

### Determination of the Working Frequency

When determining the working frequency and wavelength a) the propagation of a uniquely defined wave mode must be ensured and b) the possibility of generating this wave mode by means of the RF couplers have to be considered.

It is especially the second demand that is responsible for the choice of the  $H_{11}$  wave mode although a small loss concerning the resolution of the system has to be taken into account. Referring to [3] a uniquely defined  $H_{11}$  wave mode in a circular wave guide is given for

$$1.31 < \lambda / D < 1.71, \quad (1)$$

where

$$\lambda = 1.71 \cdot D = \lambda_k(H_{11}) \quad (2)$$

$\lambda$	Wavelength in free space
$\lambda_k(H_{11})$	Critical wavelength in free space for the $H_{11}$ wave mode
$D$	Caliber of the gun tube (without rifeling)

At wavelengths smaller than  $1.31 D$  other wave modes may occur, so that the unique identification would no longer be guaranteed. Therefore, for a 40 mm gun tube a wavelength between  $5.24 \text{ cm} > \lambda > 6.84 \text{ cm}$  and a frequency in the range from  $4.38 \text{ GHz} < f < 5.72 \text{ GHz}$  has to be chosen, respectively.

For the construction of the RF couplers described a frequency of  $f = 5.000 \text{ GHz}$  was taken. At this frequency normally coaxial components were used.

### Construction of the RF Couplers

Since there could not be found a suitable configuration for a direct transition from a coaxial line (RF output of the interferometer) to a circular wave guide (gun tube) that excites the  $H_{11}$  wave mode with sufficient efficiency, the transition was realized in two steps using a rectangular wave guide as a transition piece. Thus, the RF energy is firstly coupled from the coaxial line into the rectangular wave guide and from there into the gun tube. References for the design of the transitions and the rectangular wave guide are given in [3].

Taking into account all requirements mentioned above, at first an RF coupler for a 42 mm smooth gun tube was realized according to Figure 1. This RF coupler is attached to the muzzle of the gun barrel by means of a thread.

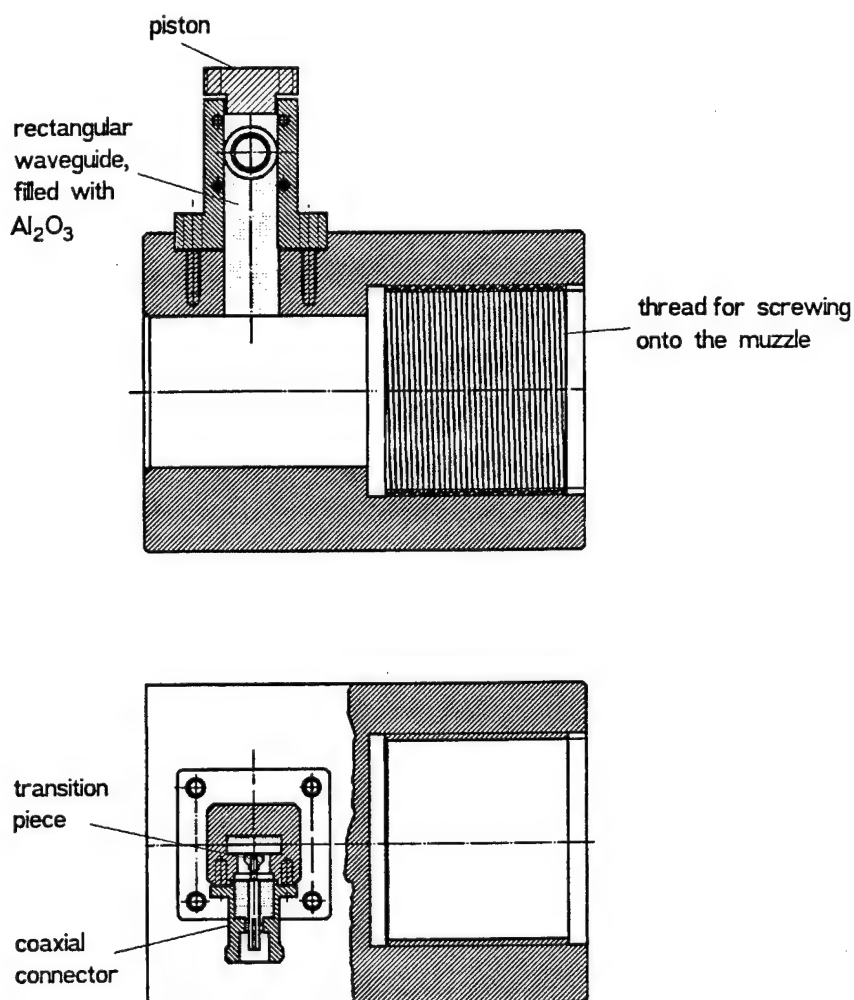


Figure 1 RF coupler for microwave interferometry with mounting thread

The two-piece rectangular wave guide is filled completely with a rectangular bar consisting of  $\text{Al}_2\text{O}_3$  ceramics (relative dielectric constant  $\epsilon_r \approx 9$ ). The  $\text{Al}_2\text{O}_3$  bar fulfills two purposes.

1. The dimensions of the rectangular wave guide will be reduced by the factor  $\sqrt{\epsilon_r}$ , that means in our case about 3.
2. The ceramics used in this case is extremely resistant against pressure and temperature. It is outstandingly suitable to withstand the muzzle pressure, and there is no erosion caused by the hot powder gases.

The base of the ceramic rod is supported by a steel piston. Between the ceramics and the piston small epoxy laminas with varying thickness may be introduced in order to optimize the RF matching. The matching of the coaxial line to the ceramic-filled rectangular wave guide has been carried out experimentally by placing transition pieces in various shapes between the surface of the ceramics and the inner conductor of the coaxial line. The criterion for the matching was an optimal interferometer signal created by a piston which has been manually moved inside the tube by means of a rod.

Except the ceramic rod and the coaxial chassis connector all parts of the RF couplers were produced in steel. The coaxial chassis connector is a commercially available part.

Figure 2 shows the RF coupler described screwed to the muzzle of a 42 mm smooth gun tube.



Figure 2 RF coupler thread mounted at the muzzle of a powder gun

Figure 3 depicts the construction of an RF coupler functioning in the same way as the RF coupler described above. However, in this case instead of a thread a flange is used for the mounting of the RF coupler.

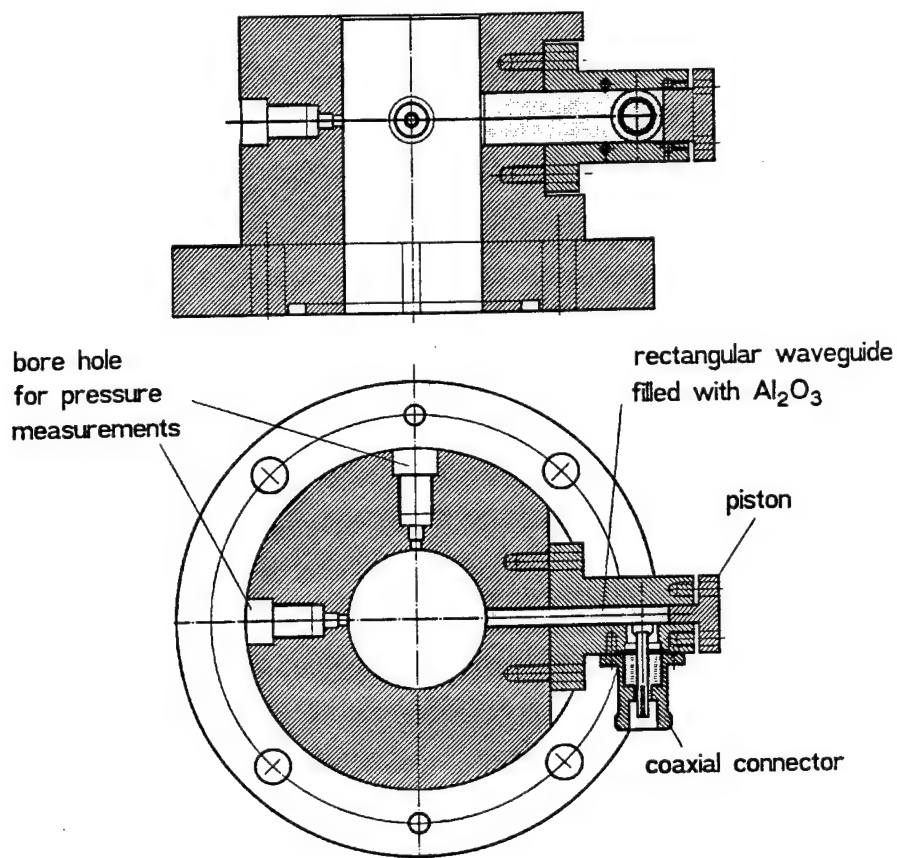


Figure 3 RF coupler for microwave interferometry with mounting flange

Figure 4 shows the RF coupler according to Figure 3, which is mounted to the muzzle of a 40 mm light gas gun.

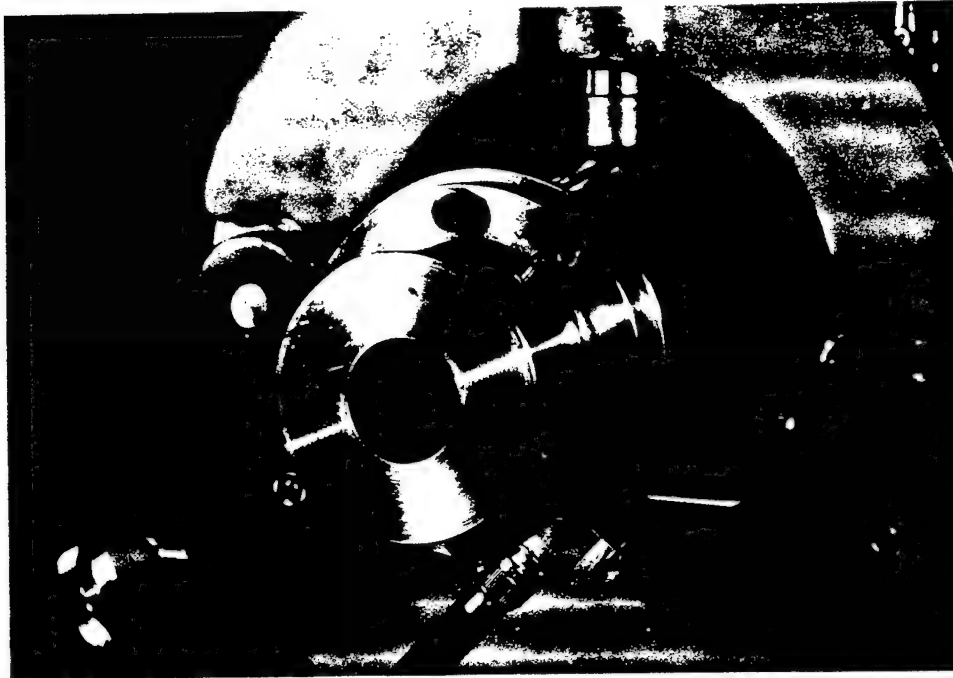


Figure 4 RF coupler flange mounted at the muzzle of a light gas gun

## MICROWAVE INTERFEROMETER

In order to carry out microwave interferometer measurements in the past at EMI the interferometer was assembled on demand using microwave components available in the laboratory. This work was time consuming, sometimes required the removal of the components from other microwave measurement setups, and it could not be carried out by any technician.

To meet the increased demand of measurements, it was necessary to construct a microwave interferometer as a complete instrument where the operator has only to connect the instrument to the RF coupler. At demand, an operational check can be carried out by moving a piston in the gun tube.

### Functional Description of a Microwave Interferometer (Type Michelson)

The principal setup of a microwave interferometer for the acquisition of the projectile motion is shown in Figure 5.

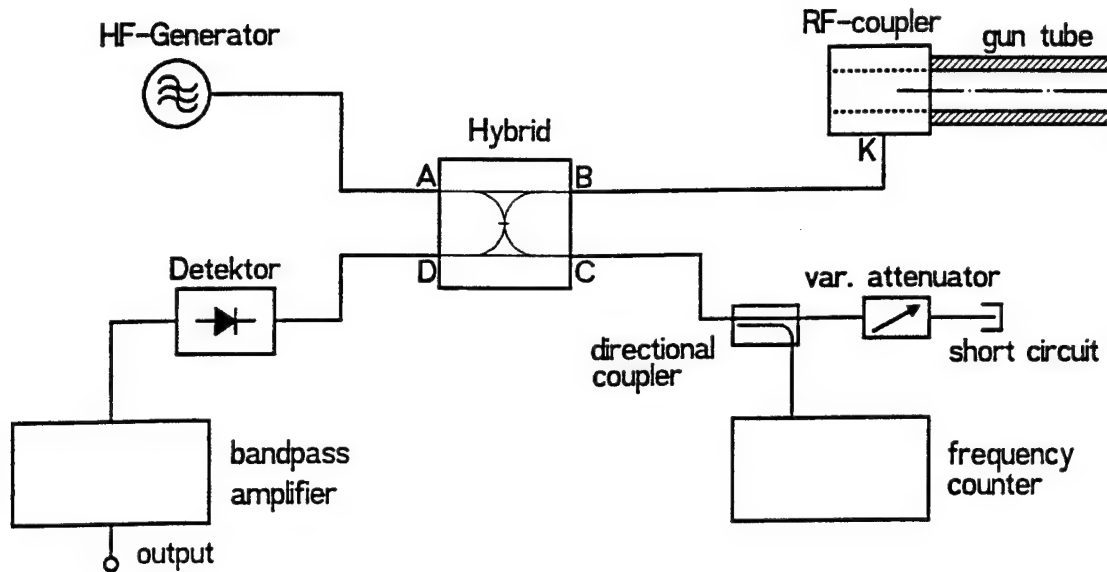


Figure 5 Basic diagram of a microwave interferometer

An electromagnetic wave with constant frequency, generated in a microwave generator, is coupled at port A into a "hybrid" (4-port) where it is split into two equal parts of power. One of the partial waves ( $TW_1$ ) reaches a short circuit via port C. There it is reflected and again split off for a second time in the hybrid into two partial waves ( $TW_{11}$  and  $TW_{12}$ ). The second partial wave ( $TW_2$ ) reaches the gun tube by passing port B and the RF coupler K. It is reflected at the projectile and scattered back to the hybrid where it is also split for a second time into the partial waves  $TW_{21}$  and  $TW_{22}$  with equal parts of power.

Each part of the waves reflected at the projectile ( $TW_{11}$ ) and at the short circuit ( $TW_{21}$ ) arrives at a detector via port D of the hybrid. Therefore, at the detector we have the superposition of two partial waves. By changing the phase of one of the partial waves, for example caused by the movement of the projectile, at a detector with square-law rectification a signal will be produced as follows

$$|E|^2 = \hat{E}_1^2 + \hat{E}_2^2 + 2\hat{E}_1\hat{E}_2 \cos(2\beta x - \Theta) \quad (3)$$

where

- $\hat{E}_1 \hat{E}_2$  Peak values of the electric field strength
- $\beta$  Wave number ( $\beta = 2\pi/\lambda$ ,  $\lambda$  wavelength)
- $x$  Displacement of the projectile
- $\Theta$  Initial phase

The accelerated movement of the projectile will therefore produce as a detector signal a sine-shaped oscillation with increasing frequency superimposed by a constant signal.

In order to evaluate the detector signal the distances in time of subsequently following minima or maxima are registered. The distances in time of two following minima or maxima correspond to a displacement of exactly half the wavelength existing in the gun tube. As a result one gets a curve where the location of the projectile is given as a function of time with measuring points spaced by half the wavelength in the wave guide.

The relationship between the free space wavelength and the wavelength in a wave guide is given by the following equation

$$\lambda_{HL} = \frac{\lambda}{\sqrt{1 - (\lambda / \lambda_k)^2}} \quad (4)$$

where

- $\lambda$  Wavelength in free space
- $\lambda_{HL}$  Wavelength in a wave guide
- $\lambda_k$  Critical wavelength (depending on the diameter of the tube and on the wave mode)

#### Design of the Microwave Interferometer

A block diagram of the device produced at EMI is given in Figure 6. Separate power supplies for the RF generator and the LF amplifier may contribute to reduce noise pickup. With the application of RF components in strip-line technique and SMA connectors the dimensions of the device could have been kept small. In order to reduce RF radiation and to get higher mechanical stability the RF components have been connected to each other by semi-rigid cables. Frequency and power of the RF generator may be checked at a special output.

The circuit diagram of the low-pass amplifier is given in detail in Figure 7. Figure 8 shows the complete device with the cover removed from the housing box.

Specifications:

Frequency	5.000 GHz
RF power interferometer output	13 dBm
Rf power check output	- 10 dBm
Output connector	Type N
LF amplification	10, 20, 50, 100
Coupling input LF amplifier	AC or DC
Bandwidth of LF amplifier	100 kHz
Dimensions	23.5 cm x 10 cm x 34 cm
Weight	3.0 kg

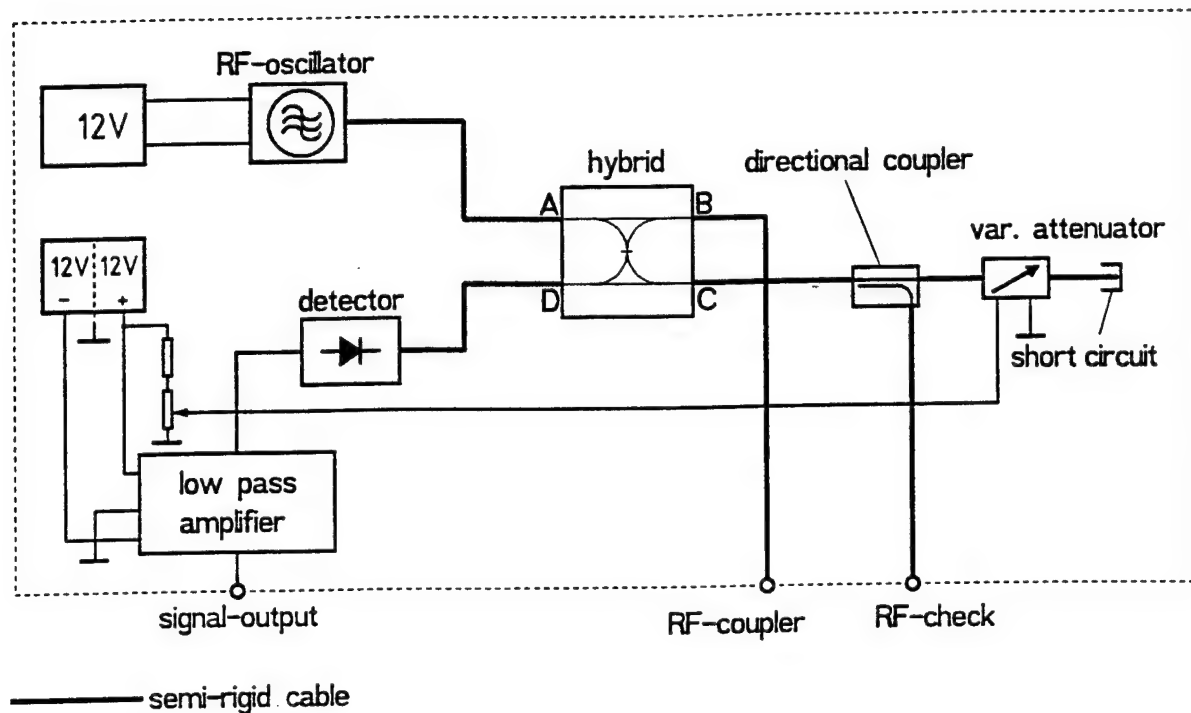


Figure 6 Circuit diagram of the 5 GHz microwave interferometer

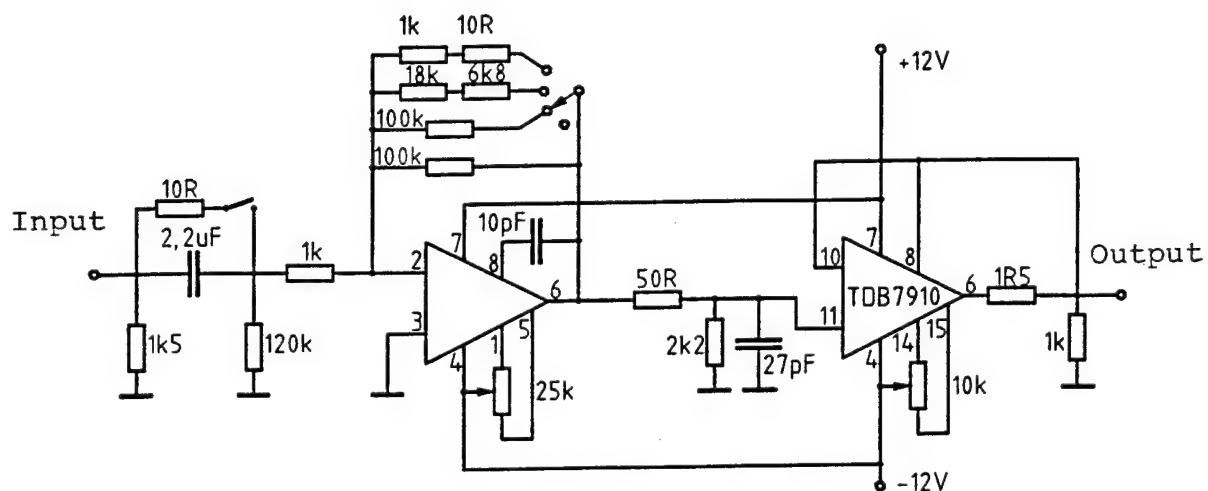


Figure 7 Circuit diagram of the LF amplifier for the microwave interferometer

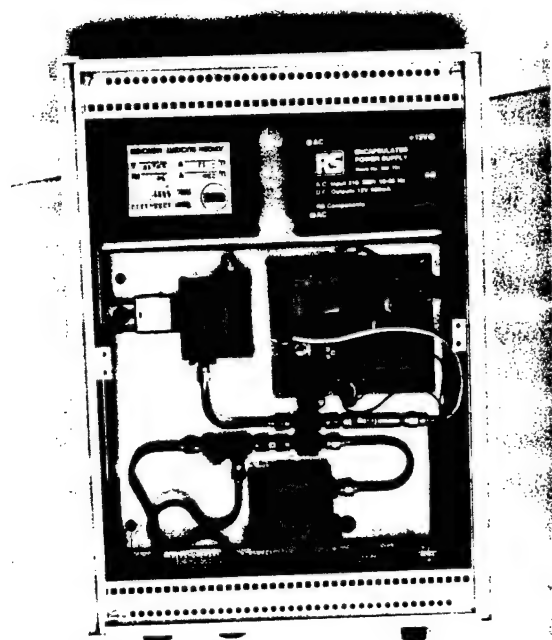


Figure 8 Microwave interferometer with removed cover

Figure 9 shows the microwave interferometer and both RF couplers described.

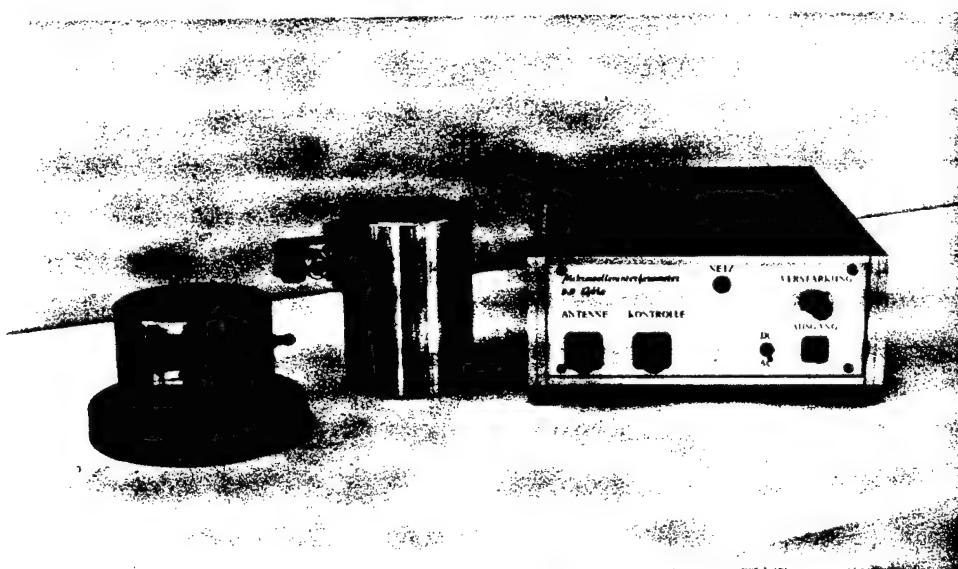


Figure 9 Microwave interferometer and RF couplers

## EXAMPLES

### Shot with a 42 mm Smooth Bore Gun

The projectile used was provided with a sabot. The muzzle velocity was about 1500 m/s. At an interferometer frequency of 5.0 GHz and a gun tube diameter of 42.45 mm the wavelength in the gun tube was calculated to be  $\lambda_{HL}(H_{11}) = 10.657$  cm.

Figure 10 shows the interferometer signal measured by the equipment described. In Figure 11 the equivalent displacement time history is depicted. This curve was gained by acquiring the maxima by means of a cursor. The position of the projectile at the start of the movement was about 50 cm related to the end of the charge chamber. The overall gun tube length was 2.8 m.

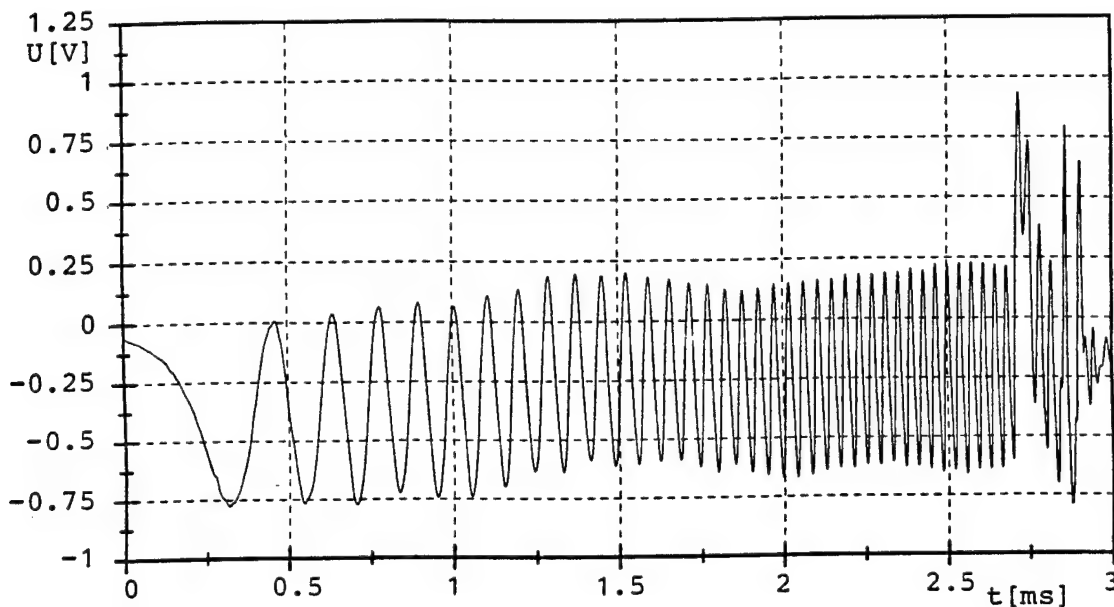


Figure 10 Interferometer signal from a shot with a 42 mm smooth bore powder gun

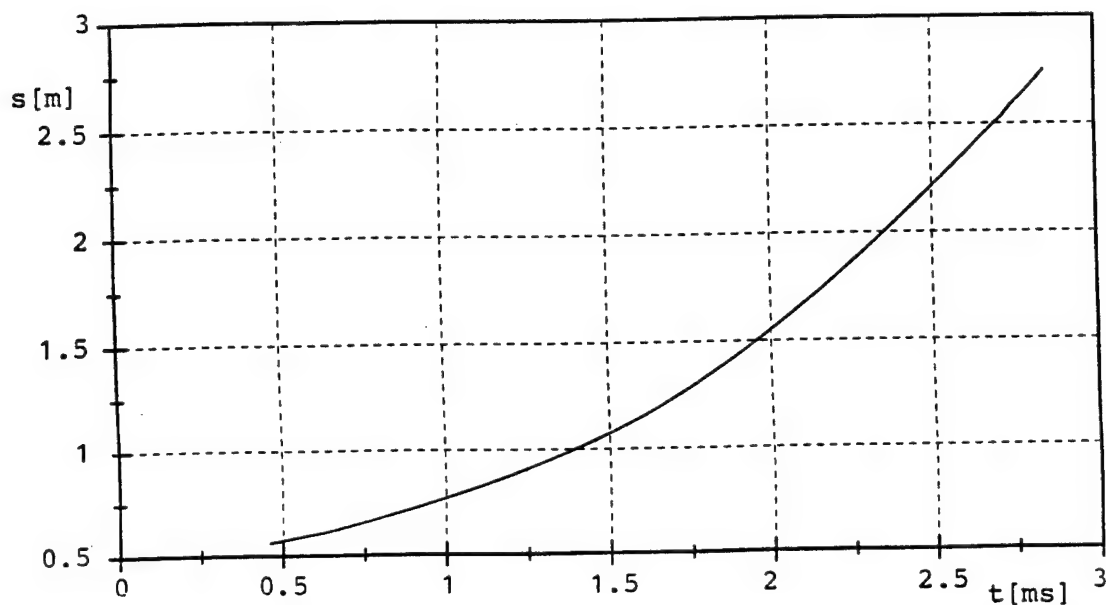


Figure 11 Displacement time curve deduced from the interferometer signal according to Figure 10

#### Shot with a 40 mm Light Gas Gun

The projectile used was equipped with a sabot. The muzzle velocity was about 1750 m/s. At an interferometer frequency of 5.0 GHz and a gun tube diameter of 40.90 mm the wavelength in the gun tube was calculated to be  $\lambda_{\text{HL}}(\text{H}_{11}) = 11.677$  cm. Figure 12 shows the interferometer signal and Figure 13 the equivalent displacement time history. This curve was gained by acquiring the maxima by means of a cursor. The position of the projectile in rest was about 20 cm. The length of the gun tube was 600 cm.

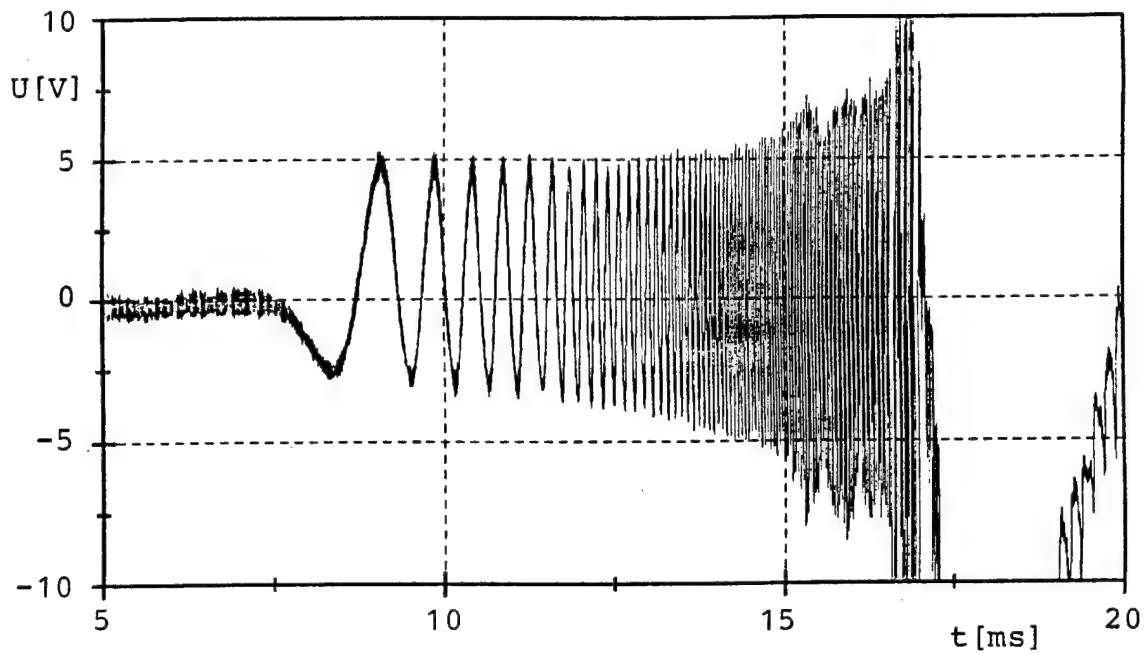


Figure 12 Interferometer signal from a shot with a 40 mm light gas gun

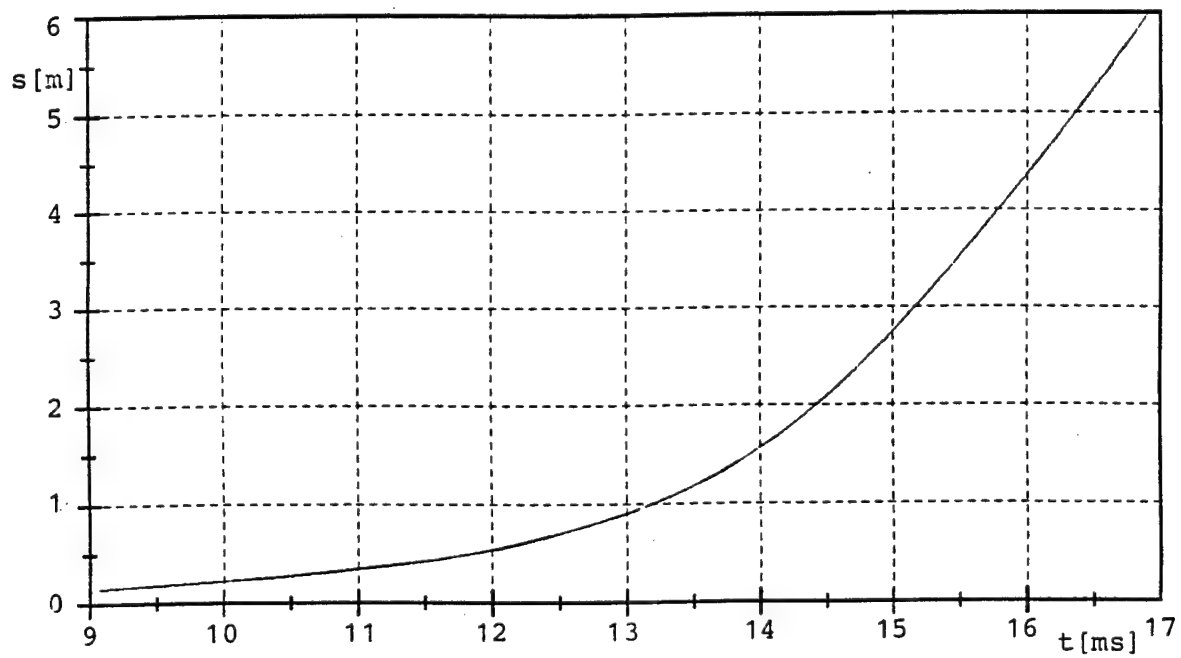


Figure 13 Displacement time curve deduced from the interferometer signal according to Figure 12

## FINAL REMARKS

When performing systematical investigations with firing arms or their ammunition in most cases the movement of the projectile is of great interest. It can be measured with good reliability by means of a microwave interferometer.

By using the RF couplers described the application of the interferometer is essentially simplified and, in addition, the reliability of the measurement is increased. The RF couplers are robust. Therefore, it is possible to make a lot of firings with the same element.

Together with the microwave interferometer one has a measuring system which is simply to handle and which can be operated by each qualified technician.

The system described, working at a frequency of 5 GHz for gun tube diameters of about 40 mm can be transformed without any problems to other frequency ranges and gun tube diameters.

## LITERATURE

- [1] L. Nappert  
Circular Waveguide Couplers for the DREV Two-Stage Light-Gas Gun  
DREV Report 4698/93, Defence Research Establishment, Valcartier, Québec, Canada
- [2] Kimmich, Groebisch, Preschern  
Ballistic Measuring Technology  
Proc. 4th International AVL Symposium on Ballistic Measurement, Werkzeugmaschinenfabrik Oerlikon-Bührle AG, Zürich, Schweiz, September 1989
- [3] Meinke, Gundlach  
Taschenbuch der Hochfrequenztechnik  
Springer-Verlag, Berlin/Heidelberg/New York, 1968

ERLINE, FISCHER

\* TITLE: First Order Dynamic Tools for Rapid Assessment of Small Changes to Major Gun and Projectile Dynamic Parameters.

AUTHORS:

Thomas F. Erline - U.S. Army Research Laboratory,  
Aberdeen, MD 21005-5066

Leo L. Fischer - United Defense,  
LP Armament Systems Division,  
Minneapolis, MN 55421-1498

\* ABSTRACT

The high cost of prototype fabrication and testing of today's complex weapon systems has placed an increasing emphasis on simulation and modeling to evaluate system design alternatives and effectiveness prior to actual hardware manufacture. In the area of large caliber gun systems, some of the most expensive tests are those required to determine the ballistic dispersion of the gun and/or its ammunition. Although there are several very sophisticated computer models available today that will accurately predict the dynamic response of large caliber gun systems during firing, these models typically require time consuming precise three dimensional models of the gun system configuration and therefore are not conducive to conducting the "quick check" type evaluations often required to assess the impact of potential design alternatives and/or proposed design modifications in a timely manner.

In a joint government-industry collaboration the U.S. Army Research Laboratory (ARL) and the Armament Systems Division of United Defense, LP have conducted a series of analyses that utilizing the "Little RASCAL" gun dynamics simulation program in conjunction with a couple of standard interior and exterior ballistics programs (i.e., "IBHGV2" and "PC-PRODAS") can provide a "quick turnaround" analysis capability to evaluate the ballistic dispersion of indirect fire gun systems.

The U.S. Navy's 5-Inch 54-Caliber Gun Mount Mark 45 and the Mk 64 projectile were selected for this study because of the Navy's recent interest in understanding the total error budget of this gun system. The results obtained from this relatively simple analysis technique have shown very good correlation with ballistic dispersion measurements made during actual firing tests. In addition, numerous parameters have been varied to provide insights into design variation trends.

**ERLINE, FISCHER**

**\*BIOGRAPHY:**

Thomas F. Erline

**\*PRESENT ASSIGNMENT:**

Mathematician, Mechanics and Structures Branch, Propulsion and Flight Division, Weapons Systems Directorate of the U.S. Army Research Laboratory.

**\*PAST EXPERIENCE:**

Mathematician, Vulnerability/Lethality Division, Ballistics Research Laboratory, 1973-1982. Research Scientist, Chemical Research and Development Command and Product Assurance Directorate, 1982-1985.

Mathematician, Mechanics and Structures Branch, Interior Ballistics Division, Ballistics Research Laboratory, 1985-1992.

**\*BIOGRAPHY:**

Leo L. Fischer

**\*PRESENT ASSIGNMENT:**

Principal Staff Engineer, United Defense, LP, Armament Systems Division.

**\*PAST EXPERIENCE:**

Junior Engineer, Mounts and Turrets Branch, U.S. Naval Ordnance Station, 1968-1969.

Engineer, Mounts and Turrets Branch, U.S. Naval Ordnance Station, 1969-1970.

Projects Engineer, Gun Systems Division, U.S. Naval Ordnance Station, 1970-1979.

Senior Engineer, Design Assurance Dept., FMC Corp. Naval Systems Division, 1979-1983.

Supervisor, Maintenance Engineering, FMC Corp. Naval Systems Division, 1983-1985.

Manager, Advanced Systems Engineering, FMC Corp. Naval Systems Division, 1985-1988.

ERLINE, FISCHER

## First Order Dynamic Tools for Rapid Assessment of Small Changes to Major Gun and Projectile Dynamic Parameters.

Thomas F. Erline U.S. Army Research Laboratory, Aberdeen, MD  
Leo L. Fischer United Defense, LP Armament Systems Division, Minneapolis, MN

### INTRODUCTION

The high cost of prototype fabrication and testing of today's complex weapon systems has placed an increasing emphasis on simulation and modeling to evaluate system design alternatives and effectiveness prior to actual hardware manufacture. In the area of large caliber gun systems, some of the most expensive tests are those required to determine the ballistic dispersion of the gun and/or its ammunition. Although there are several very sophisticated computer models available today which will accurately predict the dynamic response of large caliber gun systems during firing, these models typically require precise three dimensional models of the gun system configuration and its mass properties. Therefore, these models are not well suited to conducting the "sanity check" type evaluations often required to assess the impact of potential design alternatives and/or proposed design modifications in a timely manner.

In a joint government/industry collaboration the U.S. Army Research Laboratory (ARL) and the Armament Systems Division of United Defense, LP have investigated the feasibility of utilizing the "Little RASCAL" (LR) [ref. a] gun dynamics simulation program in conjunction with "standard" interior and exterior ballistics programs to provide a "desktop" analysis capability to evaluate the ballistic dispersion of intermediate caliber gun systems. The gun system chosen for analysis in this study was the U. S. Navy's 5-Inch 54-Caliber Gun Mount Mark 45. The Mark 45 is the main gun armament of the majority of current U. S. surface combatants and is slated to be upgraded in capability as part of the Naval Surface Fire Support (NSFS) program. Therefore, considerable interest exists in obtaining a more detail understanding of the system error budget.

The analysis procedure described in this paper has been shown to yield reasonable estimates of the ballistic dispersion of an intermediate caliber indirect fire weapon and offers a relatively simple method for obtaining "first order" estimates of the impact of proposed design changes to either the weapon or its ammunition and can provide a useful tool for gun system designers to assess the potential impact of small changes to major parameters affecting gun and projectile dynamics.

### BACKGROUND

This study was based on two ARL developed computer models; the IBHVG2 [ref. b] interior ballistics program, the LR gun dynamics program and the commercially available projectile design and analysis program PRODAS™.

IBHVG2, which stands for "Interior Ballistics of High Velocity Guns, version 2," is a lumped-parameter, interior ballistic computer code. The code, which was developed at ARL, is an updated version of the classic Baer-Frankie interior ballistic code. IBHVG2 is used to calculate interior ballistic trajectories, including gas pressure, projectile displacement and projectile velocity as a function of time. IBHVG2 was used to compute the interior ballistic cycle of the standard 5-Inch Propelling Charge Mk 67. The Mk 67 charge is designed to produce a nominal new gun velocity of 2,650 ft/sec with a 70 lb. projectile. The projectile velocity and breech pressure versus time data computed by IBHVG2 were used as input to the LR gun dynamics program.

The Little RASCAL is a comprehensive modeling code for lateral gun dynamics and projectile dynamics. When fired, the bore riding projectile undergoes a complex sequence of mechanical and gas dynamic interactions on its way out the barrel. The Little RASCAL gun and projectile dynamics program is capable of simulating the inertial loading conditions brought about by the projectile interacting with the barrel in a plane as it accelerates the length of a gun tubes unique centerline. Thus, in tracking the projectile interacting with the barrel the initial launch conditions of the projectile at shot exit can be predicted. Projectile pitch and pitch rates as well as muzzle motion are calculated and available for the exterior ballistics programs.

The Little RASCAL gun and projectile dynamics program is a dynamic displacements code employing a direct structural dynamics analysis approach to the simulation of firing a projectile from a gun. Both the gun system and the projectile are modeled using a series of equally spaced cylindrical elements. Nodes are centered and assigned equivalent mass and stiffness values based on standard engineering formulae. Inertial forces and flexural forces are calculated using this simplified description. Flexure at each node is approximated by a second order finite difference method, which allows the bending forces to be computed. Transverse nodal accelerations caused by these forces are integrated with respect to time to obtain transverse nodal velocities, and integrated again to obtain lateral node displacements. Loads induced by pressure effects, mounting conditions, breech center of gravity offset, and the projectile interaction forces with the barrel are accounted for in the LR program. All forces are then integrated by a predictor-corrector technique stabilized by a numerically stiff ordinary differential equation solver [ref. c].

The gun system (which includes the breech, barrel and two gun supports) and the projectile system are two separate models. They are accounted for individually except for a variational algorithm that handles their interaction. The interaction of the projectile with the barrel occurs through contact points. The two contact points defined on the projectile are usually positioned where they occur geometrically. The two projectile contact point positions on the barrel are dynamic and change as the projectile traverses the bore. The gun system model and the projectile model are two separate flexible entities, with each projectile contact point requiring a user defined spring constant. The spring constants serve to define the interface loads between the projectile model and the gun model.

## ERLINE, FISCHER

The LR program has proven that simple modeling techniques in which the primary components of a gun system are included can produce reasonably accurate results in a timely manner. The code is generic enough so that almost any gun system and projectile can be modeled in a simple manner. Gun dynamics predictions made by LR of barrel motion have been shown to agree quite well with experimental results over a wide range of gun system size and type. [ref. d]

The PRODAS<sup>TM</sup> program is a multi-faceted projectile analysis package. The principal features of the program used for this study were the muzzle exit analysis feature and the six degree-of-freedom (6DOF) trajectory model. The Muzzle Exit segment of PRODAS was used to compute the initial muzzle exit tip-off angle and tip-off rate resulting from the clearance between the projectile and the bore of the gun. The 6DOF trajectory model was used to determine the effect on achieved range of various initial pitch and yaw angles and angular rates.

The projectile geometry and mass properties used throughout the study were based on the standard 5-inch Mk 64 projectile body (see Figure 1) with high explosive load and Mk 73 CVT proximity fuze. The mass properties of the projectile are summarized in Table 1.

**Table 1 Projectile Mass Properties**

Weight (lbs.)	68.49
CG from Nose (in)	16.56
Axial Moment of Inertia (lbm-in <sup>2</sup> )	240.83
Transverse Moment of Inertia (lbm-in <sup>2</sup> )	2803.50

As with any gun dynamics model, the accuracy of the results obtained from the LR model are dependent upon detailed, precise knowledge of the weapon being analyzed. Since the Mk 45 Gun Mount has been in production for over 20 years, a considerable volume of detailed information concerning the geometry, mass properties, and stiffness of various system components was available to facilitate the modeling process. This was also true for the ammunition components. The single area where detailed information did not exist was the gun barrel. Although dimensional and mass property data existed for the 5-inch Gun Barrel Mk 19, there was little, if any, information on the centerline variations existent in previously manufactured gun barrels. To overcome this lack of information, centerline measurements of two Mk 19 Mod 2 gun barrels, serial numbers; 518 and 17343, were made by ARL personnel using laser measuring equipment expressly designed for this purpose. A third gun barrel, serial number 17423, was also measured; however, data from this barrel became available too late to be included in this study.

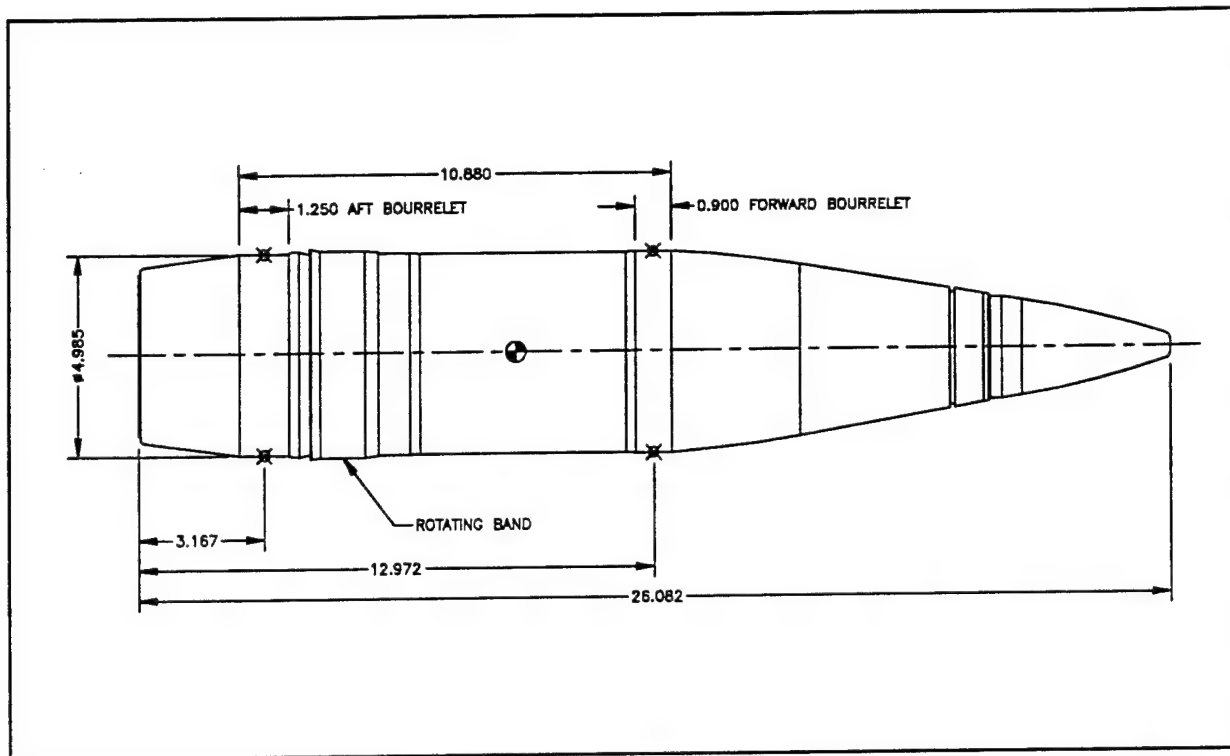


**Figure 1 5-Inch Projectile Mk 64**

The original objective of this study was to determine the ability of the LR program to accurately predict the dynamic response of the Mk 45 Gun Mount during firing for the purpose of gaining a greater understanding of the total error budget of the system. However, as the analysis proceeded, it became apparent that the analysis methodology being employed could be utilized as a relatively simple means of assessing the potential impact of changes to certain key system design parameters upon the ballistic dispersion of the system.

## APPROACH

The analysis methodology developed during this study involves a four step process: 1) the LR model is used to predict the projectile pitch and yaw angles and angular rates resulting from the dynamic response of the system during firing. 2) The tip-off angle and angular rate resulting from the in-bore yaw of the projectile is computed for both nominal and maximum projectile clearance conditions. These muzzle exit conditions are combined numerically with the LR results to obtain a set of initial projectile launch conditions to be used with the 6DOF trajectory model. 3) The 6DOF trajectory model is used to compute the range to impact for each of the initial conditions defined in step 2. 4) The results of the trajectory calculations are tabulated and the mean and standard deviation of the achieved range computed to give an estimate of the ballistic dispersion which would result from the system configuration being modeled.

The LR modeling process involves describing the projectile, projectile interior ballistics, and the gun system. The projectile is described by its geometry and mass properties, plus a definition of the location and spring constant for each of the two contact points between the projectile and the gun barrel. The interior ballistic information consists of the projectile velocity versus time history for the in-bore cycle. The gun system information required includes the geometry and mass description of the gun barrel and breech along with breech center of gravity offsets, if any, trunnion and elevation support locations and their equivalent spring constants. The final gun system data requirement is the data describing the variations in the centerline of the gun barrel.

A simplified schematic representation of the gun system, as modeled in the LR program is shown in Figure 2. The breech assembly of the Mk 45 has a weight of 2344 pounds and its center of gravity is offset 0.141 inch vertically and 0.0302 inch horizontally. The trunnion supports are located 19 inches forward of the rear face of the breech assembly and were assigned a spring constant of 3,200,000 lbs/in. The effective elevation support of the gun assembly is located 17 inches aft of the trunnion and was assigned a spring constant of 134,000 lbs/in. As previously stated, the centerline variations of two 5-inch Mk 19 Mod 2 Gun Barrels (S/N 518 & S/N 17343) were measured by ARL personnel for use during this study. The vertical and horizontal centerline deviations of the two barrels are shown in Figures 3 and 4.

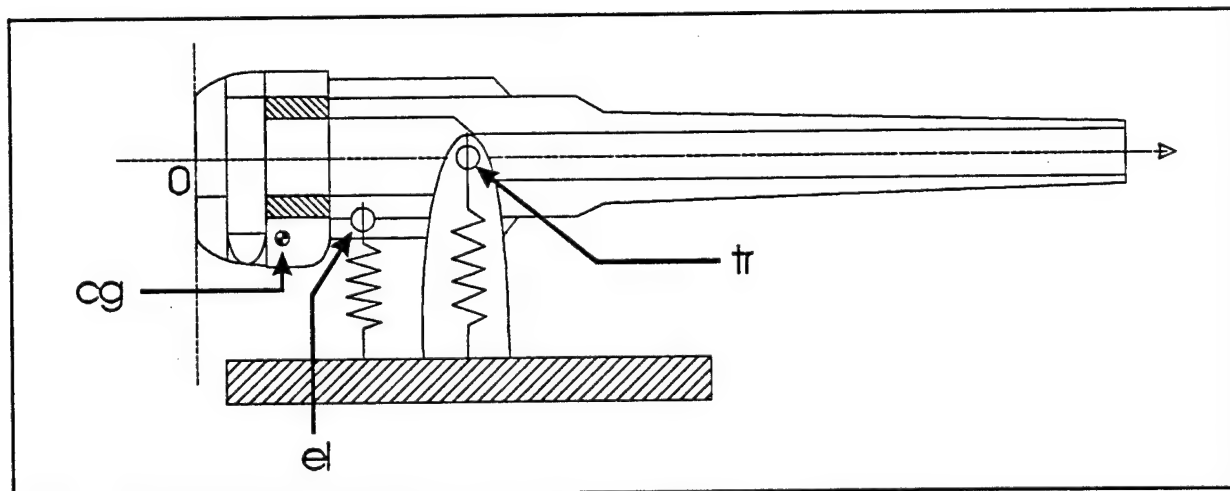


Figure 2 Gun System Model

The muzzle exit conditions computed by the PRODAS program include the magnitude of the tip-off angle and tip-off rate resulting from the bore to bourrelet clearance and spin of the projectile. The dimensional tolerances on the bourrelet of the projectile and the bore of gun barrel were examined to define the extreme clearance conditions likely to occur in fielded systems and the tip-off angle and angular rates for minimum and maximum clearance conditions computed. Since the orientation of these exit conditions, i.e., up, down, left, right, etc., is random in nature, a baseline set of 32 possible combinations of angle and angular rate for each clearance condition were established for use in the analysis. These combinations of pitch and yaw angle and angular

rate were combined numerically with the results from the LR program to produce a matrix of initial launch conditions for the 6DOF trajectory model. Thus a total of 64 possible launch conditions were established for each case to be analyzed.

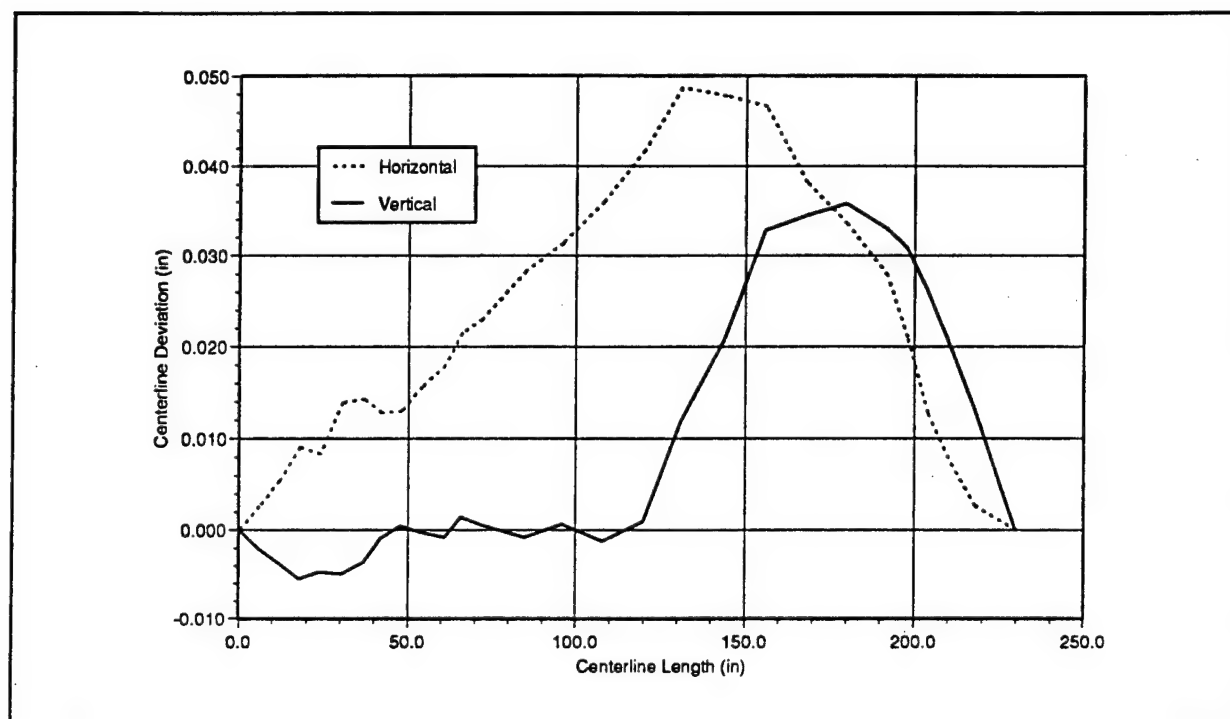


Figure 3 Gun Barrel S/N 518 Centerline Data

Prior to beginning the analysis, the 6DOF trajectory model was "calibrated" by adjusting the projectile input data to obtain range results under standard conditions which corresponded to published information [ref. e] on the range performance of the 5"/54 gun system. Once the trajectory model was calibrated, the launch condition matrices were used to generate input data files for the trajectory model. Computation time for the test case trajectories varies between 2 and 20 minutes depending on the gun elevation being used and the speed of the individual computer.

To facilitate analysis and manipulation of the data, the trajectory results were compiled in a computer spreadsheet. This approach permitted rapid computation of various statistical data such as the mean and standard deviation of the range results and plotting of the data.

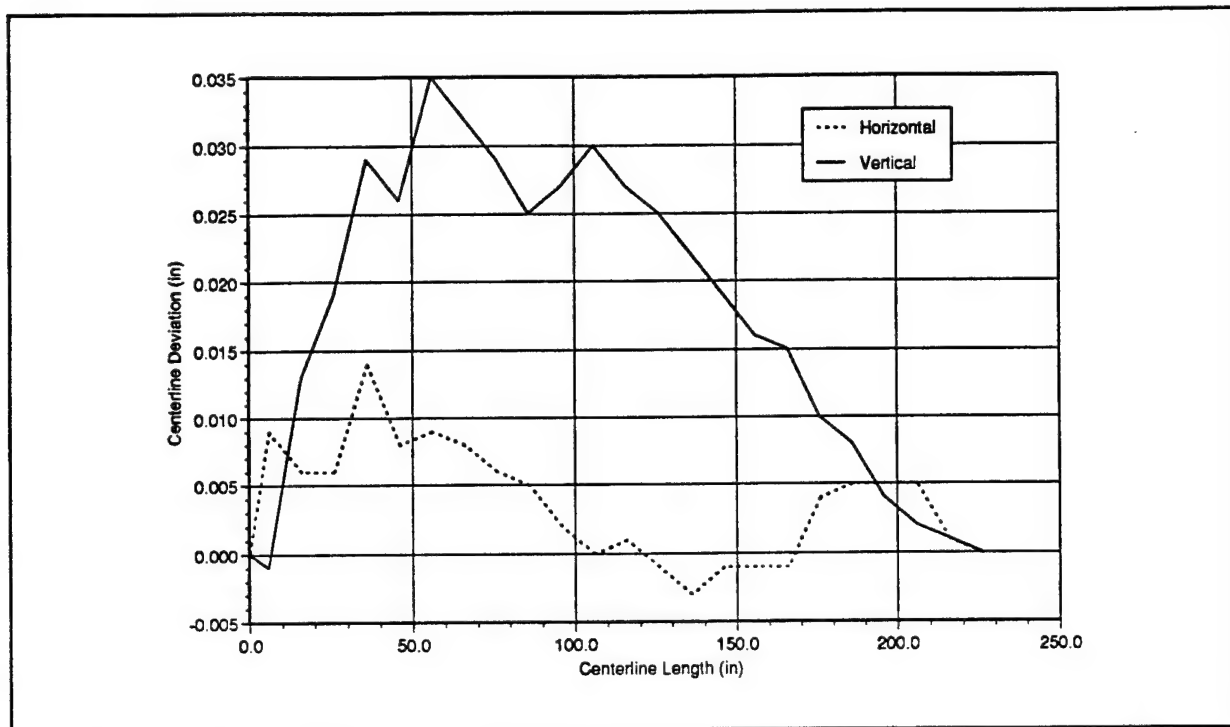


Figure 4 Gun Barrel S/N 17343 Centerline Data

## RESULTS

The initial series of simulations performed using the LR model consisted of determining the dynamic response of each gun barrel at seven different gun elevation angles. The elevation angles chosen corresponded to nominal gun ranges of 1000, 2000, 5000, 7500, 10000, 15000, and 20000 yards.

The results obtained from this initial modeling of the Mk 45's dynamic response at various elevation angles was used to assess the ability of methodology established for this study to provide a reasonable estimate of the of the ballistic dispersion which would result in actual gun firing. Trajectory calculations were made using the results from both barrel centerlines at each elevation angle. The range standard deviation obtained in each case was then compared to the best available estimates [ref. f] of actual gun system performance under proving ground conditions. The results of this assessment are shown in Figure 5.

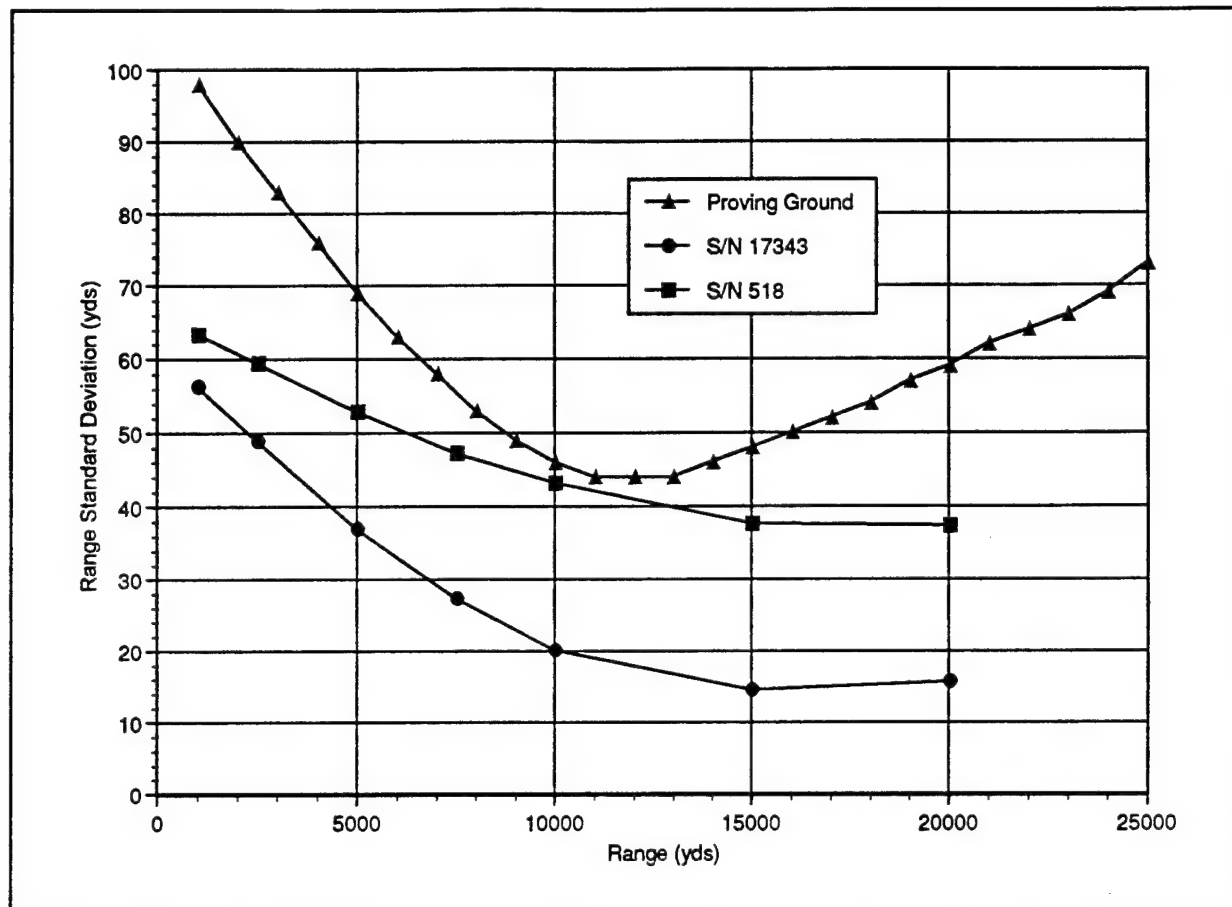


Figure 5 Calculated and Proving Ground Range Dispersion

The proving ground range dispersion values shown in Figure 5 are based on post-test analysis of a large volume of firing data collected by the Naval Surface Warfare Center/Dahlgren Division over the last 20+ years from numerous 5"/54 gun systems under various firing conditions. These values are derived during the post-test data reduction process and may be characterized as the standard deviation of the residual uncertainty which exists between the observed range of each round and the value computed when all known conditions (i.e., met conditions, projectile weight, actual muzzle velocity, etc.) are factored into the standard 5"/54 fire control equations. It has also been noted that observed ballistic dispersion of the 5"/54 gun system has been declining in recent years. This is evident in the results of a recent shipboard ammunition effectiveness test [ref. g] conducted under closely controlled conditions at a gun-target range of approximately 18,000 yds., the observed standard deviation error in range was 48 yds. (12 yds. less than the established proving ground value). While the reasons for this decline in dispersion are beyond the scope of this paper, a major contributing factor could be the improvements in dimensional consistency achieved in projectile bodies manufactured using numerical controlled machining processes.

The distinctive "U" or "bathtub" shape of the proving ground range dispersion curve is characteristic of most naval gun systems. Because naval guns employ a single service charge for both direct and indirect fire targets, variations in the departure angle of the projectile tend to be the dominate cause of range dispersion at short range, while factors which affect the drag and flight characteristics of the projectile (i.e., dimensional variations, surface finish, CG location, inertia, etc.) are the dominate source of error at long range. In addition, transient meteorological effects have a greater impact on the long range trajectories.

A further detail which must be taken into consideration when interpreting the results illustrated in Figure 5, is effect on the projectile initial tip-off angle and angular rate caused by the torsional response of the gun barrel due to the rifling reaction as the projectile is spun up during the ballistic cycle. This response is not modeled in the LR program and could account for the under-prediction of dispersion at the shorter ranges.

In light of the considerations discussed above, and the limited amount of barrel centerline data available, it was concluded that the analysis methodology developed for this study was providing a reasonably accurate "first-order" indication of the effect of the dynamic response of the gun during firing upon range dispersion. In addition, further analysis of the trajectory results revealed that the average achieved range of rounds fired from gun barrel S/N 518 was always less than that achieved by gun barrel S/N 17343 as illustrated in Figure 6.

While it has frequently been observed that some guns are "long shooters" and others "short shooters" and that retubing can change a gun from a "long shooter" to a "short shooter" and vice versa, the cause of this phenomena has never been adequately explained or investigated. Although the limited sample size used in this study precludes any definitive conclusions concerning the cause of this phenomena, the authors feel that further investigation of the effect of gun barrel centerline variations on average achieved range could lead to a more thorough understanding of this phenomena.

Encouraged by these initial results, the authors set out to determine if the analysis technique could be used to characterize the effect on ballistic dispersion of changes to major system design parameters. The system parameters chosen for further analysis were the effective spring constants of the gun trunnions, the elevation support structure, and the forward and aft bourrelets of the projectile body. Since design changes to both the trunnions and elevation drive of the Mk 45 gun mount are currently being considered as part of the NSFS upgrade package, the potential impact of changes in these components on ballistic dispersion was of particular interest. Although the significance of accurate estimates of projectile body spring constants on LR analysis results had been previously investigated [ref. h], the impact of changes or variations in these physical characteristics of the projectile upon the ballistic dispersion of indirect fire weapons had not been explored.

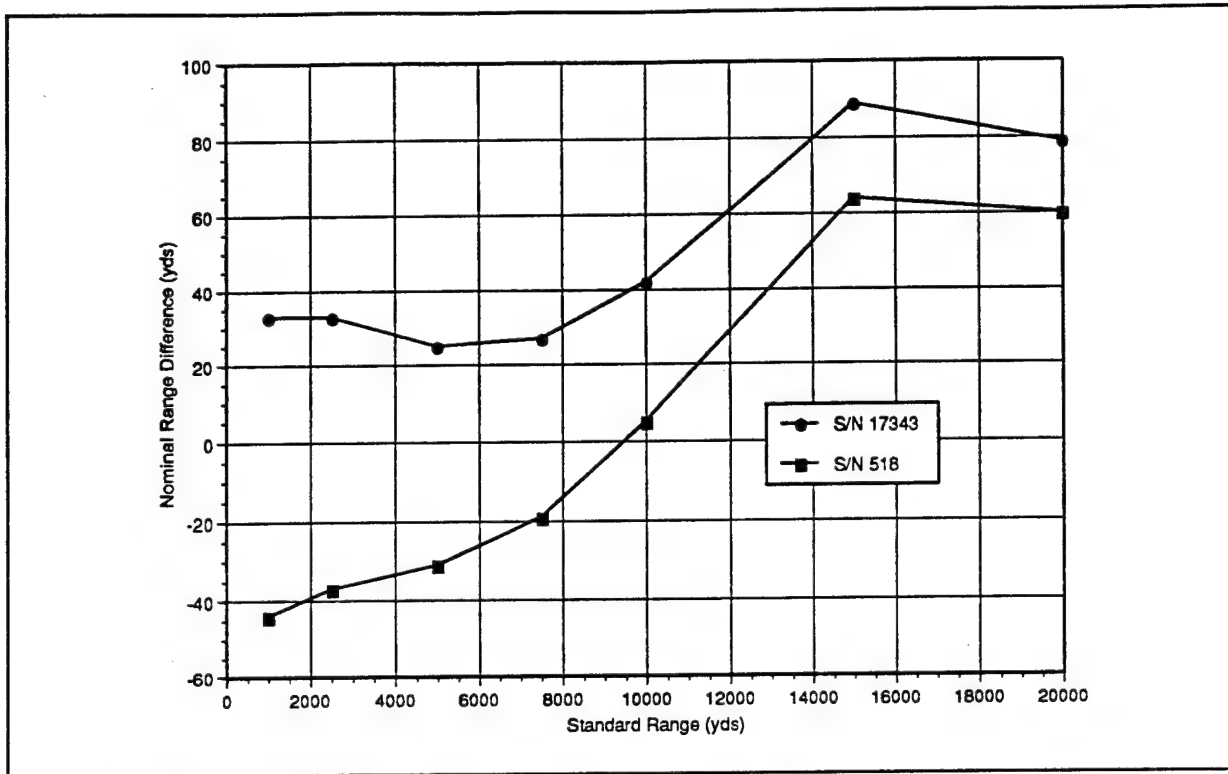


**Figure 6 Achieved Range Differential of Gun Barrels S/N's 518 & 17343**

To assess the utility of the analysis methodology in the characterization of the sensitivity of system ballistic dispersion to variations in the identified system parameters, additional calculations were conducted using the range of values shown in Table 2. Each parameter was varied over the range of values while all the others were held constant at the baseline values previously established for the system. Separate calculations were conducted for each of the two gun barrel centerlines.

**Table 2 System Parameters Varied during Analysis**

	Spring Constant (lb/in)				
	1.92E+6	2.24E+6	2.72E+6	3.20E+6	
Trunnions	1.92E+6	2.24E+6	2.72E+6	3.20E+6	
Elevation Support	109,440	123,120	135,800	150,480	164,160
Fwd Bourrelet	0.5E+6	0.8E+6	1.18E+6	2.0E+6	3.0E+6
Aft Bourrelet	0.5E+6	0.8E+6	1.08E+6	2.0E+6	3.0E+6

## ERLINE, FISCHER

The range of values chosen for the trunnions and the elevation support were based on engineering experience and the results of numerous shock and vibration analyses and tests that have been conducted on the Mk 45 Gun Mount since its introduction to the fleet in the early 1970's. The range of spring constants for the projectile bourrelets was based on test results from two Mk 64 projectile bodies and data collected by ARL on the radial stiffness of 120mm tank projectiles. [ref. i] The results obtained from the LR model for the variations of the gun mount parameters are shown in Table 3 and the results for variations of the projectile parameters are shown in Table 4.

**Table 3 Gun Mount Parameter Variation Results**

Parameter	Barrel S/N	Parameter Value	Pitch Angle (rad)	Yaw Angle (rad)	Pitch Rate (r/s)	Yaw Rate (r/s)
Elevation Support	518	164160	6.9920e-04	6.7707e-04	1.7406	0.4797
		150480	6.9905e-04	6.7707e-04	1.7405	0.4798
		135800	6.9871e-04	6.7707e-04	1.7404	0.4798
		123120	6.9876e-04	6.7707e-04	1.7403	0.4798
		109440	6.9816e-04	6.7707e-04	1.7402	0.4798
	17343	164160	-7.7922e-04	4.9129e-04	-0.8651	1.5032
		150480	-7.7956e-04	4.9129e-04	-0.8656	1.5032
		135800	-7.7990e-04	4.9130e-04	-0.8661	1.5032
		123120	-7.8023e-04	4.9131e-04	-0.8666	1.5032
		109440	-7.8058e-04	4.9131e-04	-0.8671	1.5032
Trunnions	518	3200000	6.9871e-04	6.7707e-04	1.7404	0.4798
		2720000	7.0022e-04	6.7708e-04	1.7412	0.4798
		2240000	7.0154e-04	6.7709e-04	1.7419	0.4798
		1920000	7.0241e-04	6.7709e-04	1.7423	0.4798
	17343	3200000	-7.7990e-04	4.9130e-04	-0.8661	1.5032
		2720000	-7.7990e-04	4.9132e-04	-0.8662	1.5032
		2240000	-7.7992e-04	4.9133e-04	-0.8663	1.5032
		1920000	-7.7991e-04	4.9134e-04	-0.8663	1.5032

The small changes in projectile initial conditions which resulted from rather large changes in the spring constants of the gun trunnions and elevation support would seem to indicate that the ballistic dispersion of the Mk 45 gun system is relatively insensitive to major changes in these parameters.

The changes in the initial projectile pitch and yaw angles and angular rates resulting from the changes in the spring constants of both the forward and aft bourrelets are shown in Table 4.

**Table 4 Projectile Parameter Variation Results**

Parameter	Barrel S/N	Parameter Value	Pitch Angle (rad)	Yaw Angle (rad)	Pitch Rate (r/s)	Yaw Rate (r/s)
Fwd Bourrelet	518	3000000	1.7604e-04	3.6752e-03	-4.4191	1.5883
		2000000	1.2332e-03	3.7083e-03	-1.4797	6.1585
		1185000	6.9871e-04	6.7707e-04	1.7404	0.4798
		800000	-4.0800e-04	1.3737e-03	-0.3266	-1.6183
		500000	-2.8924e-04	1.9709e-03	-3.3228	-0.5196
	17343	3000000	1.7451e-03	2.7548e-04	-0.5799	3.4469
		2000000	1.5485e-03	2.0303e-03	3.9567	0.1358
		1185000	-7.7990e-04	4.9130e-04	-0.8661	1.5032
		800000	5.5708e-04	1.3142e-03	-0.0378	-1.8546
		500000	1.3455e-04	1.8419e-04	1.5311	0.2972
Aft Bourrelet	518	3000000	1.0206e-04	7.6987e-04	1.0323	4.1891
		2000000	8.3561e-04	5.9081e-04	2.1809	1.0394
		1085000	6.9871e-04	6.7707e-04	1.7404	0.4798
		800000	4.7562e-04	9.9157e-04	1.8221	-0.7687
		500000	8.1551e-05	1.5270e-04	1.5868	-0.1344
	17343	3000000	-6.9767e-04	9.4122e-04	0.6385	2.2155
		2000000	-7.2585e-04	8.1648e-04	-0.3713	3.4534
		1085000	-7.7990e-04	4.9130e-04	-0.8661	0.4798
		800000	-6.4252e-04	5.0799e-04	-1.2817	0.2990
		500000	3.4813e-04	2.1200e-03	0.8365	1.6513

The dynamic shape of the two gun barrels during firing is shown in Figures 7 and 8. Each figure illustrates the shape of the barrel when the projectile has traveled 3/4 of the distance to the muzzle, 7/8 of the distance to the muzzle, and at muzzle exit. The reference for gun barrel motion in these figures is: at time zero all nodal displacements are zero. The dynamic response of the two gun barrels as evident in their dynamic shapes in the vertical plane, as shown in Figures 7 and 8, is unique to their individual centerline variations. These unique reaction characteristics are also evident in the transverse velocity of the gun muzzle during the in-bore cycle. As can be seen in Figures 9 thru 12, the frequency and amplitude of the transverse velocity response shifts with changes in the spring constant of the forward bourrelet of the projectile. This frequency shift is due to a change in the projectile's rigid body rocking modes. Since there are two rocking modes, [ref. j] changing the spring constants of projectile bourrelets changes the the response of the gun barrel. Without presenting all of the results generated during this study, it was noted that the changes in the spring constant of the forward bourrelet produced much larger changes in the dynamic response of the system than changes to the spring constant of the aft bourrelet. The dominate influence of the forward bourrelet results from

ERLINE, FISCHER

several factors. The most obvious being that the forward bourrelet is the first point on the projectile body to encounter the variations in the barrel and that the center of gravity of the projectile is closer to the forward bourrelet.

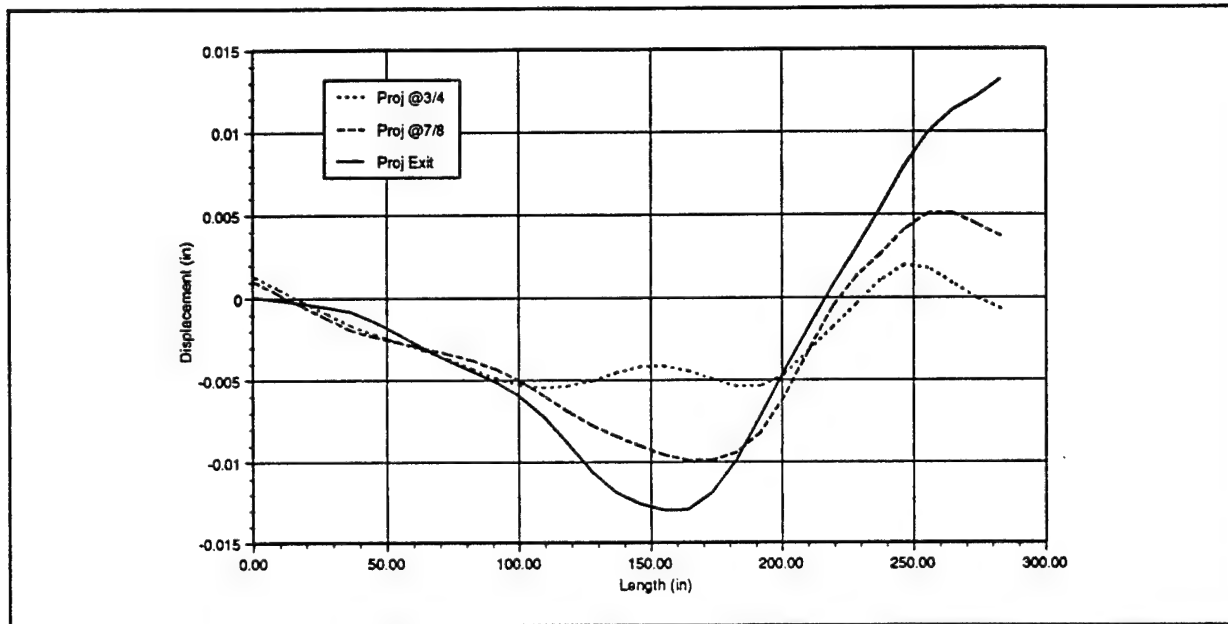


Figure 7 Dynamic Shape of Barrel S/N 518 During Firing

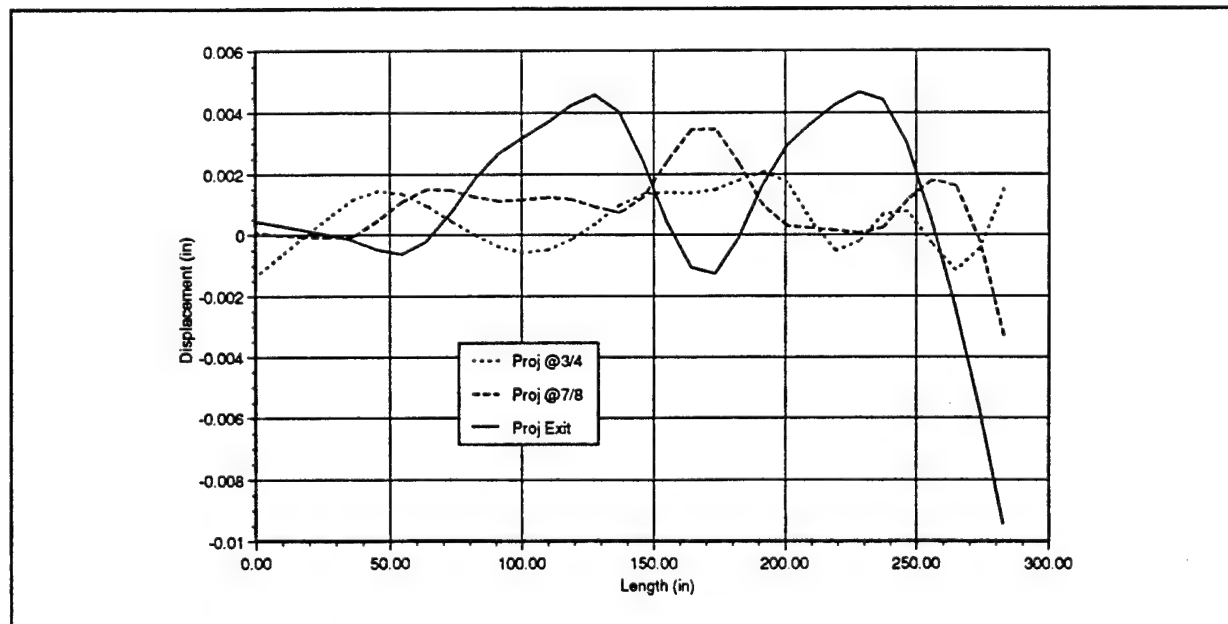


Figure 8 Dynamic Shape of Barrel S/N 17343 During Firing

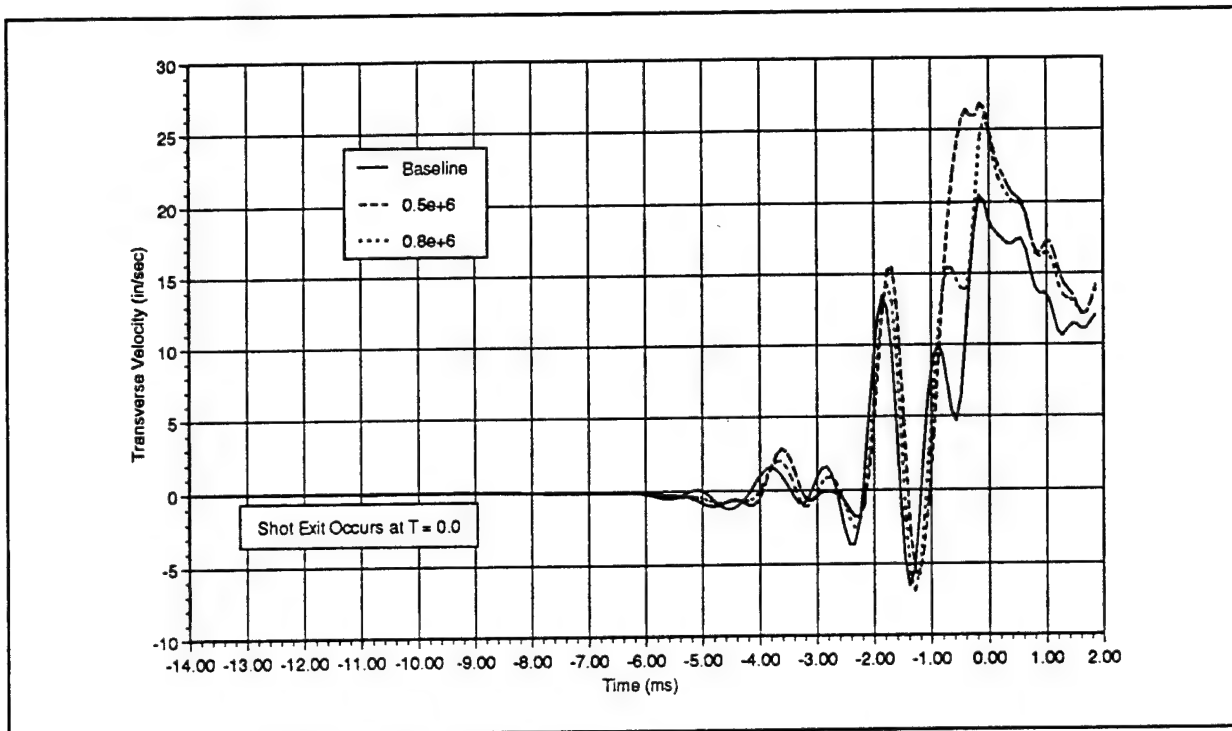


Figure 9 Transverse Velocity of Gun Muzzle (S/N 518)

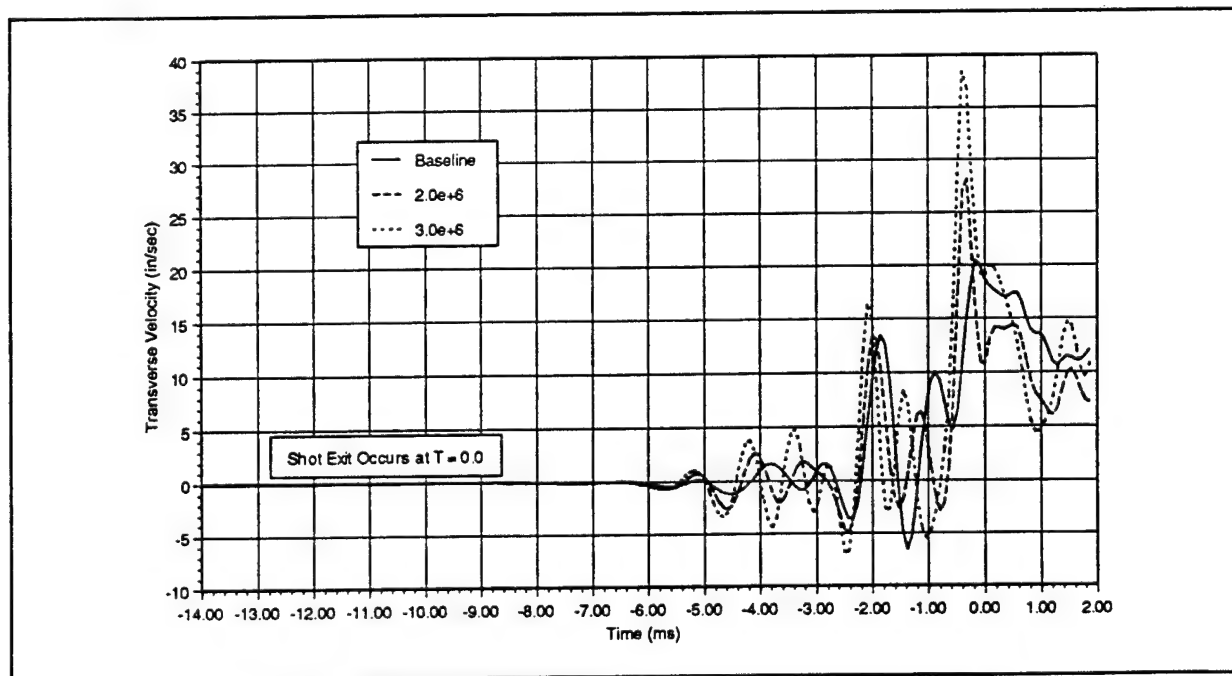


Figure 10 Transverse Velocity of Gun Muzzle (S/N 518)

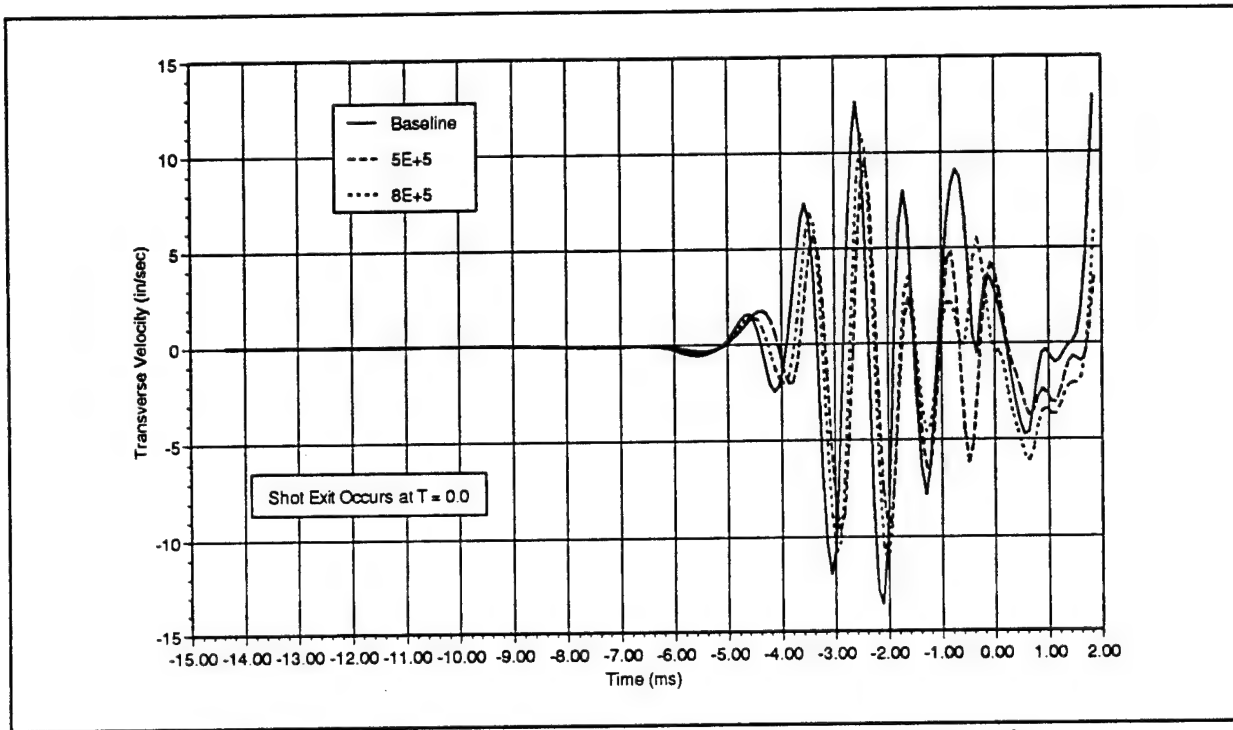


Figure 11 Transverse Velocity of Gun Muzzle (S/N 17343)

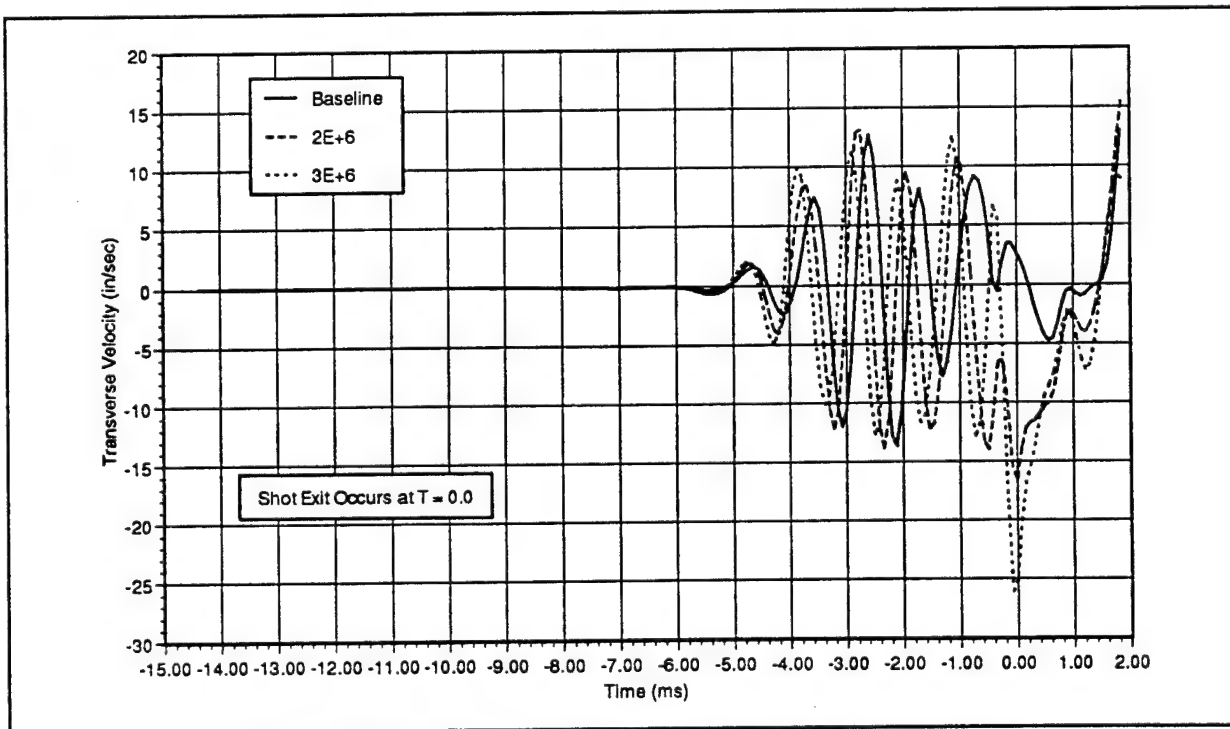
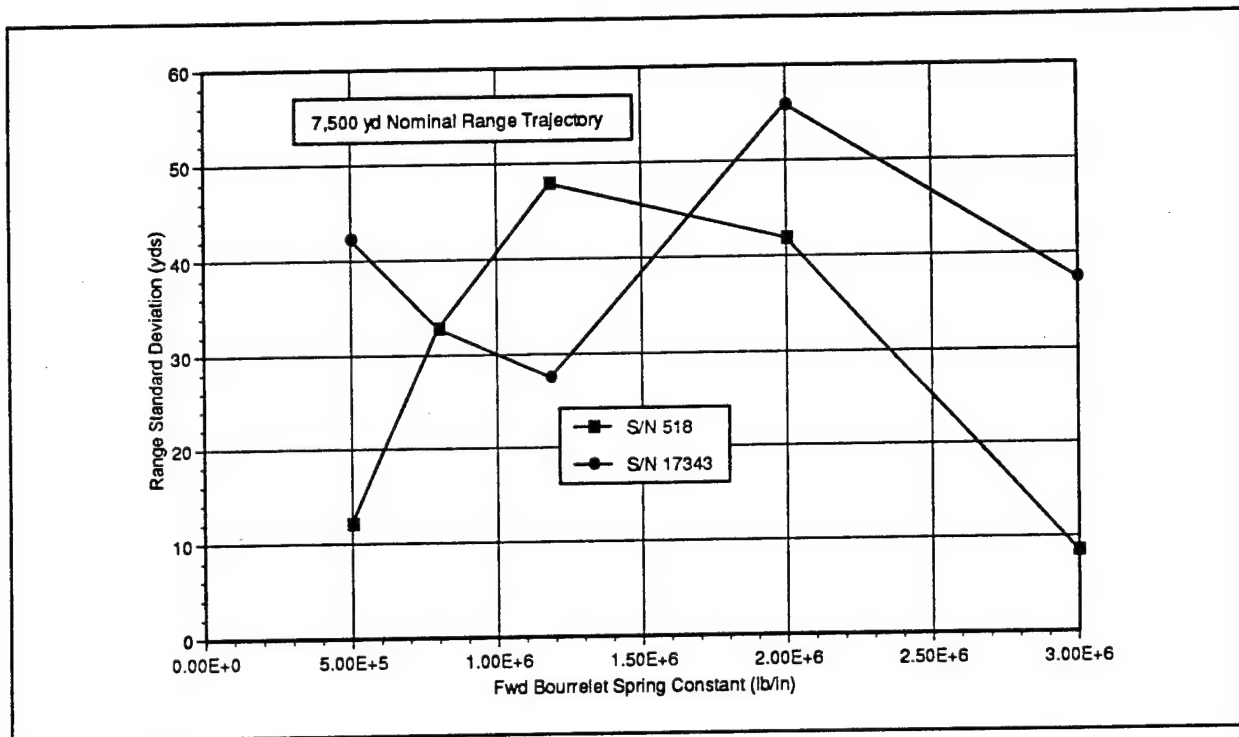


Figure 12 Transverse Velocity of Gun Muzzle (S/N 17343)

These results prompted further investigation of the potential impact of changes to the forward bourrelet spring constant on range dispersion. Using the procedure previously described, a series of trajectory calculations were performed for each initial condition at a gun elevation corresponding to a nominal range of 7,500 yds. The results of these calculations are shown in Figures 13 and 14.



**Figure 13 Effect of Variations in Forward Bourrelet Spring Constant**

As expected, the changes in range dispersion which resulted from changes to the spring constant of the forward bourrelet are significantly larger than those for corresponding changes to the aft bourrelet. Although this study analyzed the response of only two individual gun barrels, these results would seem to indicate that if further improvements in the ballistic dispersion of the 5"/54 gun system are to be realized, then attention must be focused on the gun barrel manufacturing process with the objective of producing gun barrels whose characteristic centerline variations more consistent.

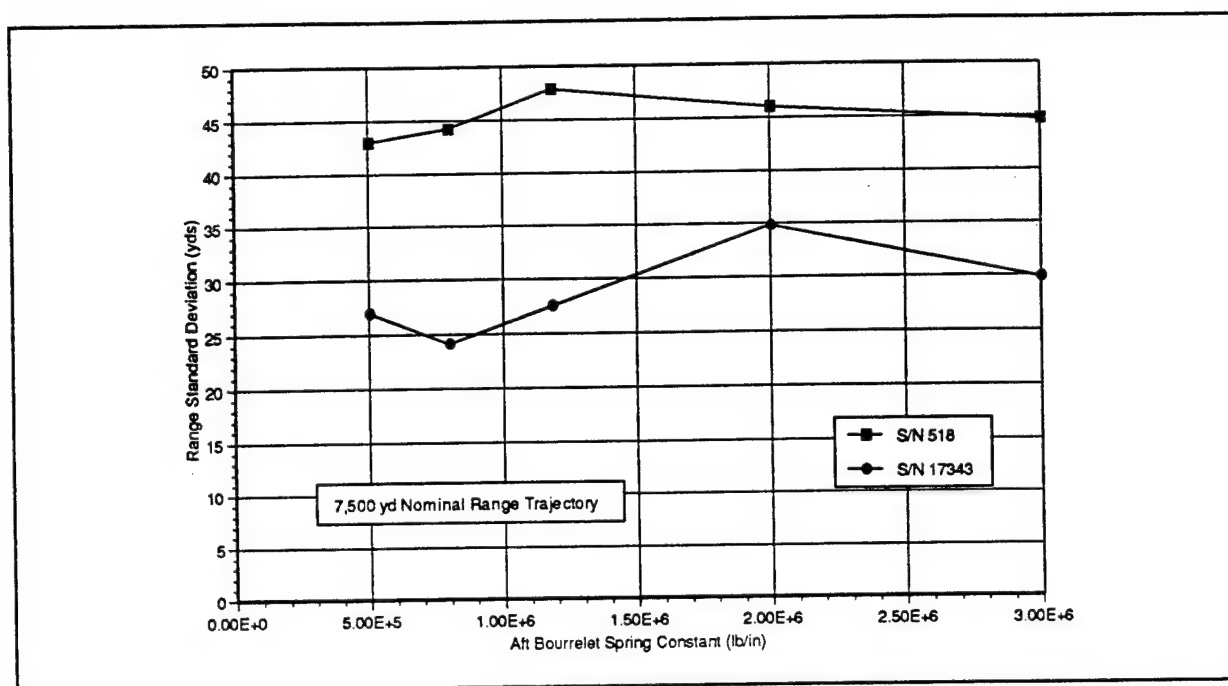


Figure 14 Effect of Variations in Aft Bourrelet Spring Constant

## SUMMARY AND CONCLUSIONS

The first order ballistics tools used in this study are proven products. They are fast, and have been shown to produce reasonably accurate results. When utilized in the analysis methodology previously described in this paper, these models produced estimates of the ballistic dispersion of the 5"/54 gun system which compare favorably to available proving ground data. In addition, simulations analyzing the effect on shot exit conditions due to changes on a single major parameter of the gun mount or the projectile were also conducted. The results of these analyses indicate that major changes in the spring constant of the gun supports produce negligible effect on the projectile at shot exit. Much more noticeable changes in shot exit conditions occur when the projectiles contact spring coefficient change. This is especially true when the forward bourrelet spring constant is changed.

One of the more important conditions to note in this gun system is that the very small center of gravity offsets in the breech have an insignificant effect on the dynamic response of the gun. The results indicate that each individual gun barrel centerline produces a unique gun response. This unique response appears to cause the mean achieved range for a fixed set of firing conditions to be different for each gun barrel. This unique response characteristic may be the root cause of the "short shooter" - "long shooter" characteristic often observed in the 5"/54 and other gun systems.

## ERLINE, FISCHER

The analyses conducted during this investigation have yielded a considerable volume of information about the overall dynamic response characteristics of the 5"/54 gun system. A complete presentation of the data derived to date is far beyond the scope of this paper. The interperation of this information is an ongoing process and will undoubtedly lead to a more complete understanding of the key factors which influence the ballistic dispersion of the Mk 45 Gun Mount.

While the dynamic response of large caliber indirect fire gun systems is a relatively minor contributor to the overall delivery error, the importance of understanding the magnitude and source of all errors cannot be overstated. As the range of indirect fire gun weapon systems is increased and greater emphasis is placed on improving delivery accuracy at these extended ranges, the need to identify, quantify, and understand the interdependencies of all sources of error will become increasingly important. Because of the ever increasing cost of conducting live firing tests, computer modeling and simulation is often the only affordable means available to acquire the necessary knowledge and understanding required to make intelligent decisions concerning the overall accuracy potential of a gun weapon system. However, as the speed and power of computers has continued to increase, so has the sophistication and complexity of the models. Although these models are capable of providing precise information, often at levels of detail heretofore impossible to instrument, the time and expense required to develop and calibrate these models for existing weapon systems is often prohibitive. Therefore, there is a definite need for an accurate and simple means of conducting the "quick look" type analyses and "first order" effect assessments necessary to guide and focus the application of more sophisticated techniques.

Although this study has admittedly been limited in scope, the authors believe that the analysis methodology developed during the investigation and described in this paper offers a relatively simple and effective means of characterizing the dynamic response of a large caliber gun system and assessing that system's sensitivity to changes in key parameters which affect its dynamic response. This "desktop" procedure provides the gun and ammunition designer with an effective tool to quickly and economically assess the potential impact of proposed changes to key system parameters and can also provide design guidance during the early stages of new system development.

## REFERENCES

- a. Erline, T. F., M. D. Kregel, and M. Pantano, "Gun and Projectile Flexural Dynamics Modeled by the Little Rascal - A User's Manual -", BRL-TR-3122, Ballistic Research Laboratory, Aberdeen Proving Ground, MD, 1990.
- b. Anderson, R. D. and K. D. Fickie, "IBHVG2 - A User's Guide", BRL-TR-2829, Ballistic Research Laboratory, Aberdeen Proving Ground, MD, 1987.
- c. Kregel M.D. and E.L. Lortie, "Description and Comparison of the "K" Method for Performing Numerical Integration of Stiff Ordinary Differential Equations",

ERLINE, FISCHER

- BRL-TR-1733, Ballistic Research Laboratory, Aberdeen Proving Ground, MD, July 1973.
- d. Erline, T. F., M. D. Kregel, "Modeling Gun Dynamics with Dominant Loads", BRL-MR-3683, Ballistic Research Laboratory, Aberdeen Proving Ground, MD, July 1988.
  - e. SW323-AB-ORD-020, "Range Table for 5-Inch 54-Caliber Guns Firing Projectiles Mark 41 and Mark 64 (Surface Targets) (Full Service Charge, ICAO Atmosphere)", Naval Sea Systems Command, Washington, D.C., 1985.
  - f. Updike, E. G., Private Communication, Dahlgren Division, Naval Surface Warfare Center, Dahlgren, VA, February 1996.
  - g. Jones, J. H. and E. G. Updike, "Quick-Look Results of 5-in./54 HECVT Ammunition-Effectiveness Test Against Land Targets Fired in USS LABOON on 2 Jun 1995", NSWCDD/TR-95/144, Dahlgren Division, Naval Surface Warfare Center, Dahlgren, VA, 1995.
  - h. Erline, T. F., "Projectile Spring Constants: Significance to Modeling with the Little Rascal Gun Dynamics Program", BRL-TR-3224, April 1991.
  - i. Lyon, D., "Radial Stiffness Measurements of 120mm Tank Projectiles", ARL-TR-392, U.S. Army Research Laboratory, Aberdeen, MD, April 1994.
  - j. "Theory of Vibrations with Applications", W. T. Thomson, Prentice-Hall, NJ, 1981, p142

DESIGN TRADEOFFS FOR A VERY LIGHTWEIGHT 155-MM  
HOWITZER FOR THE U.S. ARMY LIGHT FORCES  
LAWRENCE W. BURTON, CHRISTOPHER P. R. HOPPEL, AND  
ROBERT P. KASTE  
U.S. ARMY RESEARCH LABORATORY AMSRL-WT-PD  
ABERDEEN PROVING GROUND, MD 21005-5066

ABSTRACT

An investigation to determine a sensible design weight for a lightweight howitzer was undertaken. After choosing 7,000 lb as a design goal, the study undertook to ascertain the feasibility of such a system while attempting to maintain a 155-mm gun range and lethality.

Details of the estimated weight savings attributable to composite replacement parts, incorporation of a soft recoil system, and restriction of the maximum charge to the M119A2 are presented to demonstrate the possibility of a 7,000-lb (3,175 kg), lightweight 155-mm howitzer. The results showed that a 7,000-lb towed howitzer is possible using available technologies. While such a weapon would not have a range capability equivalent to the current M198 155-mm system, it would bring an upgraded firepower capability to the light maneuver forces, which presently use 105-mm artillery, and increase their current engagement range capability.

BIOGRAPHY:

PRESENT ASSIGNMENT: Mechanical Engineer, Mechanics & Structure Branch, Weapons Technology Directorate, U.S. Army Research Laboratory, Aberdeen Proving Ground, MD.

PAST EXPERIENCE: Mechanical Engineer, U.S. Ballistic Research Laboratory (1984-1992); Mechanical Engineer, U.S. Army Research Laboratory (1992-Present).

DEGREES HELD: M.S. Mechanical Engineering, The Johns Hopkins University, Baltimore, MD, 1991; B.S. Mechanical Engineering, Virginia Polytechnic Institute & State University, Blacksburg, VA, 1984.

## Design Tradeoffs for a Very Lightweight 155-mm Howitzer for the U.S. Army Light Forces

Lawrence W. Burton\*, Christopher P.R. Hoppel, and Robert P. Kaste  
U.S. Army Research Laboratory  
AMSRL-WT-PD  
Aberdeen Proving Ground, MD 21005-5066

### 1.0 INTRODUCTION

The roles of field artillery on the battlefield include providing a deep-strike capability, allowing for fire in all weather and terrain, and having the ability to mass fires without moving the weapon platforms. An important requirement for field artillery is that it must be at least as mobile as the unit that it supports. Such a prerequisite poses a dilemma for the light maneuver forces, which need a very mobile artillery piece and typically must sacrifice both range and lethality in the interest of mobility. Recognition of this difficulty resulted in a study being initiated to determine what size howitzer was most beneficial and practical to the U.S. Army light forces.

Thus, a study to determine the feasibility of designing a 7,000-lb (3,175 kg) 155-mm towed howitzer was undertaken. The weight limit imposed was chosen to ensure the howitzer was liftable by the UH-60 Blackhawk helicopter and make it towable by a 2.5 ton truck over rough terrain. It was hoped that the weight goal of the towed howitzer could be attained while maintaining 155-mm firepower. The primary means of achieving the 7,000-lb goal weight were to adopt improved recoil techniques, substitution of lightweight materials for various components, and gun barrel designs optimized to the in-bore pressure profile. Alternate means of weight reduction such as shorter gun barrels and reduced charge requirements would also be considered, realizing that these things could adversely affect the range capability of the 155-mm howitzer. The details of these tradeoffs and the projected performance of a very lightweight howitzer are presented in this paper.

### 2.0 SYSTEM WEIGHT SELECTION

In order to make sound decisions on the desirable features of a lightweight 155-mm howitzer, it is first imperative to define "lightweight". A review of past and present towed howitzers was made to determine their mass and vehicle towing requirements.

Table 1 provides a listing of various towed howitzers, their total weight, the maximum firing range of both nonassisted and rocket-assisted (RA) projectiles, and the size vehicle typically used to transport the weapon system on the ground [1]. The 105-mm M119, the replacement howitzer for the M102, is currently in service and available to the light forces. It provides a very light system but lacks the firepower and lethality of the 155-mm M198 system.

Table 1. U.S. Army Howitzers - Characteristics and Performance

Howitzer	Caliber (mm)	Weight (lb)	Tow Vehicle (Truck)	Range	
				Nonrocket Assist	Rocket Assist
M102	105	3,300	2.5 ton	11,500 m	15,100 m
M119	105	4,100	2.5 ton	14,000 m	20,100 m
M114	155	12,800	5 ton	14,600 m	19,300 m
M198	155	15,800	5 ton	22,000 m	30,300 m

To be of benefit to the light force community, a lightweight howitzer, in 155-mm caliber, must be transportable by the UH-60, or Blackhawk, utility helicopter. It is the Army's most frequently employed rotary-wing aircraft for delivering cargo and equipment and is capable of lifting 8,000 lb (3,629 kg) via sling [2].

Another consideration in the selection of the howitzer design weight is the preference that the system be towable by a 2.5-ton truck. A 2.5-ton truck is capable of towing up to 10,000 lb (4,535 kg) on paved roadways but is limited to a load of 6,000 lb (2721 kg) for cross-country conditions [3]. Ideally, a 155-mm system weighing 6,000 to 7,000 lb would be desirable to allow for off-road transport.

Based on this transportation information, a 7,000-lb (3,175 kg) design goal weight was chosen. At this weight plateau, the lightweight 155-mm may be lifted by a Blackhawk helicopter and also be towed off-road by a 2.5 ton truck in all except the most extreme conditions. These facts make such a system beneficial to the light forces. The tradeoffs required to reach this goal weight are detailed in the following sections.

### 3.0 LIGHTWEIGHT MATERIAL SUBSTITUTION OF COMPONENT PARTS

Several previous investigations attempting to reduce the weight of specific component parts in towed howitzer systems have been

conducted. The U.S. Army Materials Technology Laboratory (MTL)<sup>1</sup> studied the effects of optimizing the weight of the M198 trails [4]. In the MTL study, the trails were designed as tapered box beams, with a length of 110 in (2.8 m), and were able to withstand the shear and bending loads imposed by a cookoff loading condition. The analytic investigation resulted in the lightest trail weight design using steel, aluminum, and several different composite materials. The resulting design weights are summarized in Table 2.

Table 2. Trail Weight for a 155-mm Lightweight Towed Howitzer

Material System	Trail Weight (lbs/kg)
High Strength Steel	518/235
High Strength Aluminum	362/164
Glass-Fiber-Reinforced Epoxy	185/84
Graphite-Fiber-Reinforced Epoxy	114/52
Combination of Graphite-Fiber-Reinforced Epoxy and Kevlar-Fiber-Reinforced Epoxy	106/48

The weights predicted in this study are much lower than the present weight, 927 lb (420 kg), of the M198 trails. It should be noted that these trails were only designed for the loads associated with firing at peak pressure. Issues such as loads due to towing and durability were not addressed. Therefore, the trail weights for a fielded system may be higher than those shown in Table 2. However, it is significant to note the lightest composite design shows an 80% weight savings over the steel system and a 70% weight savings over an aluminum system.

In a separate project, the U.S. Army Armament Research, Development, and Engineering Center (ARDEC) performed a paper study on how to reduce the weight of specific component parts on the M198 howitzer by replacing steel with either titanium, boron-fiber-reinforced aluminum, or graphite-fiber-reinforced epoxy. A Pro Engineer computer-aided design model [5] of the M198 was constructed to evaluate each component for possible weight reduction. Table 3 lists the reduced weights for the various parts. This effort shows the system component weight may be reduced 20%, for a weight savings of 3,288 lb (1,491 kg).

However, this study was limited in scope in that it only examined modifications to the existing M198 weapon platform and did not consider changes to the recoil components which account for 45%

---

<sup>1</sup> The Materials Technology Laboratory (MTL) has since been reorganized as the Materials Directorate of the U.S. Army Research Laboratory.

Table 3. Weight Reduction of the M198 Howitzer Components

Components (# of)	Current Weight (lb)	Modified Weight (lb)	Total Weight Savings (lb)	Factors Affecting Future Reductions
Equilibrator (2)	128 each (steel)	102 each (Titanium)	52	Height of the Gun
Speed Shift	104 (steel)	68 (Ti)	36	
Actuator	47 (steel)	31 (Ti)	16	
Traversing Mechanism	67 (Al & steel)	48 (Al & Ti)	19	
Friction Clutch	47 (Al & steel)	34 (Al & Ti)	13	
Wheel/Axle Assembly	1,283 (steel)	763 (Boron/Al)	520	Weight of the Gun
Elevating Screws (2)	147 (steel)	103 each (Ti)	88	Weight of the Gun
Spade (2)	178 (steel)	55 each (Boron/Al)	248	Recoil Force
Cradle/ Ballistic Shield	933 (steel & aluminum)	706 (Boron/Al & Aluminum)	227	Recoil Force
Top Carriage Weldment	850 (Al & steel)	560 (Al & Carbon/Ep)	290	Recoil Force
Top Carriage Parts	61 (steel)	34 (steel)	27	Recoil Force
Bottom Carriage Weldment	1,477 (steel)	538 (Boron/Al)	939	Recoil Force
Trail Weldments (2)	927 (Aluminum)	627 each (Carbon/Ep)	600	Recoil Force
Other Misc. Parts	477 (steel)	264 (Ti & Boron/Al)	213	Some Dependent on Recoil Force
Total	8,108	4,820	3,288	

of the system's total weight. Also, the effects of changing the howitzer's center of gravity as a result of material substitution were neglected. Any change in these areas requires alteration of the entire gun structure.

#### 4.0 LIGHTWEIGHT 7,000-LB HOWITZER STUDY

The M198, a 155-mm towed howitzer, was taken as the baseline system for this study. The study procedure was to implement changes to the M198 in an attempt to reach the 7,000-lb goal weight. Incorporating the findings of the previous ARDEC and MTL studies on the substitution of lightweight materials for M198 components was a logical first step. As reported in a preceding section, a 25%

decrease in mass from the baseline M198 system was deemed possible through the use of composite materials and lightweight metals, resulting in a 12,000-lb (5,443 kg) "M198-equivalent" howitzer.

Other weight saving changes were investigated and adopted where prudent in an attempt to meet the 7,000-lb goal weight. Barrel weight calculations based on estimated fatigue life were made to eliminate parasitic mass from the cannon tube design. The effect of reducing the maximum cannon breech operating pressure was also examined as a means of facilitating the reduction of barrel weight. A number of techniques to improve the recoil capacity of the howitzer were considered, and soft recoil was chosen for application on the new lightweight howitzer. Geometry changes affecting the howitzer trails, recoil cylinder length, and trunnion height were other aspects explored in the study in an attempt to reduce weight. Finally, tradeoffs of barrel length versus range were made to allow for even further reduction of the system weight. The subsequent sections detail the specifics of what was considered for each weight savings measure and quantify the projected mass reduction.

#### 4.1 BARREL WEIGHT REDUCTION

The M198 towed howitzer uses the M199 gun barrel. The barrel weighs 3,850 lb (1,742 kg) [6] and is designed for 11,000 fatigue cycles [7] and 2,500 cycles in wear [8]. One reason the barrel has a fatigue life more than four times its wear life is that the recoil system of the M198 requires a large mass for the recoiling parts as a means of absorbing the recoil energy. Thus, substantial reductions in overall system weight are achievable by designing a 155-mm barrel with a reduced fatigue life.

The approach taken here is to determine the optimum barrel design for a specific fatigue life. Since the pressure due to firing a projectile decreases along the length of the gun barrel, the gun barrel should have a tapered form to match the pressure profile. Pressure profiles were generated for several charges of interest for 155-mm howitzers using the IBHVG2 computer code [9]. From these curves, it was determined that the M203A1, a zone 8s charge, produced the maximum pressure of all the charges with a value of 63.3 ksi (437 MPa). The resulting pressure from the M203A1 was greater than the pressure of the five-increment Modular Artillery Charge System (MACS) along the entire length of the barrel. Figure 1 shows a comparison the two pressure profiles.

To investigate the effects of a reduced pressure on the weight of a barrel, a second family of charges was considered. Figure 1 also shows the pressure profiles generated by the M119A2, a zone 7 charge, and a four-increment MACS. Note that the pressure due to the M119A2 charge is initially greater than the four-increment MACS at the chamber during shot start but subsequently drops below it near muzzle exit. The compilation curve shown on Figure 1 was generated to represent a barrel design capable of firing both charges.

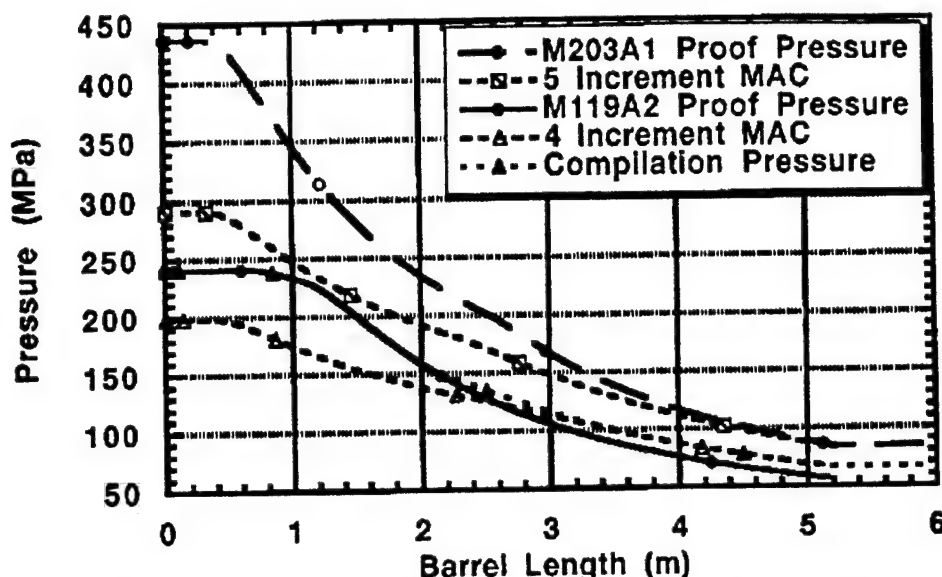


Figure 1. Pressures produced along the barrel length by various charges with a 95-lb projectile

The stress state on the inner surface of a gun barrel with a small crack will depend on the applied pressure profile, crack size, the ratio of the outer barrel radius to the inner radius, and the residual stress due to autofrettage of the barrel. The tensile hoop stress,  $S_p$ , at the inner radius of a pressurized cylinder in the region of a stress concentration can be expressed as

$$S_p = -P \left[ \frac{(2k_t - 1)W^2 + 1}{W^2 - 1} \right], \quad (1)$$

where  $P$  is the applied radial pressure,  $k_t$  is the local stress concentration factor, and  $W$  is the ratio of the outer to inner radius of the gun barrel [10]. It should be noted that if the local stress concentration is equal to 1.0, equation 1 reduces to the Lamé' stress for the inner radius of a thick cylinder subject to internal pressure. The maximum residual stress due to autofrettage,  $S_R$ , of the gun barrel is expressed as

$$S_R = S_Y k_t \left[ 1 - \ln W \left( \frac{2W^2}{W^2 - 1} \right) \right] \quad (\text{if } S_R \leq S_Y) \quad (2a)$$

and

$$S_R = S_Y \quad (\text{if } S_R > S_Y), \quad (2b)$$

where  $S_Y$  is the material yield strength, which represents the maximum possible residual stress due to autofrettage.

The effective stress at a crack in the inner radius of an internally pressurized, autofrettaged cylinder can be expressed as

$$S_{eff} = S_p + S_R - P, \quad (3)$$

where  $S_{eff}$  is the effective stress at the crack. Knowing the stress

state at the inner radius, the fatigue crack growth rate can be calculated based on the Paris law [11] [12], which states the rate of fatigue crack growth is proportional to the range of stress intensity factors at the crack tip. Expressed quantitatively [13],

$$\frac{da}{dN} = A(\Delta K)^m, \quad (4)$$

where  $da/dN$  is the crack growth rate,  $\Delta K$  is the stress intensity factor range ( $\Delta K = K_{\max} - K_{\min}$ ), and  $A$  and  $m$  are material constants determined experimentally. The stress intensity factor,  $K$ , is proportional to the applied global stress times the square root of the crack length and is expressed mathematically as

$$K = Y\sigma\sqrt{a}, \quad (5)$$

where  $Y$  is a parameter accounting for the crack geometry,  $\sigma$  is the stress applied to the cracked area, and  $a$  is the crack length [14].

As a crack grows through the thickness of the gun tube, its length increases an amount,  $da$ , with every loading cycle, and the stress intensity factor increases proportionally. When the stress intensity factor reaches a critical value, the plane strain fracture toughness,  $K_{Ic}$ , the material fails catastrophically [13]. The crack length at  $K_{Ic}$  is the critical crack length,  $a_c$ , expressed as

$$a_c = \left( \frac{K_{Ic}}{Y\sigma_{\max}} \right)^2, \quad (6)$$

where  $\sigma_{\max}$  is the maximum applied stress.

The fatigue life for the material can then be calculated by integrating equation 4 with respect to the flaw size,  $a$ , and the number of cycles,  $N$ . The limits of integration on the flaw size are the starting flaw size,  $a_o$ , and the final flaw size,  $a_c$ . The limits of integration on the number of cycles are the initial number of fatigue cycles,  $N_i$ , and the final number of fatigue cycles,  $N_f$ . If the initial number of cycles is zero, then the number of cycles to failure can be expressed as follows [14]:

$$N_f = \frac{2}{(m-2) * A * Y^m \sigma_m} \left[ \frac{1}{a_o^{\left(\frac{m-2}{2}\right)}} - \frac{1}{a_c^{\left(\frac{m-2}{2}\right)}} \right]. \quad (7)$$

Equation 7 can be used to predict the number of cycles to failure (CTF) for a barrel if the applied stresses, the starting flaw size, the geometric shape parameter for the flaw, and the various material parameters are known. Equation 7 can be solved for the stress-state,  $\sigma$ , to produce a given fatigue,  $N_f$ , and may be rewritten as

$$\sigma = \left( \frac{2}{(m-2) * A * Y^m N_f} \left[ \frac{1}{a_o^{\left(\frac{m-2}{2}\right)}} - \frac{1}{a_c^{\left(\frac{m-2}{2}\right)}} \right] \right)^{\frac{1}{m}}. \quad (8)$$

For a gun barrel with a crack in the inner surface, the stress state,  $\sigma$ , can be set equal to  $S_{eff}$  from equation 3. Thus, a relationship is established between the ratio of the outer radius to the inner radius,  $W$ , and the fatigue life,  $N_f$ . A computer program was written to solve for the minimum ratio of the outer to inner radius to produce a given fatigue life along the pressure curves shown in Figure 1. The fatigue life constants used in the analysis were taken from other studies on gun tube steels [10][15]. The initial flaw size was chosen as 0.051 inch (1.3 mm), which is a typical size flaw due to heat checking in gun barrels [10].

The weights of gun barrels having fatigue lives ranging from 100 to 100,000 cycles were calculated for the M203A1 and the M119A2 charges. The results are shown graphically in Figure 2, which also depicts the weight and fatigue life for existing barrels. The Vickers Shipbuilding and Engineering Limited (VSEL) and Royal Ordnance barrels are for 9,000-lb (4,082 kg) howitzer systems they are currently developing. Notice that although these two barrels, plus the M284 and M199 barrels, were all designed for the M203A1 charge, their weights are greater than those predicted by the fatigue calculation. This is likely due to a factor of safety margin being incorporated into the barrel design. Since the predictions in this report are based on theoretical equations, which are based on a 50% failure criteria, corrections are needed to predict a reliable design. To provide a margin of safety, the results were normalized to the weight of the VSEL barrel design. Figure 3 shows a plot of these normalized results. Notice that the M199 barrel weight falls on the revised curve, indicating this modification to the calculated data provides a reasonable safety factor.

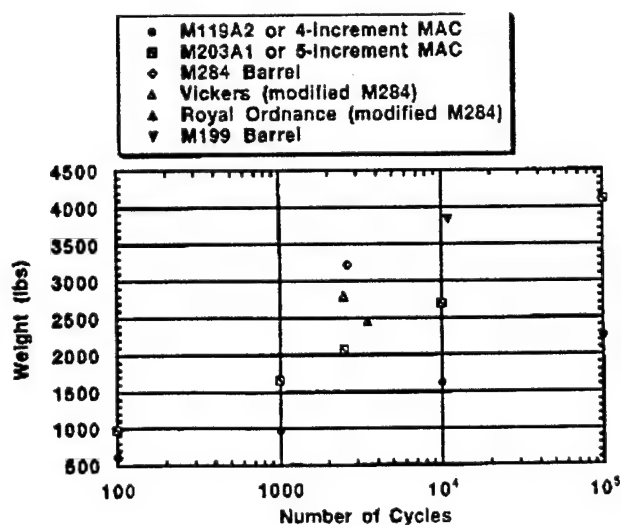


Figure 2. Calculated barrel weights for a fixed fatigue life

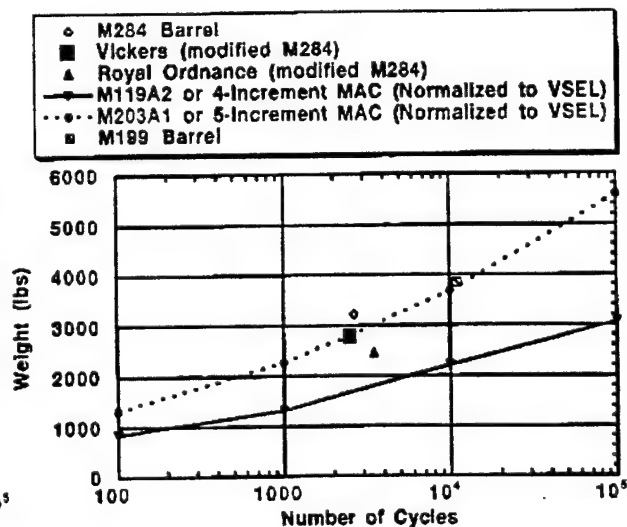


Figure 3. Barrel weight data normalized to VSEL design

## 4.2 SOFT RECOIL

Adoption of an improved recoil system was another area investigated in an attempt to achieve the desired system weight of the towed howitzer. The term soft recoil is used as a designation for the process of imparting forward momentum to the recoil mass, prior to firing the gun, to subsequently reduce the rearward recoil impulse, which must be dissipated by the recoil system.

The rearward impulse is a reaction to the forward acceleration of the projectile, propellant, and propellant combustion gases and must be dissipated and controlled to maintain weapon stability and structural integrity of the weapon system. A standard technique for dissipating the rearward momentum of a howitzer uses hydropneumatic recoil and recuperator systems, which allow some part of the weapon system to move rearward against a resistive force, thus producing relatively long duration but a lower reactionary force load. This permits the weapon to remain at its firing position without tipping over. The recuperator acts as a temporary storage device, using some of the energy dissipated in the recoil operation to return the recoiling parts forward and positioning them properly for the initiation of the next shot.

While a hydropneumatic recoil system acts to control the rearward momentum imparted to the recoiling parts, it does not reduce the magnitude of the rearward impulse. One common method used to reduce the rearward impulse imparted to the recoiling parts is the addition of a muzzle brake to the cannon. The muzzle brake uses the energy of the expelling combustion gases to impart a forward-acting impulse on the gun tube to reduce the net rearward impulse, which must be dissipated by the recoil system. Practical muzzle brakes use 0.7 to 1.0 times the momentum of the combustion gases to provide a forward-acting impulse on the recoiling parts. Theoretically, even more efficient muzzle brakes could be utilized. However, the forward impulse produced by a muzzle brake comes at the penalty of blast overpressure at the muzzle.

Soft recoil, by imparting forward-acting momentum to the recoiling parts, also reduces the net rearward impulse, which must be dissipated by the recoil system. The magnitude of the forward-acting impulse that can be applied has two major constraints. First, it cannot be more than the rearward impulse resulting from the round being fired in order to properly cycle the weapon. More importantly, the second constraint limits the amount of energy available for imparting the forward impulse, for as the magnitude of this stored energy increases, the required strength and size of the system components increase, which is counterproductive to the concept of a reduced weight weapon system.

Typical impulses for various 155-mm howitzer charges firing a 95.0-lb (43.1 kg) projectile are given in Table 4. These values come from previous work done in examining range-versus-weight tradeoffs of a 155-mm towed howitzer [16]. The impulses are broken down into various components.  $I_1$  is the impulse due to the

Table 4. 155-mm Charge Impulse Values

Charge-Type	$I_i$ (kN·s) [lb·s]	$I_g$ (kN·s) [lb·s]	$I_T$ (kN·s) [lb·s]	$I$ (kN·s) [lb·s]
M203A1	40.76 [9,174]	14.13 [3,180]	54.89 [12,354]	45.00 [10,128]
M119	32.81 [7,384]	9.99 [2,249]	42.80 [9,633]	35.81 [8,059]
M4A2 (zone 7)	25.77 [5,800]	6.10 [1,373]	31.87 [7,173]	27.60 [6,212]
M4A2 (zone 3)	12.11 [2,725]	1.54 [347]	13.65 [3,072]	12.57 [2,830]

acceleration of the projectile and propellant in-bore.  $I_g$  is the impulse due to expelling combustion gases after the projectile exits the muzzle.  $I_T$ , the total impulse, equals the sum of  $I_i$  and  $I_g$ , while  $I$ , the net rearward impulse, equals  $I_T - 0.7(I_g)$ , where 0.7 is the muzzle brake efficiency.

Table 4 shows a wide range of values for the total impulse depending on the charge and zone fired. In order to facilitate the use of soft recoil over this range in a practical application, it is necessary to include some compromises. If, for example, the recoil system is designed to allow low-impulse rounds such as the M4A2, zone 3 to be fired without using the soft recoil technique, the forward momentum imparted via a soft recoil system could be increased to accommodate charges such as the M203A1 and M119, which produce higher recoil impulses. This compromise alleviates the first system constraint discussed previously by maximizing the forward impulse of the soft recoil stroke for high-impulse firings while ensuring sufficient energy is available to return the barrel to the battery position at lower impulse firings.

However, because of the second constraint, it is also necessary to limit the forward impulse from the soft recoil to reduce the amount of stored energy required to impart the momentum to the recoiling parts. For a hydropneumatic system, this keeps the weight down, as well as reduces potential safety and operating problems associated with a weapon having highly loaded activation devices such as springs or pressure cylinders.

For a 155-mm howitzer, a forward impulse of 10.2 kN·sec (2,300 lb·sec), or about 20% of the high-impulse M203A1 charge, seems appropriate. This reduction in impulse combined with the forward impulse contribution from the muzzle brake yields net impulses for dissipation by the recoil system. These resultant impulses are 7,828 lb·s (34.8 kN·s) and 5,759 lb·s (25.6 kN·s) for the M203A1 and M119 charges, respectively.

### 4.3 GEOMETRY CHANGES

The recoiling mass of the M198 howitzer is 7,000 lb (3,175 kg), divided between the M45 recoil system (2,150 lb, 975 kg) and the M199 cannon assembly (4,850 lb, 2,200 kg) [17]. The M199 barrel weighs 3,840 lb (1,742 kg), with a muzzle break weight of 250 lb (113 kg), and a breech weight of 760 lb (345 kg) [6].

The recoil force is calculated as

$$F_r = \left( \frac{1}{2} \right) \left( \frac{I^2}{m_r L_r} \right), \quad (9)$$

where  $F_r$  denotes the recoil force,  $I$  is the impulse imparted by the cannon to the system,  $m_r$  is the mass of the recoiling parts, and  $L_r$  is the length of the recoil stroke [16].

The maximum recoil stroke length of the M198 is 72 in (1.83 m). The maximum ballistic impulse is 10,128 lb·s (45 kN·s) for an M198, equipped with a muzzle break, firing the M203A1 charge [16]. Substitution of these values into equation 9 yields a recoil force of 39,321 lb (175 kN). This represents the maximum force that must be absorbed during the recoil cycle of the M198 with its current recoil system, the M45.

Benet Laboratories estimated that an improved hydropneumatic recoil system could be designed, resulting in a 1,750-lb (794 kg) recoil mechanism [16]. The mass estimate for the barrel based on the fatigue analysis of section 1.2 is 2,800 lb (1,270 kg), allowing for a cannon with 2,500 CTF, which is equivalent to the wear criterion in place for both the M199 and M284 barrels [8]. Royal Ordnance has shown a weight savings of 100 lb (45 kg) can be attained by substituting titanium for the steel when fabricating the muzzle brake. The sum of the recoiling components for this system is listed in Table 5 as Variation A. A similar listing of the M198 baseline is provided for the sake of comparison.

The adoption of a soft recoil system similar to that detailed in the previous section allows for a 2,300-lb·s (10.2 kN·s) reduction in the impulse imparted to the gun system. Incorporating this reduction into the calculation of the recoil force, equation 9 produces a recoil force 23% less than that of the M198. Thus, the M45 recoil system is overdesigned in its capability to handle the recoil requirements of the Variation A howitzer design.

An assumption was made at this point that there is a linear relationship between the recoil length and the weight of the recoil mechanism. It was also assumed that the decrease in the recoil mechanism's load-carrying capacity could be no greater than the percent decrease in the recoil length. For example, based on these assumptions, a 5% reduction in the recoil stroke would result in a 5% reduction in the mass of the recoil mechanism, and the allowable recoil force would be 95% of the original system's.

Table 5. Mass Tradeoff Summary of Cannon and Recoil Assemblies

	Barrel Wgt (lb)	Muzzle Brake, Breech (lb)	Cannon Assemb (lb)	Recoil Mech (lb)	Total Recoil Wgt (lb)	Recoil Force (lb)	Recoil Length (ft)
Baseline M198, 155-mm, towed howitzer							
M198	3,840	1,010	4,850	2,150	7,000	39,321	6.0
Reduced barrel weight (2,500 cycles to failure), soft recoil (SR), & lightweight recoil mechanism and muzzle brake							
A	2,800	910	3,710	1,750	5,460	30,115	6.0
11% Reduction of recoil stroke length & mechanism mass, SR							
B	2,800	910	3,710	1,558	5,268	35,070	5.34
2,500 CTF Barrel, M119A2 Maximum Charge, soft recoil							
C	1,700	910	2,610	1,750	4,360	20,412	6.0
20% Reduction of recoil stroke length & mechanism mass, SR							
D	1,700	910	2,610	1,400	4,010	27,742	4.8
29 Caliber, Soft Recoil							
E	1,520	910	2,430	1,400	3,830	29,046	4.8

Employing these assumptions led to Variation B of the howitzer study, which assumed an 11% reduction in recoil stroke with a corresponding mass reduction of the recoil mechanism. The input values for equation 9 are listed in Table 5 along with the calculated recoil force. A comparison of this calculated recoil force to the M198 baseline shows it to be 11% less, nearly equivalent to the assumed reduction in stroke length. This equivalence signifies that further shortening of the recoil system would yield recoil forces in excess of its load carrying capability.

The result of these calculations was a system whose recoiling mass was 5,268 lb (2,390 kg). Adding this to the weight of the lightweight components from the ARDEC study given in section 3.0 results in a howitzer weighing approximately 10,000 lb (4,536 kg). Although other weight reduction techniques were considered, it became apparent that the 7,000-lb goal weight was not attainable while maintaining M198-equivalent performance.

Achieving significant decreases in the weight of the howitzer required that more drastic steps be taken. Thus, the decision was made to pursue a reduced system weight by backing off the high-impulse M203A1 charge. It was recognized that such an approach

would decrease the range capability of the system; however, it was deemed the most practical way of attaining the desired goal weight.

The M119A2 was selected to be the maximum allowable charge considered. The M119A2 produces an impulse of 8,059 lb·s (35.8 kN·s) when fired from the M198 with a muzzle brake having an efficiency of 0.7 [16]. Adding in a soft recoil capability equivalent to that assumed previously results in a system impulse of 5,759 lb·s (25.6 kN·s). Reducing the charge allows for a less massive barrel, with the weight of 1,700 lb (725 kg) (taken from Figure 3) for a fatigue life of 2,500 cycles. The input parameters for this 4,360-lb (1977 kg) recoil system are listed as Variation C in Table 5 along with the calculated recoil force. The recoil force is well below the load-carrying capacity of the M45 system due to the ballistic impulse being only about half that of the M198 with the M203A1. This system then requires a much shorter recoil stroke and makes it possible to shorten the recoil mechanism components considerably. Reducing the recoil length by 20% provides a corresponding decrease in the mass (based on the earlier assumptions). This variation, D in Table 5, has a shortened recoil mechanism with a weight of 1,400 lb (635 kg) and a recoil force only 76% that of the M198 baseline.

A recoil mechanism having a 1,400-lb mass represents a significant reduction from the M45 recoil mechanism used on the M198. The M45 weighs 2,150 lb (975 kg), and its principal assemblies are tabulated in Table 6 [17]. Table 6 also provides the mass of various components which make up the M45 [18]. This is an average value obtained by weighing seven different disassembled M198s. Note that the sum of the component masses is 140 lb (63.5 kg) shy of the 2,150-lb (975 kg) mass quoted for the M45. The shortfall results from not having a mass value for the sleeve bearing assembly, plus the mass associated with some smaller components is not listed. A recoil system with a 20% reduction in stroke length would allow for shorter rails, recoil cylinder assemblies, and recuperator cylinder assembly. Applying a comparable 20% mass savings to these components yields a 195-lb (88.4 kg) weight savings. The counterweight can be eliminated, netting an additional 454 lb (210 kg) for a total savings of 649 lb (294 kg). The effect of eliminating the counterweight on the weapon systems stability is addressed in the next section.

Additionally, the three yoke assemblies are steel and have a combined mass of 466.3 lb (211.5 kg). Titanium's density, 0.16 lb/in<sup>3</sup>, is 43% less than steel's, 0.283 lb/in<sup>3</sup>. Direct material substitution of titanium for steel nets an additional mass savings of 202.6 lb (92 kg). Direct substitution of materials is probably somewhat unrealistic since a titanium component would likely need to be larger to provide the same load-carrying capability. However, since the lightweight system will have a lower ballistic impulse due to restricting the system to the less severe M119A2 charge and incorporation of a soft recoil system, the components will be required to carry a reduced load. Therefore, the estimate provided by direct material substitution is deemed reasonable. This savings,

Table 6. M45 Recoil Mechanism Component Mass

M45 Recoil Mechanism Component	Component Weight (lb)	Modified Component Weight (lb)
Recuperator Cylinder Assembly	470	376 (20% leng. reduction)
Recoil Cylinder Assembly (2)	271.6 (135.8 ea)	217.3 (20% leng. reduction)
Replenisher Cylinder Assembly	43.6	43.6
Sleeve Bearing Assembly	Not Available	Not Available
Air Cylinder Assembly	70.5	70.5
Rear Yoke	238.8 (steel)	135.0 (titanium)
Middle Yoke	85.7 (steel)	48.5 (titanium)
Front Yoke	141.8 (steel)	80.2 (titanium)
Rails (2)	233.6 (116.8 ea)	186.9 (20% leng.reduction)
Counterweight	454.4	0
Totals	2,010	1,158

plus that achieved by shortening the various recoil components produces a total mass 850 lb (385 kg) less than the M45, resulting in a 1,300-lb (590 kg) recoil mechanism. This is comparable to the 1,400-lb weight cited earlier and lends some credibility to that estimate.

Even with this much lighter recoil mechanism, the total recoil weight stands at 4,010 lb (1,819 kg) (Variation D in Table 5). This is still excessive for achieving a 7,000-lb system. The next attempt at significantly reducing the mass of the recoiling parts was to examine the feasibility of a shorter gun barrel. This represented a departure from the 39-caliber systems presently used by the U.S. Army. Interior ballistic code calculations were made using IBHVG2 [9] to determine at what length of travel the M119A2 charge completely burns out. It was estimated that shortening the cannon length to 29 calibers would provide 23 calibers of travel and optimize the tube length to the burnout rate of the M119A2 charge. The 29-caliber tube reduces the cannon weight by 180 lb (82 kg) getting the recoil mass down to 3,830 lb (1737 kg). This system is reflected in Table 5 as Variation E.

The principal means of reducing the recoil was adopting a soft recoil system to lower the rearward impulse of the recoiling parts.

This allowed the length of the recoil stroke to be shortened and for the overall system weight to be reduced. However, the question arises, is such a soft recoil system feasible? To determine the plausibility of such a soft recoil system design, calculations were made based on soft recoil work done at Rock Island Arsenal (RIA) [19].

Equation 9 can be used to calculate the driving force needed to impart the forward impulse of the soft recoil process. It is assumed that the forward travel distance is one-third of the rearward recoil travel. Based on Variation E in Table 5, the forward travel length would be 1.6 ft (0.49 m). The recoil mass is 3,830 lb (1,737 kg), and the forward impulse was earlier assumed to be 2,300 lb·s (10.23 kN·s). Employing these values in equation 9 produces a resultant force of 14,271 lb (63.4 kN). Using RIA's estimates for fluid and frictional losses [19], an additional force of 3,800 lb (16.9 kN) is added for a total required driving force of approximately 18,100 lb (80.5 kN). Dual 3-in-diameter (76.2 mm) hydraulic cylinders were assumed, and calculations were made using RIA design equations to ascertain the viability of this sizing.

The resultant load-carrying capacity of the dual 3-in cylinders was calculated as 46,789 lb (208 kN). The actual recoil force anticipated is listed in Table 5 as 29,046 lb (129.2 kN). Therefore, the recoil system will operate as desired under normal operating conditions. The details of firing at nonzero elevation and the timing of round ignition to optimize the forward impulse are beyond the scope of this study. However, it should be noted that major concerns for a soft recoil system are the malfunction conditions that occur when there is either a misfire, and no rearward impulse is applied, or when there is a premature fire, so that the round is fired from the latch position with no forward impulse imparted. Traditionally, a redundant recoil system has been required to safeguard against these conditions. This approach is costly and undermines the concept of a lightweight howitzer. It is imperative that any secondary backup system be lightweight to minimize the total system weight.

To protect the system from a failure during firing or recoil, it is proposed to place crushable composite tubes both fore and aft of the barrel as shown in Figure 4. The crush tubes behind the breech would dissipate the recoil energy in the event that the soft recoil cycle failed. The smaller crush tubes forward of the breech provide a means of absorbing the energy due to the forward momentum of the gun during the soft recoil cycle in the event of a misfire. A U.S. patent has been applied for on this technology [20]. In general, the purpose of a crushable tube is to absorb energy through the progressive deformation or fracture of material. This process can be enhanced and controlled through the use of composite materials in the construction of the crush tube.

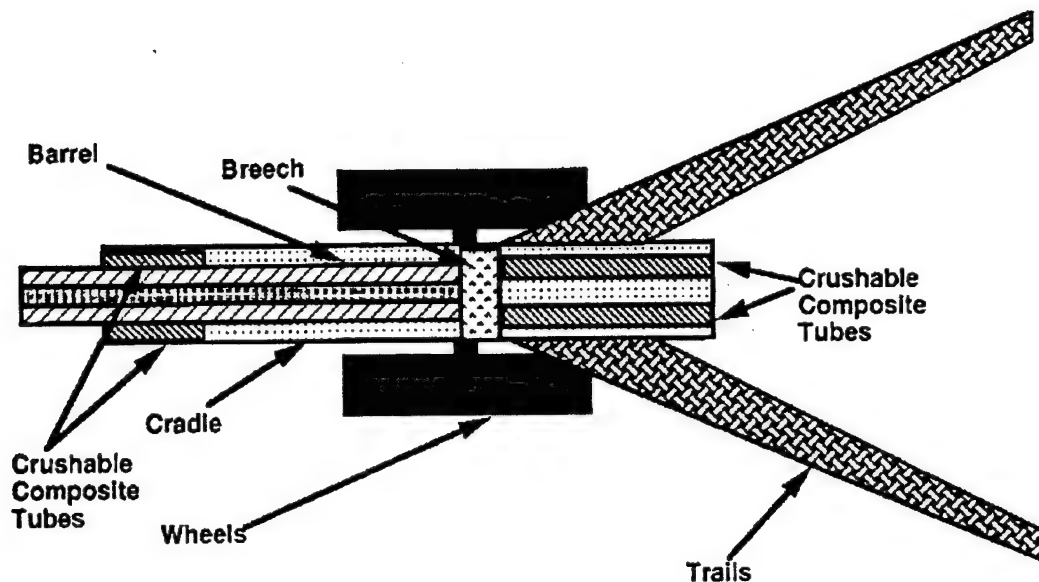


Figure 4. Placement of crushable composite tubes as a secondary backup recoil system

Other advanced recoil mitigation techniques were considered in an attempt to further improve the efficiency of the recoil mechanism. One possible advance currently being researched is the use of electrorheological (ER) fluids, which can be used to increase the viscosity of the fluid in the recoil system to minimize the recoil force. Likewise, "smart" recoil systems, which apply a variable braking force, as needed, during the recoil event, are under investigation [21]. While both techniques show some promise as a means of mitigating recoil, they were not incorporated into the present study because they are considered to be immature technologies at the present time.

#### 4.4 BARREL LENGTH AND CHARGE TRADEOFFS

In order to entirely burn the M119A2 charge in-bore, a minimum travel of 23 calibers is required. This results in a cannon tube having a total length of 29 calibers.

The tradeoff of going to a 29-caliber cannon, of course, is a reduction in the system's effective range. The IBHVG2 code was used to determine the muzzle velocity of a 95-lb (43.1 kg) projectile fired from 39- and 29-caliber 155-mm cannons with the M119A2 charge.

The M119A2 charge, in the 39-caliber M199 cannon, will fire the 95 lb (43.1 kg) M107 round, with a muzzle velocity of 2,260 ft/s (689.0 m/s) to a maximum range of 18,200 m. The muzzle velocity for the M107 round fired with the M119A2 charge from a 29-caliber barrel is 2,080 ft/s (634.6 m/s), resulting in a maximum range of 16,700 m. The reduction in muzzle velocity is approximately 8%. The resulting

reduction in range is also about 8%. Range calculations, using muzzle velocities determined from IBHVG2, were made using the General Trajectory Model (GTRAJ3), which is based on firing tables data [8].

The muzzle velocities for various charges fired in the 29-caliber barrel were determined. The resulting reduction in muzzle velocities produced about a 7 to 9% reduction in maximum range for the various round types examined. Table 7 presents the range capabilities of the 105-mm M119, a 155-mm with the M199 barrel (39 caliber), and the lightweight 155-mm (29 caliber) howitzers for various projectiles and charges. Although the lightweight 155-mm howitzer's reduced charge capability (use of the M119A2 charge instead of the M203A1) and shorter barrel reduce its range performance in comparison to the M198, they provide an approximately 19% percent improvement in maximum range capability over the 105-mm M119 for a nonrocket-assisted launch. For the rocket-assisted (RA) launch, the lightweight 155-mm howitzer has an 8% improvement in range versus that of the 105mm. The lightweight 155-mm howitzer not only provides a range capability superior to the 105-mm M119, but allows for the carrying of substantially greater mass and volume to increase the lethality of the deliverable payload.

Table 7. Range Capability Comparisons

105-MM M119 HOWITZER		
ROUND	CHARGE	RANGE (M)
M913 (RA)	M229	20,100
M760	M200	14,000
M444	M67 ZONE 7	11,200
155-MM M198 HOWITZER (39 CALIBER M199 CANNON)		
ROUND	CHARGE	RANGE (M)
M549A1 (RA)	M203A1	30,300
M549A1 (RA)	M119A2	23,700
M483A1	M119A2	17,800 (air burst)
M107	M119A2	18,200
155-MM LIGHTWEIGHT HOWITZER (29 CALIBER)		
ROUND	CHARGE	RANGE (M)
M549A1 (RA)	M119A2	21,800
M483A1	M119A2	16,300 (air burst)
M107	M119A2	16,700

One concern about adopting a shorter length gun barrel is the affect of the blast overpressure exposure on the crew. To address this concern, two sets of overpressure calculations were made to determine if any deleterious effects were introduced by having a 29-caliber barrel.

First, the 39 caliber, M199 barrel, used on the M198, firing the M203A1 charge was investigated to provide a baseline comparison. The second case looked at a 29-caliber gun barrel firing the M119A2 charge, the top zone charge for the proposed lightweight system. Both cannons were assumed to employ a muzzle break with an efficiency of 0.7. There was little discernible difference between the resulting pressure contours for the two systems. However, the muzzle being 10 calibers closer to the crew for the 29-caliber gun subjects the crew to a higher sound pressure. The calculations found the level at the rear of the 29-caliber gun to be 30 kPa (4.35 psi) versus 22 kPa (3.19 psi) at the breech of the 39-caliber gun.

MIL-STD-1474D sets limits on the maximum permissible impulse noise for an open-air firing of an Army system [22]. To apply the standards, it is necessary to convert the pressure levels to decibels. The sound pressure levels of the 39- and 29-caliber barrels convert to 180.8 dB and 184.1 dB, respectively.

Figure 5 plots lines W, X, Y, and Z to show the allowable exposure limit impulses for various durations. Those data are taken directly from MIL-STD-1474D, as is the information in Table 8 that lists the maximum permissible number of exposures per day for the various impulse noise limits for someone wearing both ear plugs and muffs for hearing protection [22]. Under the guidelines in MIL-STD-1474D, sound pressures above the Z-level are considered to be excessive for military systems.

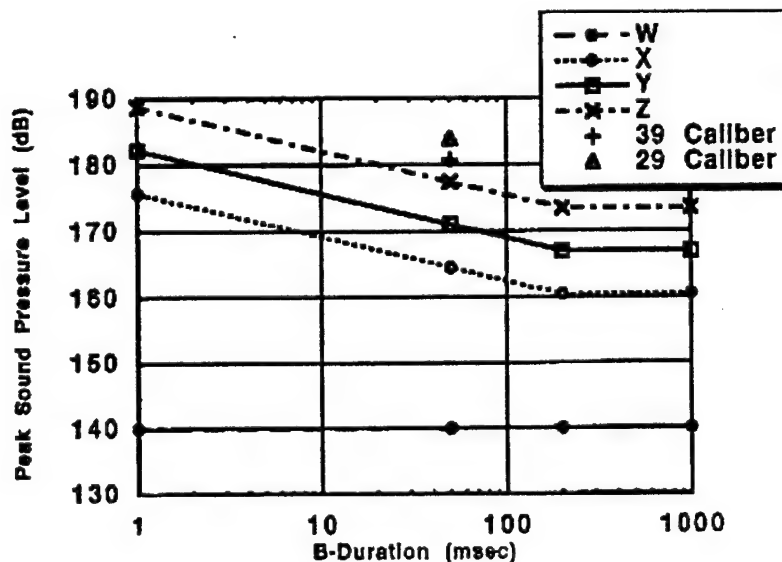


Figure 5. Peak sound pressure limits vs. B-duration for impulse noise

Table 8. Impulse Noise Daily Exposure Limits

Impulse Noise Limit	Maximum Permissible Number of Exposure/Day		
	No Protection	Either Plugs or Muffs	Both Plugs and Muffs
W	-----Unlimited Exposure -----		
X	0	2,000	40,000
Y	0	100	2,000
Z	0	5	100

The sound pressure values for the 29 and 39 caliber gun barrels are shown in Figure 5, and both exceed the Z-level limit imposed by MIL-STD-1474D. Therefore, based on the MIL-STD, both systems are unacceptable. However, the 39-caliber case corresponds to the M198 howitzer, which is a fielded system. Further research found that previous work had identified the M198 as exceeding the allowable impulse noise limits [23]. This work helped spur a review of the sound pressure limits by the Office of the Surgeon General and ultimately resulted in proposed changes to Blast Overpressure (BOP) Health Hazardous Assessment (HHA) procedures. These new HHA procedures proposed a new allowable peak impulse level of 187 dB for 100 exposures/day for a system, such as a howitzer, having a B-Duration of less than 60 ms [24]. The HHA also states that for peak pressure levels below 187 dB, the allowable number of rounds per day will be doubled for each 3-dB decrease. Thus, under the Surgeon General's guidelines, the 29-caliber barrel becomes a viable option for a 155-mm howitzer with an allowance of up to 200 rounds/day for a given gun crew. In addition, it should be noted that rotation of the crew to various weapon service stations would reduce the individual exposures and permit an increase in the allowance of rounds fired per day by a particular crew.

#### 4.5 FURTHER COMPONENT WEIGHT REDUCTIONS

Combining the recoil system listed as Variation E in Table 5, having a weight of 3,830 lb (1,737 kg), and the howitzer components derived from the ARDEC study listed in Table 3, weighing 4,820 lb (2,186 kg), yields a howitzer with a mass of 8,550 lb (3,878 kg). Further reductions in mass of the howitzer components are achievable because of the reduced system recoil, 26% less than the M198, and the overall lightening of the structure.

The data for the MTL designed trails in Table 2 may be scaled up to estimate the weight of a trail 12 ft (3.66 m) long. The lightest design in the MTL study weighed 106 lb (48 kg) for a length of 110 in (2.8 m), which scales to 139 lb for a 12-ft design. This represents a significant mass savings from the 627 lb (284 kg)

individual trail weight used in the ARDEC study. This translates to a total weight savings of 976 lb (443 kg) for the two trails, putting the mass of lightweight howitzer at 7,575 lb (3,436 kg).

Table 3 lists numerous components that may be made less massive due to the reduction in recoil force. With modifications to the trails having already been made previously, the three largest components where weight savings may be attained are the carriage weldments, both top and bottom, and the cradle. Assuming a weight reduction equivalent to the reduction in recoil force, 26%, produces a total weight savings of 469 lb (213 kg).

A final area for consideration of weight reduction is the wheel and axle assembly. The ARDEC study design was based on the wheels and axle supporting the weight of the M198. The lightweight howitzer design has a weight of less than half the M198 so it is reasonable to assume that the wheel and axle assembly weight may be cut in half. This provides another 380-lb (172 kg) weight savings.

Table 9 is a compilation of the various howitzer components and provides a comparison against the ARDEC study values from Table 3. The recoil mechanism is taken from Variation E listed in Table 5. The total system weight for the lightweight howitzer adds up to 6,821 lb (3,094 kg). This meets the goal of a howitzer weighing less than 7,000 lb and provides some room for weight growth if some estimates in the analysis prove to be overly optimistic.

Table 9. Lightweight Howitzer Component Mass

System Component	ARDEC Wgt (lb)	LWT How. Wgt (lb)	Basis for Wgt Reduction
Recoil System & Cannon	-----	3,730	Variation E in Table 5
Trails	627 ea	139 ea	Scaled MTL Design
Wheel & Axle Assembly	763	380	50% Reduction in Overall System Weight
Top Carriage	560	414	26% Reduced Recoil
Bottom Carriage	538	398	26% Reduced Recoil
Cradle	706	522	26% Reduced Recoil
Other Components	999	999	No Change
Total Weight		6,821	

## 2.6 STABILITY CONSIDERATIONS

The analysis has shown that significant mass reductions are achievable on a 155-mm howitzer. One consequence of having a lighter system is it becomes more difficult to minimize the howitzer "jump" or "hop", which necessitates repositioning prior to the next shot and subsequently reduces the firing rate. Thus, it was necessary to determine the 7,000-lb howitzer's stability requirements before declaring it as a realistic possibility.

Figure 6 shows a simple representation of a howitzer. The vector  $W_w$  represents the entire system weight acting through the weapon's center of gravity.  $F_r$  is the recoil force acting along the axis of the gun barrel. The figure is drawn showing a horizontal firing plane with the height at which the recoil force acts above ground denoted as  $H$ . The horizontal or direct-fire position represents the most severe overturning moment and is considered to provide a worst case for the stability analysis. The trail length is shown as  $L$ . These parameters are used in the governing stability equation [16] given as

$$F_r * H < W_w * L \quad (10)$$

Equation 10 can be rearranged to

$$H < \frac{W_w * L}{F_r} \quad (11)$$

Using values from the mass tradeoffs in the previous section, a weapon weight of 7,000 lb, a trail length of 12 ft, and the recoil force from Variation E of Table 5 can be used to calculate the maximum allowable trunnion height. Substitution of the values into equation 16 shows that the lightweight howitzer must have a trunnion height of less than 33.8 in (0.86 m). The current M198 trunnion height is 48 in (1.2 m). However, a lower trunnion height of 25.6 in (0.65 m) has been employed successfully by VSEL [25]. Therefore, the 7,000-lb howitzer's stability can be assured with a 30-in (76 cm) trunnion height. The lower trunnion height also provides the added benefit of requiring a smaller and, in turn, less massive lower carriage as was assumed as part of the previous geometry modifications.

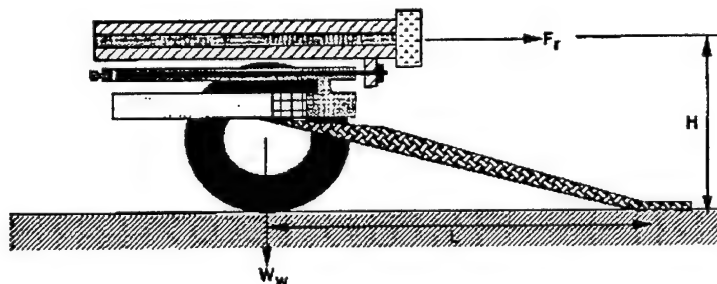


Figure 6. Howitzer sketch with reaction loads

### 3.0 CONCLUSIONS

The purpose of this study was to identify an artillery system capable of providing the light maneuver forces with 155-mm firepower and lethality while meeting their mobility requirements. A review of the towing capacity of various vehicles showed that a howitzer weighing 7,000 lb could be towed off-road by a 2.5 ton truck and lifted by a Blackhawk helicopter, thus making it a viable option for a light force unit.

Subsequently, a study was done to see what weight saving measures could be taken to reach the 7,000-lb goal weight. It was hoped that starting with the 15,800-lb M198 system, changes could be implemented to reach the design goal weight while maintaining the range capability.

Use of composite materials and lightweight metals such as titanium provided a 20% mass savings. Tailoring the barrel geometry to more closely match the in-bore pressure profile and incorporating a soft recoil system provided a further weight reduction from the M198 of 10%. Subsequent geometry changes to the rear trails and recoil cylinder were not substantial enough to reduce the projected weight of the howitzer below 8,500 lb (3,856 kg).

Restricting the maximum allowable charge to the M119A2 (as opposed to the M203A1) proved to be the final step needed to reach the desired weight level. The less severe M119A2 charge allowed for a less massive breech and barrel and a shorter caliber cannon and reduced the size of the howitzer support structure. The combination of these changes resulted in a 7,000-lb lightweight howitzer being deemed possible. This restriction reduced the maximum range of a nonrocket-assisted projectile from 22.0 to 16.7 km. However, this 16.7-km range still exceeds the capability of the current 105-mm towed howitzer employed by the light forces.

This study, while being purely analytical, used realistic projections based on today's technologies. The results of the study predict that a 7,000-lb howitzer can be designed by adopting composite component parts, adding a soft recoil system, and using the M119A2 as the top zone charge. Such a system would provide 155-mm lethality at ranges beyond those currently attainable by 105-mm howitzers.

### REFERENCES

- [1] Foss, C. F. Editor. *Jane's Armour and Artillery 14th Edition 1993-1994*. Coulsdon, Surrey, UK: Jane's Information Group Limited, Sentinel House, 1993.
- [2] Headquarters, Department of the Army. "Transportation Reference Data," Field Manual No. 55-15, Washington, DC, 9 June 1986.

- [3] *Jane's Military Vehicles and Ground Support Equipment 1986*. Coulsdon, Surrey, UK: Jane's Information Group Limited, Sentinel House, 1986.
- [4] MTL. "Material Tradeoff Studies for the Trails of the 155mm Lightweight Towed Howitzer," Draft Report, U.S. Army Materials Technology Laboratory, October 21, 1982.
- [5] Fire Support Armaments Center. "M198 Weight Reduction Report," Draft Technical Report, U.S. Army Armament Research, Development, and Engineering Center, Artillery Armaments Division, 1995.
- [6] Restifo, S. U.S. Army Armament Research, Development, and Engineering Center, Close Combat Armaments Center, Benet Laboratories, Watervliet, NY. Private Communication with L. W. Burton, U.S. Army Research Laboratory, Weapons Technology Directorate, September 1995.
- [7] Paladin - Office of the Product Manager. "155mm Artillery Weapon Systems Reference Data Book," U.S. Army Armament Munitions & Chemical Command, Picatinny Arsenal, NJ, December 1990.
- [8] Firing Tables. "Firing Tables for Cannon, 155mm Howitzer, M199 on Howitzer, Medium, Towed, 155mm, M198 Firing Projectile, HE, RA, M549A1," FT-155-AO-0, U.S. Army Research Laboratory, Aberdeen Proving Ground, MD, June 1991.
- [9] Anderson, R. D., and K. D. Fickie. "IBHVG2 - A User's Guide." BRL-TR-2829, U.S. Army Ballistic Research Laboratory, Aberdeen Proving Ground, MD, July 1987.
- [10] Underwood, J. H., and A. P. Parker. "Fatigue Life Analysis and Tests for Thick-Walled Cylinders Including the Effects of Overstrain and Axial Grooves," U.S. Army Armament Research, Development and Engineering Center Close Combat Armaments Center, Benet Laboratories, ARCCB-TR-94038, September 1994.
- [11] Paris, P. C. "Fatigue - An Interdisciplinary Approach," *Proceedings, 10th Sagamore Conference*, Syracuse University Press, Syracuse, NY, p. 107, 1964.
- [12] Paris, P. C., R. E. Gomez, and W. E. Anderson. "A Rational Analytic Theory of Fatigue," *The Trend in Engineering*, Vol. 1, n. 1, University of Washington, 1961.
- [13] Ewalds, H. L., and R. J. H. Wanhill. *Fracture Mechanics*, Edward Arnold, New York, 1989.
- [14] Hertzberg, R. W. *Deformation and Fracture Mechanics of Engineering Materials, Third Edition*, John Wiley & Sons, New York, 1989.
- [15] Parker, A. P., and J. H. Underwood. "Stress Concentration, Stress Intensity, and Fatigue Crack Growth Along Evacuators of

Pressurized, Autofrettaged Tubes," U.S. Army Armament Research, Development and Engineering Center Close Combat Armaments Center, Benet Laboratories, ARCCB-TR-94046, December 1994.

[16] Fire Support Armaments Center. "155mm Lightweight Towed Howitzer Range vs. Weight Trade-off Study," U.S. Army Armament Research, Development, and Engineering Center, Artillery Armaments Division, 1991.

[17] Medium Artillery Systems Office. "Howitzer, 155mm, Towed, M198 - Revision 3," Weapons Systems Management Directorate, HQ, U.S. Army Armament, Munitions, and Chemical Command, Rock Island, IL, March 1989.

[18] Murray, R. M. Provided experimental measurements for the components of seven M198 howitzers. U.S. Army Research Laboratory, Aberdeen Proving Ground, MD, 1995.

[19] Bowrey, G. "Feasibility Study - Lightweight 155mm Howitzer Using Hybrid Recoil Concept," Draft Technical Report, Science and Engineering Directorate, Rock Island, IL, October 1994.

[20] Hoppel, C. P. R., L. Burton, R. Kaste, and B. Burns. "Devices for Dissipating Recoil Energy," U.S. Patent Pending, U.S. Army Research Laboratory, Aberdeen Proving Ground, MD, February 1996.

[21] Floroff, S. G. "Recent Advances in Artillery Recoil Design," U.S. Army Armament Research, Development, and Engineering Center, Presented at the Recoil Workshop, Aberdeen Proving Ground, MD, November 14, 1994.

[22] Department of Defense. "Interface Standard for Noise Limits," MIL-STD-1474D, Missile Command, Redstone Arsenal, AL, 30 June 1993.

[23] Salsbury, Mark J. "Blast Overpressure," ARLCD-TR-81022, U.S. Army Research and Development Command, Dover, NJ, September 1981.

[24] Department of the Army. "Proposed Changes in Blast Overpressure Health Hazard Assessment Procedures, Final Recommendations," Memorandum from the Commander, U.S. Army Medical Research and Development Command, Fort Detrick, Frederick, MD, December 1990.

[25] Floroff, S. G., G. Powers, L. Marazita, and J. Lipinski. "Evaluation of the Vicker's Shipbuilding and Engineering Limited's Lightweight 155mm Towed Howitzer," ARFSD-TR-91037, U.S. Army Armament Research, Development, and Engineering Center, Picatinny Arsenal, NJ, January 1992.

**TITLE: DESIGN SOFTWARE AND VERIFICATION STUDIES FOR FIBRE  
COMPOSITE OVERWRAPPED GUN BARRELS**

A.GROVES\*  
A.HOWARD  
M.J.HINTON

STRUCTURAL MATERIALS CENTRE  
DEFENCE RESEARCH AGENCY  
FORT HALSTEAD  
SEVENOAKS  
KENT  
TN14 7BP  
ENGLAND

\*TEL 01959 - 515043

\*FAX 01959 - 515069

**ABSTRACT**

The requirement to increase the strike velocity of long rod penetrators for the defeat of advanced armour has led to the need to design tank gun barrels with increased length, calibre and working pressure. The penalties resulting from this are increased barrel weight and a detrimental movement in the centre of gravity away from the breech. In addition, there may be a reduction in the natural frequency of flexural vibrations, which can lead to a loss of accuracy.

For a tank barrel the adverse movement of the centre of gravity of the barrel has particularly serious consequences. For example, the inevitably larger countermass bulk in the breech region area sweeps out greater volume within the turret as the gun is slewed. This, in turn, increases the height and length of the turret leading to increased vehicle signature. This effect is also likely create severe problems if an upgraded gun is deployed within existing vehicles.

Advanced fibre composites have unidirectional specific strengths and stiffnesses of the order of five times those of gun steels. The use of such materials has the potential to greatly alleviate some of these problems by allowing the steel, in selected sections of the gun barrel, to be replaced by a composite overwrap of similar volume and much lower density. Several options are possible; a lighter gun can be built with the same performance of an all steel design, a substantially higher working pressure for the same weight, or a longer barrel with no outward shift in barrel C of G. The latter permits operation within existing limits on trunnion balancing moments.

The high specific moduli of advanced composites can also be used to improve accuracy via reduced muzzle droop, enhanced flexural stiffness and increased natural frequency.

The Defence Research Agency (DRA) has been actively researching the use of composite overwrap technology for tank gun main armament for the last 8 years. This

work has embraced a number of facets, including fundamental materials research through to barrel manufacture and firing trials. Firing trials have been conducted at both small (30mm) and large (120mm) calibres.

The design of such barrels represents a significant departure from conventional design theories. As a result, it is essential that new design capabilities are developed if overwrapped barrels are to reach their full potential. Such a design capability is being developed within DRA and includes the following features:

- Predicting the stress state in the barrel due to fabrication, firing and thermal effects.
- Analysing the stress distribution at the overwrap termination position.
- Predicting barrel thermal response as a function of firing scenario.
- Assessing barrel frequency response and muzzle droop as a function of overwrap configuration.
- The provision of a comprehensive materials data base.
- Barrel optimisation routines
- Simple to use pre- and post-processor modules.

All design software is fully underpinned by comprehensive trials and testing programmes.

This paper provides a summary of this design capability and reviews the underlying validation exercises performed to date.

\* **BIOGRAPHY:** Entered MOD in 1980 PERME Westcott. Rocket Motor Research. Gained PhD through R & D activities. Transferred to DRA Fort Halstead 1989 undertaking novel materials applications for land based systems.

\* **PRESENT ASSIGNMENT:** Technology Chief - Composite Structures

\* **PAST EXPERIENCE:** Design and development of high performance pressure vessels and weapon platforms

\* **DEGREES HELD :** BSc(Hons) Aeronautical Engineering.  
PhD Overwrapped Rocket Motors.

## **DESIGN SOFTWARE AND VERIFICATION STUDIES FOR FIBRE COMPOSITE OVERWRAPPED GUN BARRELS**

A Groves\*  
A Howard  
M J Hinton

Structural Materials Centre  
Defence Research Agency  
Fort Halstead  
Sevenoaks  
Kent  
TN14 7BP  
ENGLAND

\*Tel 01959 - 515043  
Fax 01959 - 515069

### **1 Introduction**

For the last 150 years or more, almost all gun barrels, from the small hand guns of the 19th century to the large ordnances mounted on battleships in World War Two, have been fabricated from steel. As a consequence, the metallurgy, fabrication routes and design procedures for steel gun barrels are highly developed. There remain a number of areas for further development of steel gun technology, but, perhaps with the exception of breakthroughs in coating technology to extend the wear life, these are likely to provide small increments in performance over the current situation.

With the now widespread adoption of advanced fibre reinforced composite materials into military equipments, it is logical to consider if the high specific strengths and stiffnesses of these materials may offer the gun designer a major technological advance. It is perhaps interesting to note that the Chinese had already pioneered the concept of using fibre reinforcement in lightweight siege guns in the 15th century, and the Dutch had constructed ship mounted cannons in the 17th century, using a malleable liner reinforced with shrink fit hoop 'windings'. Bearing in mind these previous lessons, the UK Defence Research Agency (DRA) has an active research programme to investigate the practicalities of designing gun barrels with today's advanced materials.

The approach taken by the DRA is based on the principle that advanced fibre composites can be used to strengthen and/or stiffen selective regions of a steel gun barrel. The more radical approach, which is to fabricate a gun barrel entirely from advanced composites, has not been pursued to date, as a steel liner is considered to be essential to provide the necessary wear life and rifling features. At a future juncture, wear resistant ceramic liners may provide a more promising alternative. An overwrapped demonstrator barrel is shown in figure 1.

The principal focus of the UK programme is, therefore, to develop reliable design tools for selectively reinforced gun barrels. This paper provides an overview of the progress to date.

## **2 Design Code Philosophy**

The DRA has, over a number of years, developed a generic, menu driven, conventional gun barrel design capability for use on a high performance PC computer. The capability covers all issues pertinent to the design and integration of an all-steel gun barrel into a gun platform, albeit a main battle tank or artillery gun. The capabilities therefore cover:

- Strength of design based on known material properties and acceptable autofrettage conditions
- Gun recoil, covering the types of recoil systems and resulting recoil forces based on the systems adopted
- Barrel frequency and droop response as a function of support configuration and barrel furniture
- Barrel heating at the C of R as a function of charge mass and type, projectile muzzle velocity, atmospheric conditions, etc

Since this capability was already in existence, it was considered vital that any software developed for composite reinforced barrels should form an integral part of this design package for the following principal reasons:

- Any composite barrel design will use a considerable number of features common to an all steel barrel design, i.e. common internal ballistic, common gun steels for the liner, gun barrel heating, frequency and droop behaviours, etc.
- Minimise learning times and make composite overwrap design techniques more straight forward to designers familiar with all-steel barrel designs
- Enable design improvements to be easily assessed by comparing all-steel vs composite reinforced barrel designs
- Avoid software duplication and associated support costs

As a result five additional modules, **MATDBASE**, **RADHT**, **GTUBE1**, **GTUBE2** and **OVERWIND** were implemented into the gun barrel design suite to cover those design issues relevant to composite reinforced gun barrels. These modules perform the following functions:

- **MATDBASE** - A materials and charge data base into which all design input parameters are stored.

- **RADHT** - Barrel heating. It is recognised that a composite reinforced barrel will heat up quicker due to the overwraps insulatory properties.
- **GTUBE1** - Predicting barrel droop and frequency response as a function of overwrap position. This is a heavily automated module so that effect of overwrap position and length on barrel behaviour can be easily assessed.
- **GTUBE2** - Models the pre-stressing process of the overwrapped gun barrel. Several mechanisms are available to achieve this objective including tension winding, shrink-fitting and autofrettage. At the time of writing an autofrettage pre-stressing route is not available since it was felt that insufficient pre-stress can be achieved in a thin walled steel liner via this route. This philosophy is, however, currently being reviewed.
- **OVERWIND** - Modelling the overwrap termination region to avoid potential areas of stress concentration.

The manner in which these modules are implemented and called from the design code is illustrated in figures 2 and 3. In these two figures, the first two menus on entering the gun design software are shown. Figure 2 outlines the principal options available, these being:

- **Composite Total Design.** This option provides a completely automatic design procedure for a composite reinforced gun barrel based on a very small number of input parameters to define internal ballistic requirements, material properties and shot length. This option automatically calls the appropriate design modules as necessary. This element of the code is still under development, but uses all of the individual codes discussed below.
- **Individual Access to Design Codes.** This provides direct access to the modules described earlier together with **Barrel Design** (design modules for all-metal barrels) and **Recoil Design**. These options are illustrated in figure 3.
- **Ancillary Design Codes.** This facility covers a number of additional codes that cover, essentially, systems studies and earlier design codes which have been retained for checking purposes. They do not form part of the composite gun barrel modules and therefore are not discussed further.

A description of the five composite gun barrel modules is given in the following section, together with a summary of module operation, features and verification activities.

### 3 COMPOSITE GUN BARREL DESIGN MODULES

#### 3.1 Materials and Charge Data Base

The development of a materials and charge data base was seen as a vital element of the composite reinforced barrels design package. This requirement arose to ensure that:

- Material properties are retained and protected
- Data can be automatically accessed from the composite reinforced gun barrel design modules to ensure that consistent data is used in all studies
- Data is validated. This is particularly acute for orthotropic materials where violation of the thermodynamic constraints on material properties can be easily achieved. This information is stored in four menu options. The first two modules are broadly identical and contain the material constants necessary for gun design, including barrel heating. A typical data base screen for the composite reinforcement is illustrated in figure 4. Methods for obtaining this data are described latter in chapter 4.

The remaining two options are for the charge. This split arises from historical developments and efforts are in hand to merge the two databases. The data bases are essentially identical in appearance to figure 4. Data covers all internal ballistics information including charge mass and muzzle velocity. Methods for obtaining the gas conductivity, viscosity, flame temperature, etc, are heavily dependant on complex combustion physics which is beyond the scope of this paper.

In all data base options, a range of facilities are offered including search and editing of data together with various options for printing the data either by particular material or charge or as a complete database.

### **3.2 RADHT**

#### **3.2.1 Description**

RADHT is a one-dimensional radial heat transfer code for predicting the transient heating of a gun barrel, albeit all-metal or composite reinforced. The use of a one dimensional code is considered fully acceptable for predicting barrel heating, particularly for those areas away from the breech block or overwrap termination regions where radial heat transfer dominates the problem. For those other regions, the increased thermal mass offered by the additional steel present reduces barrel heating. In so, doing programme predictions always remain conservative. This is seen as a prudent design philosophy given the relatively low operating temperatures of composite overwraps compared to steel.

The programme utilises its own internal ballistics module for predicting the heat transfer to the bore of the barrel, based on barrel dimensions, material properties, charge details, firing scenario and barrel cooling parameters (both internal and external). Environmental conditions are also covered within the programme through adjustments in the external heat transfer conditions. An initial uniform temperature of the barrel can also be prescribed.

Since the code is one-dimensional, barrel temperatures are calculated at defined axial positions, or sample sections. The thermal results can then be plotted, either as a function of radial position for a specified time, as a function of time for a particular

radius of the barrel or finally as a function of barrel axial position for a given radial position and time.

### **3.2.2 Module operation**

As per the materials data base module, all data is input, analysed and post processed via a simple menu facility. The options within this menu are reviewed below.

**Geometry** - this is used to input barrel liner geometry as a series of blocks, the external radii at the start and finish of each block being requested automatically, as is block length. The bore radius is the first parameter requested when entering this menu option. A typical geometry is shown in figure 5. Additional features offered include a modification facility to edit existing geometry details, a vertical scale multiplication factor to magnify barrel radial thickness to aid viewing and a delete option to remove blocks. Composite reinforcement is provided through the reinforcement table, whereby overwrap or axial reinforcement thicknesses are defined for a particular block. Reinforcement thicknesses are held constant over a block length. The use of a tapered layer of reinforcement is considered unlikely due its additional manufacturing complexities.

**Material Properties** - provides the facility to define component material properties. This is provided by an identical graphical image to that shown in figure 5 with the exception of an additional display of the thermal material data at the bottom of the screen. Material selection is then performed via movement of the mouse, with data being taken directly from the materials data base. Geometry colour is changed to assist in identifying which barrel material is being defined.

**Charge Details** - enables the internal ballistics to be defined. As for material definition, charge details are taken directly from the charge data bases. Selection is achieved via movement of the mouse and a typical screen is shown in figure 6. Additional data requested includes initial barrel temperature and ambient temperature. Two further inputs are required to define the time step for numerical solution to the transient heat transfer equations and the output time interval. These are provided to give the operator control over the solution process. Clearly large numbers give rapid run times but poor numerical accuracy, small numbers vice-versa.

**Fire Scenario And Bore Cooling** defines the firing scenario and bore cooling details. Here a table is entered covering rate of fire (rounds per minute), period of firing or cooling followed by the internal heat transfer coefficient and internal fluid (gas) temperature, see figure 7. Calculation of the heat transfer coefficient is complex, but since barrel cooling via the bore is generally small, experience has shown that a value of  $5 \text{ W/m}^2\text{K}$  yield satisfactory results. A limitation of the module is the inability to charge adjust, but this is currently being rectified.

**External Barrel Cooling Details** dominates the cooling process and is defined via a table, similar in the form, to the firing scenario. Barrel cooling parameters are defined for each barrel block. Since heat transfer can be both via convection and radiation, parameters are required for the heat transfer coefficients and surface emmissivities. As

these parameters are recognised as being key elements to barrel cooling, graphs and tables are available for these parameters based on surface finish and environmental conditions.

**Sample Sections** defines the axial positions for analysis. These axial positions are input into a box located beneath an image of the barrel to illustrate their positions visually. Each sample position is given a unique identification number, as depicted in figure 8.

**Graphs** enables a selection of graphs to be plotted following programme execution. These are:

- barrel heating through the wall at a selected time
- temperature vs time for a selected sample section and radius
- along the barrel length for a selected time and surface

Typical barrel temperature plots are shown in figures 9 and 10. In figure 9 the temperature variation through the barrel is shown for sample position 1, i.e. at the commencement of rifling 900 seconds after firing. In the latter figure the temperature history at the same sample position is shown but for the outside of the barrel. Hardcopy plots plus tabulated results can be output as required.

### 3.2.3 Code validation

In order that the heating code can be used with confidence a considerable number of gun barrel heating studies have been conducted for a range of ordnance, from small arms to artillery and tank guns. For smaller calibre barrels firing trials have been undertaken within DRA using instrumented barrels and accurately controlled firing scenarios. For the larger calibre barrels results have been taken from various instrumented firing trials conducted under various MOD programmes including both deep bored and surface thermocouples.

To illustrate a typical program accuracy, theoretical vs measured temperature histories are plotted in figures 11 for a UK artillery gun. As can be seen, given the relative simplicity of the programme, the correlation between theory and experiment is excellent.

## 3.3 GTUBE1

### 3.3.1 Description

**GTUBE1** is a comparatively straightforward beam element finite element code for predicting the droop and natural frequency response of a gun barrel tube. No damping options are available at present. The barrel is assumed to be rigidly fixed at the rear of the barrel, either at the breech or more frequently at a barrel support or bearing position. This is fully consistent with traditional design practices.

In general such codes usually request the data to be input in the form of a beam length together with its second moment of area, which can differ at either end of the beam if

tapers are used. While for gun barrels, which are essentially simple beam structures, the evaluation of the second moment of area is a straight forward exercise it was nevertheless felt that inputting barrel geometry into the module via a simple menu driven interactive pre-processor would facilitate data entry and minimise errors. The menu format was also designed to be fully compatible with all other modules in the gun barrel design suite.

In addition to facilitating data input, considerable attention was given to offering an optimisation capability such that the overwrap position and length on the barrel can be optimised to maximise barrel frequency response, while minimising barrel droop. An ability to compare any benefits directly to a reference barrel, essentially a monolithic steel barrel variant, was also considered as highly beneficial. These two objectives were met via the following module options:

- The overwrap is permitted to "float" on the exterior surface of the barrel. That is for two adjacent beam element sections the external overwrap termination position is permitted to vary automatically from the start of one section to the finish of the other. Thus plots of barrel frequency, droop and weight trends can be plotted vs overwrap position along the barrel.
- By splitting the module into essentially two identical sub-modules, the first defining the reference barrel, the second the re-designed barrel. These two sub-modules only differ in that the overwrap "float" option is not available for the reference barrel option, although composite overwraps can be applied if desired.

With these two powerful features very quick design optimisation can be achieved with minimal effort on part of the design engineer.

Barrel furniture, e.g. MRS, fume extractor, muzzle brake, cannot at present be added in the form of point of point loads, but this can be resolved by applying a pseudo reinforcement layer of appropriate density to yield the correct loading.

### **3.3.2 Operation**

Initiation of the **GTUBE1** module is achieved by selecting **GTUBE1** from the Main Analysis Selection menu; figure 3. On entering the module the option is made available to select either the reference barrel or design barrel sub-module. As described previously these two sub-modules are broadly identical, with the exception of the overwrap "float" option not being available for the reference barrel. For the purposes of this paper the procedure for setting up a design barrel is therefore described. It is assumed, however, that a reference barrel has been pre-defined and has been selected as the reference barrel from which design comparisons can be made.

Barrel geometry is achieved via the Geometric data input screen, see figure 12, although prior to the screen illustrated, the bore radius and number of beam element lengths will have been requested. Data is then entered systematically, providing each beam length followed by the radii at its start and finish. Overwrap thicknesses are then requested, up to a maximum of three layers, with zero thickness interpreted has no

overwrap material present. As per **RADHT**, the overwrap thickness is taken constant over a beam length for the reasons previously stated.

Material selection is then defined automatically for the liner material and the various reinforcement layers. A manual override is nevertheless supplied if required. A zoom facility is also provided to enlarge barrel regions to aid manual material selection, the very large aspect ratios of gun barrels making it difficult to identify the various components of the barrel, as is seen in figure 12.

Barrel optimisation can then be invoked via the **Fixed Selection Menu** as illustrated in figure 13. For the example shown, the overwrap is permitted to "float" over beam sections 3 and 4. In this case the overwrap start position is assumed to start at the end of section 4 while the termination region "floats" from the end of beam section 4 (no overwrap all metal barrel) to the start of section 3 (overwrapped over the full length of sections 3 and 4). The approach of permitting the overwrap to start at the forward end of the barrel and progress rearwards arises directly from a consideration of the behaviour of beams. Both frequency and droop are improved if weight is reduced at the front of a cantilever beam.

On completion of the analysis, option facilities are available to plot the barrels frequency, droop, mass and muzzle angle as a function of overwrap position, either non-dimensionalised relative to a pre-selected reference barrel or individually. A typical non-dimensionalised plot is shown in figure 14.

It is perhaps interesting to consider the trends shown in figure 14, particularly those relating to barrel droop and frequency responses. As can be seen, these go through distinct optima, which to a first order approximation, indicates that only the forward half of the barrel need be overwrapped if these parameters are the principle design drivers. The effect of axially stiffening, not shown, yields a similar result, although the optimum overwrap length is considerably longer than then depicted here and not so pronounced. Such features illustrate the potentials offered by overwrap technology and the need for easy to use automated design software.

### 3.3.3 Validation

Two validation techniques have been employed. The first for droop has been to compare, for simple problems, predicted results against theoretical predictions using classical engineering bending theory modified to include multi-material structures. In all cases assessed, accuracy has been well within 1%.

For frequency predictions a series of barrel vibration tests have been undertaken. Such a test consists of fixing an axially strained gauged barrel into a rigid mounting and then taping the muzzle to initiate barrel vibrations. A typical set up is shown in figure 15. Using transient data capture techniques, the longitudinal strain arising from barrel vibrations is then recorded. Given that high quality of the strain results are obtained, fast Fourier processing can then be conducted to determine at least the first 3 modes of vibration. These results have then been compared with theoretical predictions and found to be within 2-5% difference. This simple test can also be used to explore barrel damping characteristics, particularly for composite reinforced barrels, where damping

may be significant. If so this is seen as a further major benefit of overwrap technology. If so damping will be included into **GTUBE1**.

### **3.4 GTUBE2**

#### **3.4.1 Description**

**GTUBE2** is a series of closed form analytical stress and strain solutions for predicting overwrapped barrel pre-stress either via tension winding or shrink-fitting. The use of an autofrettage route is not available at present, but is an additional feature which is currently being considered for implementation.

The underlying theory is based on classical elasticity theory and structures of revolution but include the necessary additional orthotropic materials parameters for the composite overwrap.

Tension winding is modelled as the application of a succession pre-stressed bands, each band being applied one on top of each other. The induced pre-stress in the liner is then the summation of the pre-stresses for each applied layer. A similar approach is adopted for the overwrap, with the resulting stress being the sum of its winding stress plus stress reductions due to the application of subsequent layers. A further refinement to the code is to replace the resulting summations in the programme by an integral expression to greatly aid run times, particularly when large quantities of thin layers are applied.

For the shrink-fit option the barrel is assumed to be cooled and the overwrap sleeve then applied. This arises from the fact that the composite overwrap exhibits negligible expansion due to its low thermal expansion coefficients. Theory is again classical elasticity theory.

In addition to the pre-stressing facilities, the module also includes facilities for modelling barrel response to internal pressure and temperature excursions about ambient. The latter assumes the temperature gradient is exponentially varying through the overwrap and liner to facilitate the development of an analytical solution. An optimisation routine is also supplied to determine the optimal overwrap thickness vs liner thickness, for a prescribed winding tension, to satisfy a required barrel bore stress.

A full post-processing facility is provided in the form of graphs plotting stress and strain vs radius in all three principal directions. For the optimisation routine, where reinforcement thickness vs liner thickness is plotted, an interactive stressing option is provided to enable liner and overwrap stresses to be assessed for selected liner configurations.

#### **3.4.2 Operation**

The module is again menu driven, in the form of a series of automated input screens for entering material properties, geometry and component loading. The material input and title screen is shown in figure 16, and covers both the liner and overwrap material. Material selection is via mouse selection direct from the materials data base.

Component dimensions and loading is via the analysis selection screen, as shown in figure 17. Dimensions are requested first, as indicated. For the overwrap optimisation option, the upper and lower limits on liner thickness are specified together with an option to define the number of data points between these limits.

Pre-stressing is via tension winding or shrink-fitting as previously discussed. For tension winding the winding stress can be either constant for the whole winding event or varied between a start and finish value. Alternatively for shrink fitting, the liner temperature is specified relative to ambient.

Internal pressure is also specified within this table as is the temperatures at the bore, liner/overwrap interface and external surface. A reference temperature is also supplied, denoting the ambient temperature at which manufacture took place.

Finally two end constraints are provided. Open ended, whereby the barrel is free to move axially as the barrel radial distorts under applied loading, and fixed ends whereby the barrel is not free to move axially. The latter can exert very high axial loads in the barrel. These two options nevertheless provide bounding stressing solutions for gun barrel design if required.

On running the programme, the designer is automatically presented with a circumferential stress plot as shown in figure 18. Other options, to look at the stresses and strains in the three principal directions, are also available under the **Next** option. For example a radial strain plot is shown in figure 19. In all plots available the three components of stress or strain are presented, i.e. pre-stressing, pressure and temperature, together with the combined solution. This enables the dominating loading component to be identified for corrective action as necessary. In line with all the design modules, facilities are provided to obtain hard copies of the results, both plots and tabulated.

### **3.4.3 Validation**

Validation of the code was achieved entirely theoretically. However this approach was split into two elements.

The first was to model, via plane stress finite elements, the stress distribution in an overwrapped steel barrel with no pre-stress but subjected to an internal pressure. Dimensions and material data were identical in both cases. These results were in excellent agreement validating the fundamental equations of state were derived correctly.

In the second case, a winding macro was developed for use with finite element techniques to model the winding process as a series of tensioned bands. The macro was required to facilitate mesh generation, which was found to be excessively labour intensive. Although this resulted in a coarse overwrap, i.e. each radial finite element represents many layers of overwrap, the results particularly in the liner, were typically less than 2-3% of the **GTUBE2** solution. Due to the coarse nature of the model, overwrap accuracy was not so favourable, but this was fully anticipated.

Some experimental testing has also been conducted to aid validation, but this is covered in more detail in the material characterisation element of this paper.

### **3.5 OVERWIND**

#### **3.5.1 Description**

While the **GTUBE2** module discussed previously models the tension winding process for pre-stressing barrels, it is only valid in the long parallel regions of the barrel, i.e. away from end termination's. Since the liner thickness of the overwrapped portions of a barrel is very much less than those portions not reinforced, it is potentially possible that due to the pre-stressing process adverse stress concentrations could occur in the transition area between these two region arising from local bending, etc.

In order to model this area a linear elastic axisymmetric finite element package has been modified with a menu driven pre-processor. Several options are available to cover generic barrel profiles at the termination regions. Reinforcement material can be either recessed into the dimensions of an existing barrel (hoop overwrap) or applied over the external surface to model axial reinforcement for joint design concepts. Pre-stressing is achieved via specifying the overwrap stress for a particular layer. This is then interpreted as a residual stress within the finite element code from which equivalent nodal forces are evaluated. Component stressing is then evaluated. At present a new analysis is undertaken for each layer in turn, but in the longer term it is proposed to improve run times via resolve techniques. All boundary conditions are automatically defined, these being zero axial displacements at the left hand end.

Additional features that have been introduced to the module include modelling the pressure gradient across the projectile obturator band. This takes the form of a step pressure change, zero pressure to the front of the band, the gas pressure behind. Furthermore, an ability to input axial loads is also available to cover issues arising from barrel bend and joint design for axial reinforcement material.

Post-processing capabilities are broadly as for any finite-element package, offering plots of component deformation through to component stress and strain contours. All information can be plotted on high resolution printers.

#### **3.5.2 Module operation**

The principle features on entering the module are:

- To select a generic overwrap transition area as illustrated by the three icons shown at the top of figure 20.
- To define the overall dimensions of the area minus the overwrap recess.

Once defined, the introduction of composite reinforcement, applied either externally to the selected transition area or recessed into the liner, can be undertaken. For recessed layers, the recessed layers table screen is invoked where up to eight layers of tensioned

overwrapped can be recessed into the barrel section, see figure 21. The start position of the overwrap can be defined by cursor or dimensions. Furthermore, the slope at the start of the overwrap can be defined, a 90° slope being shown here. Alternatively a radius can be chosen if believed to yield improved stressing in this region.

Material properties are defined as per the **RADHT** module in that the component is displayed graphically and materials then selected via the mouse, material properties being shown at the top of the screen. Different material colours are again provided to aid material allocation, as illustrated in green in the figure 23.

Component loading is then invoked through the Pressure Loading Table, see figure 23. As discussed a pressure step is offered to model projectile motion, with the position of the pressure step being defined either by cursor or dimensions as shown in the figure. Pressure values to the left and right of the cursor are requested. In order to gain a pseudo picture of projectile motion up to eight cursor positions can be defined. Resolve facilities are then used within the programme to obtain the eight solutions in a minimal time period. Finally to account for axial loading arising from recoil, barrel bend, etc. a facility is offered to introduce axial loading to the structure. Finite element meshing is then performed automatically.

On completion of the finite element analysis deformation and stressing plots can be undertaken in line with most finite element stressing packages. Boundary conditions and applied loading can also be plotted if required. For the design example shown in figure 22 the resulting deformation plot, multiplied by 50, is shown in figure 23. The corresponding circumferential stress plot is shown in figure 24. If a winding analysis had been invoked a series of plots are offered automatically for the number of layers specified. This is also the case if a series of pressure steps were defined to simulate projectile motion. Enlarging of a particular area is offered via a zoom facility.

For the preparation of hardcopy output a border is provided together with options for inputting titles and dates. A typical border is illustrated in figure 24.

### **3.5.3 Verification**

The overwind module is still currently being developed, and at present it has yet to be fully validated. However, some preliminary checks have been performed for an overwrapped barrel subjected to pressurisation and the results compared to the **GTUBE2** results and other finite element solutions with excellent agreement. For a step pressure a several preliminary checks have been undertaken against analytical solutions and other finite results, the results to which have again been in good agreement. For the tension winding process no checks have been performed to date, but comparisons against **GTUBE2** and other finite elements will be performed as detailed in section 3.4.2.

## **4 Material Properties for Tensioned Composite Overwrap**

In the preceding chapters, a number of composite gun barrel design modules have been described to aid in the designing of high performance composite reinforced gun barrels.

While considerable efforts have been extended to validating these codes, it is clear that unless good quality material data is available for these modules the quality of results will be much reduced.

The characterisation of composite materials is in itself a subject area, but for composite gun barrels the problems are further increased by virtue of the fact that the production process will effect the resulting properties. This is particularly true for tension winding whereby very high fibre compactions can be achieved. Since removal of the material from the steel liner is not permissible, to do so would result in failure of the material due to its high residual stress state, methods have been derived for estimating properties whilst wound on the steel mandrel. For the mechanical and thermal properties, these methods are summarised below.

#### **4.1 Mechanical properties**

The principal technique for evaluating the material constants, e.g. modulus and poisson's ratio, has been achieved via the filament winding and dilation measurements of cannon calibre test specimens, a typical test specimen being shown in figure 25.

Three dilation measurements are undertaken:

- Barrel dilation before cure using bore gauges
- Barrel dilation after cure, again using bore gauges
- Barrel dilation due to applied internal pressure via externally applied strain gauges.

These three sets of measurements are undertaken to assess the material constants when the overwrap is applied as a pre-preg and in its cured state, which can result in differing properties particularly in the through thickness direction. The intermediate stage provides information on the loss of liner pre-stress due to the curing process, which may be significant.

Since finite-element techniques have validated the stress equations embodied within **GTUBE2**, material properties are obtained by undertaking data fitting exercises. However, it is assumed that the circumferential modulus is accurately predicted from the measured overwrap volume fraction and the classical rule of mixtures methods. The properties of the steel must also be known for this exercise, but such properties can be easily evaluated from conventional tensile testing techniques.

While the above technique has found to yield sound design data, it is recognised that some of the inherent assumptions embodied within the approach, particularly for the circumferential modulus, may result in property data that is not truly accurate. As a result, alternative methods are being explored. One such technique is to use an indenter, which is pushed into the overwrap along the specimen length. By measuring resulting load and indenter deflection, further estimates can be made into predicting the mechanical constants. These can then be compared with barrel dilation techniques. This alternative method is still to be fully validated, but has shown promise for overwrap materials with very low transverse properties, such as, Kevlar.

In addition to the evaluating mechanical constants, the pressure test can be used to determine failure data for the overwrap. Failure can be initiated either via tensile failure of the fibres, or alternatively via transverse radial compression. Establishing which dictates the mode of failure is complex, but can be ascertained from examinations of failed fibres and trends in burst pressures.

#### **4.2 Thermal properties**

The laser flash technique is by far the most versatile and widely used method for evaluating the thermal transport of solid materials. The technique involves the thermal pulsing (laser) of a small disk of known thickness with the elapse time and temperature rise times being recorded on the rear surface. Analytical equations are then used to evaluate the thermal diffusivity using the measured information.

For the overwrap material such a process is not directly applicable for the reasons previously discussed, i.e. the overwrap will break-up if attempts are made to remove from the steel liner. Nevertheless the technique can be modified for use with an overwrapped steel liner. In this case the overwrapped test specimen is subjected to a thermal input at the bore after which elapse time and temperature rise times are recorded on the outer surface. By knowing the properties for the steel and the resulting temperature diffusion times, the thermal diffusivity of the overwrap can be calculated. For convenience, a cooling input is used within DRA in the form of injecting water into the bore of a heated overwrapped specimen, a schematic of the apparatus being shown in figure 26.

Thermal conductivity is then evaluated as the product of thermal diffusivity and material heat capacity, the latter being derived via Differential Scanning Calorimetry for the overwrap constituent materials and overwrap volume fraction.

### **5 Conclusions**

A series of design modules have been described to aid the design of composite reinforced gun barrel tubes. These modules have been implemented into an existing all steel gun barrel design suite and provide the following features:

- A comprehensive materials and charge data base
- A one dimensional transient heat transfer code for predicting barrel heating for specified firing scenarios
- Barrel droop and frequency response as a function of reinforcement thickness and position
- Barrel pre-stressing via either tension winding or shrink-fitting
- Modelling the termination region of the overwrapped portion of the barrel

A summary of the underlying theories for each of the analysis modules is described as is validation methods. Discussions on the execution of each of these additional features is also provided.

Finally methods for obtaining material data for use with these design features has been reviewed.

## **6 Acknowledgements**

The authors acknowledge the assistance of Mr J Coleman and Mr D Wallington of the Weapons Sectors, DRA Fort Halstead, in developing the software detailed in this paper.

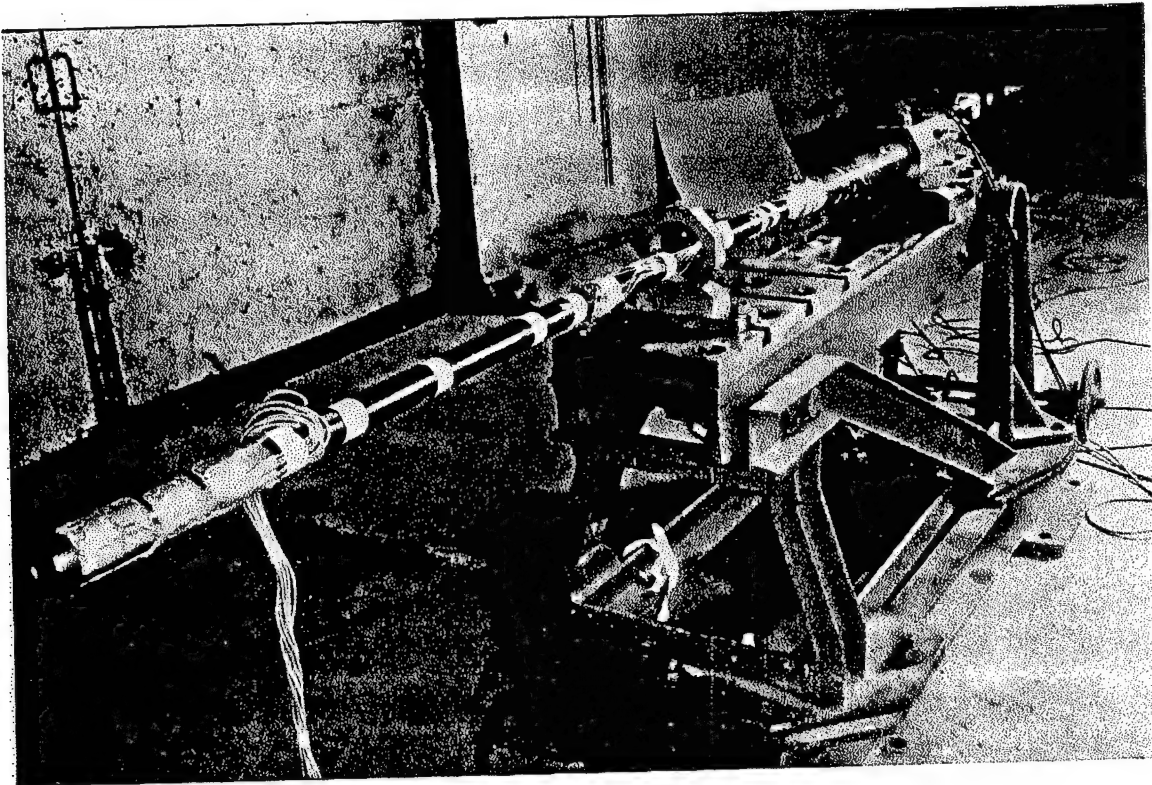


Figure 1 Overwrapped Barrel Demonstrator

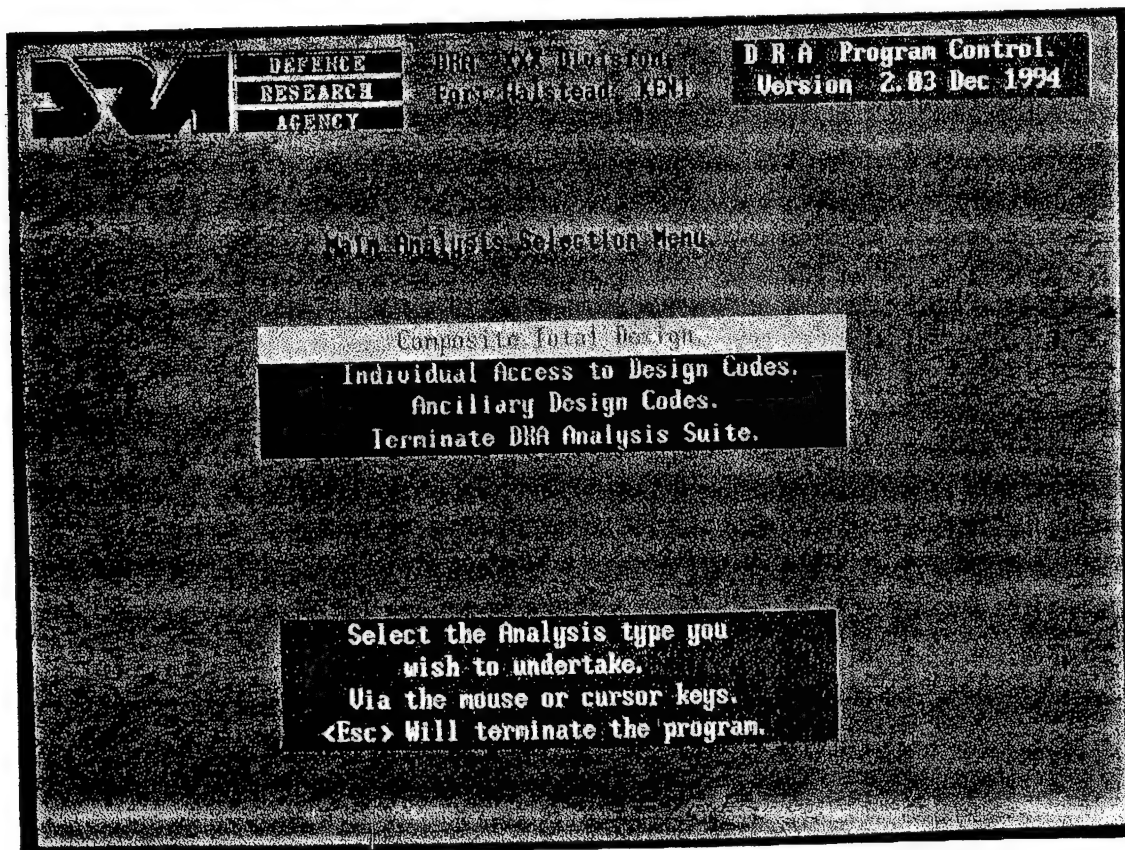


Figure 2 Main Analysis Selection Menu

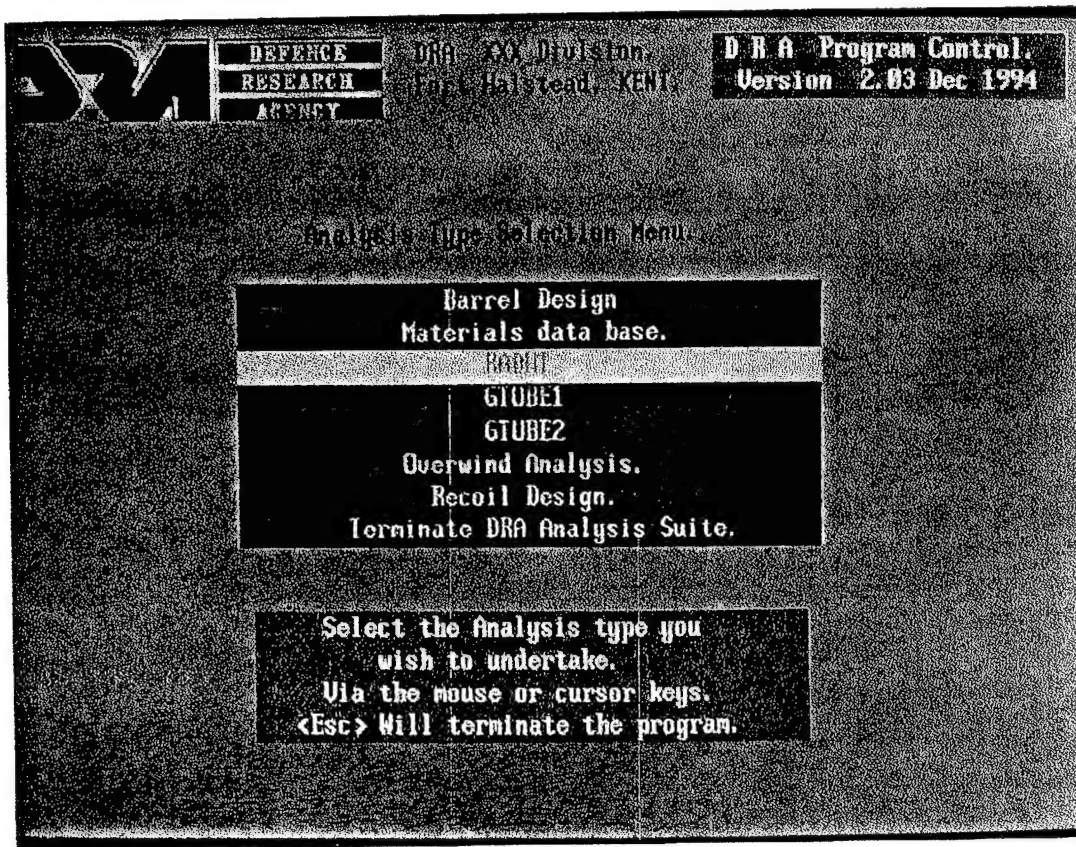


Figure 3 Analysis Type Selection Menu

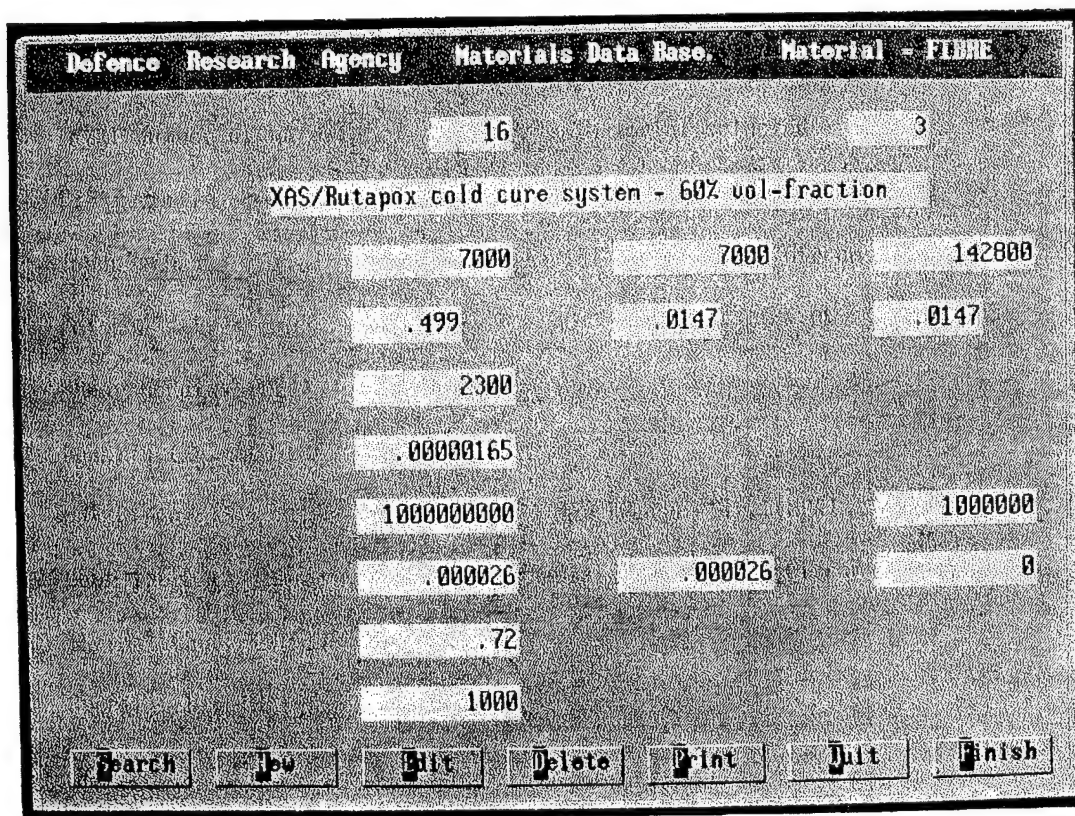
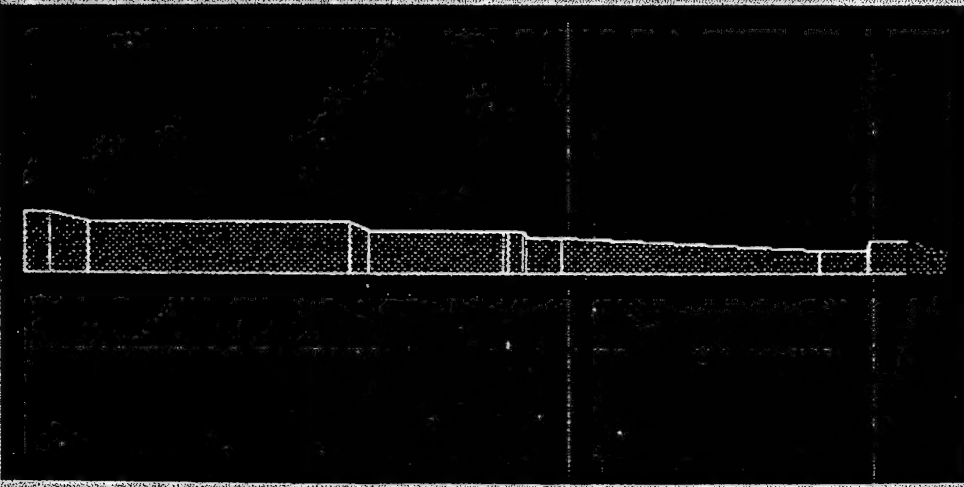


Figure 4 Overwrap Material Data Screen

**RADHT: Geometry input data collection.** **Project - EXAMPLE**

Total Length of Tube - 5811.3



Selections		Bore Rad	Barrel		Reinforcement
<b>Add.</b>	Delete	78.277	Length	210	LAY 1- 0
Select	Modify	U Scale	R1	113.5	LAY 2- 0
Bore Rad U Scale		5	R2	102.5	LAY 3- 0

Figure 5 RADHT Geometry Input Screen

**RADHT: Charge material property specification.** **Project - EXAMPLE**

SELECT CHARGE DETAILS

Charge Mass	Gas Conductivity	Gas Viscosity	Flame Temperature	Radiation Temperature
12.25	.09375	.00005	2561	861

Muzzle Velocity	Time Constant	Decay Factor	Add. Scal Factor
827	.0092	-.02	0

All temperatures in degrees C.

Time Step

Output Interval

Amb. Temp. on Tube

Initial Temperature

Figure 6 RADHT Charge Selection Screen

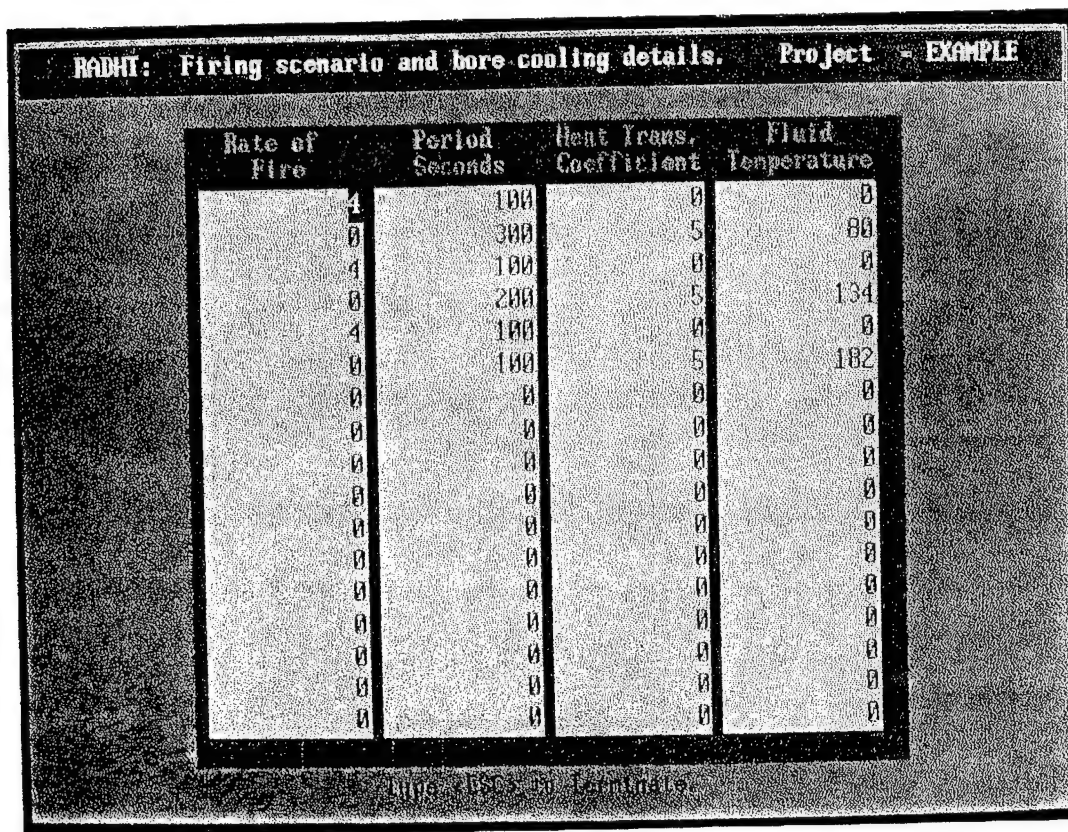


Figure 7 RADHT Firing Scenario and bore cooling data screen

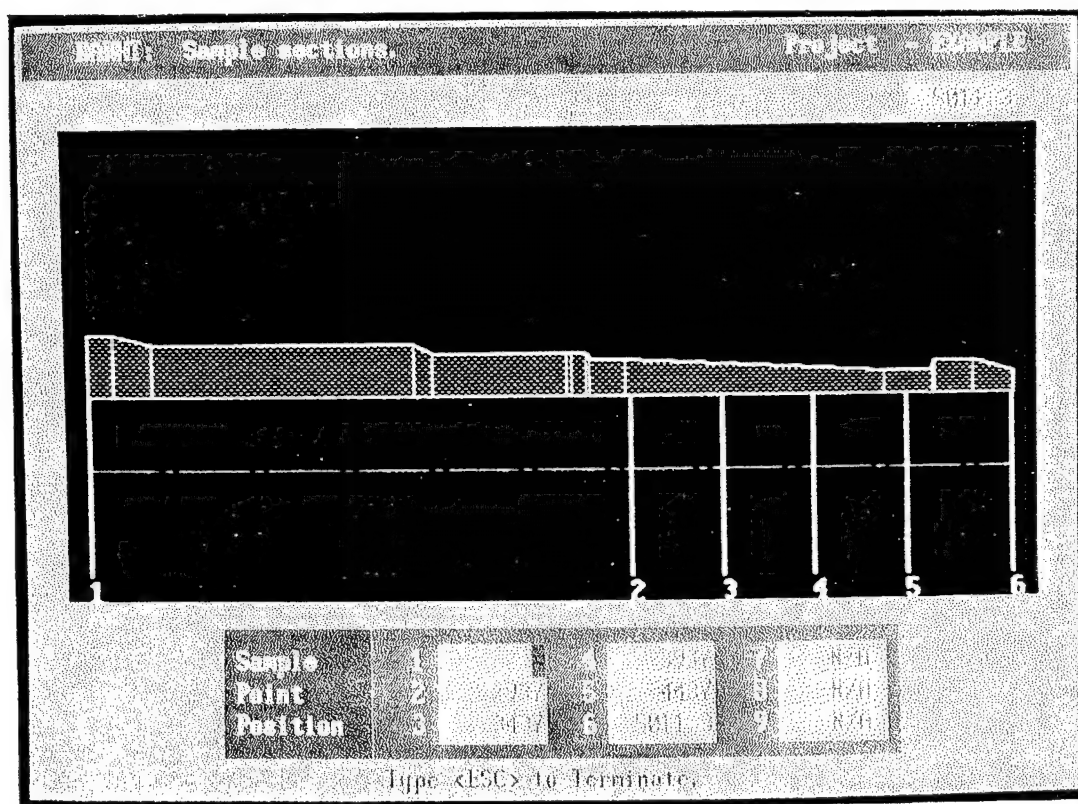


Figure 8 RADHT Sample Sections Screen

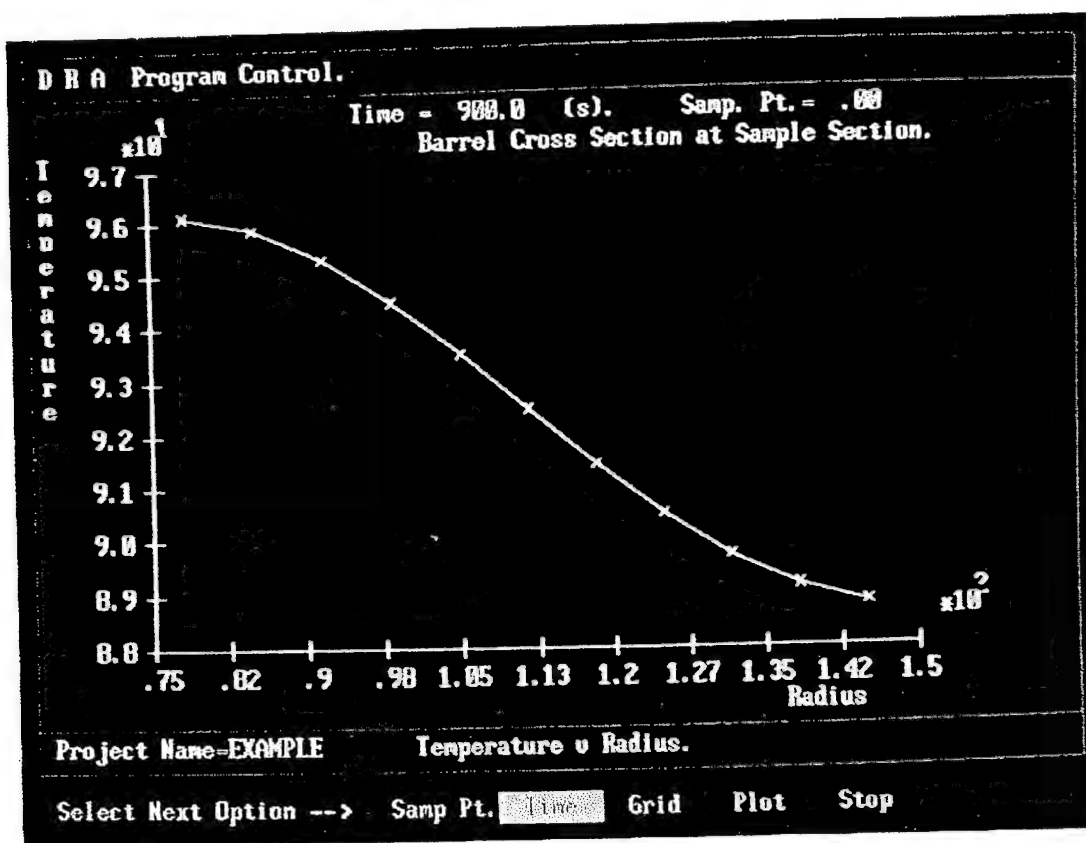


Figure 9 Barrel Cross Section Heating Plot

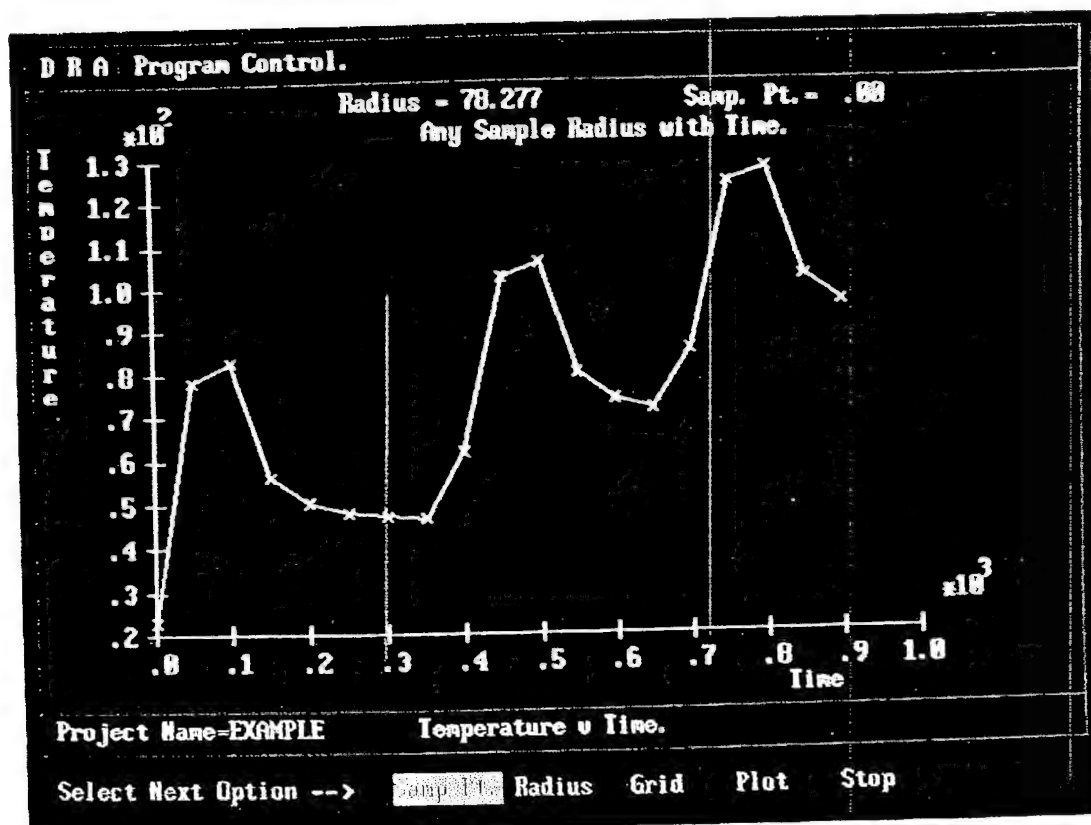


Figure 10 Barrel Temperature vs Time

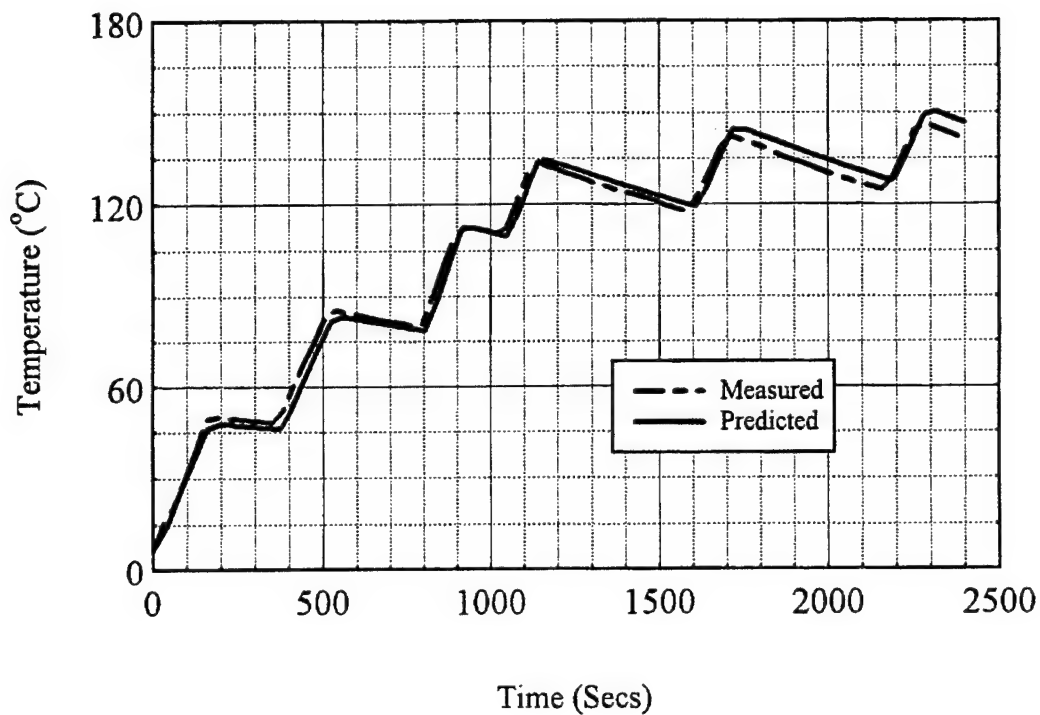


Figure 11 RADHT and Measured Temperature vs Time Plots; Artillery Gun

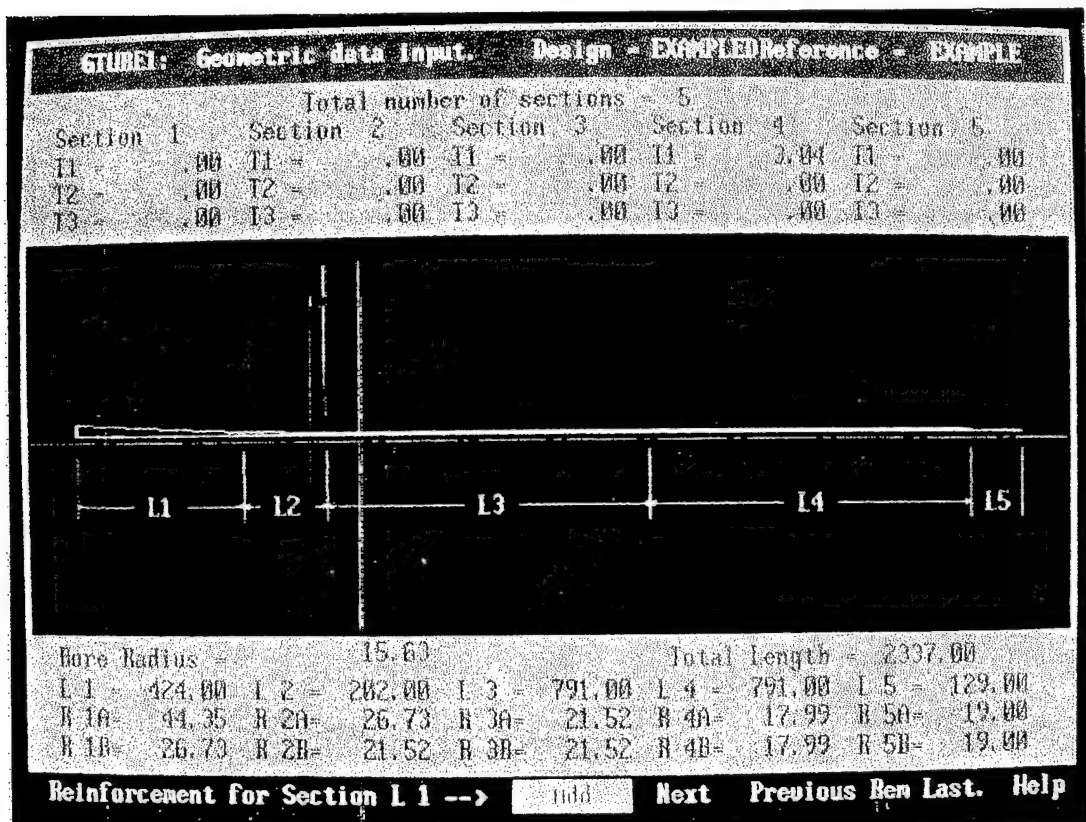


Figure 12 GTUBE1 Geometric Data Input Screen  
16-23

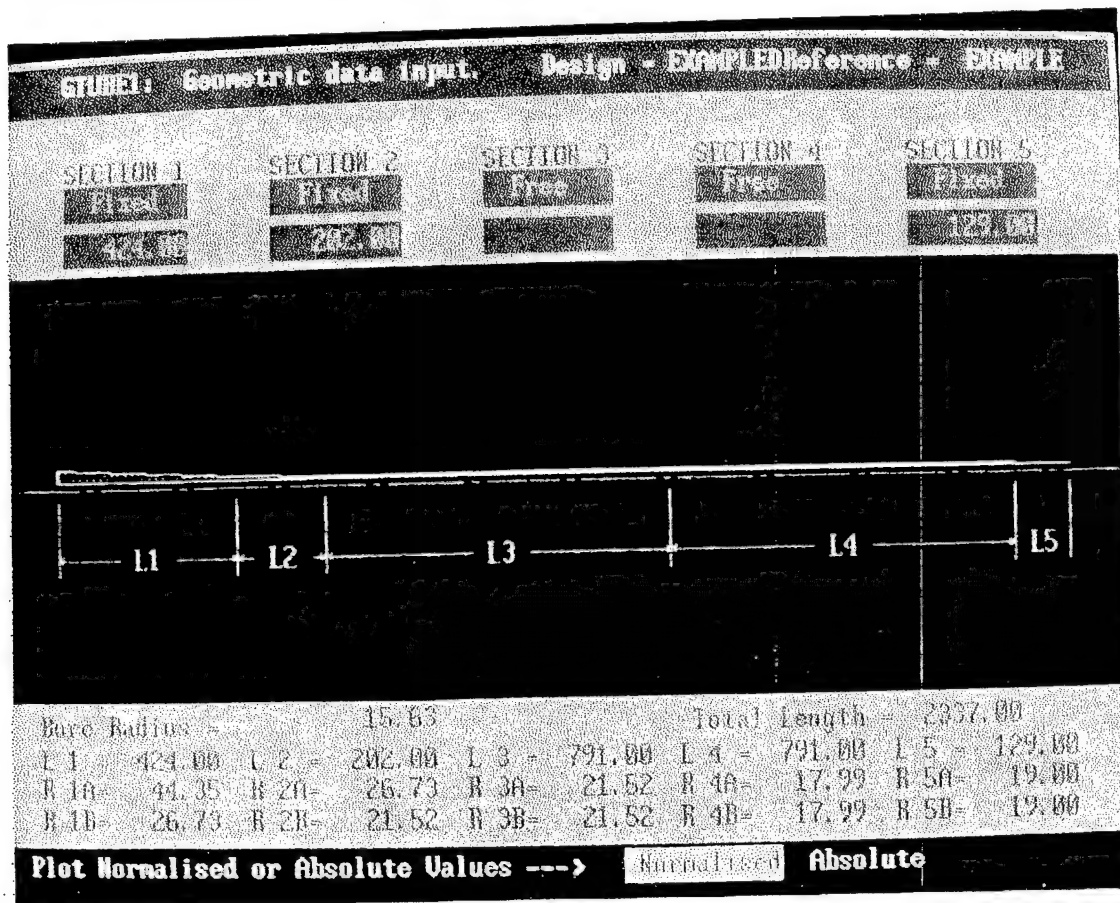


Figure 13 GTUBE1 Fixed/Free Selection Menu

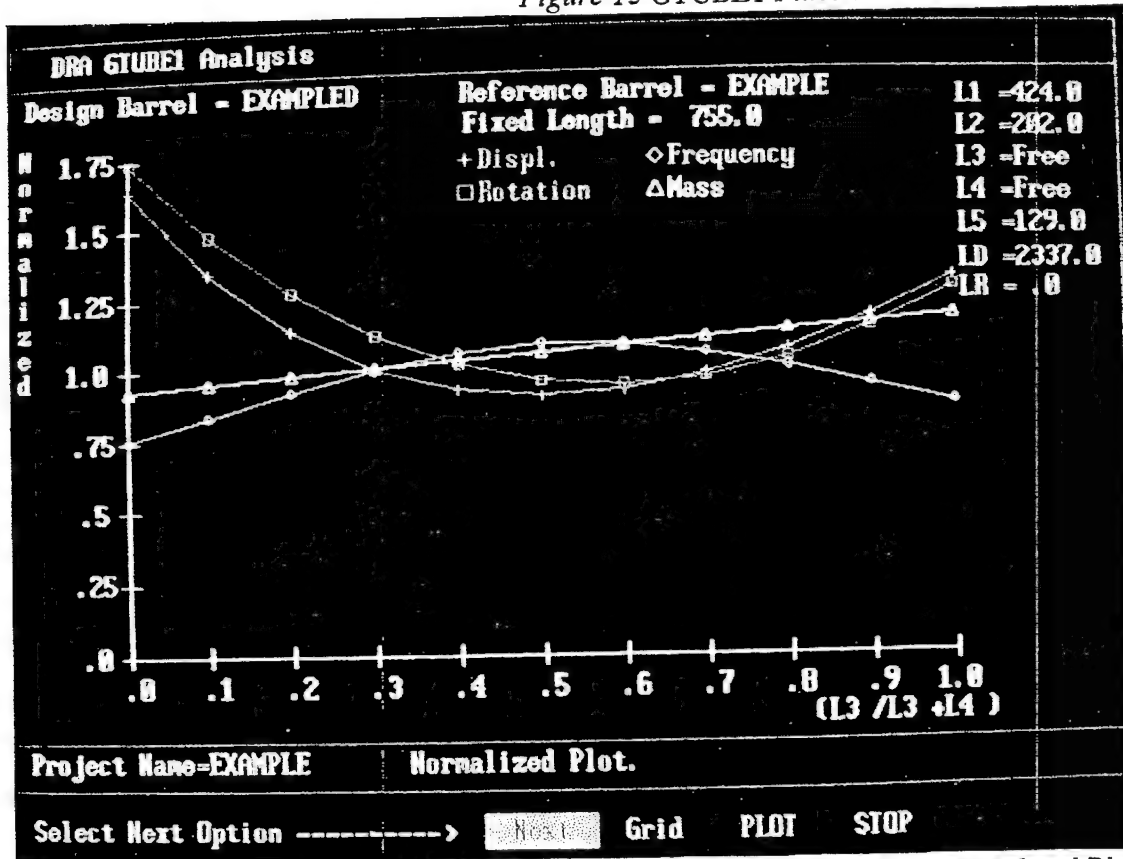


Figure 14 GTUBE1 Normalised Plot

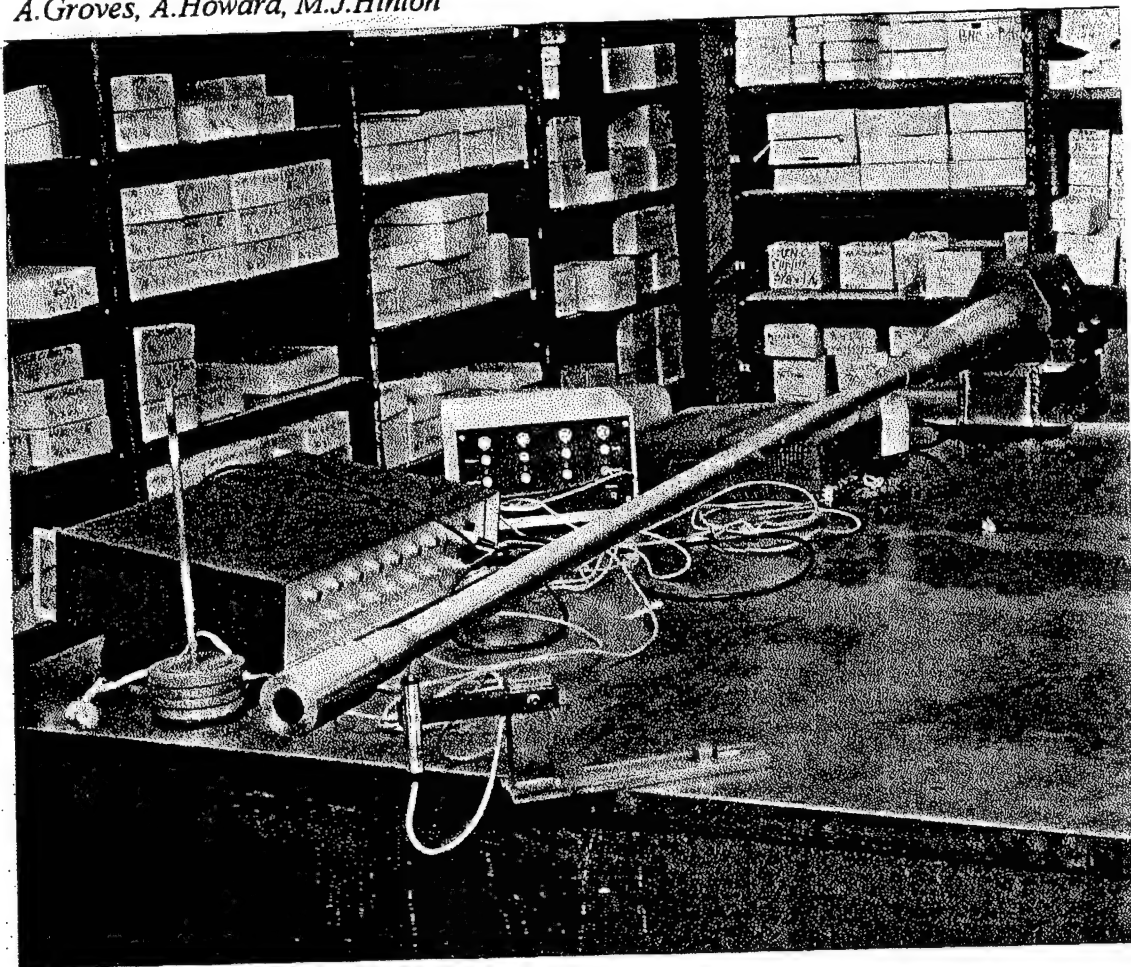


Figure 15 Frequency Test Apparatus

GTUBE2 : Title and material selection. Project - EXAMPLE

---

Strain vs Pressure results

Gun Steel

E	P.R.	Yield	Alpha	Density	Max Stress
2.07E+05	.205	1055.000	.125E-04	.700E-05	472.600

Select fibre material properties

XAS/Rutapnx cold cure system - 60% vol-fraction

Er	Ec	Ea	Urc	Uar	Uac
7.00E+00	.147E+01	7.00E+00	.147E-01	.499	.147E-01
Alpha R		Alpha C	Alpha A	Density	
.770E-04		.1000	.250E-04	.150E-05	

Figure 16 GTUBE2 Title and Material Selection Screen  
16-25

**GTUBE2 : Analysis selection screen.** Project - EXAMPLE

---

ANALYSIS TYPE       

Bore Rad.    Iface. Rad.    Extern. Rad.

Winding Ten.        Int Pressure

TEMPERATURES

Reference    Bore    Extnal    Outside

CONSTRAINT TYPE

Figure 17 GTUBE2 Analysis Selection Screen

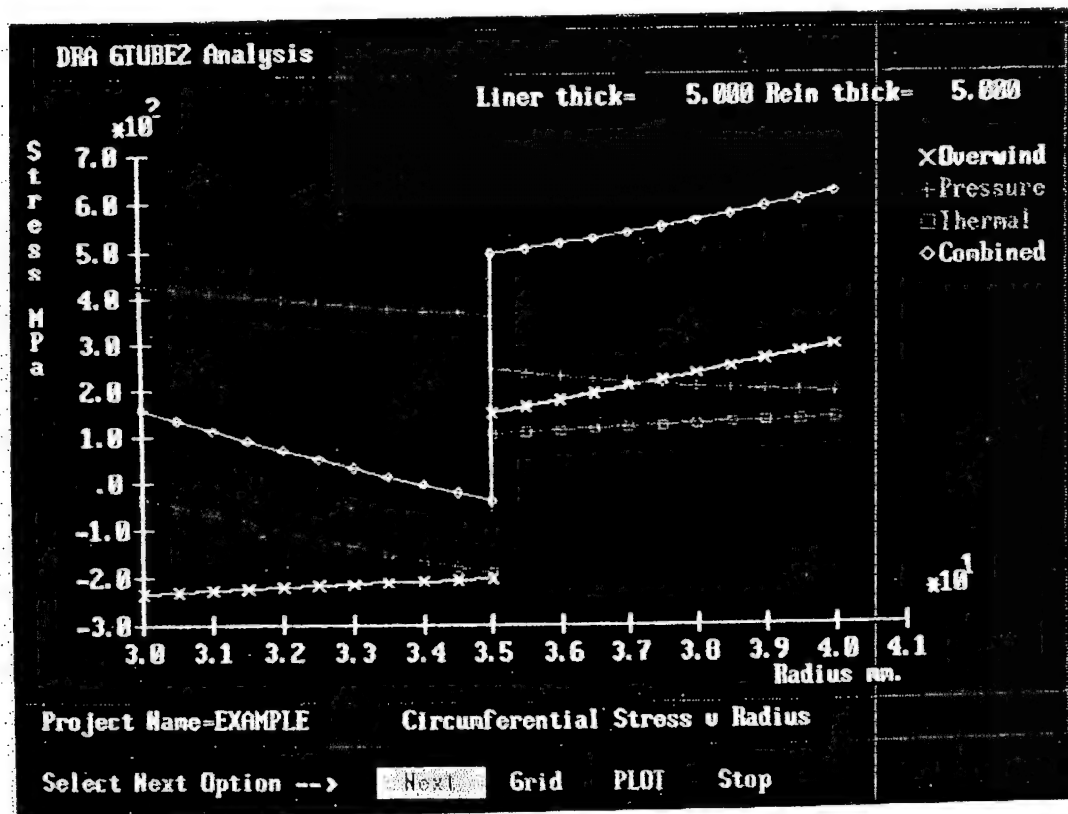


Figure 18 GTUBE2 Circumferential Stress Plot  
16-26

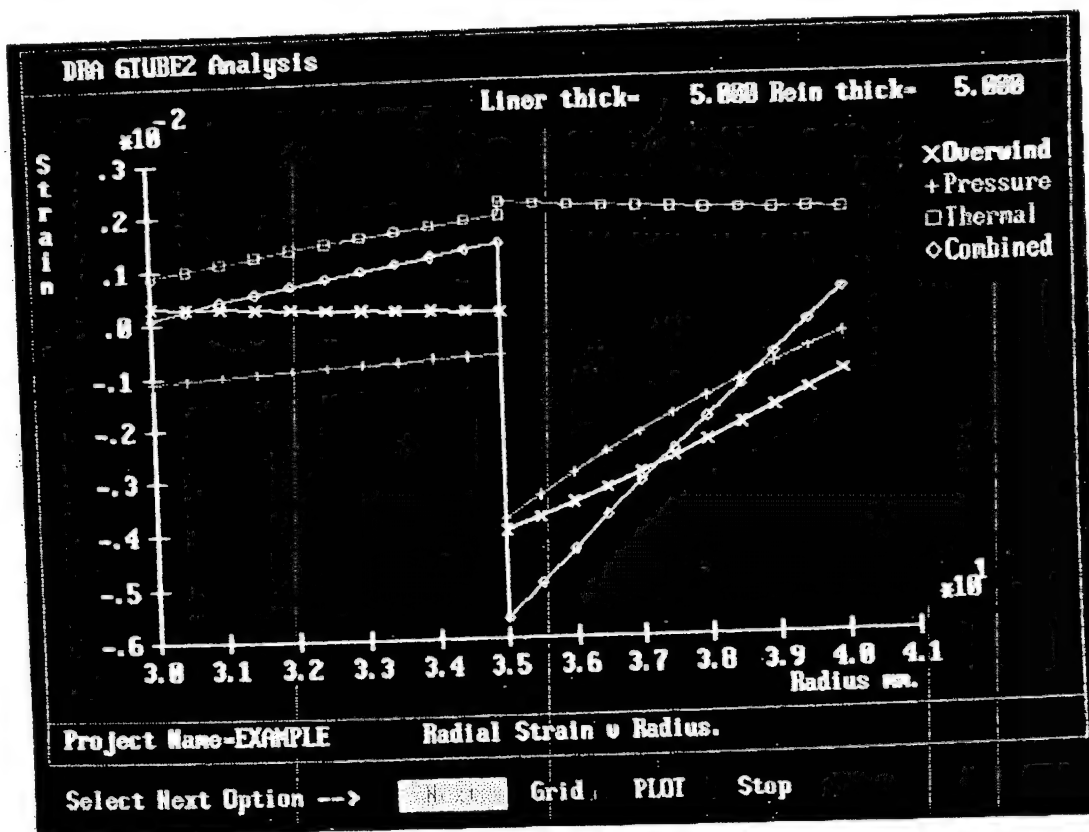


Figure 19 GTUBE2 Radial Strain Plot

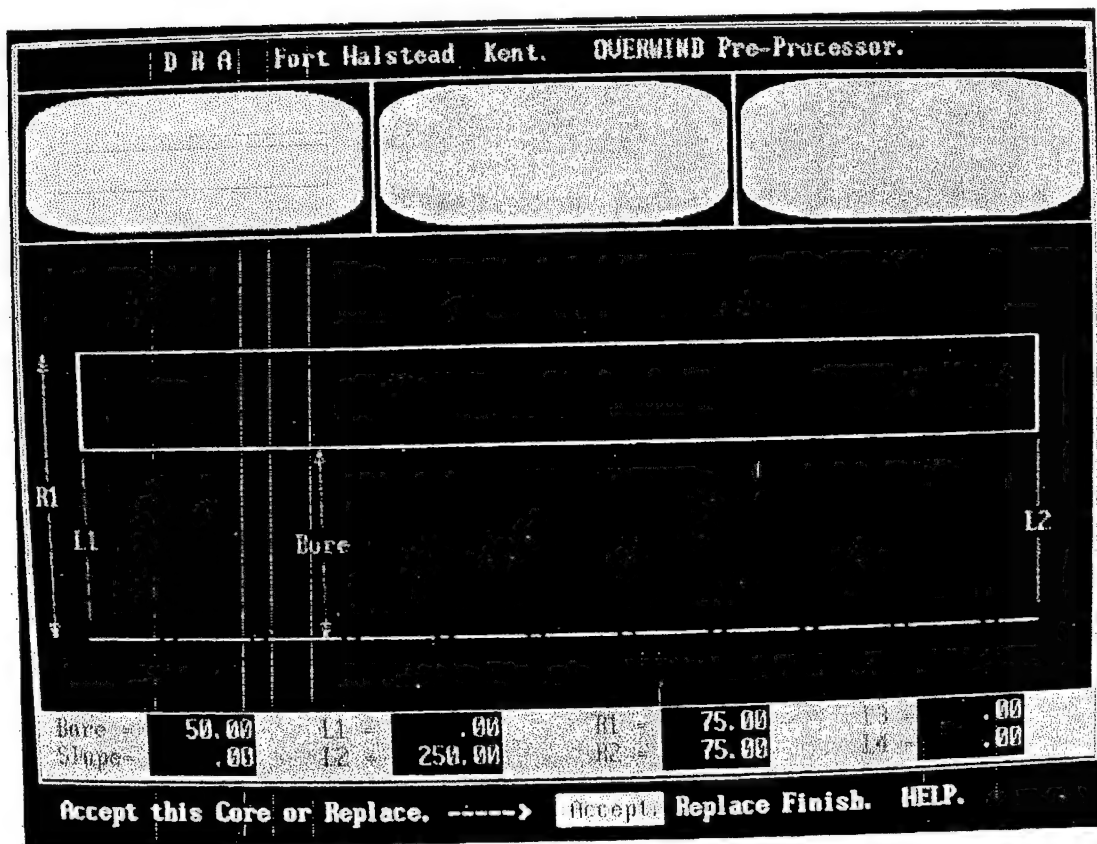


Figure 20 OVERWIND Termination Region Icon Screen  
16-27

**D R A Fort Halstead Kent. OVERWIND Pre-Processor.**

Recessed Layers Table.

Thick1= 5.00	Ten1= .00	Thick2= Unused	Ten2= Unused
Thick3= Unused	Ten3= Unused	Thick4= Unused	Ten4= Unused
Thick5= Unused	Ten5= Unused	Thick6= Unused	Ten6= Unused
Thick7= Unused	Ten7= Unused	Thick8= Unused	Ten8= Unused

Bore Slope: 50.00 L1 = .00 R1 = 75.00 L2 = .00  
 .00 L2 = 250.00 R2 = 75.00 L4 = .00

Edit Recessed Layers. ----->

Figure 21 OVERWIND Recessed Layers Table Screen

**D R A Fort Halstead Kent. OVERWIND Pre-Processor.**

Pressure Loading Table.

X1= 100.00	X3= Unused	X5= Unused	X7= Unused	X9= Unused
X2= Unused	X4= Unused	X6= Unused	X8= Unused	X0= Unused

Pressure Left = 100.00 Right = .00 Axial Load = .00

Bore Slope: 50.00 L1 = .00 R1 = 75.00 L2 = .00  
 .00 L2 = 250.00 R2 = 75.00 L4 = .00

Position by Cursor or Dimension -->

Figure 22 OVERWIND Load Definition Screen  
 16-28

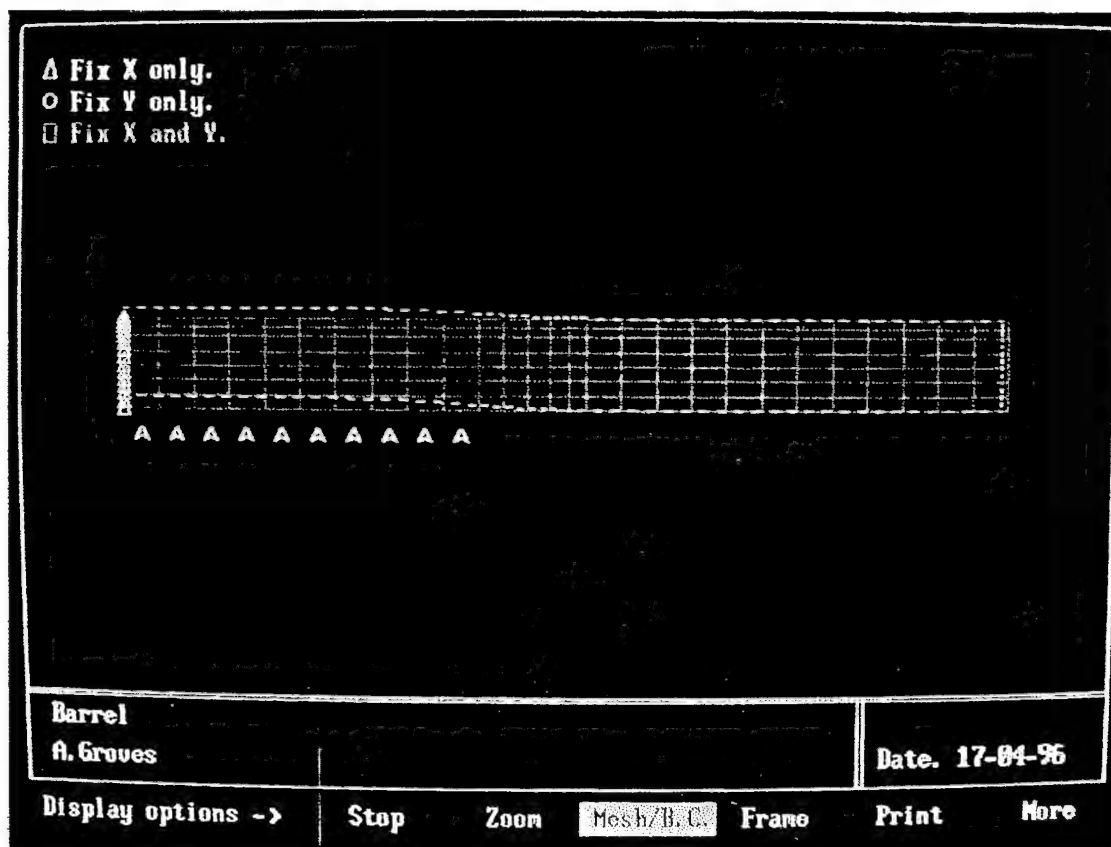


Figure 23 OVERWIND Deformation Plot

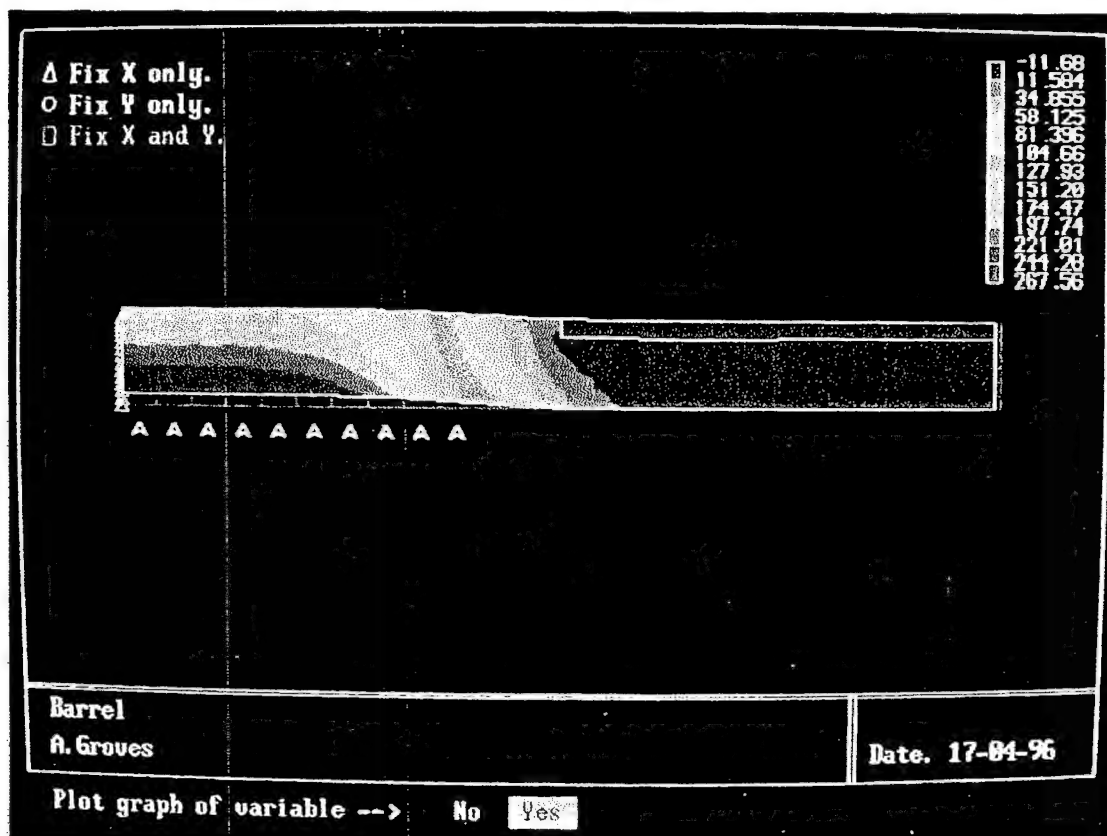


Figure 24 OVERWIND Stress Contour Plot

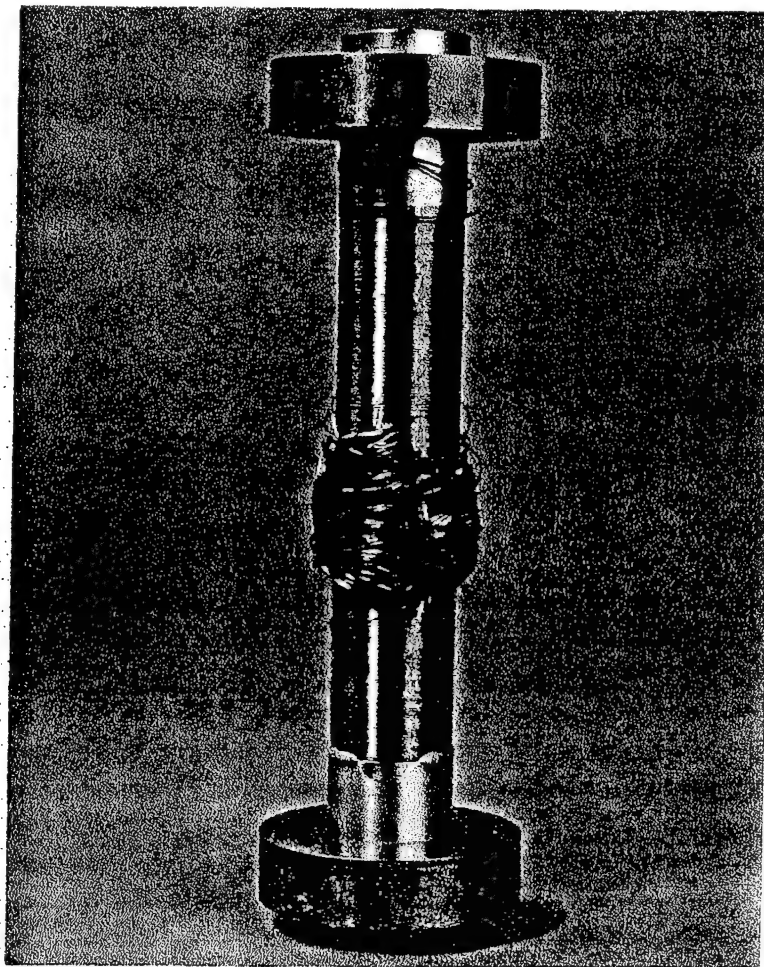


Figure 25 Cannon Calibre Overwrapped Test Specimen

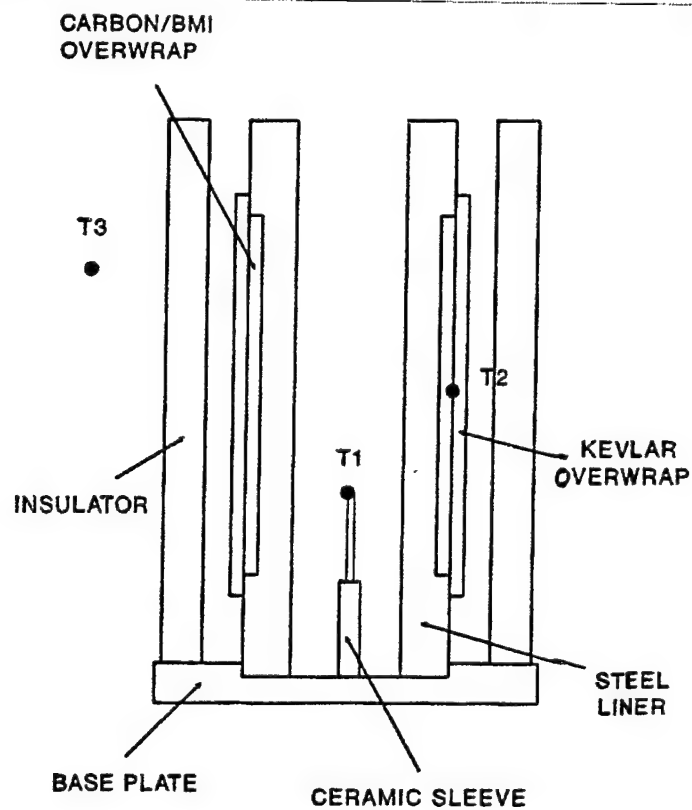


Figure 26 Thermal Diffusivity Test Procedure  
16-30

**SESSION IV**

**MODELING, SIMULATION, AND FINITE ELEMENT ANALYSIS**

**TITLE: Thermochemical Erosion Modeling of M242 Gun Systems**

Samuel Sopok, Peter O'Hara, George Pflegl

US Army Benet Laboratories, Watervliet, New York 12189

Stuart Dunn, Douglas Coats

Software and Engineering Associates, Inc., Carson City, Nevada 89701

**ABSTRACT**

The MACE gun barrel thermochemical erosion modeling code addresses wall degradations due to transformations, chemical reactions, and cracking coupled with pure mechanical erosion for M242 gun systems. This predictive tool provides gun system design information that is expensive, if not unattainable, by experiment. This complex computer analysis is based on rigorous scientific thermochemical erosion considerations that have been validated in the reentry nosetip and rocket nozzle/chamber community over the last forty years. The five module gun erosion analyses includes the standard gun community XNOVAKTC interior ballistics code (somewhat modified), the standard gun community BLAKE nonideal gas thermochemical equilibrium code (somewhat modified), the standard rocket community TDK / MABL mass addition boundary layer code (significantly modified for gun barrels), the standard rocket community TDK / CET gas-wall thermochemistry code (significantly modified for gun barrels), and the standard rocket community MACE wall material ablation conduction erosion code (significantly modified for gun barrels). These five analyses provide thermochemical ablation, conduction, and erosion profiles for each material as a function of time, travel, and shot in sequence.

For this gun system example erosion comparisons are made for two round types (M791, 616W), at two axial positions (6", 12"), predicted for shots 1 and shot 150 (cycle A, approximately 70 rpm) and for a bore surface of cracked and uncracked 0.002" chromium plated gun steel, cracked and uncracked 0.002" tantalum sputtered gun steel, and nitrided gun steel.

**BIOGRAPHY:**

Samuel Sopok

**PRESENT ASSIGNMENT:**

Research Chemist, Benet Laboratories, U.S. Army ARDEC,  
Watervliet, NY, 1980-Present

**PAST EXPERIENCE:**

**DEGREES HELD:**

B.S. Chemistry, State University of New York at Albany  
M.S. Chemistry, Rensselaer Polytechnic Institute  
PhD. Chemistry, Rensselaer Polytechnic Institute

## **THERMOCHEMICAL EROSION MODELING OF M242 GUN SYSTEMS**

Samuel Sopok, Peter O'Hara, George Pflegl  
US Army Benet Laboratories,  
Watervliet, New York 12189

Stuart Dunn, Douglas Coats  
Software and Engineering Associates, Inc.,  
Carson City, Nevada 89701

### **INTRODUCTION**

Aerothermochemistry is the study of chemical reactions in flow systems and was first described by von Karman in 1951 [1]. The modification of the heat transfer coefficient by a blocking effect for the mass addition of chemically reacting wall material into the boundary layer was first described by Reshotko and Cohen in 1955 [2,3]. The thermochemical erosion of reentry vehicle (RV) heat shield material for various chemically reacting systems was first studied by Denison and Dooley in 1957 [4].

Denison and Dooley's thermochemical erosion analysis regarding convective heat transfer with mass addition and chemical reactions was unified and summarized by Lees of California Institute of Technology (consultant to the Ramo-Wooldridge Corporation) in 1958 [5]. From early thermochemical erosion models, to JANNAF standardized current models [6,7], the near exclusive use of Lees' analysis has stood the test of time, and demonstrates that the major assumptions in his 1958 paper are still reasonable and valid for reentry vehicle nosetips and rocket chambers/ nozzles.

In the last twenty years, gun barrel technology has primarily focused on mechanical and metallurgical aspects with a secondary focus on erosion. Catastrophic gun barrel failures have been nearly eliminated, while thermochemical erosion (thermochemical ablation with mechanical erosion) problems have intensified due to performance requirements demanding the use of high flame temperature propellants. The erosion of gun barrels is generally attributed to both thermal ablation (bore surface phase transformations with aerodynamic flow removal) and thermochemical ablation (gas-wall chemical reactions with aerodynamic flow removal) although the surface temperature should remain below the solidus temperature for a practical gun design.

In 1990, the U.S. Army Benet Laboratories (Benet) conducted an extensive literature search of military, NASA, and commercial sources which revealed no "shrink-wrapped" thermochemical erosion modeling codes for gun barrels. This search did reveal the JANNAF standardized rocket

community counterpart which includes the Two-Dimensional Kinetics (TDK; chemistry by CET, mass addition boundary layer by MABL) and the Materials Ablation Conduction Erosion (MACE) modeling codes for predicting thermochemical erosion for rocket chambers, nozzles, and nosetips [6-8]. Software and Engineering Associates, Inc. (SEA), is now the sole maintainer and developer of the TDK / MACE rocket erosion codes.

In 1991, Benet and SEA mutually determine that these rocket codes should be modified for guns and that these codes actually exceeded gun erosion code requirements and expectations [9]. It became obvious that two of the analytical tools needed to begin the thermochemical erosion analysis of gun barrels were already available in the gun community. These tools were Freedman's BLAKE thermodynamic equilibrium code with compressibility [10], and Gough's NOVA interior ballistics code [11]. SEA and Benet successfully modified the BLAKE, NOVA, TDK, and MACE codes into what appears to be the first unified gun erosion code [9].

A joint SEA/Benet research seminar was given at Benet on this first unified gun erosion code presenting its capabilities using a gun system example where erosion cannot be explained by thermomechanical effects alone [9,12]. Several JANNAF sponsored gun erosion meetings have implied a gun system specific thermochemical erosion component for many previous gun systems [13]. For the referenced gun system example, with its solid propellant product-A723 steel (or chromium plated A723 steel), an ablative scale-like oxidation of iron and chromium by gas-wall diffusion of oxygen predominates, and the crack-rich brittle scale layer is easily removed by mechanical erosive forces. US Army experimental data supports the existence of gun barrel oxidation [14]. For these systems, oxidation lowers melting point by 100° to 200°C for A723 steel and raises the melting point by 400° to 500°C for chromium, based on respective phase diagrams which further justify chromium plating of steel. In July 1995, the first known gun barrel thermochemical ablation - mechanical erosion modeling code was published [15] by Benet and a summary is presented in this paper. In October 1995, ARL published its thermal ablation - mechanical erosion gun modeling code and has not published the important chemical component to date [16].

## PROCEDURE

The thermochemical erosion analysis procedure for the 25-mm Bushmaster gun system [12] consists of five analyses, including the NOVA [9,11] (interior ballistics & core flow), BLAKE [9,11], (gas thermochemistry & compressibility), TDK / MABL [6,9] (heat transfer modified by boundary layer mass addition, decoupled from core flow), TDK / CET [6,8,9] (gas-wall thermochemistry), and MACE [7,9] (ablation, conduction, & erosion profiles) codes.

The TDK / MABL module generates transport properties, Mollier gas properties, adiabatic conditions, and cold wall heat transfer conditions using NOVA / BLAKE data as input. The TDK / CET module generates H-B Mollier chart linkage files for nonreacting (inert) walls, reacting nitrated A723 walls, reacting cracked and uncracked chromium plated A723 walls, and reacting cracked and uncracked tantalum sputtered A723 walls using NOVA / BLAKE data as input; combustion product omissions are based on experimental testing and a U.S. Army report [14]. The MACE code calculates the transient thermochemical response and generates ablation,

conduction, erosion surface and depth profiles as a function of time, travel, and shot. MACE uses NOVA, BLAKE, MABL, and CET data as input for the cracked (1.0% area) and uncracked 0.002" chromium plated A723 steel walls, the cracked (0.3% area) and uncracked 0.002" tantalum sputtered A723 steel walls, and the nitrided A723 steel wall using two round types (M791, 616W) at two axial locations (6", 12") and two shots (#1, #150 using Cycle A scenario at approximately 70 rpm). MACE gas-wall chemical kinetics data are based on testing and the literature [9].

The 616W designation is for a non-standard round selected, assembled and used solely for the aggressive testing of gun barrels and bore coatings. The 616W is assembled using the same cartridge case, primer and ignitor as the M919 (APFSDS-T) round. The projectile is the same as that used in the M791; a spin stabilized tungsten penetrator weighing 135 grams. The propelling charge is 97 grams of HES9053. HES 9053 has a flame temperature above 3550°K. For comparison, JA-2 used in several KE tank rounds has a flame temperature of 3410°K and HC-33 used in the M791, under 3200°K. This 616W has proven to be a very aggressive round producing a barrel life of less than 300 rounds in the standard (non-plated) M242 barrel.

This modeling effort uses the chemistry of A-723 gun steel. This material (in type II form) is currently the material used for manufacture of barrels for the M256 tank cannon. The original barrel in the M242 was of D6AC. Current barrels can be manufactured of D6AC or CrMoV steels. A-723 and D6AC are variants of the 4340 class of steels. A-723 and D6AC have similar reactivity with the propellants used in the analysis

## RESULTS AND DISCUSSION

For this thermochemical erosion analysis, any propellant-wall combination can be modeled, each mechanism's importance is identified, computer resources are modest (high end PC), parametric analysis is possible, and incremental upgrades are feasible. However, this approach requires engineering judgement and extrapolations are questionable.

The NOVA analysis outputs the pressure, velocity, and temperature core flow as a function of time and travel. The BLAKE analysis outputs pressure-temperature-compressibility data as well as thermochemistry data.

The TDK / MABL analysis outputs adiabatic wall recovery enthalpy ( $H_r$ ) and adiabatic wall temperature ( $T_{aw}$ ) data as a function of time and travel. The recovery enthalpy is the potential chemistry driver where the heat transfer approaches zero and the adiabatic wall temperature is the potential temperature without reactions. The TDK / MABL analysis also outputs cold wall heat transfer rate ( $Q_{cw}$ ) data as a function of time and travel. This heat transfer rate is the wall heat flux evaluated at the cold wall temperature.

The TDK / MABL heat and mass transfer model includes the following three equations. The first equation for mass addition to the boundary layer, the second equation for heat-to-mass transfer ratio, and the third equation for the overall correlation between the first and second equations:

$$r_e U_e Ch_o = Q_{cw}/(H_r - H_{gw}) \quad (1)$$

$$r_e U_e Ch_b = Mdot_g/B_a; Le = 1 \quad (2)$$

$$Ch_b/Ch_o = f(B_a, M_w) = 1 - (h Mdot_g/r_e U_e Ch_o) \quad (3)$$

where  $r_e$  is edge density,  $U_e$  is edge velocity,  $Ch_o$  is Stanton number without blowing,  $Q_{cw}$  is cold wall heat transfer,  $H_r$  is recovery enthalpy,  $H_{gw}$  is gas-wall enthalpy,  $Ch_b$  is Stanton number with blowing,  $Mdot_g$  is gas mass transfer,  $Le$  is the Lewis number,  $B_a$  is ablation potential,  $M_w$  is molecular weight,  $h = a(M_{wc}/M_{wi})^{**b}$ ,  $h$  is related to the molecular diffusion of the gas into the boundary layer,  $M_{wc}$  is the molecular weight of the inviscid core at the edge of the boundary layer,  $M_{wi}$  is the molecular weight of the injected gas,  $a$  is the coefficient, and  $b$  is the exponent <sup>9</sup>.

The TDK / CET analysis outputs inert gas-wall enthalpy ( $H_{gw}$ ) and reacting gas-wall enthalpy ( $H_{gw}$ ) data as a function of pressure and temperature for nitrided A723 walls, cracked and uncracked chromium plated A723 walls, and cracked and uncracked tantalum sputtered A723 walls. This analysis also outputs condensed phase mass fraction ( $C_{cg}$ ) and ablation potential ( $B_a$ ) data as a function of pressure and temperature for these five walls. Choosing chemical equilibrium species requires considerable experience, since they may not actually exist due to kinetic blocking. These products are confirmed by experimental gas-wall analyses for metal combustion products and other applicable literature data [9].

The TDK / CET thermochemical gas-wall analysis is a practical approximation of the gun barrel bore surface due to sufficient combustion gas activation energy (high temperature) and collisions (high pressure) needed for fast gas-wall reaction rates. The TDK / CET ablation model assumes that as the gas diffuses to the wall, it reacts to form products as follows:

$$B_a = (C_w - C_{cg})/C_g = (C_{pg} - C_g)/C_g \quad (4)$$

where  $B_a$  is the ablation potential,  $C_w$  is the mass fraction of wall material,  $C_g$  is the mass fraction of the gas edge,  $C_{cg}$  is the mass fraction of condensed phase products, and  $C_{pg}$  is the mass fraction of product gas [9].

Figure 1a plots experimental system-specific gas-wall kinetic rate data, normalized mass fraction versus temperature, from a thermogravimetric analysis of the gas-A723, gas-chromium, and gas-tantalum couples needed for MACE code input. Notable features include the gas-wall reaction-limited temperature ( $T_r$ ) and gas-wall diffusion-limited temperature ( $T_d$ ) [9].  $T_r$  is about 800 F for gun steel, 1800 F for chromium, and 2000 F for tantalum. Figure 1b plots experimental material-specific wall softening data, normalized hardness versus temperature, from a thermomechanical analysis of these materials needed for MACE code input. Notable features include the transformation temperature ( $T_t$ ) of about 1300 F for A723 steel. Additional wall softening data includes the melt temperature ( $T_m$ ) of about 2700 F for A723 steel, 3300 F for chromium, and 5300 F for tantalum.

The MACE code calculates the actual thermochemical response including wall ablation, conduction, and erosion using the output of the above analyses and experimental or literature gas-

wall kinetic rate data. Figures 2a and 2b plot respective shot 1 and shot 150 MACE analysis outputs of nitrided A723 wall temperature ( $T_w$ ) data as a function of time at two axial positions (6", 12") and using two round types (M791, 616W). Figures 3a and 3b plot respective shot 1 and shot 150 MACE analysis outputs of 0.002" chromium plated A723 wall temperature ( $T_w$ ) data as a function of time at two axial positions (6", 12") and using two round types (M791, 616W). Figures 4a and 4b plot respective shot 1 and shot 150 MACE analysis outputs of 0.002" tantalum sputtered A723 wall temperature ( $T_w$ ) data as a function of time at two axial positions (6", 12") and using two round types (M791, 616W). For the M242 analysis with its two round types (M791, 616W), independent of shot number (#1, #150), notable features predict the 1.3 - 1.4 times higher refractory metal (both chromium plated A723 and tantalum sputtered A723)  $T_w$ 's compared to nitrided A723 due to A723 steel's higher ablative boundary layer thickening and lower thermal conductivity. For both round types and a given wall, a 100 - 180 F decrease is predicted from the 6" to 12" axial position. For the M791 round type and a given wall, approximately a 300 - 350 F increase in wall temperature is predicted from shot 1 to shot 150. For the 616W round type and a given wall, approximately a 350 - 400 F increase in wall temperature is predicted from shot 1 to shot 150.

Temperature calculated by the MACE module were compared to temperatures calculated by the FDHEAT code [17]. FDHEAT is a finite difference heat transfer program that calculates the transient temperature distribution in a multilayered cylinder where each layer is characterized by an orthotropic material definition. The program models radial heat flow and axial heat flow separately. The material properties are assumed to be a function of temperature. An implicit numerical scheme is used to solve the radial heat conduction equation. Heat transfer to the bore surface is derived from interior ballistics modeling, usually using the program XNOVAKTC.

T in °F	SHOT 1			SHOT 150		
CASE	$T_{FDHEAT}$	$T_{MACE}$	$\Delta$ (%)	$T_{FDHEAT}$	$T_{MACE}$	$\Delta$ (%)
Cr-791-06	1493	1587	-6.3	1860	1937	-4.1
Cr-791-12	1357	1408	-3.8	1708	1788	-4.7
Ta-791-06	1629	1570	3.6	1975	1900	3.8
Ta-791-12	1483	1473	0.1	1798	1823	-1.4
Cr-616-06	1596	1604	-0.1	2004	2004	0.0
Cr-616-12	1435	1452	-1.2	1818	1852	-1.9
Ta-616-06	1739	1691	2.8	2138	2091	2.2
Ta-616-12	1557	1558	0.0	1922	1958	-1.9

TABLE 1

The TABLE 1 compares the maximum calculated temperatures at the coating - A723 interface at the two axial positions (6", 12") for the two round types (M791, 616W) and the two bore coating materials (Ta, Cr). The MACE calculations used an average rate of 70 shots per minute to represent the Cycle A firing scenario while the FDHEAT program modeled the actual bursts of the firing cycle. This comparison is made because the FDHEAT program has been proven accurate when compared to actual test firing results.  $[(T_{FDHEAT} - T_{MACE})/T_{FDHEAT}] \times 100 = \Delta (\%)$ .

Figures 5a and 5b plot respective shot 1 and shot 150 MACE analysis outputs of nitrided A723 wall erosion (Log S; S= in / shot) data as a function of time at two axial positions (6", 12") using two round types (M791, 616W). Figures 6a and 6b plot respective shot 1 and shot 150 MACE analysis outputs of 0.002" uncracked chromium plated A723 wall erosion (Log S; S= in / shot) data as a function of time at two axial positions (6", 12") using two round types (M791, 616W). Figures 7a and 7b plot respective shot 1 and shot 150 MACE analysis outputs of 0.002" cracked (1.0% area by metallography) chromium plated A723 wall erosion (Log S; S= in / shot) data as a function of time at two axial positions (6", 12") using two round types (M791, 616W). Figures 8a and 8b plot respective shot 1 and shot 150 MACE analysis outputs of 0.002" uncracked tantalum sputtered A723 wall erosion (Log S; S= in / shot) data as a function of time at two axial positions (6", 12") using two round types (M791, 616W). Figures 9a and 9b plot respective shot 1 and shot 150 MACE analysis outputs of 0.002" cracked (0.3% area by metallography) tantalum sputtered A723 wall erosion (Log S; S= in / shot) data as a function of time at two axial positions (6", 12") using two round types (M791, 616W).

For the M242 analysis with its two round types (M791, 616W), at two axial positions (6", 12"), predicted shot 1 and shot 150 (cycle A, approximately 70 rpm) erosion comparisons are made for cracked and uncracked 0.002" chromium plated A723 steel, cracked and uncracked 0.002" tantalum sputtered A723 steel, and nitrided A723 steel. For this analysis with its two round types (M791, 616W), notable features predicted thermochemical erosion is 2.0 - 2.5 times lower for cracked chromium plated A723 steel compared to nitrided A723 steel and 4.0 - 6.4 times lower for cracked tantalum sputtered A723 steel compared to nitrided A723 steel. Since uncracked chromium plated and tantalum sputtered A723 steel is virtually uneroded (approximately  $1E-9$  in/shot), it appears that A723 steel ablation at the chromium and tantalum cracks leaves unsupported chromium and tantalum, which is subsequently removed by the high-speed gas flow. For both round types (M791, 616W) and a given wall, a 3 - 5 times decrease in erosion is predicted from the 6" to 12" axial position. For the M791 round type and a given wall, a 5 - 30 times increase in erosion is predicted from shot 1 to shot 150. For the 616W round type and a given wall, a 12 - 50 times increase in erosion is predicted from shot 1 to shot 150. For the five eroded walls and two type round combinations in Figures 5 - 9, the  $T_w$ 's from Figures 2 - 4 applied to Figures 1a - 1b show gas-wall reactions and cracking predominate since each of these combinations exceeded their  $T_r$ 's, but none exceeded their  $T_i$ 's.

In his portion of the report on M242 barrel-ammunition analyses [18], Cox reports that barrel number 12374 was exposed to 205 shots with effect exactly like that of 616W. Material loss measured at 5.5" from the rear face of the tube ( approximately 6" from base of case) was .011". This averages to  $5.4E-5$ " per shot compared to  $3.2E-5$ " per shot calculated by the MACE analysis. Extrapolated, the MACE analysis would predicts .0066". Experience with actual firing and with the code suggests that erosion is not linear with shot number but tends to increase as

firing continues. Thus the extrapolated value of .0066" may be considered a low value. Still the difference between the calculated value and the measured value is only about 40% of the measured value. This is certainly the right order of magnitude and indicates very good agreement without the laboratory determination of the reaction rates of combustion gas species - wall reaction that could be done to further refine the modeling.

## REFERENCES

1. von Karman, T., *Sorbonne Lectures*, 1951-1952; see also *Princeton University Lectures*, 1953; "Fundamental Approach to Laminar Flame Propagation," *AGARD Selected Combustion Problems*, Butterworths, London, 1954; and "Fundamental Equations in Aerothermochemistry," *Proc. 2nd AGARD Combust. Colloq.*, Liege, Belgium, 1955.
2. Reshotko, E., and Cohen, C.B., "Heat Transfer at the Stagnation Point of Blunt Bodies," NACA TN Number 3513, July 1955.
3. Cohen, C.B., Bromberg, R., and Lipkis, R.P., "Boundary Layers with Chemical Reactions Due to Mass Additions," Report No. GM-TR-268, The Ramo-Wooldridge Corporation, Los Angeles, CA, 1957.
4. Denison, M.R., and Dooley, D.A., "Combustion in the Laminar Boundary Layer of Chemically Active Sublimators," Publication No. C-110, Aeronutronic Systems, Inc., Glendale, CA, 1957.
5. Lees, L., "Convective Heat Transfer with Mass Addition and Chemical Reactions," *Combustion and Propulsion, Proc. 3rd AGARD Combust. Colloq.*, Palermo, Sicily, Pergamon Press, NY, 1958; see also *Recent Advances in Heat and Mass Transfer*, McGraw-Hill, New York, 1961.
6. Nickerson, G., Berker, D., Coats, D., and Dunn, S., "Two-Dimensional Kinetics (TDK) Nozzle Performance Computer Program," Software and Engineering Associates, Inc., Carson City, NV, 1993.
7. Dunn, S., "Materials Ablation Conduction Erosion Program (MACE)," Software and Engineering Associates, Inc., Carson City, Nevada, 1989.
8. Gordon, S., and McBride, B., "Computer Program for Calculation of Complex Chemical Equilibrium Compositions, Rocket Performance, Incident and Reflected Shocks, and Chapman-Jouguet Detonations (CET)," NASA SP-273, NASA Lewis Research Center, Cleveland, OH, 1971.
9. Dunn, S., and Sopok, S., Private Communications: Joint Modification & Linkage of the BLAKE, NOVA, TDK, and MACE Codes for Gun Barrel Erosion, and Benet Seminar on Gun Erosion Code System Example, Software and Engineering Associates, Inc., Carson City, NV, and U.S. Army Benet Laboratories, Watervliet, NY, 1992-1993.
10. Freedman, E., "BLAKE - A Thermodynamic Code Based on Tiger: User's Guide and Manual," Technical Report #ARBRL-TR-02411, U.S. Army Ballistic Research Laboratory, Aberdeen Proving Ground, MD, 1982.
11. Gough, P., "The XNOVAKTC Code," Paul Gough Associates, Portsmouth, NH, 1990.
12. 25-mm M242 / M919 / M791 Bushmaster Gun System Drawings, U.S. Army ARDEC, Dover, NJ, 1991.
13. Picard, J., Ahmad, I., and Bracuti, A., *Proceedings of the Tri-Service Gun Tube Wear and Erosion Symposiums*, U.S. Army ARDEC, Dover, NJ, 1970, 1972, 1977, and 1982.
14. Alkidas, A., Morris, S., Christoe, C., Caveny, L., and Summerfield, M., "Erosive Effects of Various Pure and Combustion-Generated Gases on Metals - Part II," U.S. Army Materials and Mechanics Research Center, Watertown, MA, 1977; see also Part I, 1975.
15. Dunn, S., Sopok, S., Coats, D., O'Hara, P., Nickerson, G., and Pflegl, G., "Unified Computer Model For Predicting Thermochemical Erosion In Gun Barrels," *Proc. 31st AIAA Propulsion Meeting*, San Diego, CA, July, 1995.
16. Conroy, P., Weinacht, P., Nusca, M., "ARL Tube Erosion Code (ATEC)," *Proc. 32nd JANNAF*

Sopok, O'Hara, Dunn, Coats, Pflegl

*Combustion Meeting*, Huntsville, AL, October, 1995.

17. Witherell, Mark D., Private Communications regarding the code FDHEAT.

18. Capsimalis, G., Cox, J., O'Hara, P., Witherell, M., Sopok, S., Underwood, J., Pflegl, G., and Cote, P., "Benet Laboratories M242/M919 Multi-Disciplinary Analyses", U.S. Army ARDEC, Dover, NJ, April, 1992, Special Report: Distribution Limited (Note: this report references the analyses of pre-production M919 ammunition.)

## Elastic-Plastic Comparison of Three Thread Forms

G. Peter O'Hara  
Benet Laboratories  
Watervliet Arsenal  
Watervliet NY 121289

### ABSTRACT

The performance of a threaded connection is dependent on the shape or form of the screw threads used. This paper demonstrates the elastic-plastic behavior of three thread forms which have been isolated from any specific structure. Single pairs of threads, from a long chain of identical thread pairs, are analyzed using identical displacement loads. In this way the basic characteristics of the forms may be studied without the confusion of a more complex structure. A shear deformation is applied which takes each thread to near failure, with the results plotted as the Shear Transfer Stress vs. Shear Deformation. The work is a comparison of three different threads, a 3 degree buttress thread, the 7 degree buttress, and the 20 degree buttress. The results clearly show that the 20 degree buttress thread can support a greater shear load before failure.

### INTRODUCTION

The threaded connection is an important part of many complex structures and is frequently a critical fatigue or safety element. Nearly everyone is familiar with the common bolt system which may include high strength aircraft and Class 8 bolts. High strength bolts make use of close control of the thread shape and material properties as defined in a series of National and International Standards documents. This type of design control is necessary for bolts and related fasteners, because they are meant for general usage and maximum interchangeability. This system uses the 30 degree 'V' thread form and has been very successful for many decades. The breech closure of cannons usually has a threaded connection between the breech ring and the gun barrel and may have another between the breech ring and the breech block. There are some cannons in the field with a fourth major element in the breech closure which is a bushing between the block and the ring, which adds another threaded connection. These are distinctly uncommon connections where general interchangeability is of no value and is required only between components of the same gun type. Here the 30 degree 'V' is never used and nearly all guns use some type of buttress thread. The buttress style thread is

characterized as an asymmetric form with a 45 degree angle on the unloaded flank.

While this author has knowledge of 18 different buttress thread forms this report will concentrate on only 3 of them. These three were chosen because of they all are in use on large cannon and are all characterized as high performance threads. The 3 degree buttress thread is used on the 120 mm M256 Tank gun which was originally developen in Germany. It will be identified in this report as the FRG thread. The 7 degree buttress thread, used on the 105 mm Gun M68 which was originally designed in England and will be referred to as the UK thread. The last is the 20 degree buttress thread which has been used on all US designed cannon since its development in 1962 (1-2). It will be referred to as the Benét thread. They all are high performance threads and feature generous root radii to help control the stress concentration at the thread root. Because this report will attempt to compare the fundamental characteristics of the threads all dimensions will the the nominal size for a thread of unit (1.0) pitch. These dimensions are given in Table I.

Table I  
Thread Dimensions for a Unit Pitch

	Thread Type		
	FRG	UK	Benét
Loaded Face Angle	3.0	7.0	20.0
Read FaceAngle	45.0	45.0	45.0
Root Radius	0.125	0.120	0.133
Addendum	0.230	0.1875	0.2013
Dedendum	0.270	0.3045	0.2774
Tip Radius	0.040	0.030	0.0480
Bearing Height	0.3842	.3223	0.3394
Shear Width	0.6595	0.7107	0.7311

#### ELASTIC ANALYSIS

The elastic analysis can proceed on two levels, the strength of materials approach and the Finite Element approach. The strength on materials approach is as simple as the load divided by area to calculate the average bearing stress or shear stress. The stress in the root fillet of the thread requires a more complex approach because this is a set of two different

stress concentration factors. One stress concentration is a function of the thread load and the other is a tensile stress concentration related to the general stress field in the component. The thread load concentration can be calculated from the work of R.B. Heywood (3) and the Tensile stress concentration from Neuber's (4) work. The combination has been explored by this author (5) in a report "Stress Concentrations in Screw Threads". This paper will concentrate on the fundamental effects of the variation in shape of individual thread teeth and will only report the tensile stress concentration without further comment.

The key item in any stress calculation is the selection an appropriate applied load. In the case of screw threads this is a complicated issue because the individual thread loads are not known apriori and can only be determined by a complex analysis of the loaded joint. But this report is a comparison of thread forms and requires only a consistent load for all cases. Here it is useful to use the concept of 'shear transfer', or the local average shear stress transferred at the pitch cylinder. This will be used as a nominal stress for calculating thread related stress concentrations. Using the strength of materials approach for the three subject thread forms are given in table II. The tensile stress concentration factor (SFC) is based on nominal stress in the component not the thread loads.

Table II  
Thread Stress Concentration factors  
Thread Type

	<u>FRG</u>	<u>UK</u>	<u>Benét</u>
Fillet stress	9.886	8.584	5.940
Bearing Stress	2.910	3.103	2.946
Shear Stress	1.424	1.497	1.421
Tensile SCF	2.377	2.565	2.538

#### ELASTIC-PLASTIC ANALYSIS

Elastic-plastic analysis cannot be done by simple strength-of-materials analysis and must be done by the finite element method. Again this is a comparative report and the analysis will be done for a single pair of mating threads with a unit pitch and a small portion of the adjoining structure. This is called isolation analysis in which a small part of a larger problem is isolated for a specific analytic goal. In this case comparing different geometries under similar loads and boundary conditions. In this case the following assumptions are made.

- 1) This is an axisymmetric problem (no helix angle).
- 2) This is one pair of a long set of identical thread pairs.
- 3) Load is transferred away from the threads in shear only.
- 4) There is no general tensile stress field.
- 5) Radial displacement on the left and right boundaries is zero.
- 6) All threads in the set have equal loads.
- 7) A shear load will be applied across the outer boundaries.

The first assumption is satisfied by the selection of an 8 node quadrilateral axisymmetric element type. The next four require an extensive set of fixed constraints and constraint equations. These constraints cover all boundaries of the model except the thread form itself, i.e. the left, right, top and bottom boundaries. The two individual threads interact through an Slide Line contact with zero friction.

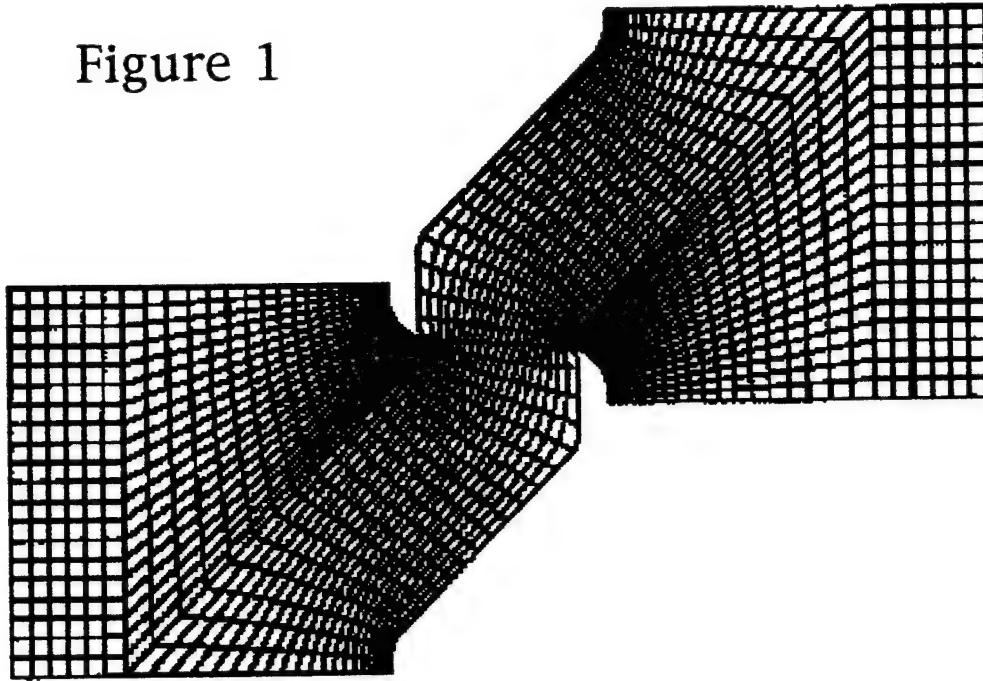
While an applied load was used for elastic analysis, a displacement load is more appropriate to the goals of elastic-plastic work where the structure will be taken to near failure conditions. In this case the left (inner) boundary will be held at zero displacement and the right (outer) will be displaced in, in the axial direction by 4% of the pitch dimension. This is sufficient to bring all thread forms to near failure in shear. This displacement is applied in an average sense by using constraint equations and giving the fixed constraint to a single node. The final results will then be given as a plot of shear transfer stress vs. displacement from 0 to 0.04 pitch units. A second load step will then be used to release the fixed constraint and allow the thread pair to unload to a new deformed shape.

## MODELING

Each two body model consisted of identically shaped thread teeth, interacting along the zero friction sliding contact surface. In the isolation analysis concept a small portion of the adjoining bodies is retained which consisted of an square 1.0 pitch high and 1.0 pitch in the radial direction. Each of these bodies was modeled as 920 elements, which allowed about 20 elements on the contact surface and 20 in the primary fillet. It also allowed a high element density across the base of the thread where the plastic behavior will occur. The ABAQUS (5) finite element code was used, with a typical mesh is shown in figure 1. It should be noted that all of the meshes in this study were topologically similar with the same node numbers on all boundaries fillets and contact surfaces. The radius of the

pitch cylinder is 10.0 with the centerline to the left. This makes the left thread the external thread and the right the internal one.

Figure 1



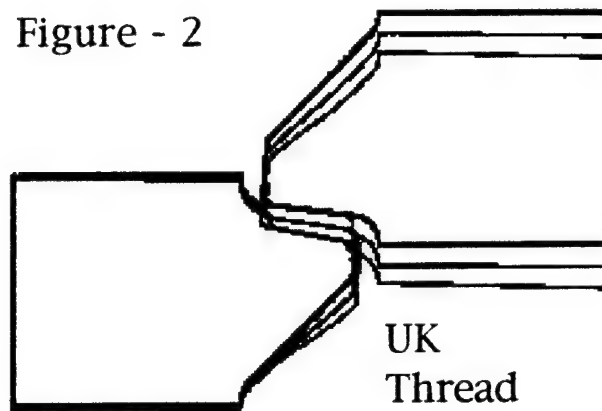
A typical mesh of a thread pair

The material model was the same high strength steel for each tooth and each thread geometry. The model was a bilinear shape with a Young's modulus of 196,700 mPa. and a Poisson's Ratio of 0.285. The yield stress of 1122 mPa. was followed by a small hardening slope of 2,732 mPa. The deformation was 0.040 (4%) was applied to the right hand boundary. A second load step was used to release the applied load on calculate the permanent deformation.

## RESULTS

The results for all three thread forms are similar in appearance and only a sample of the general results will be given here. Figure 2 shows an outline of the UK thread pair along with superimposed deformed outlines of the shape at maximum load. The two deformed outlines are for a displacement magnification of 2.5 and 5.0 times the actual deformation. Figure 3 is a contour plot of maximum Mises Equivalent Stress for the FRG

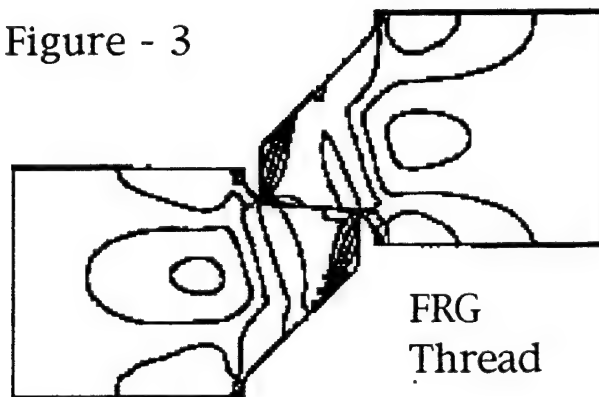
Figure - 2



Undeformed and  
Deformed Outlines  
at Maximum load.

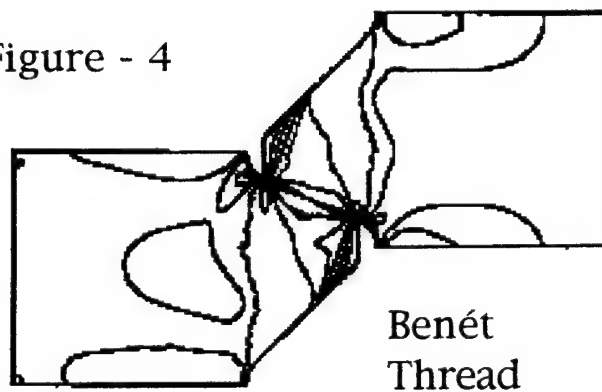
Undeformed  
Magnification = 2.5  
Magnification = 5.0

Figure - 3



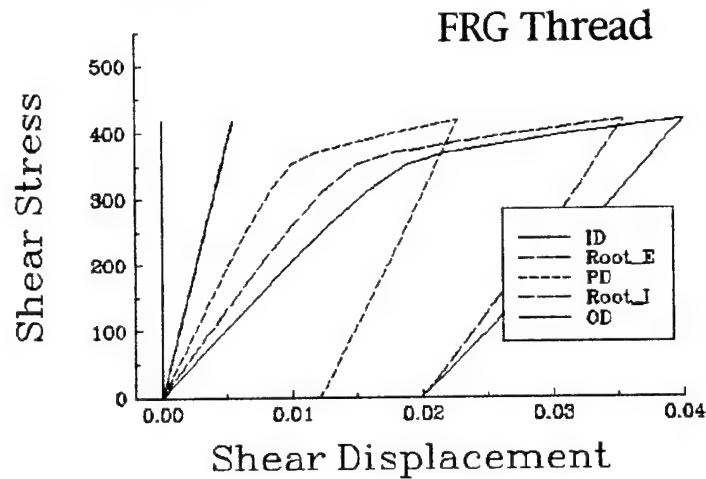
Contours of the  
Mised Stress

Figure - 4



Contours of the  
R-Z Shear Stress

Figure - 5



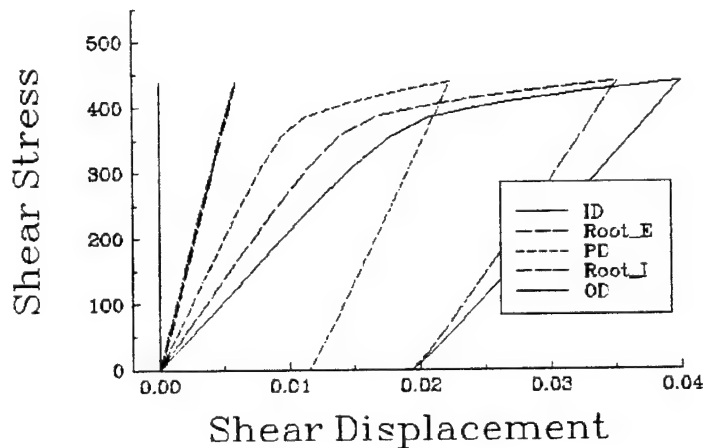
Plots of the Shear  
Transfer Stress

vs.

Shear Displacement

Figure - 6

**UK Thread**

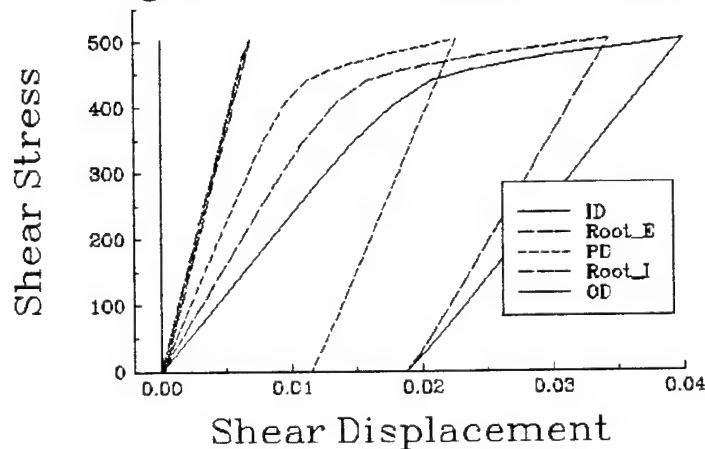


for five critical  
locations in the  
thread pair.

- 1) ID boundary
- 2) External Root
- 3) Pitch Cylinder
- 4) Internal Root
- 5) OD Boundary

Figure - 7

**Benét Thread**



thread. Figure 4 is another contour plot but this time it is the R-Z Shear Stress for the Benét thread.

The final three Figures 5 - 7 show plots of Shear Transfer Stress (Shear Stress) vs. Shear Displacement for five points in the problem. The first point is the left hand boundary which is fixed at zero and shows only the maximum shear stress. The second is the root of the inner or external thread and is the deformation of the inner body caused by the applied thread load. This is nearly linear and with only a small plastic deformation. The third curve is the average contact surface deformation at the pitch line and displays a strong plastic deformation with a large permanent set. The fourth curve is the deformation of the root of the right or internal thread. This shows the elastic-plastic deformation of both threads in the pair plus the left body portion. it is strongly nonlinear and shows substantial permanent set. The last curve is the right hand boundary with a maximum deformation of .04 which is the applied deformation. The permanent set of the fourth and fifth curves is the same, which demonstrates the linear behavior of the outer body portion.

The last result shown here is the stress stress condition which is calculated using the elastic stress factors and the maximum load in the elastic=plastic analysis. These can be compared with the tensile yield of 1122 mPa. and shear yield of 561 mPa.

Table III  
Elastic Stresses calculated from the maximum load.

	Thread Type		
	<u>FRG</u>	<u>UK</u>	<u>Benét</u>
Shear Transfer	418	438	503
Fillet stress	4133	3759	2988
Bearing Stress	1217	1359	1482
Shear Stress	595	655	715

## DISCUSSION

As noted above the general behavior of all three threads is similar in appearance, however the details are substantially different. The first elastic analysis results show a strong difference in the basic fillet stress of the different thread forms. The data given here is supported by the work in reference 2 and other unpublished finite element analysis. This is the

one of the factors which control fatigue life of threaded connections. The other is the tensile stress concentration factor which is not substantially different. In the Elastic-plastic analysis all threads show a well defined zone of high shear across the base of the thread starting at the tip of the mating thread (figures 3 and 4). This shear effect is larger on the external thread because the shear zone is at a smaller radius and therefore is smaller in size. This effect could be different if the two threads in a pair were made of different materials, with different yield strengths. Another similarity is that all the threads show a strong elastic recovery upon unloading. However one of the most important things to note is that the change from nearly linear behavior to plastic behavior is rather sharp and looks much like the stress-strain curve of a common tensile specimen. At the maximum deformation of 4% in these solutions these threads are all progressing to failure with little increase in load and will only need sufficient energy to progress to final failure.

The data from Table III shows that at the large deformation is required to produce shear failure, all the threads show similar problems. The average bearing stress is over the material yield and a detailed examination of the deformed shapes do confirm this fact. A more striking fact is that the fillet stress exceeded yield by a factor of 2.6 to 3.7. Clearly the actual design load for these threads must be set well below any level which would reasonably approach the shear failure load and that load will be set from fillet stress or bearing stress considerations. Another problem is that shear stress is frequently calculated at the pitch line which has nothing to do with any reasonable failure mode in cannon.

This work addresses two other areas of concern about the behavior of threads in threaded connections. First is the idea that a thread to thread pitch error can be corrected by plastic deformation. Second the question of whether or not moderate overloads will cause serious consequence. This work tends to downplay the first idea because the behavior remains nearly linear at substantial deformations of 0.75 to 1.0 % of the pitch dimension. One percent of a 10 mm pitch would be 0.10 mm which would be a large thread to thread error. At the same time the analysis shows a strong elastic recovery after the 4%. This would tend to reinforce the second idea, that threads may be damage tolerant when subjected to moderate overloads.

The last point is that this report is an outline of an analytical tool which

can easily be expanded to study a wide range of other loading and material conditions. An example of this is that the radial deformation of either the left or right boundaries could be set to any desired value or a general axial stress condition can be simulated in either body of the analysis. This type of analysis could be useful in design, analysis of the evaluation of failure conditions and the study of the residual stresses in threads.

## CONCLUSIONS

This report outlines an analytic method which may be very useful in the detailed study of threaded connections. However many of the results are not new and only tend to reinforce conventional notions of thread failure.

The results also tend to reinforce the use of the Benét thread for cannon breech closures. This thread form has achieved a shear failure stress which is in excess of the failure stress calculated from the simple strength of materials analysis.

## REFERENCES

- 1) Weigle, E.R., Lasselle, R.R., and Purtell, J.P. "Experimental Investigation of the Fatigue Behavior of Thread-type Projections", Experimental Mechanics May 1963
- 2) Weigle, E.R. and Lasselle, R.R., "Experimental Techniques for Predicting Fatigue Failure of Cannon-breech Mechanisms", Experimental Mechanics, February 1965
- 3) Heywood, R.B. "Designing by Photoelasticity" Chapman & Hall Ltd., London, 1952, Pages 205-215
- 4) Neuber, H. "Theory of Notch Stresses", Translated for David Taylor Model Basin, US Navy, by F.A. Ravin, J.W. Edwards, Ann Arbor 1946
- 5) O'Hara, G.P. "Stress Concentrations in Screw Threads", US Army Armament Research and Development Command Technical Report, ARLCB-TR-80010, April 1980
- 6) ABAQUS Version 5.5-1, A product of Hibbitt, Karlsson and Sorensen Inc. (HKS), 1000 Main Street, Pawtucket RI, 1995

MCMULLEN

**\*TITLE:** Application of Sub-Models to Explore Geometric Effects in Medium  
Caliber Gun Barrels

P.J. MCMULLEN  
CONCURRENT TECHNOLOGIES CORPORATION  
1450 SCALP AVENUE  
JOHNSTOWN, PA 15904

**\*ABSTRACT**

To understand the influence of geometry on the thermal gradients established in a 25mm M242 gun barrel during a firing sequence, three sub-models of common near-bore features are analyzed. The first sub-model is used to study the effect of land/groove configuration on development of the radial thermal gradient. The analytical results are compared to data obtained from actual firing tests. The second sub-model is used to study the effect of a variation in the bore surface chrome plating thickness on the radial thermal gradient. The final sub-model is used to study the effect of a near-bore thermocouple hole itself on the radial thermal gradient in a gun barrel. Since this sub-model is computationally intensive, simplified sub-models are used to study various near-bore thermocouple hole depths. Results indicate that the thermocouple hole does influence development of the radial thermal gradient.

**\*BIOGRAPHY:** Technical Staff - Concurrent Technologies Corporation, Johnstown, PA

**\*PRESENT ASSIGNMENT:** Technical Lead on Numerical Modeling for the Advanced Gun  
Barrel Project

**\*PAST EXPERIENCE:** 1992-Present: Concurrent Technologies Corporation, Johnstown, PA  
1989-1992: AEA O'Donnell, Inc., Pittsburgh, PA

**\*DEGREES HELD:** B.S. Mechanical Engineering (1989),  
University of Pittsburgh at Johnstown

## **APPLICATION OF SUB-MODELS TO EXPLORE GEOMETRIC EFFECTS IN MEDIUM CALIBER GUN BARRELS**

P.J. McMullen  
Concurrent Technologies Corporation  
Johnstown, Pennsylvania, USA 15904

### **ABSTRACT**

To understand the influence of geometry on the thermal gradients established in a 25mm M242 gun barrel during a firing sequence, three sub-models of common near-bore features are analyzed. The first sub-model is used to study the effect of land/groove configuration on development of the radial thermal gradient. The analytical results are compared to data obtained from actual firing tests. The second sub-model is used to study the effect of a variation in the bore surface chrome plating thickness on the radial thermal gradient. The final sub-model is used to study the effect of a near-bore thermocouple hole itself on the radial thermal gradient in a gun barrel. Since this sub-model is computationally intensive, simplified sub-models are used to study various near-bore thermocouple hole depths. Results indicate that the thermocouple hole does influence development of the radial thermal gradient.

### **INTRODUCTION**

Medium caliber gun barrels are required to operate at increasing rates of fire, approaching 1000 shots per minute (SPM), with sustained bursts of 150 rounds for a 6000 round life. High impetus propellants used to accelerate modern high kinetic energy projectiles generate flame temperatures up to 3550K, placing severe demands on barrel and rifling integrity for sustained high accuracy. These requirements are dictated by advanced gun system performance specifications that demand more ordnance on target at a longer range, leading to a higher kill probability and a greater safety factor. The desired performance is beyond the capability of current gun barrel materials.

In response to this need, the Advanced Gun Barrel Technology Initiative is being conducted by the National Center for Excellence in Metalworking Technology to improve gun barrel performance through a coordinated materials/product/process effort. The project

---

This work was conducted by the National Center for Excellence in Metalworking Technology, operated by Concurrent Technologies Corporation, under contract to the U.S. Navy as part of the U.S. Navy ManTech Program.

emphasizes application to U.S. Navy gun systems, such as the Phalanx weapon system, but the technology will also be applicable to weapon systems in all Services and adaptable to a wide range of gun calibers [1].

A major aspect of this work is the understanding and control of heat generation and transfer during firing. Since the rate of energy transferred from the hot propellant gases to the bore surface of the gun barrel is so much greater than the rate of energy transferred radially through the barrel wall, the rate of energy stored in the gun barrel is high. This causes large thermal gradients near the bore surface. By introducing geometric discontinuities in areas where large thermal gradients are present, a change in both magnitude and direction of the thermal gradient can occur. Three specific sub-models are used to determine the effect of near-bore geometric features on thermal gradients that occur during a firing sequence. The purpose of this paper is to present the results of these analyses and their implications for further development.

## DESCRIPTION OF MODELS

### Land/Groove Configuration Model

The purpose of the Land/Groove Configuration Model is to determine the effect of rifling in a gun barrel on the development of the radial thermal gradient during a firing sequence. To take advantage of symmetry in the rifling, a two-dimensional finite element model of a 10° segment cut through half of a land and half of a groove is used for the transient thermal analysis (see Figure 1). This segment is located approximately 172mm from the breech end of the gun, the area where the largest thermal gradients occur. The analysis was run using the ANSYS® finite element code. In order to accurately model the thermal response of the gun barrel to a firing sequence, a transient thermal analysis is required. Gas temperature and film coefficient predictions with respect to shot time for the M791 round were generated by a Benét Laboratories<sup>1</sup> internal ballistics code. These thermal boundary conditions are applied to the entire edge of the land and the groove for a five round burst fired at 85 SPM. The actual time to fire five shots is 3.54 seconds. A cool-down time of 6.46 seconds after the fifth shot is included in the model to compare analytical results to actual firing test temperature data.

Modeling assumptions are: 1. Axial conduction is negligible; 2. Temperature independent material properties for the chrome plating and the steel jacket are used in the model; 3. Radiation effects are negligible; 4. Chrome plating is a constant thickness of 0.102mm (0.004 inch) on both the land and the groove; 5. The initial temperature of the barrel is constant at 68°C; 6. The interface between the chrome plating and the steel jacket is perfect (100% conduction from chrome plating to steel jacket).

---

® ANSYS is a registered trademark of SAS IP, Houston, PA 15342

<sup>1</sup> Benét Laboratories, Watervliet, New York 12189

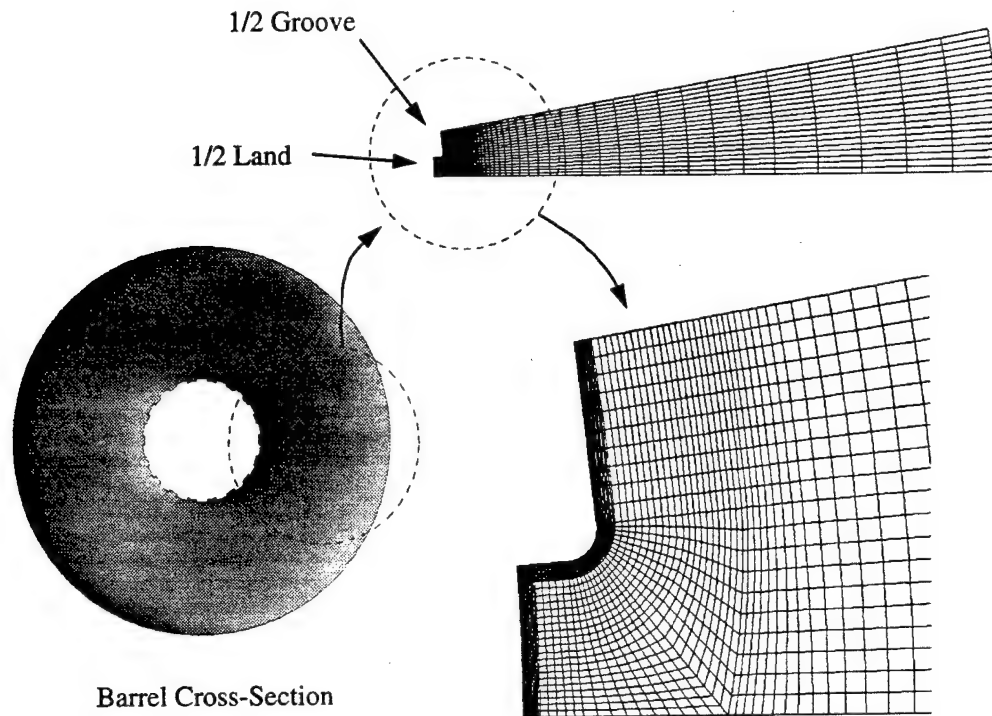


Figure 1: Land/Groove Configuration Model

### Chrome Plating Thickness Comparison Model

The purpose of the Chrome Plating Thickness Comparison Model is to determine the effect of a variation in the bore surface chrome plating thickness on the radial thermal gradient. The same type of model used for the Land/Groove Configuration study is used to study the effects of varying chrome plating thicknesses. The two cases analyzed are considered to be the limiting cases. Case one, which represents the minimum amount of chrome that should be present in this barrel, assumes a constant chrome plating thickness of 0.102mm (0.004 inch). Case two, which represents the maximum amount of chrome that should be present in this barrel, assumes a constant chrome plating thickness of 0.254mm (0.010 inch). Figure 2 shows the difference between the two finite element models. Modeling assumptions are the same as those specified for the Land/Groove Configuration Model.

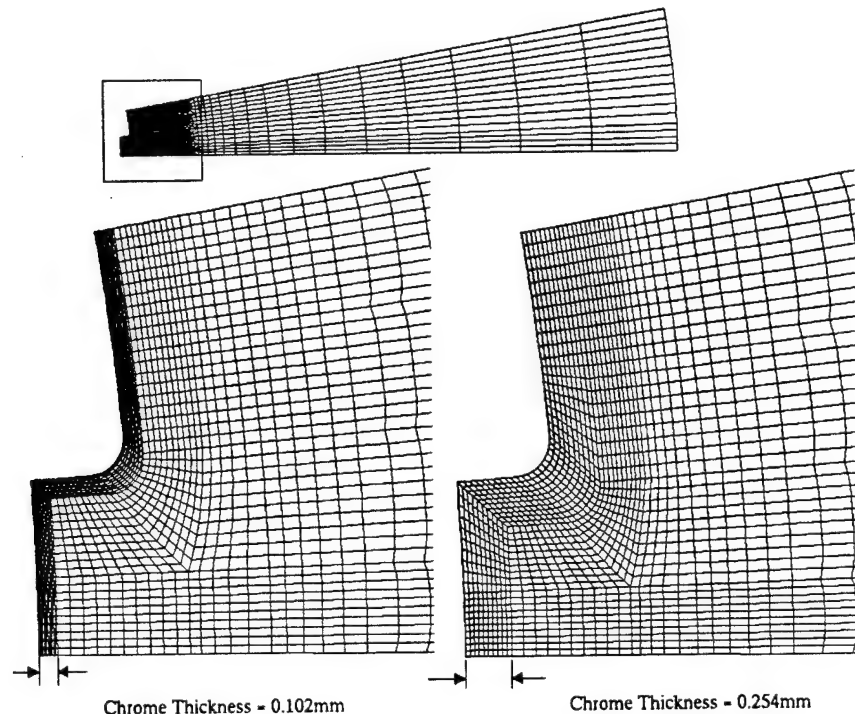


Figure 2: Chrome Plating Thickness Comparison Models

### Near-Bore Thermocouple Hole Model

The purpose of the Near-Bore Thermocouple Hole Model is to determine the effect of a near-bore thermocouple hole itself on the radial thermal gradient in the gun barrel during a firing sequence. Figure 3 shows a wireframe segment of the gun barrel with the entire thermocouple hole included. To take advantage of symmetry in the rifling and the thermocouple hole, but neglecting any circumferential thermal effects, a three-dimensional finite element model of a  $10^\circ$  segment cut through half of a land and half of a groove (1/4 of the thermocouple hole located at a land centerline is included) is used for the thermal analysis (see Figure 4). This segment is located approximately 172mm from the breech end of the gun. There are 23,750 8-noded hexahedral elements and 26,682 nodes in the model. Since large thermal gradients occur near the bore, a very fine mesh is used in this region. The analysis was run using the ANSYS<sup>®</sup> finite element code. In order to accurately model the thermal response of the gun barrel to a firing sequence, a transient thermal analysis is required. Gas temperature and film coefficient predictions with respect to shot time for the 616W round were generated by a Benét Laboratories internal ballistics code. These thermal boundary conditions are applied to the entire surface of the land and groove for a 21 round burst fired at 250 SPM. The actual time to fire 21 shots is 5.04 seconds. The model includes a 15mm axial segment of the barrel referenced from the centerline of the thermocouple hole. This segment is modeled to compare the thermal gradient at the hole location to a location where the thermal gradient is not influenced by the hole.

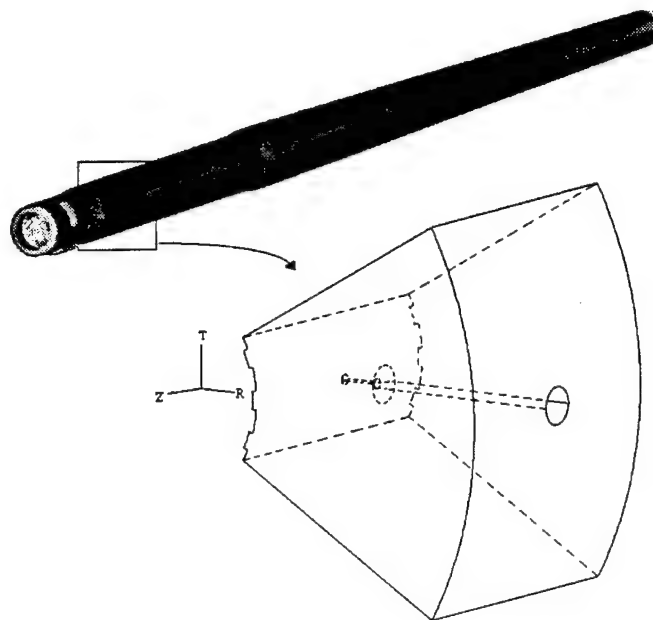


Figure 3: Wireframe Segment of Near-Bore Thermocouple Hole

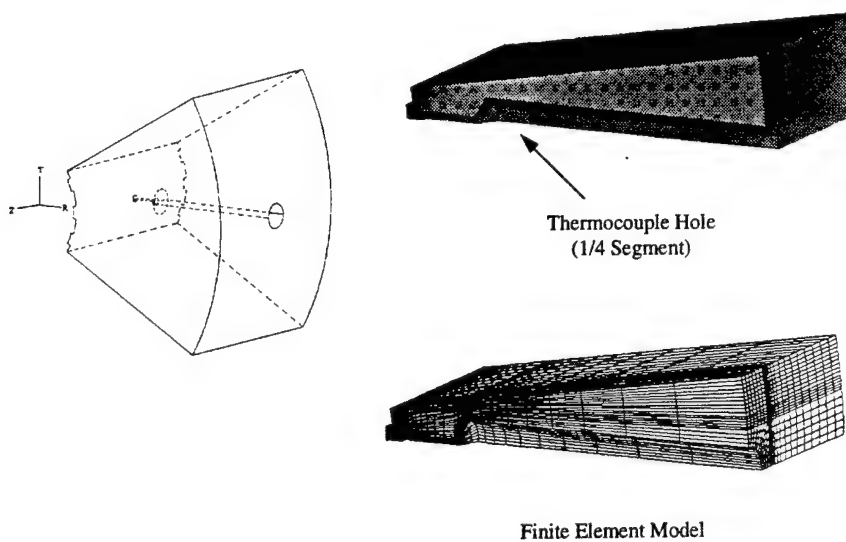


Figure 4: Near-Bore Thermocouple Hole Model

Modeling assumptions for the Near-Bore Thermocouple Hole Model are: 1. Temperature independent material properties for the chrome plating and the steel jacket are used;

2. The surface of the thermocouple hole is adiabatic since the volumetric heat transfer to the air in the hole is minimal compared to the amount of heat transferred to the barrel; 3. Seven points from the calculated film coefficient and gas temperature versus time curves are used for each shot (This is an approximation of the original curves which contain about 130 points. Three points are used for the blowdown phase of each shot.); 4. Radiation effects are negligible; 5. Chrome plating is a constant thickness of 0.102mm on the bore surface; 6. The initial temperature of the barrel is constant at 68°C; 7. The interface between the chrome plating and the steel jacket is perfect (100% conduction from the chrome plating to the steel jacket); 8. For this segment, film coefficient and gas temperature are constant in the axial direction of the barrel (These conditions actually vary along the length of the barrel during any given shot. This assumption, for comparison purposes only, is made to eliminate any potential near-bore axial thermal gradient that may influence the development of the radial thermal gradient.); 9. The film coefficient and the bulk temperature on the outer surface of the barrel are constant at  $25\text{W}/(\text{m}^2\cdot^\circ\text{C})$  and  $21.1^\circ\text{C}$  for the entire shot sequence (This simulates a natural convection boundary condition on the exterior of the gun barrel.).

Since the Near-Bore Thermocouple Hole Model is computationally intensive (approximately one day in CPU time to calculate temperatures for one shot), simplified sub-models were developed to study the effect of various near-bore thermocouple hole depths on the development of the radial thermal gradient. Four two-dimensional axisymmetric (symmetric about the thermocouple hole axis) finite element models with different thermocouple hole depths are used for the transient thermal analyses (see Figure 5).

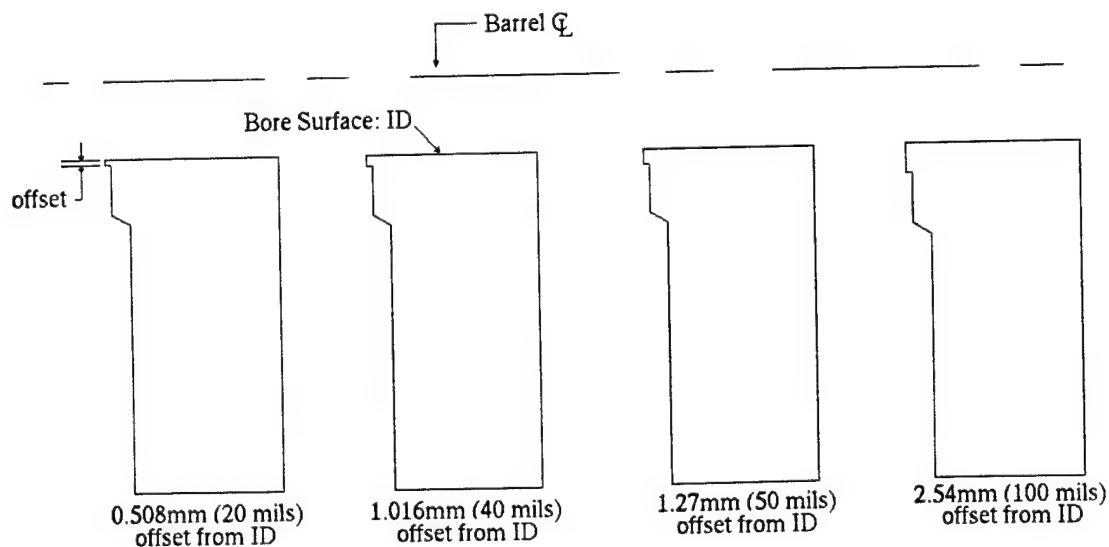


Figure 5: Two-Dimensional Axisymmetric Near-Bore Thermocouple Hole Models (Edge Plots)

The purpose of these sub-models is to study the effect of various near-bore thermocouple hole depths on the thermal gradient with reduced computation time and without the influence of the rifling. Each sub-model is analyzed for a 15 round burst of 616W ammunition fired at 500 SPM. This high rate of fire is chosen to quickly obtain a thermal gradient around the thermocouple hole.

## RESULTS AND CONCLUSIONS

### Land/Groove Configuration Model

For the specific five round burst shot schedule of M791 ammunition studied, the calculated temperature difference between the land and groove at locations consistent with the actual thermocouple locations reached about  $30^{\circ}\text{C}$ . Figure 6 shows the thermocouple hole locations relative to the land and the groove. Temperatures for thermocouple 1A are taken from the location in the groove region where an actual thermocouple is placed for the test measurements (1.27mm from the surface of the groove). Temperatures from thermocouple 1B are taken from the location in the land region where an actual thermocouple is placed for the test measurements (1.27mm from the surface of the land).

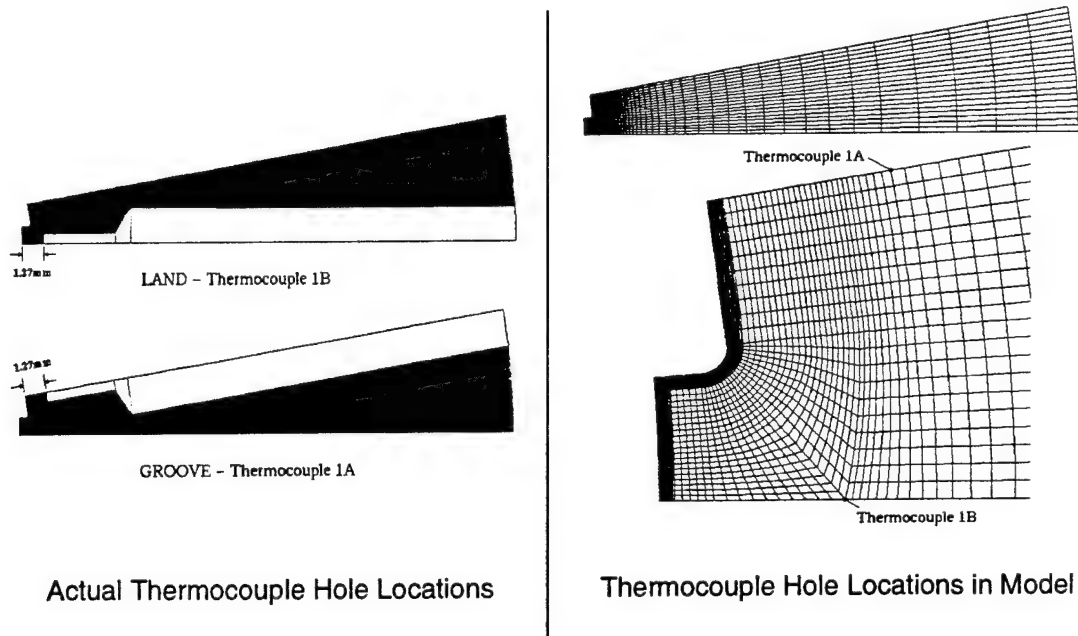


Figure 6: Actual/Model Thermocouple Hole Locations

The calculated results for the specific shot schedule show a lag in the thermal response of thermocouple 1A of about  $30^{\circ}\text{C}$  when thermocouple 1B shows a peak temperature for the fifth

shot (see Figure 7). The temperature contour plot of the land/groove region can be seen in Figure 8 for the fifth shot at 2.935 seconds in the shot sequence. The calculated temperatures at thermocouple 1B and thermocouple 1A locations are 230.18°C and 199.40°C respectively.

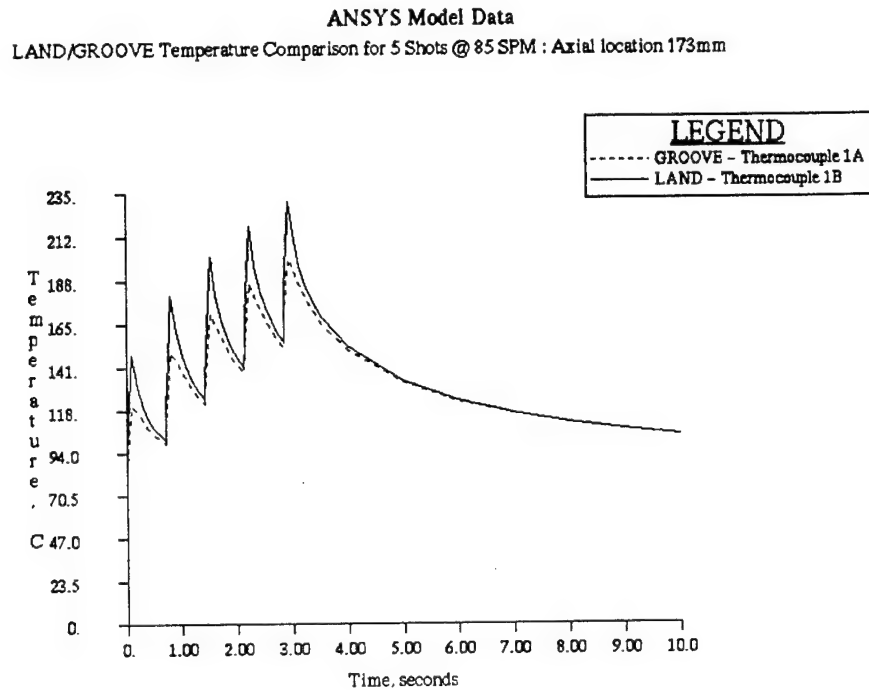


Figure 7: ANSYS Results - Temperature Profile for Land and Groove Thermocouple Locations

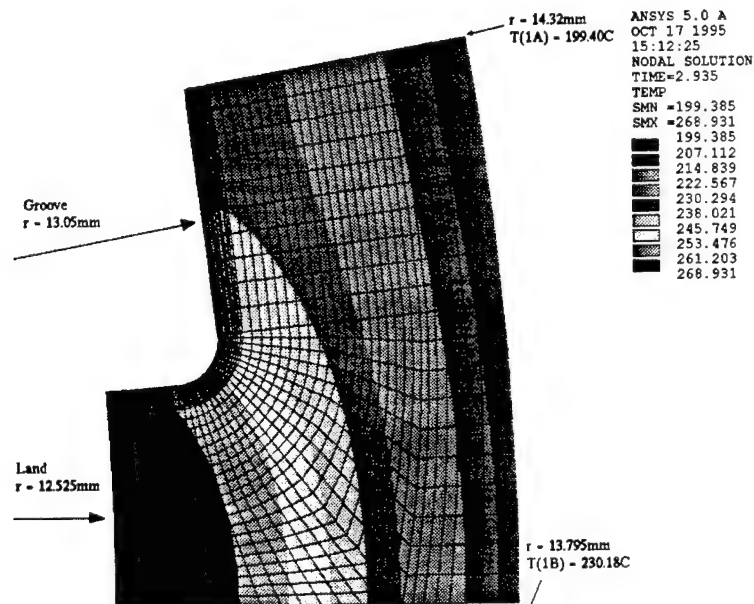


Figure 8: Land/Groove Temperature Profile at Time = 2.935 seconds

The test measurements for the specific shot schedule show the same trend found in the calculated results (see Figure 9). The groove thermocouple (1A) reading lags by about  $30^{\circ}\text{C}$  when the land thermocouple (1B) reads a peak temperature for the fifth shot. Temperature values for the calculated results do not accurately correspond with temperatures from the test measurements. This is due in part to modeling assumptions as well as potential errors in the film coefficient and gas temperature predictions.

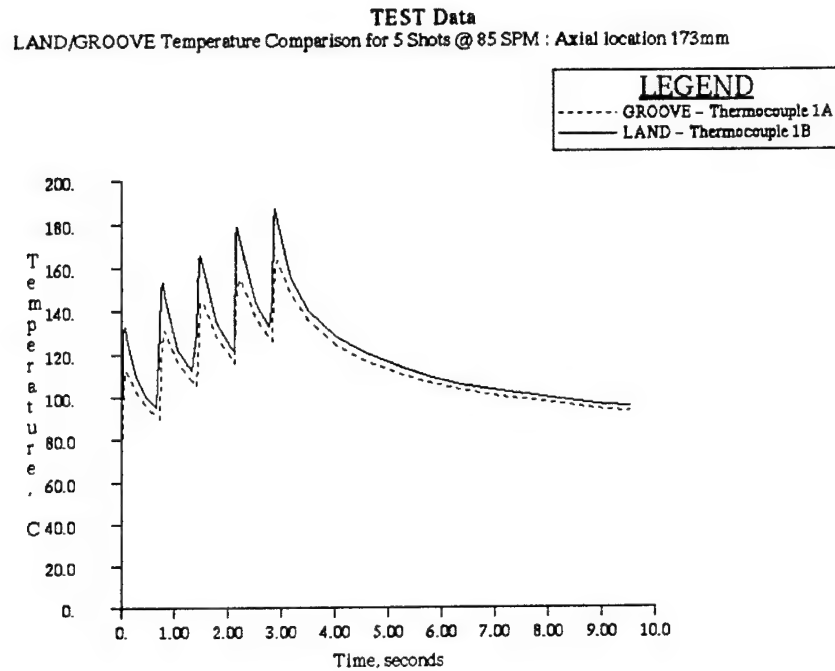


Figure 9: Actual Temperature Measurements from Land and Groove Thermocouples

From this study, it is concluded that the thermal gradient is greatly influenced by the land/groove configuration. Knowing precise thermocouple locations in the land/groove region is important when using temperature measurements to validate an analytical model of this region. It is also concluded that if an analytical model of a gun barrel does not included a land/groove region, steps must be taken to account for the temperature differences that exist in this region.

### Chrome Plating Thickness Comparison Model

From the two limiting cases studied (0.102mm and 0.254mm of chrome plating), the maximum temperature difference at thermocouple 1A and 1B locations reached about  $5^{\circ}\text{C}$  as the chrome plating thickness was changed. Figures 10 and 11 show the temperature profile comparisons. For the specific five round burst of M791 ammunition studied, temperatures for the 0.102mm chrome thickness model lag the temperatures for the 0.254mm chrome thickness

model in both the land and groove regions. This temperature difference may increase with longer bursts but is not expected to be significant.

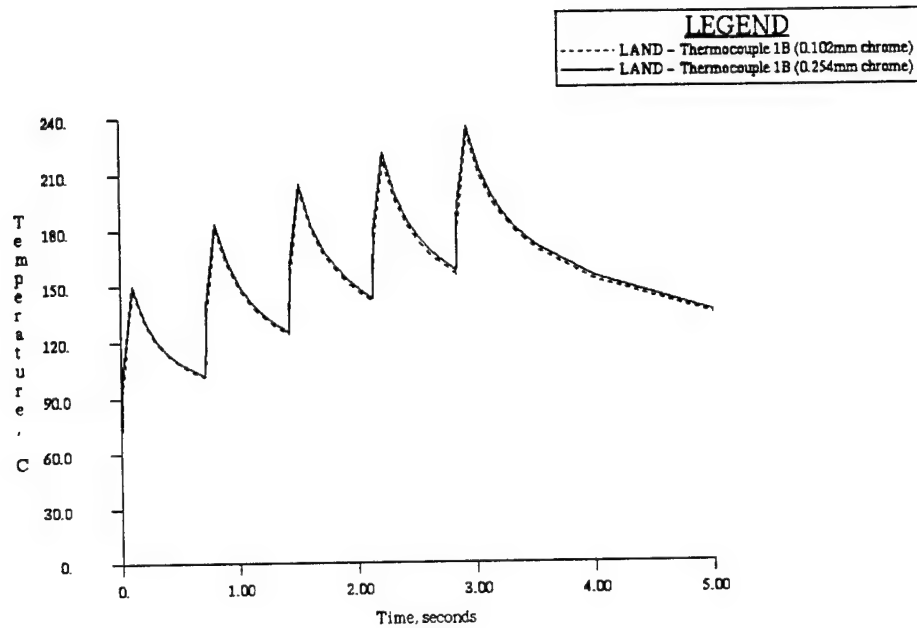


Figure 10: Chrome Plating Thickness Comparison (Land Region) - 5 Shots @ 85 SPM

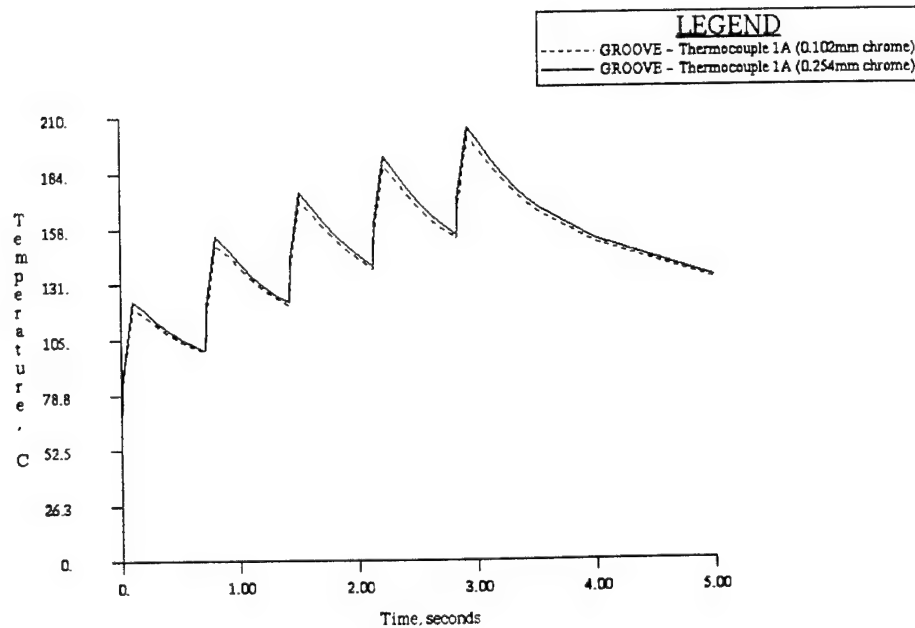


Figure 11: Chrome Plating Thickness Comparison (Groove Region) - 5 Shots @ 85 SPM

From this study, it is concluded that a variation in chrome plating thickness on the bore surface does not significantly affect the radial thermal gradient. However, when combined with other geometric effects, temperature predictions can deviate from actual temperature values.

### Near-Bore Thermocouple Hole Model

For the specific 21 round burst shot schedule of M919 ammunition studied, the calculated temperature at the thermocouple hole location was about  $45^{\circ}\text{C}$  greater than the temperature at the same radial location but 15mm away in the axial direction. Figure 12 shows the locations of the two nodes used for the temperature comparison. The bottom of the thermocouple hole is located 1.27mm radially outward from the surface of the land.

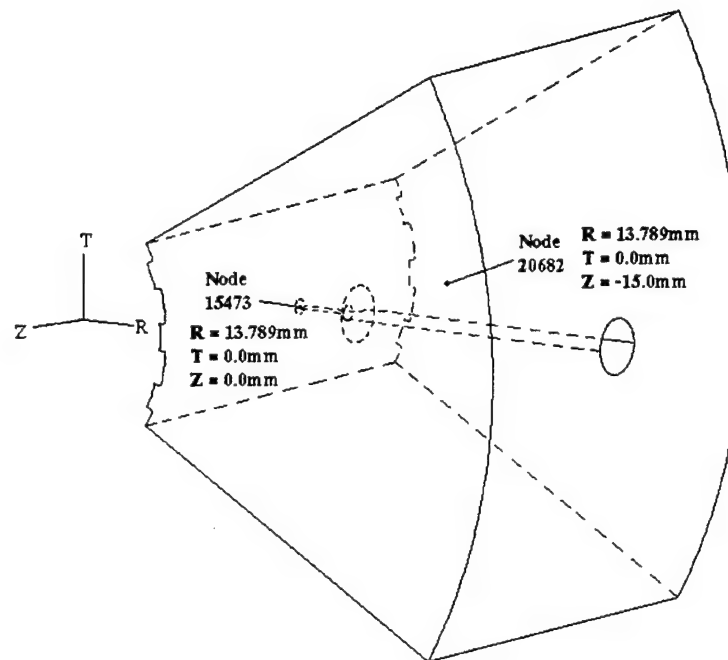


Figure 12: Node Locations for Temperature Comparisons

After 21 shots, the temperature difference between the two nodes continues to diverge but at a slower rate than earlier in the shot sequence. Figure 13 shows the temperature profiles of both nodes for 21 shots. A plot of peak temperature difference between the two locations versus time shows the temperature difference begins approaching a constant value of about  $45^{\circ}\text{C}$  (see Figure 14).

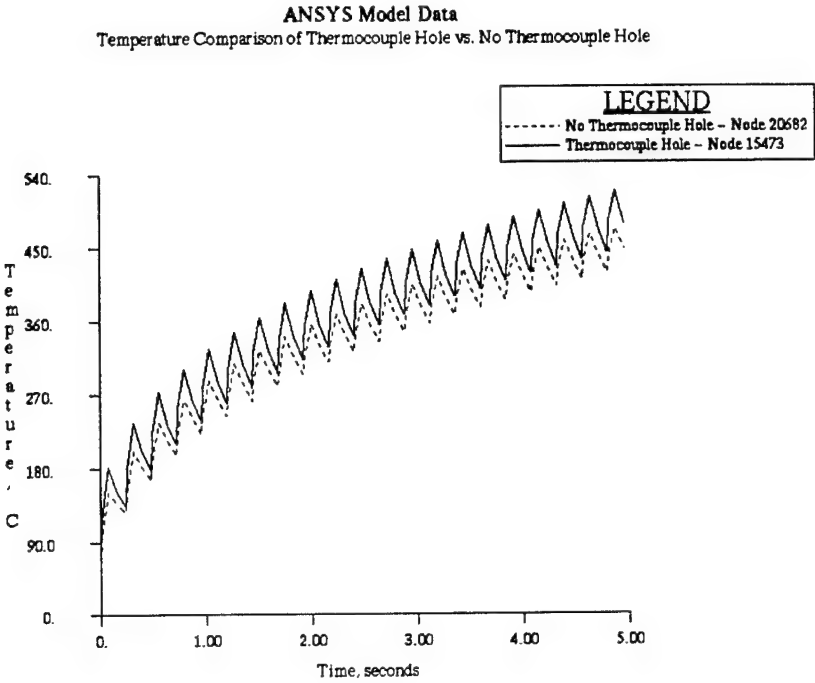


Figure 13: Nodal Temperatures for 21 Shots

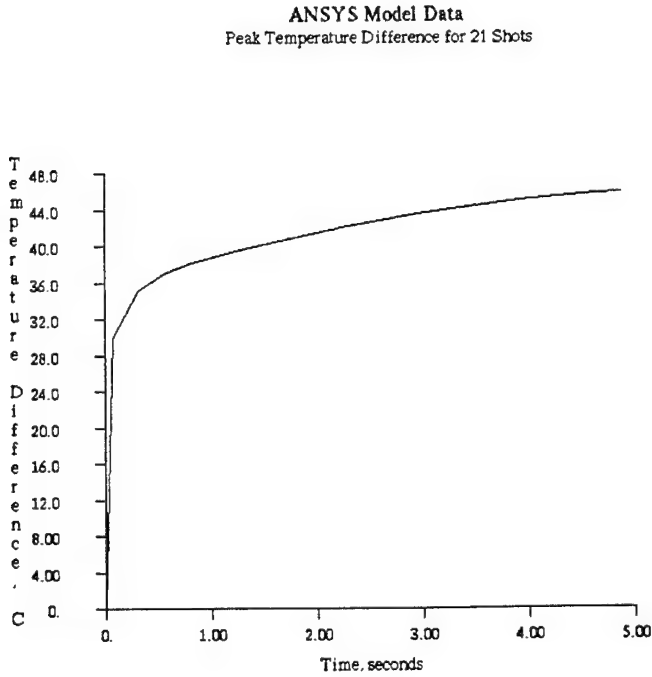


Figure 14: Peak Temperature Difference Versus Shot Time

Figures 15 and 16 show significant differences in the thermal gradients between the beginning of a shot and the end of a shot (0.24 seconds for one complete shot). At the beginning of shot 17, the temperatures at the bore surface and the bottom of the thermocouple hole are 1249°C and 410°C, respectively, leading to a thermal gradient of 661°C/mm. At the end of shot 17, the temperatures are 427°C and 419°C, respectively, leading to a gradient of 6°C/mm.

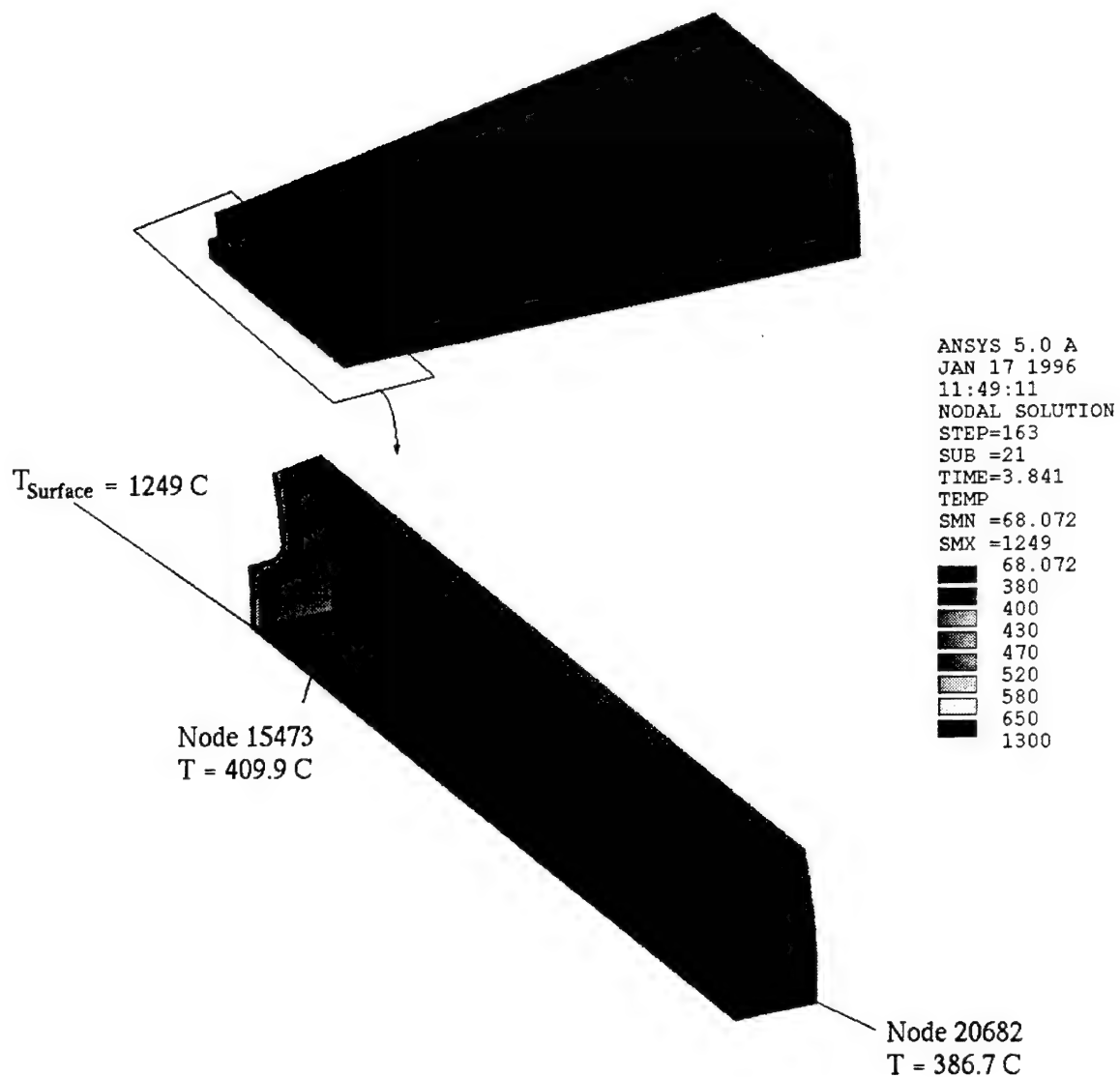


Figure 15: Temperature Contour Plot at the Beginning of Shot 17 - Time = 3.841 seconds

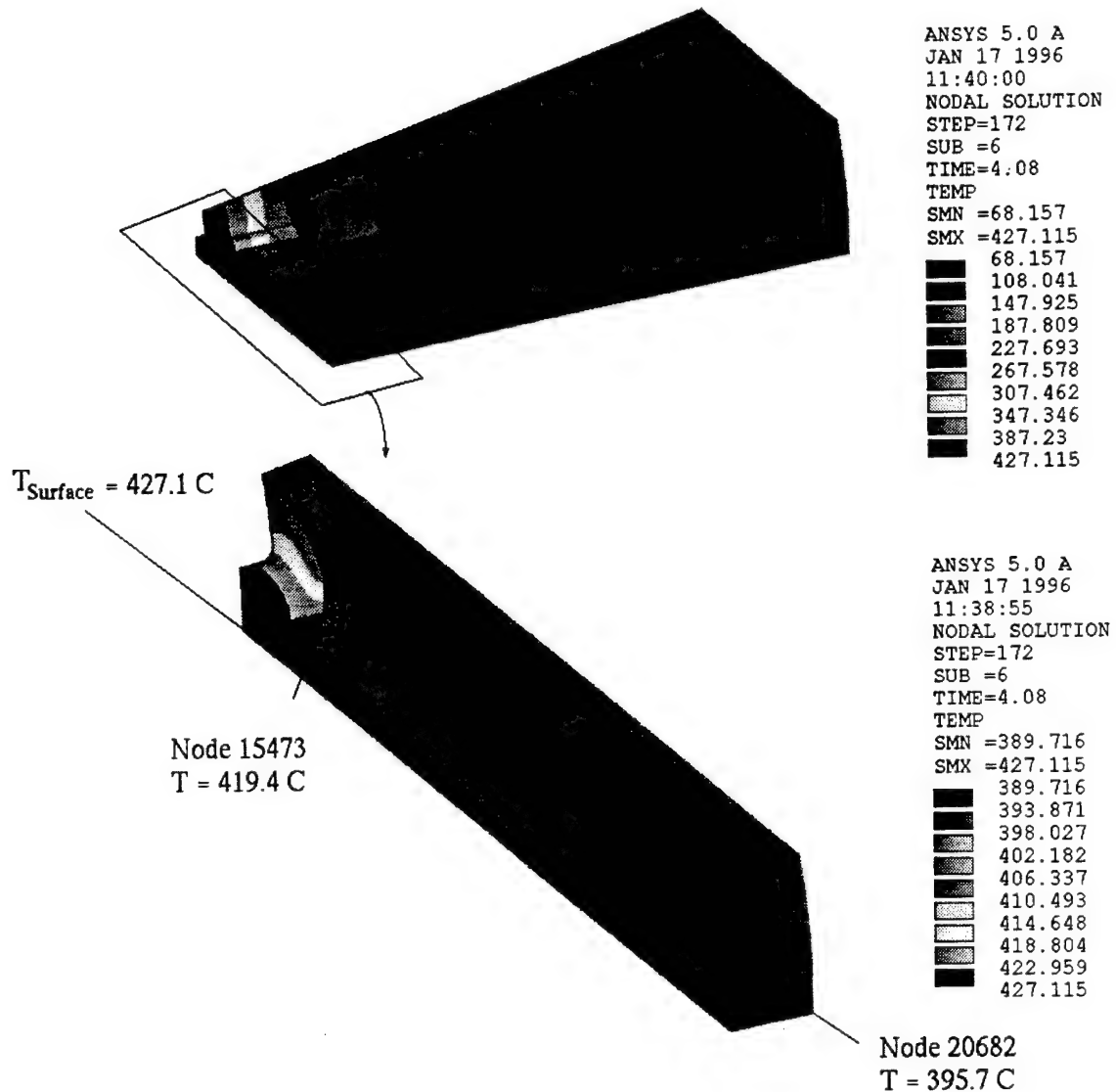


Figure 16: Temperature Contour Plot at the End of Shot 17 - Time = 4.08 seconds

To better understand the effect of varying near-bore thermocouple hole depths on the thermal gradient, simplified two-dimensional sub-models that ignore the land and groove geometric effects are used. These models require less computation time than the three-dimensional model of the near-bore thermocouple hole. There are two important findings from these models: the first is an understanding of how the thermal gradients are developed for various thermocouple hole depths; the second is a demonstration of how the thermal gradient is affected by the hole itself at various thermocouple hole depths. Figure 17 is a temperature contour plot of the four models at the end of the fifteenth shot. This figure shows that a hot spot

occurs near the bottom of the hole. This hot spot diminishes in size when the thermocouple is located farther away from the bore surface of the barrel.

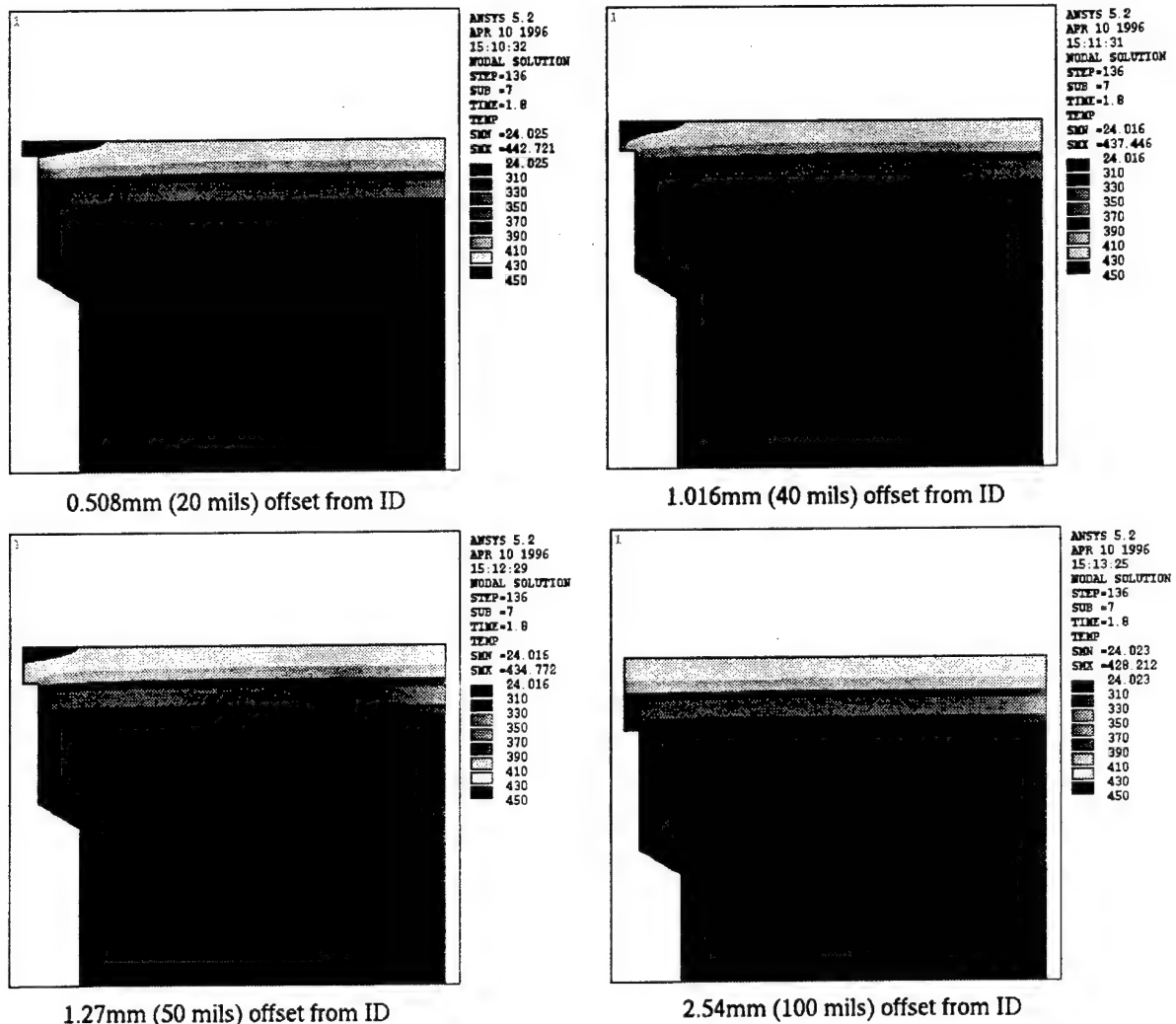


Figure 17: Temperature Contour Plots of Four Different Thermocouple Hole Depths

Temperature profiles for all four thermocouple hole depths are shown in Figure 18. From the same models, temperature profiles for the no thermocouple hole conditions (same barrel radial location as the bottom of the thermocouple hole but far enough away to be unaffected by the hole) show lower temperatures and differing peak amplitudes (see Figure 19). The results from these models show that the actual temperature at a thermocouple hole located between 0.508mm and 2.54mm from the bore surface can differ by as little as 30C° or as much as 125C° from the temperature measured by a thermocouple in the hole (see Figure 20).

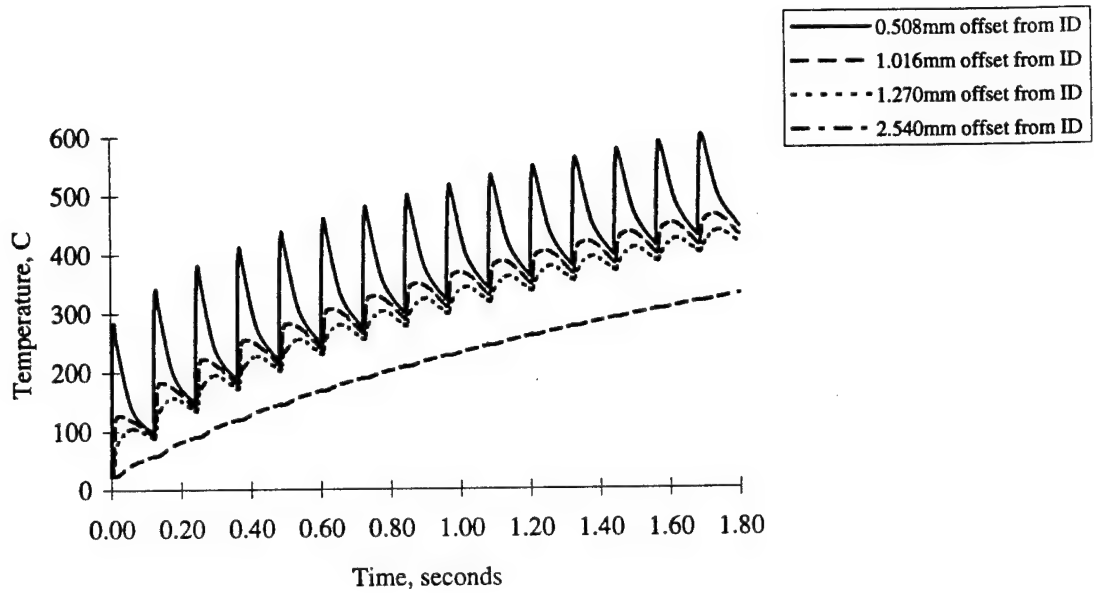


Figure 18: Temperature Profiles for Thermocouple Hole Locations - 15 Shots @ 500 SPM

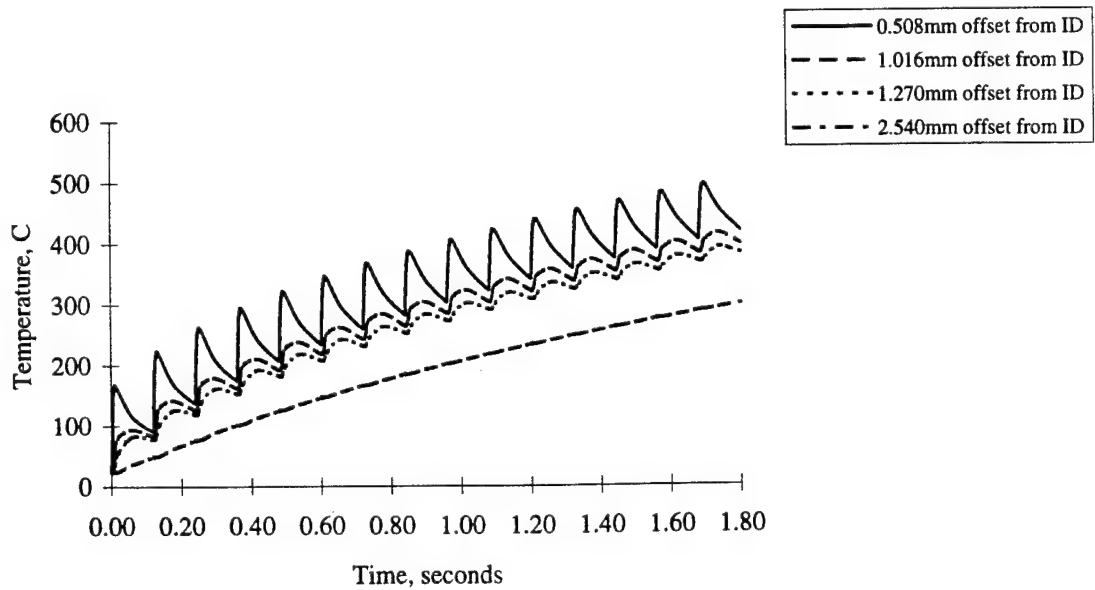


Figure 19: Temperature Profiles for No Thermocouple Condition - 15 Shots @ 500 SPM

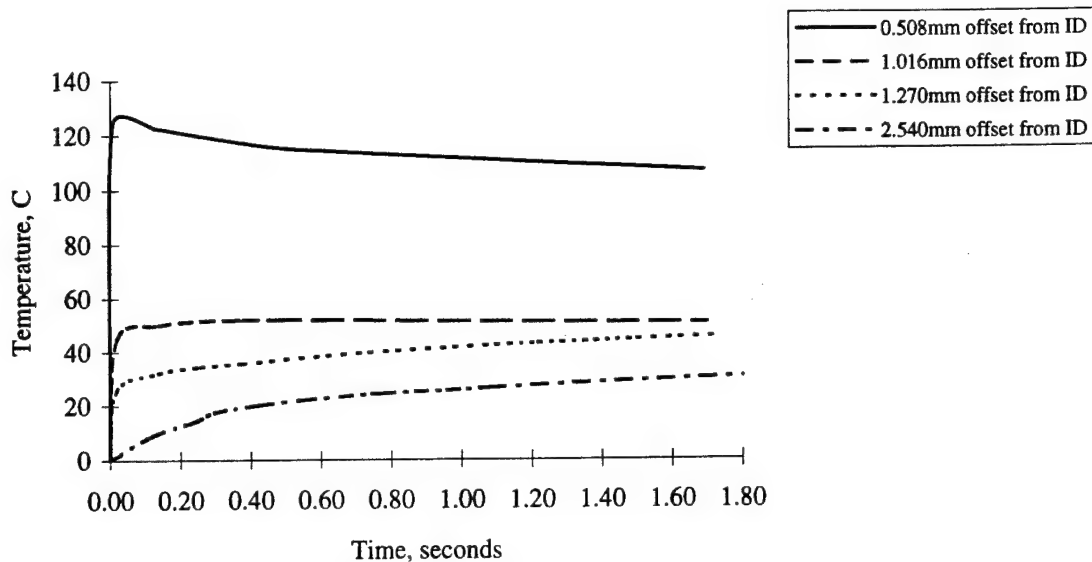


Figure 20: Peak Temperature Difference Between Hole and No Hole Conditions - 15 Shots @ 500 SPM

From the results of the Near-Bore Thermocouple Hole sub-models, it is concluded that a near-bore thermocouple hole greatly influences the radial thermal gradients established during a shot sequence. The actual temperature (no thermocouple hole present) at the same radial location (i.e., 0.508mm to 2.54mm radially offset from the bore surface) as the thermocouple hole can differ by as much as 125°C from the temperature measured by a thermocouple in the hole. These findings provide a text book example of the Heisenberg Uncertainty Principle in practice. The Heisenberg Uncertainty Principle states "*The precept that the accurate measurement of an observable quantity necessarily produces uncertainties in one's knowledge of the values of other observables*" [2]. In relation to this example, it means that the methods by which temperature measurements are taken can affect the actual temperature being measured.

## SUMMARY AND FUTURE WORK

There are many factors that influence the thermal response of a gun barrel during a firing sequence. The geometry of the rifling (i.e., land and groove) greatly influences the thermal gradients in this region. If temperatures from thermocouple measurements are used to validate an analytical model, it is important to know the precise location of the thermocouple in relation to the land and groove to obtain an accurate comparison. Steps must be taken to account for the temperature differences in this region if an analytical model of the gun barrel does not include the complexity of the land/groove configuration. Future work is planned to determine what these steps must be for various firing conditions.

The main purposes for chrome plating on the bore surface are for wear resistance and for protection of the steel jacket from the high gas temperatures inside the bore. Therefore, some amount of chrome plating is required for this type of barrel. For short duration shot bursts, the amount of chrome plating thickness on the bore surface does not significantly affect the radial thermal gradient. Future work is planned to determine if the amount of chrome plating thickness affects the thermal gradient with longer shot bursts.

When a gun barrel is configured with thermocouples to measure temperatures, a near-bore thermocouple hole itself greatly influences the measured temperature. The radial thermal gradients are affected by the void in the material where the thermocouple hole is located. The actual temperature (no thermocouple hole present) at the same radial location as the thermocouple hole can differ significantly from the temperature measured by a thermocouple in the hole. The amount varies with the distance the thermocouple hole is offset from the bore surface. Future work is planned to develop an appropriate scale factor to be applied to temperature measurements for various shot conditions and thermocouple configurations.

#### REFERENCES

- [1] C. Bagnall, J.R. Cook, K.C. Bearden, J.B. Boley, Advanced Gun Barrel Technology Initiative Project Plan Revision, National Center for Excellence in Metalworking Technology, TR No. 95-068D, Concurrent Technologies Corporation, Johnstown PA, (Dec. 31, 1995)
- [2] S.P. Parker, McGraw Hill Dictionary of Scientific and Technical Terms, Fourth Edition, McGraw Hill, New York, NY, p. 870, (1989)

PURDY

**TITLE:                   MODELLING AND SIMULATION OF A WEAPON CONTROL  
SYSTEM FOR A MAIN BATTLE TANK**

**D. J. PURDY  
ROYAL MILITARY COLLEGE OF SCIENCE  
SHRIVENHAM, SWINDON, ENGLAND, SN6 8LA**

**ABSTRACT:**

A generic non-linear model of the elevation mechanics for an electric drive weapon control system for a main battle tank is developed. The barrel is modelled by breaking it down into two rigid sections which are pin-jointed together and linked by a torsional spring and damper. The effects of hull motion are coupled into the model. This type of model allows different controllers for weapon control systems to be evaluated efficiently.

Results from simulating the weapon control system for a range of conditions are presented. The effects of non-linear friction are shown to degrade the performance of weapon control systems.

**BIOGRAPHY:**

**PRESENT ASSIGNMENT:**      **Lecturer Cranfield University (RMCS), ENGLAND**

**DEGREES HELD:**              **BSc. Mechanical Engineering (1981) Leeds University  
England, PhD. Cranfield University (RMCS) England.**

## **MODELLING AND SIMULATION OF A WEAPON CONTROL SYSTEM FOR A MAIN BATTLE TANK**

**D J Purdy**

**Royal Military College of Science, Shrivenham  
SWINDON, ENGLAND, SN6 8LA**

### **INTRODUCTION**

A non-linear model of the elevation mechanics for a Main Battle Tank (MBT) with an electrical drive is developed. The flexibility of the gun barrel is modelled by breaking it down into two rigid sections which are pin-jointed together and linked by a torsional spring and damper. In this paper, this type of model is referred to as a Lumped Parameter Flexible Beam Model (LPFBM). Non-linear friction (static and kinetic) are included in the model, both at the drive and trunnions. The effects of MBT hull motion is coupled into the model. Results from simulating the model for a range of conditions are presented and discussed. All modelling and simulation has been performed using the MATLAB/SIMULINK environment [1].

The primary objective of the Weapon Control System (WCS) on an MBT is to maximise the chance of hitting a stationary or moving target with the first round, in the shortest possible time, from a stationary or moving vehicle. Non-linear friction has a detrimental effect on the performance of a WCS from both a stationary and moving MBT. The model presented, allows the performance of different control techniques to be compared efficiently.

### **DESCRIPTION OF THE ELEVATION MECHANICS FOR AN MBT**

A diagram of an MBT illustrating the elevation mechanics is shown in Figure 1. The MBT hull has twelve wheel stations which support it and filter out the ground disturbances to it. A mathematical model of the hull which has been used to determine its response to ground inputs is given in Appendix A. The turret is mounted onto the hull via a slew-ring, which allows motion in traverse. The gun barrel, breech and cradle are pivoted at the trunnion bearings, thus allowing angular motion in elevation. The elevation drive (motor and gearbox) is connected to the cradle by a rack and pinion. A block diagram of the elevation drive-line is shown in Figure 2. The input to the elevation drive is a voltage to the servo-amplifier. The servo-amplifier produces a current, proportional to its input voltage [2]. The prime mover is a d.c. servo-motor and in conjunction with the amplifier, can be considered as producing torque proportional to its input current [2]. The remainder of the drive-line consists of a gearbox, and rack and pinion. The servo-amplifier, motor and gearbox are represented by a single drive torque constant  $K_t$ . Sensors are used to measure the angular rate of the motor, and angular rate and position of the cradle.

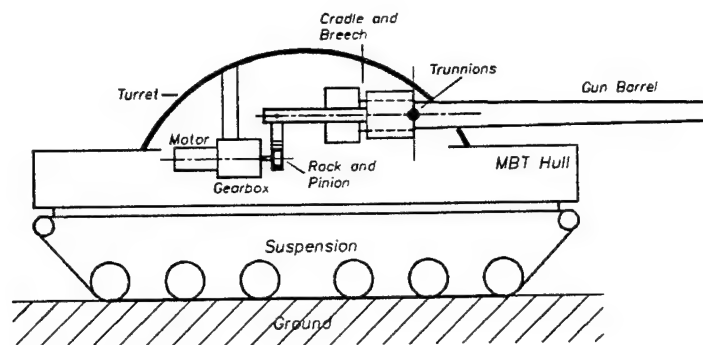


Figure 1 Elevation mechanics for an electric drive MBT.

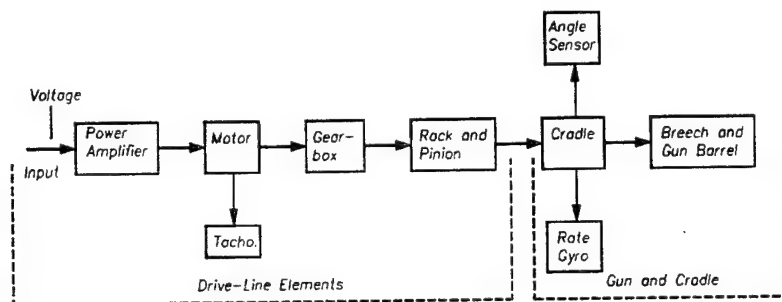


Figure 2 Block diagram of the elevation mechanics.

### COUPLING OF THE MBT HULL MOTIONS INTO THE ELEVATION MECHANICS

A simplified model of an MBT hull is shown in Figure 3. The motions of the hull are characterised by its vertical motion  $y_p$  and rotation  $\theta_p$  at its centre of gravity. For small angular motions, the input to the elevation channel can be reduced to a linear vertical motion  $y_t$  and a rotation  $\theta_p$  at the trunnions. These disturbances couple into the elevation motion by the vertical acceleration at the trunnions  $\ddot{y}_t$ , trunnion friction and the relative motion of the drive with respect to the cradle ( $X_t\theta_p$ ), Figure 4. The vertical acceleration at the trunnions is given by;

$$\ddot{y}_t = \ddot{y}_p + \ddot{\theta}_p X_t \quad [1]$$

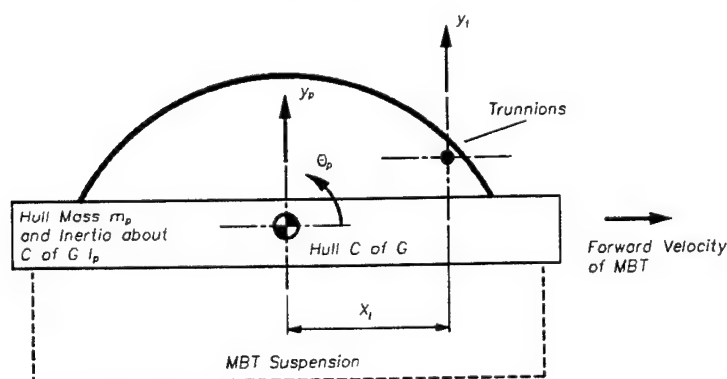


Figure 3 MBT hull model.

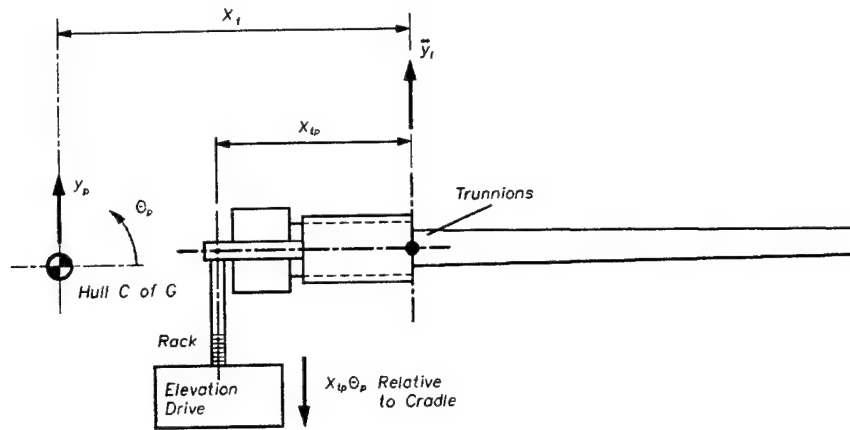


Figure 4 Coupling of the hull motion into the elevation model.

### MBT LINEAR ELEVATION MODEL

A diagram of the elevation channel model is shown in Figure 5. Data for the model is given in Appendix B.

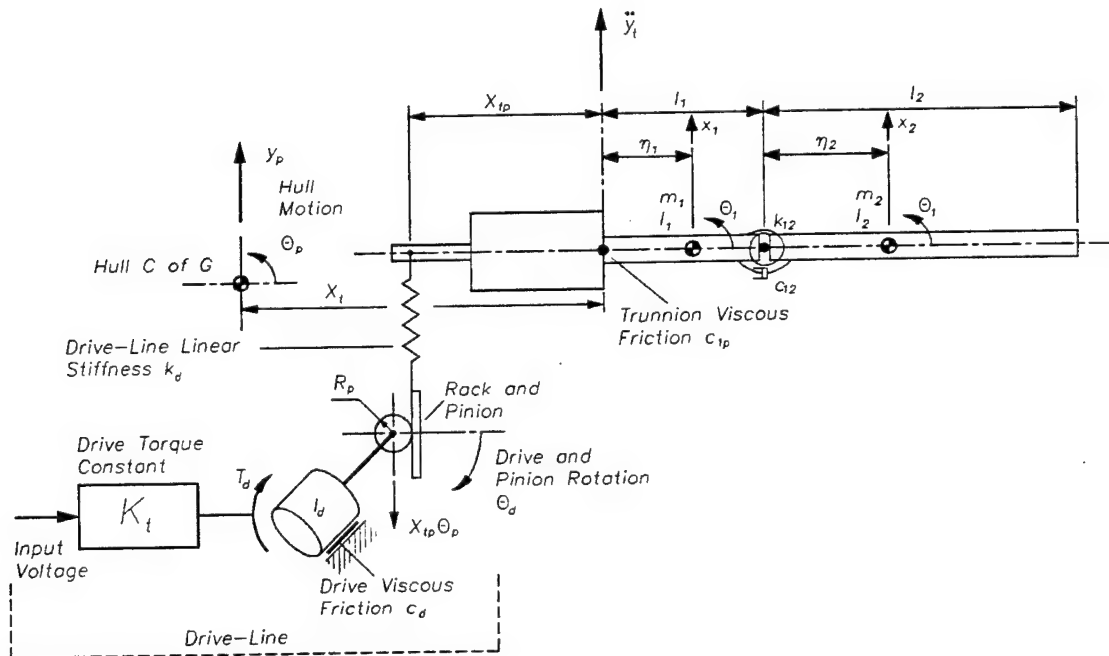


Figure 5 MBT elevation model with two section LPFBM barrel.

The drive inertia  $I_d$  represents the motor inertia referred to the output of the gearbox and the drive torque is given by;

$$T_d = K_t v_i \quad [2]$$

where  $K_t$  is the drive torque constant and  $v_i$  is the input to the servo-amplifier. The viscous friction at the drive is  $c_d$ . The radius of the pinion is  $R_p$ . The drive-line stiffness  $k_d$  has been lumped

between the rack and the cradle, which is equivalent to the model in [2]. The cradle, breech and gun barrel in this model have been broken down into two rigid sections, of length  $l_1$  and  $l_2$ , mass  $m_1$  and  $m_2$ , and moment of inertia about the centre of gravity  $I_1$  and  $I_2$ . The distance to the centres of gravity are  $\eta_1$  and  $\eta_2$ , the pin-joint linking the two sections has a torsional stiffness of  $k_{12}$  and viscous friction  $c_{12}$ . This type of model has been used to simulate and control flexible space-borne manipulators [3,4,5] and to investigate the design of GCSs [6]. The method used to select the lengths of the rigid sections is given in [3], in which the muzzle displacement and rotation for the first cantilever mode are matched to a finite element model, Figure 6. The torsional spring rate is calculated to make the first cantilever mode frequencies of the LPFBM and finite element models equal.

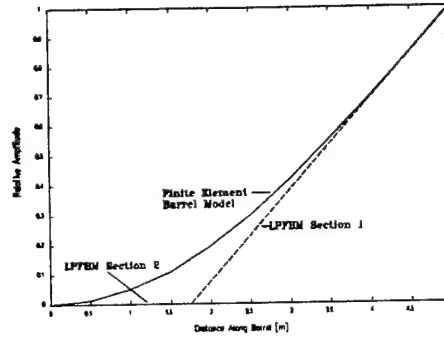


Figure 6 Section length selection for the two section LPFBM.

The inputs to the model are the voltage to the servo-amplifier  $v_i$ , the trunnion vertical acceleration  $\ddot{y}_t$  and the MBT hull pitch rate  $\dot{\theta}_p$ . The outputs from the model are the drive angular velocity  $\dot{\theta}_d$ , the breech angle  $\theta_b$  and velocity  $\dot{\theta}_b$  and the muzzle angle  $\theta_m$ .

A free body diagram for the system, assuming small motions, is shown in Figure 7. The lateral forces between the LPFBM sections is  $f_{12}$  and the vertical force at the trunnions is  $f_y$ . Longitudinal forces have been ignored.

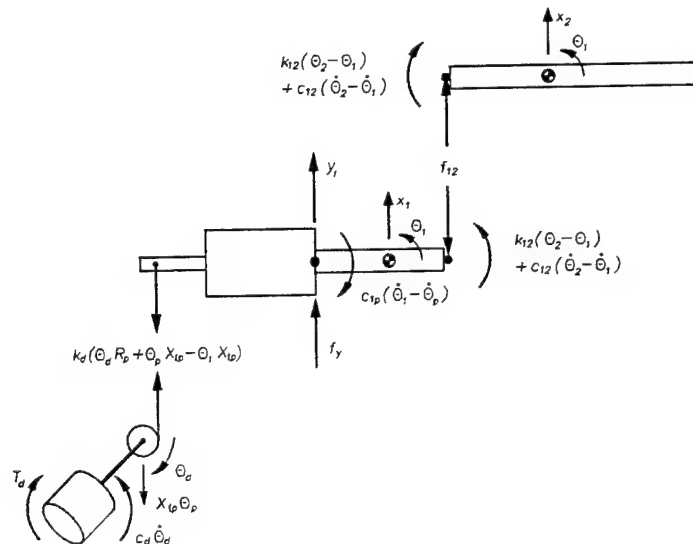


Figure 7 Free body diagram of the elevation model for small rotations.

The equations of motion for the components of the system are;

drive;

$$I_d \ddot{\theta}_d = T_d - c_d \dot{\theta}_d - k_d (\theta_d R_p + \theta_p X_{tp} - \theta_1 X_{tp}) R_p \quad [3]$$

breech section;

$$\begin{aligned} m_1 \ddot{x}_1 &= f_y - k_{d1} (\theta_d R_p + \theta_p X_{tp} - \theta_1 X_{tp}) - f_{12} \\ I_1 \ddot{\theta}_1 &= k_{d1} (\theta_d R_p + \theta_p X_{tp} - \theta_1 X_{tp}) (X_{tp} + \eta_1) - c_{1p} (\dot{\theta}_1 - \dot{\theta}_p) \\ &\quad - f_y \eta_1 - f_{12} (l_1 - \eta_1) + k_{12} (\theta_2 - \theta_1) + c_{12} (\dot{\theta}_2 - \dot{\theta}_1) \end{aligned} \quad [4]$$

muzzle section;

$$\begin{aligned} m_2 \ddot{x}_2 &= f_{12} \\ I_2 \ddot{\theta}_2 &= -f_{12} \eta_2 - k_{12} (\theta_2 - \theta_1) - c_{12} (\dot{\theta}_2 - \dot{\theta}_1) \end{aligned} \quad [5]$$

The equations of constraint for the breech and muzzle sections are;

$$\begin{aligned} y &= x_1 - \theta_1 \eta_1 \\ y + l_1 \theta_1 &= x_2 - \eta_2 \theta_2 \end{aligned} \quad [6]$$

The equations of motion for the system are obtained by eliminating the linear coordinates  $x_1$  and  $x_2$  to give;

$$\mathbf{M}_1 \{\ddot{\theta}\} + \mathbf{C}_1 \{\dot{\theta}\} + \mathbf{K}_1 \{\theta\} = \mathbf{I}_1 \{\mathbf{u}\} \quad [7]$$

where the mass  $\mathbf{M}_1$ , damping  $\mathbf{C}_1$ , stiffness  $\mathbf{K}_1$ , and input  $\mathbf{I}_1$  matrices are given by;

$$\begin{aligned} \mathbf{M}_1 &= \begin{bmatrix} I_d & 0 & 0 \\ 0 & I_1 + m_1 \eta_1^2 + m_2 l_1^2 & m_2 l_1 \eta_2 \\ 0 & m_2 l_1 \eta_2 & I_2 + m_2 \eta_2^2 \end{bmatrix} & \mathbf{C}_1 &= \begin{bmatrix} c_d & 0 & 0 \\ 0 & c_{12} + c_{1p} & -c_{12} \\ 0 & -c_{12} & c_{12} \end{bmatrix} \\ \mathbf{K}_1 &= \begin{bmatrix} k_d R_p^2 & 0 & -k_d R_p X_{tp} \\ 0 & k_{12} + k_d X_{tp}^2 & -k_{12} \\ -k_d R_p X_{tp} & -k_{12} & k_{12} \end{bmatrix} & \mathbf{I}_1 &= \begin{bmatrix} 1 & 0 & 0 & -k_d X_{tp} R_p \\ 0 & -(m_1 \eta_1 + m_2 l_1) & c_{1p} & k_d X_{tp}^2 \\ 0 & -m_2 \eta_2 & 0 & 0 \end{bmatrix} \end{aligned} \quad [8]$$

and the vector of rotations and inputs are given by;

$$\begin{aligned}\{\theta\}^T &= \{\theta_d \quad \theta_1 \quad \theta_2\} \\ \{u\}^T &= \{T_m \quad \ddot{y}_y \quad \dot{\theta}_p \quad \theta_p\}\end{aligned}\quad [9]$$

In state space form the model is given by;

$$\begin{aligned}\dot{\mathbf{x}} &= \mathbf{Ax} + \mathbf{Bu} \\ \mathbf{y} &= \mathbf{Cx} + \mathbf{Du}\end{aligned}\quad [10]$$

where;

$$\begin{aligned}\mathbf{A} &= \begin{bmatrix} \mathbf{0} & \mathbf{I} \\ -\mathbf{M}_1^{-1}\mathbf{K}_1 & -\mathbf{M}_1^{-1}\mathbf{C}_1 \end{bmatrix} \\ \mathbf{B} &= \begin{bmatrix} \mathbf{0} \\ \mathbf{M}_1^{-1}\mathbf{I}_1 \end{bmatrix} \quad \mathbf{C} = \mathbf{I} \quad \mathbf{D} = [\mathbf{0}] \\ \{\mathbf{x}\}^T &= \{\theta_d \quad \theta_1 \quad \theta_2 \quad \dot{\theta}_d \quad \dot{\theta}_1 \quad \dot{\theta}_2\}\end{aligned}\quad [11]$$

Plots of open-loop frequency response to a command input for the elevation model and for an equivalent version with ten finite elements modelling the barrel [8], are shown in Figure 8, 9, 10 and 11. Below 40 Hz, the error in the modes around 20 Hz causes the most significant discrepancy between the three degree of freedom and the higher order model. The modes predicted by the elevation model with the LPFBM barrel are lower than those with the finite element barrel by approximately 1 Hz. The three degree of freedom model is incapable of representing more than two modes<sup>1</sup>, thus those over 40 Hz are not present in the responses. The largest errors are in the response of the muzzle, Figure 11. The accuracy of this model can be improved by increasing the number of sections and/or optimising the section lengths for a particular output, for example, the breech [6].

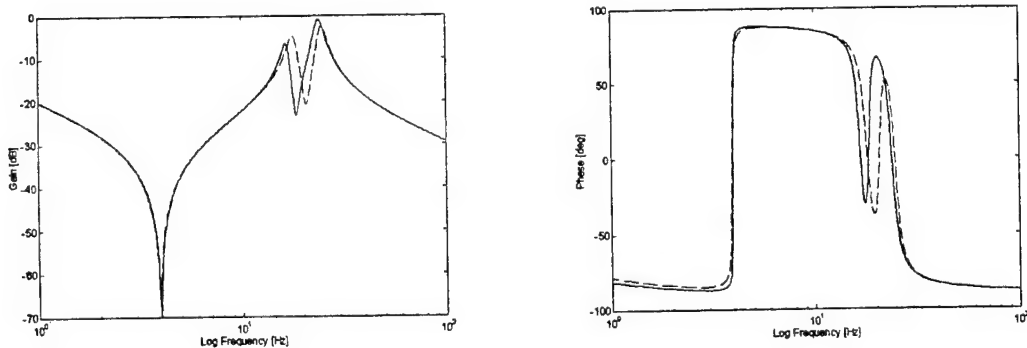


Figure 8 Plot of open-loop frequency response motor torque to drive angular velocity, with the barrel modelled using finite elements [dash] and LPFBM [solid].

<sup>1</sup> A three degree of freedom model has three modes, in this case the first is a 0 Hz and has been ignored.

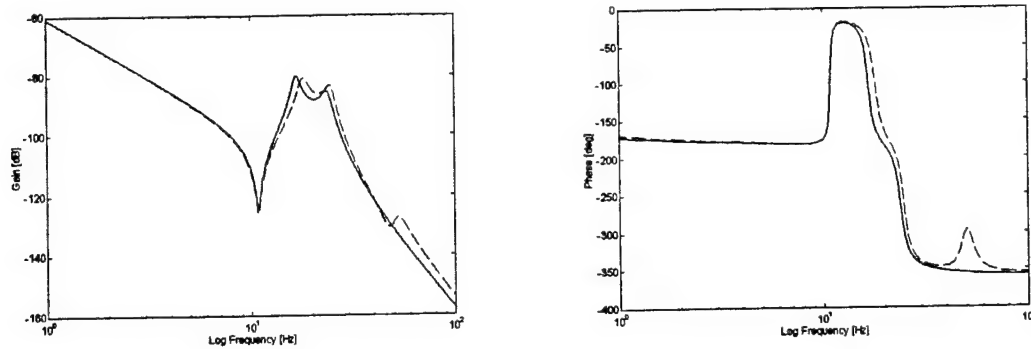


Figure 9 Plot of open-loop frequency response motor torque to breech angle, with the barrel modelled using finite elements [dash] and LPFBM [solid].

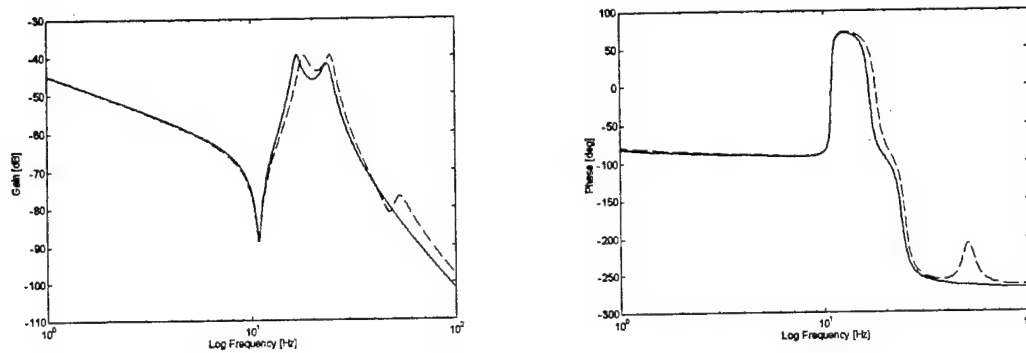


Figure 10 Plot of open-loop frequency response motor torque to breech angular velocity, with the barrel modelled using finite elements [dash] and LPFBM [solid].

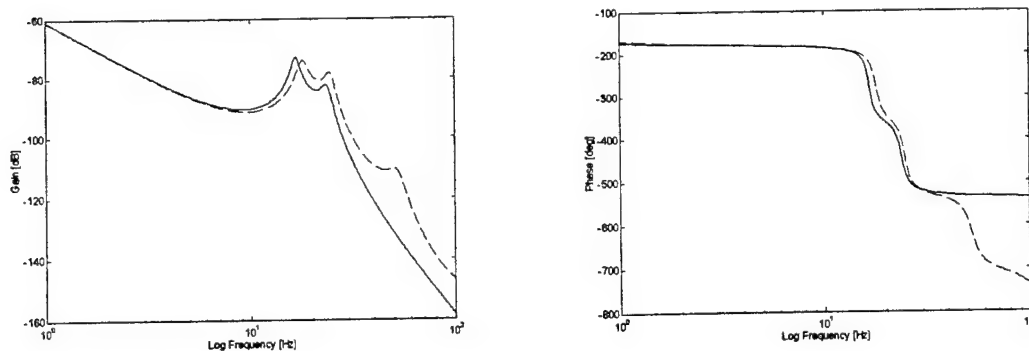


Figure 11 Plot of open-loop frequency response motor torque to muzzle angle, with the barrel modelled using finite elements [dash] and LPFBM [solid].

The response of the elevation model with the LPFBM barrel to the disturbance inputs are shown in Figure 12. The effect of the trunnions vertical acceleration, Figure 12a, has a much greater attenuation than the hull pitch rate, Figure 12b.

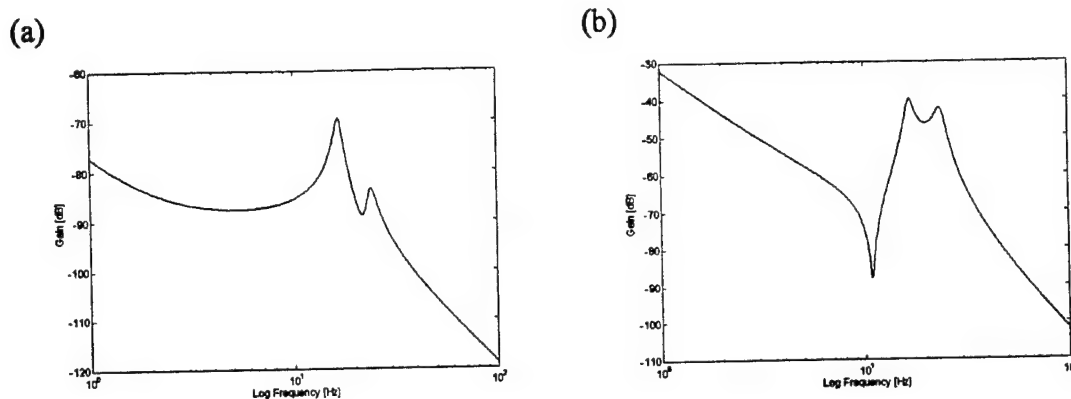


Figure 12 Disturbance frequency response of the elevation model with the LPFBM barrel to trunnion vertical acceleration (a) and hull pitch rate (b).

### MBT NON-LINEAR ELEVATION MODEL

The non-linear elevation model has been formed by incorporating non-linear friction into the drive and trunnions. The out-of-balance torque was caused by the centre of gravity of the elevating mass being 8.0 mm in front of the trunnions. The non-linear friction model used is a modified reset-integrator representation [7]. The modification to this model includes a random component of friction added into its output. This is generated by integrating white noise and adding it into the friction force, the mean level being zero and the standard deviation being approximately 1% of the kinetic (Coulomb) friction. The static friction (stiction) provides an additional 25% of the kinetic friction level. The drive friction was taken as 1% of the trunnion friction.

### CONTROLLER DESIGN

To investigate the performance of the elevation model, a classical closed-loop controller was designed, which was based on the open-loop frequency responses. The form of the controller is shown in Figure 13, and consists of an inner-loop breech rate controller<sup>2</sup> and outer-loop breech position controller. The outer-loop controller is based on a traditional proportional plus integral structure, while the inner-loop has a proportional controller augmented with a notch and low pass filter. For this controller no hull disturbance feed-forward element was used. No attempt has been made to optimise the response of the WCS.

<sup>2</sup> This used the breech rate gyro for the feedback signal.

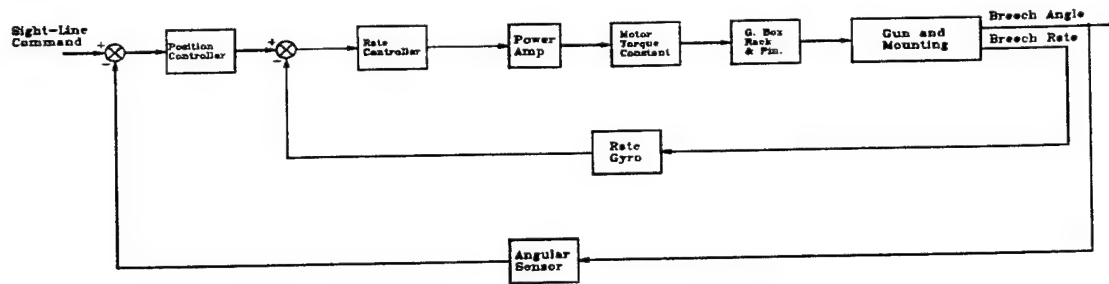
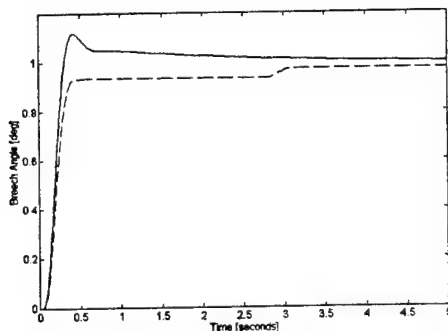


Figure 13 Closed-loop elevation control system.

### SIMULATION RESULTS STATIONARY MBT

The response of the WCS linear and non-linear models to a step input of  $1^\circ$  is shown in Figure 14a and to a tracking input of  $0.5 \text{ deg/s}$  in Figure 14b. The linear model has approximately 10% overshoot to a step input, while the non-linear model has none. The effects of the integrator can be seen to reduce the error on both responses for the non-linear model.

(a)



(b)

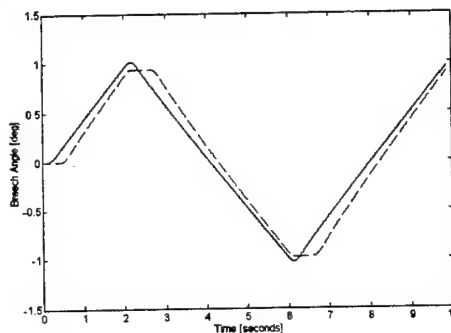


Figure 14 Step (a) and tracking (b) response of the WCS; linear [solid], non-linear [dash].

### SIMULATION RESULTS MOVING MBT

A linear MBT hull model crossing random terrain at  $5 \text{ m/s}$  has been used to generate the inputs to the elevation model, Appendix A. The simulation, including the hull model, was run for 40 seconds of simulation time which took approximately six minutes on a 75 MHz Pentium personal computer.

The output from the simulation for both the linear and non-linear (with the default value of kinetic friction) models is shown in Figure 15. The effects of non-linear friction on the drive response, Figure 15a, are negligible. The non-linear friction has increased the breech and muzzle motion by approximately 100%, Figures 15b and 15c. Due to the larger breech motion, the input to the servo-amplifier has also increased by 100%, Figure 15d. The worst case flexing of the gun barrel ( $\theta_2 - \theta_1$ ) occurred after 4 seconds, Figure 15e, and has a magnitude of almost  $3 \text{ mrad}$ ; both the linear and non-linear responses were very similar.

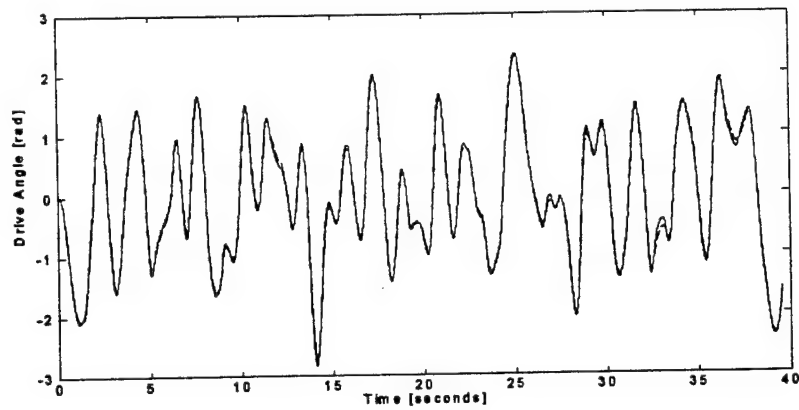


Figure 15a Drive response as MBT crosses random terrain; linear [solid], non-linear [dash].

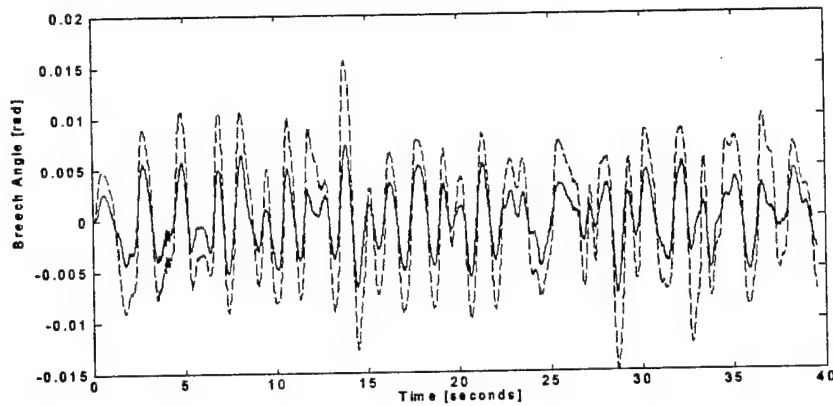


Figure 15b Breech response as MBT crosses random terrain; linear [solid], non-linear [dash].

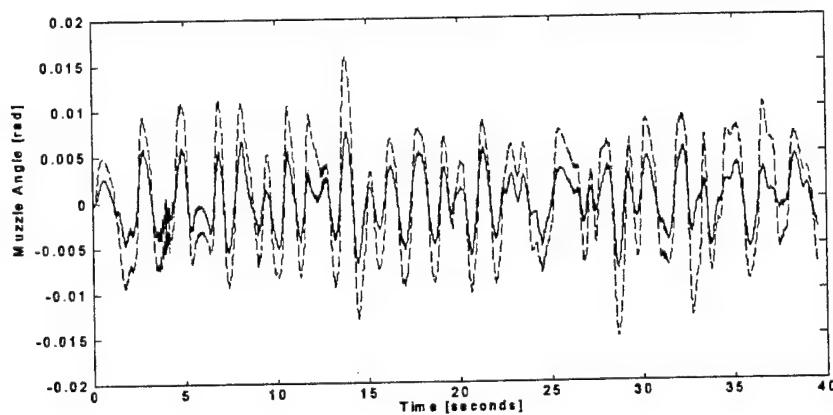


Figure 15c Muzzle response as MBT crosses random terrain; linear [solid], non-linear [dash].

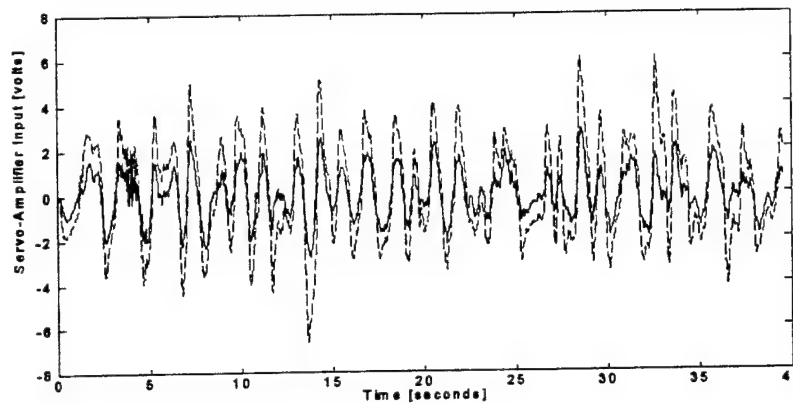


Figure 15d Servo-amplifier input as MBT crosses random terrain; linear [solid], non-linear [dash].

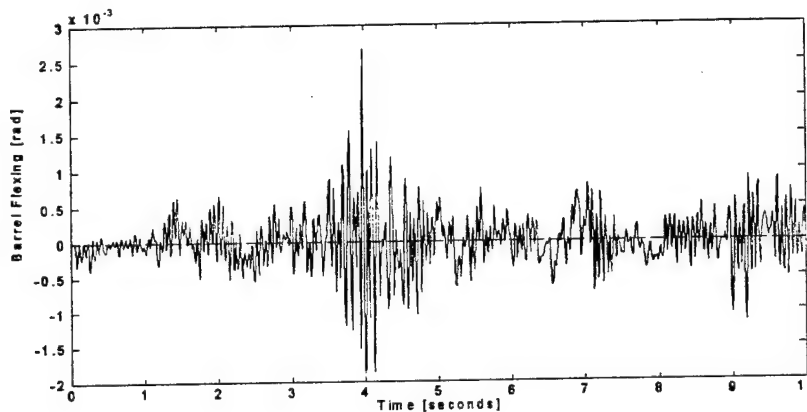


Figure 15e Gun barrel flexing as MBT crosses random terrain (first ten seconds); linear model.

The r.m.s. values for the simulated responses are given in Table 1, in addition to other runs in which the level of non-linear friction was varied. From Table 1, it is seen that the drive motion and barrel flexing are almost independent of the level of non-linear friction. The breech and muzzle motion and servo-amplifier input are seen to increase steadily.

Table 1 Effects of non-linear friction on the responses of the WCS as the MBT crosses random terrain.

Kinetic Friction [Nm]	r.m.s.				
	Breech Angle [mrad]	Muzzle Angle [mrad]	Drive Angle [rad]	Servo-Amplifier Demand [v]	Barrel Flexing [mrad]
0	2.88	2.90	1.058	1.058	0.300
100	3.26	3.28	1.057	1.194	0.300
200	3.60	3.63	1.055	1.318	0.300
300	3.87	3.90	1.054	1.419	0.301
400	4.28	4.32	1.052	1.575	0.302
500	4.72	4.76	1.052	1.730	0.303
1000 (Default)	6.17	6.23	1.046	2.288	0.312
1500	7.80	7.87	1.037	2.888	0.322
2000	8.59	8.66	1.033	3.181	0.331

The effect of reducing the amplitude of the ground profile by a factor of ten on the breech response for both the linear and non-linear models, is shown in Figure 16. From this Figure, the effect of the non-linear friction is seen to increase the breech motion by about 500% when compared to the linear model.

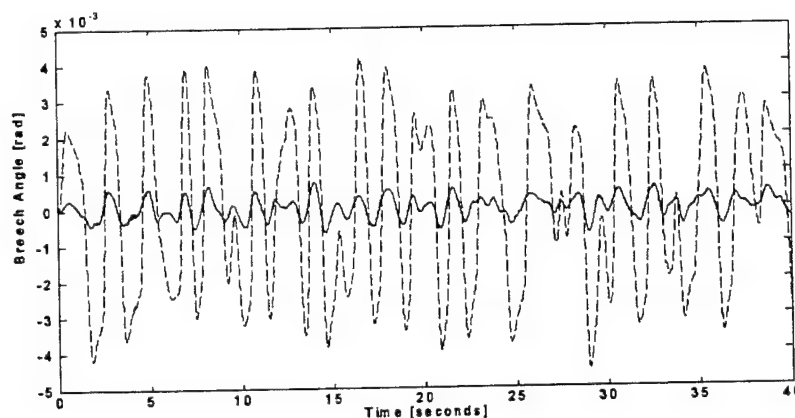


Figure 16 Breech response as MBT crosses random terrain with its amplitude reduced by a factor of ten; linear [solid], non-linear [dash].

The contribution to the breech motion caused by the vertical acceleration at the trunnions and hull pitch rate is shown in Figure 17. From this Figure, it is seen that the trunnion vertical acceleration has the least effect on the breech motion; this fact was anticipated from the disturbance responses of the linear model, Figure 12.

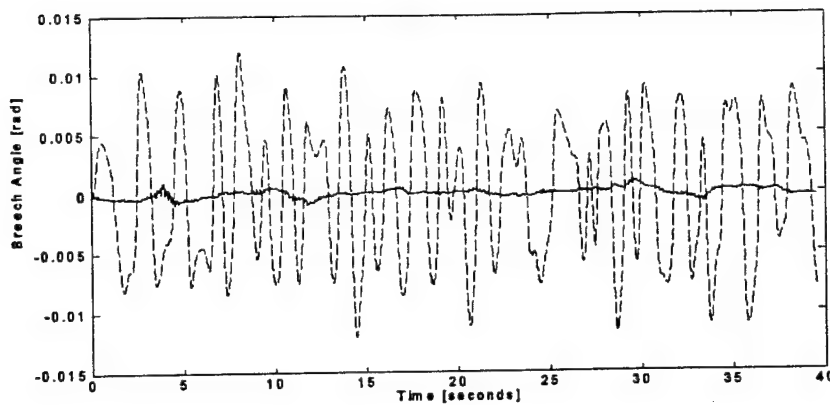


Figure 17 Effect of trunnion vertical acceleration [solid] and hull pitch rate [dash] on the breech motion.

## CONCLUSIONS

A model of the elevation mechanics of an electric drive MBT incorporating non-linear friction has been developed. The gun barrel has been represented by breaking it down into two rigid section (LPFBM), which are pin-jointed together and linked by a linear torsional spring and damper. The elevation model with the LPFBM barrel has been compared to an equivalent model with a finite element barrel and below 40 Hz the predicted modes have an error of approximately 1 Hz.

Simulations of the non-linear elevation model, have shown that the presence of static and kinetic friction degrade the performance of the WCS. The non-linear friction has a more significant effect on the accuracy of the WCS as the roughness of the terrain reduces and hence also the motions of the hull.

The model presented in this paper allows the performance of different methods of control design for WCS to be evaluated efficiently in a minimum amount of time.

## REFERENCES

- 1 MATLAB/SIMULINK reference manuals, The MathWorks, Inc., 24 Prime Park Way, Natick, Mass.
- 2 Dholiwar, D.K., Development of a Hybrid Distributed-Lumped Parameter Open Loop Model of Elevation Axis for a Gun System, Proceedings of the Seventh US Army Symposium on Gun Dynamics, Newport, Rhode Island, 11-13 May 1993.
- 3 Woerkom, P.Th.L.M., On Fictitious Joints Modelling of Manipulator Link Flexibility for the HERA Simulation Facility Pilot, National Aerospace Laboratory NLR The Netherlands, Report No. NLR TR 88086 U, 1988.
- 4 Chichester, F.D., Modular Design Attitude Control System Final Report, NASA Report No. N83-24541, October 1982.
- 5 Moch, M. and Kirk, C.L., Dynamics of Shuttle Based Flexible Antenna System, Cranfield Institute of Technology, England, College of Aeronautics Report No. 9203, January 1992.
- 6 Purdy, D.J., An Investigation into the Modelling and Control of Flexible Bodies, PhD. Thesis, Cranfield University (RMCS), England, 1994.
- 7 Haessig, D.A. and Friedland, B., On the Modeling and Simulation of Friction, Trans. of the ASME J. of Dynamic Systems, Measurement and Control, Vol. 113, Sept 1991, pp 354-362.
- 8 Cook, R.D., Malkus, D.S. and Plesha, M.E., Concepts and Applications of Finite Element Analysis, Third Edition, John Wiley & Sons, 1989, ISBN 88-27928.
- 9 Cebon, D. and Newland, D.E., The Artificial Generation of Road Surface Topography by the Inverse FFT Method, Proc. 8th Symposium on the Dynamics of Vehicles on Roads and Tracks, Cambridge, Mass, 1983.

## APPENDIX A

## MBT HULL MOTION SIMULATION

The MBT hull model used to generate the disturbance inputs to the WCS is shown in Figure 18. The twelve wheel stations have been condensed into six for this plane model. The parameters for the hull model are shown in Table 2. This simple model consists of a rigid hull with mass  $m_p$  and moment of inertia  $I_p$ , mass-less wheel stations at  $a_i$  from the hull mass centre and identical suspension components  $k_s$  and  $c_s$ . The ground inputs to the model are  $z_i$  and the forward velocity of the vehicle is  $V$ . The trunnion axis is  $X_t$  from the hull mass centre and its vertical displacement is  $y_t$ .

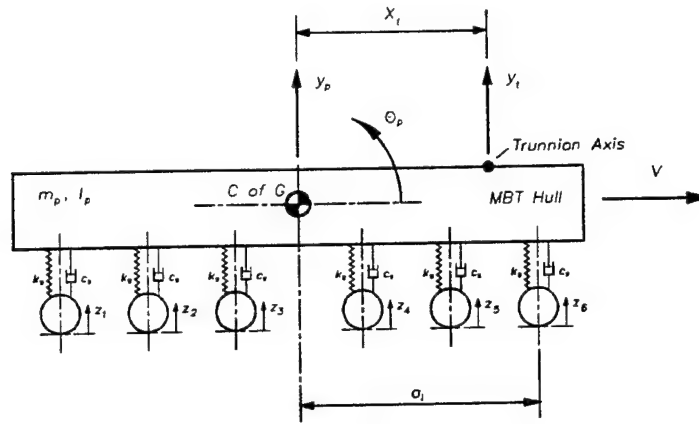


Figure 18 Side elevation of the plane MBT hull model.

Table 2 MBT hull model data.

Model Parameter	Value
Mass $m_p$	60000 kg
Inertia about C of G $I_p$	$300 \times 10^3 \text{ Kg m}^2$
Suspension Stiffnesses $k_s$	888 kN/m
Suspension Damping Coefficients $c_s$	94 kNs/m
Distance between the C of G and the Trunnion Axis $X_t$	1 m
Distance between the wheel stations and the C of G $a_i$	2.498, 1.584, 0.517, -0.397, -1.362, -2.276 m

The equations of motion for the hull model in state space form are;

$$\begin{aligned}\dot{\mathbf{x}}_h &= \mathbf{A}_h \mathbf{x}_h + \mathbf{B}_h \mathbf{u}_h \\ \mathbf{y}_h &= \mathbf{C}_h \mathbf{x}_h + \mathbf{D}_h \mathbf{u}_h\end{aligned}\quad [12]$$

where;

$$\mathbf{A}_h = \begin{bmatrix} 0 & 1 & 0 & 0 \\ \frac{-6k_s}{m_p} & \frac{-6c_s}{m_p} & \frac{-k_s \sum a_i}{m_p} & \frac{-c_s \sum a_i}{m_p} \\ 0 & 0 & 0 & 1 \\ \frac{-k_s \sum a_i}{I_p} & \frac{-c_s \sum a_i}{I_p} & \frac{-k_s \sum a_i^2}{I_p} & \frac{-c_s \sum a_i^2}{I_p} \end{bmatrix}$$

$$\mathbf{B}_h = \begin{bmatrix} 0 & \dots & 0 & \dots \\ \frac{k_z}{m_p} & \dots & \frac{c_z}{m_p} & \dots \\ 0 & \dots & 0 & \dots \\ \frac{k_z \sum a_i}{I_p} & \dots & \frac{c_z \sum a_i}{I_p} & \dots \end{bmatrix}$$

$$\mathbf{C}_h = \begin{bmatrix} \frac{-6k_z}{m_p} & \frac{-6c_z}{m_p} & \frac{-k_z \sum a_i}{m_p} & \frac{-c_z \sum a_i}{m_p} \\ \frac{-k_z \sum a_i}{I_p} & \frac{-c_z \sum a_i}{I_p} & \frac{-k_z \sum a_i^2}{I_p} & \frac{-c_z \sum a_i^2}{I_p} \\ 0 & 0 & 0 & 1 \\ 0 & 0 & 1 & 0 \end{bmatrix}$$

$$\mathbf{D}_h = \begin{bmatrix} \frac{k_z}{m_p} & \dots & \frac{c_z}{m_p} & \dots \\ \frac{k_z \sum a_i}{I_p} & \dots & \frac{c_z \sum a_i}{I_p} & \dots \\ 0 & \dots & 0 & \dots \\ 0 & \dots & 0 & \dots \end{bmatrix}$$

$$\mathbf{x}_h^T = \{y_p \quad \dot{y}_p \quad \theta_p \quad \dot{\theta}_p\}$$

$$\mathbf{u}_h^T = \{z_1 \quad \dots \quad z_6 \mid \dot{z}_1 \quad \dots \quad \dot{z}_6\}$$

$$\mathbf{y}_h^T = \{\ddot{y}_p \quad \ddot{\theta}_p \quad \dot{\theta}_p \quad \theta_p\}$$

The trunnion vertical acceleration is given by equation 1.

The power spectral density of the random profile used for the simulation [9] is shown in Figure 19.

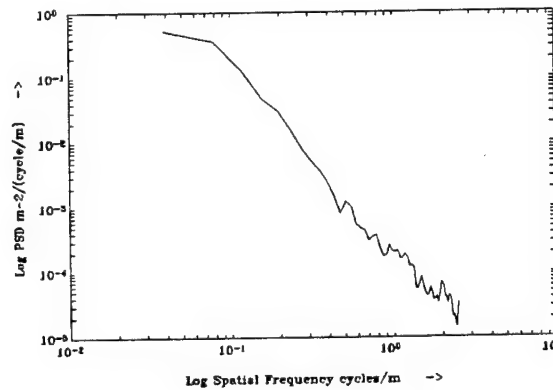


Figure 19 Spectral composition of random ground profile used in the simulation.

## APPENDIX B

## ELEVATION MODEL DATA

A generic elevation model has been used in the simulations which is not related to any in service weapon system. The configuration of the elevating mass is shown in Figure 20. The elevating mass is divided into two parts. A rigid component which consists of the cradle, breech and part of the barrel within the cradle. A flexible component which represents the gun barrel from the end of the cradle to the muzzle. The flexible barrel is taken as a tube with an inside diameter of 0.12 m and an outside diameter which tapers from 0.23 m at the cradle to 0.15 m at the muzzle. Data for the model is given in Table 3.

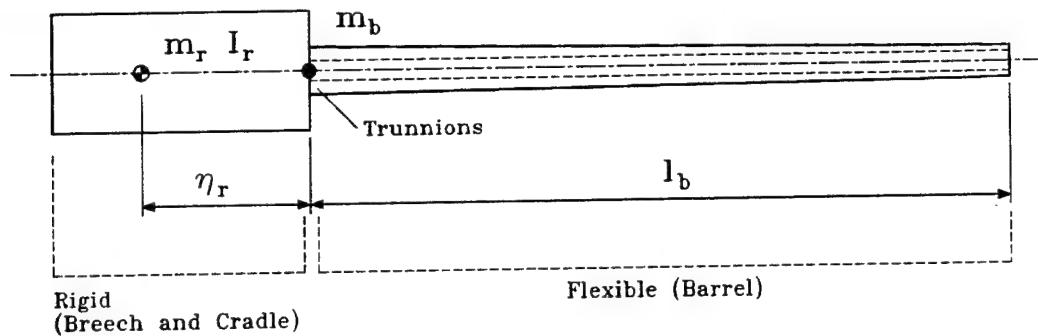


Figure 20 Elevating mass.

Table 3 Elevation model data.

Elevation Model Parameter	Value
Mass of rigid component $m_r$	1818 kg
Inertia of rigid component about its centre of gravity $I_r$	308 kgm <sup>2</sup>
Distance from trunnions to centre of gravity of rigid component $\eta_r$	1.426 m
Length of flexible barrel $l_b$	5.0 m
Mass of flexible barrel $m_b$	682 kg
Density of flexible barrel material (steel)	7800 kgm <sup>3</sup>
Modulus of elasticity of flexible barrel	200 GN/m <sup>2</sup>
Drive inertia $I_d$	0.5 kgm <sup>2</sup>
Pinion radius $R_p$	0.04 m
Drive torque constant $K_t$	60 Nm/volt
Drive-line stiffness $k_d$	6.0 MN/m
Distance from trunnions to drive $X_{tp}$	0.75 m

Trunnion viscous friction $c_{1p}$	1500 Nms/rad
Trunnion kinetic friction	1000 Nm
Trunnion static friction	25% of kinetic
Drive kinetic friction	1% of trunnion
Drive static friction	25% of kinetic
LPFBM section 1 data	
Mass $m_1$	2165 kg
Inertia $I_1$	1090 kgm <sup>2</sup>
Length $l_1$	1.75 m
Distance to centre of gravity $\eta_1$	-0.465 m
LPFBM section 2 data	
Mass $m_2$	335 kg
Inertia $I_2$	281 kgm <sup>2</sup>
Length $l_2$	3.25 m
Distance to centre of gravity $\eta_2$	1.319 m
Stiffness linking sections $k_{12}$	4.0 MNm/rad
Flexible barrel damping coefficient $\beta$	0.0005
Barrel damping $[C]=\beta \times [K]$ used for LPFBM and finite element models [8].	

**\* TITLE: GLOBAL MODELING FOR A MEDIUM CALIBRE TURRET SYSTEM**

**Bertrand COUVIN\*, Sylvain CARLIER, Josette DIAS-ALVES**  
**Giat Industries**

Branche Euro-Mobilité - Direction Technique - 13, route de la Minière  
78022 Versailles Cedex, FRANCE

**\* ABSTRACT:**

The current evolution in threats has led to an increase in power of automatic medium-calibre weapon systems, with the calibre of the weapon being between 25 and 45 mm. This situation quite naturally implies that, when an action is engaged, efficiency with an optimized number of shots fired must be looked for. With regard to the operational performances of firing anti-Infantry Combat Vehicles, the requirement is quite similar to that of high-calibre weapons. However, in order to orientate the technological choices of the future medium-calibre turret, it appears to be difficult, without further in-depth studies, to use again hypothesis or solutions that were retained for firing of high-calibre weapons. Mastery of burst-firing is an objective that requires reflection on the role of the sub-systems influencing, either primarily or secondarily, efficiency of the shots fired by a medium-calibre turret cannon. It appeared essential, for the feasibility study of this new weapon system, to have an overall simulation showing simulated behaviour and the dynamic interactions of these sub-systems. As the study advanced, it became necessary to have a macroscopic model of the elevating mass so that the performances of the future turret could be simulated realistically. This article describes the main steps in elaboration and validation of a macroscopic model of the elevating mass that allows the best estimates of performances of firing when stationary of the future medium-calibre turret weapon to be obtained.

**\* BIOGRAPHY:** Bertrand Couvin was born in Saïgon, VietNam, in 1964. He holds an engineering degree in applied & computational mathematics and mechanics of the University of PARIS-XIII and PARIS-VI, France, in 1987 and 1988. His major research interests are in the area of mechanical vibrations.

**\* PRESENT ASSIGNMENT:** Since 1991, he has been working on mechanical modeling for the Department of Weapon System Engineering, Technical Direction, Division of "Euro-Mobilité", Giat Industries.

**\* PAST EXPERIENCE:** From 1988 to 1991, he worked on numerical methods applied to flow mechanics for SIMULOG, Numerical Software Company, France.

**\* DEGREES HELD:** Applied & computational mathematics and mechanical engineering, University of PARIS-XIII and PARIS-VI.

## GLOBAL MODELING FOR A MEDIUM CALIBRE TURRET SYSTEM

**Bertrand.COUVIN\* & Sylvain CARLIER & Josette DIAS-ALVES**

Giat Industries - Branche Euro-Mobilité - Direction Technique  
13, route de la Minière, 78022 Versailles Cedex  
FRANCE

### 1. BACKGROUND

The size and the cost of such ammunition means that a minimum number of rounds should give maximum efficacy. So, the efficiency of burst-firing with a limited number of rounds, in terms of accuracy (dispersion and firing rate) is an objective that requires reflection on the role of each unit of the weapon system. In order to reduce costs and risks of development of such system, it is necessary to know how to predict its feasibility with regard to performance levels. Figure 1 shows two types of diagrams of a weapon system (Definition & Production Diagram and Functional Diagram).

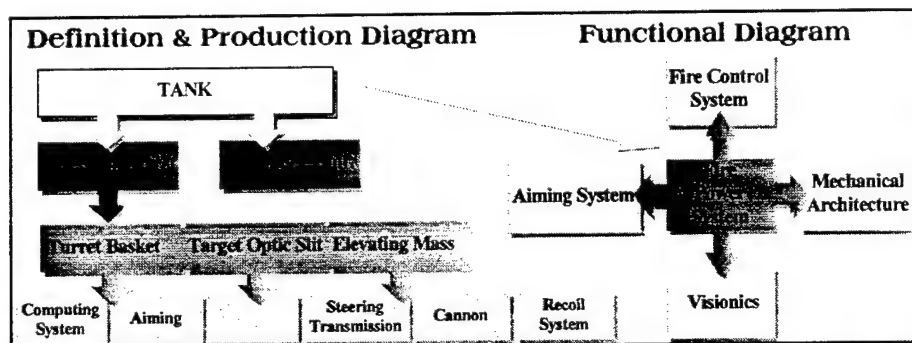


Figure 1: Weapon System Diagram

The weight of the firepower system can represent 40% to 60% of the cost of a turret. So, before developing the weapon system, it is necessary to know what kind of technology can be retained. Viewed by the system designers, elaboration of the macroscopic model gives the best estimate of the firing performance levels of the weapon system to be defined.

In 1992, the "Euro Mobilité" Branch of Giat Industries carried out a study in parallel with the feasibility study of the future medium-calibre turret. The aim of the study was to comprehend better, through experimentation, the macroscopic phenomena which degrade performances in burst-firing. The study therefore necessitated a firing test bench. In order to minimize the costs of the tests and to have an experimental device that could rapidly be

exploited, the best solution appeared to build a test bench from an elevating mass comprising a light tank and a turret equipped with a 25 mm weapon. The light tracked vehicle was assembled on trestles to avoid low frequencies of pitch and roll distortions (1 Hz) due to the suspension of the tank during firing. The turret was modified as follows : the traverse drive was removed and the movements in traverse were blocked by a reinforced traverse nut, and the elevation drive was replaced by a linear system with springs (see figure 2). The system thus allows compensation of the unbalance of the elevating mass (gun and cradle/mantlet).

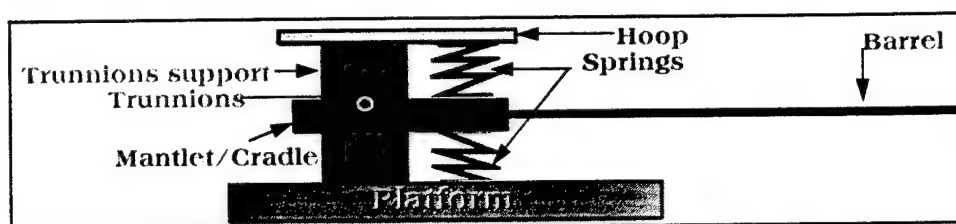


Figure 2 : Sketch of the principle of the elevating mass

This configuration is more interesting than a conventional mount (the elevating mass is clamped in elevation) for it allows, on one hand, access to the intrinsic characteristics of the weapon and, on the other, obtaining the boundary conditions, as seen by the weapon, which are representative of a classical turret assembly. The frequency of the small damping resonance of the first mode of the gun can be modified by adding to the end of the barrel a weight of 2 kgs (the first mode of the barrel is lowered by 2.5 Hz). During firing, instruments (13 sensors) give the movements of the elevating mass, the turret and the barrel. The movements of the barrel are detected by laser sensors associated with dedicated surface reflectors used because of the conicity and ribbing of the gun. The firing sequences are videoed and the impacts on a target at 100 metres are recorded. A data processing of the measurements is used to deal with all the parameters recorded during the different tests. About a hundred shots were fired and, each time, a recording was made of the physical parameters allowing determination of the respective behaviour of the weapon and its platform. As an example, analysis of the horizontal movements of the gun is given in this article. During single-shot firing, the movements of the gun, with or without the weights, are shown in Figure 3.

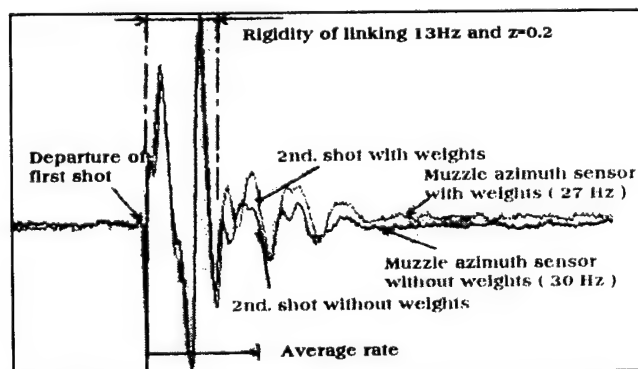


Figure 3 : Horizontal movements of the extremity of the gun during single-shot firing - Measurements made with a laser sensor placed at the end of the gun

Analysis of these movements shows, on one hand, that the phenomena are no-correlated and, on the other, understanding of the position of the gun in traverse at the second shot of a burst according to the firing rate. The whipping movements of the barrel stopped 350 ms after launch of the shot. The dynamic behaviour of the barrel therefore has no influence on burst-firing with shots separated for more than 350 ms. This was confirmed by analysis of firing at a low rate (500 ms interval between shots). But, in an average rate when the shots are separated by about 150 ms, the whipping movements greatly influence the distribution of shots in the target. In fact, from measurements taken during single-shot firing (see graphs of figure 3), it can be predicted for the average rate that :

- for the barrel without a weight, the second shot will be negative relative to the muzzle reference
- for the barrel with a weight, the second shot will be positive relative to the muzzle reference.

This extrapolation is shown to be justified by the statistical analysis of firing at an average rate (the discrepancy between the two positions is several times the dispersion of the weapon/ammunition for single-shot firing). If the results of the firing are averaged, it is possible to show that the dispersion of the second shot without a weight is three times less than the one that obtained by firing with a weight. This difference is linked to the irregularity of the rate ( $\pm 20$  shots per minute), and introduces an uncertain initial condition (the value and slope of whipping) seen by the second shot of the burst. The dispersion of the second shot of the burst is linked mainly to the efficient value of the sinusoidal signal, slightly dampened, generated by the first mode of the barrel.

Such work oriented the theoretical and experimental study on the elevating mass of the future medium calibre turret. Because of the technical and financial stakes linked to the medium-calibre turret programme, the system designers and weapon ordnances of Giat Industries started and financed a common study called "Firing dynamics of the MCF (Future Medium Calibre)", which was partly based on the methodology used during the study of the 25 mm test bench. The aim was to carry out a theoretical and experimental study so that the number of prototypes to be manufactured, and shots to be fired, could be reduced. The work started in 1992. In 1992, Giat Industries had a platform firing only single shots, with a spring recoil mechanism, and a heavy barrel for adjustment of medium calibre telescoped ammunition (figure 4).

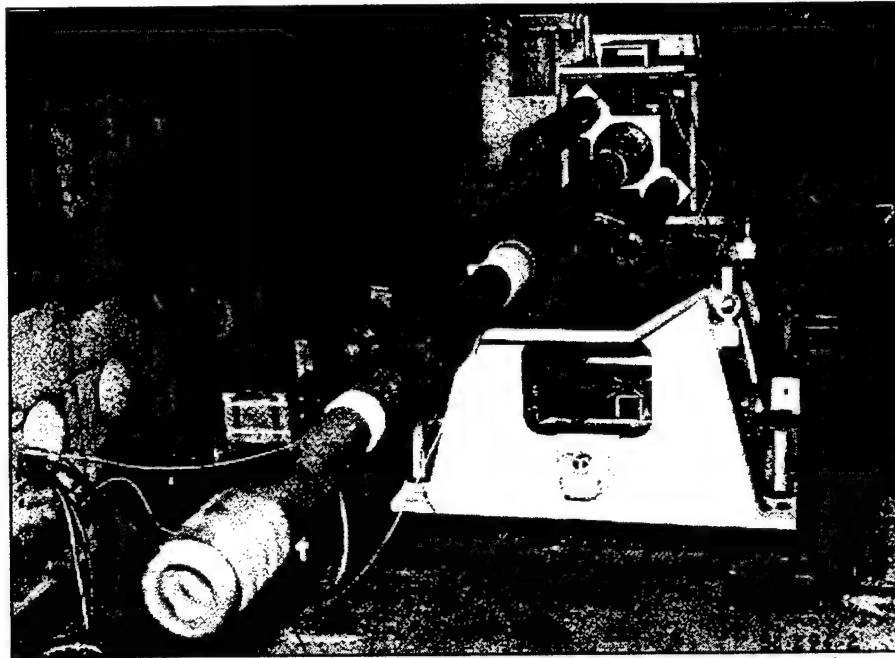


Figure 4: Platform firing only single shot with a heavy barrel

The architecture of the platform (rigid trunnions support, symmetrical cradle compared to the force of the recoil mechanism, centre of gravity of the recoiling mass on the firing axis) was particularly adapted to a constructive comparison of the information measured and the results of simulation. The theme of study was of "disturbances linked to firing". The main simulations were as follows:

- Accurate simulation of internal ballistics (work of weapon ordnances) with the SIMBAD software (Simulation of Barrel Dynamics) which shows in detail the dynamic interactions of the ammunition/barrel influencing the precision of shots. The SIMBAD data were used as initial conditions in a programme of external ballistics in the Giat Industries Research and Technological Studies Department, to estimate the position of impacts on a target in terms of mean and standard deviation.

- Macroscopic simulation of the elevating mass (system designer's work) which would be integrated into overall simulation of the study of performances of firing when stationary or moving of the future medium-calibre turret. These two simulation steps are necessary and complementary. Macroscopic simulation allows the system designer to organize into a hierarchy the problems linked to each sub-system. It also gives the weapon ordnance the possibility to deal with interactions between the ammunition and the weapon. In order to satisfy the above aims, the initial weapon system was modified by placing the elevating mass onto a springs mounting (figure 5 & 6). The stiffness of elevating gear box of a weapon system can be represented by springs.

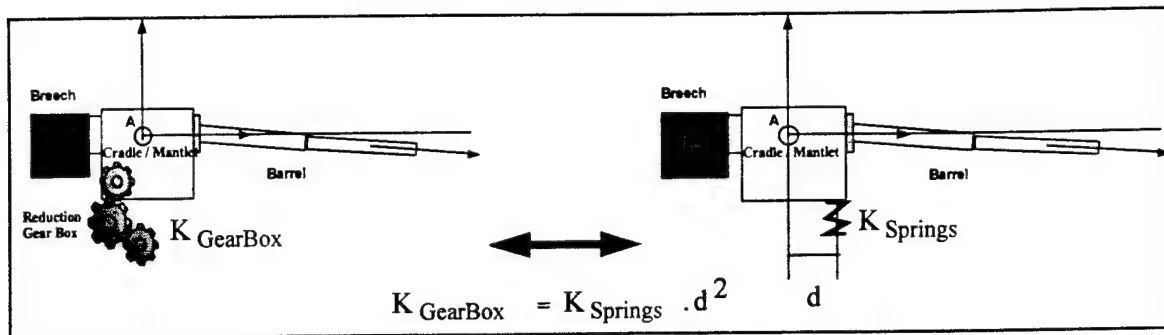


Figure 5 : Equivalent gun assembly

The first macroscopic simulation, based on the theory of modal analysis, was therefore elaborated.

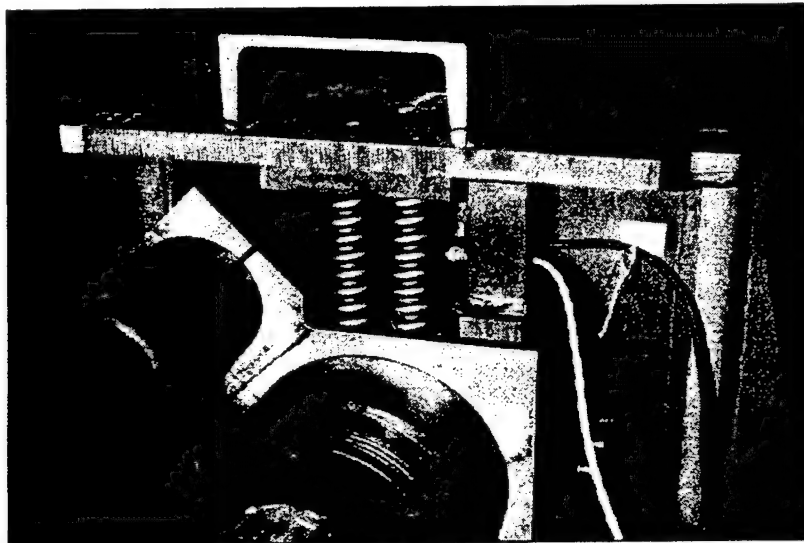


Figure 6 : Flexible gun assembly

The study continued in 1993 on a test bench with a weapon capable of firing in burst-mode. The results showed that, with a minimum number of shots fired, and analysis of the measurements, the dynamic behaviour of the bench can modify the intrinsic performances of a weapon when firing at a medium rate. The weapon ordnance and system designers of Giat Industries therefore decided to continue their common study in 1994.

The elevating mass is composed of a cradle in which the recoiling mass slides. This is checked, during firing, by the recoil mechanism between the cradle and the breech sleeve into which the gun barrel is fitted.

The supporting stiffness represents the link between the cradle/breech sleeve/barrel. It represents macroscopically the rigidity of the parts allowing the gun barrel to be fitted into the cradle/mantlet (figure 7).

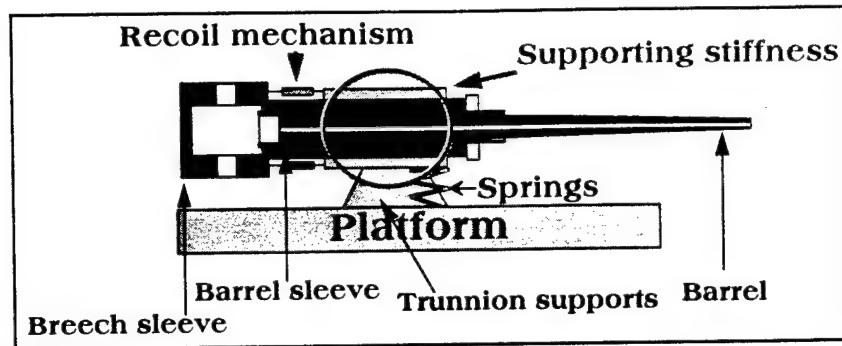


Figure 7 : Simulation of gun assembly of the Future Middle Calibre turret showing links between the recoil and the cradle/mantlet

## 2. EQUATIONS OF THE MODEL

At the beginning of 1994, theoretical studies were started so as to have a better estimate of the position and speed of the muzzle at the moment the ammunition is fired. These parameters condition precision of the shots. Analysis of international articles [1], [2] & [3], and the Giat Industries' expertise served as a basis for a quite original macroscopic simulation. Under the effect of firing, the elevating mass (figure 8) can have an absolute pitch movement  $\theta$  and each point of the barrel has a movement (angular and linear)  $w$  relative to the pitch movement  $\theta$ .

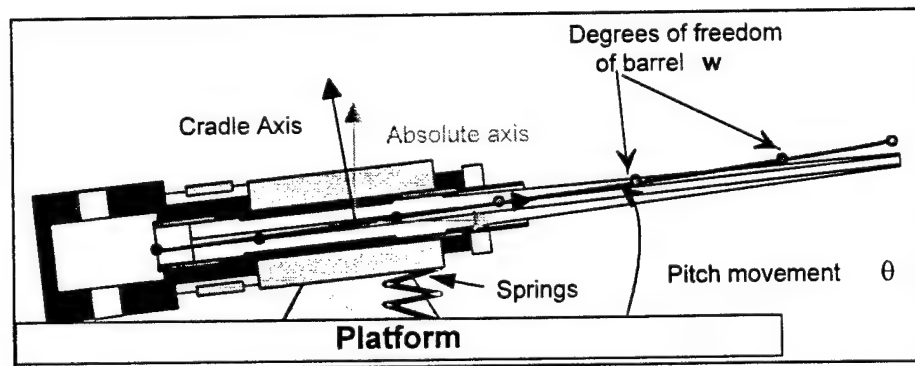


Figure 8 : Elevating Mass

The following hypothesis are retained for simulation : two-dimensional simulation of the elevating mass, the cradle-mantlet is supposed infinitely rigid (frequencies beyond 200 Hz), the barrel is simulated only in flexion by a simulation of the Euler-Bernoulli type (1), the connection between the barrel and its assembly is simulated by linear and angular supporting stiffness, the links between the solid parts are supposed to be whether with mechanical backlash or not, evolution of pressure in the barrel is extrapolated from the pressure in the breech measured during firing, the ammunition is considered as a material point (because the movement of the ammunition compared to the barrel has a high frequency (1 to 2 KHz) compared to the first two modes of the barrel situated in the range (5 to 50 Hz).

$$\int \left[ \frac{\partial^2}{\partial s^2} \left( E \cdot I(s) \cdot \frac{\partial^2}{\partial s^2} w \right) + \rho(s) \cdot \ddot{w} + \rho(s) \cdot (s - x - d) \cdot \ddot{\theta} + \rho(s) \cdot g \right] ds + \sum_{i=1}^{nss} k_i \cdot w_i + \sum_{k=1}^{nm} m_k \cdot [\ddot{w}(s_k) + (s_k - x - d) \cdot \ddot{\theta}] = \sum_{j=1}^7 f_j \quad (1)$$

with for (1):

s	Curvilign abscissa of the barrel
I(s)	Area cross section moment of inertia
E	Young's modulus of elasticity
w	Deformation of the barrel which depends on the s abscissa and t time ( w(t,s) )
x	Position of trunnions in the barrel coordinates
d	Recoil of the recoiling mass
θ	Pitch movement of the elevating mass relative to the absolute coordinates
ρ(s)	Mass per unit length
k <sub>i</sub>	Supporting stiffness (linear and angular) if it exists
nss	Number of supporting stiffness
w <sub>i</sub>	Deformation of the barrel at position of the i <sup>th</sup> contact with the barrel support
m <sub>k</sub>	Non-structural masses on the barrel at s <sub>k</sub> abscissa
nm	Number of non structural masses on the barrel
f <sub>j</sub>	Seven load functions described in reference [1], [2] & [3]:
	- Recoil inertia load
	- Pressure curvature load
	- Projectile trajectory load
	- Projectile eccentricity load
	- Projectile rotational load
	- Stationary mass eccentricity
	- Support reactions

The third term of first member of (1) represents the coupling Equipped Barrel/Cradle.  
The equation of elevating mass is (2):

$$I_{em}(d) \cdot \ddot{\theta} + K_{GearBox} \cdot (\theta - u) + \int \rho(s) \cdot (s - x - d) \cdot \ddot{w} \cdot ds + \sum_{k=1}^{nm} m_k \cdot (s_k - x - d) \cdot \ddot{w}(s_k) = \sum_{j=1} Torque_j \quad (2)$$

with for (2):

$I_{em}(d)$  Inertia of elevating mass is variable. It depends on the position of the recoiling mass.  
 $u$  Angular position of electrical motor.

$$\sum_{j=1} \text{Torque}_j = (Flh \cdot dlh - Flb \cdot dlb) - (dt * F_{fire}) - (F_{recoil} - F_{fire}) \cdot Y_g \quad (3)$$

with for (3):

$Flh$  Force of superior recoil mechanism  
 $Flb$  Force of inferior recoil mechanism  
 $dlb$  Distance between the axis of inferior recoil mechanism and axis of the trunnions  
 $dlh$  Distance between the axis of superior recoil mechanism and axis of the trunnions  
 $dt$  Distance between the gases' pressure axis and axis of the trunnions  
 $F_{fire}$  Force of gases' pressure (-pressure\*bore section)  
 $F_{recoil}$  Total force of the recoil mechanism ( $Flb+Flh$ )  
 $Y_g$  Offset of recoiling mass

The first term of (3) corresponds to the dissymetry torque of the recoil mechanism. The second term to the torque linked to the de-centering of the force of the gases' pressure relative to the axis of the trunnions and, the last term to the torque linked to the de-centering of the centre of gravity of the recoiling mass relative to the axis of the trunnions

The last equation of the system is the equation of the recoiling mass. In first order, we have:

$$(F_{fire} - F_{recoil}) \approx M_{rm} \cdot \ddot{d} \quad (4)$$

with for (4) :

$M_{rm}$  Mass of recoiling mass. Note that the dampening and stiffness of (4) are included in  $F_{recoil}$ .

The method of the finite elements allows the equations describing the system to be linearized for each section of the barrel. The displacements and their curves are approximated by four HERMITE polynomes of order 3 for each section of the barrel ( $\phi_1 \psi_1 \phi_2 \psi_2$ ). At each node of the barrel,  $w$  has 2 degrees of freedom that we note:

$$w = \begin{pmatrix} y(t,s) \\ \alpha(t,s) \end{pmatrix}, \text{ with } y \text{ the linear deformation (length unit) and,}$$

$$\alpha(t,s) = \frac{\partial y(t,s)}{\partial s} \text{ the angular deformation (radian unit)}$$

We have thus for each section of the barrel:

$$w = w(t,s) = (\varphi_1(s) \quad \psi_1(s) \quad \varphi_2(s) \quad \psi_2(s)) \begin{pmatrix} y_1(t) \\ \alpha_1(t) \\ y_2(t) \\ \alpha_2(t) \end{pmatrix} \quad (5)$$

The result of the numerical method (1)+(2) is a system of ordinary differential equations. The theoretical study gave the following analytical results (6) with matrix structure defined in (6.1) and (6.2):

$$M_o \cdot \ddot{W}(t) + C_o \cdot \dot{W}(t) + K_o \cdot W(t) = M(t) \cdot \ddot{W}(t) + C(t) \cdot \dot{W}(t) + K(t) \cdot W(t) + P(t) \quad (6)$$

$$W(t) = \begin{bmatrix} w = \begin{pmatrix} \text{Deformation} \\ \text{of} \\ \text{barrel} \end{pmatrix} \\ \theta = \begin{pmatrix} \text{Absolute\_position} \\ \text{of} \\ \text{Elevating\_mass} \end{pmatrix} \end{bmatrix} \quad (6.1)$$

$$\text{Matrix Structure} = \begin{bmatrix} \begin{pmatrix} \text{Matrix} \\ \text{of} \\ \text{Barrel} \\ \text{Characteristics} \end{pmatrix} & (\text{Coupling})^t \\ (\text{Coupling}) & \begin{pmatrix} \text{Elevating\_mass} \\ \text{Characteristics} \end{pmatrix} \end{bmatrix} \quad (6.2)$$

with for (6):

- $M_o$  Inertia matrix of the system. Its structure is defined in (6.2).
- $M(t)$  Inertia matrix of the system due to the recoil of the recoiling mass and load functions
- $K_o$  Stiffness matrix of the system including stiffness of springs of the elevating mass, barrel stiffness and supporting stiffness. Different stiffness matrix can be chosen according to backlashes of gun assembly that we note  $K_i$  ( figure 9 ).

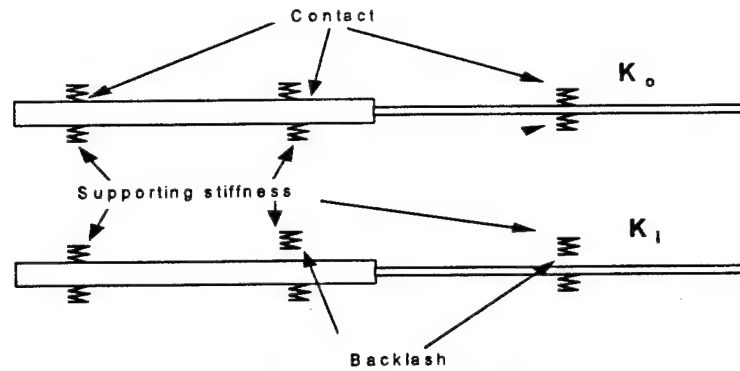


Figure 9 : Different types of Stiffness matrix

- $K(t)$  Stiffness matrix of the system due to load functions  
 $C_o$  Dampening matrix of the system  
 $C(t)$  Coriolis matrix of the system due to load functions  
 $W(t)$  Degrees of freedom ( $w$  and  $\theta$ ) of the system as defined in (6.1)  
 $P(t)$  All terms that do not depend on the variables  $w$  and  $\theta$ .

Numerically, the choice of algorithm for the integration process of (6) depends on the type of Inertia and Stiffness matrix of the mechanical system. They are generally ill-conditioned because of the non-structural masses (breech, bore evacuator, muzzle brake, etc...) and the supporting stiffnesses. High frequencies are, all the more, not necessary for system designers. The reduction procedure allowed to choose the integration process algorithm compatible with the firing dynamic system (highly non-linear, discontinuous between internal and external ballistic and, particularly only slow dynamics with frequencies less than 1 kHz). In that case, the Runge-Kutta fifth order method performs well (minimum step =  $10^{-20}$  s with an relative error of  $10^{-6}$ ). In the order case, a stiff solver as Gear method had to be used.

In order to satisfy this requirement, the equation of (6) has been reduced by using the modal analysis. The second member of this equation is calculated in Finite Elements basis. The equation of (6) becomes:

$$\ddot{Q}(t) + \mathcal{A} \cdot \dot{Q}(t) + \mathcal{D} \cdot Q(t) = \mathcal{R} \quad (7)$$

with for (7):

$$\mathcal{A} = B^{-1} \cdot M_o^{-1} \cdot C_o \cdot B \quad (7.1)$$

The reduced dampening matrix. This matrix is generally non-diagonal and replaced by the diagonal matrix with Basile's hypothesis.

$\mathcal{B}$ , is a matrix of eigen-vectors. It is the solution of:

$$\mathcal{B}^{-1} \cdot (M_0^{-1} \cdot K_0) \cdot \mathcal{B} = \mathcal{D} \quad (7.2)$$

with  $\mathcal{D}$  the eigen-values matrix.

$$Q(t) = \mathcal{B}^{-1} \cdot W(t) \quad (7.3)$$

$$\mathcal{R} = \mathcal{B}^{-1} \cdot M_0^{-1} \cdot (M(t) \cdot \ddot{W}(t) + C(t) \cdot \dot{W}(t) + K(t) \cdot W(t) + P(t)) \cdot \mathcal{B} \quad (7.4)$$

It will be noticed that the deformation of cradle can be added in the same way as the variable of the elevating mass ( $\theta$ ). The figure 10 shows the result of 3-Dimensional Finite Elements code for the dynamic behaviour of cradle. The barrel is modelled with elements given by a macroscopic model. This approach allows to estimate the coupling between dynamic behaviour of the cradle and the dynamic behaviour of the barrel when the recuperator force is applied on the cradle without load functions applied on the barrel.

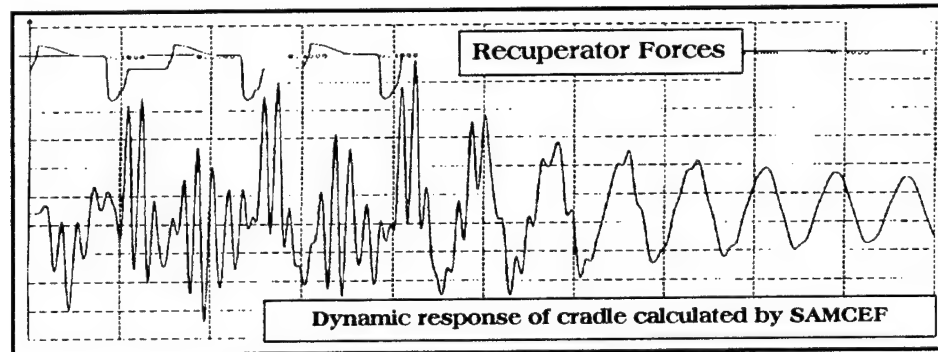
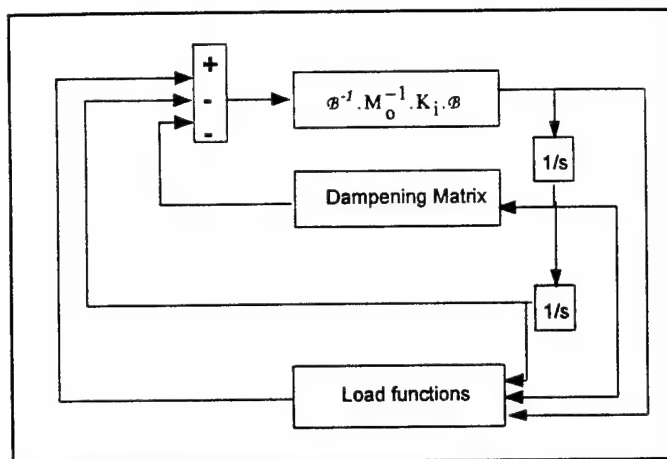


Figure 10: Dynamic response of cradle

### 3. APPLICATION

#### 3.1. Model validating

The macroscopic simulation was coded with the MATLAB and SIMULINK software. The algorithms of the macroscopic simulation were given more consistent by use of MAPLE V symbolic calculations for all components of matrix. A macroscopic simulation comprising first seven frequencies of the elevating mass was used to simulate the dynamic response of an elevating mass during firing as shown in Figure 11.



**Figure 11 : Simulink model of the elevating mass**

The studied weapon system has a barrel support in order to increase the stiffness of the barrel. The barrel support creates a third contact (between the barrel and barrel support) that it is necessary to determine its characteristics. The supporting stiffnesses (between barrel-barrel support as well as barrel-cradle) are calculated by 3-Dimensional Finite Elements Code (SAMCEF). This modeling shows that the supporting stiffnesses can be substituted by the linear and rotating springs as shown in Figure 12.

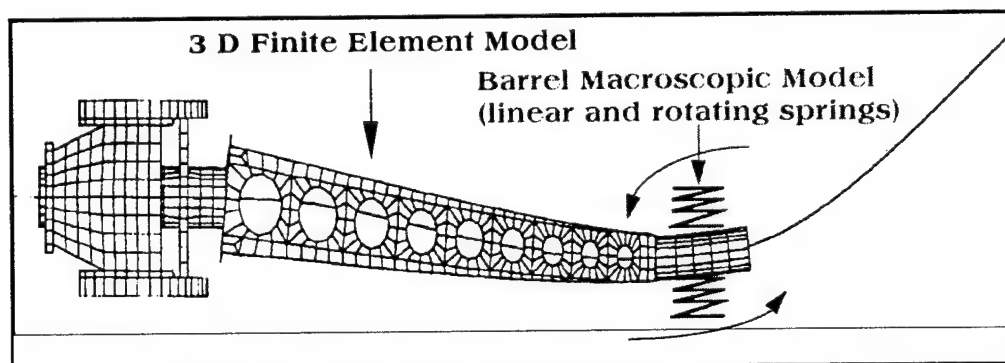


Figure 12 : Equivalent scheme of supporting stiffness

The comparison of frequency calculations between the macroscopic modeling and SAMCEF gives an error of less than 3% for the first two modes.

The simulation was validated by a specific experiment (release and firing tests).

The weapon ordnances studied this phenomenon for the cannon equipping the new french aircraft RAFALE and MCF (Future Medium Calibre) in the case of a clamped assembly of the weapon (no overall movement of the elevating mass). The system designers undertook more general steps in a turret with a more flexible assembly of the turret system.

The experimental works were carried out in 1994. The experimental mounting was a firing apparatus with an elevating mass mounting on springs.

The value of  $K_{\text{GearBox}}$  defined in (2) is replaced by  $d^2.K_{\text{Springs}}$  and  $u$  by 0. The tests allowed completion of the database constituted in 1992 with the firing apparatus equipped with a heavy barrel. The location of the sensors and their characteristics were chosen to acquire the information necessary for comparison of the simulations. The following measurements were processed: movement of the  $\theta$  pitch of the elevating mass through a linear displacement sensor, recoil of the mass, deformation of the barrel measured with strain gauges stuck on the barrel, the longitudinal and vertical accelerations of the recoiling mass (the accelerometers were assembled on a mechanical filter). Note that strain gauges give only the curvature of the barrel (8). The barrel deformations ( $w$ ) can be obtained by Finite Elements method:

$$\left[ \frac{\partial^2 w(t,s)}{\partial s^2} \right]_{s=a} = \frac{1}{2.R(a)} \left[ \frac{\Delta l_1}{l_1} - \frac{\Delta l_2}{l_2} \right]_{s=a} \quad (8)$$

with for (8):

- $R(a)$  Radius of barrel section at  $s=a$   
 $\frac{\Delta l_1}{l_1}$  Relative extension of superior strain gauge  
 $\frac{\Delta l_2}{l_2}$  Relative extension of inferior strain gauge

Release tests, carried out before the firing sequences, allowed determination of the frequencies of the first two modes of the barrel, as well as the dampening of the first mode. The frequencies of the macroscopic model are obtained by solving the eigen-values problem of (7.2). Those frequencies were compared to release tests and SAMCEF model calculations. The macroscopic simulation gave an estimate, with a several percentage discrepancy, of the different modes of the gun assembly. The most interesting comparison was obtained with the measurements carried out during the firing sequences.

Figures 12 & 13 show respectively the comparison theory/tests for the movement of  $\theta$  pitch of the elevating mass and the deformation by strain gauges. It can be noted that the movements of the elevating mass can be neglected even though the elevating mass is centred. The cause is linked to the dissymetry of the recoil mechanism creating, via the supporting stiffness, a low-frequency torque which generates an overall movement which has, through coupling, a significant influence on the barrel movements. In fact, the spectrum of the information in figure 12 shows the same amplitude of the elevating mass as the one linked to the first mode of the barrel. The strain gauges allow validation of the simulation without any modification of the intrinsic characteristics of the barrel. The displacement and speed of the barrel can be estimated from the validated simulation.

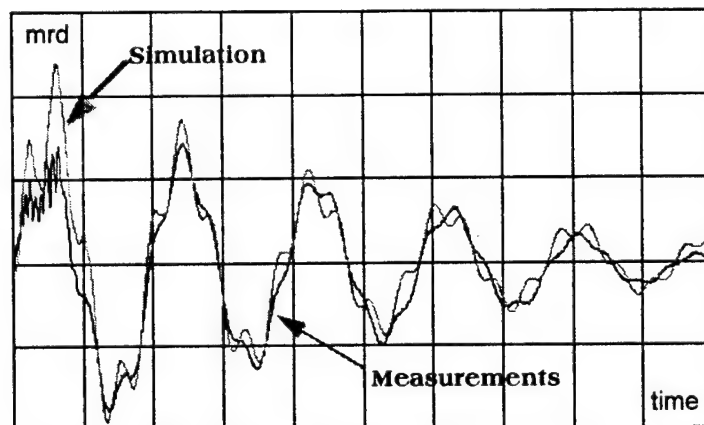


Figure 12 : Movements of the elevating mass during a single-shot firing sequence

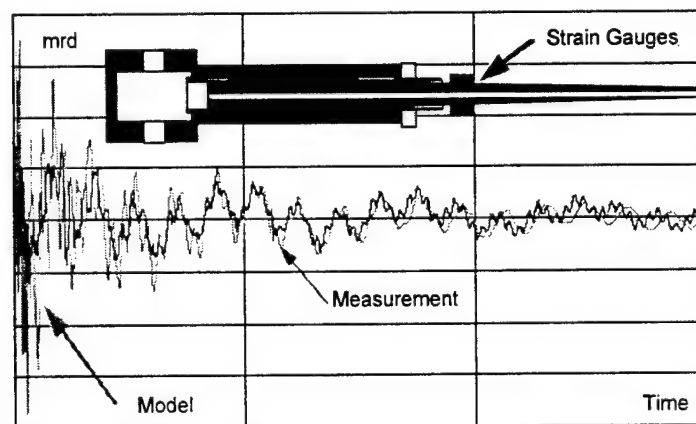


Figure 13 : Barrel deformation during single-shot firing

Note that Figure 13 shows the amplitude discrepancy during the internal ballistic phase. The dynamic rate and the magnification of macroscopic model gave a slight difference with SIMBAD than with measurements. The studies on microscopic simulation done by the weapon ordnances of Giat Industries, are delivered in this article. They did, however, permit the system designers to validate that the relative movement of ammunition in the barrel, high frequency compared to the first three modes, has an insignificant influence on the barrel movements. Studies were undertaken to show the role of the movements of the ammunition on the performances of single-shot and burst-firing sequences. The dispersion parameters of ammunition defined in load functions (ammunition eccentricity, pressure of gaz, etc...[3], [4] & [5]) allowed to verify, statistically, the dispersion estimation of the couple of elastic barrel / projectile.

### 3.2. Macroscopic simulation with aiming system

The integration of aiming system is done by the last component of (6) with the variable of elevating mass  $\theta$ . The mechanical architecture is calculated is the modal basis (figure 14). Load functions are calculated is Finite Elements basis and coded in C language. The basis

transformation module (Modal Basis  $\rightarrow$  Finite Elements Basis) has been added to allow the integration of control system.

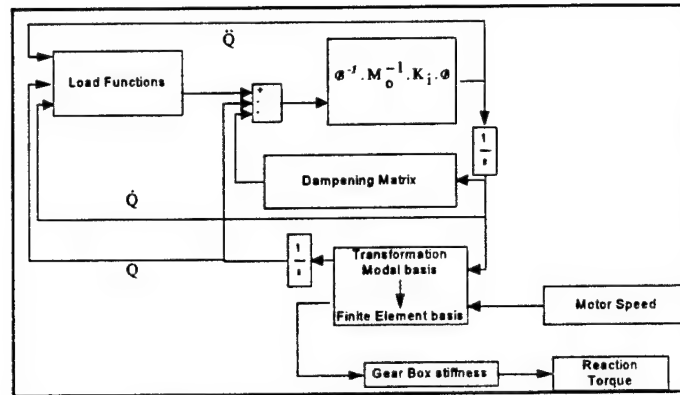


Figure 14: Coupling between Gun Assembly - Aiming System

The Dahl friction model (9) is integrated into the macroscopic model. It allows to represent better, at the contact between two surfaces, the dynamic behaviour between pur elasticity for a small displacement and Coulomb friction for important displacements. This model is integrated in the Dampening Matrix.

$$\frac{dF(\theta)}{dt} = \frac{dF(\theta)}{d\theta} \cdot \frac{d\theta}{dt} \quad (9)$$

with for (9):

$$\frac{dF(\theta)}{d\theta} = \sigma_c \left| 1 - \frac{F(\theta)}{F_c} \cdot \text{signe}(\dot{\theta}) \right|^i \cdot \text{signe} \left( 1 - \frac{F(\theta)}{F_c} \cdot \text{signe}(\dot{\theta}) \right)$$

$F_c$  Friction magnification

$\sigma, i$  Dahl parameters of elasticity behaviour

The principle of the aiming system is based on classical control principles: speed and position closed loop with tachometer motor and elevating mass gyrometer (figure 15). The gain values are dimensionned by Bode, Nyquist and Evans diagrams of elevating mass macroscopic model.

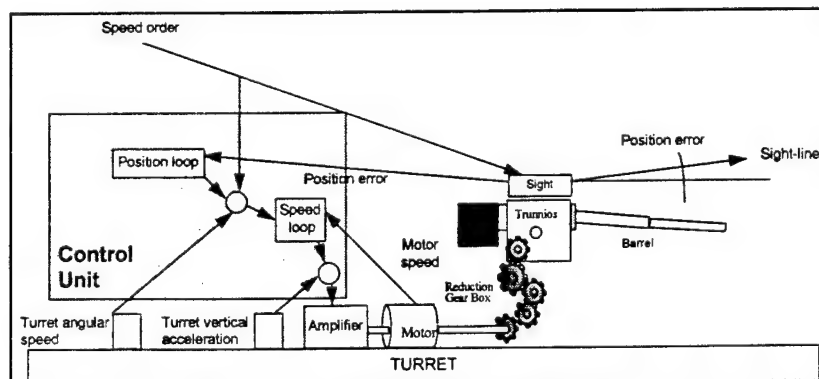


Figure 15: Aiming System Diagram

The elaboration of the macroscopic model (Mechanical Architecture and Aiming System) provides, viewed by the system designers, the estimate of the firing performance levels of the weapon system to be defined. The example below shows an example of firing stabilization of the weapon system (figure 16). The rate of fire is 400 rounds/mn. The number of rounds is 5. Four configurations were simulated:

- Unstabilized weapon system with no friction and dissymetry of recoil mechanism
- Stabilized weapon system with Dahl friction and dissymetry of recoil mechanism
- Stabilized weapon system with Coulomb friction and dissymetry of recoil mechanism
- Stabilized weapon system with Dahl friction and no dissymetry of recoil mechanism

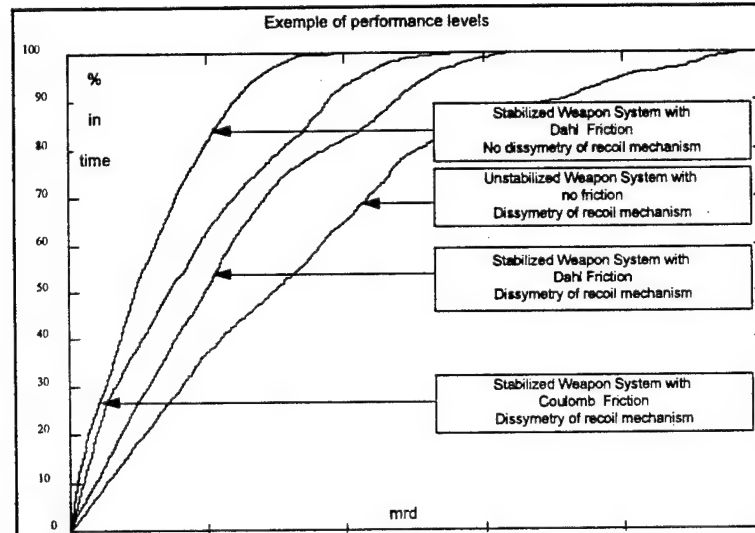


Figure 16: Performance levels example of firing stabilization

#### 4. CONCLUSION AND FUTURE PROSPECTS

The progressive and pragmatic approach adopted for creating and validating macroscopic simulation of an elevating mass produced a method of work showing, convincingly, the parameters that are estimated from simulation and those which can be measured during modal analysis tests and firing sequences with a simple gun assembly.

Modal analysis (theoretical and experimental) is a necessary tool to understand the dynamic phenomena that govern on gun assemblies with a relatively complex architecture.

The cooperation between the weapon ordnances and system designers of Giat Industries gave rise to an original and comprehensive study on the medium calibre weapon that was carried out as feasibility study for the Future Medium Calibre weapon. Analysis of the experimental data and theory led to perceiving, on one hand, the dynamic interactions generated by the single-shot firing of a simplified elevating mass with behaviour that could be controlled and, on the other hand, the dynamic phenomena of the barrel generated by single-shot firing with full calibre CTWS (Cased Telescoped Weapon System) ammunition fired with a firing device. The modes and deformations (both static and dynamic) of the barrel could thus be estimated with a discrepancy of several percent compared to the measurements

processed during the trials. The results obtained will help to adjust the overall simulation of a future turret equipped with a medium-calibre cannon firing in bursts and particularly for the study of the performances of subsystems in burst-firing.

This future study aims to reduce the numbers of prototypes to be manufactured, and to diminish the number of shots that have to be fired in order to have a well-performing gun system.

**We would like to thank the DGA (Délégation Générale de l'Armement: French MOD) for financing the study "Assembly and aiming of an automatic weapon system".**

**REFERENCES:**

- [1] : Simkins, "Transverse response of barrels to curvature-induced load functions"  
Proceeding of the 2nd U.S. Army Symposium on Gun Dynamic.  
ARLCB-SP-78013 Benet Weapons Laboratory, Watervliet, N.Y.
- [2] : Gast, "Normal modes analysis of gun vibrations by the uniform segment method"  
Technical report ARCCB-TR-87033, November 1987, Benet Weapons Laboratory,  
Watervliet, N.Y.
- [3] : Morton & Toosi, "Dispersion estimation by Monte-Carlo simulation for an elastic gun  
tube/projectile system"  
Mc Donnell Douglas Helicopter Company, Mesa, Arizona
- [4] : Cayzac & Carette & Mennechet, "Sources of dispersion occurring with APFSDS launch  
dynamics".  
15 th International Symposium on Ballistics, Jerusalem, Ireal, 21-24 May 1995  
Giat Industries ( CRET ) & Direction de la Recherche et de la Technologie ( DRET ),  
France.
- [5] : Carlier, Couvin, Guisneuf & Pichot "Shooting dynamic of automatic weapons"  
2nd Technical and Scientific Symposium of Giat Industries (Satory 13 & 14 Decembre  
1994 ), France

## **Simulation of Projectile Balloting in Hypervelocity Launchers**

**Burdett K. Stearns**

Arrow Tech Associates, Inc.  
1233 Shelburne Road, Suite D-8  
South Burlington, Vermont, USA 05403

**John R. Burnett, Jr.**

Arrow Tech Associates, Inc.  
1233 Shelburne Road, Suite D-8  
South Burlington, Vermont, USA 05403

### **Abstract**

Two conflicting goals are currently driving the design of launch vehicles utilized in conjunction with hypervelocity launchers such as the AEDC Range G light gas gun. First, the desire to achieve first shot success tends to drive test projectile designs toward the robust. Second, the desire to launch lighter weight payloads at ever increasing velocities pushes the projectile design to small margins of safety. This second goal, coupled with a failure to predict the influence of transverse loads due to projectile balloting, has resulted in projectiles, or their components, that are frequently designed with insufficient strength to withstand the launch loads.

Hypervelocity testing is a time consuming and costly process, requiring extensive preparation for launcher and instrumentation set-up. The test projectiles utilized are usually one of a kind with tight manufacturing tolerances that make them difficult and expensive to build. Therefore, whenever a projectile fails in-bore, or is deformed sufficiently to invalidate test results, two undesirable things happen. There is a test schedule delay and the expense of a re-test is incurred.

Balloting analysis has been used for many years in conventional guns to help design efficient, light weight, highly stressed projectiles which are launched without failure. Unfortunately, current balloting codes address only part of the critical balloting influences for hypervelocity launches.

This paper summarizes the various phenomena which influence hypervelocity balloting, and discusses certain challenges involved in achieving realistic simulations. A workable approach to achieving this end is also presented.

## **Simulation of Projectile Balloting in Hypervelocity Launchers**

**Burdett K. Stearns**

Arrow Tech Associates, Inc.  
1233 Shelburne Road, Suite D-8  
South Burlington, Vermont, USA 05403

**John R. Burnett, Jr.**

Arrow Tech Associates, Inc.  
1233 Shelburne Road, Suite D-8  
South Burlington, Vermont, USA 05403

### **1. Introduction**

Two conflicting goals are currently driving the design of launch vehicles utilized in conjunction with hypervelocity launchers such as the AEDC Range G light gas gun. First, the desire to achieve first shot success tends to drive test projectile designs toward the robust. Second, the desire to launch lighter weight payloads at ever increasing velocities pushes the projectile design to small margins of safety. This second goal, coupled with a failure to predict the influence of transverse loads due to projectile balloting, has resulted in projectiles, or their components, that are frequently designed with insufficient strength to withstand the launch loads.

Hypervelocity testing is a time consuming and costly process, requiring extensive preparation for launcher and instrumentation set-up. The test projectiles utilized are usually one of a kind with tight manufacturing tolerances that make them difficult and expensive to build. Therefore, whenever a projectile fails in-bore, or is deformed sufficiently to invalidate test results, two undesirable things happen. There is a test schedule delay and the expense of a re-test is incurred.

Balloting analysis has been used for many years in conventional guns to help design efficient, light weight, highly stressed projectiles which are launched without failure. Unfortunately, current balloting codes address only part of the critical balloting influences for hypervelocity launches.

This paper summarizes the various phenomena which influence hypervelocity balloting, and discusses certain challenges involved in achieving realistic simulations. A workable approach to achieving this end is also presented.

### **2. Hypervelocity Balloting**

Balloting is defined, herein, as any transverse motion of the projectile during inbore travel. The following phenomena are considered to affect this motion in hypervelocity launches:

## 2.1 CG Offset

When the projectile center of gravity (CG) and principal axis are offset from the bore centerline, the applied base pressure force forms an overturning couple with the resisting axial inertia force, producing balloting motion (see Figure 1). Initial offset can be produced by projectile machining and assembly. It can also occur during projectile chambering (when, in addition, a specific angular orientation is established). Clearances between the bore rider(s) and the launcher surface also permit lateral displacement.

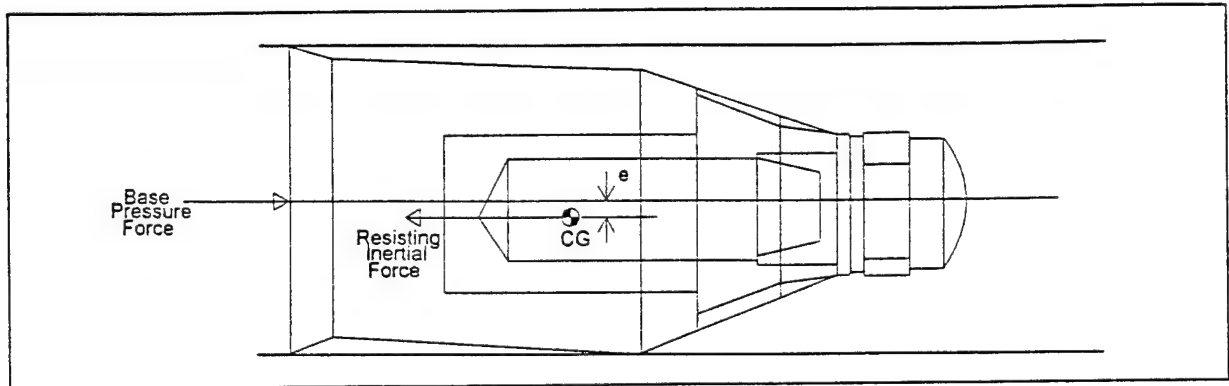


Figure 1: Center of Gravity Offset

## 2.2 Gas Pressure

Hypervelocity gas dynamics produces high frequency pressure variation at the projectile base, which is evident even in the relatively low level distribution shown in Figure 2. Ram pressure forward of the projectile may also be irregular. Balloting motion from CG offset is a direct function of the net high frequency pressure variation applied over the surface of the projectile.

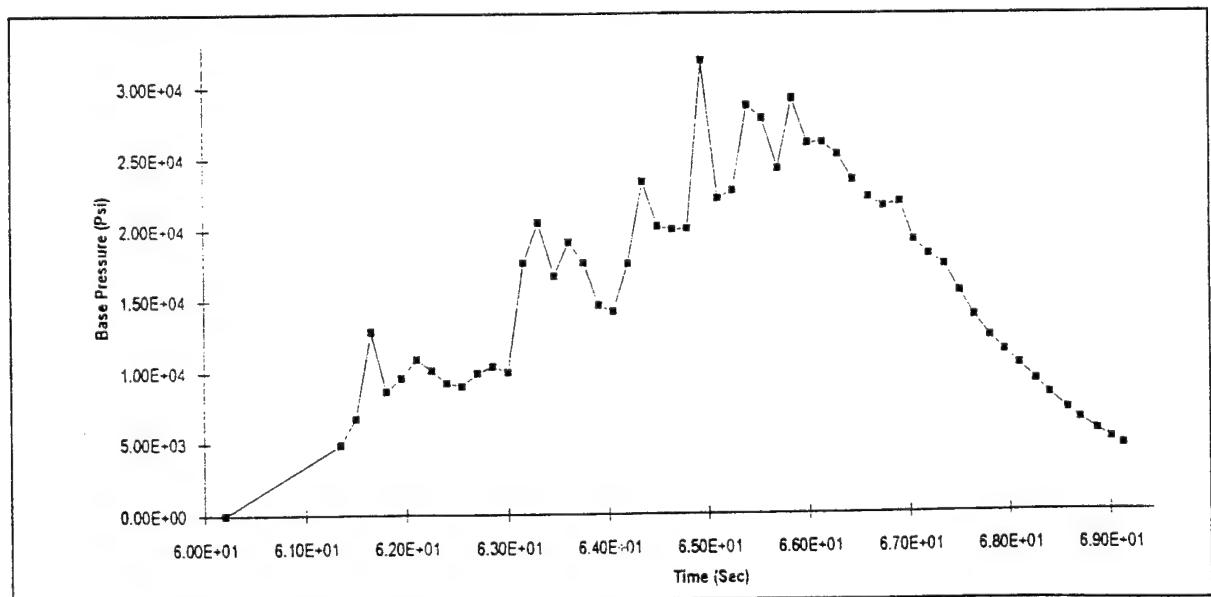


Figure 2: Gas Pressure Profile

Figure 2: Gas Pressure Profile

### 2.3 Stiffness/Mass

The stiffness/mass distribution of the projectile configuration determines its response to overturning moments and lateral impact forces. A more flexible structure permits greater CG displacement, thereby providing a further increase in offset and subsequent balloting motion.

### 2.4 Surface Wear

Wear, at projectile contact surfaces with the bore, produces or widens clearances permitting increased CG offset (see Figure 3a). Wear may also modify the obturation preload, and in some cases may remove the preload altogether, resulting in blow-by. Additionally, loss of projectile material alters the contact stiffness between projectile and launcher.

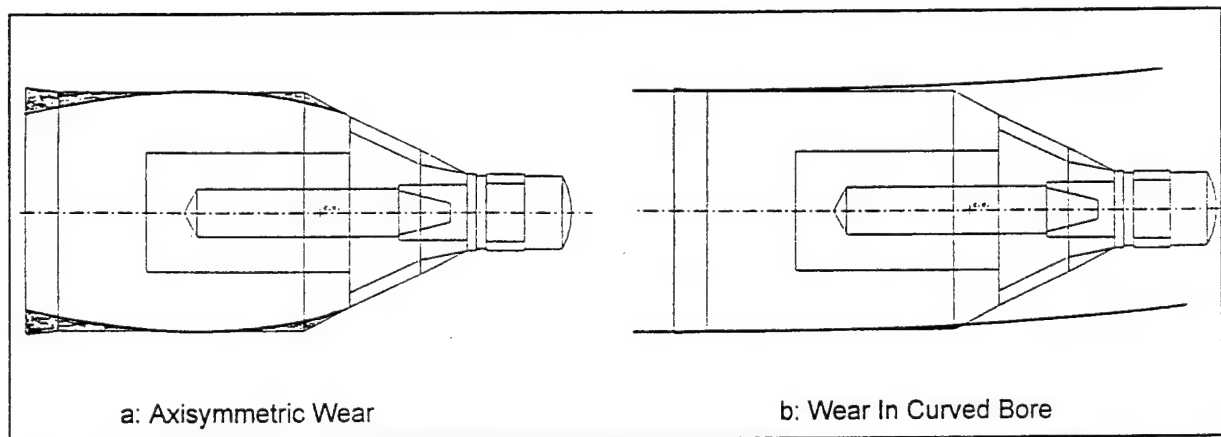


Figure 3: Surface Wear

### 2.5 Bore Curvature

Any curvature of the bore will produce centrifugal forces in the projectile, inducing balloting motion. Although hypervelocity launchers are carefully monitored and their straightness profiles are maintained to rigorous standards, some local curvature does exist. The severity of induced balloting is dependent upon the abruptness of the curvature and the velocity and mass of the projectile. Gravity droop of the launcher forms a small part of the bore curvature in well supported hypervelocity launchers.

A curved bore can also produce surface wear, as indicated in the sketch shown in Figure 3b.

### 2.6 Bore Diameter

Variation in bore diameter with axial distance effectively changes radial clearances and/or radial preload between the projectile and launcher as a function of travel.

## 2.7 Spin Devices

Rifling or spin producing devices cause rotational motion of the projectile about its longitudinal axis, adding another component of radial force to an offset CG.

## 2.8 Launcher Response

The launcher deflects transversely as the projectile travels its course. It interacts with the projectile in an exchange of loading. Multiple transverse supports are usually provided which minimize this movement. Set-back inertial loading has a straightening effect, but the so-called Bourdon Tube effect (pressurization in a curved cylinder) produces transverse motion. The launcher also expands radially under the action of gas pressure loading. Stress waves, at critical velocities, may amplify this increase in bore diameter in the vicinity of the projectile, altering the surface preload and/or clearance.

## **3. Simulation Challenges**

Projectile balloting at hypervelocity differs from that at conventional powder gun velocities in many respects, and presents certain challenges to the simulation process. To be able to replicate the significant balloting behavior of different projectile configurations in the various types of hypervelocity launchers, the relative importance of these differences must be evaluated and an approach found to include them in the simulation as appropriate. Certain of these challenges are discussed in the following paragraphs.

### 3.1 Hypervelocity Wear

Projectile surface wear is a function of velocity, normal force (balloting and radial preload), friction force, and temperature dependent material properties. The frictional heat generated can raise the temperature of the projectile to a point where ablation occurs. Extensive wear can occur at high velocities resulting in unusual behavior of the projectile. In some cases, wear can progress to the point of permitting blow-by, which may result in an unsuccessful test. Asymmetric pressure distribution along the length of the projectile will increase balloting motion.

If blow-by does occur (in a smooth bore), the projectile may rotate about its longitudinal axis, due to repeated impacts with the tube wall. This is believed to be produced by offset transverse impacts of worn smaller diameter bourrelets in the slightly larger diameter bore. As an illustration, consider the sketch in Figure 4 of a small disk undergoing repeated elastic impacts with a rigid tube wall. If the disk velocity vector at impact is not in alignment with the center of the tube, the disk will rebound at an angle. Friction developed at the surface during impact will produce a rotation of the disc. At each subsequent impact the disc will be forced to rotate in the same direction.

The disk analogy can be extended to include projectile yawing and pitching motion. Then, the direction of rotation will be governed by the largest impact forces which occur along the

contacting surface. Although the total rotation at exit may be relatively small, if spin orientation is significant in testing, blowby can effect the desired results.

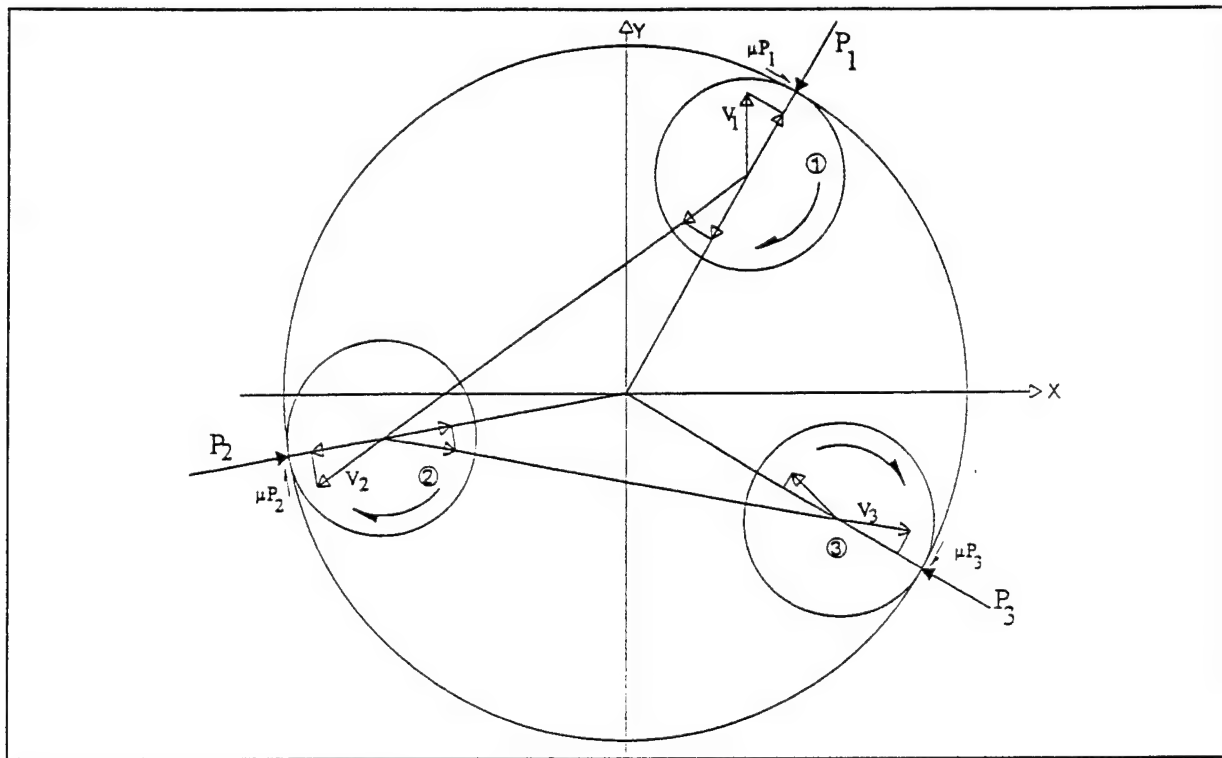


Figure 4: Elastic Impact of a Disk in a Tube

### 3.2 Gas Dynamics

The principal gas dynamic effects on projectile balloting are transmitted through the gas pressures exerted on the projectile surfaces. These include the base pressure imposed by the compressed light gas, or other propelling gas, the nose pressure exerted by the launch tube gas and peripheral pressures imposed by blow-by.

The base pressure is presently calculated by numerical integration of the equations for quasi-one-dimensional unsteady flow [1]. Any asymmetric variation of pressure in the radial direction will apply an added overturning moment to the projectile, as will an asymmetric distribution of gas pressure over the surface of the projectile developed during blow-by (see Figure 5).

Calculations must be made at relatively small time intervals to replicate the actual high frequency pressure oscillations which have a direct effect on balloting motion.

For two-stage launchers, it is necessary to consider the simultaneous motion of both the pump tube piston and the projectile in a determination of dynamic pressure variations. Their relative positions in time determine gas volume and axial distance between reflecting surfaces.

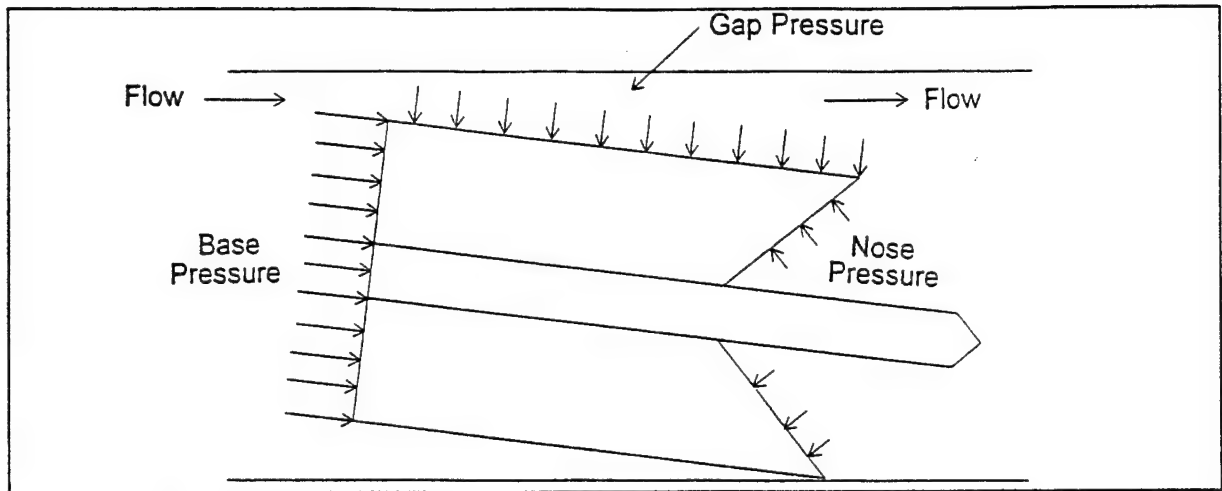


Figure 5: Blow-By Flow Field

### 3.3 Bore Curvature

In spite of using multiple supports and straightening adjustments, the bore of any launcher remains curved to some degree, and even a small curvature is significant in balloting at high velocity.

The radial acceleration (in g units) of a point mass moving at velocity  $V$ , along a curved path of radius  $R$ , is given by the expression  $N_g = V^2 / (g \cdot R)$ . Applying this, as an example, to a rigid body projectile traveling at a velocity of 18000 fps in a launcher having a local bore radius of curvature of 500 feet (6000 inches), the radial acceleration is calculated to be over 20000 g's. This is on the order of 20 times the g level expected for projectiles fired in conventional powder guns.

Bore curvature may be obtained by measurement of centerline offset, in both a vertical and horizontal plane, at a discrete number of locations along the length of the launcher. The curvature between these locations is then determined by curve fitting of the point data, as illustrated in Figure 6, for a short section of launcher. Here, a simple piece-wise cubic curve is drawn through the precise points measured in the vertical plane. Many schemes are used to provide curve definition [2], but care must be taken with smoothing, as it is the local curvature that will induce the greatest lateral accelerations.

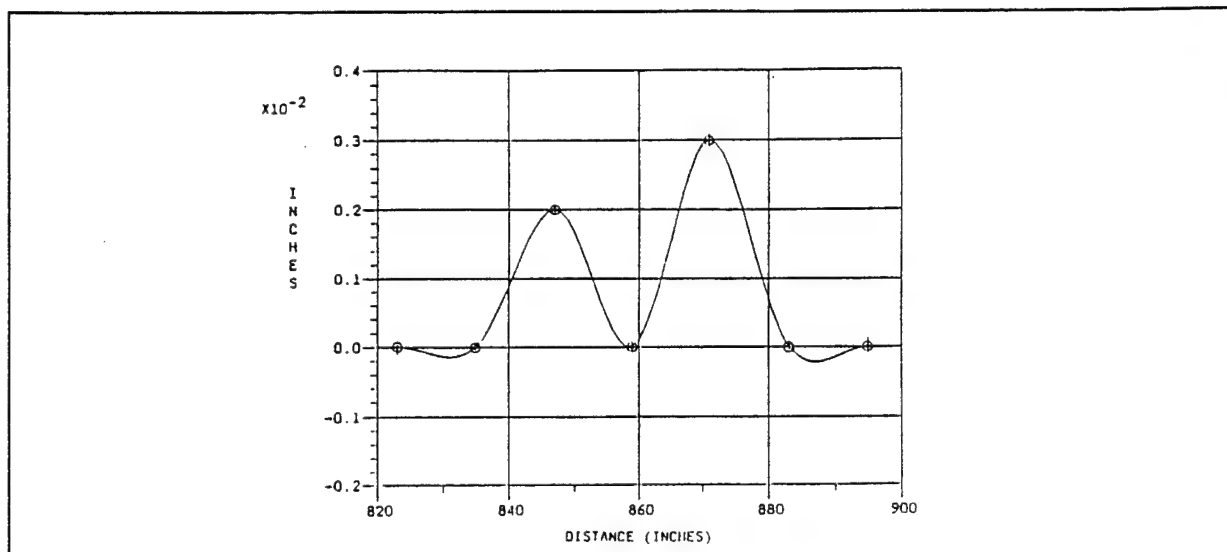


Figure 6: Curve Fit of Vertical Bore Profile

The actual bore compound curvature can be visualized in a view from the rear of the launcher looking forward. A Lissajous plot of a typical bore profile is shown in Figure 7.

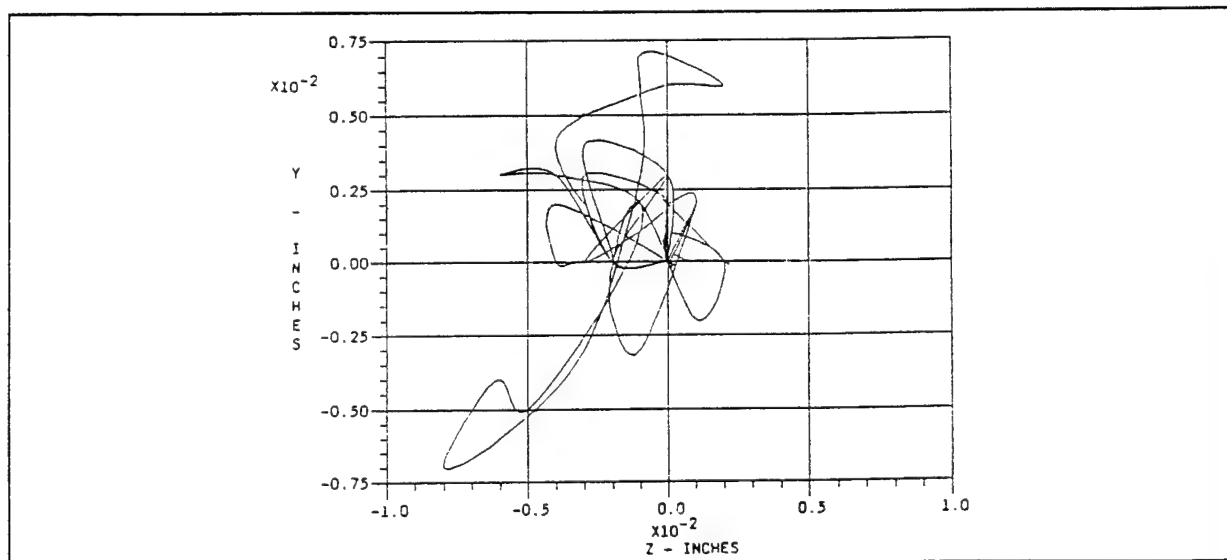


Figure 7: Bore Profile Lissajous Plot

The effects of straightening attempts in the forward section of the bore may be observed in Figure 8, where radial offset is seen to be greatly reduced. However, sharp local curvature may still exist.

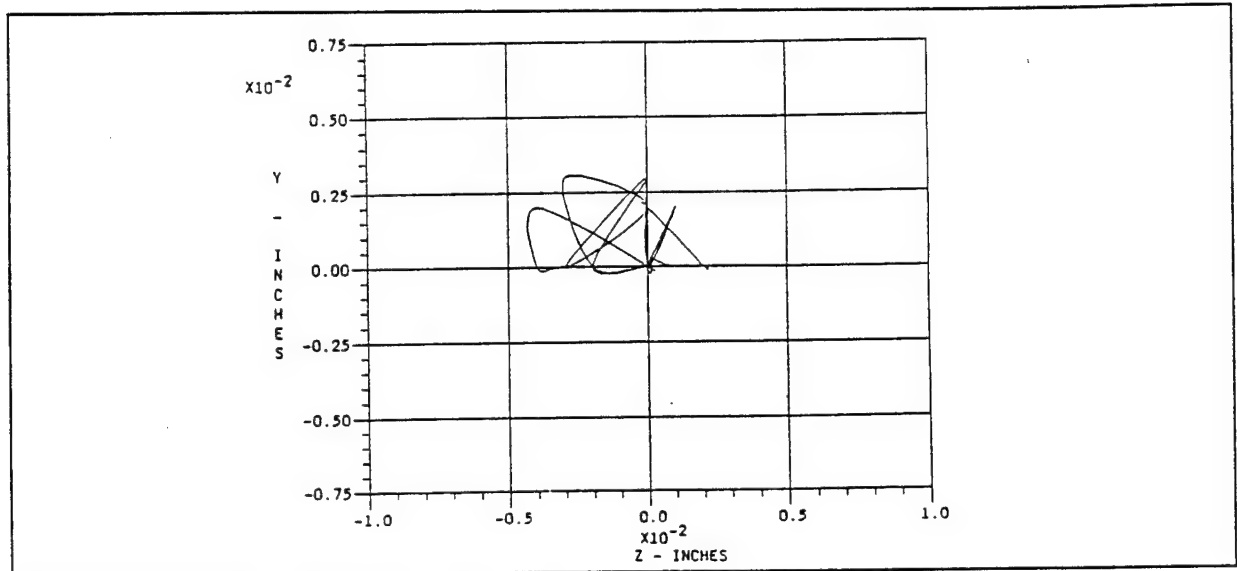


Figure 8: Bore Forward Section

### 3.4 Bore Diameter

Variation in diameter of the bore may also be obtained by measurement at a number of discrete locations along the launcher, and described continuously by curve fitting procedures. An accurate description of the diameter profile is especially significant if the bore is intentionally tapered to overcome the effects of progressive wear.

### 3.5 Stress Waves

The gas pressure behind the projectile expands the launcher tube to increase the bore diameter. The nominal static radial deflection under this loading may be obtained with the Lamé' equation for a cylinder of infinite length, and might be on the order of 2 or 3 thousandths of an inch (see Figure 9). However, this value can be amplified at the pressure front, in the vicinity of the projectile, at certain critical velocities.

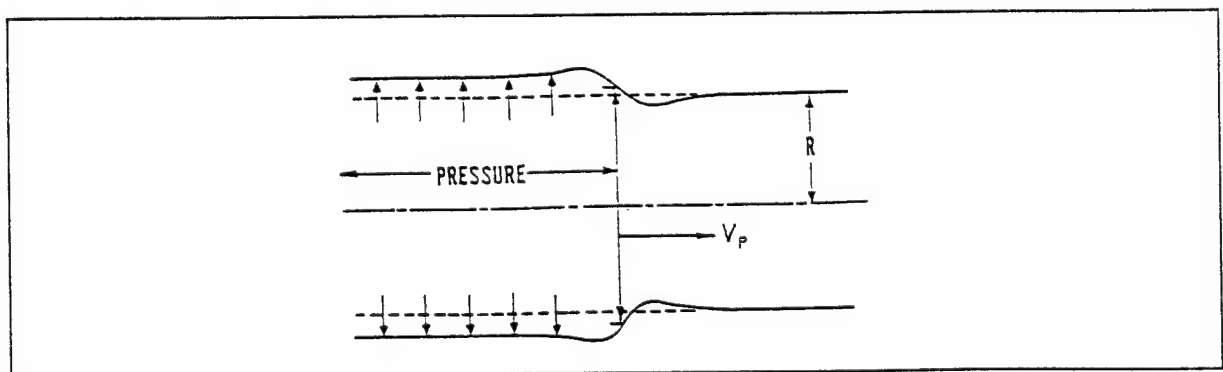


Figure 9: Infinite Cylinder with Moving Pressure

Although theoretically, the maximum dynamic amplification for a projectile traveling at the critical velocity of dilatation waves is unbounded (Figure 10), tests have shown a maximum of 4 times the steady state radial displacement [3]. The amplification which can occur when the projectile is traveling at the critical velocity of axial stress waves is unknown.

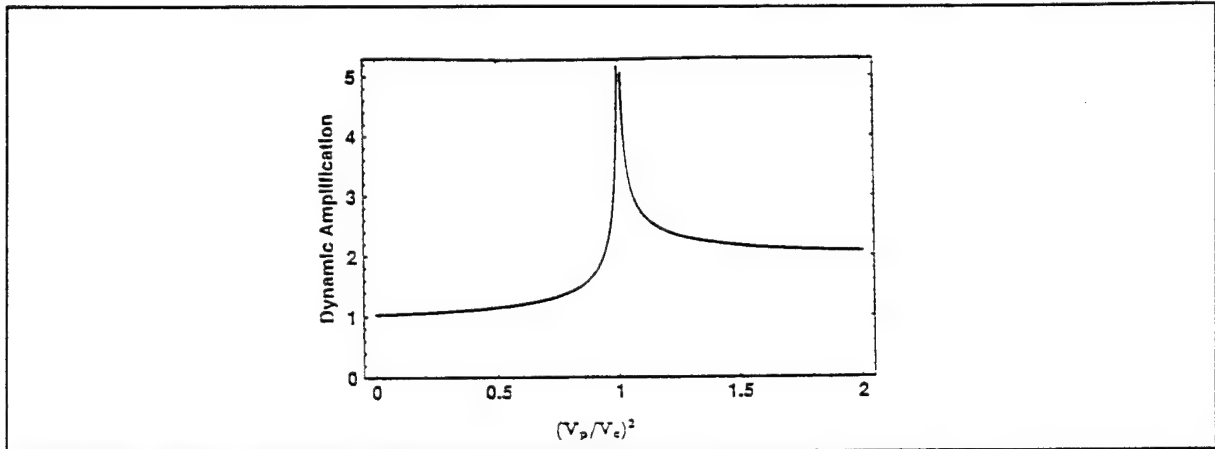


Figure 10: Effect of Pressure Velocity on Maximum Radial Displacement

### 3.6 Two-Stage Launcher

The pump tube and launch tube of a two-stage launcher are connected to form a very long structure. Movement of one affects the other. However, modeling this great length as a single entity requires considerable computational resources.

### 3.7 Practical Solution

A useful hypervelocity balloting simulation must provide the necessary information for projectile design with reasonable effort in a timely manner. The approach must be easily adaptable to include new developments.

#### 4. Approach

Arrow Tech Associates, Inc. has investigated modifications to its existing balloting simulation code, called BALANS, so that it is applicable for hypervelocity launches. Although many changes must be made to meet the aforementioned challenges, the same modeling and solution technique used in BALANS can be retained for the hypervelocity version, HYPERBAL. A block diagram of the basic modules of the proposed code is shown in Figure 11.

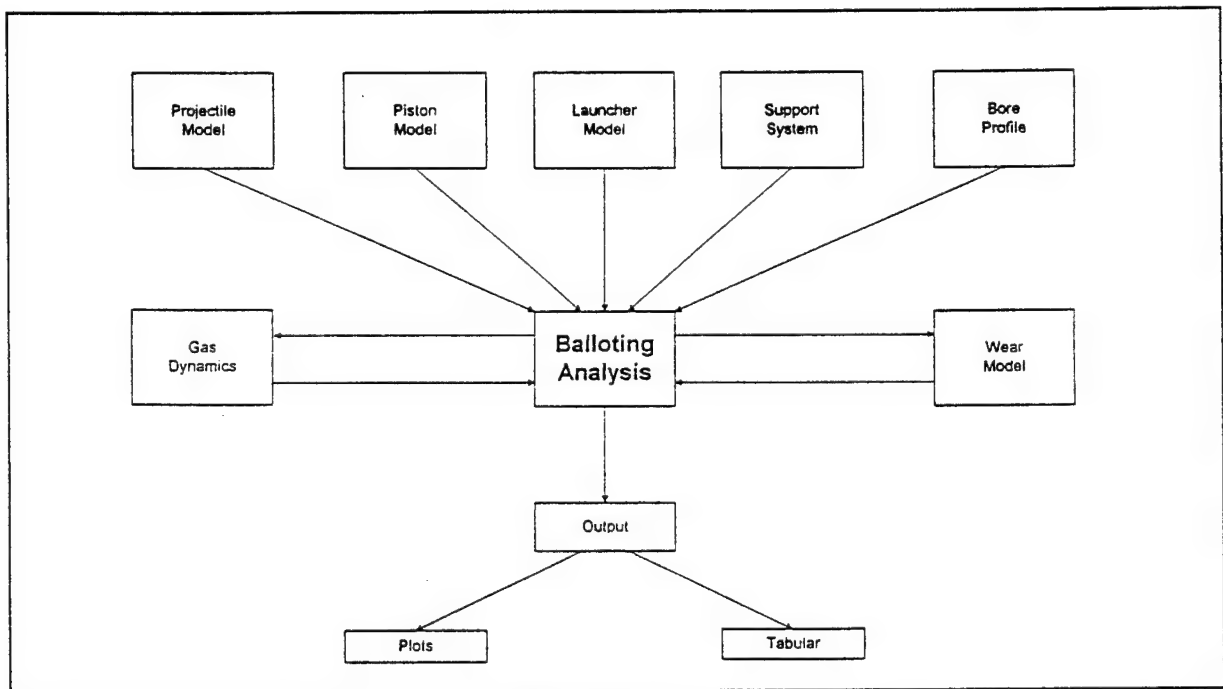


Figure 11: Hypervelocity Code Block Diagram

The current code is based on a timestep iteration of lumped mass, beam type finite element models of the projectile (Figure 12) and launcher. Non-linear spring (Figure 13) are used for support of the launcher and for projectile/launcher interaction [4]. Model masses are lumped at the beam end nodes and their motion is calculated at each time step. Three dimensional motion is considered, including the effects of spin, bore curvature, and bore diameter variation. Axial, bending and shear stresses are calculated for each projectile beam element at all designated output print steps.

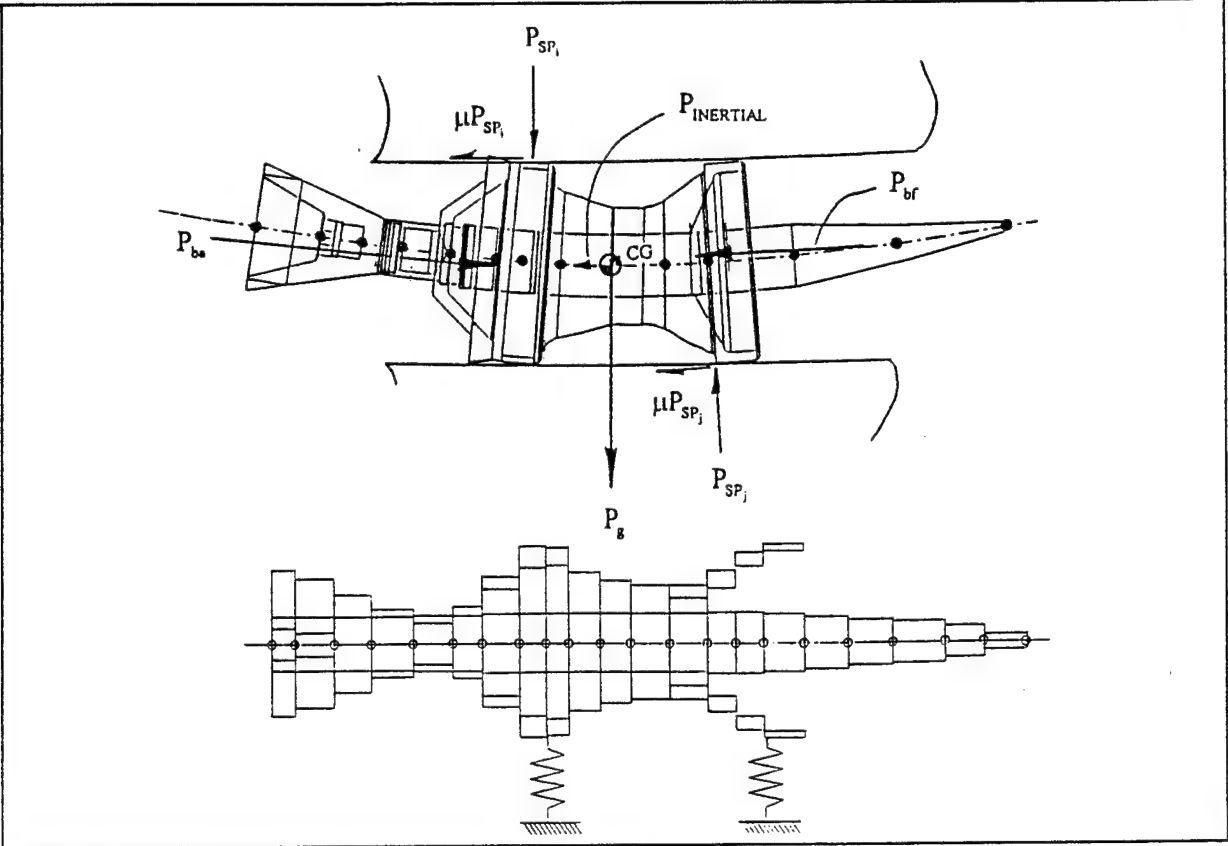


Figure 12: Projectile Loads and Balloting Model

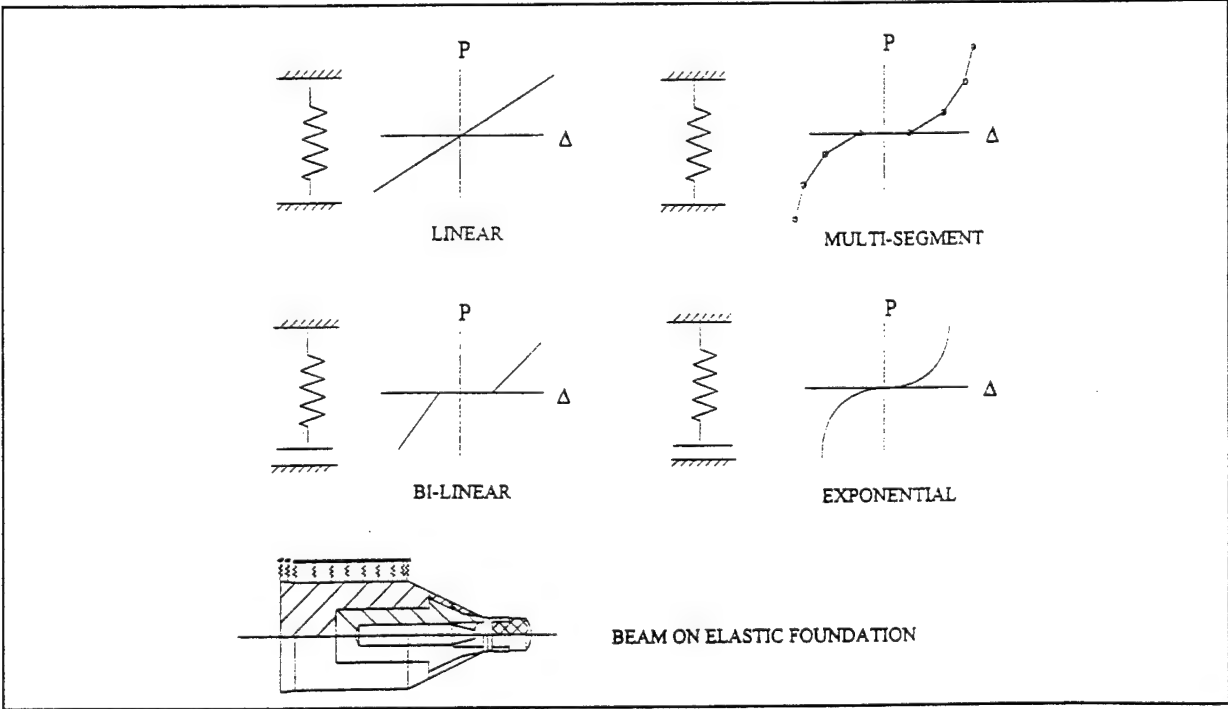


Figure 13: Spring Type Elements

The primary changes to be made to the existing code are summarized in the following paragraphs.

#### 4.1 Modeling and Solution

Since the most complex balloting analysis is believed to be required for two-stage launchers, the code is designed for this capability, with the option to analyze balloting in all other launcher types. This means that up to four (4) discrete models must be available, the piston, projectile, launcher tube (including pump tube), and launcher support structure. These will be interconnected, at contact surfaces, with spring elements.

The governing differential equations of motion for the assembled models are expressed in matrix form as:

Gun Tube

$$[M_1]\{\ddot{X}_1\} + [C_1]\{\dot{X}_1\} + [K_1]\{X_1\} = \{P_1\} + \{P_{cs1,2}\} + \{P_{cs1,3}\} + \{P_{cs1,4}\} \quad \text{Eq. 1}$$

Piston

$$[M_2]\{\ddot{X}_2\} + [C_2]\{\dot{X}_2\} + [K_2]\{X_2\} = \{P_2\} + \{P_{cs2,2}\} \quad \text{Eq. 2}$$

Projectile

$$[M_3]\{\ddot{X}_3\} + [C_3]\{\dot{X}_3\} + [K_3]\{X_3\} = \{P_3\} \quad \text{Eq. 3}$$

Tube Support Structure

$$[M_4]\{\ddot{X}_4\} + [C_4]\{\dot{X}_4\} + [K_4]\{X_4\} = \{P_4\} \quad \text{Eq. 4}$$

where

$X, \dot{X}, \ddot{X}$  = Displacement and Derivatives

$M$  = Diagonal Mass Matrix

$C$  = Damping Matrix

$K$  = Assembled Stiffness Matrix

$P$  = Pressure, Inertial, centrifugal, and other loads

$P_{cs}$  = Connecting Spring Forces

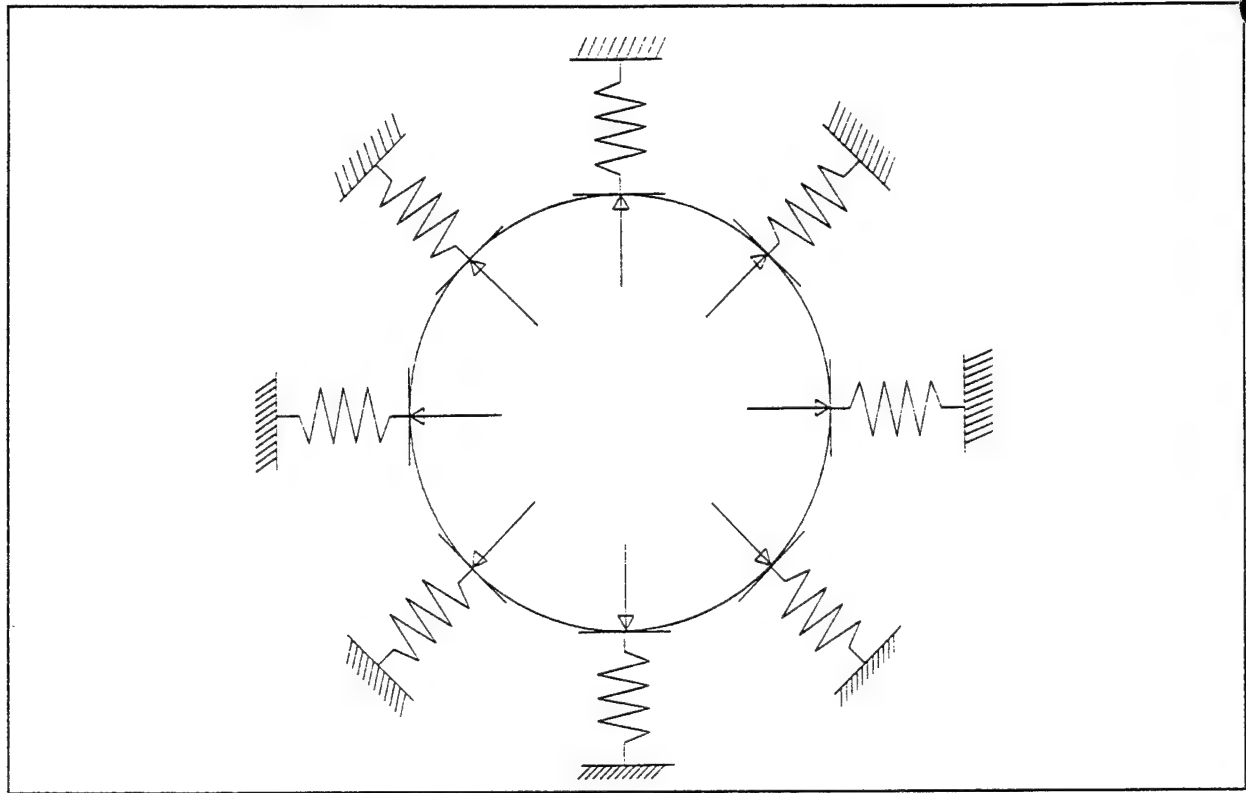


Figure 14: Bore/Projectile Contact Spring Model

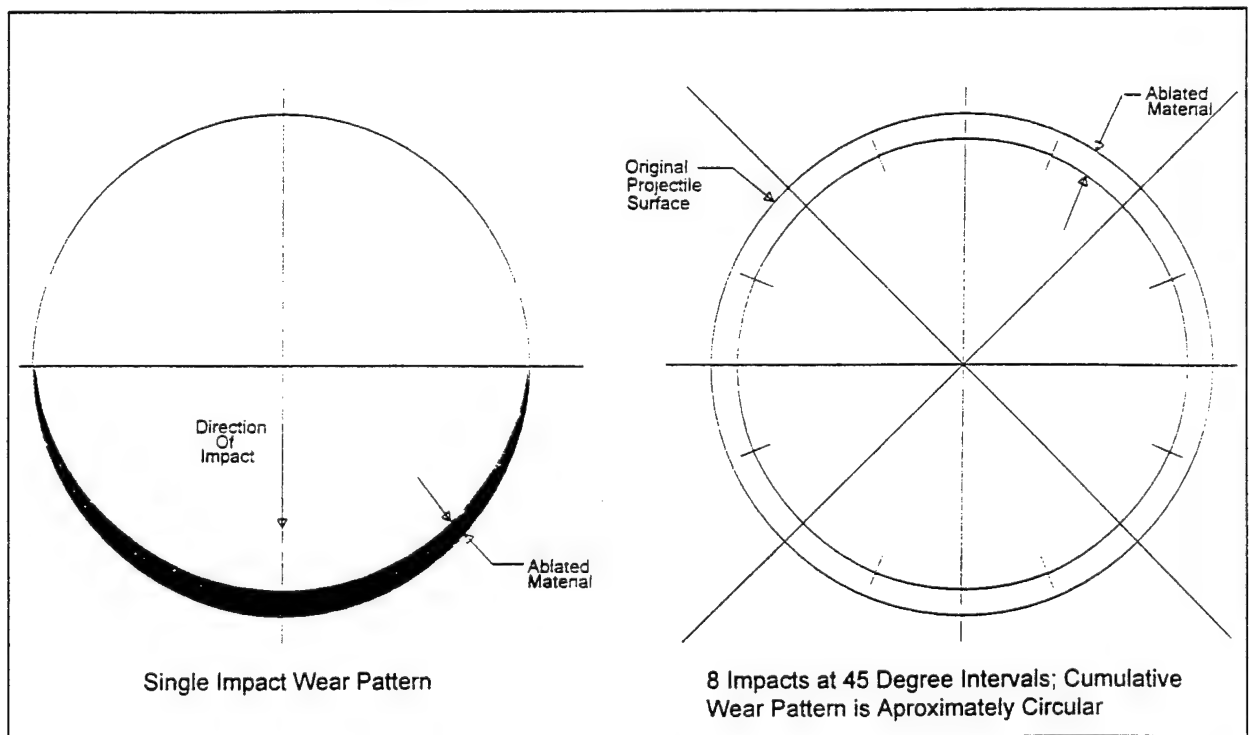


Figure 15: Cumulative Wear from Multiple Impacts

#### 4.5 Bore Expansion and Diameter Variation

Bore expansion, from internal pressurization and dynamic amplification near critical velocities, can be added to static bore diameter variation at any specified time and location along the launcher. These values can be updated at each time step, along with a redefinition of projectile support spring behavior. Changes in bore diameter alter radial preload and clearances. The dynamic amplification calculations will be carried out within the main balloting routine.

#### 4.6 Automation

The original BALANS code was a file driven batch style code with very little user interaction other than manual editing of data files in preparation for a balloting run. The emerging system contains mixed languages with a window based graphical user interface (GUI) and established data linkages between contributing modeling and analysis segments.

### **5. Summary**

Several phenomena, which occur during projectile in-bore travel, become more significant in producing balloting motion at hypervelocity than at lower velocities. The effects of these phenomena have been neglected in simulation codes developed to date. Thus, there currently is no means of predicting the resultant balloting forces for hypervelocity launches. It is critical to know the magnitude of these forces in order to ensure that a projectile is designed for successful launch.

The simulation of projectile balloting in hypervelocity launchers is very complex. The different phenomena involved require gas dynamics, structural dynamics, heat transfer and wear analyses to be performed simultaneously.

Arrow Tech Associates, Inc. has investigated the challenge of developing a simulation code specifically for the prediction of projectile balloting at hypervelocity. The use of this code could help design efficient, light weight, highly stressed projectiles which can be launched without failure.

## 6. References

- 1) R.W. Courter, "Light Gas Gun Performance Studies," Proceedings, 44th Meeting of the Aeroballistic Range Association, Munich, Germany, September 13-17, 1993.
- 2) R.G. Gast, "Experimental Investigation and Modeling of the Effect of Bore Curvature on Muzzle Motions of 60-MM Guns," *Proceedings of the Seventh U.S. Army Symposium on Gun Dynamics*, ARCCB-SP-93034, Benet Laboratories, Watervliet, NY, 11-13 May 1993, pp.251-271.
- 3) T.E. Simkins, "Dynamic Strains in a 60-MM Gun Tube - An Experimental Study," *Sixth U.S. Army Symposium on Gun Dynamics*, ARCCB-SP-90015, Benet Laboratories, Watervliet, NY, 15- 17 May 1990, pp. 253 -271.
- 4) D.H. Lyon, "Radial Stiffness Measurements of 120-mm Tank Projectiles," ARL-TR392, U. S. Army Ballistic Research Laboratory, Aberdeen Proving Grounds, MD, April, 1994.
- 5) E.S. Powell, "Range "G" Sabot Launch Wear Analysis Summary", Calspan Corporation/AEDC Division, Arnold Engineering Development Center, Arnold Air Force Station, Tennessee, Air Force Systems Command, United States Air force, September 1985.
- 6) E.S. Powell, J.R. Dewitt and A.J. Cable, "Further Study of Model Wear in a Two-Stage Light-Gas Launcher," Proceedings, 37th Meeting of the Aeroballistic Range Association, Courcellete, Canada, September 9-12, 1986.

## **Aircraft Trajectory Prediction Using a Radius of Curvature Model**

**Luis C. Cattani**  
University of Detroit Mercy  
Department of Mechanical Engineering  
Detroit, MI 48219-0900

**Paul J. Eagle**  
University of Detroit Mercy  
Department of Mechanical Engineering  
Detroit, MI 48219-0900

**Frank P. Kuhl**  
U.S. Army Armament Research, Development  
and Engineering Center  
Picatinny Arsenal, NJ 07806-5000

### **Abstract**

A new method for increasing the accuracy of remote predictions of aircraft trajectory has been developed based on a radius of curvature estimator (RC). This approach provides a means of increasing the accuracy for fire control systems based strictly on a new tracking algorithm.

This work represents a novel addition to the work done on attitude translation estimators (AT) at the U.S. Army Armament Research Development and Engineering Center (ARDEC) and the circular arc aimed munitions (CAAM) system developed at the U.S. Army Material Systems Analysis Activity.

The AT estimator used both translation and attitude data coupled with a target's specific dynamic characteristics to improve the accuracy of conventional trackers (1st and 2nd order fire control systems). The new method uses translation and attitude measurements as well. However, it represents the target aircraft dynamics without use of aircraft specific parameters and improves the target trajectory prediction by the application of regression based estimated measurements.

The radius of curvature (RC) method uses sequential estimates of the radius of curvature in the trajectory of an airborne target to provide a basis for lead angle prediction in a fire control system. This paper presents the implementation of the new tracking algorithm and comparisons to other tracking techniques using actual flight data for high performance aircraft recorded using an aircrew combat training system. Results are presented for maximum and average predictive errors derived from existing advanced tracking algorithms and the radius of curvature approach.

CATTANI, EAGLE, KUHL

## **Aircraft Trajectory Prediction Using a Radius of Curvature Model**

**Luis C. Cattani**

University of Detroit Mercy  
Department of Mechanical Engineering  
Detroit, MI 48219-0900

**Paul J. Eagle**

University of Detroit Mercy  
Department of Mechanical Engineering  
Detroit, MI 48219-0900

**Frank P. Kuhl**

U.S. Army Armament Research, Development  
and Engineering Center  
Picatinny Arsenal, NJ 07806-5000

### **1. Introduction**

The CAAM system was developed at the U.S. Army Material Systems Analysis Activity in the 1980s. The system relied upon the observation that currently used flight control systems cause the target at times to maneuver in 2D planes, fixed in 3D space, in circular arcs (a so-called coordinated turn). A pilot is compelled to maneuver in an uncoordinated turn to increase his survivability against such as a system. However, this type of maneuver is undesirable from a human factors point of view due to the fatiguing lateral force that will be generated. Determination of the target's 2D fixed planar orientation, the assumption that the target movement during a projectile time-of-flight is described by a circular arc, and the determination of the maneuvering acceleration (normal to the velocity and directed toward the center of the arc) are the key features of the CAAM concept.

The radius of curvature (RC) method follows the CAAM idea of modeling the target as a point moving in 3D space and estimates the instantaneous radius of curvature of the target as it moves on a curvilinear path. This radius of curvature coupled with the velocity and tangential acceleration of the target are used to estimate the target's total acceleration. The main differences between the CAAM and the RC systems are: the RC does not make any assumption about a circular path motion, the RC does not assume a load acceleration normal to the target's velocity and the RC needs attitude data for an accurate estimate.

### **2. Integrated Tracking and Prediction Technique**

The overall tracking and prediction approach for the RC method (schematized in Figure 1) is based on state measurements of the target at a specific instant by a vector consisting of orientation (roll, pitch and yaw), position (range, azimuth and elevation) and the corresponding

positional derivatives. The basic sequence of operations in the tracker begins with tracking the target for a period of time using inherently noisy measurement data. The trajectory measurement data are modeled using a piecewise regression technique. A linear Kalman filter is used to optimally estimate the trajectory measurements. The linear Kalman filters predict future target measurement data (for the projectile time-of-flight time), generating artificial measurement data for a non-linear Kalman Filter estimator which uses a radius of curvature model for target dynamics.

This method uses nine linear Kalman filters running in parallel to estimate the dynamics of the measurement data. These filtered estimates of the measurement data are presented to the extended Kalman filter, which then, estimates target dynamics. Ultimately, when measurement data are not available (during the lead prediction interval), the algorithm will use regression estimates of measurement data (artificial measurements) as input to the extended Kalman filter to predict the target's position.

### 3. Radius of Curvature State Model

The most innovative aspect of this approach is a tracking algorithm based on a radius of curvature estimator. This approach has a significant advantage over the existing attitude/translation based tracking algorithms. Both vehicle position and attitude are used to estimate vehicle dynamics without requiring vehicle-specific inertial data. This approach provides analytical coupling of target attitude and translation without relying on mass properties. A totally unknown target class can now be tracked with all the advantages of attitude-translational dynamic models.

The radius of curvature estimator is derived from the definition of the curvature of a particle trajectory in terms of its positional derivatives. The total acceleration of an airplane is defined as the load acceleration plus gravity:

$$a = a_L + g \quad 1$$

The load acceleration can be defined as the tangential acceleration plus the normal acceleration:

$$a_L = a_T + a_N \quad 2$$

For any particle moving along a smooth curve in three dimensional space, the velocity and load acceleration vectors can be written as:

$$v = \frac{ds}{dt} T \quad 3$$

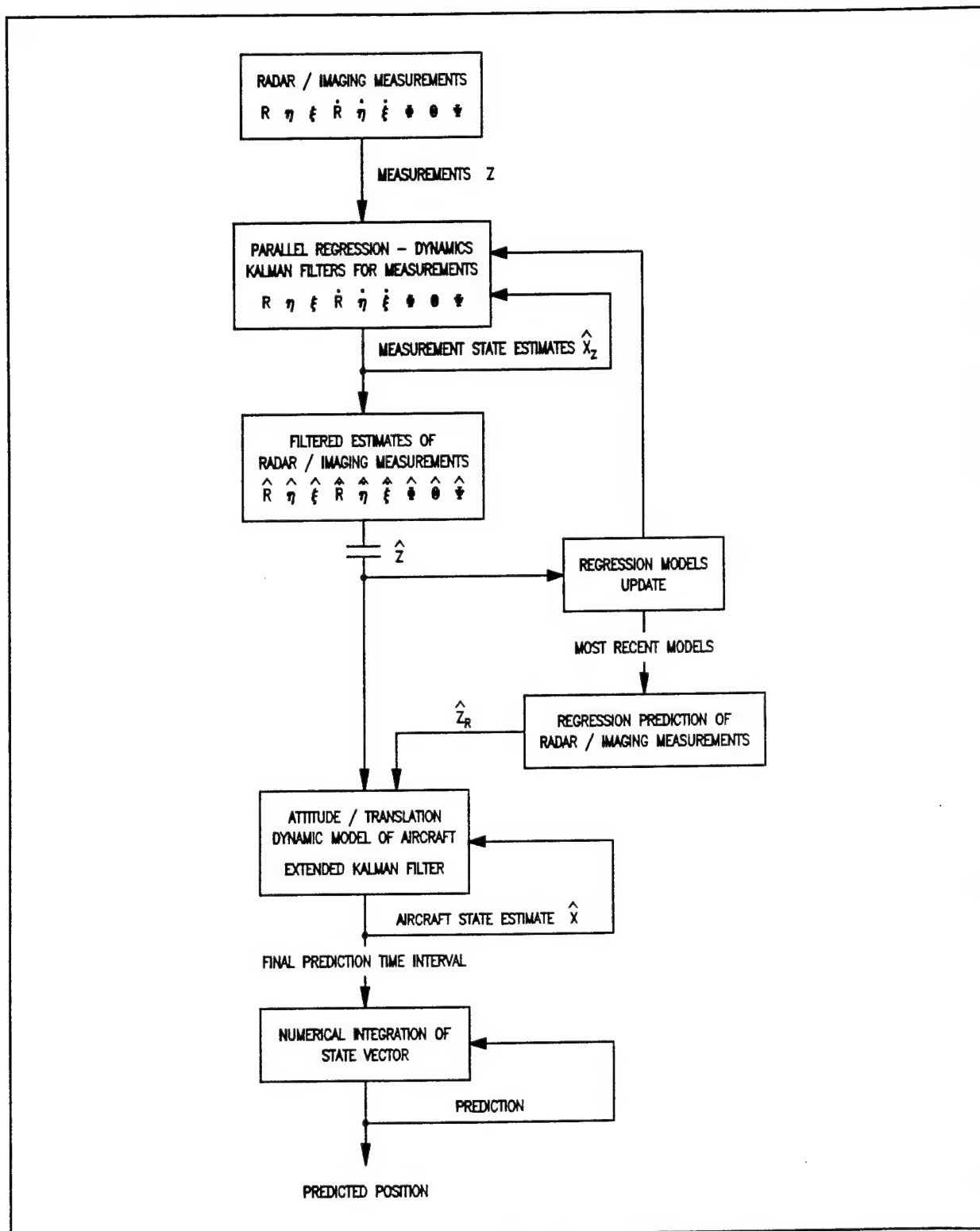


Figure 1 Schematic of Trajectory Tracking and Prediction Technique

$$a_L = \frac{d^2s}{dt^2} T + \kappa \left( \frac{ds}{dt} \right)^2 N \quad 4$$

where  $s$  is an arc-length parameter for the curve and  $T$ ,  $N$  and  $\kappa$  denote the unit tangent vector, unit normal vector and curvature, respectively.

If the position vector at time  $t$  in the inertial coordinate system is given by:

$$\mathbf{r} = x\hat{i} + y\hat{j} + z\hat{k} \quad 5$$

then

$$\frac{ds}{dt} = \left\| \frac{d\mathbf{r}}{dt} \right\| = \sqrt{\dot{x}^2 + \dot{y}^2 + \dot{z}^2} \quad 6$$

and

$$\frac{d^2s}{dt^2} = \frac{\ddot{x}\dot{x} + \ddot{y}\dot{y} + \ddot{z}\dot{z}}{\sqrt{\dot{x}^2 + \dot{y}^2 + \dot{z}^2}} \quad 7$$

Squaring both sides, the first time rate of change of  $s$  may be found as:

$$\left( \frac{ds}{dt} \right)^2 = \dot{x}^2 + \dot{y}^2 + \dot{z}^2 \quad 8$$

Given the standard definition of  $\kappa$  :

$$\kappa = \frac{\|\dot{\mathbf{r}} \times \ddot{\mathbf{r}}\|}{\|\dot{\mathbf{r}}\|^3} \quad 9$$

or

$$\kappa = \frac{\sqrt{(\dot{y}\ddot{z} - \dot{z}\ddot{y})^2 + (\dot{x}\ddot{z} - \dot{z}\ddot{x})^2 + (\dot{x}\ddot{y} - \dot{y}\ddot{x})^2}}{[\sqrt{\dot{x}^2 + \dot{y}^2 + \dot{z}^2}]^3} \quad 10$$

the magnitude of the tangential acceleration can be expressed as:

$$a_T = \frac{d^2s}{dt^2} = \frac{\ddot{x}\dot{x} + \ddot{y}\dot{y} + \ddot{z}\dot{z}}{\sqrt{\dot{x}^2 + \dot{y}^2 + \dot{z}^2}} \quad 11$$

and the magnitude of the normal acceleration can be expressed as:

$$a_N = \kappa \left( \frac{ds}{dt} \right)^2 = \frac{\sqrt{(\dot{y}\ddot{z} - \dot{y}\ddot{z})^2 + (\dot{x}\ddot{z} - \dot{x}\ddot{z})^2 + (\dot{x}\ddot{y} - \dot{x}\ddot{y})^2}}{\sqrt{\dot{x}^2 + \dot{y}^2 + \dot{z}^2}} \quad 12$$

The components of the tangential acceleration in the inertial coordinate system can be obtained with the definition of the unit tangent vector:

$$\mathbf{T} = \frac{\dot{\mathbf{r}}}{\|\dot{\mathbf{r}}\|} \quad 13$$

The components are given by:

$$a_{T_x} = \frac{\dot{x}(\ddot{x}\ddot{x} + \dot{y}\ddot{y} + \dot{z}\ddot{z})}{\dot{x}^2 + \dot{y}^2 + \dot{z}^2} \quad 14$$

$$a_{T_y} = \frac{\dot{y}(\ddot{x}\ddot{x} + \dot{y}\ddot{y} + \dot{z}\ddot{z})}{\dot{x}^2 + \dot{y}^2 + \dot{z}^2} \quad 15$$

$$a_{T_z} = \frac{\dot{z}(\ddot{x}\ddot{x} + \dot{y}\ddot{y} + \dot{z}\ddot{z})}{\dot{x}^2 + \dot{y}^2 + \dot{z}^2} \quad 16$$

The components of the normal acceleration in the inertial frame can be obtained by decomposing the normal vector into the body axis reference frame and rotating the resultant frame into the inertial frame by use of the Euler angles:

$$a_{N_x} = (\cos\psi \cos\theta \sin\alpha - \cos\psi \sin\theta \cos\phi \cos\alpha - \sin\psi \sin\phi \cos\alpha) a_N \quad 17$$

$$a_{N_y} = (\sin\psi \cos\theta \sin\alpha - \sin\psi \sin\theta \cos\phi \cos\alpha + \cos\psi \sin\phi \cos\alpha) a_N \quad 18$$

$$a_{N_z} = (-\sin\theta \sin\alpha - \cos\theta \cos\phi \cos\alpha) a_N \quad 19$$

Given these components, the definitions of the cartesian accelerations can be expressed as:

$$\begin{aligned} \ddot{x} = & [c_1 \sin\alpha + (c_2 + c_3) \cos\alpha][(\dot{y}\ddot{z} - \dot{y}\ddot{z})^2 + (\dot{x}\ddot{z} - \dot{x}\ddot{z})^2 \\ & + (\dot{x}\ddot{y} - \dot{x}\ddot{y})^2]^{1/2} [\dot{x}^2 + \dot{y}^2 + \dot{z}^2]^{-1/2} \\ & + \dot{x}(\ddot{x}\ddot{x} + \dot{y}\ddot{y} + \dot{z}\ddot{z})[\dot{x}^2 + \dot{y}^2 + \dot{z}^2]^{-1} \end{aligned} \quad 20$$

$$\begin{aligned}
\ddot{y} = & [c_4 \sin \alpha + (c_5 + c_6) \cos \alpha][(\dot{y}\ddot{z} - \ddot{y}\dot{z})^2 + (\dot{x}\ddot{z} - \ddot{x}\dot{z})^2 \\
& + (\dot{x}\ddot{y} - \ddot{x}\dot{y})^2]^{1/2} [\dot{x}^2 + \dot{y}^2 + \dot{z}^2]^{-1/2} \\
& + \dot{y}(\dot{x}\ddot{x} + \ddot{y}\dot{y} + \dot{z}\ddot{z})[\dot{x}^2 + \dot{y}^2 + \dot{z}^2]^{-1}
\end{aligned} \tag{21}$$

$$\begin{aligned}
\ddot{z} = & [c_7 \sin \alpha + c_8 \cos \alpha][(\dot{y}\ddot{z} - \ddot{y}\dot{z})^2 + (\dot{x}\ddot{z} - \ddot{x}\dot{z})^2 \\
& + (\dot{x}\ddot{y} - \ddot{x}\dot{y})^2]^{1/2} [\dot{x}^2 + \dot{y}^2 + \dot{z}^2]^{-1/2} \\
& + \dot{z}(\dot{x}\ddot{x} + \ddot{y}\dot{y} + \dot{z}\ddot{z})[\dot{x}^2 + \dot{y}^2 + \dot{z}^2]^{-1} + g
\end{aligned} \tag{22}$$

where:

$$\begin{aligned}
c_1 &= \cos \psi \cos \theta \\
c_2 &= -\cos \psi \sin \theta \cos \phi \\
c_3 &= -\sin \psi \sin \phi \\
c_4 &= \sin \psi \cos \theta \\
c_5 &= -\sin \psi \sin \theta \cos \phi \\
c_6 &= \cos \psi \sin \phi \\
c_7 &= -\sin \theta \\
c_8 &= -\cos \theta \cos \phi
\end{aligned}$$

The observed Euler angles can be preconditioned with linear Kalman filters making the terms  $c_1, c_2 \dots c_8$  constant between discrete time steps. Alternatively, the terms can be treated as states. The latter option greatly increases the complexity of the state transition Jacobian.

Using the first option, the following state transition variables can be defined as:

$$d_1 = c_4(c_2 + c_3) - c_1(c_5 + c_6) \tag{23}$$

$$d_2 = c_7(c_2 + c_3) - c_1 c_8 \tag{24}$$

$$d_3 = c_7(c_5 + c_6) - c_4 c_8 \tag{25}$$

The system dynamics can be described as:

$$\dot{x}_1 = \frac{x_1}{\tau_1} + w_1 \tag{26}$$

$$\dot{x}_2 = \frac{x_2}{\tau_1} + w_2 \quad 27$$

$$\dot{x}_3 = \frac{x_3}{\tau_1} + w_3 \quad 28$$

$$\dot{x}_4 = [(d_1 x_5 + d_2 x_6) f_1 + x_4 f_2] f_3 + x_{10} + w_4 \quad 29$$

$$\dot{x}_5 = [(-d_1 x_4 + d_3 x_6) f_1 + x_5 f_2] f_3 + x_{11} + w_5 \quad 30$$

$$\dot{x}_6 = [(-d_2 x_4 + d_3 x_5) f_1 + x_6 f_2] f_3 + g + x_{12} + w_6 \quad 31$$

$$\dot{x}_7 = x_4 \quad 32$$

$$\dot{x}_8 = x_5 \quad 33$$

$$\dot{x}_9 = x_6 \quad 34$$

$$\dot{x}_{10} = x_{10}/\tau_2 + w_7 \quad 35$$

$$\dot{x}_{11} = x_{11}/\tau_2 + w_8 \quad 36$$

$$\dot{x}_{12} = x_{12}/\tau_2 + w_9 \quad 37$$

where the functions  $f_1$ ,  $f_2$  and  $f_3$  are defined as:

$$f_1 = \sqrt{(x_5 x_3 - x_2 x_6)^2 + (x_4 x_3 - x_1 x_6)^2 + (x_4 x_2 - x_1 x_5)^2} \quad 38$$

$$f_2 = x_4 x_1 + x_5 x_2 + x_6 x_3 \quad 39$$

$$f_3 = \frac{1}{x_4^2 + x_5^2 + x_6^2} \quad 40$$

The jerk is modeled as a Markov process. The terms  $w_1, w_2 \dots w_9$  represent additive Gaussian noise. The state variables  $x_{10}$ ,  $x_{11}$  and  $x_{12}$  are process noise added to compensate for unmodeled lateral accelerations and gusts.

The positional derivative data, used in conjunction with necessary attitude estimates (to perform transformations between the aircraft body axis and the inertial axis), provide the basis for a set of state equations (Equations 26-37). This state model is used to construct a robust-continuous-discrete extended Kalman filter estimator.

## 4. Prediction Performance

A high g turn was used to perform a comparative study between the performance of the Attitude/Translation (AT) Predictor and the Radius of Curvature (RC) Predictor with artificial measurements. The variance of the measurement noises are given in Table 1.

MEASUREMENT	VARIANCE
$\phi$	0.00076 rad
$\theta$	0.00076 rad
$\psi$	0.00076 rad
$R$	2500 ft
$\eta$	0.000004 rad
$\xi$	0.000004 rad
$\dot{R}$	2500 ft/s
$\dot{\eta}$	0.000016 rad/s
$\dot{\xi}$	0.000016 rad/s

Table 1 Measurement Noise

A long duration trajectory for a high performance aircraft was used to compare the performance in a high dynamic maneuver as illustrated in Figure 3.

A 4.5 g turn to the left while diving was the selected maneuver to test the comparative performance of the predictors. This maneuver is seen in the upper right hand corner of Figure 3. The turn had accelerations ranging from 0.5 to 4.5 g and velocities close to Mach 0.7. The maximum bank angle was close to 90 degrees. The total duration of the selected trajectory was 45 seconds. Clearly, this is a demanding test for a prediction algorithm due to the high accelerations witnessed by the aircraft.

All comparisons were based on a continuous one second forward prediction of aircraft trajectory. It should be noted that the error measurements are not necessarily an absolute indication of the tracking or prediction accuracy, since the measurements were made at a distance of 6-7 miles away. Furthermore, the measurements were made on a real aircraft with a radar cross section that varies with attitude.

The results of the prediction performance are summarized in Table 2 in terms of Euclidean errors (square root of the sum of squares). A maximum Euclidean distance and the Euclidean arithmetic average of the errors are given.

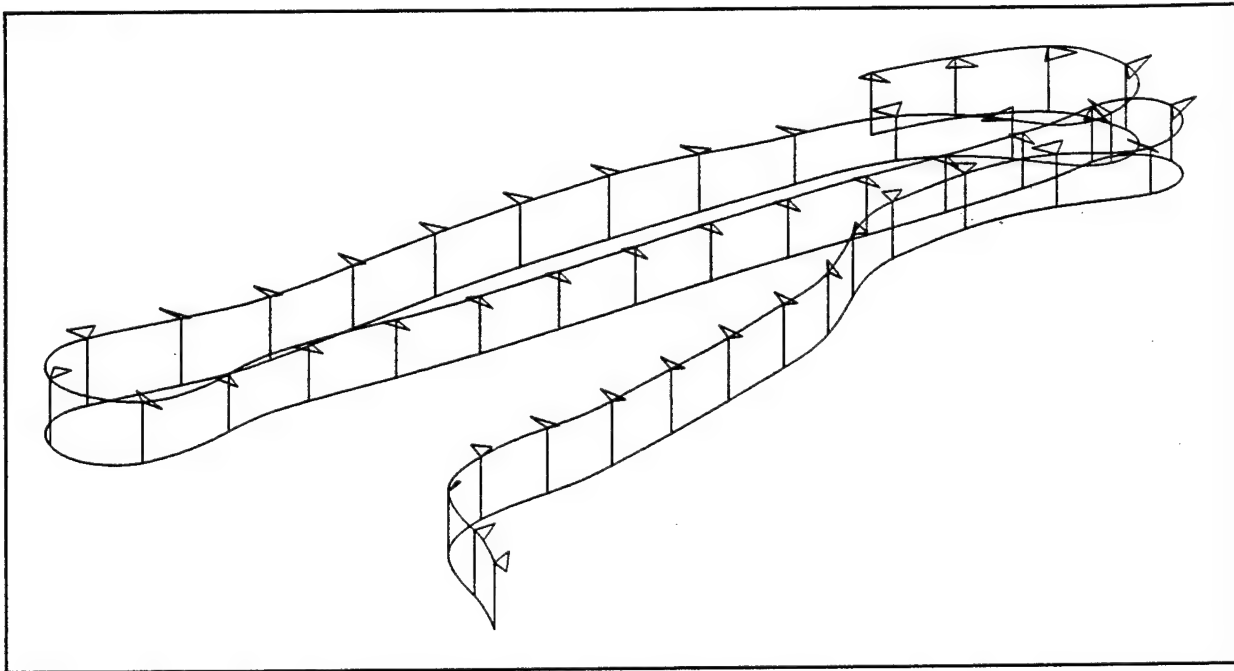


Figure 3 High Performance Aircraft Trajectory

EUCLIDEAN ERRORS		
	MAXIMUM (Feet)	AVERAGE (Feet)
Existing Attitude/Translation Estimator with Runge Kutta Prediction	226	127
Radius of Curvature Estimator with Artificial Measurements	216	110

Table 2 Error Statistics

The comparisons show an improvement in average and maximum prediction errors when the RC estimator with artificial measurements is used instead of the AT estimator with Runge-Kutta prediction. The results shown by the RC estimator compare favorably with the AT approach, especially when considering the fact that no vehicle specific information is needed. It should be noted that the ultimate performance of each approach cannot really be defined since the comparisons are being made with real radar data rather than theoretically exact simulation data. Therefore, there is no ground truth for comparison to the actual position of the aircraft.

## 5. Conclusions

The radius of curvature (RC) method represents a flexible and productive means of increasing the accuracy of lead angle prediction in a fire control system. This technique is able to achieve results comparable to or better than techniques that require substantial vehicle specific information about the target. The RC approach may be able to offer more accurate lead angle prediction than other circular arc estimators due to its more complete modeling of the 3D kinematics of the target.

## BIBLIOGRAPHY

- [1] Andrisani, D., and Kuhl, F.P., "Attitude Based Trackers for Airplane, Helicopter and Ground Targets," Remote Sensing Reviews, Vol. 6, No. 1, 1992.
- [2] Andrisani, D., Kim, E.T., and Kuhl, F.P., "Tracking Accuracy Improvement Using Noisy Target Orientation Measurements," Remote Sensing Reviews, Vol. 6, No. 1, 1992.
- [3] Andrisani, D., Tao, X., and Kuhl, F.P., "A Comparison of Aircraft Trajectory Predictors for Target Tracking Using Simulated Data," Remote Sensing Reviews, Vol. 6, No. 1, 1992.
- [4] Andrisani, D., and Kuhl, F.P., "Target Tracking Using Image Data," Remote Sensing Reviews, Vol. 6, No. 1, 1992.
- [5] Andrisani, D., F.P. Kuhl and D. Gleason, "A Nonlinear Tracker Using Attitude Measurements," IEEE Transactions on Aerospace and Electronic Systems, Vol. AES-22, No. 5, September 1986.
- [6] Andrisani, D., Gleason, D., and Kuhl, F.P., "A Tracker for Maneuvering Vehicles," Wescon/85, November 19-21, 1985, San Francisco, CA.
- [7] Andrisani, D., "Aircraft Trackers Using Attitude Measurements, Interim Report for the Period August 1985 - April 1986," School of Aeronautics and Astronautics, Purdue University, West Lafayette, IN, 1986.
- [8] Andrisani, D., "New Linear Tracking Filters," Proceedings of the 1985 American Control Conference, June 19-21 1985.
- [9] Andrisani, D., Kim, E.T., Schierman, J., and F.P. Kuhl, "A Nonlinear

- Helicopter Tracker Using Attitude Measurements," IEEE Transactions on Aerospace and Electronic Systems, Vol. AES-27, No. 1, January 1991.
- [10] Burke, H. H., "A Gun Fire Control System Predictor Concept for Improving Performance Against Maneuvering Targets (U), U.S. Army Materiel Systems Analysis Activity Technical Report TR-342, November, 1981, Unclassified.
- [11] Burke, H., "Circular Arc Aimed Munition (CAAM): A Concept for Improving Gun Fire Predictor Systems," 21st Asilomar Conference on Signals and Computers, November 2-4, 1987.
- [12] Burke, H.H., "White Paper: Circular Arc Aimed Munitions (CAAM) and the CAS/BAI Mission (U)," JTCG/AS Methodology Subgroup Meeting, NPGS, 16 August 1989, Unclassified.
- [13] Wald, J.K. and Burke, H.H., "A Comparison of Parabolic and Circular Arc Prediction (U)," U.S. Army Ballistic Research Laboratory, Technical Report BRL-TR-3091, March 1990, Unclassified.
- [14] Cattani, Luis C., "Target Aircraft Identification, Trajectory Tracking and Prediction Using Regression-Based Kalman Filter Techniques," Doctoral Dissertation, Department of Mechanical Engineering, University of Detroit, December 1993.
- [15] Eagle, Paul and Tabrizi L.H., "State Model Estimation for Kalman Filter Application," Journal of Industrial Mathematics, (Accepted for Publication).
- [16] Eagle, Paul and Tabrizi L.H., "Regression Modelling Technique for State Model Estimation and Kalman Filter Application", Proceedings of the 1990 IEEE Conference on Systems, Man and Cybernetics, 1990.
- [17] Eagle, Paul and Tabrizi L.H., "State Model Estimation for Kalman Filter Applications Using Regression Techniques", Proceedings of the 29th IEEE Conference on Decision and Control, 1990.

**TITLE:** Neural Network Based Smart Structural Control Systems  
Rajendra Damle and Vittal Rao  
Department of Electrical Engineering and  
Intelligent Systems Center  
University of Missouri-Rolla, Rolla, MO 65401

**Abstract:**

In recent studies, many neural network controller configurations for structural control have been suggested. Many of these controllers have been successfully implemented in simulation as well as using PC based data acquisition hardware. These studies have shown that in addition to conventional controller design methodologies, neural networks offer an effective basis for design and implementation of controllers. With the introduction of the Electronically Trainable Analog Neural Network (ETANN) chip i80170NX by Intel and a digital neural network chip Ni1000 by Nestor Corp., hardware implementation of neural network based controllers has been made possible. These neural network chips have also found applications in other areas such as signal processing and character recognition.

In this paper, capabilities of the ETANN based robust controllers for smart structures have been investigated. Robust controllers like LQR, modified LQG/LTR and  $H_2/H_\infty$  were implemented on a cantilever plate system which used shaped PVDF film sensors and PZT actuators. The controller design methods using Linear Matrix Inequalities (LMI) theory are investigated for the accommodation of limited actuator forces in smart structural systems. The robust controllers were implemented using two different neural network architectures suggested by Narendra and Parathasarathy. For structural systems, these neural network architectures use past values of the systems and multi-input multi-output systems. Modified back propagation algorithms like the adaptive learning rate algorithm and selective training algorithm were developed to enhance the learning and significantly reduce the training time.

Analog hardware components used in the interface between the ETANN chip, the actuators and the sensors on the smart structure test article have been described in detail. Special considerations about the fully analog implementation of the controllers which can be ignored in simulation have been pointed out. Practical consideration in training the analog neural network chip for optimal performance has also been described. Experimental results of the closed loop performance and robustness properties of the smart structural system are presented.

**SESSION V**

**KINETICS, VIBRATIONS, AND WAVE MOTION**

**TITLE: GAS DYNAMICS OF BORE EVACUATOR EJECTORS†**

**CHARLES A. ANDRADE**  
U.S. ARMY ARMAMENT RESEARCH, DEVELOPMENT, AND ENGINEERING CENTER  
CLOSE COMBAT ARMAMENTS CENTER  
BENÉT LABORATORIES  
WATERVLIET, NY 12189-4050

**DONALD G. MESSITT**  
MECHANICAL ENGINEERING, AERONAUTICAL ENGINEERING, AND MECHANICS  
RENSSELAER POLYTECHNIC INSTITUTE  
TROY, NY 12180-3590

**ABSTRACT:**

Three-dimensional flow simulations are presented for constant diameter ejectors inclined at 30° with respect to a flat plate. A flat plate is used to approximate the small bore surface curvature, relative to that of the ejector, present in gun bore evacuators. The effectiveness of the bore evacuator depends upon several factors, including the details of mixing processes between the supersonic jets and the augmented flow. The NPARC code was employed to calculate the Euler solution for a pressure ratio 6.5 supersonic jet. Experimental observations confirmed that with a small flow exit divergence, a significantly different jet structure was obtained which resulted in more efficient mixing. The CFD solution demonstrated qualitative and quantitative agreement with experimental data, and demonstrated the need for a fine mesh to resolve the structure of the supersonic jet. Comparison with experimental jet Mach number profiles illustrated that although the Euler solution captured some important features of the ejector flow field, a fully viscous solution is needed.

**BIOGRAPHY:**

**PRESENT ASSIGNMENT:** Charles A. Andrade is a Mechanical Engineer in the Infantry and Special Projects Branch at Benét Laboratories, assigned as Principal Investigator, "Bore Evacuator Computational Fluid Dynamics."

**PAST EXPERIENCE:** gas dynamics and thermochemistry of bore evacuator flows; emission spectroscopy of flames in a shock tube.

**DEGREES HELD:** Ph.D. Mechanical Engineering, Rensselaer Polytechnic Institute; M.S. Physics, Rollins College; B.S. Engineering Physics, University of California

---

†Sponsored in part by the Program Manager's Offices: Tank Main Armament Systems, PALADIN (DAAA22-91-C-1149), and AFAS (DAAA22-95-M-1108).

## GAS DYNAMICS OF BORE EVACUATOR EJECTORS

C. A. Andrade\*  
Benét Laboratories  
Watervliet, NY 12189-4050

D. G. Messitt  
Rensselaer Polytechnic Institute  
Troy, NY 12180-3590

### ABSTRACT

Three-dimensional flow simulations are presented for constant diameter ejectors inclined at 30° with respect to a flat plate. A flat plate is used to approximate the small bore surface curvature, relative to that of the ejector, present in gun bore evacuators. The effectiveness of the bore evacuator depends upon several factors, including the details of mixing processes between the supersonic jets and the augmented flow. The NPARC code was employed to calculate the Euler solution for a pressure ratio 6.5 supersonic jet. Experimental observations confirmed that with a small flow exit divergence, a significantly different jet structure was obtained which resulted in more efficient mixing. The CFD solution demonstrated qualitative and quantitative agreement with experimental data, and demonstrated the need for a fine mesh to resolve the structure of the supersonic jet. Comparison with experimental jet Mach number profiles illustrated that although the Euler solution captured some important features of the ejector flow field, a fully viscous solution is needed.

### INTRODUCTION

Gun bore evacuators are ejector pumps which remove residual propellant gases from the barrel after firing. The effectiveness of the bore evacuator depends upon several factors, including the details of mixing processes between the supersonic jets and the augmented flow. It is desirable to improve the ejector pump efficiency to ensure that these toxic gases do not flow back into the crew cabin when the breech is opened.

#### Bore Evacuator Development at The Benét Laboratories

Thirty years after the initial work on cannon bore evacuators [1], emerging high energy propellant and rapid fire development with the 120 mm M256 tank gun necessitated modern bore evacuator design flow code modeling. Present work grew from initiatives at Benét in 1984 to attempt predictions of field test measurements. The field test prediction method linked interior ballistics codes to one-dimensional (1D) models for the evacuator charge/discharge cycle. Resulting quasi-1D codes have been developed, beginning with one called BLISCHARGE used to predict the time and amount of total flow throughput due to air induced by the evacuator after the breech is opened. This code inputs canister and ejector geometry, breech opening time and the ballistic data. To validate the discharge model, bench-top tests using steady room temperature air were conducted at Rensselaer Polytechnic Institute (RPI) on a 42 % scale evacuator beginning in 1986. These tests verified the steady 1D flow results for the existing M256 design; but only for the case where the canister pressure is held at a steady constant value. Steady-state laboratory measurements also verified performance predictions obtained with BLISCHARGE, but field test measurements were found to be inconclusive. These early calculated results, given in an internal document, were thus used as a guide for the relative scale of flow throughput in the cannon, given a range of breech opening times. Theoretical and experimental aspects of this work were presented in January, 1989 [2] and on March 16-17 of the same year at the 1st Benét Bore Evacuator Seminar.

Improvements in laboratory test procedures and modeling began with FY90 initiatives: (a) use of the RPI shock tube to test the 65% scale canister charge gas dynamics; (b) test a full scale bore evacuator on the M256 tube, using steady room temperature air flow; (c) apply thermochemical methods to determine propellant toxic gas compositions and effect on the flow model due to real gas effects. These efforts reported supersonic jet effects due to the discharge ejectors [3], postulated and analyzed the shock ignition mechanism, due to sudden opening of the evacuator charge inlets, to explain the anomalous two-fold pressure rise at first fire as a manifestation of secondary combustion following shock ignition of fuel rich propellant gases [4,5], and produced improved 1D perfect gas models, now validated by the RPI measurement program [6].

Experimental Determination of Bore Evacuator Performance

Experimental studies have been undertaken to determine the baseline performance of a generic bore evacuator modeled on a currently fielded design [7]. The ejector nozzle geometry for currently fielded weapons consists of constant diameter cylinders angled at  $30^\circ$  through the barrel wall. Additional experiments investigated several ejector modifications intended to improve bore evacuator pump efficiency [7-9]. In particular, experiments in Ref. 8 illustrated the importance of ejector geometry and jet structure in determining the ability of the evacuator to induce air through the breech. In these experiments, the initially constant diameter nozzle was given a shallow exit divergence of  $14^\circ$ , resulting in an increased mass flow augmentation ratio up to 35% above the baseline bore evacuator's performance for constant diameter ejectors inclined  $30^\circ$  to the weapon axis.

Experimental observations confirmed that with this small flow exit divergence, a significantly different jet structure was obtained which resulted in more efficient mixing. Because of the importance of the ejector flow in determining the velocity of air induced through the breech, tests were conducted to investigate the behavior of the divergent supersonic jet expansions [8]. Pressure distributions and schlieren photographs were obtained for constant diameter and diverging nozzle ejectors inclined at  $20^\circ$ ,  $30^\circ$ , and  $90^\circ$  to a flat plate. These experiments verified that the supersonic jet was deflected upstream after exiting the constant diameter ejectors. The jet angle for the diverging nozzles remained nearly the same as the geometric ejector angle.

Figure 1 presents schlieren photographs taken from Ref. 8, for both constant diameter and diverging nozzle ejectors. Diverging nozzle ejectors had a nozzle half-angle of  $7^\circ$  and an expansion ratio of 1.48. The small expansion for the diverging nozzle had a large effect on the flow, resulting in less spreading of the jet and no upstream deflection, as compared with the constant diameter case. These results agree qualitatively with an experimental study, by Wlezien and Kibens [10], of supersonic jets issuing from asymmetric nozzles. Figure 2 [8] presents a comparison of mass flow augmentation ratio for constant diameter and diverging nozzle ejectors installed at  $20^\circ$  and  $30^\circ$  in model gun bore evacuators. The diverging nozzle ejectors increased the mass flow augmentation ratio by 35% at high reservoir pressures, for ejectors inclined  $30^\circ$  to the weapon axis, and up to 45% for ejectors inclined at  $20^\circ$ .

Benét and RPI team members have advanced ideas to improve the evacuator performance: including substitution of a shallow  $14^\circ$  flared nozzle flow exit at the bore wall, instead of the constant diameter exit; staggered and/or swirl nozzles; also the possible combinations of these innovative nozzle ideas. The idea of a pre-reservoir was suggested for the tank cannon. The pre-reservoir would result in longer effective operation of the evacuator by increasing the charge-up pressure of the main reservoir. Because conventional cannon bore evacuator design is generic, the Tank Main Armament and Advanced Field Artillery Systems Offices have sponsored these initiatives.

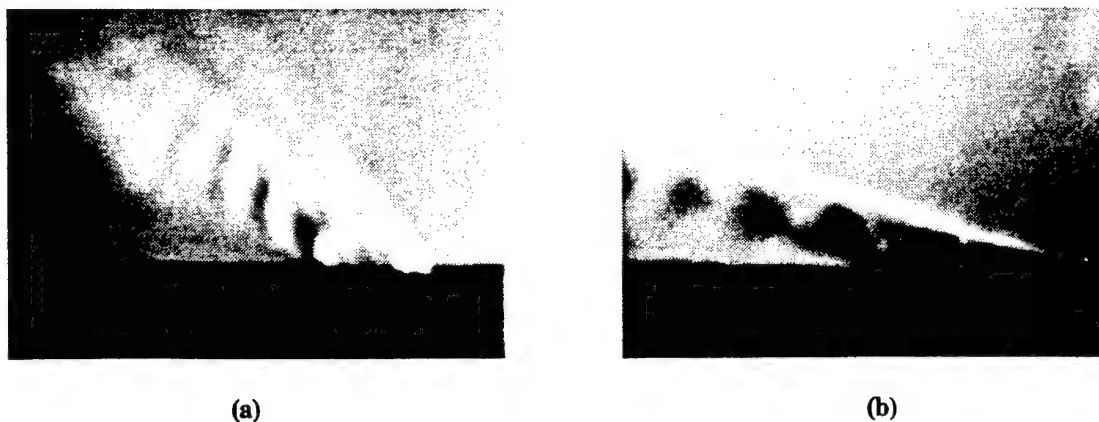


Fig. 1 Schlieren photographs of (a) constant diameter and (b) diverging nozzle ejector supersonic jets; the ejectors were inclined at  $20^\circ$  to a flat plate.

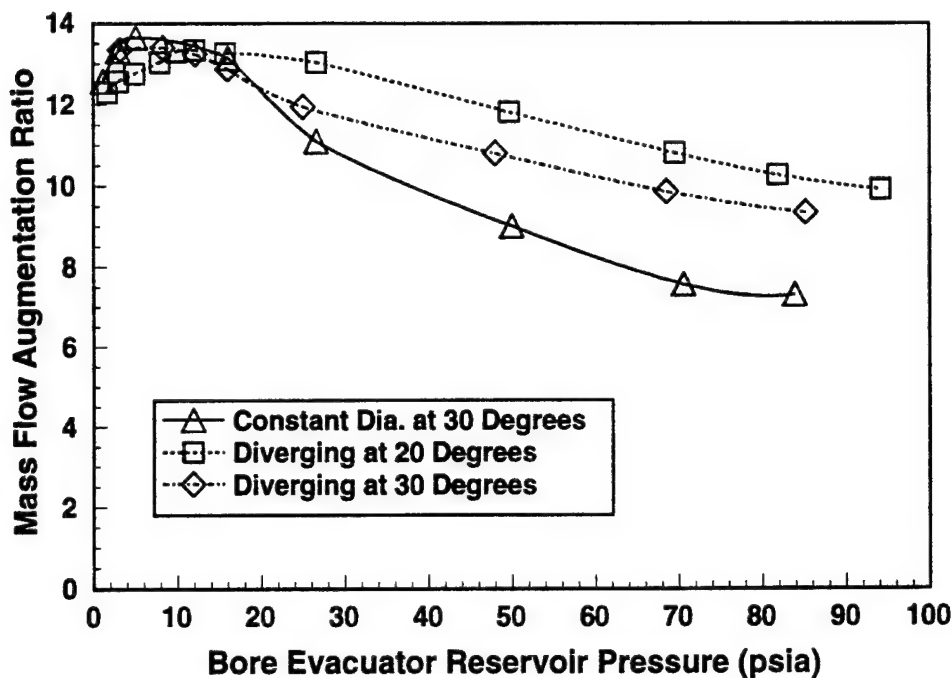


Fig. 2 Mass flow augmentation ratio for constant diameter and diverging nozzle ejectors [8].

#### Finite Element Bore Evacuator Design Flow Code

Bore evacuator designs would benefit greatly from a numerical model which could enable engineers to select the most promising ideas for evaluation in scale model and full scale experiments. CFD solutions can be much more valuable than scale model or full scale test data, since the numerical results provide detailed information over a large region of the flow. This information is much more detailed than available from any experiment, since it provides properties which are difficult or impossible to measure. Typical results from a CFD study supply enough information to calculate any flow property at any point in the flow, limited only by the assumptions entailed in the computer code used to determine the solution. Calculations can also take into account equilibrium or finite rate chemistry, allowing the chemical composition at any point in the flow to be determined.

A computer program to simulate cannon bore evacuator flow is currently being developed [11]. This code must be checked against real world data to gain the confidence necessary to use it during the design process. The computer code must be verified to ensure that it solves the equations correctly, then compared to experimental data to confirm that it incorporates the proper physical models [12]. The initial phase involves using the code to obtain solutions to model problems which are related to, but simpler than the full bore evacuator flow. These solutions should be compared to analytical results to confirm that the code solution process is free of errors. An established, previously verified code, such as NPARC [13], may be used when analytical solutions are unavailable. Experimental results are not necessary for this procedure; indeed, they are meaningless for validating proper code execution, i.e., obtaining stability, convergence, and simulation accuracy.

Favorable comparison between calculated solutions with different codes, or between computed and analytical solutions, can provide confidence that the codes are operating properly, i.e., that they are solving the equations correctly. However, the results of numerical simulations must also be compared to actual physical measurements to confirm that the equations incorporated in the code are adequate to simulate the physics of the problem. This code validation process must be performed on problems which have similar flow features as the problem of interest; this step is independent of the verification that the code operates properly, as indicated above.

It was postulated that improved gas dynamic modeling would be required for a flow code designed to predict the optimum prototype performance from among the several flow configurations suggested. The model must be three-dimensional (3D) to capture the basic physics of the problem. In 1990, Benét submitted a solicitation to the ARDEC Small Business Innovation Research (SBIR) office for sponsorship of cannon bore evacuator design flow code development. Computational Mechanics Corp. (CMC), TN, was awarded a Phase I contract to obtain validation of a finite element, CFD technique. Sufficient merit with a two-dimensional (2D) method was developed

in Phase I [14] for continuation with a 3D, Phase II effort. CMC's 3D evacuator simulations for subsonic-to-supersonic charge flow conditions and supersonic-to-subsonic turbulent discharge flow has challenged computational resources, first on the Army Research Laboratory (ARL) KSR-1 parallel processing machine and currently on the Cray T3D at Eglin AFB. Results of cooperative efforts by Benét and CMC were presented in Ref. 11. The CMC deliverable code, called AKCESS.BOREVAC, is developed on their licensed platform, a special purpose Unix shell called AKCESS.\*, which performs well with algorithms designed for incompressible porous flows, but is currently slow with nonlinear and dynamically changing conical type [15] flow conditions in the region about the ejector ports. To quote their code development assessment by CMC as it approached the twenty-third month of Phase II:

This research stems from realization by technical principals at Army's Benét Laboratories, and at CMC, that CFD simulation capabilities were emerging potentially applicable to bore evacuator performance assessment. Many ingredients are required to make this feasible, important among which are advanced CFD computational theories, in particular the finite element method, the emergence of Unix graphics-work stations, and practical maturation of parallel processing to achieve 3-dimensional simulations in reasonable wall clock time. *CMC proposed integrating innovative ideas and leading edge technologies into a desktop environment for the design engineer.* The demanding simulation character is the large disparity in length scales present in the artillery piece. The evacuator reservoir ejector ports have diameters on the order of millimeters, while the bore is centimeters in diameter and meters in length [a total ejector to bore flow area ratio = 0.007 for the M256]. The ejector ports are drilled at angles to the bore center line, presenting a very demanding discretization character to CFD procedure. CMC brought forefront research achievements in finite element CFD methodology particularly applicable to this stringent requirement. [...] The net result is stable computations using highly skewed meshes containing cells with inordinate aspect ratios, while operating at diverse pressure ratios (up to 1500:1 atm). CFD computations are very compute-intensive, and take considerable machine resources to obtain a simulation. *The 3D simulation of the complete artillery piece during the entire operation cycle is presently beyond the capabilities of modern parallel computer hardware systems.* Therefore, a domain decomposition procedure is developed to segregate various performance aspects of the bore evacuator system, taking advantage of admissible boundary conditions as appropriate [16].

One of these domains can be simplified further by considering 3D flow through a single ejector over the symmetry plane containing the ejector nozzle's axis, solving only the Eulerian problem with appropriate slip boundary conditions at the wall. Although this solution is non-dissipative, it remains rotational so that the entropy structure associated with the Mach shock bottle is captured by the equation set cast in its divergence free formulation. The ensuing inviscid flow of a perfect gas (air at room temperature) has been simulated with the NPARC code and compared to pressure measurements and with schlieren photography, the principle topic of this report.

There are several different levels of confidence which can be associated with the term validated when used to describe a CFD code, depending upon the type and extent of experimental data used to evaluate the code's performance. Extensive experimental data along boundary surfaces and within the flow field is required for the strictest definition of a validated code. Comparison of performance data or limited surface data results in a design-validated code, if the comparison is favorable for parameters important for design (e.g., discharge coefficient,  $C_d$ ). Such a code can be used to accurately predict only the quantities for which it was validated [17]. The validation process establishes the extent to which a calculated solution can be expected to match real flows.

The purpose of the current study is to provide a solution of a flow problem related to conditions experienced by a gun bore evacuator. The solution was obtained using the NPARC code, which has been verified and validated for supersonic jet flows [13]. The solution was used to gain insight into the pumping action of the inclined ejectors mounted in gun bore evacuators. This result can also be compared to calculations from the code of Ref. 11, for the purpose of verifying that the AKCESS.BOREVAC code is free of errors. In addition, measurements of the CPU time requirements for NPARC can be useful in judging the relative efficiency of other codes.

#### Euler Simulation of Single Ejector Flow

The proper simulation of the entire gun bore evacuator cycle is a very challenging problem. It involves large scale flow through the gun bore driven by small flow scales near the ejectors. A typical ratio of total ejector area to bore area is  $10^{-3}$ . In addition, the flow is unsteady, with portions of the domain laminar, transitional, and turbulent at different times during the bore evacuator cycle, and the fluid can undergo chemical reactions. Current computer and algorithm technology is probably not yet at the stage where a detailed calculation of the complete

evacuator cycle is realistic. However, significant advances in knowledge can be obtained by investigating portions of the flow field and bore evacuator cycle.

The most important region for determining the bore evacuator performance is the flow in and around the ejectors. Small changes in the ejector geometry can cause very large increases in the induced velocity, as demonstrated experimentally in Ref. 8. Any attempt to analyze the bore evacuator process, therefore, should concentrate on this area as modifications here have the greatest potential payoff. With this in mind, the present study has developed a solution and grid generating procedure for the single ejector experiments of Ref. 8. Results could be extended in the future to multiple ejector geometries, or configurations with an induced flow.

The NPARC code was chosen for this analysis. NPARC is a robust, flexible CFD program for solving the Navier-Stokes equations in two or three dimensions. Its capabilities and the theory involved in its development are discussed in detail in Refs. 13 and 18. It has been used extensively to compute solutions to many fluid flow problems, including subsonic, supersonic, and hypersonic flows. Reference 13 contains a large bibliography, which includes verification and validation cases where NPARC was applied to supersonic jets.

Proper selection of the equation set, solver parameters, and boundary conditions is essential for obtaining a useful solution. The single ejector jet was observed to be a viscous, supersonic flow [8] which would be best represented by the Navier-Stokes equations. The CPU time required to obtain a solution using NPARC is presented in Table 1. The execution speeds in the table represent three-dimensional calculations, and either were directly measured, or were extrapolated from the observed speed of NPARC solving two dimensional viscous and three dimensional inviscid problems, as indicated on the table. Calculations were performed on IBM RS/6000, SGI PowerChallenge, and Cray YMP computers. The total CPU times were obtained by assuming a maximum of one million grid points, and took into account the computations on differently refined grids necessary in any CFD study to properly characterize the numerical error. Based on Table 1, a Cray supercomputer is necessary to calculate the viscous supersonic jet. Because such a computer was not available, this report discusses a three-dimensional solution of the Euler equations, using RS/6000 and SGI PowerChallenge workstations. Although the solution cannot completely represent the actual flow, the structures in the solution are instructive for understanding the mechanism by which the surrounding fluid is induced by the jet. In addition, the computation provides information on code parameters which will be helpful for the eventual computations using the Navier-Stokes equations on a Cray supercomputer.

## NUMERICAL METHOD

Version 2.2 of the NPARC [13] CFD code was applied to the problem of a supersonic jet exiting from a constant diameter ejector inclined  $30^\circ$  to a flat plate. The problem domain is sketched in Fig. 3, and was chosen to simulate conditions generated in experiments reported in Ref. 8. The outer boundaries for the computations are indicated in the drawing, and were chosen to be far away from the jet flow, extending over 20 ejector diameters downstream of the ejector exit. The high pressure reservoir system which supplied air to the ejector in the experimental work was modeled, although an approximate upstream boundary condition could have been applied to reduce grid generation complexity and solution time [19].

### NPARC Version 2.2

The NPARC code can be used to calculate approximate solutions to either the Euler or the Navier-Stokes equations for two-dimensional, axisymmetric, and three-dimensional problems. The code determines the flow

Table 1. CPU Time Estimates

Equation Set:	Euler			Navier-Stokes		
Architecture:	RS/6000	SGI Power Ch.	Cray YMP	RS/6000	SGI PowerCh.	Cray YMP
CPU/pt/time step:	90.12 $\mu$ s	90.14 $\mu$ s	4.1 $\mu$ s <sup>†</sup>	297 $\mu$ s <sup>††</sup>	297 $\mu$ s <sup>††</sup>	13.9 $\mu$ s <sup>†</sup>
Total CPU time:	250.3 CPU hrs 10.4 CPU days	250.4 CPU hrs 10.4 CPU days	11.4 CPU hrs 0.47 CPU days	825 CPU hrs 34.4 CPU days	825 CPU hrs 34.4 CPU days	39 CPU hrs 1.6 CPU days

<sup>†</sup>Estimate based upon measured 2D performance.

<sup>††</sup>Estimate based upon measured 3D Euler and 2D Navier-Stokes performance.

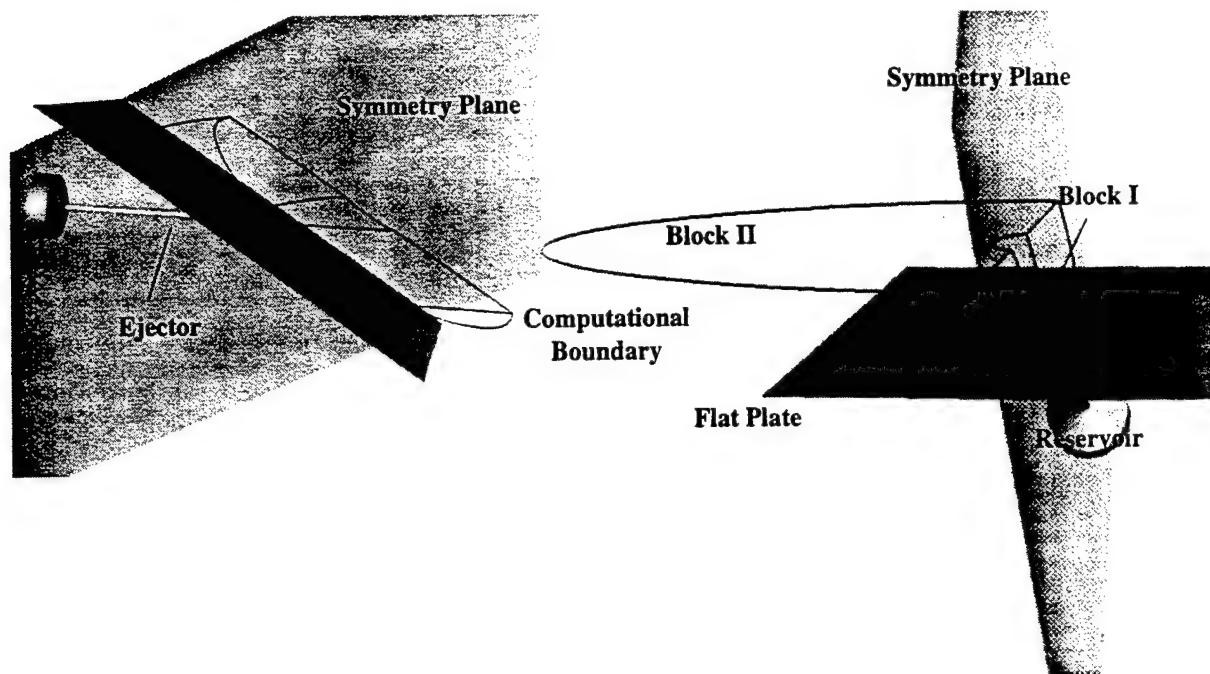


Fig. 3 Single ejector problem domain viewed from two different angles.

properties at mesh points distributed in the solution domain. The mesh is composed hexahedral cells along general, curvilinear coordinate directions. The solution domain may be decomposed into several blocks, allowing gridding and solution of flow problems around very complex configurations.

NPARC employs a Taylor series linearization of the governing equations, and an approximate factorization to decouple the spatial directions. Central difference operators are applied for the spatial derivatives, and the resulting equations are formally second order accurate in space and first order in time. The Navier-Stokes equations are given by:

$$\frac{\partial Q}{\partial t} + \frac{\partial F_j}{\partial x_j} - \frac{1}{\text{Re}} \frac{\partial G_j}{\partial x_j} = 0$$

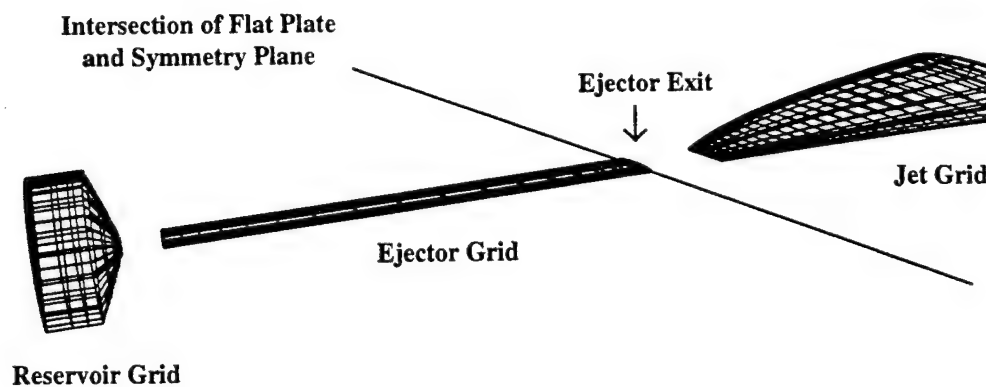


Fig. 4 Block I grid assembled from three parts

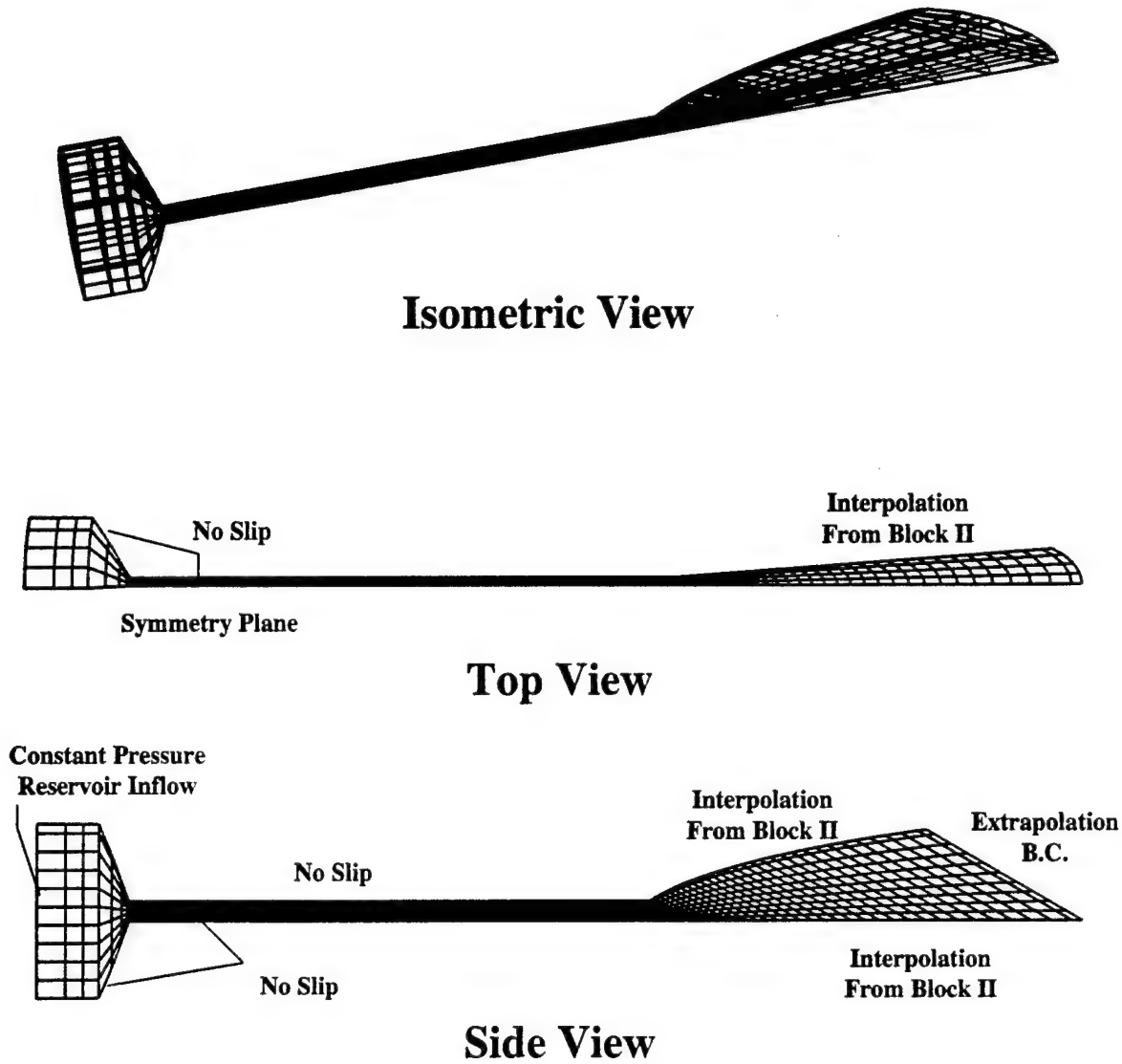


Fig. 5 Block I grid, containing reservoir, ejector, and jet regions, with boundary conditions.

where  $Q = \{\rho, \rho u, E\}^T$ ,  $F_j = \{\rho u_j, \rho u_i u_j + p \delta_{ij}, u_j(E + P)\}^T$ , and  $G_j = \{0, \tau_{ij}, u_i \tau_{jk} - q_j\}^T$  [18], with the obvious simplification for inviscid flows. The ideal gas assumption is employed, and various turbulence models are available to close the equation set. The application of central differences to the above results in a block pentadiagonal set of equations. The NPARC algorithm diagonalizes the equations, resulting in a set of pentadiagonal scalar equations which are much less expensive to solve than the block pentadiagonal set produced by the unmodified equations. The viscous fluxes are time-lagged in order to allow the equations to be uncoupled; this has negative implications for time accuracy and for stability [18].

#### Inclined Ejector Grid and Boundary Conditions

The single ejector flow was three-dimensional, with a symmetry plane running down the center of the ejector, as illustrated in Fig. 3. The computational grid was constructed from two blocks to simplify the task of fitting the inclined, cylindrical ejector with the exterior region surrounding the jet and the flat plate, and took advantage of the geometric symmetry. The Block I grid was assembled from three parts to facilitate grid point clustering, as depicted in Fig. 4. The assembled grid is shown in Fig. 5. The actual mesh was much finer than presented in these figures; points were removed from the drawing for clarity.

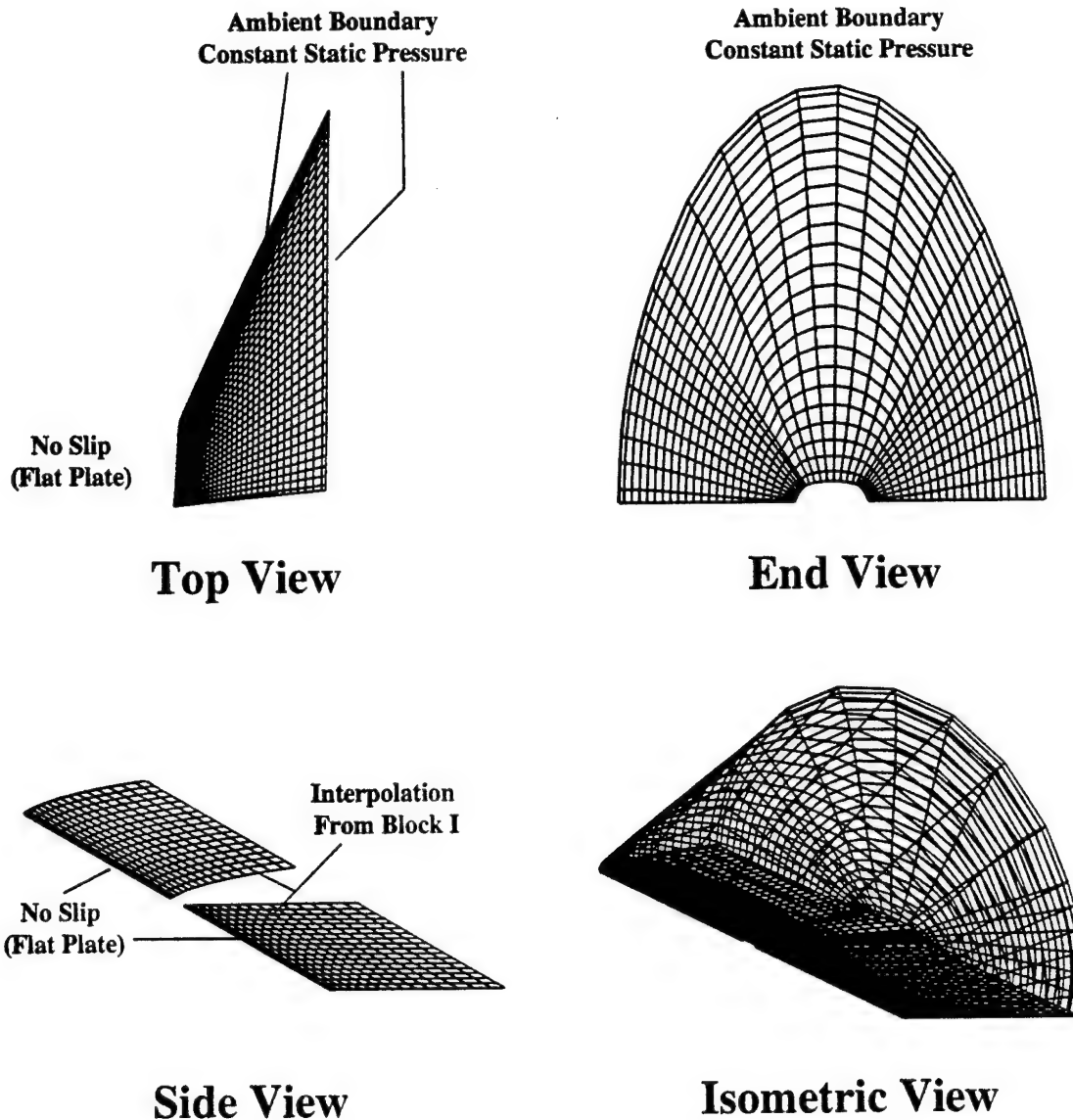


Fig. 6 Block II grid, containing region outside ejector and flat plate, with boundary conditions.

The Block II grid was constructed to mate with the outer boundary of the jet grid section of Block I, and encompassed the flat plate and the surrounding, ambient fluid. Figure 6 contains a three-view drawing of this grid, and the assembled, multi-block grid is shown in Fig. 7. Mesh points were also removed from these plots, for clarity.

Experiments reported in Ref. 8 showed that the inclined, supersonic jet contained several shock cells which were formed as the flow overexpanded after exiting the ejector. These shock cells were captured by the calculations, but were not well resolved on the initial grid, which had 64 points in the axial direction inside the supersonic jet region. The Block I grid was subsequently refined by doubling and then quadrupling the number of axial points inside the jet portion of the grid. The final Block I grid had dimensions of  $300 \times 20 \times 20$ ; the Block II grid was  $60 \times 58 \times 69$ .

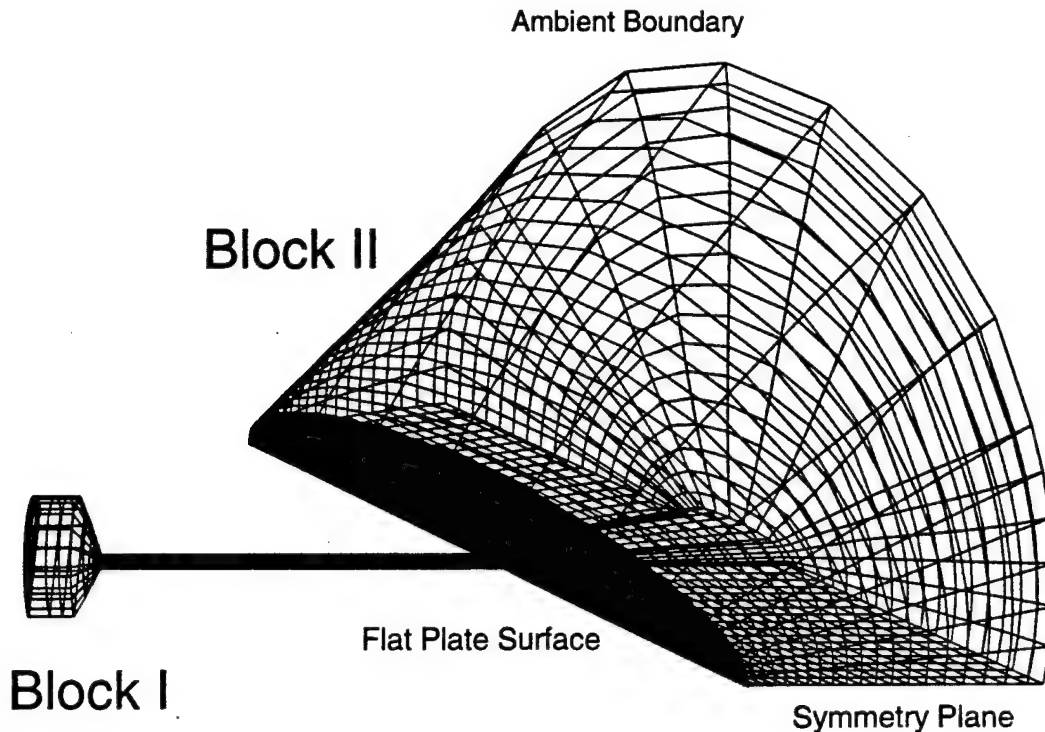


Fig. 7 Assembled Block I and Block II grids. Plot is coarser than actual.

The boundary conditions were chosen to reproduce the experiments of Ref. 8, and are marked on Figs. 5 and 6. The calculations were conducted with a pressure ratio of 6.5, reproducing the experiments with a 96 psia reservoir. The reservoir boundary was maintained at a constant total pressure throughout the simulation, while the static pressure was fixed at ambient on the external boundaries. The flat plate, ejector and reservoir surfaces, and the symmetry plane were slip surfaces, with the velocity normal to the surface set to zero.

The Euler equations were calculated on the multi-block grid using RS/6000 computers at Rensselaer and a SGI PowerChallenge at Benét Laboratories. The measured execution times of the NPARC code obtained during this study are presented in Table 1. The results of the calculations were transferred to SGI workstations at Benét and RPI for flow visualization using FAST [20].

## CALCULATED RESULTS

The supersonic ejector flow was calculated on three grids which had differing number of points in the supersonic jet region. Figure 8 presents contours of the shock function (based on the pressure gradient) for the three grids, with 64, 128, and 256 axial points in the jet grid portion. The shock cells in the supersonic jet were not well resolved on the coarsest mesh, and the supersonic region of the flow extended more than twenty ejector diameters downstream from the exit. This does not agree with the large experimental database, where, for the 6.5 pressure ratio, the supersonic region would not be expected to extend more than approximately ten diameters (e.g., Ref. 21).

The shock cells were much better resolved on the finer grids, with a corresponding reduction in the supersonic core length. The attenuation of the shock cells in a supersonic jet by a coarse computational mesh is a well known phenomena, and it is important for simulations of bore evacuator flows, which have been conducted with grids much more coarse than even the coarsest employed in the current study [11,14].

The structure of the supersonic jet exiting the ejector has been experimentally demonstrated to have a large effect on bore evacuator performance [8]. Figure 2 presents the measured performance of a generic bore

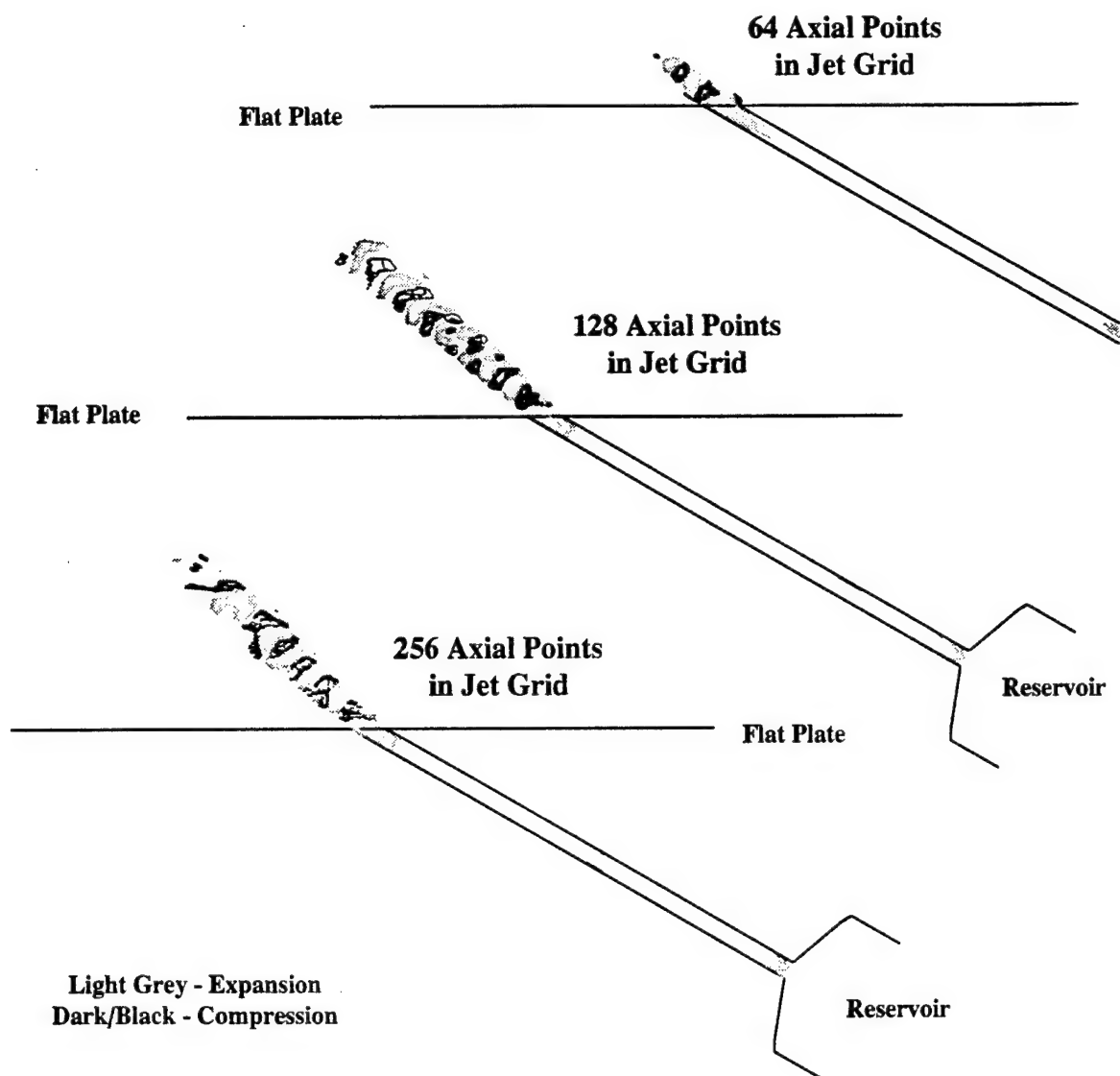


Fig. 8 Symmetry plane contours of the shock function based on pressure gradient.

evacuator with three different ejector designs. The constant diameter ejectors, similar to the ejector in the present study, were inclined  $30^\circ$  to the axis of the gun tube. The diverging nozzle ejectors had an expansion angle of  $14^\circ$  and area ratio of 1.48, had the same choked area as the constant diameter ejectors, and produced the same hole discharge coefficient. The performance of the nozzle ejectors was as much as 35% greater than the constant diameter ejectors at the higher pressure ratios, because the ejector flow was fully expanded supersonically before the ejector exit, eliminating the upstream deflection of the jet and reducing losses associated with shock waves in the jet [8]. These observations indicate that although the resolution of the supersonic expansion and the shock cell structure is computationally expensive, it is important for bore evacuator simulation since small changes in the ejector geometry have been observed to have a large impact on the measured bore evacuator performance.

The constant diameter ejector modeled in the current CFD study caused the jet to deflect in the upstream direction, as noted in Refs. 8 and 10. This upstream deflection was partially responsible for the lower than ideal measured evacuator performance, when compared to simple one-dimensional calculations [2,3]. The three-dimensional, Euler flow CFD analysis predicts this upstream deflection. Figure 9 presents contours of the jet axial momentum. A line is plotted on this plot extending out from the ejector exit into the fluid flow region in and

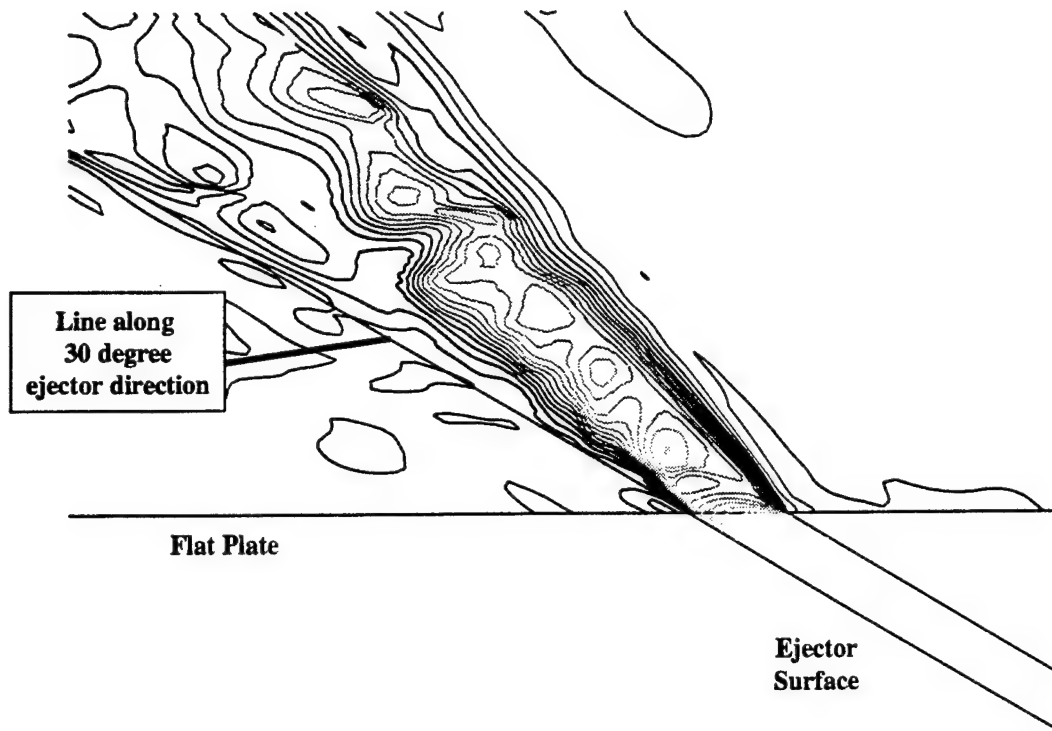


Fig. 9 Jet axial momentum contours on the symmetry plane, illustrating upstream deflection of the jet.

around the jet. This line is at a  $30^\circ$  angle to the flat plate, and represents the direction the jet would take if it followed the geometric ejector angle following the exit. The jet is clearly deflected upstream by the interaction of the expansion fan near the exit with the extended lip of the inclined ejector hole. The jet edge angles measured from this plot compares well with experimental data extracted from schlieren photographs [8], cf. Fig. 10.

Figure 11 compares the measured and computed static pressure distributions inside the ejector, near the exit. The pressures are plotted along the line on the downstream side of the ejector, with the axis origin as depicted in the insert to Fig. 11. The calculated results agree fairly well with the measurements, especially considering that the numerical predictions resulted from calculations of inviscid flow. A 3D, laminar flow solution using the finite element code of Ref. 11 is also provided for comparison. The added complexity of the full Navier-Stokes solution did not significantly improve the predicted ejector pressure. However, the viscous solution was carried out on a very coarse mesh, and additional mesh refinement may yield improved prediction of the pressure distribution.

The computed Mach number distribution along the jet centerline is compared with measurements [21] in Fig. 12. The measurements were carried out for a Mach 1.4 jet exiting an axisymmetric, converging nozzle. The experimental Mach numbers were determined from pitot pressure and thermocouple temperature measurements. The Euler CFD calculations compare surprisingly well with the measurements, considering that the experiments were conducted on an axisymmetric jet at a somewhat lower pressure ratio. The viscous dissipation far downstream of the exit was not present in the CFD results. These results, together with the favorable pressure comparison and excellent agreement of jet angles, indicates that the inviscid CFD solution captures the primary characteristics of the supersonic ejector flow.

## CONCLUSION AND FUTURE WORK

Gun bore evacuators are ejector pumps which remove residual propellant gases from the barrel after firing. The effectiveness of the bore evacuator depends upon several factors, including the details of mixing processes between the supersonic jets and the augmented flow. It is desirable to improve the ejector pump efficiency to ensure that these toxic gases do not flow back into the crew cabin when the breech is opened.

Experimental observations confirmed that with a small flow exit divergence, a significantly different jet structure was obtained which resulted in more efficient mixing. These experiments indicated that the most

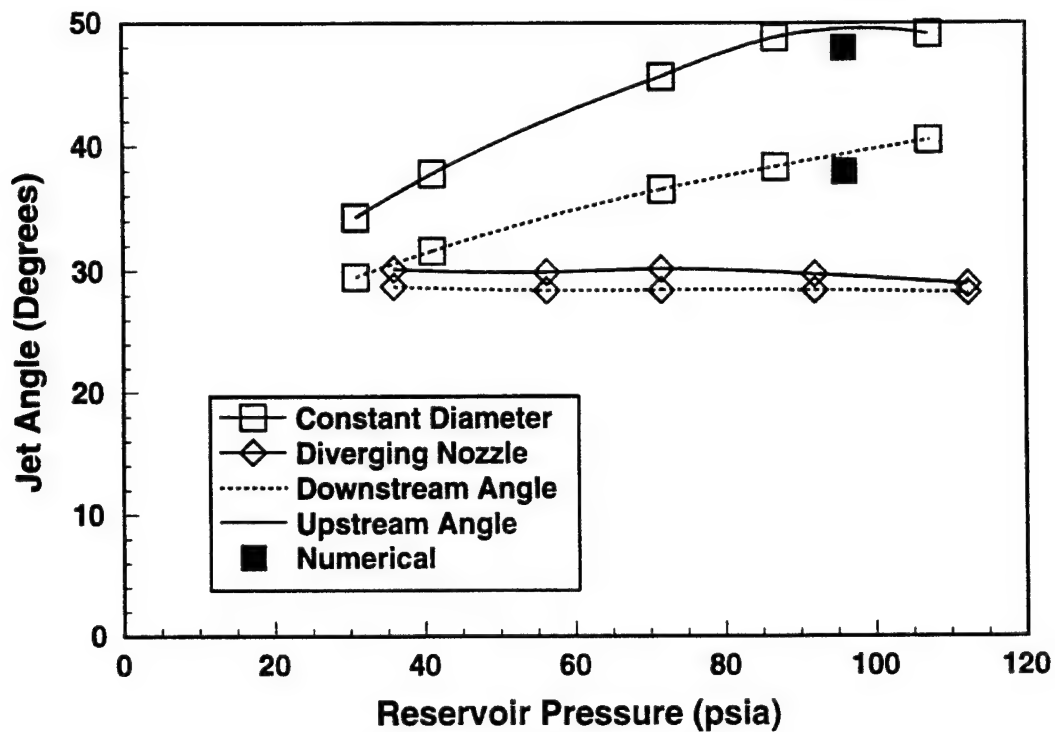


Fig. 10 Comparison of measured and calculated jet deflection angles.

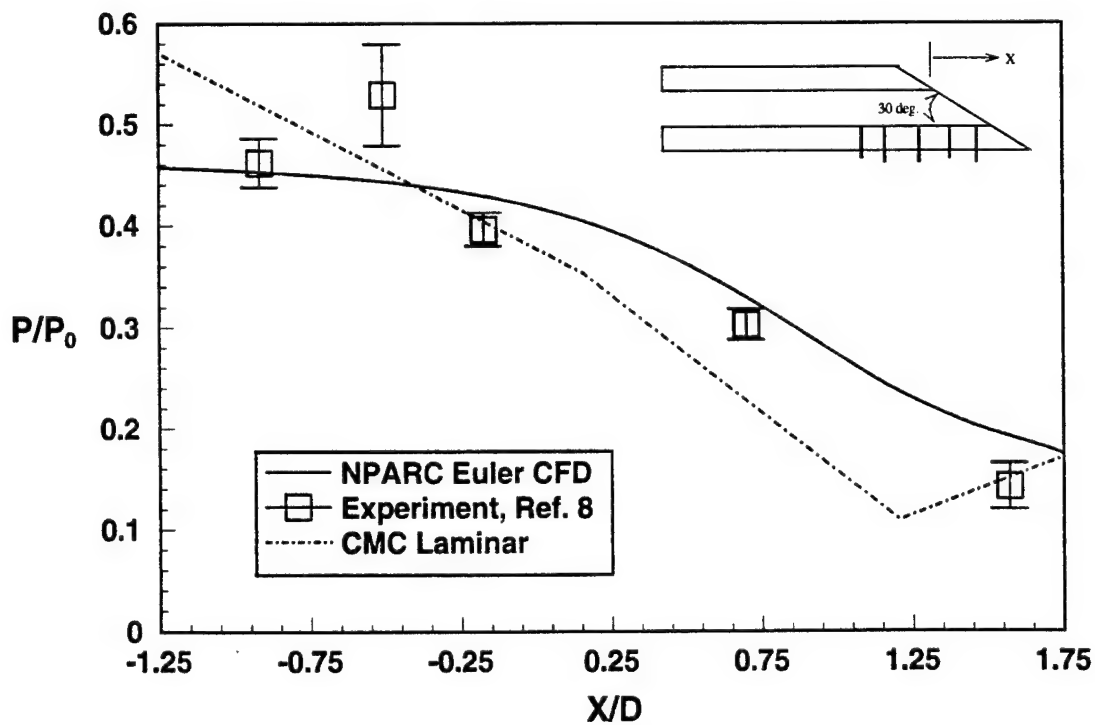


Fig. 11 Comparison of computed and measured static pressure along the downstream side of the ejector.

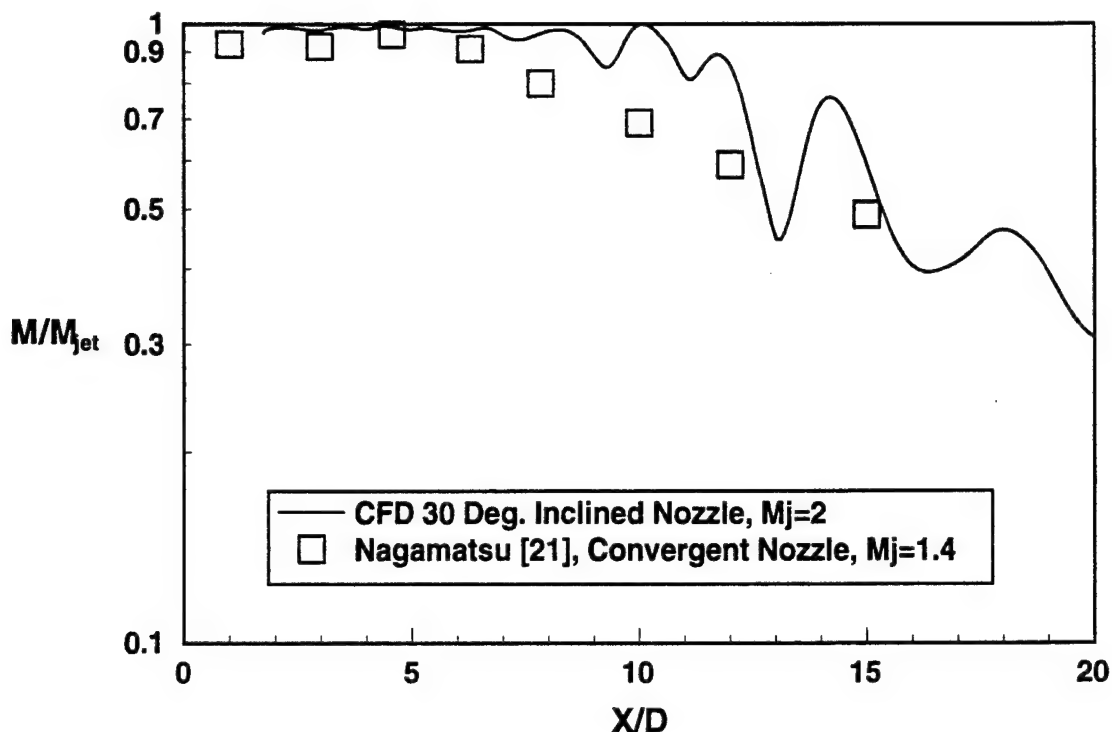


Fig. 12 Comparison of measured and computed jet centerline Mach number. Measurements from Ref. 21.

important region for determining the bore evacuator performance is the flow in and around the ejectors. Small changes in the ejector geometry can cause very large increases in the induced velocity, as demonstrated experimentally in Ref. 8. Therefore, a numerical investigation of the ejector flow was undertaken to increase understanding of the inclined, supersonic jet, and to demonstrate the capability of current computer algorithms and hardware to assist in bore evacuator performance determination.

The NPARC code was employed to calculate the solution for a pressure ratio 6.5 jet inclined 30° to a flat plate. The viscous flux vector was dropped from the equation set due to computer hardware limitations; a parallel or vector supercomputer is required to calculate realistic, three-dimensional viscous problems. The resulting solution demonstrated qualitative and quantitative agreement with experimental data. A fine mesh was required to adequately resolve the structure of the supersonic jet. Resolution of the jet structure is important for determining bore evacuator performance, since experimental observations have shown that small changes in the ejector geometry have produced large changes in evacuator performance.

This work may be extended to viscous flow, provided a powerful, vector supercomputer is available. The grid generation process was very time consuming, and the results may be immediately moved to a Navier-Stokes solution. In addition, the Euler results may be used to start the Navier-Stokes solution, further reducing the time required. Other interesting extensions involve examining an induced flow, multiple ejector configurations, or altered ejector geometry (i.e., diverging nozzles).

#### ACKNOWLEDGEMENTS

The authors wish to thank Benét Laboratories' Management, particularly Messers Russ Fiscella, Rick Hasenbein, and Dr. John Santini for their support; the Project Leaders, Messers Jim Bendick and Ciro Morales for their technical assistance; and Aeronautical Engineering Research Prof. (Active Emeritus), Henry T. Nagamatsu, RPI, for continuous scientific and technical guidance during these theoretical and experimental investigations, leading to the present CFD work. Finally, conventional cannon bore evacuator design is generic, facilitating computational fluid dynamics techniques that can reduce time and cost for the prototype production of high

performance evacuators. Accordingly, both Tank Main Armament and Advanced Field Artillery Systems Offices have sponsored the present initiatives.

# REFERENCES

1. Fagen, W., "Bore Scavenging Study of Case-Loaded Cannon Mounted in Closed-Cab Vehicles," AMF Projects MR 1014 and 1030, Mechanics Research Department, American Machine and Foundry Company, September 1954 and June 1955.
2. Andrade, C.A., Nagamatsu, H.T., and Duffy, R.E., "Theoretical Compressible Flow in Generic Bore Evacuators and Experimental Verification", AIAA 89-0652, January, 1989.
3. Nagamatsu, H.T., Duffy, R.E., and Andrade, C.A., "Experimental and Numerical Study of Supersonic Jet Ejectors For Gun Bore Evacuators," AIAA-90-1620, June, 1990.
4. Andrade, C.A. and Haas, J.E., "Generic Bore Evacuators II. Non-Ideal and Real Propellant Gas Transients," *Proceedings, 6th U.S. Army Symposium on Gun Dynamics, I*, Benét Laboratories, ARDEC Report ARCCB-SP-90015, May, 1990.
5. Andrade, C.A., Clauss, C.W., Nagamatsu, H.T., Myrabo, L.N., and Messitt, D.G., "Investigation of Shock Ignition in the Injector Ports of an Annular Reservoir," *Proc. 7th U.S. Army Symposium on Gun Dynamics*, Report ARCCB-SP-93034, Ed: T.E. Simkins, Benét Laboratories, ARDEC, 11-13 May, 1993, pp. 61-80.
6. Nagamatsu, H.T., et. al., "Generic Bore Evacuators I. Experimental & Aerodynamic Investigations," ARCCB-SP-90015, *Proceedings, 6th U.S. Army Symposium on Gun Dynamics, I*, Benét Laboratories, ARDEC Report ARCCB-SP-90015, May, 1990.
7. Nagamatsu, H.T., Myrabo, L.N., Messitt, D.G., Ekonomidis, C., Greenman, M.D., and Yagle, P., "An Experimental Investigation of the Gasdynamic Performance of Gun Bore Evacuators Mounted on 155MM Self-Propelled Howitzers," U.S. Army Contractor Report ARCCB-CR-95019, March, 1995.
8. Nagamatsu, H.T., Myrabo, L.N., Messitt, D.G., Greenman, M.D., and Peterson, K.G., "Experimental Investigation of Innovative Gun Bore Evacuator Concepts for Generic 155mm Self-Propelled Howitzers," Final Report for U.S. Army Contract DAAA-22-93-C-0106, Rensselaer Polytechnic Institute, May, 1994.
9. Nagamatsu, H.T., Myrabo, L.N., and Messitt, D.G., "Experimental Investigation of Innovative Gun Bore Evacuator Concepts for Generic 155mm Self-Propelled Howitzers," Final Report for Extension of Army Contract DAAA-22-93-C-0106, August, 1994.
10. Wlezien, R.W., and Kibens, V., "Influence of Nozzle Asymmetry on Supersonic Jets," *AIAA Journal*, Vol. 26, No. 1, 1988, pp. 27-33.
11. Andrade, C.A., Manhardt, P.D., Schaub, E.G., Clauss, C.W., and Baker, A.J., "120mm Gun Bore Evacuation Simulated by Finite Element CFD," *Proceedings of the 30th JANNAF Propulsion Meeting*, Nov., 1993.
12. Mehta, U.B., "Guide to Credible Computational Fluid Dynamics Simulations," AIAA Paper 95-2225, 1995.
13. Sirbaugh, J.R., Cooper, G.K., Smith, C.F., Jones, R.R., Towne, C.E., and Power, G.D., "A User's Guide to NPARC Version 2.0," Arnold Engineering Development Center, <http://info.arnold.af.mil/nparc/>, Nov., 1994.
14. Andrade, C.A., Nagamatsu, H.T., Sodergren, O.F., and Iannelli, G.S., "Cannon Bore Evacuator Flow Theory, CFD, and Experimental Validation," American Institute of Aeronautics and Astronautics Paper AIAA 92-0832, Jan. 1992.
15. Joseph, D.D., Renardy, M., and Saut, J-C., "Hyperbolicity and Change of Type in the Flow of Viscoelastic Fluids," *Arch Rational Mechanics and Analysis*, Vol. 87, No. 3, 1985, p. 213.

16. Baker, A.J., Private Communication, April 21, 1994.
17. Mehta, U.B., "Computational Requirements For Hypersonic Flight Performance Estimates," *Journal of Spacecraft and Rockets*, Vol. 27, 1990, pp. 103-112.
18. Cooper, G.K., and Sirbaugh, J.R., "PARC Code: Theory and Usage," AEDC-TR-89-15, Arnold Engineering Development Center, 1989.
19. Lakshmanan, B., and Abdol-Hamid, K.S., "Investigation of Supersonic Jet Plumes Using an Improved Two-Equation Turbulence Model," *Journal of Propulsion and Power*, Vol. 10, No. 5, Sept.-Oct., 1994, pp. 736-741.
20. Walatka, P.P., Clucas, J., McCabe, R.K., Plessel, T., and Potter, R., "FAST User's Guide," NASA Ames Research Center, October, 1993.
21. Nagamatsu, H.T., Sheer, R.E., Jr., and Bigelow, E.C., "Mean and Fluctuating Velocity Contours and Acoustic Characteristics of Subsonic and Supersonic Jets," Rept. No. 70-C-391, General Electric Corporate Research and Development Laboratory, October, 1970.

**TITLE:** Modal Analysis of Mortar Baseplates  
Mario P. Rivera, Elwood Eisler  
Department of Mechanical Engineering  
Union College, Schenectady, New York, 12308  
Carlos I. Gutierrez  
Benet Laboratories, Close Combat Armaments Center  
Watervliet Arsenal, Watervliet, New York, 12189-4050

## **ABSTRACT**

The dynamic behavior of mortar baseplates due to shock loading, especially in large caliber mortars, has traditionally led to a number of conjectures amongst the community of ordnance engineers in regards to baseplate structural failure modes such as cracking, gross plastic distortion, etc. Strain field measurements indicate that stress are high with considerable vibration activity of offensive nature, these events have led to analytical investigations of mortar baseplates using Finite Element Analysis (FEA), most of these analyses have predicted large deformation gradients which have motivated concerns on vibration levels.

The manufacture of some baseplates, notably the 120 mm mortar base plate, is quite laborious this type of baseplate consists of a monocoque weldment which has more than 64 parts joined by no less than 100 ft. of weld-joints. It follows then that it would be highly advantageous to have a simple dynamic acceptance criteria for these baseplates in terms of simple bench instrumented "ringing check out tests."

The purpose of this investigation was to determine and describe the dynamic behavior of 120 mm mortar baseplate through the use of experimental modal analysis. The information presented in this paper may be used to validate advanced FEA theoretical models relative to the dynamic behavior of these type of structures and also may be utilized as a baseline for developing the aforementioned manufacturing "ringing" acceptance criteria for assessing mortar baseplate quality, notably the presence of undesirable defects such as gaps, poor weldments, etc.

The investigation includes the results of more than 200 individual measurements from the structure. The results are presented in computer animation format as well as the traditional graphical and tabular formats.

Finally, the experimental results are compared to theoretical predictions of simplified finite element analysis.

## **BIOGRAPHY:**

**PRESENT ASSIGNMENT:** Associate Professor, Mechanical Engineering Department, Union College (1985 to present). Mechanical Engineer, WAE, Infantry and Special Projects Branch, Development Engineering Division, Benet Laboratories (1985 to present).

**PAST EXPERIENCE:** Assistant Professor, Aeronautical-Mechanical and Mechanics Engineering, Rensselaer Polytechnic Institute, Troy, New York (1979-1985). Research mechanical Engineer, Tribology and Lubrication Branch, AFML, Wright Patterson AFB (1973-1979).

**DEGREES HELD:** B.S.A.E. (1968), M.S. Mech. (1970), Ph.D. (1973) all at Rensselaer Polytechnic Institute.

Modal Analysis of Mortar Baseplates  
Mario P. Rivera, Elwood Eisler  
Department of Mechanical Engineering  
Union College, Schenectady, New York 12308  
Carlos I. Gutierrez  
Benet Laboratories, Close Combat Armaments Center  
Watervliet Arsenal, Watervliet, New York 12189-4050

## INTRODUCTION

The following investigation deals with the experimental Modal Analysis of a monocoque isotropic shell type structure. The experimental technique is well established a basic description is given by Ewins [1]. The technique and methodology are advanced by investigating the dynamical behavior of a rather complex geometry provided by the 120 mm mortar baseplate shown in Figure 1. The resulting principal modes of vibration are provided in animated computer simulated form.

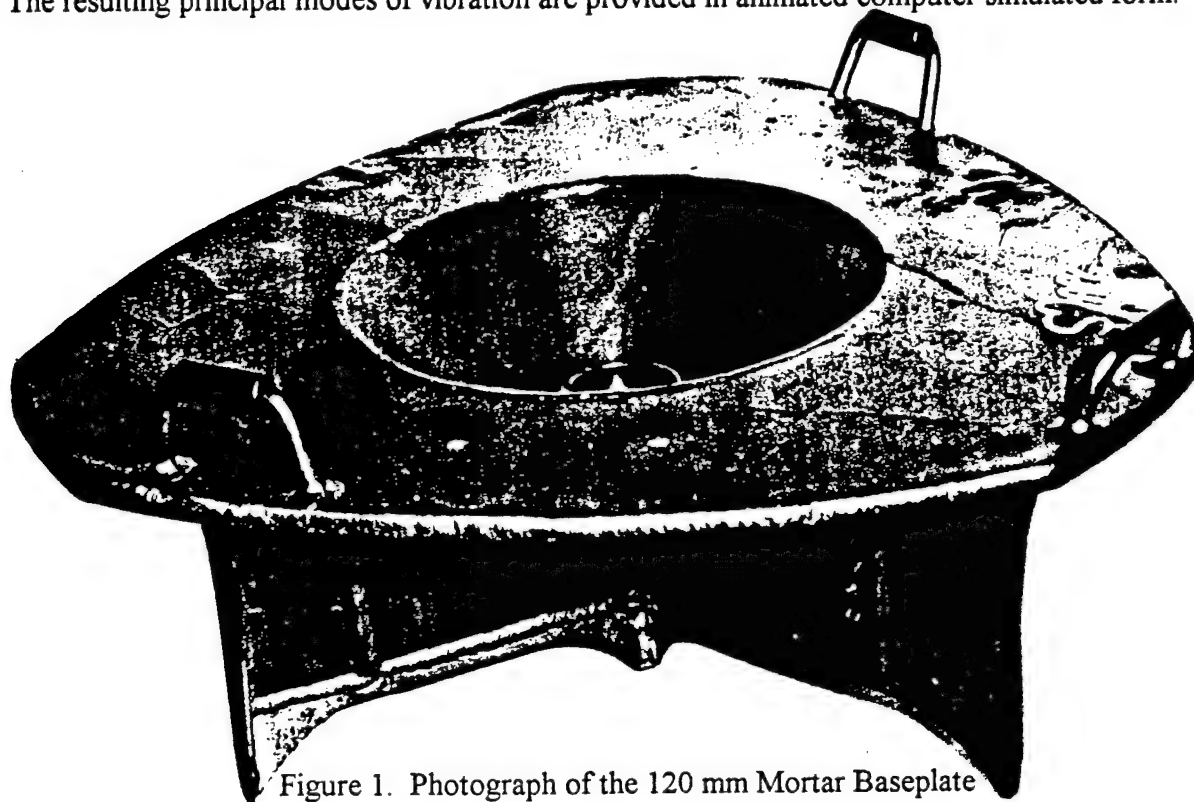


Figure 1. Photograph of the 120 mm Mortar Baseplate

The M9 Mortar is a particularly powerful defensive weapon which is subject to extreme vibration and impact shock loading during field operation. The nature of this excitation in combination with an insufficient damping contribution from some soil conditions in which the mortar is embedded can lead to large deflections and stresses, and a significant reduction in service life of the component.

The manufacture of some baseplates, notably the 120 mm mortar baseplate, is quite laborious. This type of baseplate consists of a monocoque weldment which had more than 64 parts joined by

less than 100 ft. of weld-joints. It follows then that it would be highly advantageous to have a simple dynamic acceptance criteria for these baseplates in terms of simple bench instrumented "ringing check out tests."

The purpose of this investigation was to determine and describe the dynamic behavior of 120 mm mortar baseplate through the use of experimental modal analysis. The information presented in this paper may be used to validate advanced FEA theoretical models relative to the dynamic behavior of these type of structures and also may be utilized as a baseline for developing the aforementioned manufacturing "ringing" acceptance criteria for assessing mortar baseplate quality, notably the presence of undesirable defects such as gaps, poor weldments, etc.

## **BRIEF HISTORICAL PERSPECTIVE OF EXPERIMENTAL MODAL ANALYSIS**

Experimental Modal Analysis has been widely used in various forms for the past sixty years. In the 1930's resonance testing was performed with eccentric mass shakers and modal deflection patterns were visualized by observing sand patterns. In the 1940's Kennedy and Pancu [2] presented resonance testing based on complex Admittance. It is from this work that Structural Impedance testing was performed by many engineers through the mid 1960's. In the 1950's Lewis and Wislisy [3] along with others developed multishaker test methods for isolating single modes and determining the concept of modal damping. In the early 1960's Stahle [4] introduced the first frequency domain Experimental Modal Analysis utilizing a Co-Quad Meter and tracking filters.

In the early 1970's experimenters such as Klosterman [5] furthered Frequency Domain Analysis through the use of broadband excitation and Parameter Estimation techniques used to match Experimental Modal Analysis measurements to analytical models. In the mid 1970's Richardson and Potter [6] carried out Frequency Domain Analysis using dual channel Fast Fourier Transform (FFT) with both random and transient excitation. They also began estimating modal parameters using least square curve fitting techniques to the Frequency Response Function. In the 1980's, and the early part of this decade, advances in testing and data analysis include multi-point force inputs, poly reference, direct parameter estimation, Ibrahim Time domain, and modal assurance criteria to mention a few. Presently, Experimental Modal Analysis is being used to aid in developing new and better designs. There are systems which allow automated comparison between Experimental Modal Analysis and Finite Element Analysis. One of the most popular implementations in recent times, which was due to computer advances in both software and hardware, is computer animation. Anything that can be drawn can be animated.

## **ANALYTIC BACKGROUND**

Since the behavior of complex multidegree of freedom (MDOF) Systems may be modeled as the linear superposition of a number of single degree systems [1]. The SDOF systems are combined using matrix algebra which are evaluated using standard linear algebra techniques to determine the natural frequencies (eigenvalues), mode shapes (eigenvectors), and the Frequency Response Function (FRF).

For a system with  $n$  degrees of freedom the generalized equation of motion is:

$$[m]\{\ddot{x}\} + [c]\{\dot{x}\} + [k]\{x\} = \{p(t)\} \quad [1]$$

where the brackets represent an  $n \times n$  matrix and the curly braces represent  $n$  component column vectors. There is one natural frequency associated with each degree of freedom for a total of  $n$ . As before, the associated equation for the free undamped oscillation of this system is used to determine the  $n$  resonances. By substitution  $\{x\} = \{u\}e^{j\omega t}$  this equation becomes:

$$[k - \omega^2 m]\{u\} = \{0\} \quad [2]$$

for a non-trivial solution this reduces to:

$$| [k] - \lambda [m] | = 0 \quad [3]$$

where  $\lambda = \omega^2$ . Expanding the determinant results in the eigenvalues  $\lambda_r$ , which are substituted back into equation [2] to find the eigenvectors,  $\{u(r)\}$  where  $r = 1, 1, \dots, n$ . These eigenvectors are components of the modal matrix  $[u]$  which fully describes the mode shape displacements. To get the orthonormal set of eigenvectors we matrix multiply through the mass matrix as follows:

$$\{u(r)\}^T [m] \{u(r)\} = 1 \quad [4]$$

In the orthonormal form, the modal mass  $M_r$  reduces to unity and the values for the modal stiffness  $K_r$  are equal to  $\lambda_r$ . The modal damping is found by matrix multiplying the eigenvectors through the damping coefficient matrix as follows:

$$\{u(r)\}^T [c] \{u(r)\} = C_r \quad [5]$$

The equations of motion are then uncoupled by substituting  $\{x\} = [u]\{s\}$  into [1] and taking advantage of the principle of orthogonality to achieve the following result:

$$[M]\{\ddot{s}\} + [C]\{\dot{s}\} + [K]\{s\} = [u]^T \{p\} \quad [6]$$

Assuming that  $s(t) = S(\omega)e^{j\omega t}$  and  $p(t) = P(\omega)e^{j\omega t}$ , substituting into [6] and rearranging terms the equation becomes:

$$S_r = \frac{\{u(r)\} \{P\}}{M_r(\omega_r^2 - \omega^2 + j\zeta_r\omega_r\omega)} \quad [7]$$

$$\zeta_r = \frac{C_r}{(K_r M_r)^{1/2}} \quad [8]$$

It follows that  $\{X\} = S_1\{u(1)\} + S_2\{u(2)\} + \dots + S_r\{u(r)\}$  which leads to the FRF:

$$H_{rk} = X_r/P_k \quad [9]$$

Equation [9] is a complex function of frequency,  $\omega$ . It is also noteworthy to mention that for a linear mechanical system this response matrix exhibits a symmetry across the main diagonal according to Maxwell's reciprocity theorem. For such a system, the following can be assumed:

$$H_{rk} = H_{kr} \quad r = k \quad [10]$$

## EXPERIMENTAL SETUP AND PROCEDURE

### Test Description

The M9 Mortar Baseplate, weighs about 200 pounds and consists of a triangular shaped ½ inch thick steel plate approximately 33 inches across. A cast conical section with maximum diameter of 19 inches has been welded into a circular hole at the center of the plate. At this location, the mortar barrel interfaces with the baseplate through the use of a ball socket joint which provides the mortar with its pitch variation. The entire assembly rests upon a trunk made up of over 30 individual steel plates welded together to provide structural support and stability. The mortar is initially installed in the field by firing the cannon from the desired point of installation. Three legs protruding from the base serve as earth movers during this process, and firmly entrench the component in a bed of soil.

The objective of the experimental portion of the analysis is to measure and record the system response to an impulse excitation in the form of a complex function of frequency. Application of the impulse and corresponding measurements were taken at discrete locations on the test component surface called nodes. Due to the complexity of the test piece and the relatively large number of nodes required to sufficiently describe its geometry, it is practically impossible to make measurements at every combination of input and output nodes required to fully populate the complex frequency response matrix. Therefore the principles of geometric similarity and reciprocity were utilized to reduce the minimum number of experimental data points necessary to fully describe the system response.

### Test Setup

One of the goals of the present investigation was to develop ringing quality control qualification procedures. The test setup therefore consists of the component free standing on the laboratory floor in an upright position as demonstrated in Figure 2. The primary operating environment of the unit is with the trunk firmly embedded in soil, which can be argued to provide a degree of damping to the response of the structure.

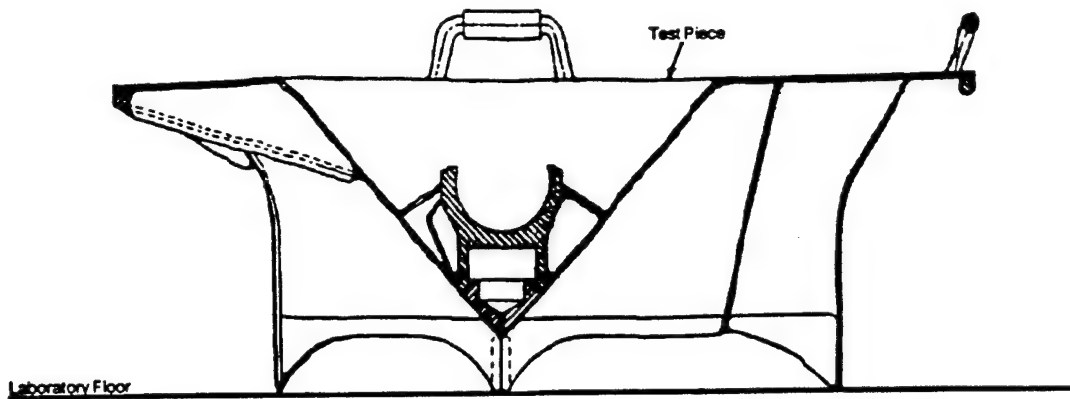


Figure 2. Test Piece Orientation

An impact hammer and accelerometer in concert with a spectrum analyzer will be used to stimulate and record the response of the test piece. The accelerometer was applied to the surface of the test component through the use of a thin layer of wax. The steel hammer tip was selected because of the impact resistance of the test component and the performance of the tip across a wide frequency range. Additionally, the accelerometer required signal amplification via a conditioning amplifier. The data was recorded on a micro computer from which the test was directed. Figure 3 illustrates the configuration of the test equipment.

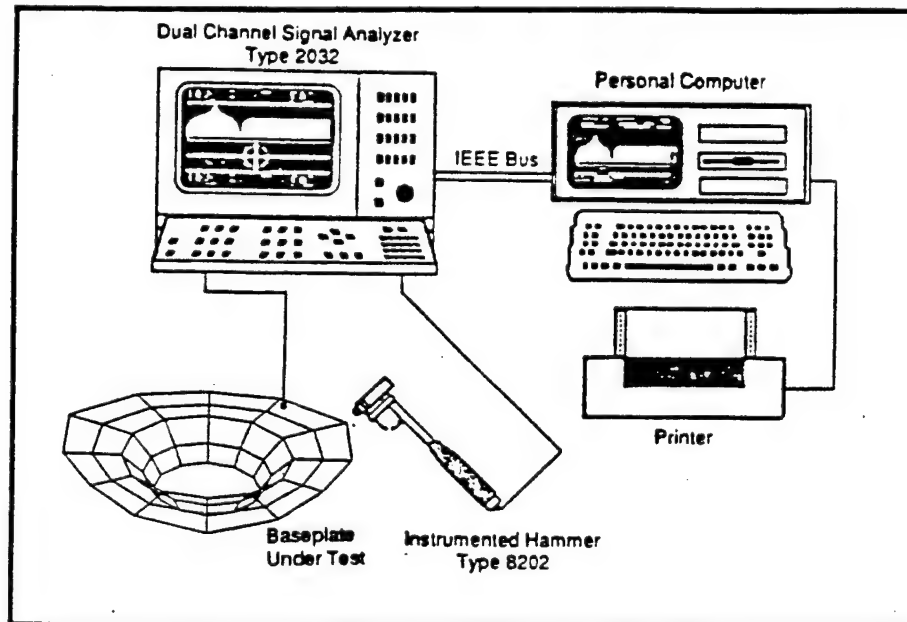


Figure 3. Test Equipment Configuration

Initially, a preliminary study was performed to determine the complexity of the mesh used to discretize the component geometry, and to locate the most reliable reference node locations. Once the preliminary study was completed, a system calibration check was performed to ensure that all of the test components were operating properly and accurately. This check was accomplished by mounting an accelerometer on a known mass so that it was capable of measuring the acceleration of the mass in a linear degree of freedom. The FRF of acceleration (the units of which are 1/mass) developed by striking the mass with the impulse hammer should result in a constant across the frequency range, the value of which provided an estimate of the mass of the calibration block. This estimate was then checked against the known mass of that block. A calibration test of this type was repeated before and after each data recording session of the experiment.

### **Instrumentation**

The following list of equipment was required to complete the experimental portion of the analysis.

- a. M9 Mortar Baseplate P/N 12576881
- b. Accelerometer Type 4384
- c. Impact Hammer Type 8202
- d. Conditioning Amplifier Type 2626
- e. Dual Channel Spectrum Analyzer Type 2032
- f. Graphics Plotter Type 2319
- g. Micro Computer
- h. IEEE 488.2 GPIB-PCII Interface Bus
- i. PC Modal Software Series, Software
- j. Calibration Mass (1.801 lbs)
- k. Wax Pencil
- l. Cleaning Agent
- m. Rags

### **Preliminary Considerations**

With the measurement equipment and test component configured as described in the previous section, the study was carried out by tapping the test piece with the impulse hammer at several structurally different locations and observing the response at a single measurement point. The process was then repeated at a few different measurement points until rough locations of response nodes and anti-nodes could be mapped out. With this information, the discretized mesh of Figure 4 was selected.

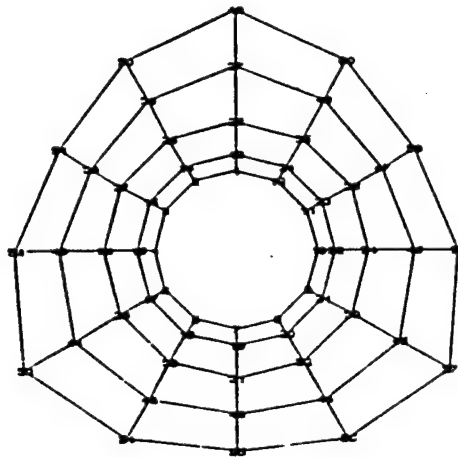


Figure 4. Discretized Mesh

The mesh consists of 60 geometric nodes and 108 connectivities plotted on a cylindrical coordinate system with the origin at the center of the test piece, in plane with the surface of the triangular top plate. Twelve radial lines containing five nodes each extend to the outside edges at 30 degree intervals. The trunk was excluded from the mesh, limiting the study to only those surfaces of the mortar exposed during operation. This decision was based on the low transmissibility of the trunk measured in the preliminary study, and field observation citing the exposed surfaces as the most critical regions. Also, as a result of the very small response recorded at the ball socket during the preliminary study, the geometry is simplified in this area to a ring of nodes along the outside face of the socket. Simplifications like these help to reduce the number of measurements and data reduction time without losing useful response information.

In order to fully populate the matrix FRF of equation [9] from section 2 with the 60 node mesh from Figure 4, the response at every node would have to be measured for the excitation at every node. This would amount to 3600 individual measurements which is neither practical nor necessary. Assuming linear behavior of the structure, allows to reduce this number by applying the principle of reciprocity. The accuracy of this assumption is checked in Figure 5. The top plot is the FRF found by exciting the structure at node 58 and measuring the response at node 56. This plot corresponds very closely with the lower FRF showing the result found by exciting at node 56 and recording the response at node 58.

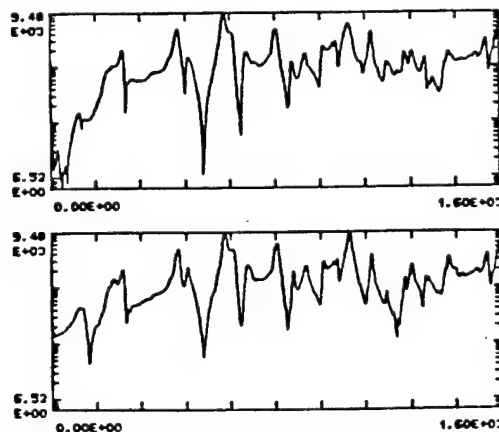


Figure 5. Reciprocity and Linearly FRF's

Taking full advantage of reciprocity only reduces the number of measurements by half to around 1800. However, for a linear mechanical system, all the information required to describe its mechanical behavior can be found in a single row or column of the transfer matrix [7]. Therefore the total number of required measurements is reduced to the number of degrees of freedom, or 60. This number was further trimmed down to 35 after taking advantage of the symmetry of the test piece itself, assuming that the mechanical behavior of structurally similar portions of the component would have somewhat similar response characteristics. Over 200 individual measurements were actually recorded in order to provide preliminary analysis data.

The mesh coordinates were then entered into the Display module of the PC Modal software and transcribed onto the surface of the test piece. With the mesh in place, a search for reference response nodes was begun. This portion of the preliminary study proceeded in much the same manner as before by tapping and measuring at labeled nodes of the mesh. During this search, careful consideration was given to avoiding an unresponsive node of the structure which could lead to erroneous findings. Referring again to Figure 4, nodes 49, 53 and 57 were found to be most responsive and number 49 was chosen as the primary test reference location. Combining the previous linearity assumptions with this reference response DOF results in the list of response excitation nodes pairs given in Table 1.

Table 1. Response-Excitation Node Pairs

#	Excitation Node	Response Node
1	1	49
2	2	49
3	3	49
4	4	49
5	5	49
6	6	49
7	7	49
8	13	49
9	14	49
10	15	49
11	16	49
12	17	49
13	18	49
14	19	49
15	25	49
16	26	49
17	27	49
18	28	49
19	29	49
20	30	49
21	31	49
22	37	49
23	38	49
24	39	49
25	40	49
26	41	49
27	42	49
28	43	49
29	49	49
30	50	49
31	51	49
32	52	49
33	53	49
34	54	49
35	55	49

The frequency range of interest was also determined during this preliminary study. The more narrow this range, the more accurately the location and magnitude of the resonance peaks can be determined, while a wider range includes more high frequency resonances which may have some significant influence on the structure. By varying the frequency scale of the FRF plots from the spectrum analyzer, comparing FRF magnitudes at resonance, and looking for significant peaks at higher frequencies, a frequency range of interest of 1.6 kHz was chosen.

## EXPERIMENTAL RESULTS

Mode shapes for the first nine resonances within the frequency range of interest were reviewed. All of the modal deflection patterns indicate that the outer edges of the M9 Mortar Baseplate flange experience significant excitation, while the interior cone remains relatively rigid.

Resonances throughout the frequency range of interest exhibited a close coupled nature, which make mode identification quite challenging.

### Mode Shape Descriptions

Table 2 lists the resonant frequencies of the first nine modes and their corresponding modal damping coefficients.

Table 2. Experimental modal Frequencies and Damping

Mode #	Modal Frequency (Hz)	Percent Damping
1	65.82	16.32
2	111.04	-1.29
3	229.70	5.35
4	259.93	3.00
5	449.88	1.71
6	482.89	0.54
7	627.68	1.50
8	656.03	1.66
9	692.53	1.55

Figure 7 through Figure 24 illustrate the deflection pattern of each of the modes found during the experimental analysis. Figure 6 shows an isometric view of the undeflected structure with node 49 (0 degrees) labeled as a reference.

Figures 7 through 24 are pairs of snapshots of the deflection pattern extremum for each of the nine modes in order of frequency. The first snapshot for each mode shows the deflection pattern at the beginning of the deflection cycle, the second shows the same pattern at the end of a deflection cycle. In each figure frequency and damping are given in the upper right hand corner of the figure.

In addition to these still frames, PC MAP provides an animation feature which allows the analyst an opportunity to view the mode shape pattern at greatly reduced speeds, with highly exaggerated deflection magnitudes. This feature allows for a much clearer interpretation of each modal deflection pattern.

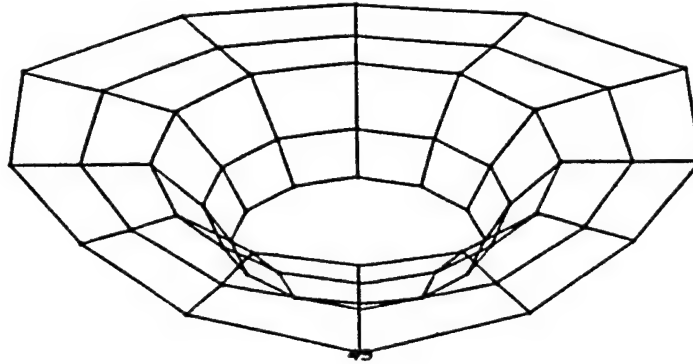
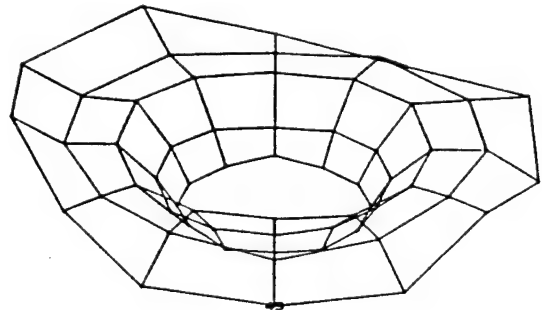
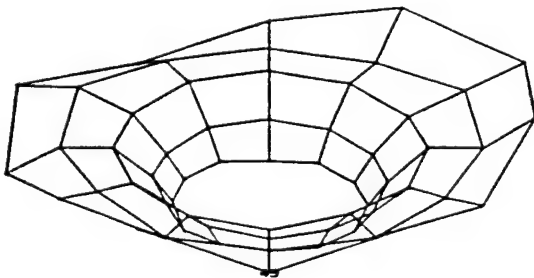


Figure 6. Isomeric View of Undeformed Baseplate

**Mode #1**

Frequency 65.8 Hz, Figures 7 and 8

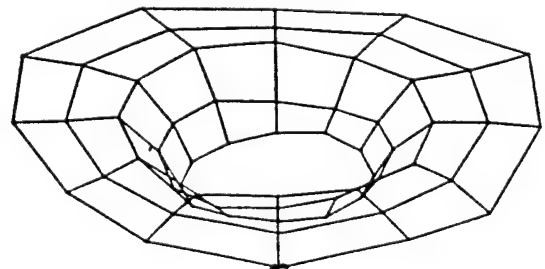
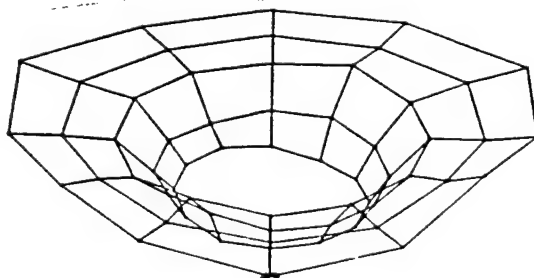
There is an asymmetric curl of the outside ring of nodes on the flange. The figures show that the deflection of the right half of the plate is 180 degrees out of phase with that of the left. The inner cone remains relatively rigid during this mode.



**Mode #2**

Frequency 111.0 Hz, Figures 9 and 10

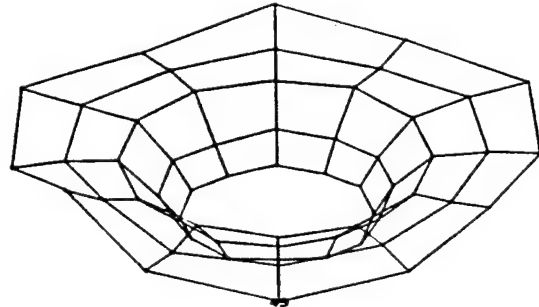
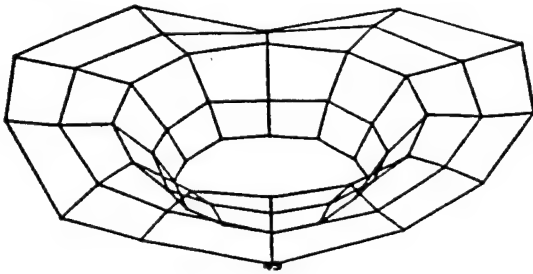
A symmetric cupping of the flange is demonstrated very clearly in this mode. In addition, the cone begins to experience some twisting about the x-axis (axis definition is shown in the lower right hand corner of each of the figures).



**Mode #3**

Frequency 229.7 Hz, Figures 11 and 12

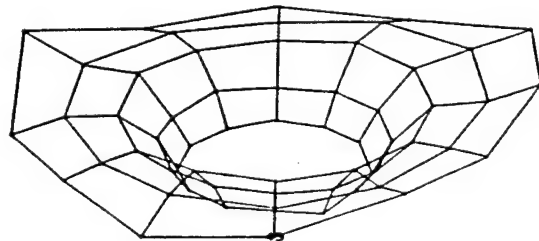
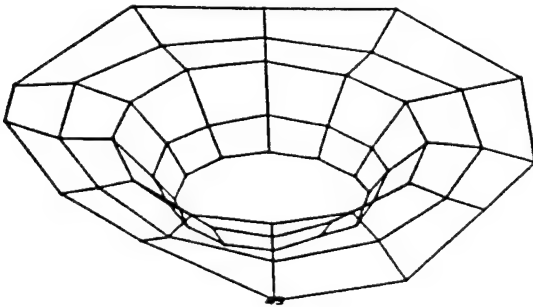
Symmetric excitation of nodes 51, 55 and 59 while the rest of the structure remains relatively rigid.



**Mode #4**

Frequency 259.9 Hz, Figures 13 and 14

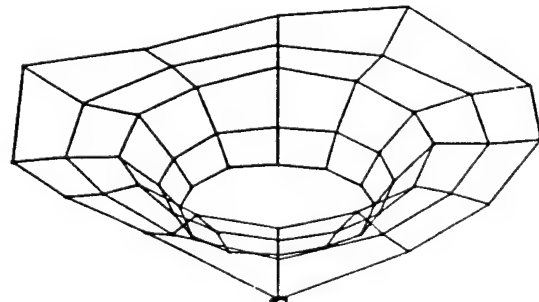
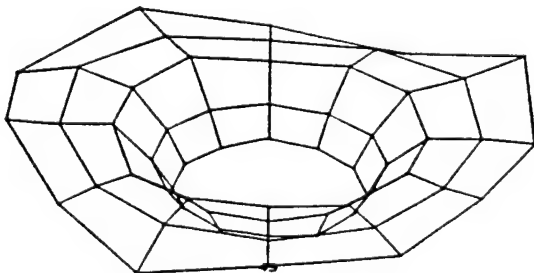
Here there is a very clear twisting of the entire baseplate about a line of action parallel to an imaginary line passing through nodes 58 and 59. In addition, there is some evidence of one of the earlier flexural modes in the lower left quadrant.



**Mode #5**

Frequency 449.9 Hz, Figures 15 and 16

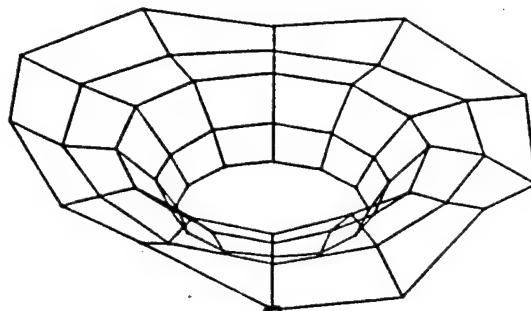
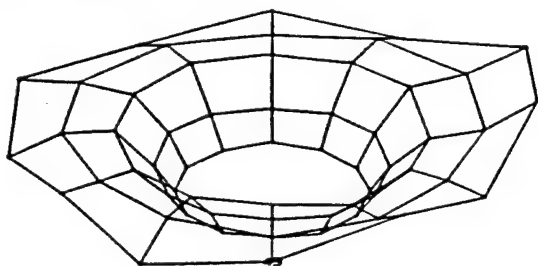
Asymmetric cupping between neighboring nodes along the upper left portion of the outside flange edge. The more symmetric behavior of the lower right quadrant suggests that some twisting along a similar line of action as mode #4 is present.



**Mode #6**

Frequency 482.9 Hz, Figures 17 and 18

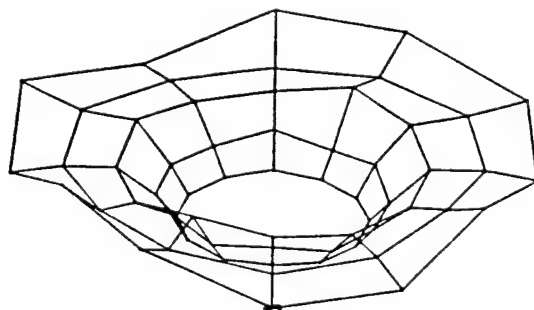
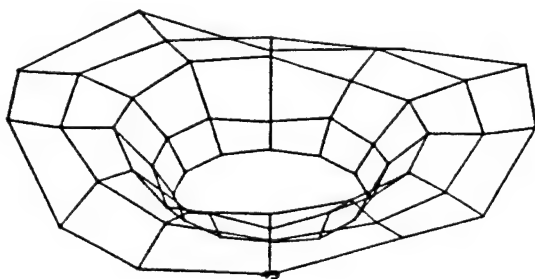
Similar to mode #5 with the twisting pattern more evident on the right half of the flange and some asymmetric flexural behavior on the left.



**Mode #7**

Frequency 627.7 Hz, Figures 19 and 20

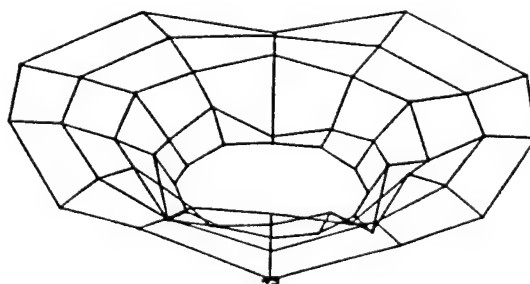
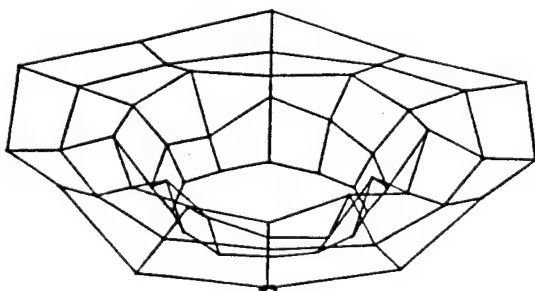
In-phase cupping of upper right quadrant as well as nodes 57, 59 and 60. Similar to Mode #5 but twist is not as evident. Nodes 30 and 36 on inner cone become active in phase with upper right quadrant deflection pattern. Remaining nodes inactive.



**Mode #8**

Frequency 656.0 Hz, Figures 21 and 22

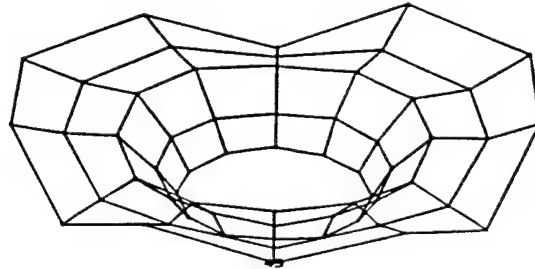
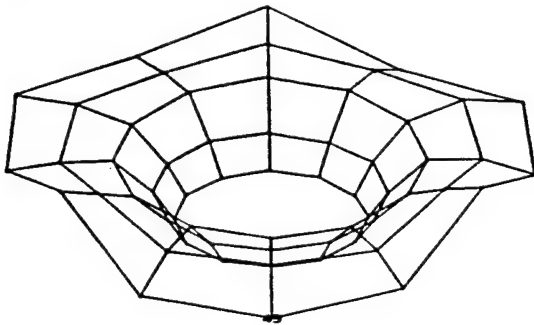
Flexural asymmetry is demonstrated between neighboring nodes on both the flange and the outer two mesh rings of the cone. The deflection pattern of the cone is out of phase with that of the flange. Nodes 1 through 12 continue to remain rigid.



### Mode #9

Frequency 692.5 Hz, Figures 23 and 24

Symmetric cupping of the flange with the exception of nodes 51, 55 and 59 which are deflecting out of phase with the flange. The inner cone is once again inactive.



### FEA VERIFICATION

In order to develop some confidence in the experimentally generated mode shape results, a comparison with analytical predictions from a finite element model is undertaken here. FEA analysis package has been selected for its simplicity and availability. The goal of this comparison is to identify similar deflection patterns between as many of the experimentally and theoretically predicted modes as possible. It is expected that many of the higher modes will not compare closely due to the intricacy of the construction of the mortar baseplate, and the limitations of the finite element model.

### FEA Package INTRO Description

The FEA analysis program employs a block diagram approach to the analysis of mechanical systems. The INTRO system used in this report is a scaled-down demonstration version of the large scale program. The principal limitation of the INTRO system in this application is a maximum number of nodes of only 25. However, the INTRO program does provide full three-dimensional analysis of beams, plates and shells; double precision computation of results; and automatic graphics generation.

### Model Description

The model consists of 25 nodes and 48 connectives arranged into quadrilateral plate, triangular plate and beam type elements. The dimensions of the annular plate are proportional to the test piece and the model has the material properties of 3/8 inch thick steel. To simulate the relative rigidity of the central portion of the test piece, stiffeners were added to the model along the conical section at connectives 2,8; 4,10; and 6,12. These elements have a rectangular cross-sectional area of and were also of steel construction. The model was fixed at nodes 14, 16 and 18 to represent the test piece resting on its three legs on the laboratory floor.

## Results and Comparison

Table 3 details the resonant frequencies found by the finite element model. There is fairly good agreement between the finite element model and the test results on several of the first few resonances. The first mode shape is quite similar with the asymmetric bending of the flange. Where the test results found one cupping mode at 111.0 Hz the analytical model found two, at 91.6 and 155.6 Hz. The fourth mode corresponds most closely both in shape and resonant frequency to the third mode found during test, although the analytical results showed more activity in the central cone section.

Table 3. Analytically Predicted Modal Frequencies

Mode #	Experimental Modal Frequency (Hz)	Analytical Modal Frequency (Hz)	Percent Difference
1	65.82	83.07	26%
2	111.04	91.61	-17%
3	229.70	155.50	-32%
4	259.93	236.55	-9%
5	449.88	378.79	-16%
6	482.89	442.07	-8%
7	627.68	451.83	-28%
8	656.03	x	x
9	692.53	x	x

The analytical results didn't locate a resonance in the range of the fourth mode from test, but the fifth test mode and the sixth analytical mode matched very closely both in frequency and the combination of asymmetric bending and twisting in the mode shape.

The higher resonances found by the finite element approach did not match as closely to the modes found in test, and in fact began repeating at mode eight. This is not surprising when the complexity of the structure and the simplicity of the model are taken into account. In general however, the results from the analytical model do support the findings from test for all but one of the first five resonances.

## CONCLUSION

The M9 Mortar Baseplate was found to have several closely coupled, low frequency modes combining both symmetric and asymmetric bending with significant torsional deflection. The unsupported outer edges of the flange were found to be most responsive whereas the inner conical section where the mortar is attached was quite rigid. The high dynamic responsiveness of the flange indicates that this section would be the most susceptible to crack formation and growth.

Despite the physical complexity of this structure, a dynamic model for the baseplate was determined by test and then verified with a simple analytical finite element representation. This model can now serve as a blueprint to predict the dynamic behavior of these structures. Acceptance criteria based on these results can be developed for this structure, which can improve the accuracy of the hardware inspection while reducing the time required to complete such an inspection.

A suggestion for future study would be a test similar to the one described here, where the test configuration consisted of the baseplate imbedded in soil as it is during field operation. This would provide some measure of the damping effects on the flange deflection during resonance and give insight into the level of concern these resonances should provoke.

## REFERENCES

1. Ewins, D.J., "Modal Testing: Theory and Practice," Research Studies Press Ltd., 1986.
2. Kennedy, C.C., and Pancu, C.D.P., "Use of Vectors in Vibration Measurement and Analysis," *Journal of Aeronautical Sciences*, 14 (11), 1947.
3. Lewis, R.C., and Wrisley, D.L., "A System for the Excitation of Pure Natural Modes of Complex Structures," *Journal of Aeronautical Sciences*, 17 (11) 1950, pp. 705-722.
4. Stahle, C.V., "Modal Test Methods and Applications," *Journal of Environmental Sciences*, Jan./Feb. 1973, p. 4.
5. Klosterman, A.L., "Modal Surveys of Weakly Coupled Systems," AE Paper No. 760876, Nov. 1976.
6. Richardson, M., and Potter, R., "Identification of Modal Properties of an Elastic Structure From Measured Transfer Function Data," Instrument Society of America, ISA ASI 74250, 1974, pp. 239-246.
7. Døssing, O., Structural Testing: Part II, Brüel and Kjaer, Naerum, Denmark, p. 22, 1988.

# **Dynamic Response of Overwrapped Composite Gun Tubes Subjected to a Moving Internal Pressure**

Jerome Tzeng and David Hopkins  
U.S. Army Research Laboratory  
Weapons Technology Directorate  
Aberdeen Proving Ground, MD 21005-5066

Rodney Hubbard  
U.S. Naval Surface Warfare Center  
Dahlgren, VA 22448

## **ABSTRACT**

The dynamic response of a overwrapped composite gun tube subjected to a moving pressure front is investigated. The effect of a stress wave in the wall of the gun tube is modeled using both closed-form analytic and finite element methods. Results indicate that very high amplitude and high frequency strains are induced in the tube at the instant and location of pressure front passage as the velocity of the projectile approaches the fundamental propagation velocity of the axially symmetric flexural wave. The dynamic effects are especially critical on overwrapped composite gun tubes because of the multi-material construction, anisotropy and thermal degradation of material properties, and the design goals inherent in light weight structures applications.

## **INTRODUCTION**

Very high amplitude and high frequency strains develop in a gun tube at the instant and location of projectile passage. This phenomena is commonly referred to as dynamic strain amplification within the ballistic community. It is caused by resonance as the moving pressure front approaches a critical propagation velocity of the axially symmetric flexural waves in the tube. The dynamic response of a gun tube subjected to moving pressure loads has been investigated by Taylor (1942) [1], Jones and Bhuta (1964) [2], Tang (1965) [3], and Reismann (1965) [4]. More recently, Simkins (1987) [5] investigated the response of flexural waves in constant cross-section tank gun tubes. Evidence of dynamic strain amplification in the 120 mm tank guns has been observed. Hopkins (1991) [6] used the finite element method to study the dynamic strain response in more realistic gun tube geometries subjected to a moving pressure front for which analytic solutions are not easily available. Currently, research of the

dynamic strain effect in gun tubes has been limited to tubes made of isotropic material constructions. In this paper, the dynamic response in an overwrapped composite tube with a steel liner is investigated. The results are applicable to light weight composite cylinder designs such as gun tubes and high pressure piping systems .

This dynamic strain effect is especially critical for overwrapped composite gun tubes which are designed to achieve enhanced performance with relatively light weight. From a design point of view, the weight savings in general decreases the rigidity and inertia of the tubes under dynamic loads. These effects are especially critical for thin-wall cylinders. Also, the response at the interface between the composite overwrap and steel liner becomes very important. The shear properties and tensile peel strength at this interface are relatively low due to poor adhesion between these materials. The stress and strain levels due to dynamic strain amplification can be two to three times higher than those attained under static loading conditions. This amplification is due to local shell bending caused by the pressure discontinuity as it travels down the tube. The deformation due to shell bending also leads to very high axial and transverse shear stresses. The transverse shear stress magnitude is critical since the shear strength of composites are generally much lower than the shear strength of metals. The dynamic cyclic strains may lead to fatigue failure of the composite materials resulting in dynamic fracture of the overwrapped tube.

## ANALYSIS

In this section, the dynamic response of a composite overwrapped gun tube subjected to a moving pressure load is investigated using both closed-form analytic and finite element methods. The critical velocity at which resonance occurs is dependent upon the specific tube geometry and material properties. Except for simple geometries, it is not possible to obtain a closed-form expression for the critical velocity as a function of these parameters. As a first approximation though, Love's thin shell theory can be used to derive a closed-form expression for the critical velocity. This is because predicted values of the critical velocity based on thin-shell theory are reasonably accurate when compared with both experimentally measured values as well as values obtained using finite element methods. A rule-of-mixture approach for determining appropriate material properties is applied to simplify the calculation procedure for a multi-material construction. The finite element solution is obtained using a version of the DYNA2D [7] hydrocode which has been modified to allow accurate modeling of the moving pressure front. This approach allows modeling both the moving pressure front and the composite cylinder geometry in sufficient detail to simulate the actual loading conditions.

### Critical Velocity

The critical velocity of a flexural wave in a cylindrical tube can be obtained from Love's thin shell theory. Although some assumptions of thin shell theory are not strictly valid for the gun tube which is thick in geometry, the predicted critical velocity does provide a good estimation of the measured critical velocity near the

muzzle. Additionally, the closed-form solution is very valuable in illustrating and understanding the important parameters which determine the dynamic response of the cylinder. These results can be compared with the critical velocity values obtained using finite element techniques.

Consider a thin orthotropic cylinder of radius  $R$  subjected to a transient and an axisymmetric radial load, e.g. a moving internal pressure  $P$ . Figure 1 shows the geometry, coordinate system, and pressure loading condition being considered. The governing equation derived from the conservation of momentum principle for this model includes a moving internal pressure front, expressed as Heaviside step function, is

$$m \frac{\partial^2 W}{\partial t^2} + D_x \frac{\partial^4 W}{\partial x^4} + \frac{12(1-\nu_{\theta x} \nu_{x\theta})}{h^2 R^2} D_\theta W = P (1-H(x-Vt)) \quad (1)$$

where  $W$  is the radial displacement, dependent upon time,  $t$ , and axial position coordinate,  $x$ ,  $m$  is the mass which is equal to  $\rho h$ ,  $\rho$  is the density of shell material,  $h$  is the thickness of the shell,  $P$  is the internal pressure, and  $V$  is the pressure front velocity which is assumed constant. The shell bending stiffness in the axial and circumferential directions are given by the expressions in Eq. (2) and Eq. (3), respectively.

$$D_x = \frac{E_x h^3}{12(1-\nu_{\theta x} \nu_{x\theta})} \quad (2)$$

$$D_\theta = \frac{E_\theta h^3}{12(1-\nu_{\theta x} \nu_{x\theta})} \quad (3)$$

where  $E_x$  and  $E_\theta$  are the effective (smeared) elastic moduli, and  $\nu_{x\theta}$  and  $\nu_{\theta x}$  are the effective Poisson's ratios of the composite material in the axial and circumferential directions, respectively. For a composite tube with cross-ply laminate construction, the shell bending stiffness is different in the axial and circumferential directions and is a function of the axial-to-hoop layer ratio.

The loading function,  $P(1-H(x-Vt))$  in Eq. (1), represents the internal pressure front traveling in the axial direction with constant velocity  $V$ .  $H(x-Vt)$  is the Heaviside step function. Accordingly,

$$\begin{aligned} P(1-H(x-Vt)) &= 0 & \text{when } x > Vt \\ &= P & \text{when } x \leq Vt \end{aligned} \quad (4)$$

The critical velocity for an orthotropic cylindrical shell, derived from the characteristic function obtained from Eq. (1), is given by

$$V_{cr,comp}^2 = \sqrt{\frac{1}{3(1-\nu_{\theta x}\nu_{x\theta})}} \left(\frac{h}{R}\right) \left(\frac{\sqrt{E_{\theta}E_x}}{\rho}\right) \quad (5)$$

Equation (5) shows that the critical velocity of an orthotropic cylinder subjected to a moving pressure front is a function of the geometry, density, Poisson ratios, and elastic moduli. The critical velocity increases when either of the elastic moduli increase as well as when the shell thickness to radius ratio increases. From a design point-of-view, a tube constructed with high stiffness and lightweight materials is preferred for dynamic loading conditions. However, Equation 5 indicates that a larger wall thickness is required for the tube geometry when a high velocity pressure front is present. It also shows that a cylinder with isotropic properties (e.g.  $E_{\theta} = E_x$ ) will have the highest critical velocity if all other material properties as well as the geometry remain the same.

For an isotropic cylinder, Equation 1 reduces to

$$m \frac{\partial^2 W}{\partial t^2} + D \frac{\partial^4 W}{\partial x^4} + \frac{Eh}{R^2} W = P(1-H(x-Vt)) \quad (6)$$

where D, the bending stiffness of shell, is given by

$$D = \frac{Eh^3}{12(1-\nu^2)} \quad (7)$$

The critical velocity at which resonance occurs in this isotropic tube is therefore given by

$$V_{cr,steel}^2 = \sqrt{\frac{1}{3(1-\nu^2)}} \left(\frac{h}{R}\right) \left(\frac{E}{\rho}\right) \quad (8)$$

The critical velocity of an isotropic cylinder, Eq. (8), is thus seen to be very similar to the critical velocity of an orthotropic cylinder, Eq. (5). As discussed previously, it is important from a design point-of-view to be able to estimate the critical velocity of gun tube constructed from various materials.

### Finite Element Solution

The closed-form solution described in the previous section can be applied accurately to a cylindrical shell under the assumption of infinite length. For a finite

length cylinder with varying cross-sectional area along its length and multi-material construction, the finite element method allows a more expedient and straightforward procedure for determining the critical velocity. DYNA2D [7], a hydrodynamic finite element code, was modified to simulate the moving pressure boundary condition. The solution obtained using DYNA2D is a reduced 3D solution resulting from axisymmetrical conditions of both geometry and loads. Accordingly, the analysis includes both the flexural and shear modes and will approach the exact solution as the mesh discretization increases.

A schematic of the finite element modeling technique is shown in Figure 2. A slideline which allows a dummy projectile to move freely along the axial direction of the cylinder is included in the finite element model of the cylinder. The instantaneous location of the pressure front is then easily determined by tracking the location of the rear face of the dummy projectile. In order to accurately capture the oscillatory dynamic response of the tube, the computation utilizes a very fine time interval ( $\sim 10^{-6}$  sec). This time interval also allows the pressure to slowly ramp to maximum value as individual element surfaces are uncovered by the moving projectile. The artificial numerical stress oscillations due to the sudden application of the pressure boundary condition on an element face are minimized. Hence, these numerical oscillations do not adversely affect the solution. While for the cases examined in this study the projectile velocity was held constant, this methodology can also be used to simulate the effect of an accelerating projectile if desired.

Since the composite tube has a laminated construction, ideally a ply-by-ply model will yield the best result and accuracy. However, this would dictate the use of many thousands of elements in the finite element model. This level of detail, coupled with the very short time step interval required for a dynamic analysis, would lead to an unreasonably long computational time. Also, an additional side effect of taking many millions of time steps would be to induce numerical instabilities due to round-off errors. To avoid these constraints, the size of finite element model was limited so that it can be analyzed within a reasonable computational time. For thick composite analysis, it is standard practice to use smeared properties for the composite laminate. These properties, which are representative of the unique layup construction of the tube, were calculated using a model developed by Alexander, Tzeng, Drysdale, and Burns (1994) [8]. The smeared property approach allows a single finite element to contain about 10 layers through the thickness of laminate. Accordingly, the size of the finite element model can be greatly reduced. The smeared properties for a composite tube composed of 25% axial (x-direction) and 75% hoop ( $\theta$ -direction) plies are shown in Figure 3. The properties are calculated based on the use of an IM7 graphite / 8551-7 epoxy composite. The unit ply properties are also given in this figure.

The cylindrical geometry used in this analysis is 100 inches long with a constant wall thickness. The steel liner and composite overwrap are 0.05 inch and 0.15 inch thick, respectively. The cylinder is equally divided into 200 elements along the axial direction and 6 elements through the thickness. These elements are divided into 2 elements representing the steel liner with 4 elements representing the composite overwrap. In all, this model utilizes 1,200 elements. The moving internal pressure is 6,000 psi. Two pressure front velocities, a sub-critical velocity of 2,500 ft/sec (Case 1)

and a super-critical velocity 3,500 ft/sec (Case 2) were performed to illustrate the dynamic effects .

The total time for the projectile to traverse the tube was 3.33 msec and 2.43 msec for Cases 1 and 2, respectively. The time increment used in the analysis was on the order of 1  $\mu$ sec , therefore, approximately 3,500-4,000 time steps were needed for each analysis. The finite element model including the composite cylinder and the dummy projectile are shown in Figures 4 and 5 at two different instants in time. Finally, because an axisymmetric model was employed, only one-half of the cylinder is shown. In Figure 4, the dummy projectile is shown at its initial position. The projectile is then given an initial velocity which is held constant throughout the analysis. Figure 5 shows the projectile when it has traveled 20 inches from the initial position. A fringe plot of the radial displacement in the neighborhood of the projectile at this specific instant is shown in Figure 6. The fringe pattern shows the stress oscillation due to induced bending boundary layer stresses in the wall of cylinder as it is subjected to a moving pressure front. The maximum displacement is located very close to the base of projectile. This corresponds the location of the pressure loading discontinuity. The displacement then decreases with increasing axial distance from the location of the pressure front discontinuity. The deformation is transient and cyclic with time and position.

The above way of presenting the data shows the spatial variation of the displacement, and consequently strain and stress, fields. This view corresponds to what an observer traveling with the projectile as it traverses the cylinder would observe. An alternative view is to pick a fixed location on the tube and observe the change in displacement as the projectile approaches this position and then passes it, e.g. a time history plot for a given location. This corresponds to what is measured with strain gauges or accelerometers attached to the tube. The radial locations at which various displacement and stress components are examined in this report are shown in Figure 7. These radial locations represent positions at which these displacement and stress components attain their greatest values as discussed in detail in the following. Since the tube is subjected to an internal pressure, the maximum hoop stress occurs at the inner surface of the liner. As the pressure front passes a given axial location, a local axisymmetric bending occurs in the wall of the tube. The maximum axial stress will thus occur at the innermost surface of the liner and the outermost surface of the composite. The maximum shear stress associated with this bending is located at the neutral axis of the cross section. Accordingly, the critical value of the shear stress in the transverse direction of composite laminate occurs near the interface of the liner and the composite overwrap.

Figures 8-13 plot the various displacement and stress components vs. time at these locations for the cylinder of Design I. The radial displacement at the innermost region of the composite (Figure 8) shows a dramatic difference in the magnitude of peak displacement as well as in temporal behavior of the oscillations as the projectile velocity changes, Case 1 vs Case 2. Prior to the projectile arriving, the cylinder at these observed locations are basically undeformed. The small oscillations that occur just before projectile arrival are real and represent stress oscillations due to the moving pressure front. Similar behavior is predicted by thin wall shell theory. It is seen that at the instant the projectile passes, the radial displacement undergoes a rapid increase.

However, for sufficiently low velocities, similar to Case 1, the displacements and stresses are still close to what would be predicted based upon Lamé's equations for a static internal pressure loading. This is not the case though for velocities near or above the critical velocity shown in Figure 8, Case 2. A very large radial displacement occurs for this case where the projectile velocity is 3,500 ft/sec. In fact, this velocity exceeds the critical velocity of the overwrapped composite tube. The peak magnitude of the radial displacement is seen to be about 1.5 times the peak magnitude of the radial displacement of Case 1 where the velocity is only 2,500 ft/sec. As the projectile moves further away from this axial location, the radial displacement approaches the same magnitude ( $\sim 7.5 \times 10^{-3}$  inch) as would be predicted by a static analysis of a pressurized tube. This is shown to be true for both Case 1 and Case 2. It is very important to realize that because the velocity for Case 2 is above the critical velocity, the peak radial displacement value is actually less than the peak value that would be obtained if the projectile had accelerated from 2,500 ft/sec to 3,500 ft/sec since in this scenario, the projectile would have passed through the critical velocity at some axial location. This would have resulted in a resonant condition at that location and the peak radial displacement would have been at least twice the Lamé prediction. In fact, for linear elastic behavior, the magnitude of dynamic response would theoretically have been infinitely large. In the analysis, the material response was limited by the internal damping of the material coupled with its behavior after yield.

Figure 9 shows the smeared hoop stress induced at the innermost region of composite. The composite overwrap is constructed with 75% hoop and 25% axial plies and the smeared hoop stress presents the average value for the laminate construction. A simple rule-of-mixtures calculation indicates that the peak unsmeared fiber stress in the hoop direction is about 86 ksi for the low velocity case and 135 ksi for the high velocity case. The effect of resonance due to a moving pressure front is again clearly indicated. Figure 10 shows the smeared axial stress at the outermost radius of composite overwrap. The axial stress mainly results from the shell bending along the axial direction. The computed fiber stress is approximately 45 ksi and 100 ksi for the low and high velocity cases, respectively based on a rule-of-mixtures approach. Figure 11 shows the shear stress,  $\tau_{rz}$  at the innermost radius of composite overwrap which is near the neutral axis of the combined steel/composite tube. The shear stress is in the transverse direction of the laminate. The stress levels are 4.3 ksi and 7.0 ksi for the low and high velocity cases, respectively. Considering manufacturing factors and the low adhesion strength at the steel/composite interface, the 7.0 ksi shear stress indicates a low margin of safety factor.

Figures 12 and 13 show the hoop and axial stresses respectively, at the innermost radius of the liner. Both the hoop and axial stresses show the resonance effect for the case of high velocity. These high frequency stress oscillations may not cause immediate failure of the liner since the peak magnitude is well below the failure stress of high quality steel, although the comments concerning the effect of an accelerating projectile as discussed previously must be kept in mind. However, of potentially more importance is the effect of these high frequency stress oscillations upon the fatigue behavior of the gun and the effect this may have in reducing the life cycle of the cylinder due to fatigue of either the liner or composite overwrap materials.

The use of a thicker steel liner also leads to a different value for the critical velocity. It is reasonable to estimate the critical velocity approximately using the thin-shell solution derived previously for a mono material design. The critical velocity is proportional to the modulus-to-density ratio if the geometry is kept to be the same. However, the critical velocity for a multi-material construction such as a steel liner wrapped with composite can no longer easily be predicted using the equation (5) and (8). A closed form solution can be obtained by solving the boundary value problem from thick shell theory. Other approach will be the finite element solution as presented in this investigation.

## CONCLUSION

The dynamic analysis of an overwrapped composite tube illustrates high magnitude strains and stresses develop in the tube at the rear face of the projectile as the projectile traverses the length of the tube. The high magnitudes are caused by a resonance condition of the flexural wave propagation with the moving pressure front velocity. This effect is commonly referred to as dynamic strain amplification. These results are important in highlighting the potential shortcomings of traditional static analysis commonly used in cylinder design. This dynamic strain effect can potentially cause damage and lead to a shortened life cycle of cylinder. The dynamic effect is particularly critical for the lightweight overwrapped composite gun barrels because of the low shear stress strength at the interface of multi-material construction and the tendency of thermal degradation of polymer composite materials to further reduce these strength levels. Finally, the goal of achieving a lightweight design leads to tubes with thinner wall thicknesses at precisely the axial location where the projectile velocity and thus the dynamic strain amplification effect will be the greatest: the muzzle. In order to arrive at a safe, optimum design then, this effect must be included. This paper illustrates one approach to analyzing proposed designs using finite element methods and including the effect of a moving pressure front.

## REFERENCES

1. Taylor, G. I., "Strains in a Gun Barrel Near the Driving Barrel of a Moving Projectile," A.C. 1851/Gn. 104, U.K. Ministry of Supply, London, England, March 1942.
2. Jones, J. P. and Bhuta, P. G., "Response of Cylindrical Shell to Moving Loads", Journal of Applied Mechanics, Vol.31, Trans, ASME, Vol. 86, Series E, March 1964, pp. 105-111.
3. Tang, S., "Dynamic Response of a Tube Under Moving Pressure," Journal of the Engineering Mechanics Division Proceedings of the ASCE, October 1965, pp. 97-122.

4. Reismann, H., "Response of a Prestressed Cylindrical Shell to Moving Pressure Load, Development in Mechanics," Solid Mechanics - Proceedings of the Eighth Midwestern Mechanics Conference, Pergamon Press, Part II, Vol. 2, 1965, pp. 349-363.
5. Simkins, T. E., "Response of Flexural Waves in Gun Tubes," Tech. Report ARCCB-TR-87008, US Army ARDEC, Benet Weapons Laboratory, Watervliet, NY, July, 1987.
6. Hopkins, D. A., "Predicting Dynamic Strain Amplification by Coupling a Finite Element Structural Analysis Code with a Gun Interior Ballistic Code," BRL-TR-3269, U. S. Army Ballistic Research Laboratory, Aberdeen Proving Ground, Maryland, September, 1991.
7. Hallquist, J. O., "User Manual for DYNA2D - An Explicit Two-dimensional Hydrodynamic Finite Element Code with Interactive Rezoning and Graphical Display", Lawrence Livermore National Laboratory, 1987.
8. Alexander, A., Tzeng, J. T., Drysdale W. H., and Bruce B. P., "Effective Properties of 3D Laminated Composites for Finite Element Applications," Proceedings of 1994 International Conference of Computer in Engineering, Vol. 2, ASME, 1994, pp. 507-518.

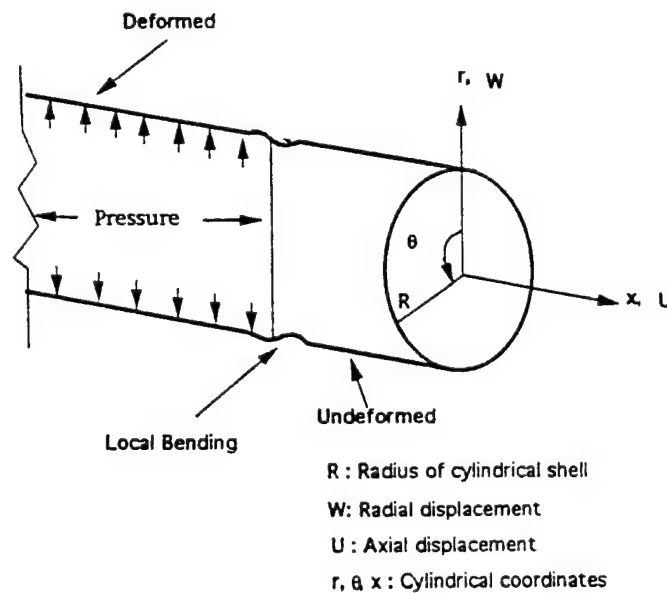


Figure 1. A cylinder subjected to a moving internal pressure

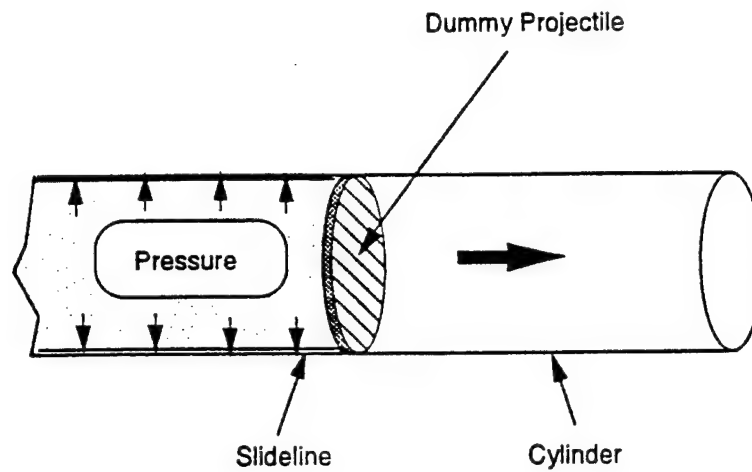


Figure 2: Finite element model of launching a projectile

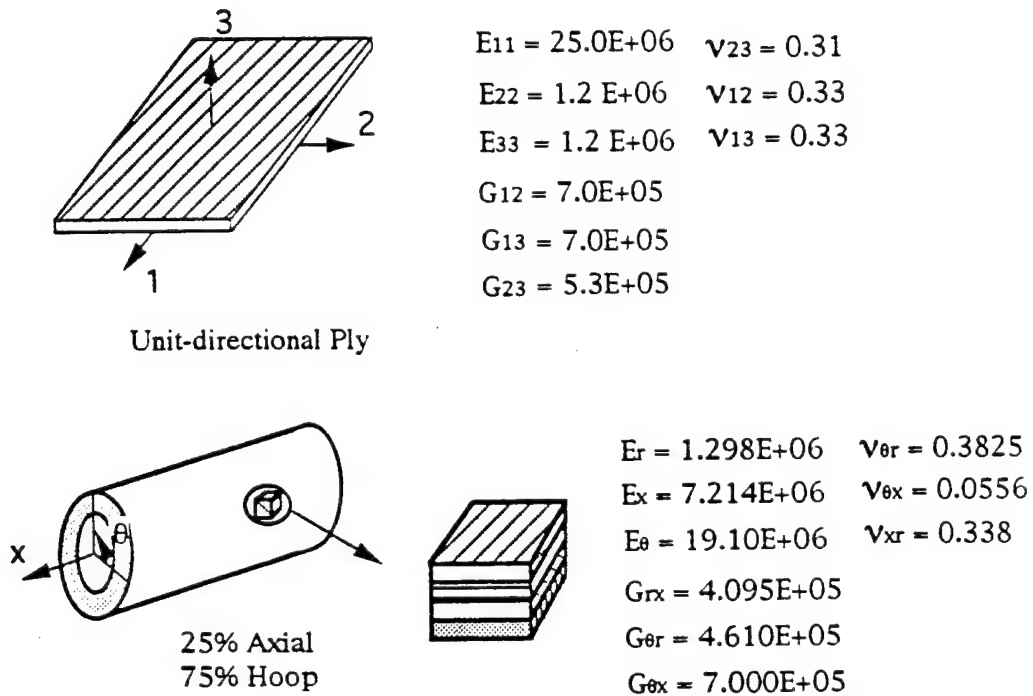


Figure 3: Smeared properties of the composite tube

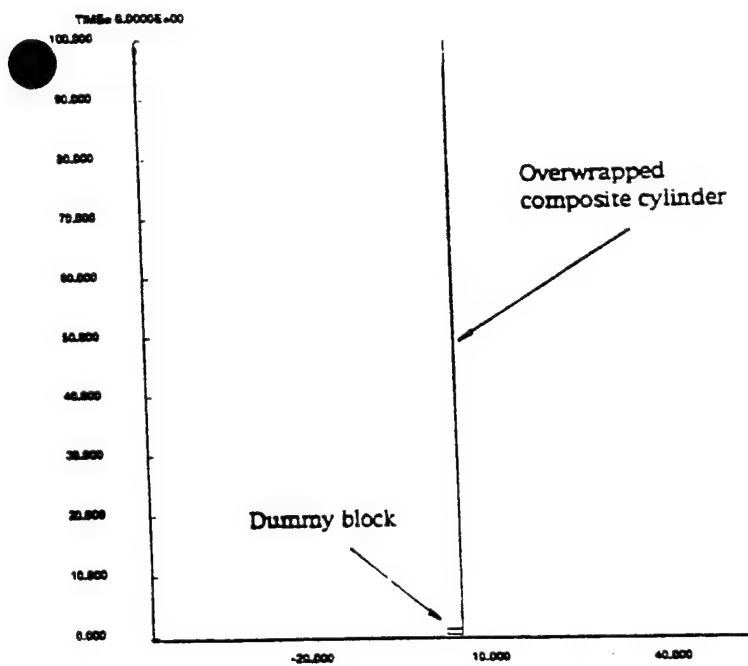


Figure 4: Finite element model with the dummy block at the initial position.

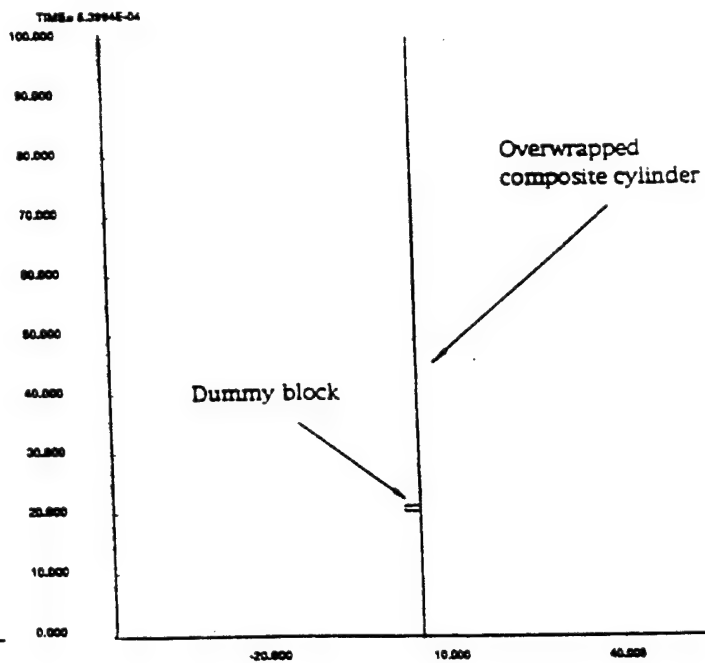


Figure 5: Finite element model with the dummy block at Time=0.53994 E-3 sec)

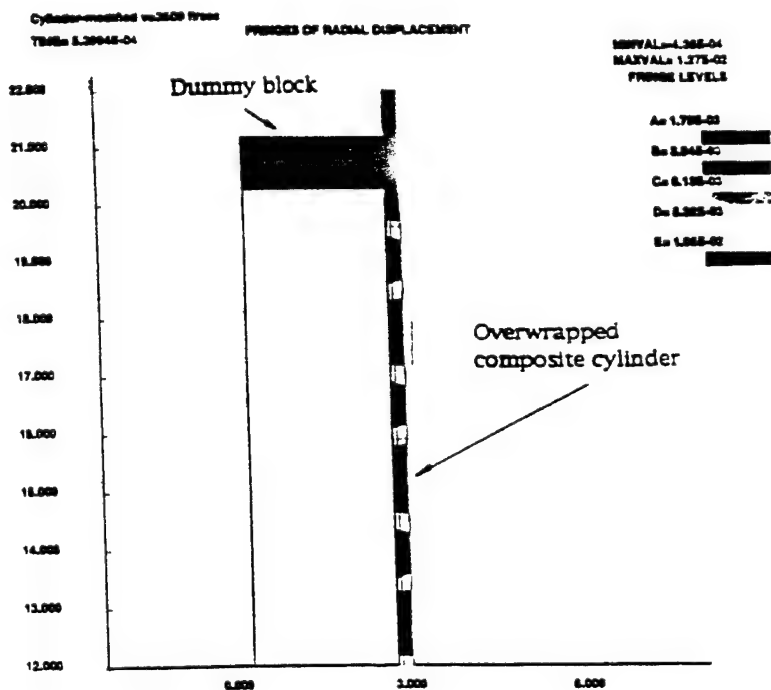


Figure 6: Oscillation of radial displacement at the vicinity of pressure front

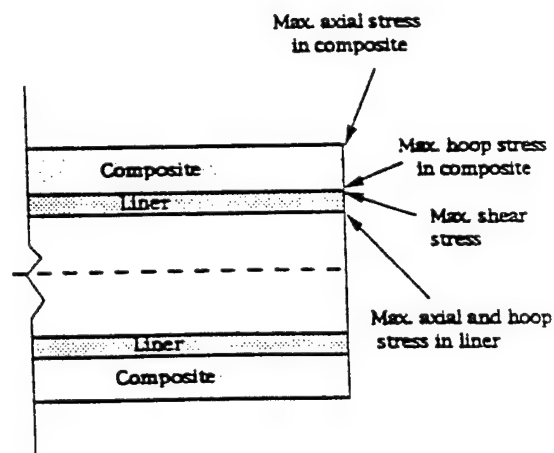


Figure 7 : Locations of the maximum stress components

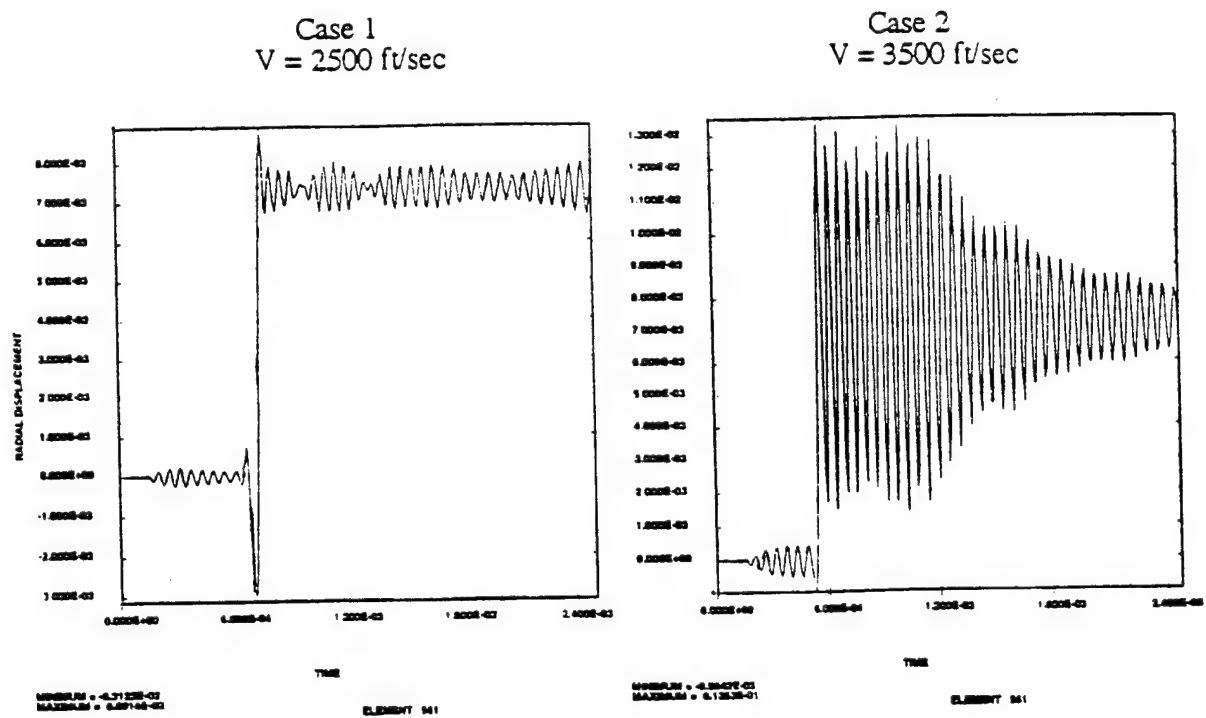


Figure 8 : Radial displacement in the innermost region of the composite overwrap

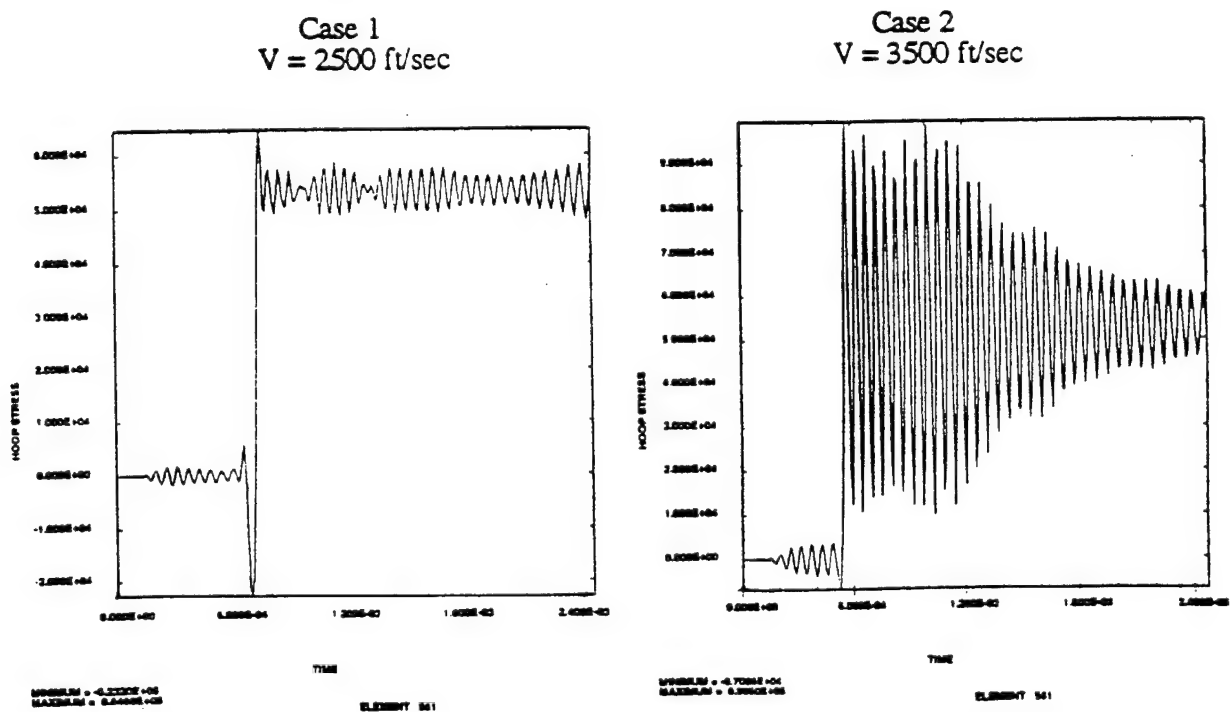


Figure 9 : Hoop stress in the innermost region of the composite overwrap

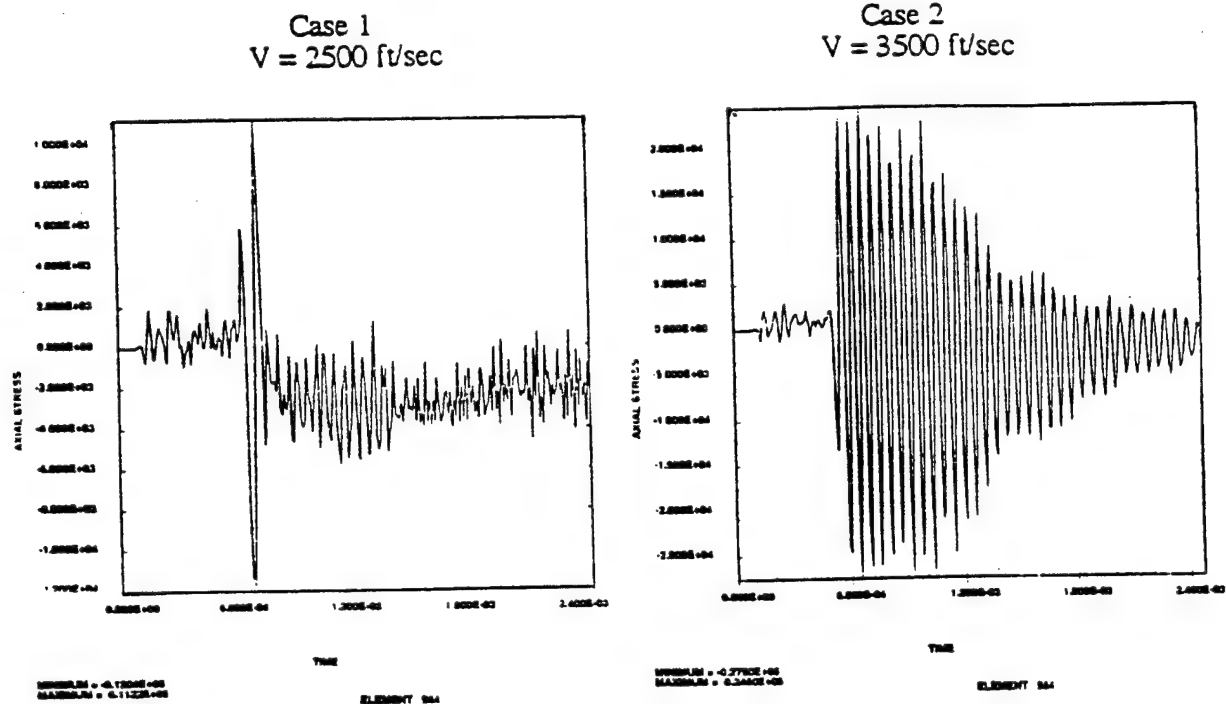


Figure 10 : Axial stress in the outermost region of the composite overwrap

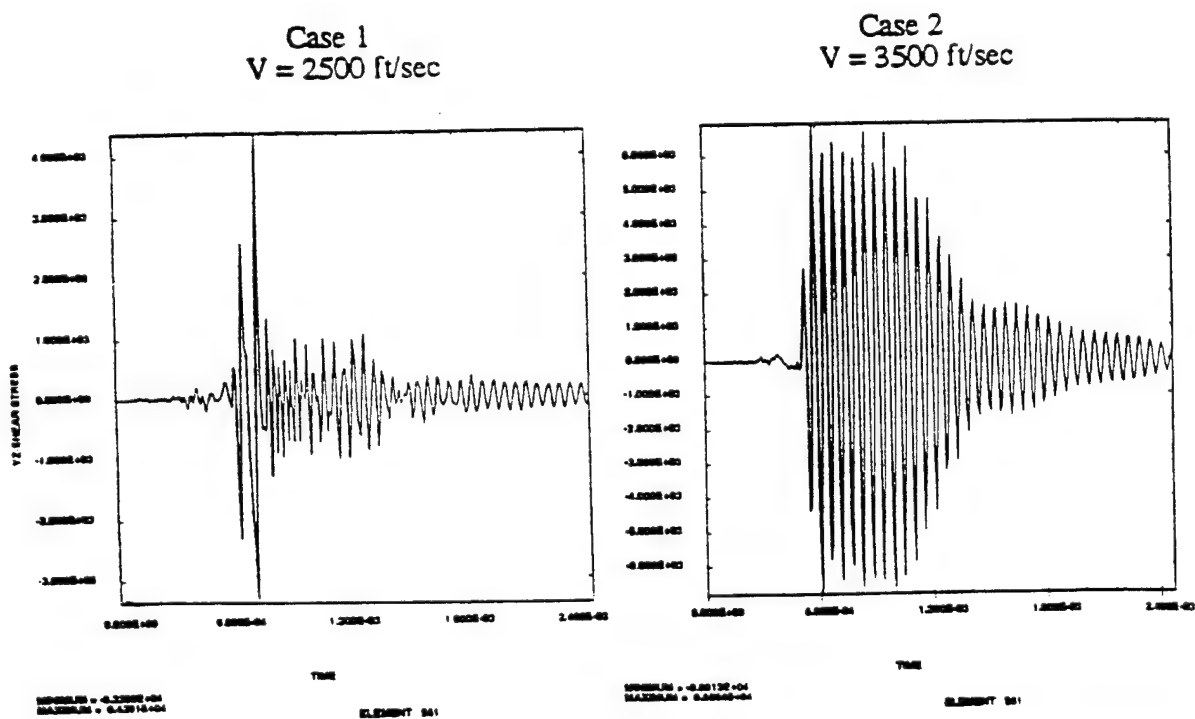


Figure 11 : Interlaminar shear stress in the innermost region of the composite overwrap

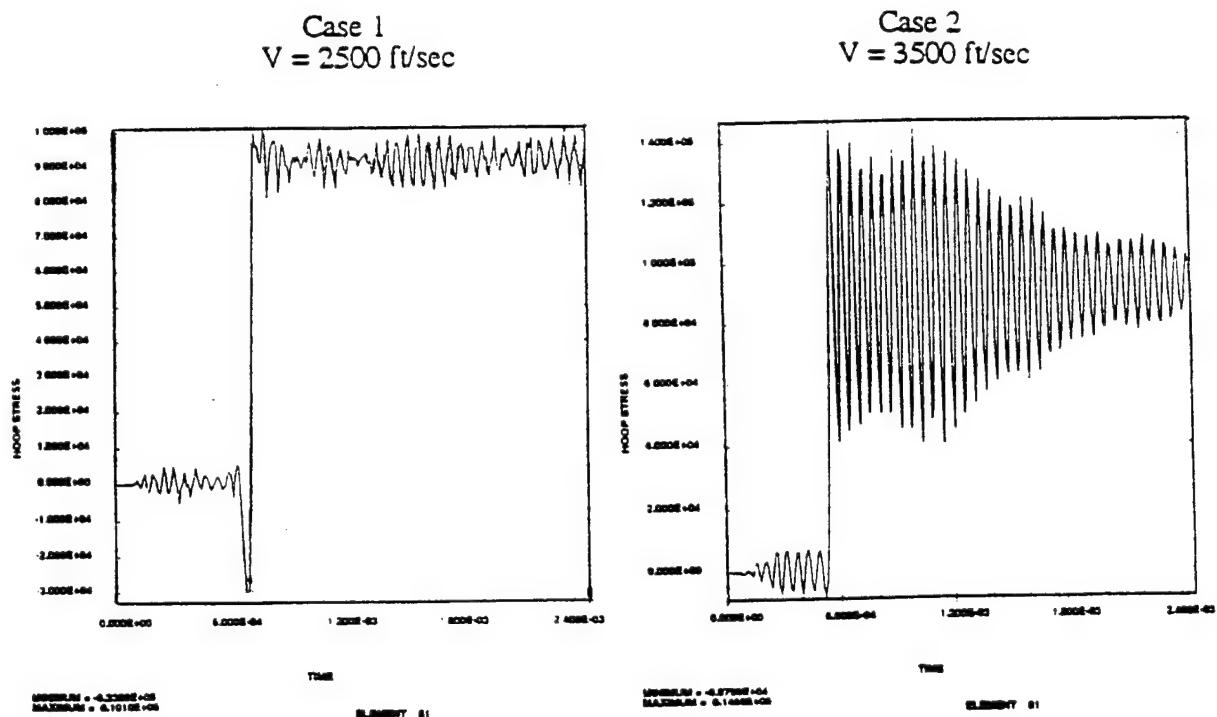


Figure 12 : Hoop stress in the innermost region of the steel liner

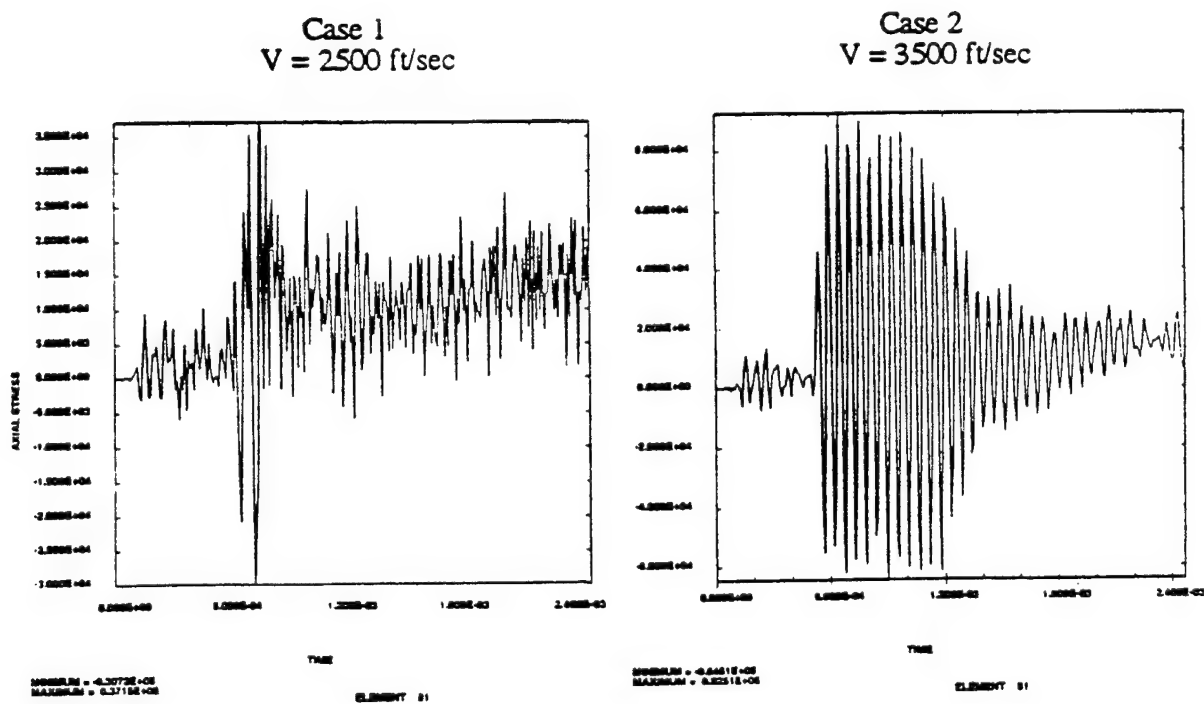


Figure 13 : Axial stress in the innermost region of the steel liner

KATHE

**TITLE:** Design of Passive Vibration Absorber to Reduce Terrain Induced Gun Barrel Vibration in the Frequency Domain

Eric L. Kathe  
US Army Armament Research, Development and Engineering Center  
Close Combat Armaments Center  
Benét Laboratories  
Watervliet Arsenal  
Watervliet, NY

**ABSTRACT:**

The purpose of this paper is to present an applied methodology for the optimal design of passive vibration absorbers to reduce terrain induced vibrations of tank cannon. The method utilizes a finite element model of the cannon formulated using the Euler-Bernoulli transverse beam approximation. This model is then transformed to the Laplace "s" domain (transfer function form) using the MATLAB® software package. Optimization of the design is achieved by assigning a scalar cost function to the frequency response of the modified barrel, to provide a metric for minimization in the design parameter space. The results indicate that the peak amplitude of the frequency response of a 1,500 Kg barrel may be cut in half by an appropriately tuned 20 Kg absorber located at the muzzle. Further, sensitivity of the design to parametric variation and modeling uncertainty is significantly reduced with Rayleigh stiffness proportional damping of the absorber in the range of  $0.02 \frac{N/(m/s)}{N/m}$ .

**BIOGRAPHY:** Eric L. Kathe

**PRESENT ASSIGNMENT:** Mechanical Engineer, Technology Division, Benét Laboratories, Watervliet Arsenal, NY.

**DEGREES HELD:** B.S. and M.S., Mechanical Engineering, Rensselaer Polytechnic Institute, Troy, NY

## Design of Passive Vibration Absorber to Reduce Terrain Induced Gun Barrel Vibration in the Frequency Domain

Eric L. Kathe<sup>†</sup>

US Army Armament Research, Development and Engineering Center  
Close Combat Armaments Center  
Benét Laboratories  
Watervliet Arsenal  
Watervliet, NY

### 1. INTRODUCTION

The purpose of this paper is to develop an applied methodology for the optimal design of passive vibration absorbers to reduce terrain induced vibrations of tank cannon. It is anticipated that this will improve the accuracy of the weapon by reducing variations in the initial conditions of the gun barrel at shot start.

Application of vibration absorbers to beams entails coupling a damped mass-spring system to the beam at the locations of greatest vibration activity. (Vibration absorbers [1] are also commonly referred to as dynamic dampers [2], vibration neutralizers [3], and tuned-mass-dampers, MTDs [4, 5].)<sup>‡</sup> This achieves two main benefits. First, the addition of the absorber may reduce the receptance of the modified beam to certain frequency bands of a disturbance force —effectively *rejecting* the disturbance energy. Second, the absorber provides the opportunity to enhance the dissipation of vibrational energy via the damping of the absorber. This may play a significant role if the damping of the unmodified structure is limited and sustained external excitement is expected, but it generally has less impact on the design. Absorbers also present the undesirable possibility of increased receptance at certain frequency bands.

The method presented in this paper utilizes an Euler-Bernoulli finite element technique to generate the second-order equations of motion of the gun barrel as a non-uniform beam, with subsequent conversion to the first-order state-space domain [6]. This model is then transformed to the Laplace “s” domain (transfer function form) using the MATLAB<sup>®</sup> software package [7, 8, 9]. (The MathWorks, Inc. / 24 Prime Park Way / Natick, MA 01760-1500.) In this domain, the frequency

---

<sup>†</sup> The author would like to thank Dr. Andrew Lemnios —Rensselaer Polytechnic Institute, Troy, NY— and Dr. Ronald Gast, Dr. Ronald Racicot, and Dr. Patrick Vottis —U. S. Army, Benét Laboratories, Watervliet Arsenal, NY— for their assistance and insightful suggestions throughout this effort.

<sup>‡</sup> In many engineering contexts, these terms may become misnomers and create confusion [3]. The design of such mechanisms may emphasize the dissipation of energy via damping or the redistribution of energy within the frequency spectrum. For this application, the absorption of energy —into other frequency bands— and the dissipation of energy by the damping element are both superseded by the *rejection* of the energy effected by reshaping the frequency response function.

response of the system is revealed via Bode analysis. Optimization of the design is achieved by assigning a scalar cost function to the frequency response function of the modified barrel, to provide a metric for minimization in the design parameter space of the vibration absorber. This provides an applied approach to the effective design of vibration absorbers. It forms a middle ground between mere numerical simulation and analytic formulation of the problem.

This paper will document the detailed development of the dynamic modeling and design of vibration absorbers for application to the XM291 gun system as an elastic beam. All explicit MATLAB® functions, in addition to the previously written m-files, are enclosed by angle brackets to distinguish them from regular text.

## 2. THE DYNAMIC MODEL

This report will leverage the software developments of a previous effort to formulate the dynamic model of the gun system [6].

### 2.1 The Barrel

The means chosen to dynamically model the barrel is the finite element method. This application utilizes the Euler-Bernoulli beam approximation and Hermite-cubic interpolation functions to form the inertial and stiffness matrices of the undamped second-order equations of motion. This is achieved by approximating the continuous non-uniform beam as an assemblage of a finite number of discrete elements. Within each discrete element, the interpolation functions are used to approximate the interior deformation. At the boundary between two adjacent elements, called a node, continuity of lateral displacement and slope are imposed. When assembled, the resulting finite element model dynamics, governed solely by the node states, closely approximates the dynamics of the non-uniform beam.

XM291 Profile &amp; Non beam Masses Versus Length in Meters, (Total Non beam Mass of 1442 Kg, or 3178 lbm)

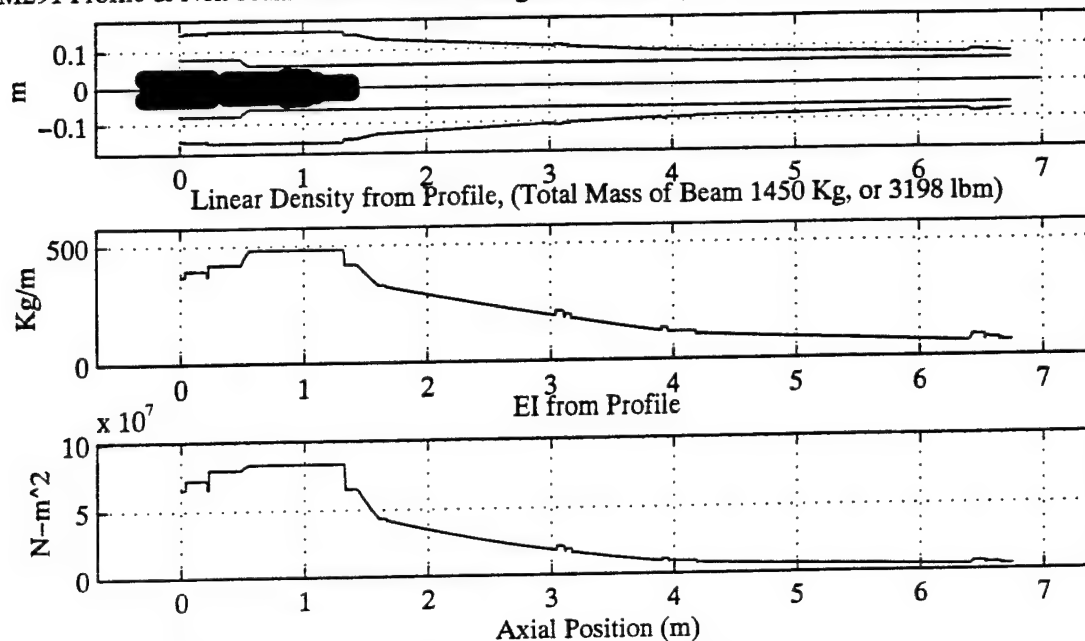


Figure 1 XM291 Geometry and Material Properties Data.

The geometry and material properties data for the XM291 is read in by the m-file `<geomf_XM291.m>` [6] and is shown in Figure 1. The upper plot depicts the inner and outer radii of the barrel with respect to the axial position. Within the confines of the inner diameter of the barrel, the distribution of the extraneous mass of components that are attached to the barrel is shown. The plot reveals that this barrel is configured with its breech and mount hardware, but not the thermal shrouds, bore evacuator, or muzzle reference mount. For clarification, the total mass of the extraneous attached hardware is shown in the title. The middle plot indicates the linear density of the barrel alone. (The purpose of segregating the inertia of the barrel from the mounted hardware is to maintain visual validation of the plots; a plot of the combined linear density could obscure the distinction between a valid plot and an erroneous one.) The final plot reveals the axial distribution of cross-sectional stiffness. These input vectors are used to formulate the finite element matrices.

For this model, the barrel will be broken-up into seven elements. This will provide ample accuracy of the model, in the frequency range of the first few flexible modes. As was shown in [6], the frequency response is greatest in the lowest modes of vibration, where the finite element model most accurately mimics the vibration of the underlying distributed parameter system.

To form the finite element mesh, three locations are specified as imposed node locations. These imposed nodes specify the locations along the barrel where external constraints may conveniently be incorporated into the dynamic model. The three external constraints will be located at the elevation mechanism location, the trunnion bearing location, and the location of the vibration absorber (0.540m, 0.988m, and 6.544m respectively). For convenience, the absorber will be located at the muzzle reference system mount, as it is a convenient location to test the design concept. In general, the location of the absorber would be a free parameter in its design. The remaining three

node locations are placed by the file <fem\_mesh.m> [6]. (For seven elements, the beam must be modeled by eight nodes. This includes the two free-ends of the beam, and the three imposed node locations, leaving three nodes to be placed by the mesh as shown in Figure 2.)

The result of the finite element modeling of the barrel realized by <fem\_form.m> [6] consists of a sixteen-by-sixteen inertial matrix and cross-sectional stiffness matrix. A damping matrix, that introduces a force opposite in direction and proportional to the velocity of the deformations, is constructed via the Rayleigh proportional damping approximation as realized by the file <fem\_lump.m> [6]. The inertial proportional damping coefficient,  $\alpha$ , is set to zero while the stiffness coefficient,  $\beta$ , is set to  $0.001 \frac{\text{N/(m/s)}}{\text{N/m}}$ . (These values are a common approximation for steel structures. Experimental measurement of these values is anticipated in a future report.)

## 2.2 Constraint/Mounting of the Barrel

Once the dynamics of the distributed parameter system of the barrel are modeled, they must be constrained by a model of the gun mount. This constraint is essentially applied to the barrel at two locations—the elevation mechanism and the trunnions—and provides constraint forces that are a function of the transverse deflections of the barrel.

Both forces are approximated by a force that is proportional to the lateral deflection of the barrel at the constraint locations, and opposite in direction. Thus the constraints are essentially modeled as springs. (For this analysis, both stiffness are set to  $500,000 \text{ lb}_f/\text{in} \sim 10^8 \text{ N/m}$ .)

Using arguments developed in [6], the stiffness and damping values of the constraints are directly added to the respective diagonal elements of the finite element matrices that correspond to the lateral motion of the constrained node. The implementation of this is also executed by the file <fem\_lump.m>.

This parametric formulation of the barrel constraints is limited; the real structure would require more than two values to accurately model. This approximation results in imprecise boundary conditions on the barrel that has the greatest impact on the lower modes of vibration. However, the model does capture many of the dynamic effects of interest, and may easily be modified to incorporate more advanced constraint approximations—including servo-control dynamics [10].

XM291 Meshing Metric & Node Locations Vs Position

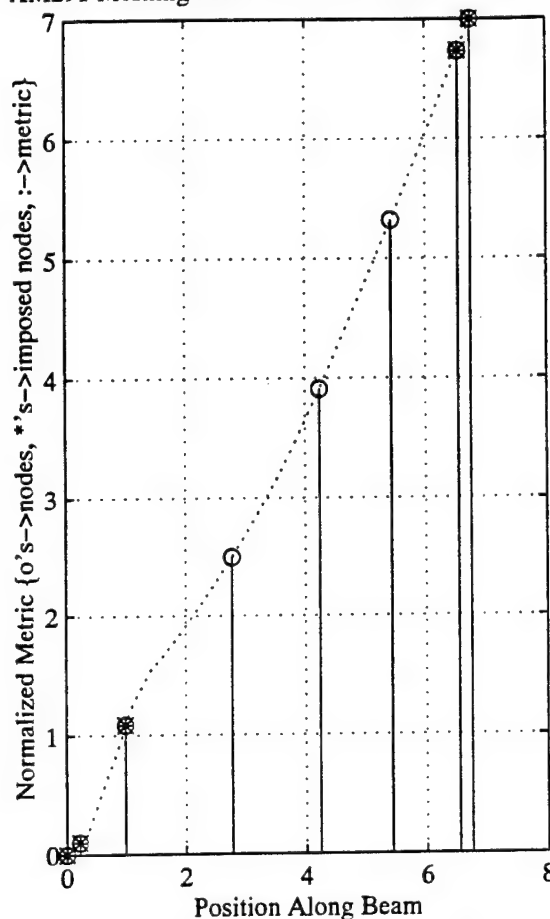


Figure 2 Node Placement by Meshing Metric.

### 2.3 Coupled External Vibration Absorbers

A very interesting dynamic effect can be achieved by coupling an external lumped mass-spring-damper system to structures. The effect of the external mechanism is to attenuate combined system vibration in a relatively narrow band near the operating frequency of the absorber, and to dissipate and disperse steady-state energy across a wider band, if the damping, stiffness, and inertial coefficients are well tuned.

With the inclusion of the absorber, a new *energy storing* degree-of-freedom has been added to the total system. This requires the inclusion of a new generalized coordinate to represent the deflection of the absorber, and its time derivatives, from its equilibrium position. This requirement will increase the size of the system matrices from sixteen-by-sixteen to seventeen-by-seventeen as shown in Figure 3. (The incorporation of the absorber is developed in [6] and implemented by the file <fem\_lump.m>.)

Figure 3 depicts the image of the completed system mass and stiffness matrices of an absorber modified system. (The absorber stiffness, and damping will be optimized later in this report.) The shaded images to the left indicate the relative magnitude of the elements of each matrix. Since the disparity in element magnitude is great, the distinction between small and zero elements may be obscured. To address this issue, the non-zero elements of both matrices, regardless of their magnitude, are revealed to the right using MATLAB's <spy> command [8]. The plots verify the cascading construction of four-by-four elemental matrices, resulting in the diagonally banded system matrices for the sixteen-by-sixteen finite element portion of the matrices. Further, the coupling of the absorber to the lateral generalized coordinate — $q_{13}$  in this case— results in the stiffness elements at  $K_{17,13}$ ,  $K_{13,17}$ , and  $K_{17,17}$ . (Interior modification at  $K_{13,13}$  is also effected by <fem\_lump.m>.) The absorber inertia results in the single element at the lower right-hand corner of the mass matrix,  $M_{17,17}$ .

### 2.4 Equations of Motion

Once the combined system matrices have been formed, the resulting equation of motion is:

$$M\ddot{q} + C_d\dot{q} + Kq = f \quad (1)$$

#### XM291 Absorber Modified Matrices

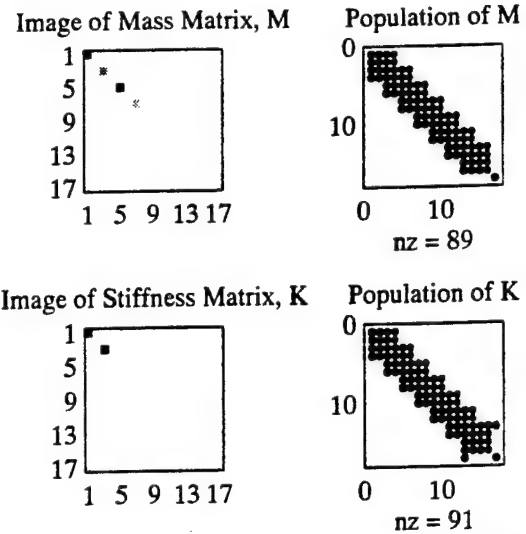


Figure 3 Image of Absorber Modified System Matrices.

where:

- $M$  is the 17 by 17 mass matrix  
 $C_D$  is the 17 by 17 damping matrix  
 $K$  is the 17 by 17 stiffness matrix  
 $\underline{q}$  is the 17 by 1 generalized coordinate vector  
 $\underline{f}$  is the 17 by 1 generalized force vector  
 $\cdot$  denotes differentiation with respect to time

In equation (1),  $M$ ,  $C_D$ , and  $K$  are the seventeen-by-seventeen mass, damping, and stiffness matrices respectively. The generalized coordinate vector,  $\underline{q}$ , and force vector,  $\underline{f}$ , may be related to the nodal displacements and forces as shown in equation (2).

$$\begin{aligned}
 \underline{q} = \begin{bmatrix} q_1 \\ q_2 \\ q_3 \\ q_4 \\ \cdot \\ \cdot \\ \cdot \\ q_{2 \times nn - 1} \\ q_{2 \times nn} \\ q_{2 \times nn + 1} \end{bmatrix} &= \begin{bmatrix} y_1 \\ \theta_1 \\ y_2 \\ \theta_2 \\ \cdot \\ \cdot \\ \cdot \\ y_{nn} \\ \theta_{nn} \\ y_{VA} \end{bmatrix} \quad (a) \\
 \underline{f} = \begin{bmatrix} f_1 \\ f_2 \\ f_3 \\ f_4 \\ \cdot \\ \cdot \\ \cdot \\ f_{2 \times nn - 1} \\ f_{2 \times nn} \\ f_{2 \times nn + 1} \end{bmatrix} &= \begin{bmatrix} F_1 \\ M_1 \\ F_2 \\ M_2 \\ \cdot \\ \cdot \\ \cdot \\ F_{nn} \\ M_{nn} \\ F_{VA} \end{bmatrix} \quad (b)
 \end{aligned} \tag{2}$$

where:

- $q_n$  is the  $n^{\text{th}}$  generalized coordinate  
 $f_n$  is the  $n^{\text{th}}$  generalized force  
 $y_n$  is the transverse displacement of the  $n^{\text{th}}$  node  
 $y_{VA}$  is the transverse displacement of the absorber  
 $\theta_n$  is the rotational displacement of the  $n^{\text{th}}$  node  
 $F_n$  is the transverse external force at the  $n^{\text{th}}$  node  
 $F_{VA}$  is the external force applied to the absorber  
 $M_n$  is the external applied moment at the  $n^{\text{th}}$  node  
 $nn$  is the total number of nodes

In general —with the exception of gravitational forces— external forces are only transmitted to the system through the mount locations (exclusive of the firing event). For example, terrain disturbance forces would be applied to the gun system through the trunnion mounts and *corrected* by the elevation mechanism ( $f_5$  and  $f_3$  respectively in this case). Gravitational forces may be neglected as they result in an equilibrium deflection solution about which the disturbance induced vibrations will oscillate. This assumption may be compromised if rapid elevation of the gun barrel —resulting in significant changes of the orientation of the gun relative to the gravity field and subsequent changes in the equilibrium deflection— occurs.

## 2.5 Conversion to First-Order State-Space

Many of the powerful MATLAB® tools for dynamic analysis and design require the dynamic equations to be in linear, time-invariant, first-order state-space form. Equation (1) is in the second-order symmetric form. This representation of the system dynamics may be converted to the first-order state-space form through the following method [6, 11]:

First, define the state-vector and its first time derivative as the combined generalized coordinates of equation (2) and their first temporal derivatives:

$$\underline{x} = \begin{bmatrix} \underline{q} \\ \underline{\dot{q}} \end{bmatrix} \rightarrow \underline{\dot{x}} = \begin{bmatrix} \underline{\dot{q}} \\ \underline{\ddot{q}} \end{bmatrix} \quad (3)$$

Second, Define the system dynamics of equation (1) in terms of the generalized coordinate vector's time derivatives:

$$\begin{aligned} \underline{\dot{q}} &= \underline{I} \underline{\dot{q}} & (a) \\ \underline{\ddot{q}} &= -\underline{M}^{-1} \underline{K} \underline{q} - \underline{M}^{-1} \underline{C}_D \underline{\dot{q}} + \underline{M}^{-1} \underline{f} & (b) \end{aligned} \quad (4)$$

Note that the form of equation (4) presumes that the mass matrix is invertible. This is always the case for beam finite element formulations. Using equations (3) and (4), a state-space representation, with all of the generalized coordinates as the output is:

$$\begin{aligned} \underline{\dot{x}} &= \underline{A} \underline{x} + \underline{B} \underline{f} \\ \underline{q} &= \underline{C} \underline{x} + \underline{D} \underline{f} \end{aligned} \quad (5)$$

Where the state-space matrices are constructed in terms of the second order system matrices, and the zero and identity matrices of compatible size. (Note, the state-space matrices have twice the number of rows and columns of the second-order system matrices.):

$$\begin{aligned}
 A &= \begin{bmatrix} 0 & I \\ -(M^{-1}K) & -(M^{-1}C_D) \end{bmatrix} & (a) & B = \begin{bmatrix} 0 \\ M^{-1} \end{bmatrix} & (b) \\
 C &= \begin{bmatrix} I & 0 \end{bmatrix} & (c) & D = \begin{bmatrix} 0 \end{bmatrix} & (d)
 \end{aligned} \tag{6}$$

The m-file <fem2ss.m> [6] computes the state-space matrices using the second-order matrices of (1) as shown in (6).

### 3. FREQUENCY RESPONSE ANALYSIS OF THE MODEL

#### 3.1 Model Truncation

Truncation of the state-space model from a multi-input/multi-output system to a single-input/single-output system facilitates frequency response analysis. With this goal in mind, the selection of which input and output to use must be made. Since the terrain disturbances are transmitted to the system via the trunnion mounts the disturbance forcing is applied at  $f_s$ . The *correction force* applied by the elevation mechanism at  $f_3$ , is simply modeled as a linear compliance. (Inclusion of the fire-control dynamics, such as previously done by Dholiwar [10], would enhance the model significantly and will be pursued, but have not yet been incorporated into this effort.) The muzzle pointing angle is selected as the sole output of the system as it should include contributions from all vibratory modes. (The muzzle is an *anti-node* of the constrained beam.) The truncation is effected by the <ssselect> command [9] as was demonstrated in [6].

### 3.2 Bode Analysis of Unmodified Barrel

XM291 Trunnion Disturbance to Muzzle Pointing Angle Bode Plot

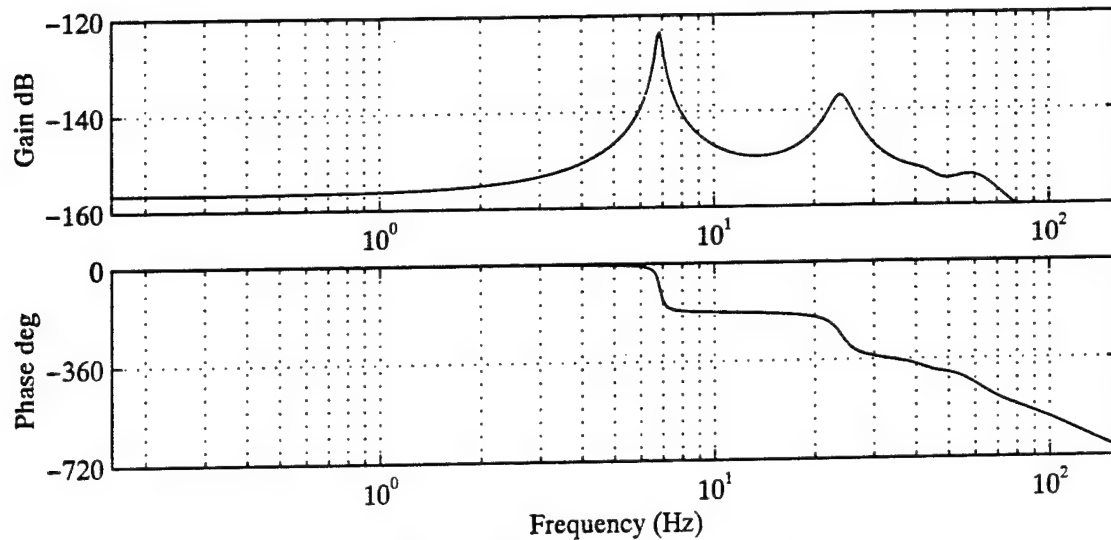


Figure 4 Base-Line Bode Plot of Unmodified XM291 Gun System.

Once in the single-input/single-output state-space realization, the frequency response of the system may be computed using the <bode> command [9]. This may be thought of as a cross section of the Laplace transfer function along the imaginary frequency axis by substituting  $j\omega$  for " $s$ ," where  $\omega$  is the radial frequency. The frequency response of a dynamic system indicates the steady-state response,  $y(t)$ , of the system to a sinusoidal input,  $u(t)$  [9]:

$$\begin{aligned} u(t) &= A \sin((2\pi f)t) \\ y(t) &= k A \sin((2\pi f)t + \phi) \end{aligned} \quad (7)$$

where:

- $u(t)$  is the input force at the trunnions
- $A$  is the amplitude of the input force
- $f$  is the cyclic frequency of the input force
- $t$  is time
- $y(t)$  is the output pointing angle of the muzzle
- $k$  is the gain
- $\phi$  is the phase lead/lag of the response

Figure 4 is a Bode plot of the response of the muzzle pointing angle to disturbance trunnion loading of the unmodified barrel. This may be used as a base-line against which modified barrels may be judged. It consists of two plots, the upper relates the gain of the system,  $k$  in equation (7), to the excitation frequency,  $f$ , and the lower depicts the phase lag,  $\phi$ , to the frequency. The gain is represented in decibels. (A decibel is related to the gain as:  $\text{dB} = 20 \log_{10}(k)$ .)

#### 4. FREQUENCY DOMAIN OPTIMIZATION OF THE ABSORBER

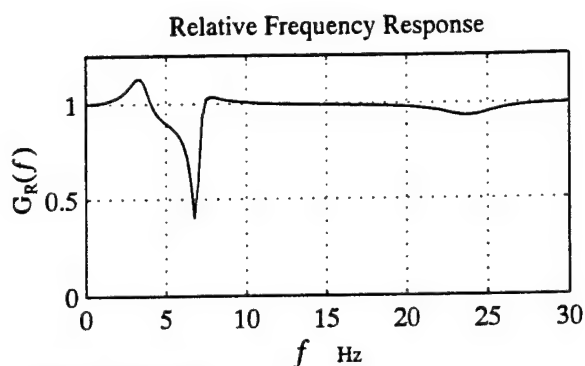
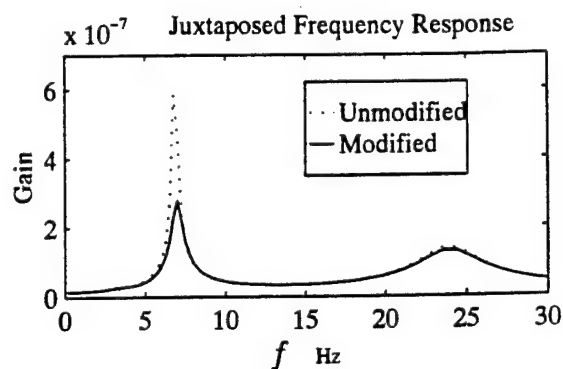
##### 4.1 Bode Analysis for Absorber Optimization

The frequency response of a modified barrel is effected in the same manner as the unmodified barrel. For this paper, two absorber parameters are varied, the stiffness,  $K_{VA}$ , and the stiffness proportional damping coefficient,  $\beta_{VA}$ . The gain function of the modified barrel is then divided by the gain of the original system, resulting in a relative frequency response as shown in Figure 5.

A weighting function is then applied to emphasize the response in the frequency range of primary interest. This function, as shown in Figure 6, was generated as the normalized response of a second order system with natural frequency,  $f_n$ , of nine Hertz and a critical damping ratio,  $\zeta$ , of 40%. In general, the weighting function may effectively combine the dynamics of the gun system, with the a priori frequency content of the disturbance forcing. (Multiplication in the frequency domain is equivalent to convolution in the time domain. [12]) Thus, this weighting function approximates *white* terrain induced trunnion force disturbance as having been passed through a second-order, damped filter.

A single scalar cost function,  $J$ , is then quantitatively computed as the integral of the weighted relative frequency response of the absorber modified system —across the frequency range of interest:

$$J = \int_{f_{low}}^{f_{high}} (G_R(f) G_W(f)) df \quad (8)$$



Absorber Parameters:

$M = 20 \text{ Kg}$ ,  $K = 1.08 \times 10^4 \text{ N/m}$ ,  $B = 0.02 \text{ (N/(m/s))/(N/m)}$

Figure 5 Juxtaposition of Modified and Un-Modified Barrels and the Resulting Relative Frequency Response.

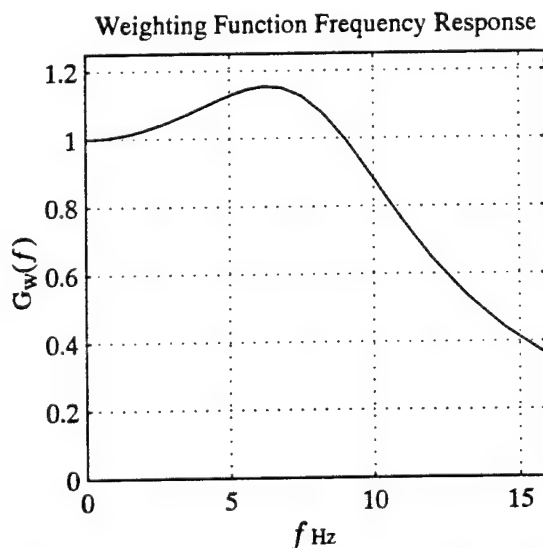


Figure 6 Weighting Function Used to Emphasize Expected Disturbance Frequency Content in the Optimization.

where:

- $J$  is the scalar cost function
- $f_{low}$  is the lowest frequency of interest
- $f_{high}$  is the highest frequency of interest
- $G_R(f)$  is the relative frequency response as shown in Figure 5
- $G_w(f)$  is the weighting function frequency response as shown in Figure 6

$J$  is subsequently normalized to be unity for  $K_{VA}$  and  $\beta_{VA}$  at zero (these values essentially eliminate the effects of the damper). Other cost functions could readily be utilized to incorporate other design considerations such as worst-case performance, or pragmatic engineering issues such as bounds on reasonable damping levels. Strategic formulation of the cost function becomes more of a concern as the dimension of the parametric design space increases, requiring multi-dimensional gradient descent methods for optimization such as the `<fmin>` command [8]. For the two dimensional case at hand, visual inspection of the optimization surface,  $J(\beta_{VA}, K_{VA})$ , is possible.

## 5. RESULTS

### 5.1 Optimization Surface

The optimization surface generated using the scalar frequency response cost function is shown in Figure 7 for a 20 Kg vibration absorber.

The plots clearly indicate that for low levels of damping,  $\beta \leq 0.005$ , the absorber design is extremely sensitive to parametric variation. This can be seen by the high density of contour lines near the peaks that indicates step gradients.

The peaks are caused by detrimental interaction of the absorber with the fundamental frequencies of the barrel. As mentioned earlier, this also implies that low level damping absorber designs are also sensitive to model uncertainty caused by the unmodeled mount and elevation servo control dynamics. This said, the contour plot does indicate that at least one low level

Optimization Surface in Parameter Space

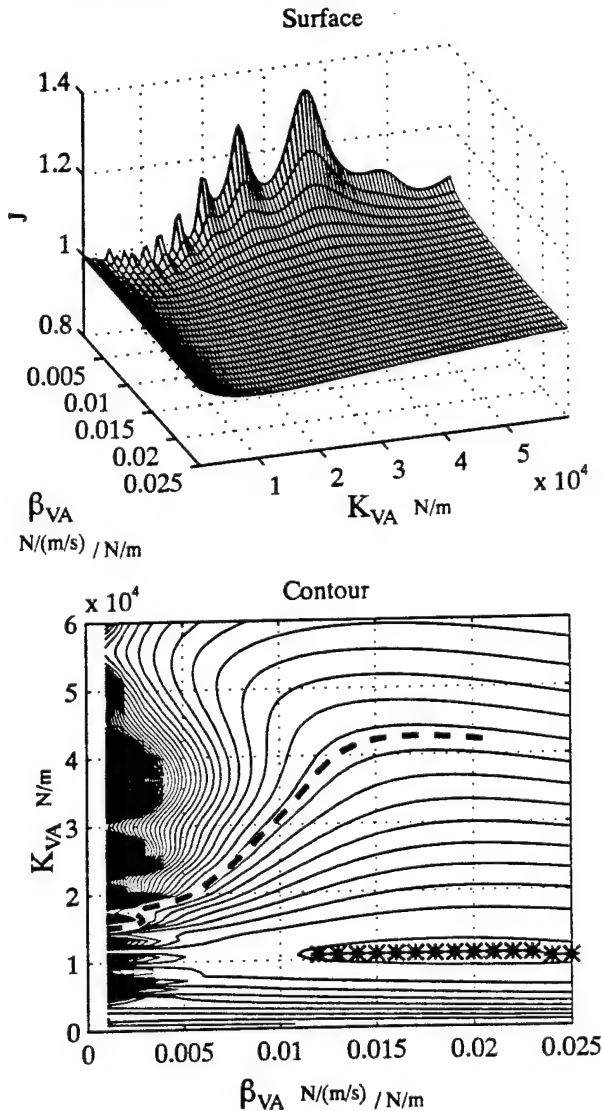


Figure 7 The Optimization Surface of a 20 Kg Absorber. The Top Plot Depicts a 3D rendering of the Surface. The Bottom Plot Reveals a Contour of the Surface; The Dashed Line Represents the Unity  $J$  Value, The Asterisks Represent Optimal Parameter Values that Minimize  $J$ .

damping design, near  $K_{VA} = 10,000$  N/m, would effect disturbance rejection by the absorber.

For higher damping levels,  $0.005 \leq \beta_{VA} < 0.030$ , the absorber design appears to be quite insensitive, especially to the level of damping.

In both cases, the lack of sensitivity to damping levels is a desirable result. Engineering obstacles with damping materials that are subject to harsh variations in temperature—as would be experienced in a weapon environment—may be relaxed due to this lack of sensitivity with respect to this challenging design parameter.

## 5.2 Relative Frequency Response

The optimization of Figure 7 demonstrates that the optimal “spring-constant” of 11,400 N/m that couples the 20 Kg absorber to the gun barrel is essentially constant for the range of  $\beta_{VA}$ 's examined. (Actually, for the low damping values, the optimization bifurcates with a slight advantage for a  $K_{VA}$  of 9,600 N/m.)

Figure 8 depicts the change in the frequency response gain due to an optimal absorber for various Rayleigh damping values. The “spikes” in the response for low damping, may be offset by the deep “notch-filter” effect that these systems exhibit. If modeling uncertainty is very low, matching the notch-filter to known problem disturbances may be a viable design methodology.

For the case at hand, this “notch-filter” approach may be viable if:

- i. Prototype hardware *tuning* of the parameters to match the real system is possible.
- ii. Interaction with the fire-control servo loop is well modeled.
- iii. Modal interaction with other unmodeled structures (such as the turret) does not coincide with the absorber “spikes.”

The advantages of a design with significant damping levels are clearly based on a lack of model and structural sensitivity. Unless there is an absolute need for a “notch-filter” level of disturbance rejection, this robust behavior is the preferred design approach.

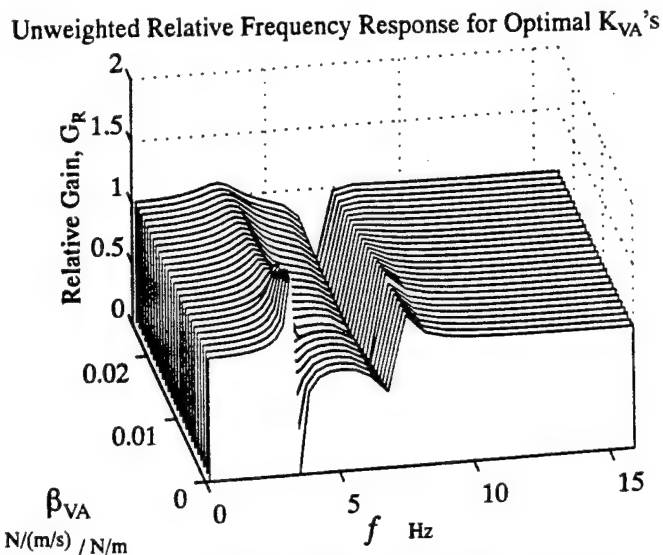


Figure 8 Relative Frequency Response of a 20 Kg Absorber for Optimal  $K_{VA}$ 's ( $\sim 10,000$  N/m) versus Rayleigh Damping  $\beta_{VA}$ 's.

### 5.3 Pole-Zero Plots in the Laplace Domain

The location of the damped eigenvalues and zeros in the Laplace domain provides insight into the dynamics of the absorber modified gun system.

Often called a pole-zero map, the unmodified system is shown in Figure 9. In this figure, the first four bending modes are revealed as the complex conjugate "x" pairs. The natural coordinate units for the imaginary axis are radians per time, but I have scaled this axis to display in the more familiar cyclic frequency of Hertz.

The polar grid correlates damped frequencies to their natural (undamped) counter parts by the arc's of constant radius.

The critical damping ratio,  $\zeta$ , for each mode is revealed by the angular displacement off of the imaginary axis. Each radial line represents 20% increments of the critical damping, from zero at the imaginary axis to 100% along the real axis.

It is important to realize that roots in this domain imply that the denominator of the transfer function goes to zero as these roots are approached. This leads to unbounded response at these locations; thus the term "pole."

Conversely, the zeros of the transfer function are depicted by the "o" marks. At these locations, the transfer function numerator is zero, nullifying any response from the system at these locations.

The effect of these values on the frequency response occurs along the imaginary axis, where the real parts of the Laplace domain "s" variables are zero. As a surface, the transfer function along

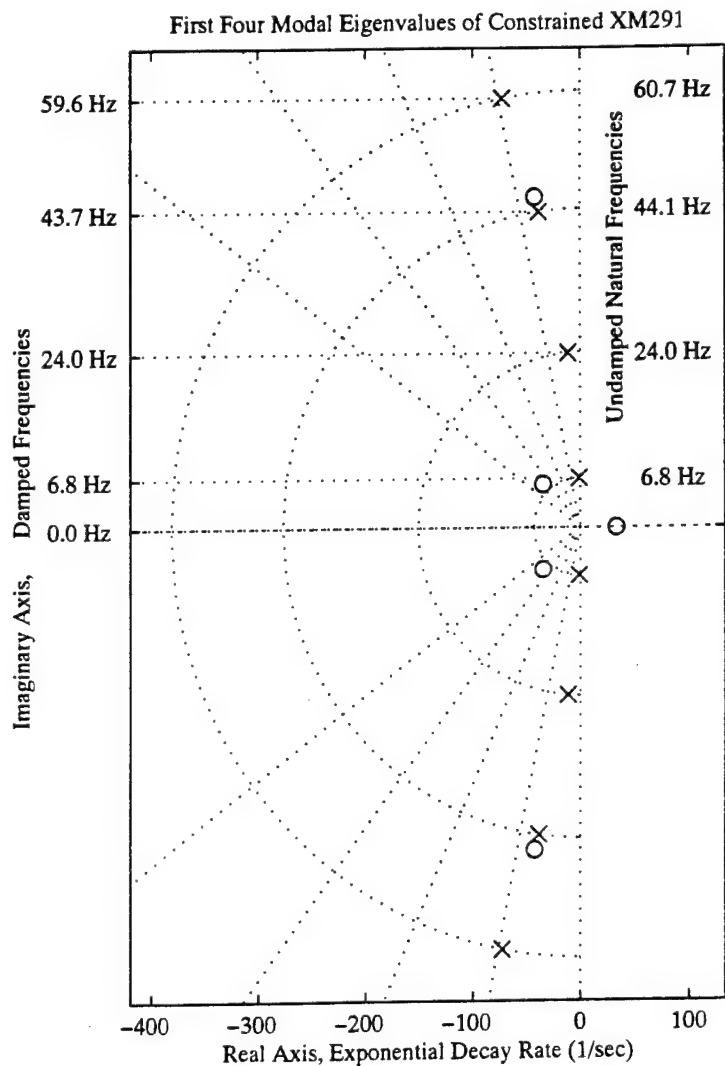


Figure 9 Pole-Zero Plot in Laplace Domain of Unmodified Gun System.

the imaginary axis closely mimics the response of the poles and zeros that near to it. Thus in Figure 9, the nearby location of the eigenvalue located at 6.8 Hz, effects a spike in the frequency response function as was seen in Figure 4 and Figure 5. Since the pole is not coincident with the imaginary axis, the spike is not unbounded as would be expected of an undamped model.

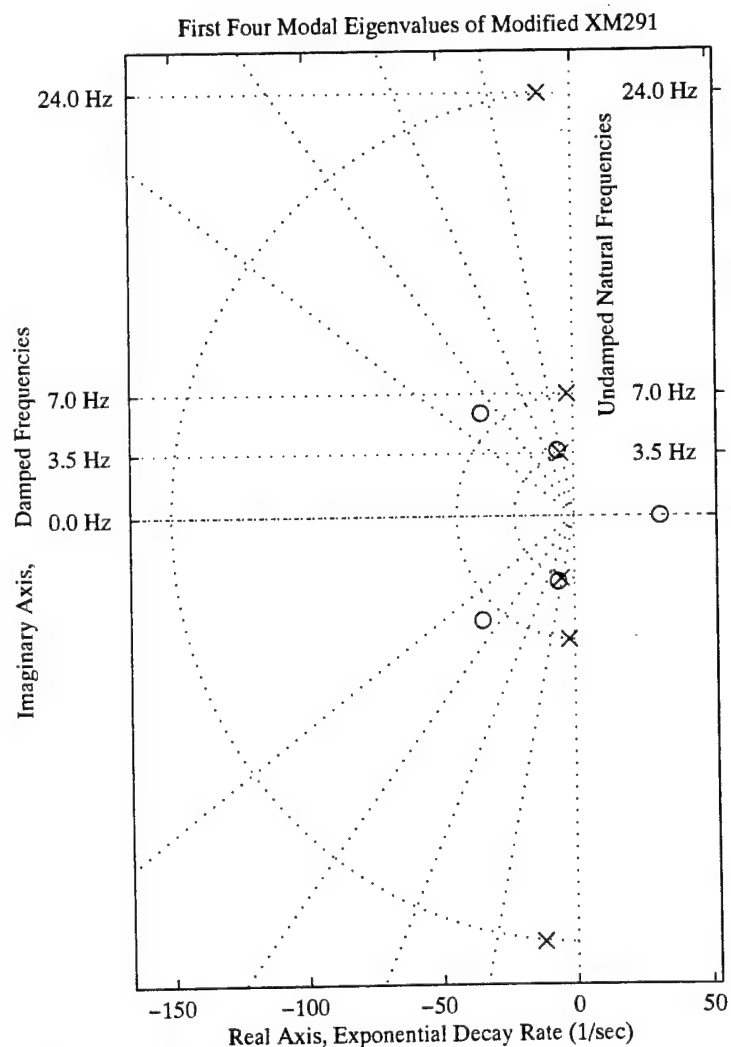
The absorber changes the pole zero map by introducing a new degree of freedom, and its subsequent poles and zeros.

Figure 10 depicts the new pole-zero map of the modified gun system. The 20 Kg absorber has created a pair of conjugate poles and a pair of conjugate zeros. The optimization has placed the new zeros very near to the new poles, with a slight translation to a higher frequency.

The absorber pole location is nearly coincident with the natural frequency that the absorber would exhibit if it were constrained to a rigid reference. This natural frequency may be evaluated as  $\omega = \sqrt{(K_{VA}/M_{VA})}$ . This value, divided by  $2\pi$  radians per cycle, is 3.70 Hertz for the absorber parameters  $M_{VA} = 20$  Kg and  $K_{VA} = 10,800$  N/m. The absorber pole—located near 3.5 Hertz—is below the rigid coupling value due to the relatively high barrel contribution to its effective inertia as opposed to stiffness, and the modest level of damping.

The close proximity of the zero to the pole, largely cancels the response of the pole. However, since the zero is shifted higher, the pole does effect a small increase in response towards the low frequency side. This effect may readily be seen in Figure 5 and Figure 8.

The zero subsequently reduces the response of the system towards the higher frequencies,



Absorber Parameters:  
 $M = 20$  Kg,  $K = 1.08 \times 10^4$  N/m,  $B = 0.02$  (N/(m/s))/(N/m)

Figure 10 The Pole-Zero Map of the Gun Modified by an Optimal 20 Kg Absorber.

especially the next pole, with a diminishing effect as the input disturbance frequency migrates up the imaginary axis.

Also note that the coupling of the absorber has slightly increased the effective stiffness of the original first mode of the gun system. This effect may be seen as the shift of the 6.8 Hz pole in Figure 9 to 7.0 Hz in Figure 10.

For the case of an absorber designed with low damping, the new pole-zero pair becomes nearly collocated with the imaginary axis, resulting in the pronounced spike and notch effects revealed by Figure 8.

#### 5.4 Mode Shape Comparison

The mode shapes (eigenvectors) of both the original, and the 20 Kg absorber modified barrels, were evaluated as shown in Figure 11 and Figure 12 using the <eigen\_20.m> file as developed in [6]. In both cases the mode shapes are mass normalized.

The x's along the barrel center line indicate the node locations. The external coupling at the elevation mechanism and the trunnions is shown by the small circle around the x. The absorber deflection in Figure 12 is depicted by the circle—constrained to the barrel—by the thin line.

Figure 12 shows the nearly decoupled mode of the vibration absorber itself. (The flexure of the barrel in this mode shape is nearly rigid body.) Although the rather large deflection of the absorber in the first mode would normally cause concern, the near *pole-zero cancellation* shown in Figure 10 largely alleviates this problem. The first mode is essentially coincident with the notch depicted in Figure 5 and Figure 8.

## 6. CONCLUSIONS

Vibration absorbers present the opportunity to reduce the receptance of gun systems to terrain

### XM291 Eigen Vectors Frequencies

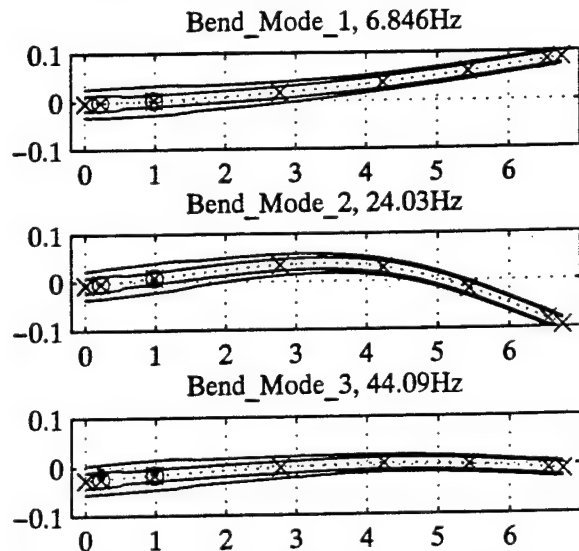


Figure 11 First Three Mode Shapes and Frequencies of the Unmodified Gun System.

### Absorber Modified XM291 Eigen Analysis

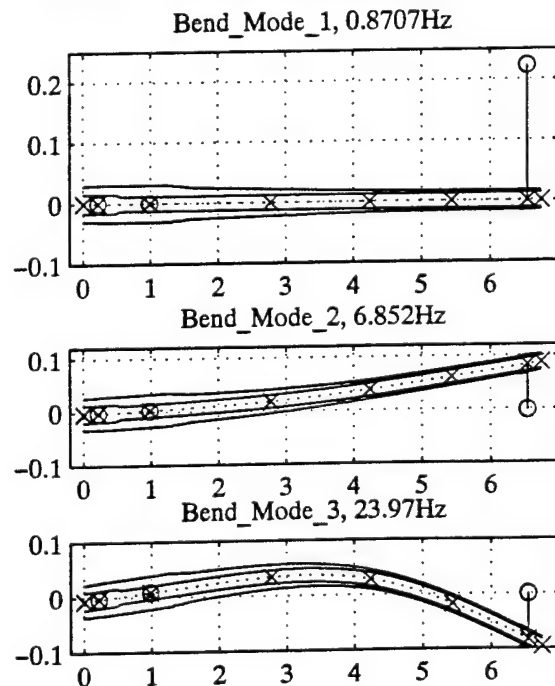


Figure 12 First Three Mode Shapes and Frequencies of the Gun System Modified by an Optimal Absorber.

induced vibrations using a simple passive mechanism. The design methodology presented in this paper, both optimizes the design and reveals the sensitivity of the design to parametric uncertainty of the absorber, as revealed by the gradient of the optimization surface. Optimization within a high dimensional parameter space has been enabled by the identification of a scalar cost-function in the frequency domain of the system that is readily computed within the MATLAB® computing environment. This cost function may be adapted to disturbances that may be characterized a priori via a weighting function in the frequency domain. This weighting in the frequency domain is equivalent to convolution in the time domain of the gun system with the approximated disturbance system.

Evaluation of absorber performance has been examined in the Laplace domain via pole-zero plots, frequency domain via Bode analysis, and using eigen techniques. These perspectives verify the advantages of designing an absorber with significant damping levels to avoid undue sensitivity to modeling and parametric uncertainties.

Sensitivity of designs that are low in damping —to slight parametric variations, model uncertainty, and unmodeled dynamics— has been shown. Also, the potential advantage of the “notch-filter” effect of such designs has been demonstrated in the event that the disturbance may accurately be characterized a priori, thus justifying significant modeling and validation efforts to reduce the potentially detrimental uncertainties. Terrain induced vibrations are unlikely to be well characterized; however, undesirable servo-control dynamics may provide a candidate for this type of approach.

## 7. REFERENCES

- [1] Thomson, W. T., Theory of Vibration with Applications, 4<sup>TH</sup> Edition, Prentice Hall, Englewood Cliffs, NJ, 1993.
- [2] Timoshenko, S., and Young, D. H., Vibration Problems in Engineering: 3<sup>RD</sup> Edition, D. Van Nostrand Company, Inc., New York, NY, 1955.
- [3] Crede, C. E., Shock and Vibration Engineering Concepts in Engineering Design, Prentice-Hall, Inc., Englewood Cliffs, NJ, 1965.
- [4] Leipholz, H. H. E. and Abdel-Rohman, M., Control of Structures, Martinus Nijhoff Publishers, Boston, MA, 1986.
- [5] Rofooei, F. R., “Active Control of Structures,” PhD Thesis, Rensselaer Polytechnic Institute, Troy, NY, May 1992.
- [6] Kathe, E., MATLAB® Modeling of Non-Uniform Beams Using the Finite Element Method for Dynamic Design and Analysis, ARDEC Technical Report ARCCB-TR-96010, April 1996.
- [7] MATLAB® User's Guide, The MathWorks, Inc., Natick, MA, July 1993.
- [8] MATLAB® Reference Guide, The MathWorks, Inc., Natick, MA, July 1993.
- [9] Control System Toolbox User's Guide, The MathWorks, Inc., Natick, MA, June 1994.
- [10] Dhaliwar, D. K., “Development of a Hybrid Distributed-Lumped Parameter Openloop Model of Elevation Axis for a Gun System,” Proceedings of the Seventh U.S. Army Symposium on Gun Dynamics, ARCCB-SP-93034, Benét Laboratories, Watervliet, NY, 11-13 May 1993, pp. 368-385.
- [11] Meirovitch, L., Dynamics and Control of Structures, John Wiley & Sons, New York, NY, 1990.
- [12] Bracewell, Ronald N., The Fourier Transform and Its Applications: Second Edition - Revised, McGraw-Hill, New York, NY, 1986.

**EDITOR'S NOTE:**

The genesis for Dr. Simkin's presentation 'Beating the Critical Velocity Problem' is contained in ARDEC Technical Report ARCCB-TR-92040, 'Criteria for the Design of a Strain Attenuating Obturator', T.E. Simkins & M. Leach, Benet Laboratories, Watervliet, NY, September 1992. The report is published here for completeness of the symposium proceedings and to aid accessibility.

## INTRODUCTION AND BACKGROUND

Previous publications by Simkins [1-3] have shown good agreement between measured dynamic strains in gun tubes and those predicted by critical velocity theory when the projectile velocity is subcritical. Moreover, even thin-wall theory predicts these dynamic strains with surprising accuracy. However, because critical velocity theory ignores end effects (an infinitely long tube is assumed), differences do occur between the measured and predicted strains. These are most easily explored via finite element simulations, which are assumed to more closely mimic physical reality. For the purpose of exposing the basic idea behind such an obturator, however, the infinitely long and uniformly thin-walled tube traversed by a moving pressure at constant velocity is most convenient.

## SECTION I - WALL DEFORMATION IN A GUN TUBE OF INFINITE LENGTH (CRITICAL VELOCITY THEORY)

Figure 1 shows the theoretically predicted radial displacement along the length of an infinitely long and uniformly thin-walled gun tube caused by a unit pressure step moving at a velocity which is 99% of the critical value, i.e.,  $V = 0.99V_{cr}$ . The displacement values have been normalized with respect to the displacement as calculated from the Lamé formula [4] so that the ordinate can be labeled the *dynamic amplification*. The abscissa  $\xi$  measures the distance from the leading edge of the step so that the deformation appears constant to an observer moving along with the step. To such an observer, the deformation is reminiscent of a static load-deformation scenario. This equivalence to a static problem (really an application of D'Alembert's Principle) can also be stated mathematically. Starting with the differential equation of motion for a thin-walled tube:

$$D \frac{\partial^4 w}{\partial x^4} + \frac{Eh}{R^2} w + m \frac{\partial^2 w}{\partial t^2} = (1 - H(x - Vt)) \quad (1)$$

where  $H$  is the Heaviside step function:

$$\begin{aligned} H(x - Vt) &= 0 \quad x < Vt \\ &= 1 \quad x > Vt \end{aligned}$$

In this equation,  $w$  is the radial displacement of the median surface of the cylinder located at a distance  $R$  from the central axis;  $h$  is the wall thickness and is assumed small compared to  $R$ ;  $m = \rho h$  where  $\rho$  is the mass density of the tube material;  $D = Eh^3/12(1 - \nu^2)$ ;  $E$  is Young's modulus of elasticity;  $\nu$  is Poisson's ratio; and  $V$  is the velocity of the moving pressure, assumed to be finite and constant.

The critical velocity derived from this thin-wall theory is given by the expression:

$$V_{cr}^2 = \frac{2}{\rho h} \sqrt{\frac{EhD}{R^2}}$$

Equation (1) expresses the relationship between load and deformation in space and time. Let  $\xi$  denote the distance from the moving step so that  $\xi = x - Vt$ . Substituting this transformation into equation (1):

$$D \frac{d^4 w}{d\xi^4} + \frac{Eh}{R^2} w + mV^2 \frac{d^2 w}{d\xi^2} = (1 - H(\xi)) \quad (2)$$

Equation (2), since it lacks the time variable, can be viewed as a *statics* problem in the *space* variable  $\xi$ . The solution to this 'statics' problem when  $V$  is subcritical is [1]:

$$W_s(\xi) = w/K = \frac{e^{d\xi}}{2} \left( -\cos c\xi + \frac{d^2 - c^2}{2cd} \sin c\xi \right) + 1, \quad \xi \leq 0 \quad (3a)$$

$$W_s(\xi) = w/K = \frac{e^{-d\xi}}{2} \left( \cos c\xi + \frac{d^2 - c^2}{2cd} \sin c\xi \right), \quad \xi \geq 0 \quad (3b)$$

where  $c = \gamma\sqrt{\frac{\lambda+1}{2}}$ ,  $d = \gamma\sqrt{\frac{1-\lambda}{2}}$ ,  $\lambda = V^2/V_{cr}^2$ , and  $\gamma^4 = Eh/R^2D$ .  $K = R^2/Eh$  approximates the Lamé displacement so that  $W_s$  represents the *dynamic amplification* caused by the moving step of pressure.

### WALL DEFORMATION CAUSED BY AN ARBITRARY LOAD DISTRIBUTION

Consider a moving pressure,  $f(\xi)$ , where the leading edge is no longer a step but any function such that  $f(0) = 0$  and  $f(\xi) = 1, \xi \leq -\alpha$ . Figure 2a is an example of such a pressure when  $\alpha = 2.4$ . The wall deformation  $W_f$  caused by this pressure distribution can be found using the expression for  $W_s$  above. To show this, we first envision a staircase approximation to  $f(\xi)$ , as shown in Figure 2b, so that  $f(\xi)$  is approximated as a sum of step distributions each of magnitude  $\Delta f_i$ .  $\eta_i$  is the distance of the leading edge of the  $i^{th}$  step from the origin  $\xi = 0$ . The distance between the leading edges of two successive steps is then  $\Delta\eta_i$ . The displacement caused by the  $i^{th}$  step is simply:

$$W_i = \Delta f_i W_s(\xi + \eta_i)$$

Because of the linearity of Equation (2),  $N$  such displacements can be summed to give the displacement caused by an  $N$ -step approximation to  $f(\xi)$ , i.e.:

$$W_{N\text{-step}} = \sum_{i=1}^N \Delta f_i W_s(\xi + \eta_i) = \sum_{i=1}^N \frac{\Delta f_i}{\Delta\eta_i} W_s(\xi + \eta_i) \Delta\eta_i$$

Taking the limit of this sum as  $N \rightarrow \infty$  and  $|\Delta\eta_i| \rightarrow 0$ , results in the integral:

$$W_f = \int_0^\alpha f'(\eta) W_s(\xi + \eta) d\eta \quad (4)$$

The simplest  $f(\xi)$  is the linear function:

$$f(\xi) = -\frac{\xi}{\alpha}$$

Since  $\eta$  increases as  $\xi$  decreases:

$$f(\eta) = \frac{\eta}{\alpha}$$

so that

$$f'(\eta) = \frac{1}{\alpha}$$

Substituting for  $f'(\eta)$  in Equation (4):

$$W_f = \int_0^\alpha \frac{1}{\alpha} W_s(\xi + \eta) d\eta \quad (5)$$

The integral in Equation (5) can be evaluated numerically once values for all parameters have been chosen.

### NUMERICAL RESULTS

In this section, the response to a moving unit step,  $W_s(\xi)$ , as given by Equations (3a,b), is compared with that due to the 'ramp-step'  $W_f(\xi)$  (Equation (5)).

## SIMKINS

The following parametric values correspond to a particular 60-mm gun tube:

$$\begin{aligned} E &= 30.3 \times 10^6 \text{ psi} & \nu &= 0.3 & h &= 0.12 \text{ in} & \rho &= 7.365 \times 10^{-4} \frac{\text{lb-sec}^2}{\text{in}} \\ R &= 1.2411 \text{ in.} & V &= 0.99V_{cr} \end{aligned}$$

Using these values,  $W_r(\xi)$  is computed using Equations (3a,b) and is shown as a dashed curve in Figure 3. From these equations the "wavelength" - that is, the distance between neighboring maxima - is  $2\pi/c$  and computes to be 1.34 inches. For this example, this is the value also chosen for  $\alpha$ , the length of the "ramp" portion of  $f(\xi)$ . The integral in Equation (5) can be evaluated numerically, and the resulting  $W_f(\xi)$  is shown as the solid curve in Figure 3. The reduction afforded by the ramp is dramatic.

It is of interest to know the effect of ramp length,  $\alpha$ , on the maximum response or dynamic amplification of the wall displacement. This is shown in Figure 4 - a plot of the maximum dynamic amplification resulting as  $\alpha$  is iterated through increasing values in Equation (5). From the figure it can be concluded that the response is nearly minimized when  $\alpha = 2\pi/c$ , the value chosen for the numerical example above.

## SECTION II - FINITE ELEMENT SIMULATIONS

The critical velocity theory employed in Section I assumes, among other things, a tube of infinite length. From actual field measurements, however, the most severe wall strains occur at or near the muzzle of a gun tube. These deformations are caused by reflections of the travelling wave at the muzzle which superpose with the remainder of the oncoming wave, at times reinforcing to create higher strain maxima. Predicting these strains via critical velocity theory, which assumes steady-state conditions, is not possible and the general procedure is to resort to numerical methods such as finite element simulations. While such simulations do not usually lead to a detailed understanding of the cause of the high strains (closed-form symbolic solutions like Equations 3a,b are not generated), they are useful to predict the strains on a case-by-case basis.

The finite element (ABAQUS) model used in this study is depicted in Figure 5. A constant ballistic pressure in the form of either a step or a ramp-step enters the breech end of a 60-mm gun tube at a constant velocity  $V = 0.99V_{cr}$ . The sudden appearance of this high velocity step of pressure at the breech end initiates a transient vibration that is not realistic of an actual firing. Previous work [5] shows that this transient continually interacts to give higher strain maxima at certain locations along the tube but decays with distance. While no evaluation of this effect has been undertaken for the ABAQUS results reported herein, based on previous experience it is not expected to be a major one. Its influence for the case of a ramp-step of moving pressure should be less than for a step.

Figures 6a-d compare the ABAQUS-computed time histories of the radial displacement at different points along the bore of the 60-mm tube in response to a moving step and a moving ramp-step of pressure. Figure 6a shows the response at a point midway along the tube, i.e., twenty-four inches from the muzzle and breech. Here the maximum displacement caused by the moving step is estimated to be 3.3 (times the Lamé displacement), whereas that due to the moving ramp-step is only 1.22. Since this location is considerably distant from the ends of the tube, both of these displacements should be, and are, in very good agreement with those predicted by critical velocity theory (Figure 3 of Section I). Figure 6b compares responses at a point only 0.24 inch from the muzzle end and shows a maximum displacement of 2.2 caused by the moving step vs. 1.40 caused by the moving ramp-step. Figure 6c compares time histories at a point which is 0.12 inch from the muzzle. The corresponding maximum displacements are 4.8 vs. 1.8. Finally, at the muzzle itself, Figure 6d shows the comparison to be 8.0 vs. 2.2. (In each figure the time of passage of the pressure front coincides with the abrupt increase in displacement. For example, in Figure 6a the pressure front passes this midlength location at approximately  $t = 0.00052 \text{ sec.}$ ) While it is tempting to conclude that the ramp-step will *always* cause displacements (and hence stresses and strains), which are less than those caused by the step, finite element simulations such as these are never conclusive. A different choice of location along the tube, for example might conceivably yield opposite results. However, from the solutions obtained by the critical velocity theory in Section I, it is certain that at a *sufficient* distance from the ends of the tube, the

## SIMKINS

moving ramp-step always causes travelling waves of lesser amplitude than the moving step. It is reasonable to expect that the reflections of these waves will also be lower in amplitude.

## CONCLUSIONS

From the work reported herein, it is apparent that dramatic reductions in dynamic strains in gun tubes can be obtained if the ballistic pressure rise in the vicinity of the projectile can be made less abrupt. It is hoped that practical schemes for doing this are possible. One idea, suggested by Benet Laboratories Director Laurence Johnson [6], proposes an obturator band that has increasing wall thickness over its length. The inner surface of the obturator would receive the ballistic pressure and expand to contact the bore of the gun tube. The pressure applied to the bore by the obturator could then be brought to zero over the length of the obturator by suitably varying its wall thickness.

References

1. T.E. Simkins, "Resonance of Flexural Waves in Gun Tubes," ARCCB-TR-87008, Benet Laboratories, Watervliet, NY, July 1987.
2. T.E. Simkins, G.A. Pfiagl and E. G. Stilson, "Dynamic Strains in a 60-mm Gun Tube: An Experimental Study," Proceedings of the 61st Shock and Vibration Symposium, Vol 3, pp 201-218, Oct 16-18, 1990.
3. T.E. Simkins, "Wave Coupling and Resonance in Gun Tubes," ARCCB-TR-89008, Benet laboratories, Watervliet, NY, March 1989.
4. S.P. Timoshenko and J.N. Goodier *Theory of Elasticity*. New York, McGraw-Hill Book Co., third edition, 1987 re-issue, 68-71.
5. T.E. Simkins, "The Influence of Transient Flexural Waves on Dynamic Strains in Gun Tubes," ARCCB-TR-89020, Benet Laboratories, Watervliet, NY, August 1989.
6. L.D. Johnson, Director, Benet Laboratories, Watervliet, NY, personal communication, May 1992.

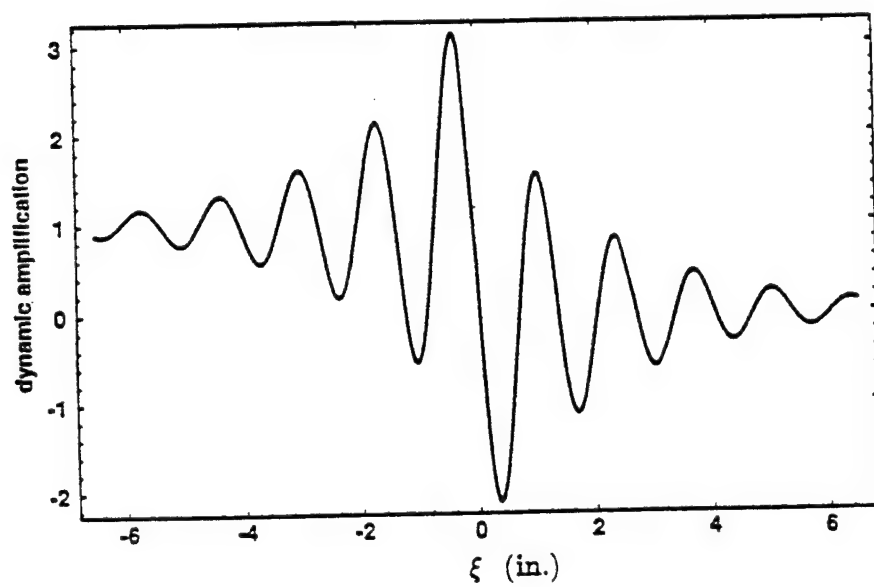


Figure 1. Dynamic amplification,  $V = 0.99V_{cr}$

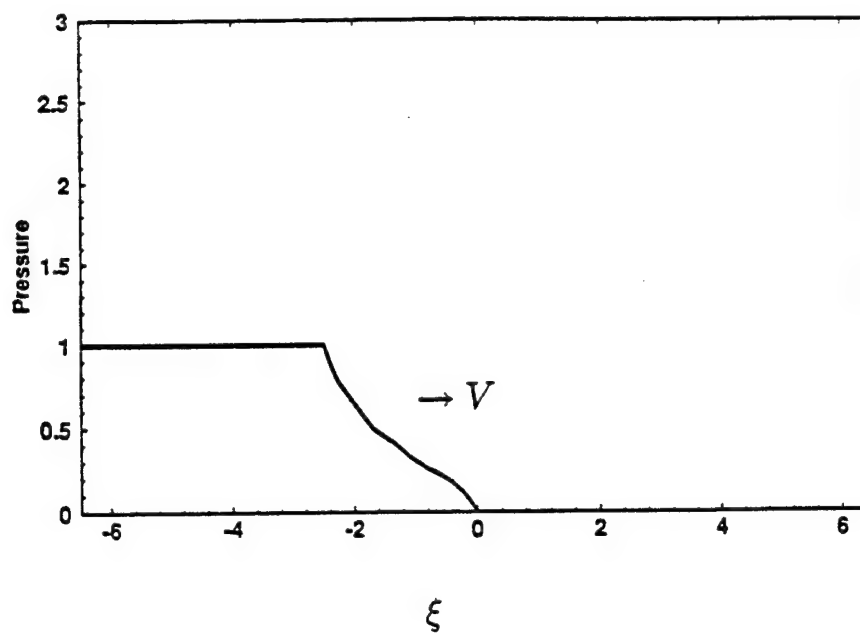


Figure 2a. Moving pressure, arbitrary leading edge.

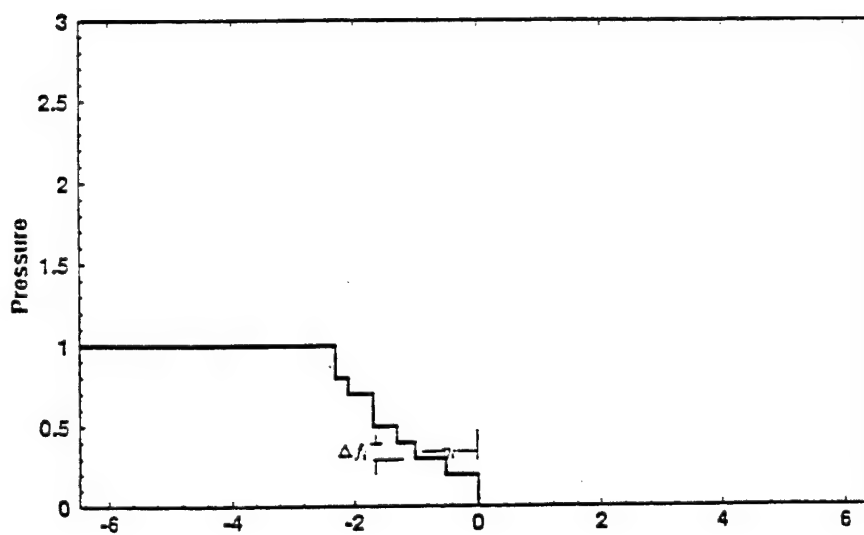


Figure 2b. Staircase approximation of Figure 2a.

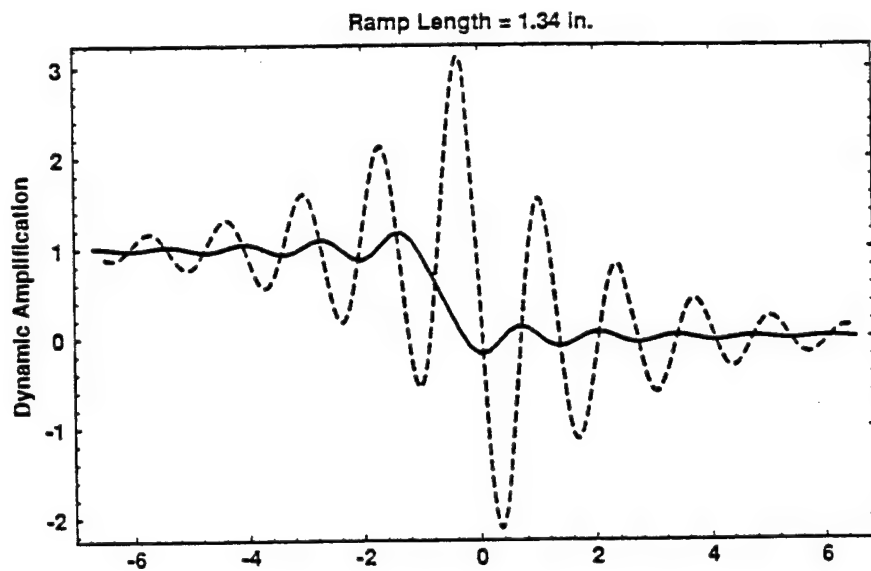


Figure 3a. Comparison of response to step (dashed) and response to ramp (solid).

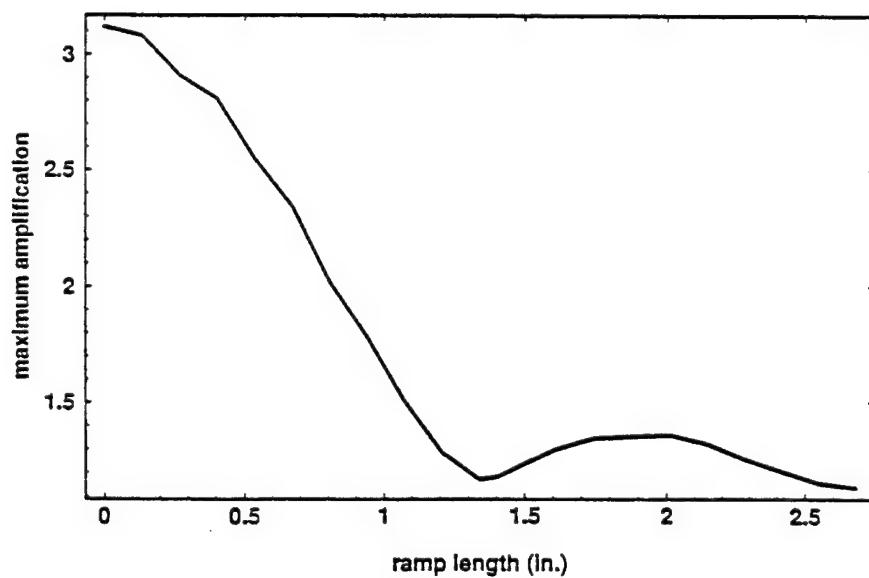


Figure 4. Effect of ramp length.

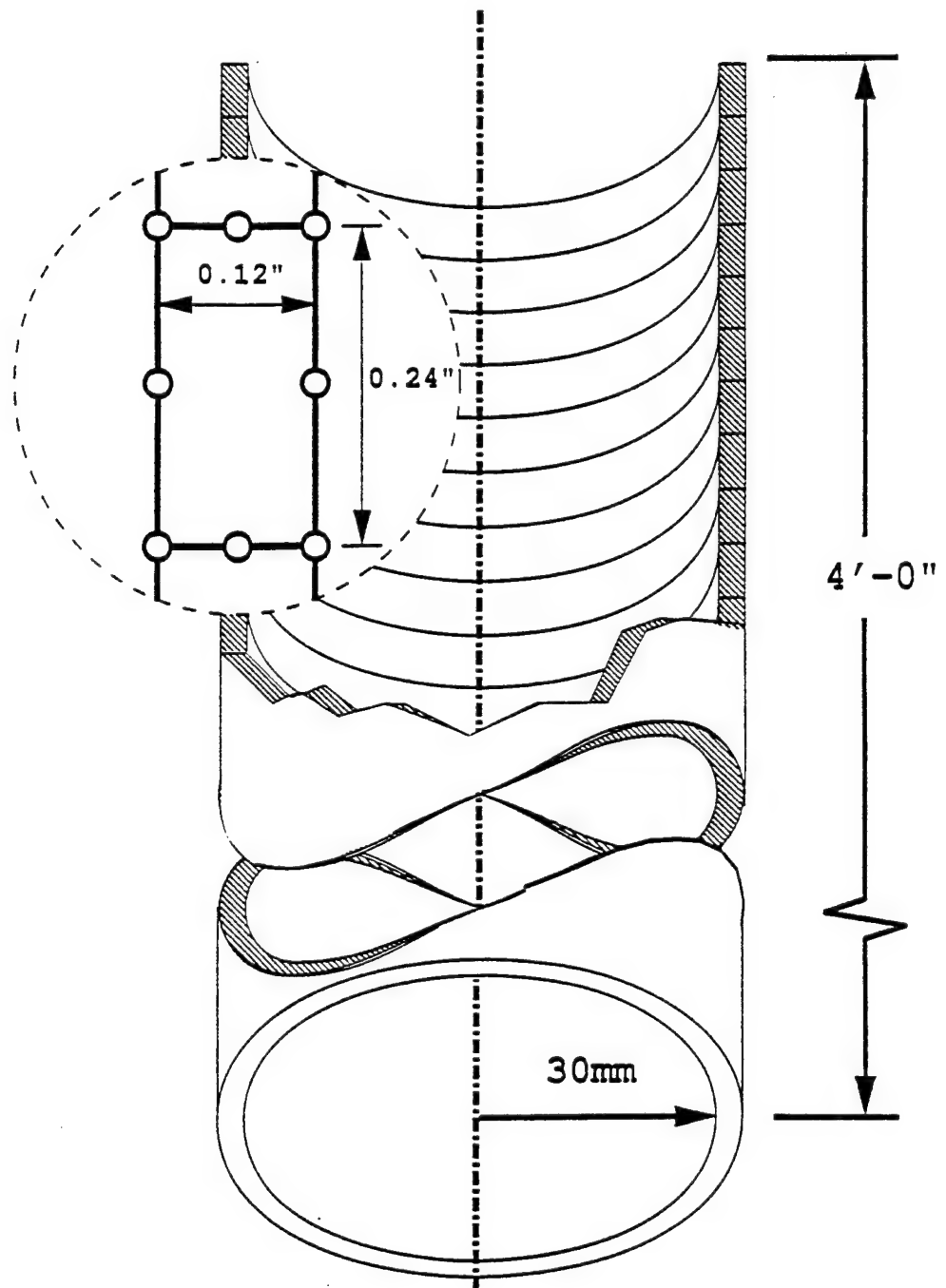
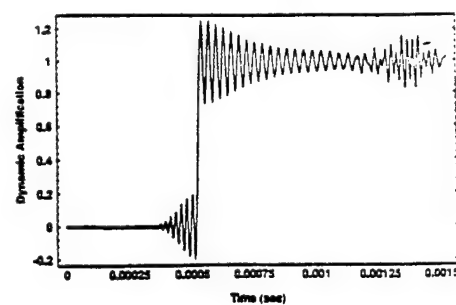
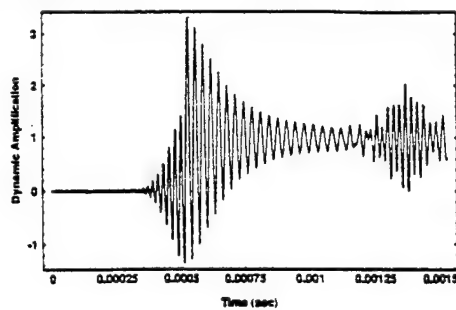
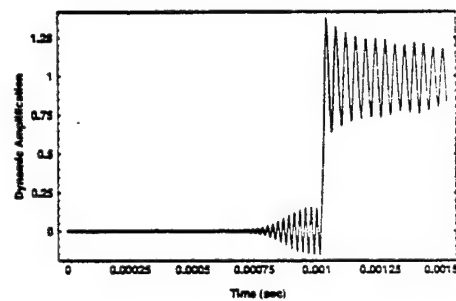
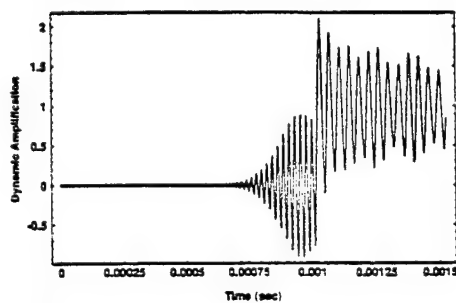


Figure 5. Finite element model.

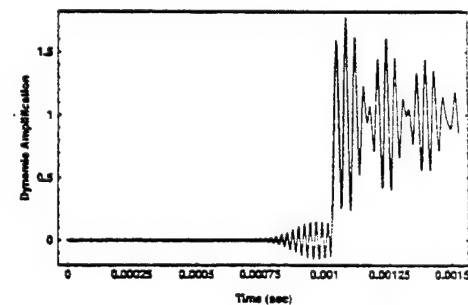
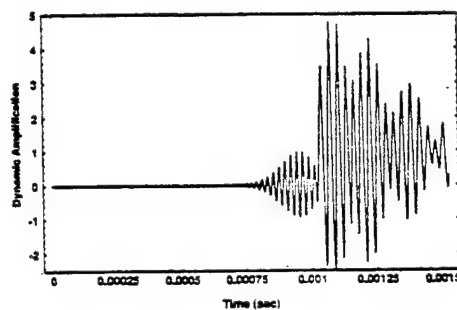
a) 24.0 in. from muzzle



b) 0.24 in. from muzzle



c) 0.12 in. from muzzle



d) at muzzle

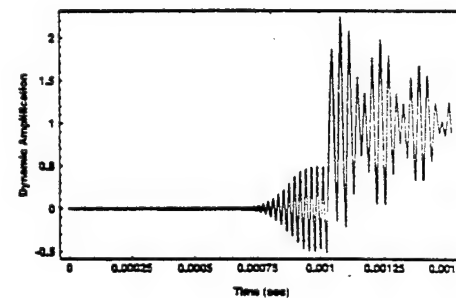
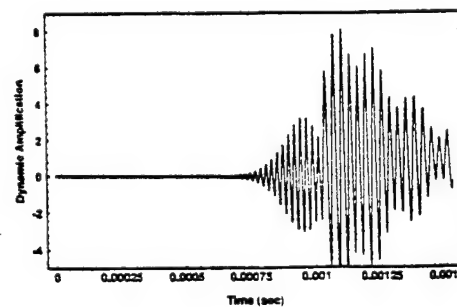


Figure 6. Response to moving step (left) and moving ramp (right).

---

TECHNICAL REPORT INTERNAL DISTRIBUTION LIST

	<u>NO. OF COPIES</u>
CHIEF, DEVELOPMENT ENGINEERING DIVISION	
ATTN: AMSTA-AR-CCB-DA	1
-DB	1
-DC	1
-DD	1
-DE	1
 CHIEF, ENGINEERING DIVISION	
ATTN: AMSTA-AR-CCB-E	1
-EA	1
-EB	1
-EC	1
 CHIEF, TECHNOLOGY DIVISION	
ATTN: AMSTA-AR-CCB-T	2
-TA	1
-TB	1
-TC	1
 TECHNICAL LIBRARY	
ATTN: AMSTA-AR-CCB-O	5
 TECHNICAL PUBLICATIONS & EDITING SECTION	
ATTN: AMSTA-AR-CCB-O	3
 OPERATIONS DIRECTORATE	
ATTN: SIOWV-ODP-P	1
 DIRECTOR, PROCUREMENT & CONTRACTING DIRECTORATE	
ATTN: SIOWV-PP	1
 DIRECTOR, PRODUCT ASSURANCE & TEST DIRECTORATE	
ATTN: SIOWV-QA	1

NOTE: PLEASE NOTIFY DIRECTOR, BENÉT LABORATORIES, ATTN: AMSTA-AR-CCB-O OF ADDRESS CHANGES.

---

---

TECHNICAL REPORT EXTERNAL DISTRIBUTION LIST

	<u>NO. OF COPIES</u>		<u>NO. OF COPIES</u>
ASST SEC OF THE ARMY RESEARCH AND DEVELOPMENT ATTN: DEPT FOR SCI AND TECH THE PENTAGON WASHINGTON, D.C. 20310-0103	1	COMMANDER ROCK ISLAND ARSENAL ATTN: SMCRI-SEM ROCK ISLAND, IL 61299-5001	1
DEFENSE TECHNICAL INFO CENTER ATTN: DTIC-OCF (ACQUISITIONS) 8725 JOHN J. KINGMAN ROAD STE 0944 FT. BELVOIR, VA 22060-6218	2	MIAC/CINDAS PURDUE UNIVERSITY 2595 YEAGER ROAD WEST LAFAYETTE, IN 47906-1398	1
COMMANDER U.S. ARMY ARDEC ATTN: AMSTA-AR-AEE, BLDG. 3022	1	COMMANDER U.S. ARMY TANK-AUTMV R&D COMMAND ATTN: AMSTA-DDL (TECH LIBRARY) WARREN, MI 48397-5000	1
AMSTA-AR-AES, BLDG. 321	1	COMMANDER U.S. MILITARY ACADEMY ATTN: DEPARTMENT OF MECHANICS WEST POINT, NY 10966-1792	1
AMSTA-AR-AET-O, BLDG. 183	1		
AMSTA-AR-FSA, BLDG. 354	1		
AMSTA-AR-FSM-E	1		
AMSTA-AR-FSS-D, BLDG. 94	1		
AMSTA-AR-IMC, BLDG. 59	2	U.S. ARMY MISSILE COMMAND REDSTONE SCIENTIFIC INFO CENTER ATTN: AMSMI-RD-CS-R/DOCUMENTS BLDG. 4484 REDSTONE ARSENAL, AL 35898-5241	2
PICATINNY ARSENAL, NJ 07806-5000			
DIRECTOR U.S. ARMY RESEARCH LABORATORY ATTN: AMSRL-DD-T, BLDG. 305 ABERDEEN PROVING GROUND, MD 21005-5066	1	COMMANDER U.S. ARMY FOREIGN SCI & TECH CENTER ATTN: DRXST-SD 220 7TH STREET, N.E. CHARLOTTESVILLE, VA 22901	1
DIRECTOR U.S. ARMY RESEARCH LABORATORY ATTN: AMSRL-WT-PD (DR. B. BURNS) ABERDEEN PROVING GROUND, MD 21005-5066	1	COMMANDER U.S. ARMY LABCOM, ISA ATTN: SLCIS-IM-TL 2800 POWER MILL ROAD ADELPHI, MD 20783-1145	1
DIRECTOR U.S. MATERIEL SYSTEMS ANALYSIS ACTV ATTN: AMXSY-MP ABERDEEN PROVING GROUND, MD 21005-5071	1		

---

NOTE: PLEASE NOTIFY COMMANDER, ARMAMENT RESEARCH, DEVELOPMENT, AND ENGINEERING CENTER,  
BENÉT LABORATORIES, CCAC, U.S. ARMY TANK-AUTOMOTIVE AND ARMAMENTS COMMAND,  
AMSTA-AR-CCB-O, WATERVLIET, NY 12189-4050 OF ADDRESS CHANGES.

---

TECHNICAL REPORT EXTERNAL DISTRIBUTION LIST (CONT'D)

	<u>NO. OF COPIES</u>		<u>NO. OF COPIES</u>
COMMANDER U.S. ARMY RESEARCH OFFICE ATTN: CHIEF, IPO P.O. BOX 12211 RESEARCH TRIANGLE PARK, NC 27709-2211	1	WRIGHT LABORATORY ARMAMENT DIRECTORATE ATTN: WL/MNM EGLIN AFB, FL 32542-6810	1
DIRECTOR U.S. NAVAL RESEARCH LABORATORY ATTN: MATERIALS SCI & TECH DIV WASHINGTON, D.C. 20375	1	WRIGHT LABORATORY ARMAMENT DIRECTORATE ATTN: WL/MNMF EGLIN AFB, FL 32542-6810	1

NOTE: PLEASE NOTIFY COMMANDER, ARMAMENT RESEARCH, DEVELOPMENT, AND ENGINEERING CENTER,  
BENÉT LABORATORIES, CCAC, U.S. ARMY TANK-AUTOMOTIVE AND ARMAMENTS COMMAND,  
AMSTA-AR-CCB-O, WATERVLIET, NY 12189-4050 OF ADDRESS CHANGES.

---

DEPARTMENT OF THE ARMY  
ARMAMENT RESEARCH, DEVELOPMENT AND ENGINEERING CENTER  
BENÉT LABORATORIES, CCAC  
US ARMY TANK-AUTOMOTIVE AND ARMAMENTS COMMAND  
WATERVLIET, N.Y. 12189-4050

OFFICIAL BUSINESS  
AMSTA-AR-CCB-O  
TECHNICAL LIBRARY

DEPARTMENT OF THE ARMY  
OFFICIAL BUSINESS

Defense Technical Information Center  
Attn: DTIC-OCF (Acquisitions)  
8725 John J. Kingman Road  
Ste 0944  
Ft. Belvoir, VA 22060-6218

DA Label 18-1, Sep 83  
Edition of Oct 74 will be used until exhausted.

BOOK RATE

BOOK RATE

BOOK RATE

